International Journal of Modern Engineering Research (IJMER)

International Journal of Modern Engineering Research (IJMER)

Editorial Board

To make a biogas energy from different sources & creating awareness between human begins – case study

Neeraj kumar[1], Gourav Dureja[2], Sandeep Kamboj[3]

Assistant Professor, Department of ME1
Lecturer, Department of CE2
Assistant Professor, Department of ME3
Maharishi Markandeshwar Group of Institutions (Ramba) Karnal, India

ABSTRACT: *Biogas from biomass appears as an alternative source of energy, which is potentially enriched in biomass resources. This article gives an overview of present and future use of biomass as an industrial feedstock for production of fuels, chemicals and other materials. However, to be truly competitive in an open market situation, higher value products are required. Results suggest that biogas technology must be encouraged, promoted, invested, implemented, and demonstrated, but especially in remote rural areas. Different types of wastes are used for production of biogas .these wastes are found very easy and an every palace. This article helps to make biogas form different wastes. From this study, it can be concluded that this method not only contributed to renewable biogas production but also improved the effluent quality.*
Keywords: Biogas, biomass, waste, biogas plant, methane, alternate source.

I. Introduction

Achieving solutions to possible shortage in fossil fuels and environmental problems that the world is facing today require long-term potential actions for sustainable development. In this regard, renewable energy resources appear to be one of the most efficient and effective solutions[1].A naturally occurring gas formed as a by-product of the breakdown of organic waste materials in a low-oxygen (e.g., anaerobic) environment. Biogas is composed primarily of methane (typically 55% – 70% by volume) and carbon dioxide (typically 30% – 45%). Biogas may also include smaller amounts of hydrogen sulfide (typically 50 – 2000 parts per million [ppm]), water vapor (saturated), oxygen, and various trace hydrocarbons. Due to its lower methane content (and therefore lower heating value) compared to natural gas, biogas use is generally limited to engine-generator sets and boilers.[2]. one type of biogas is produced by potential advantages include: The replacement of an anaerobic digestion or fermentation of biodegradable inefficient (but traditional) fuel with a more efficient and materials such as biomass, manure or sewage, municipal flexible one, the recoupment of the fertilizer value of the waste, green waste and energy crops [3].

Biogas technology is based on the phenomenon that in a number of countries when organic matter containing cellulose is fermented in After treatment biogas approximate to pure methane the absence of air (aerobically), combustible gases but with a calorific value of about 40 MJ/m . Biogas is an majorly (methane) is formed [4]. Producing and utilizing renewable energy – both in a global and a national context– is necessitated by the synergistic effect of climate change and the long term, continuous price rise of fossil fuels.[5]. there are several problems comes to run a biogas plant. in rural area a abundant amount of bio waste are discarded into river and open area which is very harmful to our heath. because it produced many dangeroures gasas. Improper handling and storage of methane is a very dangrour for human beings.[6].

II. Biomass- based Energy Production   (Biogas)

Energy is a complex system; hence, energy-production and energy-conversion require systemic thinking, for which firstly a change of aspect is necessary[6].   Biogas is generated by micro-organisms in the absence of air by a so called anaerobic metabolism. Industrial biogas is produced at sewage treatment plants (sludge fermentation stage), landfills, sites with industrial processing industry and at digestion plants for agricultural organic waste, both mesophilic (35 °C) and thermophilic (55 °C). Biogas from anaerobic digestion and landfills consists primarily of CH_4 and CO_2.[7]. In this paper biomass like different type of wastes include convert into biogas by anaerobic digestion process.
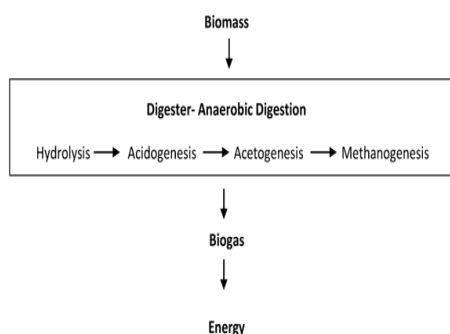
Figure No-1,Biogas coversion process

Waste includes all items that people no longer have any use for, which they either intend to get rid of or have already discarded. Additionally, wastes are such items which people are require to discard, for example by lay because of their hazardous properties. Many items can be considered as waste e.g., household rubbish, sewage sludge, wastes from manufacturing activities, packaging items, discarded cars, old televisions, garden waste, old paint containers etc. Thus all our daily activities can give rise to a large variety of different wastes arising from different sources.[8].

III. Biogas Resources

Biogas resources include different type of wastes in india.in this paper we discuss seven types of wastes which is shown in this figure.
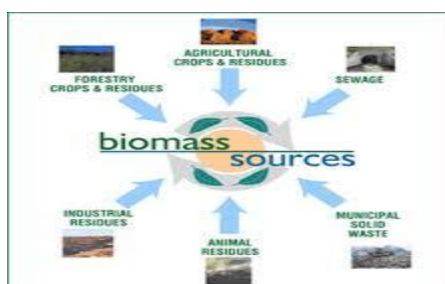
Figure No-2(Biomass sources)

3.1   Municipal solid waste
3.1.1Agricultural waste
3.I.2 Industrial waste
3.1.3Household waste
3.1.4 Hazardous waste
3.1.5Hospital waste
3.1.6 Kitchen waste

3.1.Municipal solid waste:

Municipal Solid Waste (MSW) contains organic as well as inorganic matter. the latent energy present in its organic fraction can be recovered for gainfulutilisation through adoption of suitable Waste Processing and Treatment technologies solid waste (MSW) includes Municipal wastes (household waste and similar commercial, industrial and institutional wastes) including separately collected fractions household garbage and rubbish, street sweeping, construction and demolition debris, sanitation residues, trade and non-hazardous industrial refuse and treated bio-medical solid waste. Municipal Solid Waste is defined in Ireland as household, commercial, and street cleaning wastes.[9].

Figure No-3, Munciple solid waste

3.1.1 Agricultural waste:

Agriculture waste is an organic material and can be used to produce biogas through anaerobic digestion, thus providing an alternative for Agriculture waste use and mitigating the pollution. Agriculture waste is mainly composed of three groups of polymers, namely cellulose, hemicelluloses, and lignin. Cellulose and hemicellulose are sugar rich fractions of interest for use in fermentation processes. [10]

3.1.2 Industrial waste

Anaerobic processes are largely used for the treatment of industrial wastes and waste water for more than a century and AD is today a standard technology for the treatment of variousindustrial .waste waters from food-processing, agro-industries, and pharmaceutical industries. AD is also applied to pre-treat organic loaded industrial waste waters, before final disposal. Due to recent improvements of treatment technologies, diluted industrial waste waters can also be digested.[11].

3.1.3 Household waste

The systematic development and promotion of household (Hh) biogas technology programme is over 60 years old in India. The demonstration and limited extension phase of Hh biogas plants was first initiated in India by KVIC, using their floating steel gas holder model, in 1960. However, the implementation of Hh plants got impetus in India, only after the Ministry of Non-Conventional Sources of Energy (MNES- earlier known as DNES), Govt. of India, launched a centrally sponsored scheme, known as National Project on Biogas Development (NPBD), in 1981-82.

3.1.4 Hazardous waste

Waste and waste reduction are increasingly becoming the focus of numerous national administrations and environmental agencies around the world. country must make every effort to stem the rising tide of garbage and industrial waste through a more aggressive use of waste minimization and recycling practices. international shipments of hazardous wastes are the primary focus of this document, the preamble states that the signatory parties to this convention were motivated by the idea that, "the most effective way of protecting human health and the environment from the dangers posed by [hazardous] wastes is the reduction of their generation to a minimum in terms of quantity and/or hazard potential [12].Industrial and hospital waste is considered hazardous as they may contain toxic substances. Certain types of household waste are also hazardous. Hazardous wastes could be highly toxic to humans, animals, and plants; are corrosive, highly inflammable, or explosive; and react when exposed to certain things e.g. gases. India generates around 7 million tonnes of hazardous wastes every year, most of which is concentrated in four states: Andhra Pradesh, Bihar, Uttar Pradesh, and Tamil Nadu.

3.1.5 Hospital waste

(A) Clinical Waste: this includes body fluid, drainage bags, blood collection tubes, vials, culture dishes, other types of broken/unbroken glassware that were in contact with infectious agents, gauze, bandages or any other materials that were in contact with infectious agents or blood, pathological waste including organs, body parts, tissues. These are potentially dangerous and present a high risk of infection to the general population and to the staff.

(B) Laboratory Waste: This is also high risk category waste. This includes chemicals used in the pathological laboratory, microbial cultures and clinical specimens, slide, culture dish, needle, syringes, as well as radioactive waste such as Iodine-125, iodine -131 etc.
(C) Non-clinical Waste**:** this includes wrapping paper, office paper, and plastic that has not been in contact with patient body fluid.[13].

3.1.6 Kitchen waste

Kitchen waste: This includes food waste, wash and waste water. kicthen wastes include vegetables waste, garbage, broken material which are found in homes and these are discarded into open areas. "Food waste" refers to food that is of good quality and fit for human consumption but that does not get consumed because it is discarded. Fruits, milk, paper, Fish, Food cooked but not eaten, eggs, Chicken, breasts, Mushrooms, Lemons, Fruit pies, Onions, Mixed vegetables.

Figure No-4, Kitchen waste

IV.   Biogas Production process

There are three stages which are discussed about biogas generation. and In this paper we are discussed about one by one .
4.1 Hydrolysis:
4.2 Acetogeness
4.3 Methangenesis

Anaerobic digestion is a multistep biological and chemical process that is beneficial in not only waste management but also energy creation. There are four fundamental steps of anaerobic digestion that include hydrolysis, acidogenesis, acetogenesis, and methanogenesis
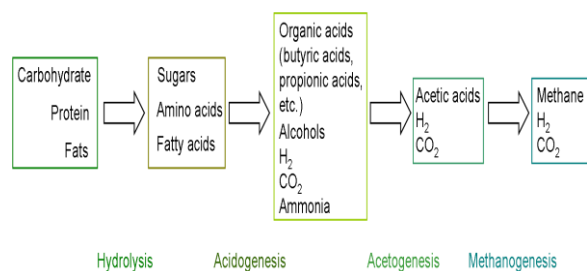
Figure No-5, biogas process

Biogas production is a three stage biochemical process comprising hydrolysis, acidogenesis/acetogenesis and methanogenesis.

$(C6H10 O5(C6H10 O5)n + nH2O \rightarrow n (C6 H12 O6)$ - Hydrolysis
$n (C6 H12 O6) \rightarrow n CH3 COOH$ -Acetogenesis/Acidogenesis
$3nCH3 COOH \rightarrow n CH4 + CO2$ – Methanogenesis

Biogas technology amongst other processes (including thermal, pyrolysis, combustion and gasification) has in recent times also been viewed as a very good source of sustainable waste treatment / management, as disposal of wastes has become a major problem especially to the third world countries[1].In a first step, known

as the hydrolysis process, carbon hydrates are broken down into simple sugars, proteins into amino acids, and fats into fatty acids. The products of the hydrolysis undergo an acidogenic process (acidogenesis) where organic acids and low alcohols are produced. The subsequent acetogenic process (acetogenesis) leads to the production of methane.The products of the acidogenic process are converted into acetic acid, carbon dioxide and hydrogen, which are the compounds required for the methanogenic process. (methanogenesis).

V. Biogas Plant
There are many types of biogas plants in India.

In this paper we study the only one type of biogas plants which is very economical. cheap and easy in construction.There are many types of plant but fixed dome type plants are very easy in construction and working.in this article we have study the fied dome plant which is very economical.

5.1 Fixed dome type biogas plant:
A fixed-dome plant comprises of a closed, domeshaped digester with an immovable, rigid gas-holder and a displacement pit, also named "compensation tank". The gas is stored in the upper part of the digester. When gas production commences, the slurry is displaced into the compensating tank. Gas pressure increases with the volume of gas stored and the height difference between the slurry levels in digester and compensation tank. If there is little gas in the gasholder, the gas pressure is low. The cost of a fixed-dome biogas plant is relatively low, and it is simple as no moving parts exist. There are also no rusting steel parts and, hence, a long life of the plant (20 years or more) can be expected. The plant is constructed underground, protecting it from physical damage and temperature changes.
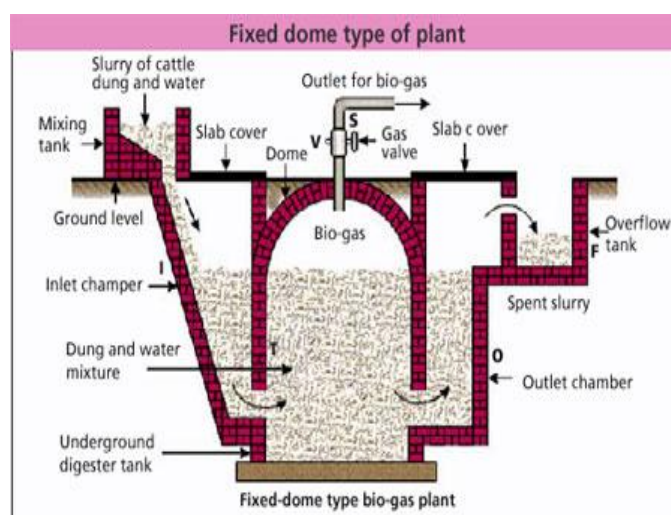
Figure No-6 , Fixed dome type biogas plant

The main parts of plants are mixing tank, overflow tank, dome type digester, inlet chamber, outlet chamber, gas valve. In this type of plant any type of waste are used like slurry of cattle dung and its mixed with water. during a retentions period a reaction takes place. And gas is produced at upper part of the tank .and this gas is used by a gas holder valve. and overflow scullery are dumped into field.

VI. Conclusion
With the help of this biogas plants we prodused a gas. And in rural area the wastes like cow dung, waste material are dumped into open area .due to this causes some dangerous gases are prodused.which are very harmful to our health. To solve this type of problems we can uses these wastes.and in a village two or three homes are make a small type of biogas plant.and biogas as a alternate sources of energy for human beings. Which is used for lighting.power gaeration , cooking purposes.the life of other conventional sources like coal,oil, fuel.are very low and we are searching a lot of energy resources.so biogas is a renewable energy resources.

REFERENCES

[1]   Ofoefule, Akuzuo U.*1, Nwankwo, Joseph I.2, Ibeto, Cynthia N.1, Biogas Production from Paper Waste and its blend with Cow dung, Pelagia Research Library,Advances in Applied Science Research, 2010, 1 (2): 1-8, ISSN: 0976-8610

[2]   Ken Krich ,Don Augenstein, JP Batmale, John Benemann ,Brad Rutledge, Biomethane from Dairy Waste: A sourcebook for the production and Use of renewable natural gas in California, page no-14/282 July 2005.

[3]   Shelef, G., H. Grynberg and S. Kimchie, 1981. High rate thermophilic aerobic digestion of agricultural wastes, Biotechnology and Bioengineering Symposium, 11: 341-342.

[4]   I.R. Ilaboya, F.F. Asekhame, 3M.O. Ezugwu, 4A.A. Erameh and 5F.E. Omofuma, Studies on Biogas Generation from Agricultural Waste; Analysis of the Effects of Alkaline on Gas Generation, World Applied Sciences Journal 9 (5): 537-545, 2010, ISSN 1818-4952.

[5]   Attila Meggyes, Valéria Nagy, Biogas and Energy Production by Utilization of Different Agricultural Wastes, Acta Polytechnica Hungarica ,Vol. 9, No. 6, 2012

[6]   E.J. DaSilva, Biogas generation: developments, problems, and tasks - an overview, Division of Scientific Research and Higher Education, Unesco, Paris, France

[7]   Patricia cekanova,natalia jasminska, Tomas brestovic,Eva schvarzba cherova, Biogas upgrading process for the production of natural gas substitute, ISSN 1848-0071 ,(24 may 2011).

[8]   Eze J. I.1,2* and Ojike O.1,2, Anaerobic production of biogas from maize wastes International Journal of the Physical Sciences Vol. 7(6), pp. 982 - 987, (2 February, 2012).

[9]   Mamdouh A. El-Messery*, Gaber AZ. Ismail*, Anwaar K. Arafa**,Evaluation of Municipal Solid WasteManagement in Egyptian Rural Areas,J Egypt Public Health Assoc Vol. 84 No. 1 & 2, (2009)

[10]   TR Sneha R. Vattamparambil, Anaerobic Microbial Hydrolysis of Agriculture Waste for Biogas Production , International Conference on Emerging Frontiers in Technology for Rural Area (EFITRA-2012)

[11]   University of Southern Denmark Esbjerg, NielsBohrsVej 9-10, DK-6700 Esbjerg, Denmark, Teodorita Al Seadi, DominikRutz, Heinz Prassl, Michael Köttner, Tobias Finsterwalder, Silke Volk, Rainer Janssen, ISBN 978-87-992962-0-: Copyright © 2008.

[12]   Christa D. Jensen, Who Generates Hazardous Wastes? Attribution of Producer and Consumer Responsibility within the US, Regional Research Institute, Department of Economics, West Virginia University, PO Box 6825, Morgantown, RESEARCH PAPER 2010-16

[13]   Nasima Akter, Medical Waste Management: A Review, Environmental Engineering Program School of Environment, Resources and Development, January, 2000

Virtualization Technology using Virtual Machines for Cloud Computing

T. Kamalakar Raju[1], A. Lavanya[2], Dr. M. Rajanikanth[2]

[1, 2] Lecturer, Dept. of Computer Science, Andhra Loyola College, Vijayawada
[3] Lecturer, Dept. of Computer Science, Govt. Degree College, Movva

Abstract: Cloud computing is the delivery of computing and storage capacity as a service to a community of end users. The name "cloud computing" comes from the use of a cloud-shaped symbol as an abstraction for the complex infrastructure it contains in system diagrams. Cloud computing entrusts services with a user's software, data and computation over a network.   End users access cloud-based applications through a web browser or mobile application or a light-weight desktop while the business software and user's data are stored on servers at a remote location. Proponents claim that cloud computing environment allows enterprises to get their applications up and running faster, with improved manageability and less maintenance, and enables IT industry to more rapidly adjust resources to meet fluctuating and unpredictable business demand. In this paper, we present a system that uses virtualization technology to allocate the data center resources dynamically based on the application demands and support green computing by optimizing the number of servers in use. This method multiplexes virtual to physical resources adaptively based on the changing demand. We use the concept of skewness metric to combine virtual machines with different resource characteristics appropriately so that the capacities of servers are well utilized.
Keywords: Cloud, Hot spot, Physical machine, Skewness, Virtual machine.

I. Introduction

Cloud computing emerges as a new computing technology which aims to provide customized, reliable and QoS (Quality of Service) guaranteed computing dynamic environments for end-users [1].Distributed processing, grid computing and parallel processing together emerged as cloud computing environment. The basic principle of cloud computing technology is that the user data is not stored locally but is stored in the data center of internet. The companies which provide cloud environment service could manage and maintain the operation of these data centers. The cloud users can access the stored data at any time by using the Application Programming Interface (API) provided by the cloud providers through any terminal equipment connected to the internet. Not only are the storage services provided but also both hardware and software services are available to the general public and business markets. The services provided by the service providers can be everything, from the infrastructure, platform or software resources. Each such cloud service(Figure 1) is respectively called as Infrastructure as a Service (IaaS), Platform as a Service (PaaS) or Software as a Service (SaaS) [2].
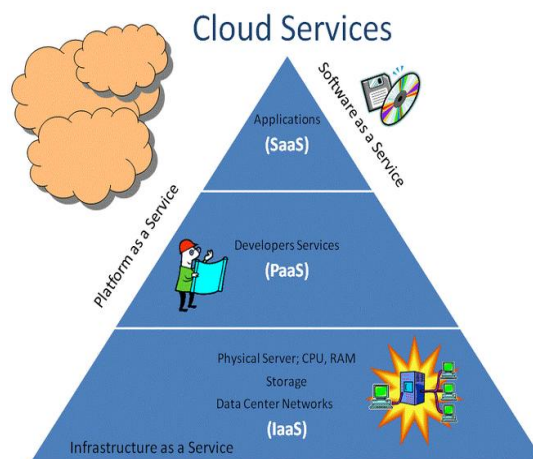

Fig. 1 Cloud Computing Services

There are numerous advantages of cloud computing technology, the most basic ones being the lower costs, re-provisioning of resources and remote accessibility. Cloud computing environment lowers cost by avoiding the capital expenditure by the company in renting the physical infrastructure from a third party provider. Due to the flexible nature of cloud computing technology, we can quickly access more resources from the cloud providers when we need to expand our business. The remote accessibility enables the cloud users to access the cloud services from anywhere at any time. To gain the maximum degree of the above mentioned benefits, the cloud services offered in terms of resources should be allocated optimally to the applications running in the cloud environment.

II. Related work

In [3], the authors proposed architecture, using the feedback control theory, for adaptive management of virtualized resources, which is based on Virtual Machine (VM). In this VM-based architecture all the hardware resources are pooled into common shared space in the cloud computing infrastructure so that hosted application can access the required resources as per there need to meet Service Level Objective (SLOs) of application. The adaptive manager use in this cloud architecture is multi-input multi-output (MIMO) resource manager, which includes three basic controllers: CPU controller, memory controller and I/O controller, its goal is regulate the multiple virtualized resources utilization to achieve SLOs of application by using the control inputs per-VM CPU, memory and I/O allocation.

In [4], the authors proposed a general two-layer architecture that uses the utility functions, adopted in the context of dynamic and autonomous resource allocation, which consists of the local agents and global arbiter. The responsibility of the local agents is to calculate utilities, for given current or forecasted workload and the range of resources, for each AE and results are transfer to global arbiter. Where, global arbiter computes near optimal configuration of the resources based on the results provided by the local agents. In [5], the authors proposed an adaptive resource allocation method for the cloud environment with preempt able tasks in which algorithms adjust the resource allocation adaptively based on the updated of the actual task executions. Adaptive list scheduling (ALS) and adaptive min-min scheduling (AMMS) algorithms are use for task scheduling process which includes static task scheduling, for static resource allocation, is generated offline. The online adaptive procedure is use for re-evaluating the remaining static resource allocation repeatedly with some predefined frequency.

The dynamic resource allocation based on the distributed multiple criteria decisions in computing cloud explain in [6]. In it, author contribution is two-fold, the first distributed architecture is adopted, in which the resource management is divided into independent tasks, each of which is performed by Autonomous Node Agents (NA) in ac cycle of three activities: (1) VMPlacement, in it suitable physical machine (PM) is found which is capable of running the given virtual machine and then assigned VM to that physical machine, (2) Monitoring, in it total resources use by hosted VM are monitored by NA, (3) In VM selection, if the local accommodation is not possible, a VM need to migrate at another PM and then process loops back to into placement. And second, using PROMETHEE method, NA carry out configuration in parallel by using multiple criteria decision analysis. This approach is potentially more feasible in large data centers than in the centralized approaches.

III. Proposed work

In this paper we develop a resource allocation method that can avoid overload in the cloud system effectively while minimizing the number of servers used. We introduce the concept of "skewness", which is used to measure the uneven utilization of a server. By minimizing the skewness, we can improve the overall utilization of the servers in the face of multi-dimensional resource constraints. We develop an effective load balancing algorithm using the Virtual Machine Monitoring to minimize or maximize different performance parameters.

A. System Overview

The architecture of the overall system is presented in Figure 2. Each physical machine (PM) runs the Xen hypervisor (VMM) which supports a privileged domain zero and one or more domain "U". Each VM in domain U encapsulates one or more applications such as the Web server, remote desktop, DNS, Map/Reduce, Mail, etc. We assume all PMs share a back- end storage. The multiplexing of the VMs to PMs is managed using the Usher framework [7]. The main logic of our cloud system is implemented as a set of plug-ins to Usher. Each node runs an Usher local node manager (LNM) on domain zero which collects the usage statistics of the resources for each VM on that node. The statistics collected at each PM are forwarded to the Usher central controller (Usher CTRL) where our virtual machine scheduler runs. The VM Scheduler is invoked periodically and then receives from the LNM the resource demand history of VMs, the capacity and the load history of the

PMs, and the current layout of VMs on PMs. The scheduler has several components, these include: The predictor predicts the future resource demands of VMs and the future load of PMs based on the past statistics. We compute the load of a physical machine by aggregating the resource usage of its VMs.
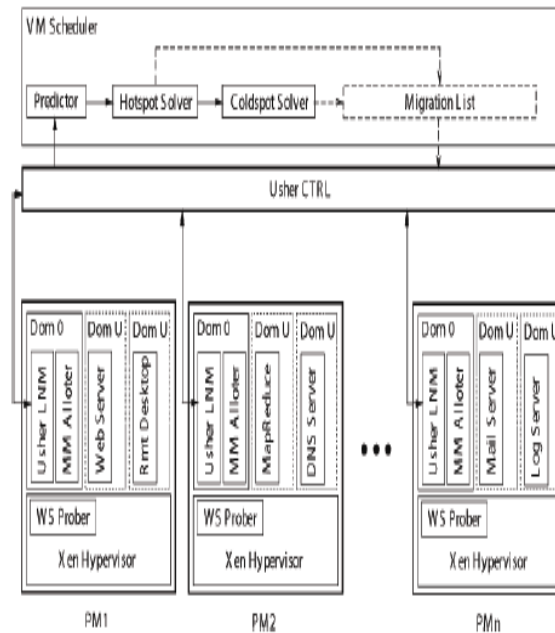

Fig. 2 System Architecture

The LNM at each node first attempts to satisfy the new demands locally by adjusting the resource allocation of virtual machines sharing the same VMM. The MM Alloter on domain zero of each node is responsible for adjusting the local memory allocation. The hot spot solver in our VM Scheduler detects if the resource utilization of any physical machine is above the hot threshold (i.e., a hot spot). The cold spot solver checks if the average utilization of an actively used PMs (APMs) is below some green computing threshold.

B. Skewness Algorithm

The skewness algorithm consists of three steps: hot spot mitigation, green computing, load balancing. Let "n" be the number of resources and "ri" be the utilization of the i-th resource. The resource skewness of a server "p" is defined as follows:

$$skewness(p) = \sqrt{\sum_{i=1}^{n} (\frac{r_i}{r} - 1)^2}$$

We use several adjustable thresholds that control tradeoff between performance and the green computing. The "hot threshold" defines the acceptable upper limit of the resource utilization. We define a server as a hot spot if the utilization of any of its cloud resources is above some hot threshold. We define the temperature of a hot spot "p" as the square sum of its resource utilization beyond the hot threshold:

$$temperature(p) = \sum_{r \varepsilon R} (r - r_t)^2$$

Where R is the set of the overloaded resources in server p and rt is the hot threshold for resource r.

The temperature of a hot spot reflects its degree of system overload. If a server is not a hot spot, then its temperature is zero. The "cold threshold" denotes the acceptable lower limit of resource utilization. A server whose utilization of all system resources is under the cold threshold is defined as a cold spot. The "green computing" threshold defines the utilization level of all active physical machines, under which the system is considered power-inefficient therefore green computing operations get involved. Finally, the "warm threshold" defines the ideal level of the resource utilization that is sufficiently high to justify having the server running but not so high as to risk becoming a hot spot in the face of temporary fluctuation of the application resource demands.

C. Hot Spot Mitigation

For each scheduling round, the skewness algorithm takes two steps, hot spot mitigation and green computing, to calculate the migration list. In hot spot mitigation, we try to solve all hot spots in the descending order of the temperature. For each hot spot, we try to migrate away the virtual machine that can reduce the server's temperature the most. In those servers that can accommodate the virtual machine without becoming a hot spot, we choose a server with most skewness reduction by accepting this virtual machine as the migration destination. This does not necessarily eliminate the hot spot, but at least reduces the temperature. Hot spot mitigation step is finished after all hot spot are processed successfully. If the overall resource utilization of the active servers is lower than the green computing threshold, a green computing step is invoked.

D. Green Computing

In the green computing step, we try to solve cold spots in ascending order of the memory utilization, which representing the efforts taken to solve the cold spot. To resolve a cold spot, all of its virtual machines need to be migrated away. The destination of a virtual machine is decided in a way similar to that in the hot spot mitigation, but its resource utilization should be below the warm threshold after accepting the virtual machine. We also restrict the number of cold spots that can be eliminated in each run of the skewness algorithm to be no more than a certain percentage, for example 6%, of the active servers in the system. These arrangements are to avoid over consolidation that may incur hot spots later.

E. Load Balancing

The Load balancing algorithm (Figure 3) is divided into three parts: The first part is the initialization phase. In initialization phase, the expected response time of each virtual machine is to be found. In the second part, efficient virtual machine is found and in the last part, the ID of efficient virtual machine is returned.

Load Balancing Algorithm:

Step 1: For each virtual machine, find expected response time. The expected response time is found with the help of resource information program.
Step 2: When a request to allocate a new virtual machine from the Data Center Controller arrives, now find the most efficient VM (efficient VM having least loaded, minimum expected response time) for allocation.
Step 3: Return the identifier of the efficient virtual machine to the Datacenter Controller.
Step 4: Datacenter Controller identifies and notifies the new allocation
Step 5: Now update the allocation table increasing the allocations count for that virtual machine.
Step 6: When the virtual machine finishes processing the request, and then the Data Center Controller receives the Response. Data center controller notifies the efficient way for the VM de-allocation.
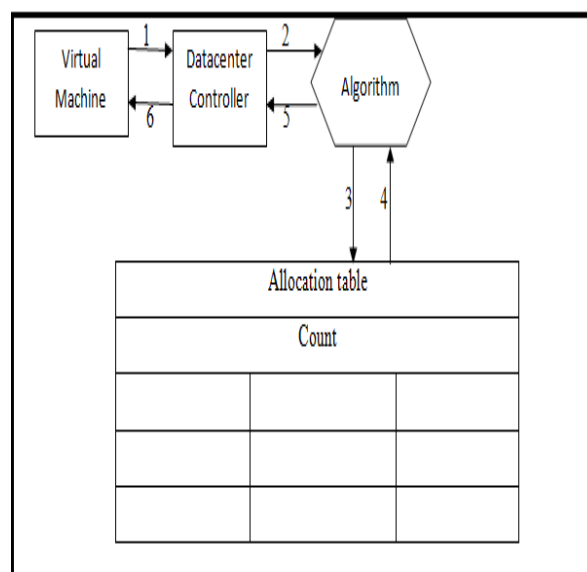

Fig. 3 Load Balancing

IV. Conclusion

Cloud computing technology emerges as a new computing paradigm which aims to provide customized, reliable and QoS (Quality of Service) guaranteed computing dynamic environments for the end

users. In this paper, we develop a resource allocation system that can avoid overload in the system effectively while minimizing the number of servers used. The capacity of a physical machine should be sufficient to satisfy the resource needs of all virtual machines running on it. Otherwise, the physical machine is overloaded and can lead to degraded performance of its virtual machines. We introduce the concept of "skewness" to measure the uneven utilization of the server. By minimizing the skewness, we can improve the overall utilization of the servers in the face of multi-dimensional resource constraints. The concept of the green computing is the number of physical machines used should be minimized as long as they can still satisfy the needs of all virtual machines. Idle physical machines can be turned off to save energy.

REFERENCES

[1] Lizhewang,JieTao,Kunze M.,Castellanos,A.C,Kramer,D.,Karl,w,"High Performance Computing and Communications",IEEE International Conference HPCC,2008,pp.825-830.

[2] ZhixiongChen,JongP.Yoon,"International Conference on P2P, Parallel,Grid,Cloud and Internet Computing",2010 IEEE:pp 250-257.

[3] "Adaptive Management of Virtualized Resources in Cloud Computing Using Feedback Control," in First International Conference on Information Science and Engineering, April 2010, pp. 99-102.

[4] W. E. Walsh, G. Tesauro, J. O. Kephart, and R. Das, "Utility Functions in Autonomic Systems," in ICAC '04: Proceedings of the First International Conference on Autonomic Computing. IEEE Computer Society, pp. 70–77, 2004.

[5] Jiayin Li, Meikang Qiu, Jian-Wei Niu, Yu Chen, Zhong Ming, "Adaptive Resource Allocation for Preempt able Jobs in Cloud Systems," in 10th International Conference on Intelligent System Design and Application, Jan. 2011, pp. 31-36.

[6] Yazir Y.O., Matthews C., Farahbod R., Neville S., Guitouni A., Ganti S., Coady Y., "Dynamic resource allocation based on distributed multiple criteria decisions in computing cloud," in 3rd International Conference on Cloud Computing, Aug. 2010, pp. 91-98.

[7] M. McNett, D. Gupta, A. Vahdat, and G. M. Voelker, "Usher: An extensible framework for managing clusters of virtual machines," in Proc. of the Large Installation System Administration Conference (LISA'07), Nov. 2007.

Finite Element Analysis of Single Point Cutting Tool

S. H. Rathod[1], Mohd. Razik[2]

1Pursuing M.E. Mechanical Engineering, Department, Babasaheb Naik college of Engineering, pusad, India
2Assistant Professor, Mechanical Engineering, Department, Babasaheb Naik college of Engineering, pusad, India

Abstract: In this project, temperature at tool-tip interface is determined, generated in high-speed machining operations. Specifically, three different analyses are comparing to an experimental measurement of temperature in a machining process at slow speed, medium speed and at high speed. In addition, three analyses are done of a High Speed Steel and of a Carbide Tip Tool machining process at three different cutting speeds, in order to compare to experimental results produced as part of this study. An investigation of heat generation in cutting tool is performed by varying cutting parameters at the suitable cutting tool geometry. The experimental results reveal that the main factors responsible for increasing cutting temperature are cutting speed (v), feed rate (f), and depth of cut (d), respectively. It is also determined that change in cutting speed and depth of cut has the maximum effect on increasing cutting temperature. Various researches have been undertaken in measuring the temperatures generated during cutting operations. Investigators made attempt to measure these cutting temperatures with various techniques during machining.
In this project, "Fluke 62 max IR thermometer" (Range -40 ^0C to 650 ^0C) is used for measuring temperature at tool-tip interface. Single point cutting tool has been solid modeled by using CAD Modeler Pro/E and FEA carried out by using ANSYS Workbench 14.5. Experimental work is done at "Khushi Engineering", Nagpur.
By varying various parameters the effect of those on temperature are compared with the experimental results and FEA results. After comparison nearly 4% variation is found in between the results.
Keywords: Single Point Cutting Tool (HSS) tool and Carbide tip tool (P - 30), Computer Aided Design (CAD), Centre lathe, Fluke 62 max IR thermometer (Range -40 0C to 650 0C), Finite Element Analysis, Solid Modeling.

I. Introduction

Machining, the most widespread process for shaping metal, has become a very significant aspect of modern society and industry. The importance of the machining process is evident by the observation that nearly every device used by humanity in day-to-day life has at least one machined part or surface. From a materials viewpoint, high speed machining is a relative term, since different materials should be machined with different cutting speeds to insure acceptable tool life. Because of this difference and the fact that cutting speed determines whether a material will form continuous or segmented chips, one way to define high-speed machining is to relate it to the chip formation mechanism. Machining is a common fabrication technique where material removed from a part using a tool with a small, hard tip. Usually the material being cut is a metal, such as aluminum or steel. In order to fabricate a part quickly, a high cutting speed desired. These higher speeds, however, lead to a faster degradation of the tool tip, which requires that the tool tip replaced more frequently. Over the history of machining, guidelines and conventions have arisen based on empirical information of tradeoffs between cutting speed and tool replacement time. Machining is a term covering a large collection of manufacturing processes designed to remove material from a work piece.

II. Literature Review

The purpose of this chapter is to provide a review of past research efforts related to single-point cutting tool and finite element analysis. A review of other relevant research studies is also provided. The review is done to offer insight to how past research efforts have laid the groundwork for subsequent studies, including the present research effort. The review is detailed so that the present effort can be properly tailored to add to the present body of literature as well as to justify the scope and direction of the present effort.

Lower and Shaw et al.[1], developed analytical prediction model for the measurement of cutting temperature during machining. They concluded that the cutting temperature is the function of cutting speed and feed rate.

$\theta t = V^{0.5} \times t^{0.3}$

Where,

θt = Average cutting temperature

V = cutting speed

t = un-deformed chip- thickness or feed rate.

Stephenson [2], suggested that the temperature distribution in the tool might be obtained by using information about the changes in the hardness and microstructure of the steel tool. It is necessary to calibrate the hardness of the tool against the temperature and time of heating and samples of structural changes at corresponding temperatures. These methods permit measurement of temperatures to an accuracy of $\pm$ 25 ^{0}C within the heat-affected region.

Miller et al [3], developed Experimental techniques using modern, digital infrared imaging and successfully applied them during this study to gather cutting tool temperature distributions from orthogonal machining operations.

Abhang L.B. et al. [4], worked to measure the tool-chip interface temperature experimentally during turning of EN-31 steel alloy with tungsten carbide inserts using a tool-work thermocouple technique. Average chip-tool interface temperatures have been experimentally studied using the tool work thermocouple technique. Based on the parametric study. the developed empirical relation agrees well in velocity with the Shaw's non-dimensional model. It has been observed that increasing cutting speed, feed rate and depth of cut lead to an increase in cutting temperature.

Federico M. Aneriro et al. [5], Investigated the influence of cutting parameters (cutting speed, feed rate and depth of cut) on tool temperature, tool wear, cutting forces and surface roughness when machining hardened steel with multilayer coated carbide tools. A standard K-type of thermocouple inserted near the rake face of the tool was used to measure the interface temperatures. They concluded that the temperature near the rake face increases significantly when the depth of cut changes from 0.2 to 0.4 mm. The increase in contact length between chip and rake face could be responsible, since it grows, together with uncut chip cross-section.

Sullivan et al. [6], measured the machined surface temperatures with two thermocouples inserted into the work piece when machining aluminum 6082-T6. The results indicated that an increase in cutting speed resulted in a decrease in cutting forces and machined surface temperatures. This reduction in temperature was attributed to the higher metal removal rate that resulted in more heat being carried away by the chip.

S.K. Chaudhary et al. [7], Predicted cutting zone temperatures by natural tool work thermocouple technique, when machining EN 24 steel work piece and HSS with 10% cobalt as the cutting tool. The results indicated that an increase in cutting speed and feed rate resulted in an increase in tool wear and cutting zone temperature increases with the increase in the cutting speed. While in the whole range of feed the temperature increases with increase in feed rate.

Huda et al [8], developed a technique for measuring temperature at the interface between a cutting tool and a chip using two-color pyrometer with fused fiber coupler for the temperature measurement of the tool-chip interface in dry and wet turning.

H.Ay and Yang [9], used a technique with K thermocouple to analyze temperature variations in carbide inserts in cutting various materials such as copper, cast iron aluminum 6061 and AISI 1045 steel. They observed oscillations in temperature near the cutting edge, which were more marked for ductile materials and less in the hard machining materials. These observations were attributed to the chip formation and its contact with the work material.

Kashiway and Elbestawi [10], investigated the effect of cutting temperature on the integrity of machined surface. It has been shown that cutting temperature has a major effect on the integrity on the machined surface. The undesirable surface tensile residual stresses were attributed to the temperature generated during machining. Therefore, controlling the generated tensile residual stresses relies on the understanding of the effect of different process parameters on the cutting temperature.

B. Findes, et al [11], studied the influence of cutting speed, feed rate and depth of cut on cutting pressures, cutting force and on cutting temperature, when machining AISI H11 steel treated to 50 HRC work piece material with mixed ceramic tool. The results show that depth of cut has great influence on the radial cutting pressure and on cutting force. The cutting pressure and cutting force increase with an increase in depth of cut and feed rate. It was found that increase in cutting speed increases cutting zone temperature rapidly

W. Grzesik [12], His work related to create a FEM simulation model in order to obtain numerical solutions of the cutting forces, specific cutting energy and adequate temperatures occurring at different points through the chip/tool contact region and the coating/substrate boundary for a range of coated tool materials and defined cutting conditions. Results showing how the tool chip interfacial friction influences the temperature distribution fields as the effect of using coated tools are the main. A good agreement was achieved, especially for uncoated and three-layer coated tools, between predicted and experimental values of cutting temperatures.

W. Grzesik, M. Bartoszuk et al. [13], the aim of this study was to create a FEM simulation model in order to obtain numerical solutions of the cutting forces, specific cutting energy and adequate temperatures occurring at different points through the chip tool contact region and the coating/substrate boundary for a range of coated tool materials and defined cutting conditions.

III.   Objective of Present Work

3.1 Project objective
The objective of the project is;
➢ To detect tool tip temperature by using "IR Thermometer" at various machining parameters
➢ Modeling by using PRO/E
➢ Finite Element Analysis by ANSYS 14.5
➢ Comparison of Experimental data with FEA data for the tool.

IV.   Project Methodology

Since there are a large number of variables controlling the process, some Experimental models are required to represent the process. In order to achieve this, FEA analysis of the experimental results will have to be processed using the analysis (ANSYS). ANSYS is a computational technique that enables the estimation of the relative contributions of each of the control factors to the overall measured response. In the present work, only the significant parameters are used to develop relation between temperature and various parameters like speed, feed and depth of cut. These models are of great use during the optimization of the process variables.

4.1 Experimental results for HSS Tool
Table 4.1 : Various Results obtained experimentally Using HSS Tool

Exp. No.	Speed (v) (RPM)	Depth of cut (d) (mm)	Experimental Temperature (T in ^{0}C)
1.		0.5	143
2.		0.7	149
3.	540	1.0	156
4.		1.3	162
5.		1.5	165
6.		0.5	150
7.		0.7	154
8.	750	1.0	163
9.		1.3	169
10.		1.5	175
11.		0.5	166
12.		0.7	171
13.	950	1.0	180
14.		1.3	189
15.		1.5	200

4.2 Experimental results for Carbide Tool
Table 4.2 : Various Results obtained experimentally Using Carbide Tool

Exp.No.	Velocity (v) (RPM)	Depth of cut (d) (mm)	Experimental Temperature (T in ^{0}C)
1.		0.5	148
2.		0.7	152
3.	540	1.0	163
4.		1.3	170
5.		1.5	172
6.		0.5	155
7.		0.7	164
8.	750	1.0	168
9.		1.3	176
10.		1.5	181
11.		0.5	168
12.		0.7	176
13.	950	1.0	186
14.		1.3	197
15.		1.5	205

Table 4.3 : Heat Flux for HSS and Carbide

Sr. No.	Speed RPM	Area	Heat Flux For HSS	Heat Flux For Carbide
1		75	1823.066	1898.4
2		73.75	1945.89	1991.8
3	540	71.87	2106.85	2216.9
4		70	2260	2389.1
5		68.75	2350.4	2465.4
6		75	1928.53	2003.8
7		73.75	2022.5	2175.7
8	750	71.87	2216.9	2292.5
9		70	2373	2486
10		68.75	2514.7	2613.3
11		75	2169.6	2199.7
12		73.75	2282.9	2359.5
13	950	71.87	2484.2	2578.5
14		70	2695.8	2825
15		68.75	2925.6	3007.8

V. Finite Element Analysis of Tool (Thermal)

5.1 Transient Thermal analysis of tool

5.1.1 Finite Element Analysis of HSS tool at

Medium speed (V- 750 RPM):
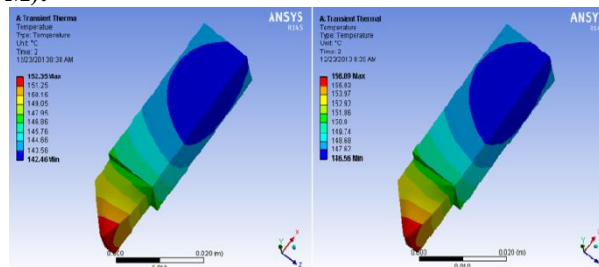
Fig. 5.1: HSS tool at Depth of cut 0.5 mm Fig.5.2: HSS tool at Depth of cut 0.7 mm
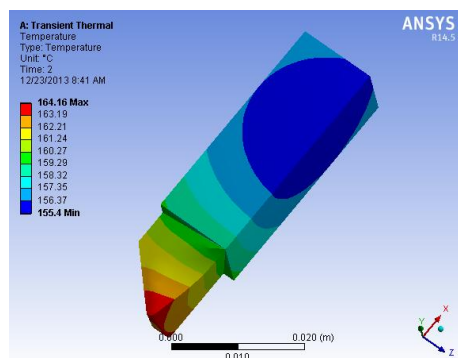
Fig. 5.3: HSS tool at Depth of cut 1.0 mm
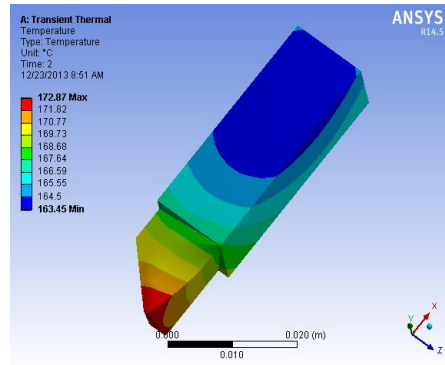
Fig. 5.4 : HSS tool at Depth of cut 1.3 mm
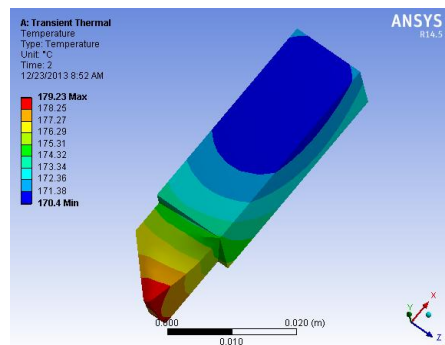
Fig. 5.5 : HSS tool at Depth of cut 1.5 mm

Speed (750) RPM	DOC	0.5	0.7	1.0	1.3	1.5
	Max^m Temp.	152.35	156.09	164.16	172.87	179.23

5.1.2 Finite Element Analysis of Carbide tool at High speed (V- 750 RPM):

Fig. 5.6 : Carbide tool at Depth of cut 0.5 mm
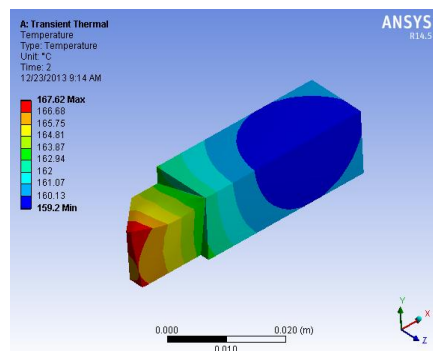
Fig. 5.7 Carbide tool at Depth of cut 0.7 mm
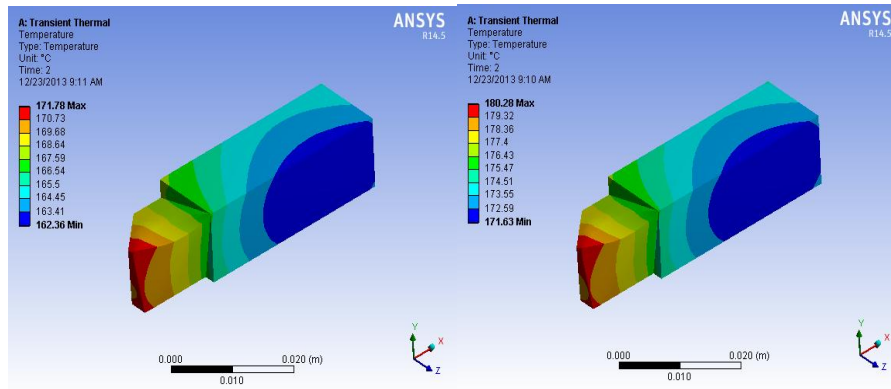
Fig. 5.8 : Carbide tool at Depth of cut 1.0 mm
Fig. 5.9 Carbide tool at Depth of cut 1.3 mm
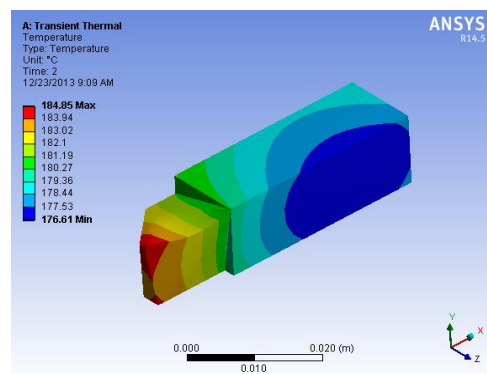
Fig. 5.10: Carbide tool at Depth of cut 1.5 mm

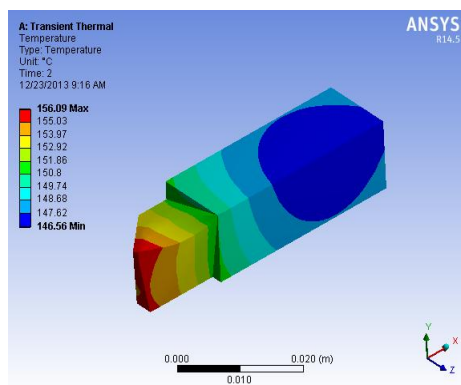| Speed	DOC	0.5	0.7	1.0	1.3	1.5
(750)	Max^m	156.	167.	171.	180.	184.
RPM	Temp.	09	62	78	28	85

VI.   Results and Discussion

Comparative results for HSS

Table 8.1 : Comparative Results obtained for HSS Tool

Exp. No.	Speed (v) (RPM)	Depth of cut (d) (mm)	Experimental Temperature (T in ^{0}C)	FEA Temperature (T in ^{0}C)	% Difference
1.		0.5	143	146.41	2.33
2.		0.7	149	150.15	2.10
3.	540	1.0	156	157.64	1.04
4.		1.3	162	165.03	1.84
5.		1.5	165	166.99	1.19
6.		0.5	150	152.03	1.335
7.		0.7	154	158.57	2.88
8.	750	1.0	163	166.06	1.84
9.		1.3	169	171.67	1.55
10.		1.5	175	179.99	2.77
11.		0.5	166	170.73	2.77
12.		0.7	171	174.94	2.55
13.	950	1.0	180	182.89	1.58
14.		1.3	189	192.25	1.69
15.		1.5	200	201.6	0.79

➢ **Effect of cutting speed for HSS tool**

As the cutting speed increase, increase in temperature occurs at tool tip interface.
Cutting speed increases from 540 RPM to 750 RPM change in temperature observed experimentally 4.66 %.
While, results observed for FEA have 5.62%.

➢ **Effect of depth of cut on cutting temperature for HSS tool**

Keeping the speed constant if we increase the depth of cut, it is observed that with increase in DOC temperature at tool tip interface also increases.
For increase in DOC from 0.5 to 0.7 mm increase in temperature is 2.72% experimentally and 2.5 by FEA.

Comparative Results for Carbide

Table 8.2 : Comparative Results obtained for Carbide Tool

Exp. No.	Velocity (v) (RPM)	Depth of cut (d) (mm)	Feed (f) (mm / rev)	Expt. Temp. (T in ^{0}C)	FEA Temp. (T in ^{0}C)	% Difference
1.	540	0.5	1	148	150.54	1.68
2.		0.7	1	152	157.06	3.22
3.		1.0	1	163	166.3	1.98
4.		1.3	1	170	172.8	1.62
5.		1.5	1	172	175.93	2.23
6.		0.5	1	155	156.09	0.7
7.		0.7	1	164	167.62	2.16
8.	750	1.0	1	168	171.78	2.20
9.		1.3	1	176	180.28	2.37
10.		1.5	1	181	184.85	2.08
11.		0.5	1	168	171.78	2.20
12.		0.7	1	176	179.17	1.77
13.	950	1.0	1	186	188.43	1.28
14.		1.3	1	197	200.03	1.51
15.		1.5	1	205	207.04	0.98

➢ **Effect of cutting speed for Carbide tool**

Cutting speed increases from 540 RPM to 750 RPM change in temperature observed experimentally 4.51%.
While, results observed for FEA have 3.55%.

➢ **Effect of depth of cut on cutting temperature for Carbide tool**

For increase in DOC from 0.5 to 0.7 mm increase in temperature is 2.63% experimentally and 4.15% by FEA.

VII. Conclusion

• From the results obtained experimentally and by FEA, the difference in temperature is not more than 4%.
• Thus, finally it can be observed that we must select the cutting parameters, which are cutting speed, feed rate, and depth of cut, in such a way so as to have the optimum temperature at the tool tip because of the heat generated, so that the minimum tool wear is encountered, and thus we could have the longest tool life and better machining economy.

REFERENCES

[1] Lowen E.G. and Shaw M.C, on the analysis of cutting tool temperatures, Transactions of the ASME, 001. 76 pp-217-231, (1954).
[2] D.A. Stephenson, Tool –work thermocouple temperature measurements: theory and implementation issues, Proceedings of winter Annual meeting of ASME, Anaheim CA. pp-18-95. November (1992).
[3] Miller Mark R., Mulholland George, Anderson Charles, Journal of Manufacturing Science and Engineering, vol. 125(2003), pp. 667-673.
[4] L. B. ABHANG and M. HAMEEDULLAHD department of Mechanical Engineering, Aligarh Muslim University, Aligarh, India "Chip-Tool Interface Temperature Prediction Model for Turning Process", 2010.
[5] Federico M. Aheiro Reginalot, Coelho, Lincdnc, Brandao, Turning hardened steel using coated carbide at high cutting speeds. J.of the Braz. soc. of Mech. sci. and Engg., vol.xxx. no. 2 1109, (2008).
[6] Sullivan D.O., Cotterell M., Journal of Material Processing Technology, vol. 118(2001), pp. 301-308.

[7]   S. K. Choudhary, G. Bartarya, Role of temperature and surface finish in predicting tool wear using neural network and design of experiments. Int. J. of machine tools and manufacture,43, 747-753, (2003).

[8]   Huda Mahfudz Al, Yamada Keiji, Hosokawa Akira, Ueda Takashi, Journal of Manufacturing Science and Engineering, vol. 124(2002),pp. 200-207.

[9]   H. Ay, W. J Yang, Heat transfer and life of metal cutting tools in turning, Int, J. Heat and mass transfer, 41, 613-623, (1998).

[10]   Kishawy, H. A. Elbestawi, M. A, Effect of edge preparation and cutting speed on surface integrity of die materials in hard machining, ASME Int. Eng. Congr, Exp. Manf.sci, Techno, 269-276, (1998).

[11]   [11]   B. Fnides, M. A. Yallese, H, Aouici, Hard turning of hot work steel AISI H11: Evaluation of cutting pressure, resulting force and temperature, ISSN1392-1207, Mecanika, Nr.4 (72), 2008.

[12]   Grzesik, W, Experimental investigation of the cutting temperature when turning with coated Index able inserts .Int.J, of Machine tools and manufacture, 39 pp 355-369,(1999).

[13]   W. Grzesik, M. Bartoszuk and P. Niesłony, 13 International scientific conference, (2005).

[14]   P.C. Sharma, "A Text Book of Production Engineering", S. Chand and Company Ltd. Delhi,

[15]   Hajra Choudhary, "Workshop Technology", Tata McGraw-Hill *Publishing* Co. Ltd., New Delhi,

[16]   M GOSTIMIROVIC, P KOVAC and M SEKULIC, "An inverse heat transfer problem for optimization of the thermal process in machining", *Sadhana* Vol. 36, Part 4, pp 489–504. Indian Academy of Sciences, August 2011.

[17]   P. L. Ballani, Data book of heat transfer, Thermal Engineering, Khanna publication, 7th Reprint, 24th Edition, pp 249, 272, 2012.

[18]   Mahesh Rathore , "Heat Transfer", Tata McGraw-Hill Publishing Co. Ltd., 914, 2010.

Design and Analysis of Bolted Joint in Composite Laminated

Amit P. Wankhade[1], Kiran K. Jadhao[2]

[1]*Pursuing M.E. Mechanical Engineering, Department, Babasaheb Naik college of Engineering, pusad, India*
[2]*Associate Professor, Mechanical Engineering, Department, Babasaheb Naik college of Engineering, pusad, India*

Abstract: *In this work plate was designed for single and four bolted joint with two different materials such as mild steel and E-glass fiber. The aim of this work is to examine the distribution of tensile and crushing stress among the different bolts by changing material of plates and bolt. The bolted joints for mild steel plate and composite laminate were analyzed by using FEA. The result shows that tensile stress and crushing stress is less for composite laminate compare to mild steel .It is concluded that Weight reduction of structure is also achieved for e-glass fiber structure. The stress concentration was reduced in composite laminate bolted joints compare to mild steel so this will improve strength of structure.*

I. Introduction

Until early 1990s, the use of fiber-reinforced polymer (FRP) composites was almost limited to only aerospace and military applications. By the mid-1990s, civil engineers started to realize the advantages of such materials especially in the structural repair and rehabilitation of existing reinforced concrete bridges and buildings. In structural applications such as in aircraft, spacecraft and civil engineering structures, composite components are often fastened to other structural members by bolted joints. Since bolted joints require holes to be drilled in the structure, large stress concentration tends to develop round the hole, which can severely reduce the overall strength of the structure [4,14]. The introduction of composite materials in the automotive industry, places new demands on the materials and manufacturing processes in terms of cost, cycle time and automation. Manufacture and assembly of composite structures require knowledge of reliable joining techniques. Mechanical fastening is a common method used to join composite materials. Mechanically fastened joints commonly adopted in aerospace structures are characterized by tight tolerances on both the fasteners and on the machined holes. Joints are the potential weakest point in the structure in order to make useful structure. Consideration is given to the ways of joining the various components of the structure [10]. In structural application such as in aircraft, space craft and in civil engineering structures the components are often fasten to the structural members by bolted joints. Since bolted joint is to be required to drill hole in the structures, large stress concentration developed around the hole, which can reduce the overall strength of the structure. The usage of composite is increasing in aerospace and other engineering industries and the study of joining methods for composite materials became an important research area. The composite materials are widely used because they have high strength to weight ratio, good fatigue resistance and high damping properties. The main objective of the bolted joint is to transfer the applied load from one part of the joint structure to the other through the fastener element. However, the presence of bolt holes induces high stress concentration which has thus recognized to be a source of damage developed during fatigue loading.

The objective of this work is to determine the various types of stress induced in bolted joints by using ANSYS 14.5 and finally comparison is made between the metal plate and FRP plate with bolted joint.

II. Description of the Problem

Load sharing in mechanically fastened joint depends upon number, size and material of the bolt and stiffness of joining members. The problem associated with bolted joint is stress concentration. High stress concentration in mechanical joint reduces strength of the structure. Strength of the structure depends on strength of joint. So present work deals with analyzing various stresses induced in bolted joint made up of two different materials.

Aim and Scope of the Work

The aim of this work is to examine the distribution of tensile and crushing stress among the different bolts by changing material of plates and bolt and to increase the strength of joint by reducing the stress concentration.

2.1   What is Composite Material

A material composed of two or more constituents is called composite material. Composites consist of two or more materials or material phases that are combined to produce a material that has superior properties to those of its individual constituents. The constituents are combined at a macroscopic level and or not soluble in each other. The main difference between composite and an alloy are constituent materials which are insoluble in each other and the individual constituents retain those properties in the case of composites, whereas in alloys, constituent materials are soluble in each other and forms a new material which has different properties from their constituents.

Classification of Composites
➢   Polymer matrix composites.
➢   Metal matrix composites.
➢   Ceramic Matrix.

Material Properties

Table 5.1 : Properties of the E-Glass fiber and mild steel.

Properties	*Unit*	*E-glass fiber*	*Mild steel*
σ_t	Mpa	2050	350
σ_c	Mpa	5000	207
ρ	(kg/m^3)	2000.0	7845
υ	_	0.3	0.27
E	Gpa	72	190

➢   **Design of rectangular plate**
➢   **Design For Single Bolted Joint for E-Glassfiber material.**

Consider,
➢   Tensile Force for mild steel, σ_t = 175 MPa; (Text Book of R.S.Khurmi, Design of Bolted Joint)
➢   Tensile Force for E-Glass Fiber, σ_t = 1025 MPa;
➢   Crushing Force for Mild steel, σ_c = 207MPa
➢   Crushing Force for E-Glass fiber, σ_c =5000MP
➢   t = 4.16 mm;   l   =100mm
➢   Ultimate Tensile stress = 2050;   Factor of safety = 2
➢ $(\sigma_t)_{theoretical}$ $= \frac{Ultimate\ tensile\ stress}{Factor\ of\ safety}$
➢   Stress (σ_t) $= \frac{Force}{Area}$
➢   F$_t$ = (b x t) x $(\sigma_t)_{theoretical}$
➢   155 x 10^3 = (37 x 4.16) x $(\sigma_t)_{Cal.}$
➢ $(\sigma_t)_{Cal.}$ = 1007.016 Mpa
➢ $(\sigma_t)_{Cal.} < (\sigma_t)_{theoretical}$

"The obtained Dimensions are safe for the Design, so the Design is safe."

Consider the Crushing Stresses induced in Single Bolted Joint made of E-Glass Fiber,
➢   **Design calculations for four bolts:**
➢   Consider Tensile Force on Plate, for four bolted joint is
➢   F$_t$ = 620 x 10^3 kN
➢   F$_t$ = n x (b x t) x $(\sigma_t)_{theoretical}$
➢   620 x 10^3 = n x 37 x 4.16 x 1025
➢   n   = 3.92
➢   i.e. n   = 4
➢   Therefore, Four Bolts are required for this force.

For Four Bolts (n = 4)
➢   620 x 10^3 =4 x 37 x 4.16 x $(\sigma_t)_{cal.}$
➢ $(\sigma_t)_{cal.}$ = 1007.01 MPa
➢   "Which is less than $(\sigma_t)_{theoretical}$. therefore, the Design is safe."

- Consider the Crushing Stresses induced in Single Bolted Joint made of Mild Steel, F_c = 27 kN
- F_c = (d x t) x $(\sigma_c)_{theoretical}$
- 27×10^3 = (d x 4.16) x 207
- d = 6.96 mm
  - let d = 8 mm
- Then,
- $27 \times 10^3 = (8 \times 4.16) \times (\sigma_c)_{Ca}$
- $(\sigma_c)_{Cal.}$ = 180.28 MPa
- $(\sigma_c)_{Cal.} < (\sigma_c)_{theoretical}$
- "The obtained Dimensions are safe for the Design, so the Design is safe."

Weight Calculation
- **I) For Composite laminate Plate:**
- Mass = Density x Volume
- = 2000 x l x b x t
- = 2000 x 0.100 x 0.037 x 0.00416
- = 0.03078 kg
- **II) For mild steel Plate:**
- Weight = M × g
- Mass = Density× Volume
- = 7845 x l x b x t
- = 7845 x 0.100 x 0.038 x 0.00416
- = 0.12401 kg

- **Weight Reduction %** $= (\frac{0.12401 - 0.03078}{0.12401}) \times 100$
- =75.17%

Geometry of Single Bolted Joint
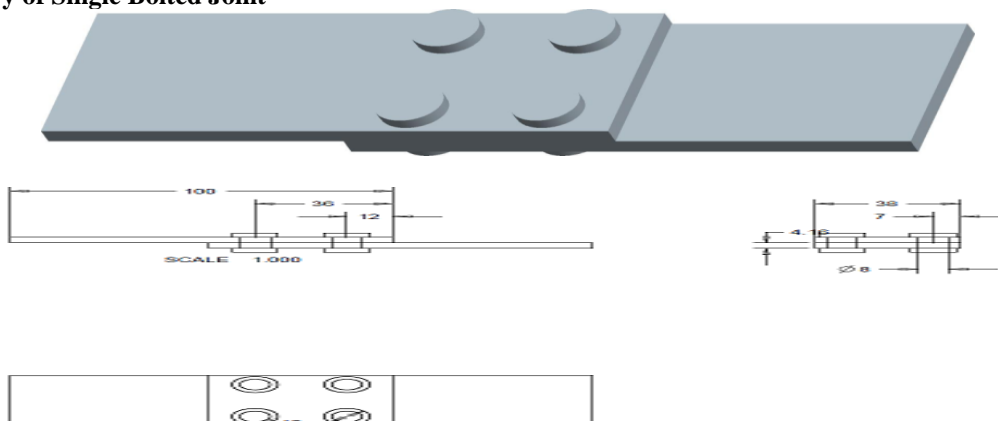
FEA analysis of Bolted joint mild steel and E-glass Fiber:

Fig : FEA analysis of single bolted joint in E-glass fiber

Fig. : FEA analysis of single bolted joint in E-glass fiber

Fig. : FEA analysis of single bolted joint in mild steel

Fig. : FEA analysis of Four bolted joint in E-Glass Fiber steel
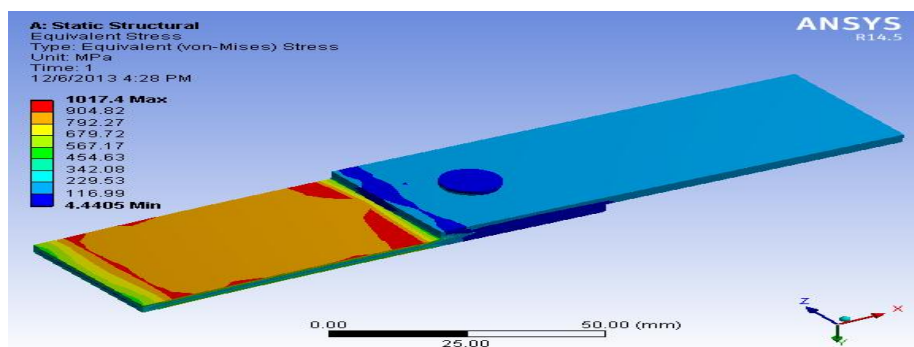
Fig. : FEA analysis of Four bolted joint in mild steel fiber
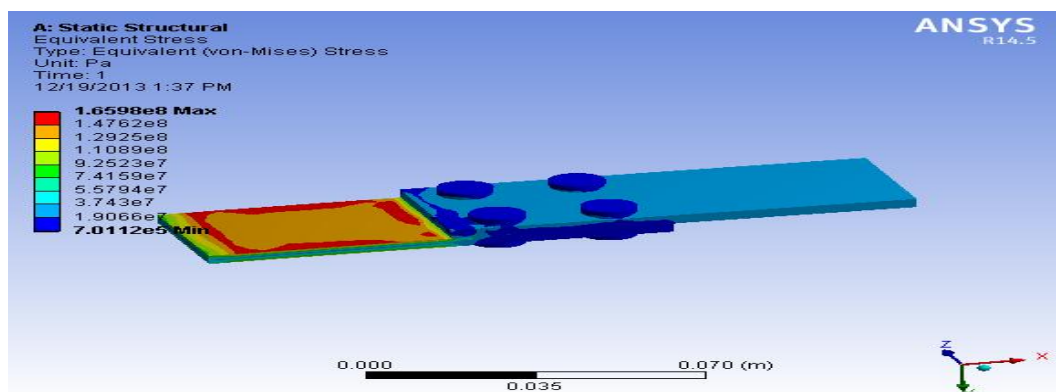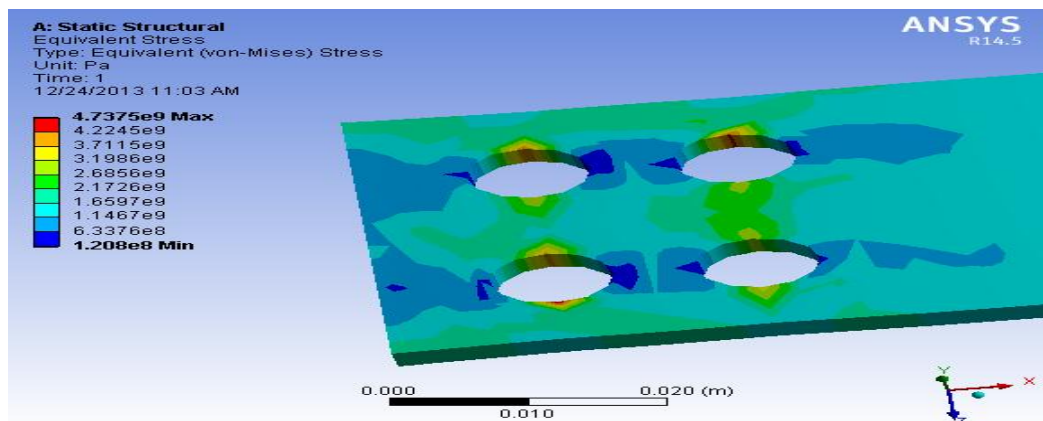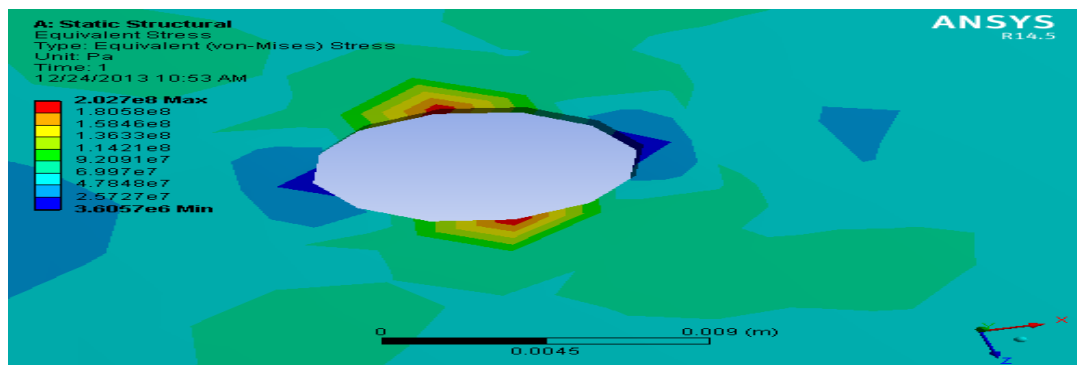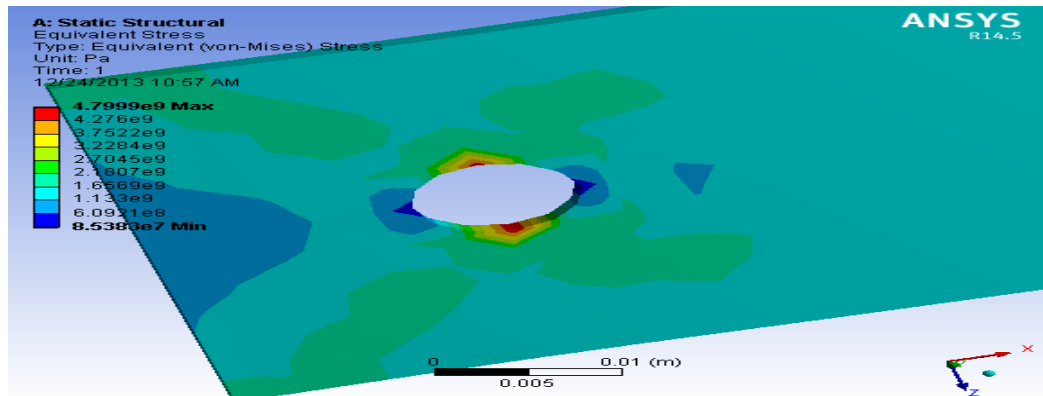
Comparison of Results
Table 8.1: Comparison of Results

NO. OF BOLTS	MATERIAL	ANALYTICAL RESULTS		FEA RESULTS		% DIFFERENCE	
		σ_t (tensile stress) MPa	σ_c (crushing Stress) MPa	σ_t (tensile stress) MPa	σ_c (crushing Stress) MPa	σ_t (tensile stress)	σ_c (crushing Stress)
Single bolted joint	E-glass fiber	1025	5000	1017.4	4799	0.741	3.28
	Mild steel	175	207	160.57	202.7	8.24	1.88
Four bolted joint	E-glass fiber	1025	5000	1069.2	4736	4.133	5.28
	Mild steel	175	207	165.20	198.3	5.6	4.202

III. Conclusion

- From the results obtained theoretically and by FEA, the difference in Tensile stress is not more than 8.24%.and for crushing stress is not more than 5.28%.
- The replacement of composite materials has resulted in considerable amount of weight reduction about 75% when compared to conventional mild steel plates.
- By using composite material there is substantial weight saving is about 75% than that of conventional mild steel plate.

Finally it is concluded that with the same geometry, plates with E-Glass Fiber have better strength. The life the joint is increased because of high resistance to corrosion, resistance to chemical attack, high stiffness to weight ratio and high strength to weight ratio of E-Glass fiber.

REFERENCES

[1] Marie-Laure Dano, Guy Gendron , Andre Picard, on Stress and failure analysis of mechanically fastened joints in composite laminates, Departement de genie civil, Universitie Laval, Sainte Foy, Que., Canada G1K 7P4 (2000).
[2] Tae Seong Lim, Byung Chul Kim, Dai Gil Lee, Fatigue characteristics of the bolted joints for unidirectional composite laminates, Mechanical Design Laboratory with Advanced Materials, Department of Mechanical Engineering, Me3221, Korea Advanced Instituteof Science and Technology, 373-1, Gusong-dong, Yusong-gu, Daejon-shi 305-701, Republic of Korea (7 December 2004).
[3] Murat Pakdil, Failure analysis of composite single bolted joints subjected to bolt pretension, Department of Mechanical Engineering, Abant Izzet Baysal University, 14280, Bolu, Turkey, (11 Sept. 2007).
[4] Marie-Laure Dano, Elhassania Kamal, Guy Gendron, Analysis of bolted joints in composite laminates: Strains and bearing stiffness predictions, Department of Mechanical Engineering, Universite Laval, Que bec, QC, Canada G1K 7P4 Available online (3 April 2006).
[5] K.I. Tserpesa, G. Labeasb, P. Papanikosb, Th. Kermanidis, Strength prediction of bolted joints in graphite/epoxy composite laminates, Laboratory of Technology and Strength of Materials, Department of Mechanical Engineering and Aeronautics, University of Patras, Patras 26500, Greece, (20 May 2002).
[6] Gordon Kelly, Stefan Hallstrom, Bearing strength of carbon fiber/epoxy laminates: effects of bolt-hole clearance, Division of Lightweight Structures, Department of Aeronautical and Vehicle Engineering, Kungl Tekniska Hogskolan, S-100 44 Stockholm, Sweden, (12 November 2003).
[7] A. Nanda Kishore, S.K. Malhotra, N. Siva Prasad, Failure analysis of multi-pin joints in glass fiber/epoxy composite laminates, Department of Mechanical Engineering, Indian Institute of Technology Madras, Chennai 600 036, India, (2009).
[8] Roman Starikov, Joakim Schon, Local fatigue behaviour of CFRP bolted joints, Division of Lightweight Structures, Department of Aeronautics, Royal Institute of Technology, SE-100 44 Stockholm, Sweden, (8 November 2001).

OPEN ACCESS

Production & Evaluation of Biodiesel from Karanja Seeds, A Seed Plentily Available In Rural Odisha

Bibhuti B. Samantaray[1], Dibyajyoti Giri[2], Ranjit K. Behuria[3],
Abhisek Samantray[4], Debasish Rath[5], Nihar R. Sahoo[6]
(Department of Mechanical Engineering, the Techno School, BPUT, Bhubaneswar-19, India)

ABSTRACT: *Energy is playing an important role in the development of economy and society both in developed and developing countries. As concern to the environment & vehicular population lead toward fuel crisis there is a trend begin to look for the alternative energy source which are more secure & less pollute. This paper is about the renewable source of Energy i.e. Biodiesel which is more secure & less pollutant as compared to fossil fuel (Diesel). This paper represent the biodiesel production from the Karanja oil which is plentily available in rural Odisha. We have set up a low cost experimental set up in which we have used the transesterification process to produce the Biodiesel and we have found out that the overall quality of the Biodiesel is optimum and satisfactory. The conversion of Crude Karanja oil to biodiesel in our experiment is around 3570 ml out of 5000 ml, which shows a good agreement in the other literature regarding the Biodiesel Production. Also in this paper we have focused on the crude glycerol formation as a byproduct and its utilization. The experiment has been conducted in a controlled environment where the temperature was around 63-67℃ and it has lasted around 92-95 min per experiment with the help of the catalyst KOH and MeOH in the proportion of 6:10 and 8:10 respectively.*
Keywords: *Bio Diesel, Catalyst, Esterification, Glycerol, Karanja Oil.*

I. Introduction

In 1895 Rudolph Diesel himself predicted that "the use of vegetable oil engine fuels may seem insignificant today. In course of time such oils may become as important as petroleum and the coal products of the present time". Due to increase in population & standard of living the demand & consumption of petroleum product is increase day by day. Hence biodiesel is the alternate coming in the way it used in any unmodified diesel engine. Vivek and A.K. Gupta [1] have studied the production of Biodiesel and they found out it has similar properties as diesel it can be also blend with diesel. Vismaya *et al* [2] has found out that the recent depletion and fluctuation in prices due to uncertain supplies for fuel, make us to search on renewable, safe and non-polluting sources of energy and reported that the vegetable oil also may used as direct fuel without refining but it make some problem. India is not self sufficient in petroleum and has to import about two third of its requirements from outside. P.K. Srivastava and Madhumita Verma [3] reported that Presently Indian government spends 90,000 cores for petroleum fuel and annual consumption is around 40 millions tons. One of the solutions is to explore the feasibility of substitution of diesel with an alternative fuel which can be produced in our country on a massive scale to commercial utilization. P.K. Sahoo and L.M. Das [4] described in their paper that India is a net importer of edible oil, hence the emphasis is on non-edible oils from plants such as Jatropha, karanja, neem, mahua, simarouba, etc. out of these plants, and Jatropha and Karanja have shown promise for biodiesel production. K.V. Thiruvengadaravi *et al* [5] said that In India the karanja trees are found in almost all rural areas. Its botanical name is "Pongamia Pinnata" of Leguminaceae family. It can grow in humid & subtropical condition having rainfall of 500-2000mm. Avinash K. Agarwal and K.Rajamanoharan [6] found that the karanja pod are of green in color at the beginning but after about 9-10 months it changes to tan color .The pods are elliptical, about 6 cm long of kidney shapes the kernels are white in color covered by a red skin with yield of 10-20 kg per tree The seed contain 29% oil, protein 18% & moisture 20%. In India production of karanja is approximately 220 million ton per annum. Malaya Naik *et al* [7] found that karanja oil is nonedible, nontoxic, biodegradable fuel. The karanja trees get most suitable condition for growth is in India in rural areas. The seeds are crushed in the expeller to get the oil. Y.C. Sharma and B Singh [8] have found that It basically contain chromanoflavones, chromencontin, furanoflavonols, furranodiketons which make it non edible & use of biodiesel. H. Raheman and A.G. Phadatare [9] found thatTransterification process is the main process of biodiesel production. In this process triglyceride oils are converted under heat to methyl or ethyl esters and glycerin by alcohol and a strong base catalyst.

Karanja oil + Potassium Methoxide $\longrightarrow$ Methyl ester + Glycerin

In Transesterification process triglyceride oils are converted under heat to methyl or ethyl esters and glycerin by alcohol and a strong base catalyst. v mamila *et al* [10] have studied that the main factors are the amount of the catalyst and alcohol, reaction temperature, pressure and time, as well as the content of free fatty acid (FFA) and water in oils by. Transesterification process is also called Alcoholysis, because it is the displacement of alcohol from an ester by another alcohol in a process similar to hydrolysis, except than alcohol is used instead of water. Md. Nurun Nabi *et al* [11] have found that Biodiesel was produced by acid Esterification followed by Transesterification process due to high FFA concentration in the karanja oil. For acid esterification h_2so_4 was used as catalyst. For base catalyzed Transesterification process methanol was used as alcohol and NAOH was used as lye catalyst. Instead of methanol and NAOH, ethanol or KOH can also be used for making biodiesel. L.M. Das *et al* [12] describe that Methanol and NAOH were used for lower cost and higher conversion efficiency. Karanja oil were filtered and preprocessed to remove water and contaminants, during alkaline (base catalyzed) Transesterification. Sara Pinzi *et al* [13] studied that Different ratios of methanol to oil were investigated for low acid value of less than 2mg KOH/g-oil and low FFA concentration of less than 1%. For acid pretreatment a round flask was used. A hot plate with a magnetic stirrer was used for heating the mixture in the flask. The karanja oil was taken into the flask and heated. H.J.Berchmans and S. Hirata [14] have found that Then methanol and 1% H_2SO_4 were added to the flask and heated continuously for an hour. It reported that for complete FFA esterification in some vegetable oils, the reaction temperature has been set to 50 °c, the reaction time 1 h and the acid to oil ratio 1% w/w. During heating and stirring the mixture, acid value and FFA concentration were tested. The FFA concentration should less than 1% so alkalized Transesterification was conducted with pretreatment karanja oil. H. Sharon   *et al* [15] have studied that it was expected to get maximum biodiesel when the acid value was less than 2mg KOH/g-oil and the FFA concentration in karanja oil was less than 1% using base catalyzed Transesterification. For base catalyzed Transesterification, different parameters including catalyst to oil ratio (w/w), methanol to oil hg (w/w), and the reaction temperature were investigated. But in this paper we have studied and produced the Biodiesel as well as Crude Glycerol form the Karanja seed, a seed plentily available in rural Odisha in a low cost experimental set up and studied the fuel characteristic and done the emission testing.

II. Experimental Set Up and Procedure

2.1 Experimental setup**:** A schematic of the experimental set-up used for the production of Glycerol is shown in Fig.1. The Experimental setup consists a heating device, a stirrer, a motor, a thermo meter, beaker, separating funnel, washing unit, diffuser unit and chemical unit. A metal frame is being used for holding up the motor and separating funnel at the same time. The crude Karanja oil is kept in the beaker and being heated by the heater with a controlled environment. A stirring rod is dipped into the solution of Karanja oil and the other chemical mixture like MeoH and KoH. The equipment like Beaker, Stirring rod, Separating Funnel, Conical Flask are made up of high resistance Glass Material. The stirrer is rotated by an electric motor of variable RPM ranging from 200 rpm to 600 rpm. A temperature measuring device i.e. thermometer is dipped in the solution for continuous temperature measurement. The beaker is covered with a glass cover to prevent reactant loss as alcohol being volatile vaporized during the reaction so it is necessary to prevent it from vaporizing. Separator is used to separate the glycerol from biodiesel after transesterification process.

2.2 Experimental procedure**:** Karanja oil is being produced from Karanja seeds through crushing in the expeller. Initially 500ml of Karanja oil was taken inside the beaker. At first it heated at 63-67℃ for the removal of moisture. The oil was then cooled down. The transterification process was carried out in a basic medium to achieve it. Here we used KOH as catalyst. The required amount of catalyst 25gm KOH taken and dissolved completely in 100 ml of pot methanol by using stirrer provided in the potassium methoxide. The alkali methoxide solution added into the oil for vigorous mixing by means of a mechanical transterification vessel. The free fatty acids cloudy looking is called glycerin, It sink to the bottom and the methyl ester- a translucent liquid, will remain on top. The required temperature of 63-67^{0}C was maintained throughout the reaction time of 92-95 minutes by means of controlled environment. The reacted mixture was then poured into the separating funnel. The mixture was allowed to separate and settle overnight by gravity into a clear liquid biodiesel on the top with light brown glycerol at the bottom. The next day, the glycerol was drained off from the separating funnel leaving the bio-diesel at the top. The raw bio-diesel was collected and water washed to bring down the pH of bio-diesel to 7. This pure bio-diesel gives the ester yield measured on weight basis and important fuel properties were determined and compared with the properties of raw oil and BIS standards for biodiesel. Transterification was

done at boiling point of mixture as that is the highest temperature achievable at normal condition. To increase the contact surface area reactants are agitated using stirrer. Hence stirrer rod also enhance the reaction rate.
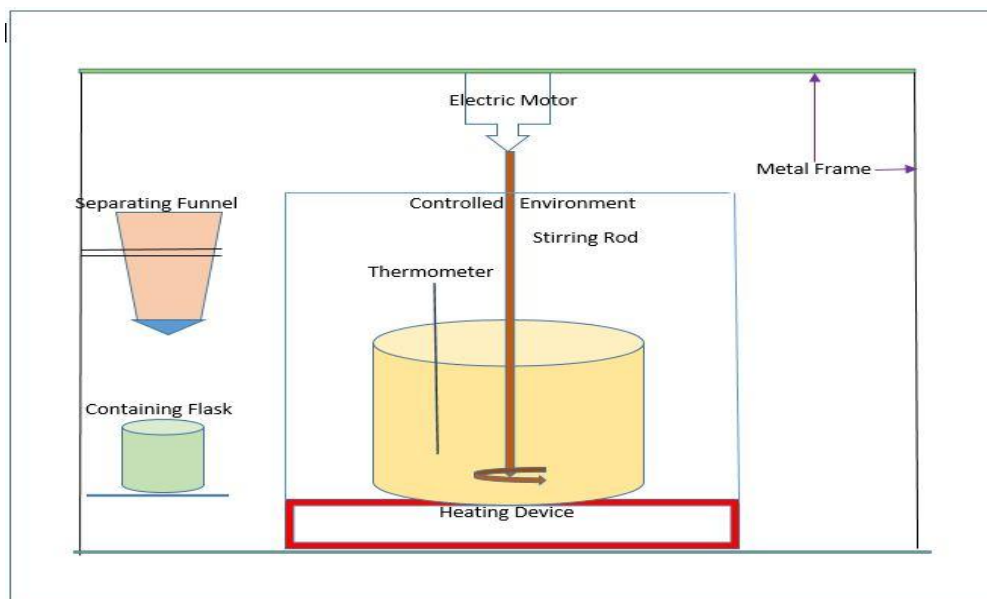

Figure.1. Schematic of the experimental setup

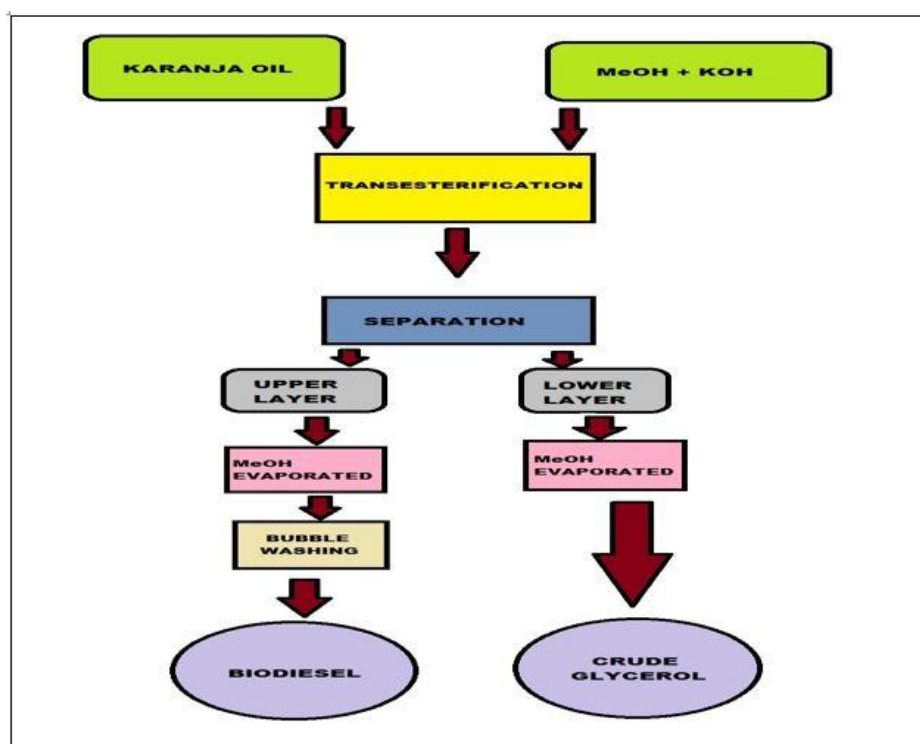Figure 2. The Detailed Biodiesel Production Process.

III. Results and Discussion

We have conducted the experiment in the above mentioned process and environment for several times to get more precession. The characteristic of the Biodiesel and the emission studies has been described below after testing.

3.1 Characteristics

After the esterification process we obtained around 3570 ml of biodiesel from 5000 ml of Karanja oil in the proportion 714 ml biodiesel from 1 liter of karanja oil. We found that color of biodiesel is turn to reddish yellow & kinematic viscosity of karanja oil was found nearly 10 times more than biodiesel at 50^0c. After esterification, the kinematic viscosity reduced to 3 times than that of pure karanja oil. Increase in diesel amount decrease the viscosity in the blend. The calorific value of biodiesel was found to be 35.88 MJ/kg, which is less than the calorific value of diesel (42.21 MJ/kg) and greater than crude Karanja oil (34 MJ/kg). As flash point is found to be more than 100^0c. Here Different property of the diesel and karanja oil are compared with the biodieel in the table given below.

Property	Diesel	Karanja oil	Biodiesel
Density (kg/m^3)	840	865	850
Viscosity (c. stokes)	3.8	5	2.8-5.1
Specific gravity	0.85	0.87	0.85
Heating value (kj/kg)	42000	36000	38285
Flash point(^{0}c)	60	208	130
fire point(^{0}c)	67	238	138

3.2 Emission Studies:

3.2.1. No$_x$ Emission

The amount of NO_x produced for B20 to B100 varied between 5 and 12 ppm as compared to 12 and 13 ppm for diesel. As compared to diesel 26% reduction in NO_x was obtained from its blends the reductions in emissions occurs generally from the complete combustion of fuel.

3.2.2. Carbon Monoxide

The diesel engine run using blends B10 to B100 have produced variation of Carbon Monoxide. The minimum and maximum CO produced were 0.005 %, 0.016% resulting in a reduction of approximately 92% and 75%, respectively as compared to diesel.

3.2.3. Smoke density

The smoke density produced during the test of fuels as per B20 to B100 were 0.8% and 3.2% with a maximum and minimum reduction of approximately 80% and 20% respectively as compared to diesel.

3.2.4. Exhaust Temperature:

The exhaust temperature for fuels in B20–B100 is measured varied between 250◦C and 320◦C as compared to 260◦C and 340◦C for diesel which is nearly same. So the exhaust heat is constant through the load range process.

IV. Conclusion

- It is confirmed that karanja oil also can used as a product for biodiesel which is used as a fuel in diesel engine as the replacement or supplementary fuel.
- The fuel properties as viscosity, density, flash point, fire point and calorific value of the biodiesel is compared with diesel which is found nearly same.
- It is found that in biodiesel blends emissions such as Carbon monoxide, smoke density and NO_x on average of 85%, 50% and 28%, respectively.
- It was found that 40% volume of biodiesel blends with diesel can be crude diesel which can be used in the diesel engine. Using the nonedible oil like karanja will surely improve the economics of the biodiesel formation process.

REFERENCES

[1]   Vivek and A.K Gupta, Production Biodiesel From Karanja Oil, Journal of scientific& Indian research,   Volume 63, 2004, 39-47.

[2]   Vismaya, W.Sapna Ei
pesona, J.R .Manjunatha, P. Srinivas and T.C. Sindhu Kanya, Extraction And Recovery Of Karanjin: A Value Addition To Karanja (Pongamia Pinnata) Seed Oil, Industrial Crops   and Products, 32, 2010, 118– 122.

[3]   P.K. Srivastava and Madhumita Verma, Methyl Ester Of Karanja Oil As An Alternative Renewable   Source Energy , Fuel 87, 2008, 1673–1677.

[4]   P.K. Sahoo and L.M. Das, Process Optimization For Biodiesel Production From Jatropha, Karanja And Polanga Oils, Fuel 88, 2009, 1588–1594.

[5]   K.V. Thiruvengadaravi, J. Nandagopal, P. Baskaralingam ,V. Sathya Selva Bala and S. Sivanesana, Acid-Catalyzed Esterification Of Karanja (Pongamia Pinnata) Oil With High Free Fatty Acids For Biodiesel Production, Fuel 98, 2012, 1–4.

[6]   Avinash Kumar Agarwal and K.Rajamanoharan, Experimental Investigations Of Performance And Emissions Of Karanja Oil And Its Blends In A Single Cylinder Agricultural Diesel Engine, Applied Energy 86, 2009,106-112 .

[7]   Malaya Naik, L.C. Meherb, S.N .Naik and L.M.Das, Production of Biodiesel from High Free Fatty Acid Karanja (Pongamia Pinnata) Oil, Biomass& Bioenergy, 2008, 354 – 357.

[8]   Y.C. Sharma and B Singh, Development Of Biodiesel From Karanja, Tree Found In Rural India, Fuel 87, 2008, 1740–1742.

[9]   H. Raheman and A.G. Phadatare, Diesel Engine Emissions & Performance From Blends Of Karanja Methyl Ester And Diesel, Biomass and Bioenergy 27, 2004, 393 – 397.

[10]   Venkata R. Mamilla, M. V. Mallikarjun, Dr. G.Lakshmi and N. Rao, Preparation Of Biodiesel   From Karanja Oil, International Journal of Energy Engineering, DOI 10.5963/IJEE0102008.

[11]   Md. Nurun Nabi , S.M. Najmul Hoque and Md. Shamim Akhter , Karanja (Pongamia Pinnata) Biodiesel Production In Bangladesh, Characterization Of Karanja Biodiesel And Its Effect On Diesel Emissions, Fuel Processing Technology, 90 ,2009, 1080–1086.

[12]   L.M. Das, Dilip K. Bora, Subhalaxmi Pradhan Malaya K. Naik and S.N. Naik, Long-Term Storage Stability Of Biodiesel Produced From Karanja Oil, Fuel, 88, 2009, 2315–2318.

[13]   Sara Pinzi , Paul Rounce , Jose M. Herreros, Athanasios Tsolakis and M. Pilar Dorado, The Effect Of Biodiesel Fatty Acid Composition On Combustion And Diesel Engine Exhaust Emissions, Fuel, 104 2013, 170–182.

[14]   H.J.Berchmans and S. Hirata, Biodiesel Production From Crude Jatropha Curcas Seed Oil With High Content Free Fatty Acids, Bioresource Technology 99, 2008, 1716–1721.

[15]   H. Sharon, R. Jayaprakash, M. Karthigai selvan, D.R. Soban kumar, A. Sundaresan and K. Karuppasamy, Biodiesel Production And Prediction Of Engine Performance Using SIMULINK   Model Of Trained Neural Network, Fuel 99 ,2012,197–203.

OPEN ACCESS

Optimized FIR filter design using Truncated Multiplier Technique

V. Bindhya[1], R. Guru Deepthi[2], S. Tamilselvi[3], Dr. C. N. Marimuthu[4]

[1] *M.E Applied Electronics, Department of ECE, Nandha Engineering College, Erode.*
[2]*M.E Vlsi design, Department of ECE, Nandha Engineering College, Erode.*
[3]*M.E Vlsi design, Department of ECE, Nandha Engineering College, Erode.*
[4]*DEAN, Department of ECE, Nandha Engineering College, Erode*

ABSTRACT: *In this paper we have proposed an efficient way of FIR filter design using truncated multiplier technique. The Multiplication operation is performed using Multiple Constant Multiplication Accumulation Truncation (MCMAT) technique. The proposed multiplier design is based on the Wallace tree compressor (WTC). As a result it offers significant improvements in area, delay and power when compared with normal Carry Propagation Addition (CPA). Usually the product of two numbers appears as output in the form of LSB and MSB. The LSB part is truncated and compressed using MCMAT technique. The proposed design produces truncation error which is not more than 1 ulp (unit of least position). While implementing the proposed method experimentally, there is no need of any error compensation circuits and the final output is precised. Hence the area can be saved and the power is also reduced.*

Keywords: *Digital signal processing (DSP), Finite Impulse Response (FIR) filter, Multiple constant Multiplication Accumulation Truncation (MCMAT), Truncated multipliers, WTC.*

I. Introduction

Digital signal processing (DSP) is one of the core technologies in multimedia and communication systems. Most of Digital signal processing (DSP) needs faster multiplication and addition operations to be performed. Multiplication is frequently required in digital signal processing for filter realization. Many research works deals with the low power design of high speed multipliers. Since the multipliers have a significant impact on the performance of the entire system, many high-performance algorithms and architectures have been proposed to accelerate multiplication [3]. Filtering is an operation usually performed to extract the needed information from a digital signal. A signal/data stored in memory contains both wanted and unwanted information (noise). On the basis of impulse response, there are two fundamental types of digital filters: Infinite Impulse Response (IIR) filters, and Finite Impulse Response (FIR) filters. Finite Impulse Response digital filter has strictly exact linear phase, relatively easy to design, highly stable, computationally intensive, less sensitive to finite word-length effects, arbitrary, amplitude-frequency characteristic and real-time stable signal processing requirements etc.FIR filter is described by differential equation. The output signal is a convolution of an input signal and the impulse response of the filter.

$$y(n) = \sum_{k=0}^{N-1} (h(k) \ x(n-k)) \qquad (1)$$

where   x(n) is the input signal.
          h(n) is the impulse response of FIR filter.

Normally, multiplication involves two basic operations as partial production generation and their partial product summation. The main bottle-neck of the area is in the multiplication of two numbers as it generates a product with twice the original bit width.. The critical path for the multiplier is on the number of partial products. The partial products generated are added using Wallace Tree Compressor (WTC).The basic idea of this work is to use WTC instead of CPA to achieve lower area and power consumption. The main advantage of this WTC logic reduces the number of full adders and half adders during the tree reduction. The design achieves less area and power which leads to have truncation error of not more than 1 ulp (unit of least position). So there is no need of error compensation circuits hence the final output will be précised.

This paper is organized as follows. In Section II, discusses the MCMAT technique. In Section III, the proposed scheme is implemented in FIR filter realization. In Section IV, the proposed scheme is compared to the previously proposed ones. Finally, Section V, concludes this paper.

II. MCMAT Technique

Multiple constant Multiplication Accumulation Truncation (MCMAT) technique is more efficient to collect all the Partial Product(PPs) into a single Partial Product Bit(PPB) matrix with Carry Propagation Addition (CPA). It is needed to truncate the partial product bits to the required precision to reduce area cost. In this technique, a single row of PPBs is made undeletable (for the subsequent rounding), and the PPB elimination consists of only deletion and rounding [2].Instead of accumulating individual multiplication for each product, it is more efficient to collect all the PPs into a single PPB matrix to reduce the height of the matrix to two, followed by final carry propagation adder is shown in Fig.1.

2.1 Operations in MCMAT technique

The MCMAT truncated multiplier consists of several operations, including deletion, truncation, rounding, and final addition. In the first step, we perform the deletion that removes all the unnecessary PP bits that do not need to be generated is shown in Fig.1. a single row of PPBs is made undeletable (for the subsequent rounding), and the PPB elimination consists of only deletion and rounding. After the deletion of PP bits, we perform the per-column reduction and generate two rows of PP bits. After reduction, we perform the truncation that further removes the first row of n − 1 bits from column 1 to column n− 1.This step of truncation introduces truncation error.

After deletion, reduction, and truncation, the PP bits are added using a CPA to generate the final product of P bits. The bits in column 2 to column n−1can be safely removed before CPA because these bits are the only bits left in the columns after the deletion and truncation processes, and thus, they do not affect the carry bit to column n + 1 during the rounding process [2]. Before the final CPA, we add a bias constant of 1∕2 ulp in order to achieve the round to nearest rounding with the rounding error. The bit at column n after the final CPA is also removed during the rounding process. Thus, the total error for the design of the MCMAT multiplier is bounded by the following equation

$$-ulp < E = (E_D + E_T + E_R) \leq ulp \qquad (2)$$
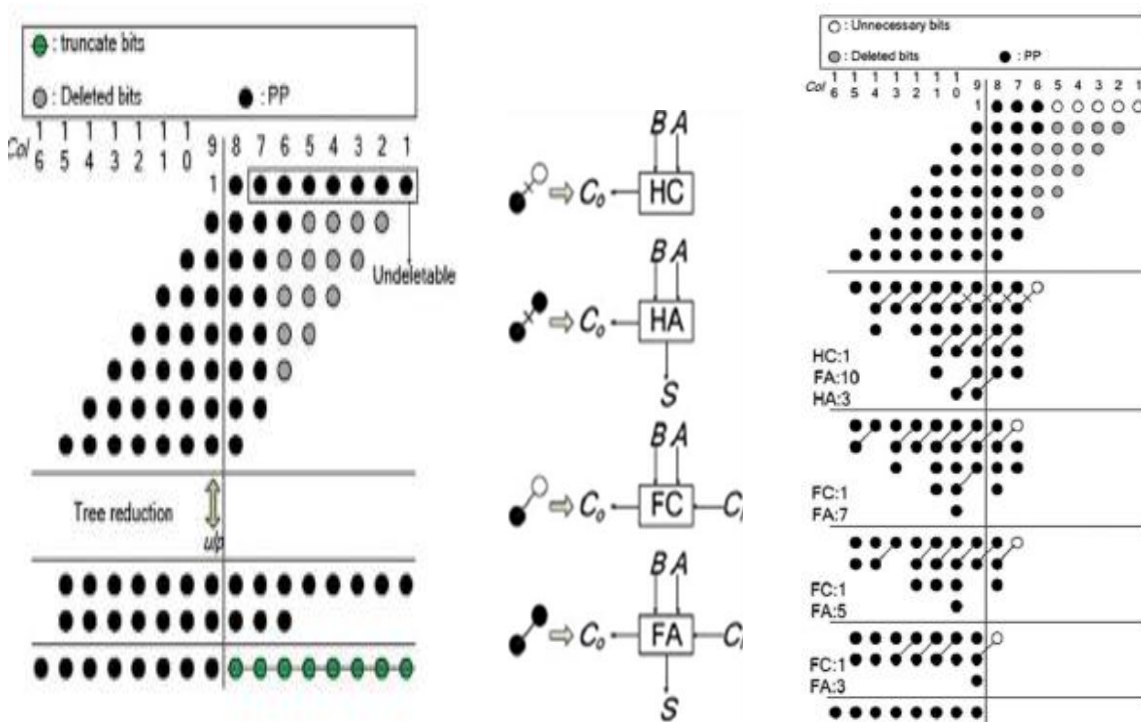

Fig.1.Truncated multiplier design using MCMAT technique

III. Proposed Work In Fir Filter Realization

Truncated multiplier can be effectively implemented in FIR filter structure. Conventional FIR filter performs ordinary multiplication of coefficient and input without considering the partial product bit length. Thus the structure can be made effective by replacing the existing multiplier with the proposed MCMAT truncated multiplier technique using Wallace Tree Compressor [4] for visible area reduction. Digital FIR filter implementation using MCMAT technique that removes unnecessary PPBs so that truncation error is not more than 1ulp, so the final result is precised.
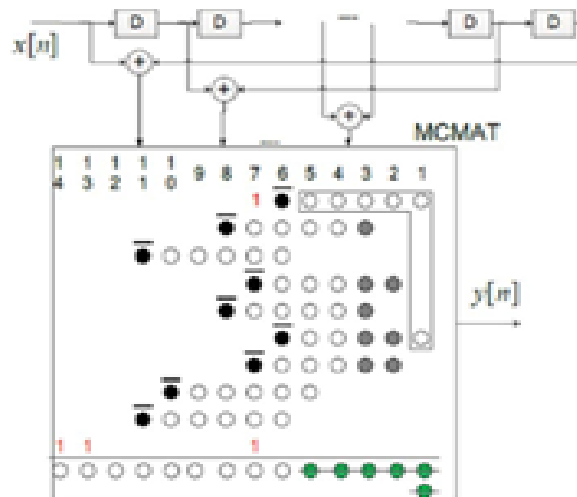

Fig.2. Digital FIR filter implementation using MCMAT technique

In Fig.2,the white circles in the L-shape block represent the undeletable PPBs. The deletion of the PPBs is represented by gray circles. After PP compression, the rounding of the resultant bits is denoted by crossed circles. The last row of the PPB matrix represents all the offset and bias constants required including the sign bit modifications. The proposed work of digital FIR filter design is implemented with MCMAT technique using Wallace tree compressor(5:2), where the results of the FIR filter structure shows the better area and power reduction compared to the conventional FIR filter.
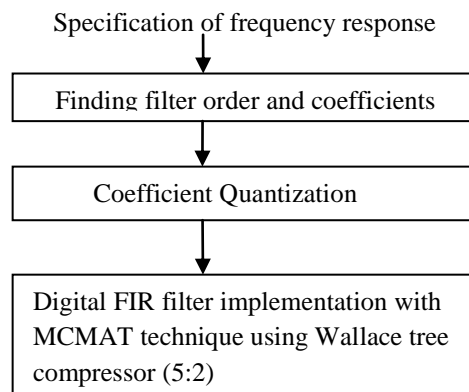

Fig.3. Digital FIR implementation with MCMAT technique using WTC

This modified FIR filter design and implementation can be divided into the following stages: Finding filter order and coefficients, coefficient quantization, digital FIR filter implementation with MCMAT technique using Wallace tree compressor is shown in Fig.3. In the first stage, the filter order and the corresponding coefficients are determined to satisfy the specification of the frequency response. Then, the coefficients are quantized to finite bit accuracy of 8 bits. The first two stages are implemented using MATLAB. Finally, optimization approaches such as MCMAT technique using WTC are used to minimize the area of hardware implementation.

IV. Results and Discussions

Multiplication plays a major role in FIR filter realization. The major aim of MCMAT technique is to provide high speed along with reduction in area. Area utilization and power utilization by the proposed method is less.

We implemented FIR filter with the low pass filter specification as given in Table I [7].M is the original filter order while EWL is the effective word length, f_{pass} and f_{stop} are the passband and stopband edge frequencies normalized to one, and A_{pass} and A_{stop} denote the corresponding peak to peak ripples.

TABLE I
Specification of the FIR filter under consideration

Filter	M	EWL	f_{pass}	f_{stop}	A_{pass} (dB)	A_{stop} (dB)
A(LP)	5	8	0.20	0.27	0.10	46

The MCMAT technique is simulated using MODELSIM and the output is shown in Fig.4. Here the inputs are given as a= 11111111 b=11111111 cf=11111111 d=11111111 e=11111111 f=11111111 g=11111111 h=11111111 k=11111111 l=11111111. For this input, outputs are produced as 11110110. For the given specifications, digital FIR filter implementation with MCMAT technique using WTC is simulated using MODELSIM and the output is shown in Fig.5.Here xn is the input,d1,d2,d3,d4 are the filter coefficients and y_n is the output.
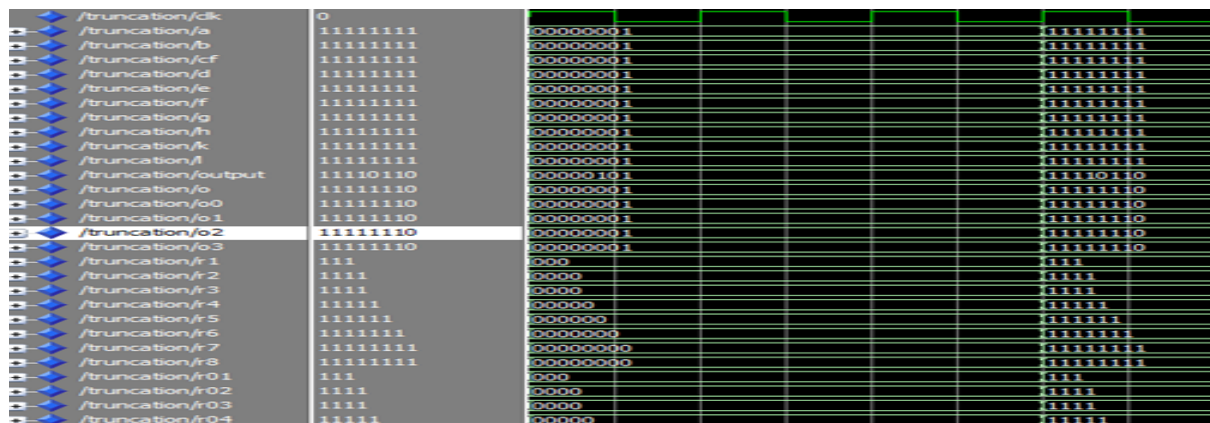

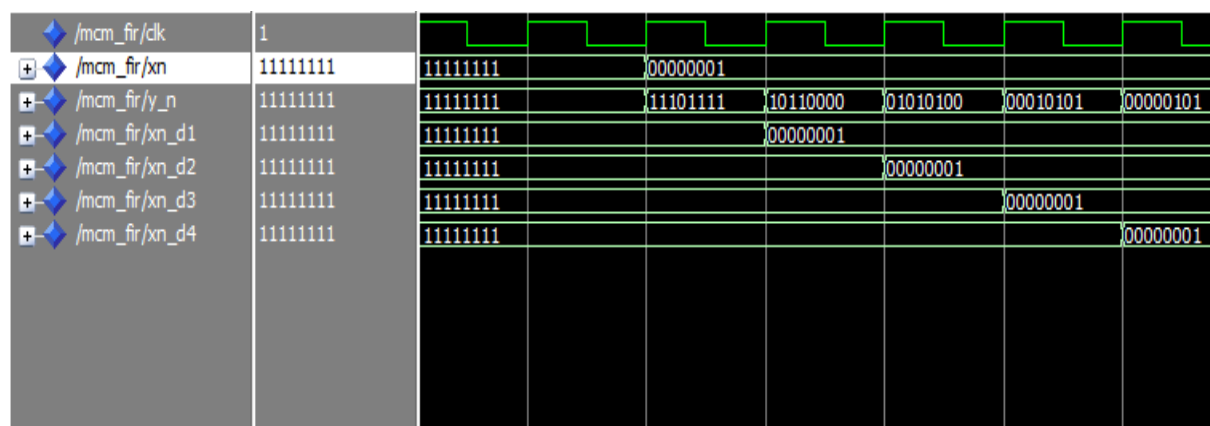Fig.4. Simulation result of MCMAT technique

Fig.5. Simulation result of digital FIR implementation with MCMAT technique using WTC

The synthesis of the design is done using Xilinx ISE simulator and the implementation is done using Verilog HDL code. The synthesized report shows that the design in terms of area and speed is optimized. The comparison of area and power for the different architectures are given in the table below.

TABLE II
Synthesis results of Filter A with 5 tap LP

Parameters	Digital FIR filter design with MCMAT technique using CPA	Digital FIR filter design with MCMAT technique using WTC
Area (gate counts)	2,203	2,136
Power (mw)	55.57	47.62
No. of latches	229	149
No. of Slice registers	213	169

From the synthesized result as given in Table II, it is found that the proposed truncated multiplier technique using WTC consumes low area and low power compared to existing truncated multiplier technique using MCMAT technique for FIR filter realization.

After FIR filter coefficient multiplication operations, the output signals have larger bit width due to bit width expansion. In many practical situations, only partial bits of the full-precision outputs are needed. For this purpose, area efficient FIR filter is designed with MCMAT technique using WTC. The proposed design can effectively reduces the number of adders and the truncation error which is not more than 1 ulp. Hence the final output will be précised.

V. Conclusion

The proposed paper implements an area efficient low power FIR filter implementation. The area can be effectively reduced by the use of MCMAT technique for the filter coefficient multiplication with a slight reduction in speed. Thus the multiplication is carried out using WTC in place of Carry Propagation Addition(CPA). The MCMAT technique with WTC consists of lesser number of logic gates and as a result, it reduces the area of the design. The power is also reduced to the effectiveness of the design.

REFERENCES

[1]   Charles. Roth Jr. ―Digital Systems Design using VHDL,Thomson Brooks/Cole, 7th reprint, 2005.
[2]   H.-J. Ko and S.-F. Hsiao, "Design and application of faithfully rounded and truncated multipliers with combined deletion, reduction, truncation, and rounding," IEEE Trans. Circuits Syst. II, Exp. Briefs, vol. 58, no. 5,pp. 304–308, May 2011.
[3]   Soojin Kim and Kyeongsoon Cho , Design of High-speed Modified Booth Multipliers Operating at GHz Ranges, World Academy of Science, Engineering and Technology 37, 2010.
[4]   Naveen Kr. Gahlan, Prabhat Shukla, Jasbir Kaur, "Implementation of Wallace Tree Multiplier Using Compressor", International journal on Computer Technology & Applications, vol. 3,pp. 1194-1199.Nov-Dec.2012.
[5]   Y. J. Yu and Y. C. Lim, "Design of linear phase FIR filters in subexpression space using mixed integer linear programming," IEEE Trans. Circuits Syst. I, Reg. Papers, vol. 54, no. 10, pp. 2330–2338, Oct. 2007.
[6]   H. Samueli, "An improved search algorithm for the design of multiplierless FIR filters with powers-of-two coefficient," IEEE Trans. Circuits Syst., vol. 36, no. 7, pp. 1044–1047, Jul. 1989.
[7]   Y. C. Lin and S. Parker, "Discrete coefficient FIR digital filter design based upon an LMS criteria," IEEE Trans. Circuits Syst., vol. 30, no. 10,pp. 723–739, Oct. 1983.

An Effective Tea Leaf Recognition Algorithm for Plant Classification Using Radial Basis Function Machine

Arunpriya C.[1], Antony Selvadoss Thanamani[2]

[1]*P.S.G.R Krishnammal College for Women, Coimbatore, India*
[2]*Nallamuthu Gounder Mahalingam College, Pollachi, India*

Abstract: *A leaf is an organ of a vascular plant, as identified in botanical terms, and in particular in plant morphology. Naturally a leaf is a thin, flattened organ bear above ground and it is mainly used for photosynthesis. Recognition of plants has become an active area of research as most of the plant species are at the risk of extinction. Most of the leaves cannot be recognized easily since some are not flat (e.g. succulent leaves and conifers), some does not grow above ground (e.g. bulb scales), and some does not undergo photosynthetic function (e.g. cataphylls, spines, and cotyledons).In this paper, we mainly focused on tea leaves to identify the leaf type for improving tea leaf classification. Tea leaf images are loaded from digital cameras or scanners in the system. This proposed approach consists of three phases such as preprocessing, feature extraction and classification to process the loaded image. The tea leaf images can be identified accurately in the preprocessing phase by fuzzy denoising using Dual Tree Discrete Wavelet Transform (DT-DWT) in order to remove the noisy features and boundary enhancement to obtain the shape of leaf accurately. In the feature extraction phase, Digital Morphological Features (DMFs) are derived to improve the classification accuracy. Radial Basis Function (RBF) is used for efficient classification. The RBF is trained by 60 tea leaves to classify them into 6 types. Experimental results proved that the proposed method classifies the tea leaves with more accuracy in less time. Thus, the proposed method achieves more accuracy in retrieving the leaf type.*

Keywords: *Leaf Recognition, Dual Tree Discrete Wavelet Transform (DT-DWT), Digital Morphological Features (DMFs), Radial Basis Function (RBF).*

I. Introduction

Leaf is the most important organ in a plant. Plant leaf features are important for the plant species identification.[1]Plant recognition is an essential and challenging task. Leaf recognition plays an important role in plant classification and its key issue lies in whether the chosen features are constant and have good capability to discriminate various kinds of leaves. The recognition procedure is very time consuming. Computer aided plant recognition is still very challenging task in computer vision because of improper models and inefficient representation approaches. The main aim of plant recognition is to evaluate the leaf geometrical morphological and Fourier moment based features.

Recently, computer vision and pattern recognition techniques have been applied towards automated process of plant recognition [2].The classification of plant leaves is a vital mechanism in botany and in tea, cotton and other industries [3], [4]. Additionally, the morphological features of leaves are employed for plant classification or in the early diagnosis of certain plant diseases [5].

Preprocessing is a technique in which an image includes removal of noise, edge or boundary enhancement, automatic edge detection, automatic contrast adjustment and the segmentation. As multiple noise damages the quality of nature of the images, improved enhancement technique is required for improving the contrast stretch in leaf images. Image enhancement is basically improving the interpretability or discernment of information in images for human viewers and providing enhanced input for other automated image processing techniques [22, 23]. During this process, one or more attributes of the image are altered. Selection of attributes and the way they are modified are specific to a given task.

Denoising has become an basic step in image analysis. Noise suppression and the preservation of actual image discontinuity is essential in image denoising in order to detect the image details and suitably alter the degree of noise smoothing. Fuzzy feature is used in single channel image denoising to enhance image information. This feature space helps to distinguish between important coefficients, which depends on image discontinuity and noisy coefficients [6]. The size of image plays an important role in order to transmit the image in lesser time and with the allotted bandwidth. DT-DWT has been successfully used in many applications such as image denoising, texture analysis, compression, and motion estimation.

The extraction of leaf features from a plant is a key step in the plant recognition process [7, 8]. This feature extraction process creates a new challenge in the field of pattern recognition [9] [10]. The data acquisition from living plant automatically by the computer has not been implemented. The main phases

involved in this research are feature extraction and the classification. All features are extracted from digital leaf image. Radial Basis Function(RBF) is used for efficient classification.

The paper can be organized as follows. Section II describes the related works involved regarding leaf recognition. Section III describes about the proposed methodology. Experimental results are illustrated in Section IV and Section V deals with the conclusion.

II.   Related Works

Stephen Gang Wu et al., [11] employ Probabilistic Neural Network (PNN) with image and data processing techniques to implement general purpose automated leaf recognition for plant classification. They implemented a leaf recognition algorithm using easy-to-extract features and high efficient recognition algorithm. They mainly concentrate on feature extraction and the classifier. Features are extracted from digital leaf image. Except one feature, all features can be extracted automatically. The features are orthogonalized by Principal Components Analysis (PCA).As to the classifier; they used PNN for its fast speed and simple structure.

Wang et al., [12] first investigated the representation efficiency of 3D DT-DWT for video and proposed a DDWT-based scalable video coding scheme without motion estimation (DDWTVC) [13]. Better coding efficiency in terms of PSNR and visual quality are reported compared with 3D SPIHT which also does not use motion compensation.

Xiao Gu et al., [14] proposed a novel approach for leaf recognition by means of the result of segmentation of leaf's skeleton based on the integration of Wavelet Transform (WT) and Gaussian interpolation. And then the classifiers, a nearest neighbor classifier (1-NN), a k -nearest neighbor classifier (k-NN) and a radial basis probabilistic neural network (RBPNN) are employed, based on Run-length Features (RF) obtained from the skeleton to identify the leaves. Ultimately, the efficiency of this approach is illustrated by several experiments. The results reveal that the skeleton can be effectively extracted from the entire leaf, and the recognition rates can be significantly improved.

Jyotismita Chaki et al., [15] proposed an automated system for recognizing plant species based on leaf images. The leaf images corresponding to three different plant types are analyzed using two different shape modeling techniques. The first modeling is based on the Moments-Invariant (M-I) model and the second on the Centroid Radii (C-R) model. The first four normalized central moments have been considered for the M-I model and studied in various combinations namely in joint 2-D and 3-D feature spaces for producing optimum results. An edge detector has been used for the C-R model to identify the boundary of the leaf shape and 36 radii at 10 degree angular separation have been used to build the feature vector. A hybrid set of features involving both the M-I and C-R models has been generated and explored to find whether the combination feature vector can lead to better analysis. Neural networks are used as classifiers for discrimination.

III.   Methodology

The tea leaf recognition method used in the proposed approach consists of three phases namely image pre processing, feature extraction and classification. The steps used in the recognition of tea leaf system is shown in the Fig.1.

3.1. Image Pre-Processing
The input tea leaf images undergo several processing steps as follows.
  A.   *Converting RGB Image To Binary Image*

The tea leaf image is obtained through scanners or digital cameras. An RGB image is firstly converted into a grayscale image. Equation 1 is used to convert RGB value of a pixel into its grayscale value.

$$gray = 0.2989*R + 0.85870*G + 0.1140*B \qquad (1)$$

Where R, G and B corresponds to the color of the pixel, respectively.
  B.   *Fuzzy Denoising Using Dual Tree Discrete Wavelet Transform*

Here the denoising is done through Fuzzy shrinkage rule. In image denoising, where a trade-off between noise suppression and the maintenance of actual image discontinuity must be made, solutions are required to detect important image details and accordingly adapt the degree of noise smoothing. With respect to this principle, use a fuzzy feature for single channel image denoising to enhance image information in wavelet sub-bands and then using a fuzzy membership function to shrink wavelet coefficients, accordingly.

Dual Tree Discrete Wavelet Transform (DT-DWT) is used as a fuzzy denoising algorithm which provides both shiftable sub-bands and good directional selectivity and low redundancy.

The 2-D dual-tree discrete wavelet transform (DT-DWT) of an image is employed using two critically-sampled separable 2-D DWT's in parallel .[16] The advantages of the dual-tree DWT (DT-DWT) over separable 2D DWT is that, it can be used to employ 2D wavelet transforms which are more selective with respect to orientation.
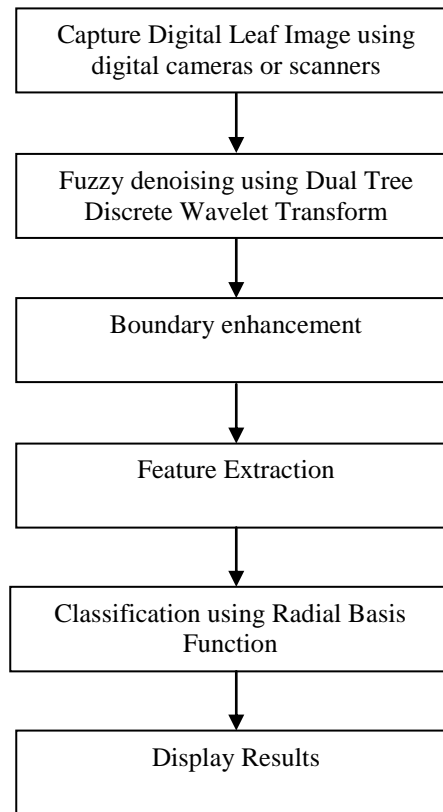

Fig. 1 Steps used in the recognition of tea leaf system

The real part or the imaginary part of DT-DWT [19] produces perfect reconstruction and hence it can be employed as a stand-alone transform. Feature vector can be calculated using magnitude of subbands. The implementation of DT-DWT is easy. An input image is decomposed by two sets of filter banks, (H_0^a, H_1^a) and $H_0^b, H_1^b)$ separately and filtering the image both horizontally and vertically. Then eight sub bands are obtained: LL_a , HL_a , LH_a , HH_a , LL_b , HL_b , LH_b and HH_b. Each high-pass subband from one filter bank is combined with the corresponding subband from the other filter bank by simple linear operations: averaging or differencing. The size of each subband is the same as that of 2D DWT at the same level. [20] But there are six high pass subbands instead of three highpass subbands at each level. The two lowpass subbands, LL_b and LL_a , are iteratively decomposed up to a desired level within each branch.

The DT-DWT (K) can be designed in two ways to have required delays. The first is based on Farras filters and the second employs Q-shift (quarter shift) filter design. The key issue in the design of DT-DWT (K) is to obtain (approximate) shift invariance using any of the filter forms.[21]To use a redundant transform for compression seems contradictory to the goal of compression which is to reduce whatever redundancy as much as possible. However if coefficients of a redundant transform are sparse enough, compression can even benefit from the introduced redundancy since most coefficients are nearly zero.

Processing is usually result from a modification of the spatial correlation between wavelet coefficients (often caused by zeroing of small neighboring coefficients) or by using DWT. DWT is shift invariance and will cause some visual artifacts in thresholding based denoising. For this reason, the fuzzy filter is used on the results of the proposed fuzzy-shrink algorithm to reduce artifacts to some extent. First, use a window of size (2 L+1) × (2 K+1) centered at (i, j) to filter the current image pixel at position (i, j). Next, the similarity of neighboring pixels to the center pixel is calculated using the following equation.

$$m(l, k) = \exp\left(-\left(\frac{Y_{s,d}(i, j) - Y_{s,d}(i+l, j+k)}{\text{Thr}} \right)^2 \right) \quad (2)$$

$$s(l, k) = \exp\left(-\left(\frac{l^2 + k^2}{N} \right) \right) \quad (3)$$

where $Y_{s,d}(i,j)$ and $Y_{s,d}(i+l,j+k)$ are central coefficient and neighbor coefficients in the wavelet sub-bands, respectively. $Thr = c \times \hat{\sigma}_n$, $3 \leq c \leq 4$, $\hat{\sigma}_n$ is estimated noise variance, and N is the number of coefficients in the local window $k \in [-K \ldots K]$, and $l \in [-L \ldots L]$.

According the two fuzzy functions, can get adaptive weight $w(l,k)$ for each neighboring coefficient:

$$w(l,k) = m(l,k) \times s(l,k) \qquad (4)$$

Using the adaptive weights $w(l,k)$, obtain the fuzzy feature for each coefficient in the wavelet sub-bands as follows:

$$f(i,j) = \frac{\sum_{l=-L}^{L} \sum_{K=-K}^{K} W(l,k) \times |Y_{s,d}(i+l,j+k)|}{\sum_{l=-L}^{L} \sum_{K=-K}^{K} W(l,k)} \qquad (5)$$

After finding the fuzzy feature, will form Linguistic IF-THEN rules for shrinking wavelet coefficients as follows:

"IF the fuzzy feature $f(i,j)$ is large THEN shrinkage of wavelet coefficients $Y_{s,d}(i,j)$ is small".

Finally, the output of post-processing step is determined as follows:

$$\tilde{x}(i,j,c) = \frac{\sum_{l=-L}^{L} \sum_{K=-K}^{K} w(l,k) \times \hat{x}(i+1,j+k,c)}{\sum_{l=-L}^{L} \sum_{k=-k}^{k} w(l,k)} \qquad (6)$$

where $\hat{x}$ is the denoised image, which can be obtained using proposed fuzzy-shrink algorithm. After the post processing process the enhanced leaf image is obtained as a result.

C. Boundary Enhancement
The margin of a leaf is highly focused in this pre processing step. Convolving the image with a Laplacian filter of 3×3 spatial mask:

$$\begin{matrix} 0 & 1 & 0 \\ 1 & -4 & 1 \\ 0 & 1 & 0 \end{matrix} \qquad (7)$$

Fig. 2.1 Enhanced image   Fig. 2.2 Boundary Enhancement

The Fig. 2 shows the enhanced image and boundary enhancement the proposed tea leaf recognition. To make boundary as a white curve on black background, the pixel values "1" and "0" are swapped.

3.2. Feature Extraction
The proposed approach uses common Digital Morphological Features (DMFs), so that a computer can obtain feature values quickly and automatically The features used for extraction in the proposed method is described as follows.

A. *Physiological Length:*

The distance between the two terminals is the physiological length. It is represented as L_p. The red line in the Fig. 3 indicates the physiological length of a leaf.
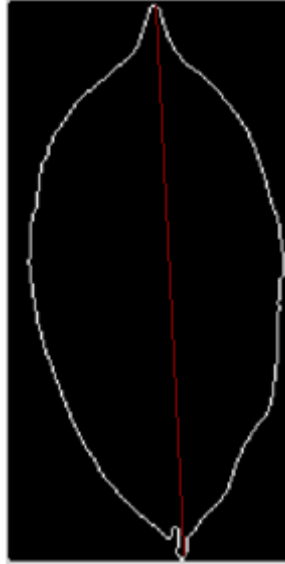

Fig. 3 Physiological length of a leaf

B. *Physiological Width:*

Drawing a line passing through the two terminals of the main vein, infinite lines can be plotted orthogonal to that line. The number of intersection pairs between those lines and the leaf margin is also infinite. At the physiological width, the longest distance between points of those intersection pairs is defined. It is represented as W_p. As the coordinates of pixels are discrete, two lines are considered as orthogonal if their degree is $90° \pm 0.5°$. The red line in the Fig. 4 indicates the physiological width of a leaf.
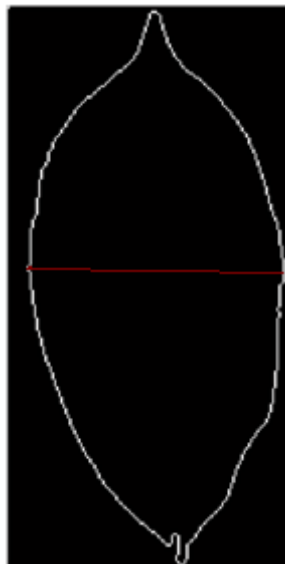

Fig. 4 Physiological width of a leaf

C. *Aspect Ratio:*

The ratio of physiological length L_p to physiological width W_p is called aspect ratio and it is given by,

$$Aspect\ ratio = \frac{L_p}{W_p} \qquad (8)$$

D.   Serration Angle:

The teeth angle of a leaf can be defined using serration angle.

$$\theta = arc \cos\left(\frac{(a.b)}{|a||b|}\right) \qquad (9)$$

Where θ is the serration angle , a is the length of first recognizable teeth from the tip of the angle and b is the breadth of first recognizable teeth from the tip of the angle.
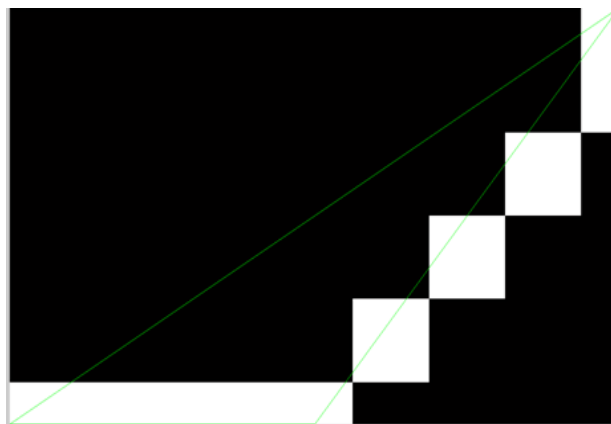

Fig. 5. Serration angle obtained from the tea leaf

The serration angle obtained from the tea leaf using equation 4 is shown in the Fig. 5.

E.   Segment

The segment of a leaf can be defined as the ratio of first recognizable teeth in the left side from the tip of the angle 'a' to the first recognizable teeth in the right side from the tip of the angle 'b'.

$$segment = \frac{a}{b} \qquad (10)$$

F.   Segment maximum width to Physiological length ratio

The leaf is divided into 10 segments as shown in the Fig. 6. Each segment width to the physiological length ratio can be determined for all the 10 segments.

Fig. 6 Segment of a leaf

G.   Tip Angle

The angle which is formed from the tip of the leaf to the first recognizable teeth on either side of the leaf is called tip angle.

The tip angle can be calculated using the formula,

$$\theta = arc\cos\left(\frac{(a.b)}{|a||b|}\right) \qquad (11)$$

Where θ is the tip angle, a and b are the first recognizable teeth from the tip of the angle on left and right side respectively. The tip angle formed from the tea leaf is shown in the Fig. 7.

Fig. 7 Tip angle obtained from the tea leaf

3.3. Classification Using Radial Basis Function
A Radial Basis Function Neural Network (RBFNN) is a special type of neural network commonly used for classification, regression, function approximation and data clustering problems. RBFNN uses Radial Basis Function (RBF) as its activation function.[18] Radial Basis Function Neural Network architecture is shown in the fig. 8.
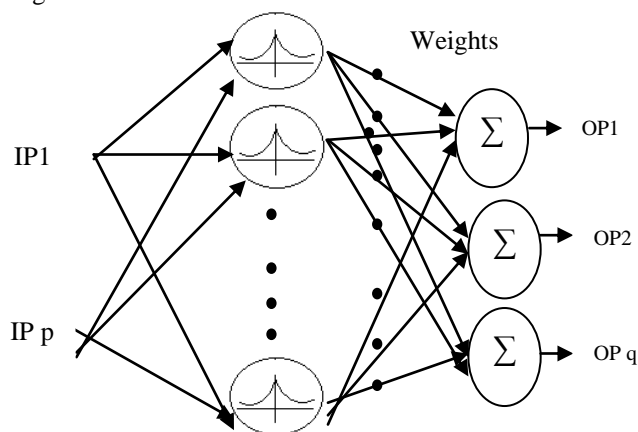

Fig 8. Radial Basis Function Neural Network Architecture

A Radial Basis Function Neural Network has three layers such as the input layer, the hidden layer and the output layer. The input layer in the RBF brings the coordinates of the input vector to each unit in the hidden layer. Activation produced by each unit in the hidden layer using the Radial Basis Function. Then, each unit of the hidden layer processes a linear combination of the activations and creates a classified output in the output layer units. The output depends on the use of the activation function used in the hidden layer and the weights related with the links between the hidden layer and the output layer.

Several learning algorithms available for RBF neural networks . The main applications of RBF is data classification. Majority of the learning algorithms determines the number of units in the hidden layer, the activation functions connected with the hidden units and the weights related with the links between the hidden and output layers.[17] The general mathematical form of the output units in RBF network is as follows:

$$f_j(x) = \sum_{i=1}^{h} w_{i,j}\, r_i(x) \qquad (12)$$

where f$_j$ is the function corresponding to the jth output unit and it is a linear combination of h radial basis functions $r_1, r_2, \ldots\ldots, r_h$.

In this paper, supervised learning algorithm based on gradient descent with momentum is used for training RBF neural networks.

A. Gradient Descent with Momentum

Gradient descent with momentum is implemented to train the RBF neural network to respond to the local gradient and to recent trends in the error surface. Momentum which acts like a low pass filter, permits the network to ignore small features in the error surface. With momentum a network can slide through a shallow local minimum.

Gradient descent with momentum depends on two parameters. The training parameter lr indicates the learning rate and the training parameter mc is the momentum constant that defines the amount of momentum. mc is set between 0 and values close to 1. The value of momentum constant 1 results in a network that is completely insensitive to the local gradient.

GDM can be used to train RBF neural network as long as its net input, weight, and transfer functions have derivative functions. RBF is used to calculate derivatives of performance $perf$ with respect to the weight and bias variables X. The variable can be adjusted based on the gradient descent with momentum,

$$dX = mc * dXprev + lr * (1 - mc) \qquad (13)$$
$$* dperf/dX$$

Where $dXprev$ is the previous change to the weight or bias. Training stops when any of these conditions occurs:
- If it reaches maximum number of repetitions.
- The maximum amount of time is exceeded.
- Performance is minimized to the goal.
- The performance gradient falls below min_grad.
- Validation functioning has increased more than max_fail times since the last time it decreased.

IV. Experimental Results

The tea leaf recognition is considered in the proposed approach. The dataset used in this approach is UPASI dataset. The performance of the proposed approach is evaluated based on the following parameters: Accuracy and Execution time. The different tea leaves taken in the proposed approach is shown in the Table 1.

TABLE I
DIFFERENT TYPES OF TEA LEAVES TESTED IN THE PROPOSED METHOD

Tea leaf name	Tested Samples	Number of Correct Recognition
TRF 1	58	53
UPASI - 3	61	56
UPASI - 9	57	52
UPASI - 10	55	49
UPASI -17	60	53
UPASI - 22	64	61

Table 2 shows the accuracy of the classification algorithms. The accuracy of the proposed Radial Basis Function classification approach is compared with K- Nearest Neighbour classification approach.

TABLE 2
COMPARISON OF THE CLASSIFICATION ACCURACY

Classification Techniques	Accuracy (%)
Radial Basis Function	86.2
K- Nearest Neighbour	78

It is clearly observed from the table 2 that the proposed Radial Basis Function classification approach outperforms the K- Nearest Neighbour classification approach. The accuracy obtained by Radial Basis Function classification is 86.2% whereas the accuracy obtained by the K- Nearest Neighbour is 78%.

TABLE 3
COMPARISON OF THE EXECUTION TIME

Classification Techniques	Time (seconds)
Radial Basis Function	2.02
K- Nearest Neighbour	3.6

Table 3 reveals the execution time of the classification algorithms. The execution time of the proposed Radial Basis Function classification approach is compared with K- Nearest Neighbour classification approach.

It is observed from the table 3 that the proposed Radial Basis Function classification approach takes only 2.02 seconds for execution where as the K-Nearest Neighbour classification approach takes 3.6 seconds.

V.   Conclusion

A new approach of tea leaf classification based on leaf recognition is proposed in this paper. The approach consists of three phases namely the preprocessing phase, feature extraction phase and the classification phase. The image is preprocessed by Dual Tree Discrete Wavelet Transform (DT-DWT) using fuzzy shrinkage rule. The features of leaf are extracted and given as an input to the classifier. Radial Basis Function Neural Network is trained using Gradient Descent with Momentum(GDM). The computer can automatically classify 6 kinds of plants via the leaf images loaded from digital cameras or scanners. The performance of the proposed approach is evaluated based on the accuracy and execution time. The proposed algorithm produces better accuracy and takes very less time for execution. The perfoemance of algorithm can be further improved by incorporating efficient kernel functions and also the performance of the classifiers can be improved.

Acknowledgement

REFERENCES

[1]   Zhihui Sun, Shenglian Lu, Xinyu Guo, Yuan Tian, "Leaf Vein and Contour Extraction from Point Cloud Data", International Conference on Virtual Reality and Visualization, 2011.IEEE DOI 10.1109/ICVRV.2011.40
[2]   J. Pan and Y. He,"Recognition of plants by leaves digital image and neural network", International Conference on Computer Science and Software Engineering, Vol. 4, pp. 906 – 910, 2008.
[3]   Cotton Incorporated USA, The classification of Cotton, 2005, http://www.cottoninc.com/ClassificationofCotton.
[4]   National Institute for Agricultural Botany, Chrysanthemum Leaf Classification. Cambridge, 2005.
[5]   N. Kumar, S. Pandey, A. Bhattacharya and P. S. Ahuja, "Do leaf surface characteristics affect agro bacterium infection in tea" J. Biosci., Vol. 29, No. 3, pp. 309–317, 2004.
[6]   Jamal Saeedi, Mohammad Hassan Moradi, Ali Abedi, "Image Denoising Based on Fuzzy and Intra-Scale Dependency in Wavelet Transform Domain", International Conference on Pattern Recognition, 2010. IEEE DOI 10.1109/ICPR.2010.655.
[7]   Y. Li, Q. Zhu, Y. Cao and C. Wang, "A Leaf Vein Extraction Method based on Snakes Technique," in Proceedings of IEEE International Conference on Neural Networks and Brain, 2005.
[8]   H. Fu and Z. Chi, "Combined thresholding and Neural Network Approach for Vein Pattern Extraction from Leaf Images," IEEE Proceedings-Vision, Image and Signal Processing, Vol. 153, No. 6, 2006.
[9]   J.-X. Du, X.-F. Wang and G.-J. Zhang, "Leaf shape based plant species recognition," Applied Mathematics and Computation, vol. 185, 2007.
[10]   F. Gouveia, V. Filipe, M. Reis, C. Couto and J. Bulas-Cruz, "Biometry: the characterization of chestnut-tree leaves using computer vision," in Proceedings of IEEE International Symposium on Industrial Electronics, 1997.
[11]   Stephen Gang Wu, Forrest Sheng Bao, Eric You Xu, Yu-Xuan Wang, Yi-Fan Chang and Qiao-Liang Xiang, "A Leaf Recognition Algorithm for Plant Classification Using Probabilistic Neural Network", 2007.
[12]   B. Wang, et al., "An investigation of 3D dual-tree wavelet transform for video coding", in Proc. Int. Conf. Image Processing, Singapore, Oct. 2004.
[13]   B. Wang, et al., " Video coding using 3-D dual-tree wavelet transforms", in Proc. Int. Conf. on Acoustics, Speech, and Signal Processing, Philadelphia, Mar. 2005.
[14]   Xiao Gu, Ji-Xiang Du and Xiao-Feng Wang, "Leaf Recognition Based on the Combination of Wavelet Transform and Gaussian Interpolation", Advances in Intelligent Computing, Vol. 3644/2005, pp. 253-262, 2005.
[15]   Jyotismita Chaki and Ranjan Parekh, "", International Journal of Advanced Computer Science and Applications (IJACSA), Vol. 2, No. 10, 2011.
[16]   Ankit A. Bhurane, Sanjay N. Talbar, Preeti N. Gophane, "Comparative Analysis of Conventional, Real and Complex Wavelet Transforms for Face Recognition", International Journal of Computer Applications, Vol 39, No.6,pp. 975 – 8887, February 2012.
[17]   M. Safish Mary, V. Joseph Raj, "Radial Basis Function Neural Classifier using a Novel Kernel Density Algorithm for Automobile Sales Data Classification" International Journal of Computer Applications , Vol. 26,No.6, 0975 – 8887, July 2011.

[18]   M. J. L. Orr, "Introduction to radial basis function networks", Technical report, Center for Cognitive Science, University of Edinburgh, 1996.
[19]   N. G. Kingsbury and T. H. Reeves, "Redundant representation with complex wavelets: how to achieve sparsity", in Proc. Int. Conf. Image Processing, Barcelona, Sept. 2003.
[20]   G.Y. Chen, B. Kegl. Invariant Pattern Recognition using Dual-tree Complex Wavelets and Fourier Features, In: Conference on Image and Vision Computing (IVCNZ 05). Newzealand, 2005.
[21]   Arokia Priya, S.PNarote, and A.V.Patil, "Dual Tree Wavelet Transforms in Image Compression".
[22]   M. Sepasian, W. Balachandran and C. Mares, " Image Enhancement for Fingerprint Minutiae-Based Algorithms Using CLAHE, Standard Deviation Analysis and Sliding Neighborhood", Proceedings of the World Congress on Engineering and Computer Science 2008 WCECS 2008, October 22 - 24, 2008, San Francisco, USA.
[23]   R.Sharmila, R. Uma, "A New Approach To Image Contrast Enhancement using Weighted Threshold Histogram Equalization with Improved Switching Median Filter", International Journal Of Advanced Engineering Sciences and Technologies Vol No. 7, No. 2,pp. 206 – 211, 2011.

Line of Balance

P. A. Badukale[1], Prof. Syed. Sabihuddin[2]

Abstract: *Now-a-days whole world facing competition in every fields, including construction industry. Large construction companies carry out big projects, according to the need of that project, they uses different methods of construction and management. Critical Path Method (CPM), Linear Scheduling Method (LSM), and Line Of Balance (LOB) are the different methods of construction project management. All the construction companies utilize these methods according their utilities and requirement of project. In this report, Line of balance method is explained with its different component on the basis of some related works discussed different alternatives and strategies to sequence activities in the long run. This report contains a study carried out in a construction company in which LOB concept is used in the initial planning phase of a high-rise residential project. Based on the information provided by different LOBs, representing different scenarios, It is further discussed with projects managers, superintendents, and crews the advantages and disadvantages of each scenario regarding the project's lead time, activities cycle time, gang sizes, batch sizes, buffers, sequencing and interferences between activities .*

Keywords: *1 Line of Balance, Preplanning methods of LOB, Advantages, Disadvantages.*

I. Introduction

In different types of construction companies different methods are used for different projects. As the requirement of a project the method like critical path method (CPM), linear scheduling method (LSM), and line of balance (LOB) are applied on it.

The construction industry currently utilizes the Critical Path Method scheduling technique (CPM) to plan and manage most construction projects. This phenomenon is depicted in a study conducted by Tavakoli and Riachi in 1990. In their study, they surveyed the use of CPM scheduling in the top ENR 400 contractors.

For the past three decades, numerous researchers have identified the various intrinsic advantages of the Line of Balance scheduling technique (LOB) in comparison to the CPM. The concept of finding a critical path is another major fundamental difference between LOB and CPM scheduling. Arditi, Tokdemir, and Suh (2001) explained how "In network analysis, at least one critical path exists. Activities which are on the critical path have to be started and completed by their assigned times if the total project duration is not to be extended." The LOB scheduling methods criticalness is based on time and resources, unlike network scheduling where it is only based on time.

The LOB method allows the team to deliver at its maximum speed, by helping balance the different activities in the production chain. In keeping with the idea of using the team's actual performance, we also propose to derive the lead-times for the so called "control points", not from an activity network as in the original LOB formulation, but from the team's "velocity". Line of Balance (LOB) is a method of showing the repetitive work that may exist in a project as a single line on a graph. Unlike a Bar Chart, which shows the duration of a particular activity, a LOB Chart shows the rate at which the work that makes up all of the activities has to be undertaken to stay on schedule, the relationship of one trade or process to the subsequent trade or process is defined by the space between the lines. If one group is running behind schedule, it will impact on the following group and this is shown by the lines intersecting.

The Line-of-Balance then would have a series of stair step offsets. Making those decisions is the job of the management team. Once the Bedding, Laying of Pipe, and Testing of the 1st segment to done, then the Backfill can begin and work continuously. However, the difficulties in using the LOB for scheduling projects have been stripped off from the method when authors have downplayed problems that surround the definition of task durations, the choice of the repetitive unit or batch size, cycle time, and the definition of buffers between tasks.

II. Line Of Balance

A simple diagram in which line shows location and time at which a certain crew will be working on a given operation is known as LOB. it is used on repetitive work such as constructing multiple dwelling units, when used on linear work such as roads and railways the technique is more accurately called Time/Location Charts or Chainage Charts which include 'blocks' to mark out chainages such as bridges and culverts that require substantial time to build and interrupt the general flow of work.

The purpose of the LOB method is to ensure that the many activities of a repetitive production process stay "in balance" that is, they are producing at a pace which allows an even flow of the items produced through a process and at a speed compatible with the goals set forth in a plan. The method does this by calculating how many items should have passed through a given operation or control point, and showing these figures alongside the number that actually did.

The LOB technique is very suitable for repetitive projects like residential buildings, however it may be adapted for non-repetitive projects as well. The main advantages of LOB schedule are its graphical presentation, easy understanding of the schedule and the goals of planning used in it. The research conducted by the authors aims to improve the LOB concepts on building construction and prove its usefulness.

The LOB method helps project managers take corrective actions such as allocating more resources or prioritizing the work when there is still time to do it. In terms of the data required to implement the LOB technique, most of it should be readily available from your defect tracking system or could be derived from it with a few calculations implemented in Excel or any other spreadsheet. Preplanning using the line of balance technique attempts to solve planning problems by making production process clearer and simpler. A preplanning method is presented which needs little detailed information about productivities and work volumes and may be rapidly produced. The plan brings an overall view of the project by grouping the main activities that are highly interdependent. The concept on the best rhythm for each group of activities focus on the sequencie of work, continuity of labor team working and completeness rather than on pure schedule goals. Many characteristics of the method support lean construction concepts, such as waste elimination, variances minimization, flexible planning and scheduling sequencing. Using line of balance concepts also suggests some control tools which are being experimented on aplication cases and are briefly described.

LOB scheduling is superior to the CPM when scheduling projects of a repetitive nature; and these projects capitalize and make use of many of LOB scheduling benefits, and explained how in repetitive projects, LOB scheduling is more beneficial in areas like managing the project resources, visualization of the project schedule, creating schedules more efficiently, managing and updating the schedule, and decreasing the chance of scheduling errors.

The lessons learned from the first jobs helped the efficient use of the developed tools for the planning of new projects and the development of the second stage of the work, which is the LOB application on multi-story building sites as a medium term planning and control tool. The LOB application is imbedded into a new model of planning and control which attempts to solve planning problems by making production control process clearer and simpler. The main idea would be: "let everybody manage his own problems and do not create new problems by managing other people's problems". The line of balance technique has many concepts close to this new model and the research is investigating them on practical site applications.

III. Preplanning Method

Repetitive projects such as multi-story building allow working with rhythmic planning. In this case, in order to find the optimum use of resources, a different type of planning is typically used. Crews and equipment are designed to yield the same production rate, in terms of construction units (i.e., one floor/week, one apartment/week, etc.). If activities are planned to be built in this way, all activities could become critical. Nevertheless, most building projects (even simple building construction projects) are not repetitive ones in all their extent. Thus, an "all activities critical" planning might not be applicable for the whole project. When planning is based in construction units (floors or apartments) and production velocities, fairly repetitive construction subdivisions can be developed. In this case the schedule is developed based on the production velocity, in such a way to generate the same work rhythm for all the involved crews. The number of optimum crews is selected so that all crews will perform the same amount of construction units in the same period of time. This approach is essentially the line of balance concept and was proved successful in the applications described in this paper and by others.

Detailed construction procedures were developed for major construction activities. The fact of working with a repetitive apartment building project eased the work and allowed development of a significant level of detail for the majority of activities on site.

The construction procedures included:
- I) Crew composition
- II) Daily construction volume
- III) Crew sizes
- IV) Required tools and equipment

IV.   Advantages

The Advantages of Line Of Balance is as :

1) Clearly shows the amount of work taking place in a certain area at a specific time of the project.
2) Has the ability to show and optimize the resources used for large number of repeated activities, executed in several zones or locations.
3) Easier cost and time optimization analysis because of all the information available for each activity in the project.
4) Ease of setup and its superior presentation and visualization.
5) Easier to modify, update and change the schedule.
6) Better managing of all the various sub-contractors in the project.
7) Allows for simpler and clearer resource management and resource optimization functions.
8) Visualization of productivity and location of crews.
9) It allows project managers to see, in the middle of a project, whether they can meet the schedule if they continue working as they have been.

V. DISADVANTAGES

1) Inability to generate a clear critical path of the project schedule, relative to the one provided by CPM schedules.
2) Could only be divided by location.
3) In CPM scheduling the user could divide project by location and other systems like trades, in LOB only location.
4) Productivity rates in LOB schedule do not include the effect of crews‟ learning curve, or if the individuals working in the crews changed.
5)

V.   Conclusion

As the Line Of Balance is more suitable than other methods and the study shows the use of LOB as a means to simulate and discuss decisions related to the design of a production system for a multi-storey building and its impacts on daily operations. As the LOBs presented to the Company, project managers, different cultural aspects surfaced regarding the adoption of Lean Construction concepts and presentation of LOB for the purpose of easy understanding is convenient.

Therefore now a days Line Of Balance is more popular method in construction management and adopted by most companies.

References

[1] Ballard, G. (1995). "Toward construction JIT." Proc. 3rd Workshop on Lean Construction, Albuquerque, ed. Luis Alárcon, Santiago, 1997, Chile: Catholic University of Chile, pp. 291 300.

[2] Ballard, G. (1997). "Lookahead planning: the missing link in production control." Proc. 5th Conf. of Lean Construction, pp. 13-25, http://www.vtt.fi/rte/lean/

[3] Lutz, J.D. and Hijazi, A. (1993). "Planning repetitive construction current practice." Construction Management and Economics, 11:99-110.

[4] Melles, B. and Welling, D.T. (1996). "Towards a different view on production control in construction." Proc. 4th Conference on Lean Construction, http://www.vtt.fi/rte/lean/

[5] Mendes Jr., R. (1998). "Modelo em planilha eletrônica para programação de edifícios— novos desenvolvimentos" (in Portuguese), Encontro Nacional de Tecnologia do Ambiente Construído—ENTAC 98, Proc., April, Florianópolis: UFSC, pp. 671-678.

[6] Kemmer, S. L. (2006) "Análise de diferentes tempos de ciclo na formulação de planos de ataque de edifícios de múltiplos pavimentos." (in Portuguese) Master's thesis. Programa de Pós-Graduação em Engenharia Civil. Federal University of Santa Catarina, Florianópolis. 122pp.

Measurement & Analysis of Harmonics & Efficacy of Different Types of Luminaries using Power Harmonic Analyzer

[1]Geena Sharma, [2] Gulshan Kumar

[1](Electrical Engg. Deptt. Baddi University of Emerging Sciences and Technology
Baddi, H.P. 173205, India
[2] (Prof. & Director, Electrical Engg. Deptt. Baddi University of Emerging Sciences and Technology
Baddi, H.P. 173205, India

Abstract: *The aim of this paper is to analyze various power quality indices and luminous efficacy of different types of luminaries (Incandescent Lamp, Fluorescent Lamp, Compact Fluorescent Lamp and Light Emitting Diode). CFLs and LEDs are considered as highly energy efficient luminaries as compared to widely prevalent, low cost incandescent lamps. The replacement of Incandescent Lamps by CFLs and LEDs have resulted in reduction in active power consumption, a reduction in peak current and reduction in distribution system losses. All these aspects have positive impact on energy consumption. However, the other aspect – viz. harmonic distortions in CFLs and LEDs is not being appropriately addressed, which might cause unforeseen problems in the power supply grids, particularly in rural feeders in India. The paper represents comparative analysis of luminous efficacy, distortion power and power factor occurring in different types of luminaries (as defined in IEEE – 1459:2000 Standard).*
Keywords: *Compact Fluorescent Lamps (CFLs), Incandescent Lamp, Light Emitting Diodes (LEDs),*
distortion power, Efficacy.

I. Introduction

The introduction of the paper should explain the nature of the problem, previous work, purpose, and the contribution of the paper. The contents of each section may be provided to understand easily about the paper.

In the recent years, Power Quality (PQ) is emerging as an issue of major concern, (globally as well as nationwide) requiring precise monitoring, in-depth analysis and adoption of planned PQ improvement initiatives. A few years back, the main concern of the electricity was reliability of supply, which could be understood as availability of power at rated voltage and frequency. The present scenario, however, has drastically changed in our country, with a large proportion of the industrial, commercial and domestic load now turning out to be non-linear due to growing use of power electronics, automation, computers and information technology [1]. The term Power Quality, in ideal terms, would refer to an uninterrupted power supply, maintained at rated voltage and frequency (within specified tolerances), and having a pure, undistorted sinusoidal wave shape .PQ problems are complex, and often require detailed diagnosis by an expert team to find an optimum techno-economic solution. In early days Incandescent Lamps were widely used in household and commercial lighting, for portable lighting such as table lamps etc. Incandescent Lamp makes light by heating a metal filament wire to a high temperature until it glows. Incandescent Lamps do not require external regulating equipment and have a low manufacturing cost and work equally well on either alternating current or direct current. But approximately 90% of the power consumed by this lamp is emitted as heat, rather than visible light. Thus due to high energy consumption and low luminous efficacy(lm/W), Incandescent lamps have been replaced in many applications by other types of electric lights such as Fluorescent lamps, CFLs, LEDs. These new technologies improve the ratio of visible light to heat generation. European Union are in process of phasing out the use of Incandescent Lamps in favour of more energy efficient lighting. In United States, federal law has scheduled Incandescent Lamp to be phased out by 2014, to be replaced by more energy efficient lighting. In Brazil these have already been phased out. Fluorescent lamp converts electrical power into useful light more efficiently than an Incandescent Lamp. A fluorescent lamp/tube is a gas discharge lamp and uses electricity to excite mercury vapour. The excited mercury atoms produce short wave ultra violet light, which causes a phosphor to fluoresce, providing visible light. Lower energy cost typically offsets the higher initial cost of this lamp .Now a days these larger Fluorescent lamps have been replaced by CFL, popularly known as energy saving lamp. CFL is a type of fluorescent lamp having electronic ballast and can fit into a fixture of general lighting service incandescent lamp. The electronic ballast of CFL has removed the problems of flickering and slow starting which are associated with magnetic ballast fluorescent lamp. It is well established that integrated CFLs presently being used have longer operating life and

different light spectrum as compared to that of incandescent lamps. On account of their high energy efficiency, CFLs are recently being promoted as an effective measure to reduce average and peak demand. This has led to aggressive promotion of CFLs, and even free distribution/subsidies in some states. Electricity consumers – both rural and urban are being encouraged to replace their existing incandescent lamps with energy saving CFLs to reduce electricity bills. Another energy efficient luminary is LED. LEDs present many advantages over above discussed luminaries such as low energy consumption, longer life time (20,000 – 50,000 hours, which is about 4 to 8 time than that of CFL) , smaller size, faster switching and greater durability and reliability. However, CFLs and LEDs are known to produce high current distortions due to high frequency switching in the electronic ballast [7]. The power quality aspect of these luminaries is an emerging issue requiring attention as excessive harmonic injections by increasing these non linear loads can adversely affect the performance of electrical feeders. In this paper, a true comparison of different types of powers (real, reactive and distortion), power factor (fundamental and distortion) and luminous efficacy are evaluated after detailed experimental work on different types of luminaries.

II.   Experiment

An exhaustive experiment has been carried out as a part of this work using Power and Harmonics Analyzer (PHA) and Lux meter to measure the type and magnitude of different harmonic components and their efficacy for different types of luminaries. The experimental work broadly comprised two parts. These are:
   (i) Measurement of harmonic contents of different luminaries using PHA
   (ii) Measurement of efficacy of different luminaries using Lux meter.

An experimental setup has been developed to measure harmonic contents of each luminary. The measurements has be en carried out using Power and Harmonic Analyzer (PHA) to find rms voltage V, rms current I, active power P, reactive power Q, Apparent power S, Total power factor pf, total harmonic distortion in voltage THD_v and total harmonic distortion in current THD_i. Power and Harmonic Analyzer (PHA) is a special purpose, graphic-based, true rms instrument. It can analyze ac voltage and current harmonics up to 99th order along with other important electrical parameters like active, reactive and apparent power, power factor, energy, average demand and maximum demand etc. The instrument consists of 512 KB memory, programmable CT/PT, an RS-232 interface and has the capability to save the captured data.

III.   Analysis Of Distortion Power In Cfl

In harmonic environment, the apparent power is given by:

$$S = V_{rms}\ I_{rms} \qquad\qquad\qquad (1)$$

where

$$V_{rms} = \sqrt{V_1^{\,2} + V_2^{\,2} + V_3^{\,2} + \cdots} \qquad\qquad (2)$$

$$= \sqrt{\sum_{h=1}^{\infty} V_h^{\,2}} \qquad\qquad\qquad (3)$$

Similarly,

$$I_{rms} = \sqrt{\sum_{h=1}^{\infty} I_h^{\,2}} \qquad\qquad\qquad (4)$$

According to IEEE-1459 Standard [4] , rms voltage and current can be decomposed into fundamental and harmonic components as below:

$$V_{rms} = V_1^{\,2} + V_h^{\,2} \qquad\qquad\qquad (5)$$

$$I_{rms} = I_1^{\,2} + I_h^{\,2} \qquad\qquad\qquad (6)$$

The total apparent power can then be expressed as

$$S^2 = (V_{rms}\ I_{rms})^2 \qquad\qquad\qquad (7)$$

$$= S_1^{\,2} + S_N^{\,2} \qquad\qquad\qquad (8)$$

In above equation, S_N is non-fundamental apparent power which comes into picture due to the presence of harmonic frequencies either in voltage or current waveform .An approach suggested by Emanuel decomposes total apparent power S as below [6]:

$$S^2 = (P_1 + P_H)^2 + Q_1^{\,2} + Q_H^{\,2} \qquad\qquad (9)$$

$$= S_1{}^2 + S_N{}^2 \qquad\qquad (10)$$

The term P_H is harmonic active power which rarely exceeds 0.005 P_1 and thus can be safely ignored. This indicates that there is negligible contribution to real power due harmonic frequencies. Q_1 is fundamental reactive power (var) and Q_H is non-fundamental or harmonic reactive power flow due to non-linear load. In harmonic analysis, an important quantity – Total Harmonic Distortion (THD) in voltage and current is expressed as:

$$THD_V = \frac{V_H}{V_1} = \sqrt{\left(\frac{V_{rms}}{V_1}\right)^2 - 1} \qquad\qquad (11)$$

$$THD_I = \frac{I_H}{I_1} = \sqrt{\left(\frac{I_{rms}}{I_1}\right)^2 - 1} \qquad\qquad (12)$$

The concept of power factor in harmonic domain is also modified to take into account voltages and currents of different frequencies . The total power factor is defined as:

$$pf_{tot} = \frac{Total\ Real\ Power\ P}{Total\ Apparent\ Power\ S} \qquad\qquad (13)$$

$$= \frac{P_1}{V_{rms} \cdot I_{rms}}$$

$$Also, V_{rms} = V_1 \cdot \sqrt{1 + \left(\frac{THD_V\ in\ \%}{100}\right)^2}, \&$$

$$I_{rms} = I_1 \cdot \sqrt{1 + \left(\frac{THD_I\ in\ \%}{100}\right)^2}$$

Assuming THD_V to be less than 10 %, which is generally the case in power system networks as well as in our above experimental work, the total power factor can be expressed as:

$$\frac{P_1}{V_1 I_1 \sqrt{1 + \left(\frac{THD_I\ in\ \%}{100}\right)^2}} \qquad\qquad (14)$$

$$= pf_{disp} \cdot pf_{dist} \qquad\qquad (15)$$

In above expression, the first term is known as fundamental or displacement power factor and second term is known as distortion power factor.

The measurements were carried out using Power and Harmonic Analyzer to find rms voltage, current, P, Q, S, total pf, and THD in voltage and current for different make of CFLs. Subsequently, the results were obtained by a MATLAB script using Emanuel method of distortion power analysis.

Various steps for assessment of distortion power and distortion power factor will include:
  (i) Input of the data from Power & Harmonics Analyzer (i.e. V, I, THD, S, P,   Q, pf)
 (ii) Calculation of Fundamental and Harmonic Voltage and Current from   the measured data.
 (iii) Analysis of total apparent power in different luminaries as per IEEE -   1459 Standard.
- Fundamental Apparent power
- Non-fundamental Apparent power
- Voltage distortion power
- Current distortion power
- Harmonic Apparent power
  (iv) Calculation of Fundamental and Harmonic
     Active (Real) powers.
  (v) Computation of fundamental and harmonic
     reactive powers as per Emanuel's method.
   (vii) Computation of Fundamental and Distortion
     Power factors.

IV. Results

The comparative analysis of distortion power, power factor and luminous efficacy of different types of Luminaries at rated voltage (230 V) is tabulated below:

TABLE 1 Distortion Power Analysis of Different Types of Luminaries

S. No.	Luminaries Parameter	Type Of Luminaries			
		GLS	*Fluorescent Lamp*	*CFL*	*LED*
1	Nominal rms Voltage applied across Luminary V (V)	230.4	229.9	229.5	231.6
2	Total rms Current flowing Through Luminary I (A)	0.680	1.245	0.744	0.174
3	Voltage THD at Luminary terminals (%)	7.7	10.4	7.3	7.7
4	Current THD in Luminary load (%)	9.2	13.9	21.1	65.8
5	Fundamental rms Voltage V_1 (V)	229.72	228.6	228.89	230.68
6	Harmonic rms Voltage V_H (V)	17.6884	24.4	16.71	18.2238
7	Fundamental rms Current I_1 (A)	0.6771	1.234	0.7280	0.1454
8	Harmonic rms Current I_H (A)	0.0623	0.165	0.1536	0.0956
9	Total apparent power S (VA)	155	286.3	169	39
10	Fundamental apparent power S_1 (VA)	155.5527	282.1	166.6261	33.5308
11	Non-fundamental apparent power S_N (VA)	13.101	48.86	28.2269	9.9170
12	Total active power P (W)	156	160	164	10
13	Fundamental active power P_1 (W)	156	160	164	10
14	Harmonic active power P_H (W)	0	0	0	0
15	Total reactive Power Q (var)	0	- 0.237	44	38
16	Fundamental reactive power Q_1 (var)	11.805	232.3	29.466	32.3
17	Non-fundamental reactive power Q_H (var)	13.101	232.2	28.2269	19.9170
18	Total power factor	1	0.57	0.97	0.23
19	Fundamental power factor	1	0.56	0.9842	0.2684
20	Distortion power factor	0.9971	0.316	0.9855	0.8569
21	Prominent Harmonic order	5th	3rd	7th	3rd
22	**Luminous Efficacy(lumens/ W)**	1.83 (min.)	9.725	10	34.78 (max.)
23	Peak Factor	1.32	1.26	1.318	1.32

V. Conclusion

- It is concluded from that Power Quality is emerging as an issue of major concern, globally as well as nationwide, requiring precise monitoring, in depth analysis and adoption of planned power quality improvement initiatives.
- Power quality problems depend on the quality of the voltage supplied by the utility, the types of loads in installation and the sensitivity of the equipment to various kinds of disturbances. There is no single generic solution for this problem. An optimum techno-economic solution needs to be designed for each site, taking into account the above three interacting factors.
- The power supply system can only control the quality of the voltage; it has no control over the currents that particular loads draw. Therefore, standards in the power quality area are devoted to maintain the supply voltage within limits. There is always a close relationship between voltage and current in any practical systems. Although the generators may provide a near-perfect sine wave voltage, the current passing through the impedance of the system can cause several disturbances to the voltage.
- Various power quality problems are transients, voltage variations (interruption , sags, swells, over voltage , under voltage, fluctuations), voltage imbalance, wave-from distortion , power frequency variation etc.

- Harmonics are one of the primary types of wave-form distortion. Harmonic distortion originates due to the non-linear characteristics of the devices and the loads on the power system. Energy shortage continues to disturb the power sector due to demand-supply mismatch,
- The state electricity boards of India have recognized that the use of CFLs can effectively meet DSM objectives. This has led to aggressive promotion of CFLs. However, CFLs are known to produce high current distortion due to   high frequency switching in the electronic ballasts.
- Luminous efficacy of LED is highest among all the luminaries tested in this experiment, but power factor. of LED is very poor which give negative impact on the power   quality.

REFERENCES

[1]   D. Matvoz and M. Maksić "Impact of Compact   Fluorescent Lamps on the Electric Power Network "International Conference on Harmonics and Quality of Power, Wolongong, NSW, 2008

[2]   Rangan Banerjee, "Energy   Efficiency   and   DSM", Integrated   Energy Policy Committee, Govt. of India, 2005.

[3]   J. Cunill-Sola   and   M. Salichs, "Study   and Characterization of Waveforms   from   Low-Watt (< 25 W) Compact Fluorescent Lamps with   Electronic Ballasts", IEEE Trans. Power Delivery, vol. 22, no. 4, Oct. 2007, pp. 2305-2311.

[4]   IEEE Trial-Use   Standard   Definitions   for the   Measurement of Electric   Power   Quantities Under Sinusoidal, Nonsinusoidal, Balanced or un-balanced Conditions, IEEE Std. 1459, Jan. 2000.

[5]   Czarnecki, L.S., "What   is   Wrong with Budeanu's Concept of Reactive and   Distortion   Power and   Why it   Should   be   Abandoned," IEEE   Transactions on   Instrumentation   and   Measurement, Vol. IM-36, No. 3, Sept. 1987.

[6]   Emanuel, A.E.., "On   the   Assessment   of Harmonic Pollution", IEEE   Transactions   on   Power Delivery, Vol. 10, No. 3, July 1995,   pp. 767-772.

[7]   A. M. Blanco and E. E. Parra "Effects of High Penetration of CFLs and LEDs on the Distribution Networks." International Conference on Harmonics and Quality of Power, Bergamo, 2010

[8]   Santoso, Surya, Dugan, R.C.,McGranaghan, M.F., Beaty, H.W.,"Electrical Power System Quality", McGraw-Hill, Second Edition, 2003.

Product Marketing Management Services In. Pln (Persero) In Manado

Meike D. Mament

Faculty of Economics, University of Manado - Indonesia

Abstract: *This study was conducted to determine how much influence marketing management product to the consumer's decision to buy the product in smart electrical services at PT. PLN (Persero) Manado area. The method used methods of quantitative analysis. The data analysis using the analysis of a single table and then testing the hypothesis using the Spearman Rank correlation studies seeking a relationship between two variables, namely the relationship between the variables X (Management product marketing services) and variable Y (Decision consumers). The population in this study amounted to 202 is a consumer and a sample of 67 respondents taro Yamane with a confidence level of 90%, 10% precision. Based on the results of the calculation of Spearman rank correlation coefficient, ie rs = 0.97, prove that there is a positive effect of the variable X (product marketing management services) with variable Y (Decision consumers) in a smart buying electrical products at. PLN (Persero) Manado area. The calculation of the coefficient of determination: (Kp = (rs) 2 x 100%) which shows the influence of variable X (Management product marketing services) with variable Y (Decision consumer) to purchase the product. The results obtained indicate Kp is equal to 94%, meaning that the presence of a smart electrical product marketing promotions, consumers / communities interested in using / buying smart electricity for their lighting needs at PT PLN (Persero) Manado Area. This is due to the influence of marketing management services to market products through smart electrical products marketing campaign that is sebsar 94%, while the remaining 6% is influenced by other factors not examined.*
Keywords: Product Marketing Management Services, Consumer Decision.

I. Introduction

Marketing management services smart electrical products depending on the results of the promotion of the product being marketed . Investment resources and increasing industrial operations to determine the level of consumption of electrical products for the smart , the role of innovation management is very important in determining the progress and market the products of a company . Each company is expected to have the right product management strategies to market their products to the public . Modern marketing strategy is not only oriented towards the development of a good product , but must be able to influence the prospective customers to be loyal kosemen . PLN should always be able to meet the needs of consumers so that consumers feel the maximum satisfaction . PT PLN (Persero) is a State -owned company engaged in the field of electricity , is the only state electricity company in Indonesia . PLN should always be able to meet the needs of the consumer as a requirement that must be met . In view of what happened today , every company is required to develop its productivity , for the PLN seeks to develop productivity in the supply of electricity . Seeing the number of consumer complaints regarding electrical service for this , it is necessary to increase innovation to satisfy customers and attract potential customers . Therefore, the company offers innovative products and services are implemented throughout the service unit or a Power Smart Prepaid Electric . How can a way to introduce a product innovation that is smart electrical products to the public , of course, with the management strategy of the company's marketing campaign . There are various marketing promotion strategies undertaken by companies to develop their products . However, researchers interested in research focused on strategies advertising campaigns run by PT . PLN (Persero) Manado area in terms of influencing consumers to use the product innovation Electric Smart . Kotller & Keller (2005:249) explains that the advertising / ads are all forms of non-personal presentation and promotion of the idea, goods or services of a particular sponsor of the company . Therefore , the need for information of interest through advertising so that consumers teratrik and decide to buy the product.

The use of electricity initially manually , electricity consumers are already accustomed to make use of the manual so that consumers sometimes do not feel attracted to smart electrical products . Beside that , because

at the time postpaid electricity usage , which will be the registrar meters assigned to record the customer for monthly usage meter , so after switching to smart electricity (prepaid electricity) meter registrar no longer get a job as usual . This causes the registrar meters take keutungan in other ways (not all cater, but only in part) , which would certainly damage the reputation of PLN . Sometimes they are looking for customers who will perform a new installation or a change of power at a cost that is not in accordance with the provisions of PLN , which means that they are very expensive to burden the cost to consumers or potential consumers on the condition that they would take care of all procedures and customers or potential customers just accept the results only . Without thinking and without knowing the actual cost information , consumers or potential consumers directly gave them to cater it. They are called illegal or unscrupulous third parties who are not responsible for (brokers) who actually should be anticipated .

Thus there are difficulties in mnemasarkan / promote a new product that is Smart Power products due to consumer confidence in the new connection fee and change the power is interrupted . In addition , also caused by illegal elements who deceive the public and because of the familiarity of consumers use electricity manually so that promotional advertising for the product need to inform ditingkatan advantage of smart electrical products . Because of the fact that there where of all electricity customers in PT PLN (Persero) Area Manado Manado Area with a population amounting to 407 473 inhabitants or - / + the number of customers approximately 32,000 families (KK) , is approximately 12,883 (40 , 25 %) customer households in the Manado area using smart electrical products , while the expectations to be achieved is the use of smart electricity evenly by 100 % has not been achieved , because there are approximately 59.75 % were not using smart electricity and will be pursued by PT PLN (Persero) Manado area for migrating

Advertising management is needed to market the product. The word comes from the Greek ads, which means less is more "lead people to the idea". The comprehensive understanding of advertising according to Kotler (2003), Advertising is "any form of presentation and promotion of ideas, goods or services by a non-personal links that require certain payments". Advertising merupakn a mass communication process that involves certain links, namely the advertisers (advertisers), which pays a mediamassa services for broadcasting the ad.

Targeted advertising is possible to market the product. Advertising (Advertising): It is the main tool for employers to influence consumers. Advertising can be done by employers through newspapers, radio, magazines, brochures, television, or in the form of posters mounted alongside a road or strategic places.

Consumer decision to purchase a product is to choose a product that is needed and in accordance with the purchasing power of consumers . After seeking and evaluating a range of alternatives to meet the needs of consumers at some point have to decide between buying or not buying , if the decision is to buy , the consumer must make a series of decisions related to brand , price , place of sale , colors , and other appropriate needed . Purchasing decisions according to Philip Kotler (2000:202) distinguishes five played the role in the purchase decision , namely : (1) Originator : someone who first proposed the idea to buy a good or service , (2) Giving effect : a person who views or decisions affecting the target (3) the decision maker : someone who takes a decision for each component purchasing decision (4) Buyer : the person doing the actual purchase , and (5) Users : people who consume or use the goods or services concerned . Furthermore, according to the theory AIDCDA , to make consumers interested in purchasing a product that stimulates action successful advertising buyers to buy products according Rhenald (1995) , should at least meet the criteria AIDCDA namely : (1) Attention ang containing attractiveness (2) Interest -containing attention and interest (3) desire which gave rise to a desire to try or have (4) conviction that raises confidence in the product (5) Decision which produces satisfaction with the product purchased and (6) Action that leads to action to buy the product . With advertising manajemn the underlying theory of consumer purchase decisions heavily influenced by management pemasarana products produced

II. Research Methodology

The method used is descriptive method kuantiutatif used to describe the data obtained from empirical observation and data collection . According to Maman (2002) : a descriptive study sought to describe a social phenomenon and analyze the data in a way to describe or depict the data collected and presented data obtained . The method used quantitative analysis methods with techniques of data analysis using the analysis of a single table and then testing the hypothesis using the Spearman rank correlation research method , the population / target of this research is the consumer of PT PLN (Persero) Manado area is determined by the researchers that consumer 202 obtained from product marketing promotional activities . Sample of 67 respondents taro Yamane with sampling techniques used are : Convenient or accidental sampling (samples incidentally) , the method of sample selection regardless of population characteristics . Who's coming and affordable by researchers sampled (Prasetya Irawan , 1999:182) . This study uses Spearman Rank Correlation studies with the formula rs = formula $rs = \frac{\sum x2 \, \Sigma y2}{2\sqrt{\Sigma x2 \, \Sigma y2}}$

III. Results

The data analysis in this study was done by the analysis of a single table and then testing hypotheses. To analyze the single table in this study using the technique of percentage with the formula: P = F / N x 100%. This study uses correlation study Spearman Rank, formula $rs = \frac{\sum x2\ \Sigma y\ 2}{2\sqrt{\Sigma x\ 2\ \Sigma y\ 2}}$, the search for a relationship between two variables, namely the relationship between the variables X (Advertising Promotion Management) and variable Y (Consumer Buying Decisions Product). Before we entered the Spearman Rank calculations, starting with the provision of the ranking variables X and Y variables to obtain results Σd2. The calculations are as follows:

Table.1
Calculation $\sum d^2$

No.	X *(Rx)*	Y (Ry)	di	di^2
1	31 (6)	31 (2)	4	16
2	37 (12)	34 (5)	7	49
3	30 (5)	34 (5)	0	0
4	39 (14)	37 (8)	6	36
5	33 (8)	35 (6)	2	4
6	29 (4)	35 (6)	-2	4
7	33 (8)	34 (5)	3	9
8	30 (5)	32 (3)	2	4
9	38 (13)	33 (4)	9	81
10	35 (10)	35 (6)	4	16
11	29 (4)	35 (6)	-2	4
12	28 (3)	33 (4)	-1	1
13	37 (12)	33 (4)	8	64
14	31 (6)	34 (5)	1	1
15	26 (2)	36 (7)	-5	25
16	29 (4)	31 (2)	2	4
17	31 (6)	35 (6)	0	0
18	33 (8)	38 (9)	-1	1
19	33 (8)	35 (6)	2	4
20	28 (3)	37 (8)	-5	25
21	36 (11)	39 (10)	1	1
22	30 (5)	39 (10)	-5	25
23	34 (9)	37 (8)	1	1
24	36 (11)	35 (6)	5	25
25	34 (9)	37 (8)	1	1
26	25 (1)	37 (8)	-7	49
27	30 (5)	32 (3)	2	4
28	38 (13)	36 (7)	6	36
29	30 (5)	34 (5)	0	0
30	39 (14)	36 (7)	7	49
31	35 (10)	29 (1)	9	81
32	29 (4)	32 (3)	1	1
33	32 (7)	40 (11)	-4	16
34	34 (9)	32 (3)	5	25
35	35 (10)	37 (7)	3	9
36	32 (7)	34 (5)	2	4
37	29 (4)	39 (10)	-6	36
38	33 (8)	33 (4)	4	16
39	33 (8)	42 (12)	-4	16
40	30 (5)	39 (10)	-5	25
41	39 (14)	36 (7)	7	49
42	29 (4)	35 (6)	-2	4
43	28 (3)	40 (11)	-8	64
44	29 (4)	31 (2)	2	4

45	26 (2)	39 (10)	-8	64
46	33 (8)	39 (10)	-2	4
47	30 (5)	39 (10)	-5	25
48	39 (14)	36 (7)	7	49
49	36 (11)	40 (11)	0	0
50	39 (14)	36 (7)	7	49
51	37 (12)	37 (8)	4	16
52	31 (6)	29 (1)	5	25
53	32 (7)	38 (9)	-2	4
54	30 (5)	37 (8)	-3	9
55	39 (14)	36 (7)	7	49
56	28 (3)	40 (11)	-8	64
57	33 (8)	38 (9)	-1	1
58	33 (8)	39 (10)	-2	4
59	35 (10)	39 (10)	0	0
60	30 (5)	40 (11)	-6	36
61	36 (11)	34 (5)	6	36
62	29 (4)	37 (8)	-4	16
63	31 (6)	29 (1)	5	25
64	37 (12)	36 (7)	5	25
65	33 (8)	34 (5)	3	9
66	28 (3)	33 (4)	-1	1
67	33 (8)	34 (5)	3	9
	2177	2387		$\sum d^2$1409

Furthermore, since there is a rank-numbered the same ranking on variable X and Y, it is necessary to factor the following correction: Correction Factor Calculation Variable X.

Table 2
Variable X Factor Correction

Same score	Total/ Jumlah	$t^3 - t / 12$
2	2	0.6
3	5	10.4
4	8	42.7
5	9	60.8
6	5	10.4
7	3	2.2
8	11	111
9	3	2.2
10	4	5.3
11	4	5.3
12	4	5.3
13	2	0.6
14	6	18
	Tx	**274.8**

Calculation of Correction Factors Variable Y

Table3
Correction factor variable Y

Same score	Total/ Jumlah	$t^3 - t / 12$
1	3	2.2
2	3	2.2
3	4	5.3
4	5	10.4

5	9	60.8
6	8	42.7
7	9	60.8
8	8	42.7
9	3	2.2
10	9	60.8
11	5	10.4
	Ty	**300,5**

With the twin figures in the variable x and variable y, then the formula to be used is:

$$\mathbf{r_s} = \frac{\mathbf{\Sigma x^2 + \Sigma y^2 - \Sigma di^2}}{\mathbf{2 \sqrt{\Sigma x^2 \Sigma y^2}}}$$

To get the value $\mathbf{\Sigma x^2}$ **dan** $\mathbf{\Sigma y^2}$ and then use the following formula:

$$\mathbf{\Sigma x^2} = \frac{\mathbf{N^3 - N}}{\mathbf{12}} - \mathbf{\Sigma Tx}$$

$$\Sigma x^2 = \frac{67^3 - 67}{12} - 274,8 \qquad \mathbf{\Sigma x^2 = 24783,2}$$

After $\mathbf{\Sigma x^2}$ ie 24783.2, then the next we specify $\mathbf{\Sigma y^2}$:

$$\mathbf{\Sigma y^2} = \frac{\mathbf{N^3 - N}}{\mathbf{12}} - \mathbf{\Sigma Ty}$$

$$\Sigma y^2 = \frac{67^3 - 67}{12} - 300,5 \qquad \Sigma y^2 = \mathbf{24757,5}$$

Then the Spearman Rank Correlation can be calculated as follows:

$$\mathbf{r_s} = \frac{\mathbf{\Sigma x^2 + \Sigma y^2 - \Sigma di^2}}{\mathbf{2 \sqrt{\Sigma x^2 . \Sigma y^2}}}$$

$$r_s = \frac{24783,2 + 24757,5 - 1409}{2 \sqrt{24783,2 . 24757,5}}$$

$r_s = $ 48131,7 / 49540,7 $\qquad$ **r_s= 0,97** $\qquad$ **r_s^2= 0,97² = 0,94**

To examine the strength of the relationship, use the formula Guilford (Sugiyono, 2002: 149): from 0.00 to 0.199 = Relationships Very Low
0.20 to 1.399 = Relationships Low
0.40 to 0.599 = Medium Relationships
From 0.60 to 0.799 = Strong Relationships
0.80 to 1.00 = Very Strong Relationship , by knowing the coefficients (rs) = 0.97; hence based on the guidelines provided Sugiyono (2002:149), it is known relationship between the two variables and Advertising Campaign Management in the Consumer Decision smart buying electrical products for the foreign Manado area is very strong and direct. To measure how much influence advertising campaign management for consumer decisions in purchasing products listrk clever, done by finding the coefficient of determination (Kp), then the formula used is as follows: **Kp = $(r_s)^2$ x 100 %**
Kp = $(r_s)^2$ x 100%
Kp = $(0,97)^2$ x 100%
Kp = 0,9409 x 100% $\qquad$ **Kp = 94,09** or **Kp = 94 %**

Kp obtained from the calculation of 94%, meaning that the consumer's decision to buy a smart power products at PT PLN (Persero) Manado area affected by the advertising campaign management sebsear 94%, while the remaining 6% is influenced by other factors such as friends, family, environment, and others. To determine whether the relationship between Advertising Campaign Management (variable X) and Decision Consumers buy products (variable Y) in Manado Area PLN significant or not, it is necessary to test the hypothesis that would prove that the promotion of good will influence consumer purchase decisions. Hypothesis testing can be done in the following way:

Ho: rs ≤ 0 = meaning no significant effect between advertising campaign management with consumer decisions to purchase products on the smart electricity company PT PLN (Persero) Manado area, or the opposite effect.

Ha: rs> = 0 means that there is a significant positive effect between the management of advertising campaigns in the consumer's decision to buy a smart power products at PT PLN (Persero) Manado area.

In determining acceptance or rejection of hypotheses, it must be sought by determining the value of ttabel degree of freedom (df) in the following manner:

df = n-2

df = 67-2

df = 65

α = 0.05, and to set the value of t it is necessary to use the following formula:

$$t = \frac{r_s \sqrt{n-2}}{\sqrt{1-r^2}}$$

$$t = \frac{0,97 \sqrt{67-2}}{\sqrt{1-0,94}}$$

$$t = 7,8 / 0,24 \quad = \quad t_{hitung} = 32,5$$

Once we determine the amount of 32.5 t then we will determine which will be obtained from the t table t distribution with α ½ opportunities. Ttabel value obtained from:

df = 65

α = 0,05

= 1- $^{1}/_{2}$ (0,05)

= 1-0,025m **= 0,975**, df = 65, table = 2.00 (see the t distribution table, because it is not listed in the list tebel 65 numbers, then look for the number that is closest to 65 is 60. ttabel so obtained is 60 = 2.00)

Gambar 1
Distribusi t
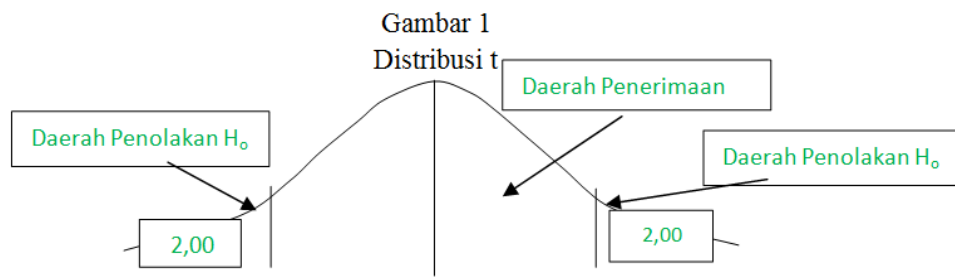
Thus there is a relationship between product marketing management services to the promotion of electric smart advertising to consumers in the purchase decision of a smart electrical products for the foreign Manado area, or significant relationships / mean.

IV. Conclusion

Marketing management through smart electricity darting through advertising campaigns snagat determine consumers to buy smart electrical products . Management needs to be improved smart electrical products to market . The result shows Spearman rank correlation coefficient , ie rs 0.97 , proving that there is a positive effect of the variable X (pemasran Promotion Management) with a variable Y (Consumer Decision) in a smart buying electrical products at PT PLN (Persero) Manado area . The result shows the coefficient of determination , the amount of influence which the presence of the role of advertising campaign management product then the consumer can buy / use smart electrical products . Results obtained Kp is equal to 94 % , meaning that the consumer 's decision to purchase a smart electrical products at PT PLN (Persero) Manado area affected by the advertising campaign management by 94 % , while the remaining 6% is influenced by other factors such as family impetus , encouragement friend and the environment . We advise the company can market the product well in order to influence consumers in a smart buying electrical products . Companies

should be wary of illegal elements , as well as enhance the security and confidence of consumers or potential consumers as unscrupulous illegal (brokers) are circulating everywhere that would damage the reputation of the product of PT . PLN Manado area . In addition to the need for intensive control of smart electricity to customers in order to minimize fraud do illegal elements in the name of PLN melayanai can deceive consumers and society .

REFERENCES

[1]   Djayakusumah . AIDCDA theory . Volume of First Instance . Jakarta . King Grafindo PT Persada . 1982
[2]   dts7.blogdetik.com/tag/promosi-periklanan . Downloaded on May 1, 2013
[3]   Kasali . AIDCDA criteria . Volume the First . Jakarta . PT Bumi Aksara.1995 .
[4]   Kotler , Philip.Manajemen terjemahan.Edisi Millennium Campaign , vol 1 . Jakarta . PT . Prenhallindo . 2002
[5]   Kotler , Philip.Marketing Management Analysis , Planning , and Control . Volume I. Index of Jakarta . .2006 . Gramedia Group.
[6]   Maman . Research Methods . Jakrta . Erland . , 2002.
[7]   Nawawi . Singarimbun . Survey Research and Data Analisys . Jakarta . Gramedia.1995 .
[8]   Nur Indriantoro . Bambang Supomo . Survey Research Methods . Jakarta . Library LP3ES Indonesia.2002
[9]   Prasetya Irawan . Sampling techniques . Bandung . PT Graha . , 1999.
[10]   Singarimbun & Efendi . Survey Research Methods , Data Analisys . Jakarta . LP3ES . , 1995.
[11]   Sugiyono . Research Methods . Yogyakarta . ANDI . , 2004.
[12]   William Wells , John Burnett and Sandra Moriart.Media Advertising . Jakarta . PT Grafindo . , 2006.
[13]   Document: Government Regulation No. 10 . 1989 About Providers and Utilization of Electricity.
[14]   Document: Act No. 20 of 2002 on Electricity.

Time Dependent Quadratic Demand Inventory Models when Delay in Payments is Acceptable

R. Venkateswarlu[1], M. S. Reddy[2]

[1]*GITAM School of International Business, GITAM University, Visakhapatnam – 530 045, India*
[2]*BVSR Engineering College, Chimakurthy - 523 226, India*

Abstract: *An EOQ model is constructed for deteriorating items with time dependent quadratic demand rate. It is assumed that the deterioration rate is constant and the supplier offers his retailer the credit period to settle the account of the procurement units. To solve the model it is further assumed that shortages are not allowed and the replenishment rate is instantaneous. We have presented the models under two different scenarios, viz., (i)the offered credit period is less than or equal to the cycle time and (ii) the offered credit period by the supplier to the retailer for settling the account is greater than cycle time. The objective is to minimize the retailers total inventory cost. Salvage value is also taken to see its effect on the total cost. A numerical example is given to study the effect of allowable credit period and the total cost of the retailer.*

Key words: *Quadratic demand, perishable, constant deterioration, trade credit, holding cost.*

I. Introduction

It is well known that 'trade credit policy' is the most effective way of a supplier to encourage retailer to buy more goods and to attract more retailers. Trade credit can also be used as a multi-faceted marketing management (or relationship management) tool which gives some information to the market or to a buyer about the firm or its products or its future plans. The EOQ model developed by Wilson was based on the assumption that the retailer will pay for the items as soon as it is received by the system. In reality the supplier may offer some credit period to the retailer to settle the accounts in a reasonable time period. Thus the delay in payment can be treated as a kind of price discount to the retailer.

The relationship between inventory policy and credit policy in the context of the classical lot size model was studied by Haley and Higgins (1973). Chapman et al. (1984) developed an economic order quantity model which considers possible credit periods allowable by suppliers. This model is shown to be very sensitive to the length of the permissible credit period and to the relationship between the credit period and inventory level. Davis and Gaither (1985) developed optimal order quantities for firms that are offered a one time opportunity to delay payment for an order of a commodity. A mathematical model is developed by Goyal (1985) when supplier announces credit period in settling the account, so that no interest charges are payable from the outstanding amount if the account is settled within the allowable delay period. Shah et al. (1988) extended the above model by allowing shortages. Mandal and Phaujdar (1989a, b) have studied Goyal (1985) model by including interest earned from the sales revenue on the stock remaining beyond the settlement period. Carlson and Rousseau (1989) examined EOQ under date terms supplier credit by partitioning carrying cost into financial cost and variable holding costs. Chung and Huang (2003) extended Goyal (1985) model when replenishment rate is finite. Dallenbach (1986, 1988), Ward and Chapman (1987), Chapman and Ward (1988) argued that the usual assumptions as to the incidence and the value of the inventory investment opportunity cost made by the traditional inventory theory are correct and also established that if trade credit surplus is taken into account, the optimal ordering quantities decreases rather than increase. Chung (1998) established the convexity of the total annual variable cost function for optimal economic order quantity under conditions of permissible delay in payments. Jamal et al. (2000) discussed the problem in which the retailer can pay the supplier either at the end of credit period or later incurring interest charges on the unpaid balance for the overdue period. Sarker et al. (2001) obtained optimal payment time under permissible delay in payments when units in an inventory are subject to deterioration. Abad and Jaggi (2003) considered the seller-buyer channel in which the end demand is price sensitive and the supplier offers trade credit to the buyer. Shinn and Hwang (2003) dealt with the problem of determining the retailer's optimal price and order size simultaneously under the condition of order size dependent delay in payments. It is assumed that the length of the credit period is a function of the retailer's order size and also the demand rate is a function of the selling price. Chung et al. (2005) determined the

economic order quantity under conditions of permissible delay in payments where the delay in payments depends on the quantity ordered when the order quantity is less than the quantity at which the delay in payments is permitted, the payment for the item must be made immediately. Otherwise, the fixed credit period is allowed. Huang (2007) examined optimal retailer's replenishment decisions in the EOQ model under two levels of trade credit policy by assuming that the supplier would offer the retailer partially permissible delay in payments when the order quantity is smaller than a predetermined quantity. Teng et. al. (2007) derived retailer's optimal ordering policies with trade credit financing.

The literature is replete in the field of trade-credit. Previously several economic order quantity inventory models were developed with trade-credit and a very few production inventory models were developed under allowable delay in payment. All these works were based on the assumption that the demand rate is either linear or exponential function of time. Several authors argued that, in realistic terms, the demand need not follow either linear or exponential trend. So, it is reasonable to assume that the demand rate, in certain commodities, is due to seasonal variations may follow quadratic function of time [i.e., $D(t) = a + bt + ct^2$; $a \geq 0, b \neq 0, c \neq 0$]. The functional form of time-dependent quadratic demand explains the accelerated (retarded) growth/decline in the demand patterns which may arise due to seasonal demand rate (Khanra and Chaudhuri (2003). We may explain different types of realistic demand patterns depending on the signs of *b* and *c*. Bhandari and Sharma (2000) have studied a single period inventory problem with quadratic demand distribution under the influence of marketing policies. Khanra and Chaudhuri (2003) have discussed an order-level inventory problem with the demand rate represented by a continuous quadratic function of time. It is well known that the demand for spare parts of new aero planes, computer chips of advanced computer machines, etc. increase very rapidly while the demands for spares of the obsolete aero planes, computers etc. decrease very rapidly with time. This type of phenomena can well be addressed by inventory models with quadratic demand rate. Sana and Chaudhuri (2004) have developed a stock-review inventory model for perishable items with uniform replenishment rate and stock-dependent demand. Recently, Ghosh and Chaudhuri (2004) have developed an inventory model for a deteriorating item having an instantaneous supply, a quadratic time-varying demand and shortages in inventory. They have used a two-parameter Weibull distribution to represent the time to deterioration. Venkateswarlu and Mohan (2011) have developed inventory models for deteriorating items with time dependent quadratic demand and salvage value. Recently Venkateswarlu and Mohan (2013) studied inventory model for time varying deterioration and price dependent quadratic demand with salvage value.

In literature we seldom find on the inventory models with trade credit policy for perishable items with time dependent quadratic demand rate. Thus, in this paper, we wish to develop a mathematical model when the units in an inventory are subjected to a constant deterioration rate and the demand rate follows a time dependent quadratic function. It is assumed that the supplier offers a credit period to the retailer to settle the account. We have also considered the salvage value for deteriorating units of the inventory. Sensitivity analysis is presented with a numerical example.

II. Assumptions and Notations

The following assumptions are used to develop the model:
- The system deal with a single item
- The demand rate R is time dependent quadratic demand
- The replenishment rate is infinite.
- The lead time is zero and shortages are not allowed.
- The salvage value, $\gamma p \ (0 \leq \gamma < 1)$ is associated to deteriorated units during the cycle time. Here *p* is the purchase cost of an item.

The following notations are used to develop the model:
- The Demand rate $R(t)$ at time t is assumed to be $R(t) = a + bt + ct^2 \quad a \geq 0, b \neq 0, c \neq 0$. Here *a* is the initial rate of demand, *b* is the initial rate of change of the demand and *c* is the acceleration of demand rate.
- $\theta \ (0 < \theta < 1)$ is the constant rate of deterioration.
- A is the ordering cost per order.
- S is the selling price per item $(S > p)$.
- Q(t) is the ordering quantity at time t=0
- h is per unit holding cost excluding interest charges per unit per year.
- I_e is the interest earned per year.
- I_c is the interest charged per stocks per year.

- M is the permissible delay in settling in the accounts, 0<M<1.
- T is the interval between two successive orders
- K(T) is the total cost per unit time.

III. Formulation and Solution of the Model

The objective of the model is to determine the total cost of the system and the demand rate of items is time dependent quadratic function with constant rate of deterioration.

Let *I(t)* be the inventory level at time t ($0 \leq t \leq T$). The inventory depletes due to deterioration and the demand, and then the differential equation which describes the inventory level at time t is given by

$$\frac{dI(t)}{dt} + \theta I(t) = -R(t), \ 0 \leq t \leq T \tag{1}$$

where $R(t) = (a + bt + ct^2)$

and   (i) $I(T) = 0$ when $t = T$, (ii) $I(0) = Q$. $\tag{2}$

The solution of equation (1) using the boundary condition $I(T) = 0$ is given by

$$I(t) = a(T - t) + (a\theta + b)(\frac{T^2}{2} - \frac{t^2}{2}) + (b\theta + c)(\frac{T^3}{3} - \frac{t^3}{3}) + c\theta(\frac{T^4}{4} - \frac{t^4}{4})$$
$$- (\theta t)\left[a(T - t) + b(\frac{T^2}{2} - \frac{t^2}{2}) + c(\frac{T^3}{3} - \frac{t^3}{3}) \right] \tag{3}$$

where we taken series expansion and ignored the second and higher powers of θ as θ is small.
Since $I(0) = Q$, we obtain

$$Q(t) = aT + (a\theta + b)(\frac{T^2}{2}) + (b\theta + c)(\frac{T^3}{3}) + c\theta(\frac{T^4}{4}) \tag{4}$$

The number of deteriorated units D (T) during one cycle is given by

$$D(T) = Q - R(T)T = \frac{a\theta T^2}{2} + \frac{b\theta T^3}{3} + \frac{c\theta T^4}{4} - \frac{bT^2}{2} - \frac{cT^3}{3} \tag{5}$$

The cost due to deterioration is given by

$$CD = pD(T) \ = p\left(\frac{a\theta T^2}{2} + \frac{b\theta T^3}{3} + \frac{c\theta T^4}{4} - \frac{bT^2}{2} - \frac{cT^3}{3} \right) \tag{6}$$

The salvage value of deteriorated units is
$$SV = \gamma CD \tag{7}$$

The inventory holding cost during the cycle is

$$IHC = h\int_0^T I(t)dt$$
$$= h\left(\frac{60aT^2 + 40bT^3 + 30cT^4 + 40a\theta T^3 + 15b\theta T^4 + 12c\theta T^5}{120} \right) \tag{8}$$

The Ordering cost is given by
$$OC = A \tag{9}$$

Following Nita Shah and Pandey (2008), we have considered the following two cases for interest charged and the interest earned:

Case-1: The offered credit period is less than or equal to the cycle time i.e., $M \leq T$.
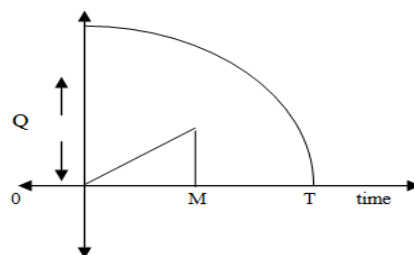
Figure-1

Case-2: The offered credit period for settling the account is greater than the cycle time i.e., $M > T$.
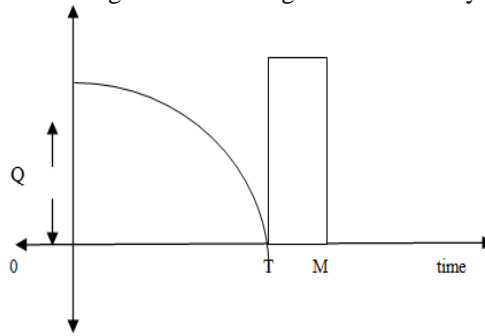
Figure-2

3.1 *Case-1*

The retailer can sale units during *[0, M]* at a sale price: '*S*' per unit which he can put an interest rate 'I_e'per unit per annum in an interest bearing account. So the total interest earned during *[0, M]* is

$$IE_1 = SI_e \int_0^M R(t)tdt = SI_e \left(\frac{aM^2}{2} + \frac{bM^3}{3} + \frac{cM^4}{4} \right) \tag{10}$$

Now, in the period *[M, T]*, the supplier will charge the interest to the retailer on the remaining stock at the rate 'I_c' per unit per annum. Hence, total interest charges payble by the retailer during *[M, T]* is

$$IC_1 = SI_c \int_M^T I(t)dt$$
$$= \frac{1}{120} (SI_c)(M-T)^2 (60a + 10M^2c + 30T^2c + 20Mb$$
$$+ 40Tb + 20T\theta a - 5M^2\theta - 2M^3\theta c + 15T^2\theta b + 12T^3\theta c$$
$$+ 20M\theta a - 10MT\theta b - 6MT^2\theta c - 4M^2T\theta c) \tag{11}$$

Now, the total cost $K_1 (T)$ per time unit is

$$K_1(T) = \frac{1}{T}(OC + IHC + CD - IE_1 + IC_1 - SV)$$

$$= \frac{1}{T} \begin{pmatrix} A + h\left(\dfrac{60aT^2 + 40bT^3 + 30cT^4 + 40a\theta T^3 + 15b\theta T^4 + 12c\theta T^5}{120} \right) \\ + (1-\gamma)p\left(\dfrac{a\theta T^2}{2} + \dfrac{b\theta T^3}{3} + \dfrac{c\theta T^4}{4} - \dfrac{bT^2}{2} - \dfrac{cT^3}{3} \right) \\ - SI_e \left(\dfrac{aM^2}{2} + \dfrac{bM^3}{3} + \dfrac{cM^4}{4} \right) \\ + \dfrac{1}{120}(SI_c)((M-T)^2(60a + 10M^2c + 30T^2c + 20Mb \\ + 40Tb + 20T\theta a - 5M^2\theta b - 2M^3\theta c + 15T^2\theta b + 12T^3\theta c \\ + 20M\theta a - 10MT\theta b - 6MT^2\theta c - 4M^2T\theta c) \end{pmatrix} \tag{12}$$

Since our objective is to minimize the total cost $K_1 (T)$ per unit time, the necessary condition for the total cost to be minimum is $\frac{\partial}{\partial T} K_1(T) = 0$ i.e.,

$$\frac{\partial K_1(T)}{\partial T} = \left(\frac{1}{T} \right)(X_1 + X_2) - \left(\frac{1}{T^2} \right)(X_3 + X_4 - X_5 + X_6) \tag{13}$$

where

$$X_1 = \frac{h(120M^2b + 120M^3c + 120Ma + 120M^2a\theta + 60M^3\theta b + 60M^4\theta c)}{120}$$
$$X_2 = (1-\gamma)(p)(M^2\theta b - Mb - M^2c + M^3\theta c + M\theta a)$$

$$X_3 = A + h\left(\frac{60aT^2 + 40bT^3 + 30cT^4 + 40a\theta T^3 + 15b\theta T^4 + 12c\theta T^5}{120}\right)$$

$$X_4 = (1-\gamma)p\left(\frac{a\theta T^2}{2} + \frac{b\theta T^3}{3} + \frac{c\theta T^4}{4} - \frac{bT^2}{2} - \frac{cT^3}{3}\right)$$

$$X_5 = SI_e\left(\frac{aM^2}{2} + \frac{bM^3}{3} + \frac{cM^4}{4}\right)$$

$$X_6 = (\frac{1}{120})SI_c((M-T)^2(60a + 10M^2c + 30T^2c + 20Mb + 40Tb +$$
$$20T\theta a - 5M^2\theta b - 2M^3\theta c + 15T^2\theta b + 12T^3\theta c + 20M\theta a -$$
$$10MT\theta b - 6MT^2\theta c - 4M^2T\theta c)$$

From equation (13), we have

$$\left(\left(\frac{-1}{T^2}\right)\left(\begin{array}{l}A + h\left(\frac{60aT^2 + 40bT^3 + 30cT^4 + 40a\theta T^3 + 15b\theta T^4 + 12c\theta T^5}{120}\right) \\ + (1-\gamma)p\left(\frac{a\theta T^2}{2} + \frac{b\theta T^3}{3} + \frac{c\theta T^4}{4} - \frac{bT^2}{2} - \frac{cT^3}{3}\right) \\ - SI_e\left(\frac{aM^2}{2} + \frac{bM^3}{3} + \frac{cM^4}{4}\right) \\ + \frac{1}{120}(SI_c)(M-T)^2(60a + 10M^2c + 30T^2c + \\ 20Mb + 40Tb + 20T\theta a - 5M^2\theta b - 2M^3\theta c + 15T^2\theta b + 12T^3\theta c + \\ 20M\theta a - 10MT\theta b - 6MT^2\theta c - 4M^2T\theta c)\end{array}\right) + \left(\frac{1}{T}\right)\left[\begin{array}{l}\frac{h(120M^2b + 120M^3c + 120Ma + 120M^2a\theta + 60M^3\theta b + 60M^4\theta c)}{120} \\ + (1-\gamma)(p)(M^2\theta b - Mb - M^2c + M^3\theta c + M\theta a)\end{array}\right]\right) = 0 \qquad (14)$$

We solve the above equation for optimal *T* using MATHCAD. For this optimal T, the total cost is minimum only if $\frac{\partial^2 K_1(T)}{\partial T^2} > 0$.

3.1.1 Numerical Example

To demonstrate the effectiveness of the models developed, a numerical example is taken with the following values for the parameters:

a =500	b=5	c=0.1	h=5	S=30	$\gamma = 0.08$
T=0.5	I$_c$=0.15	I$_e$=0.12	$\theta = 0.05$	p=20	A=200

For the above example, it is found that the optimality conditions are satisfied in all the following four cases for all *T* viz.,

(i)   *a* > 0, *b* > 0 and *c* > 0 (i.e., accelerated growth model)
(ii)   *a* > 0, *b* < 0 and *c* > 0 (i.e., retarded growth model)
(iii)   *a* > 0, *b* < 0 and *c* < 0 (i.e., accelerated decline model)
(iv)   *a* > 0, *b* > 0 and *c* < 0 (i.e., retarded decline model)

The MATHCAD output is given in Table-1 through table-4 which shows the variations of the deterioration rate, θ and the delay period, M.

From the output shown in table-1 to table-4, it is observed that the buyer's total cost decreases with the increase in delay period for a fixed value of deterioration rate. For example, if the deterioration rate is 0.05, the total cost K$_1$(T) decreases when the delay in payment increases from 15 days to 60 days in all the models. We may attribute this due to the interest earned by buyer who earns more revenue from the sold items. Further, across all the models, it can be noticed that the buyer's total cost increases when the rate of deterioration increases from 0.05 to 0.10.

Table-1: a > 0, b > 0 and c > 0 (i.e., accelerated growth model)

S.No.	θ	M=15 days		M=30 days		M=45 days		M=60 days	
		T	$K_1(T)$	T	$K_1(T)$	T	$K_1(T)$	T	$K_1(T)$
1	0.05	0.28	1345.02	0.28	1256.13	0.28	1170.07	0.28	1086.76
2	0.06	0.28	1358.57	0.28	1269.65	0.28	1183.61	0.28	1100.37
3	0.07	0.27	1371.97	0.27	1283.02	0.28	1197.01	0.28	1113.84
4	0.08	0.27	1385.24	0.27	1296.27	0.27	1210.27	0.27	1127.17
5	0.09	0.27	1398.38	0.27	1310.36	0.27	1223.41	0.27	1140.38
6	0.10	0.27	1411.39	0.27	1322.36	0.27	1236.42	0.27	1153.46

Table-2: a > 0, b < 0 and c > 0 (i.e., retarded growth model)

S.No.	θ	M=15 days		M=30 days		M=45 days		M=60 days	
		T	$K_1(T)$	T	$K_1(T)$	T	$K_1(T)$	T	$K_1(T)$
1	0.05	0.27	1367.99	0.28	1279.43	0.28	1193.75	0.28	1110.89
2	0.06	0.27	1381.29	0.27	1292.70	0.27	1207.05	0.28	1124.25
3	0.07	0.27	1394.46	0.27	1305.84	0.27	1220.20	0.27	1137.47
4	0.08	0.27	1407.50	0.27	1318.85	0.27	1233.24	0.27	1150.57
5	0.09	0.26	1420.41	0.27	1331.74	0.27	1246.15	0.27	1163.55
6	0.10	0.26	1433.21	0.26	1344.51	0.26	1258.94	0.27	1176.41

Table-3: a > 0, b < 0 and c < 0 (i.e., accelerated decline model)

S.No.	θ	M=15 days		M=30 days		M=45 days		M=60 days	
		T	$K_1(T)$	T	$K_1(T)$	T	$K_1(T)$	T	$K_1(T)$
1	0.05	0.27	1368.07	0.28	1279.52	0.28	1193.84	0.28	1110.98
2	0.06	0.27	1381.37	0.27	1292.78	0.27	1207.13	0.28	1124.33
3	0.07	0.27	1394.54	0.27	1305.92	0.27	1220.29	0.27	1137.56
4	0.08	0.27	1407.58	0.27	1318.93	0.27	1233.32	0.27	1150.66
5	0.09	0.26	1420.49	0.27	1331.82	0.27	1246.23	0.27	1163.63
6	0.10	0.26	1433.28	0.26	1344.58	0.26	1259.02	0.27	1176.49

Table-4: a > 0, b > 0 and c < 0 (i.e., retarded decline model)

S.No.	θ	M=15 days		M=30 days		M=45 days		M=60 days	
		T	$K_1(T)$	T	$K_1(T)$	T	$K_1(T)$	T	$K_1(T)$
1	0.05	0.28	1345.02	0.28	1256.22	0.28	1170.15	0.28	1086.85
2	0.06	0.28	1358.65	0.28	1269.73	0.28	1183.69	0.28	1100.46
3	0.07	0.27	1372.05	0.27	1283.11	0.28	1197.09	0.28	1113.93
4	0.08	0.27	1385.32	0.27	1296.35	0.27	1210.36	0.27	1127.26
5	0.09	0.27	1398.46	0.27	1309.46	0.27	1223.49	0.27	1140.47
6	0.10	0.27	1411.46	0.27	1322.44	0.27	1236.50	0.27	1153.54

3.2 Case-2

In this case, the interest earned is

$$IE_2 = SI_e\left[\int_0^T R(t)tdt + R(T)T(M-T)\right]$$

$$= SI_e\left[aMT + bMT^2 + cMT^3 - \frac{aT^2}{2} - \frac{2bT^3}{3} - \frac{3cT^4}{4}\right] \tag{15}$$

and the interest charges is zero *i.e.,* $IC_2 = 0$

The total cost $K_2(T)$ per time unit is

$$K_2(T) = \frac{1}{T}\left(OC + IHC + CD - IE_2 + IC_2 - SV\right)$$

$$= \frac{1}{T}\begin{pmatrix} A + h\left(\dfrac{60aT^2 + 40bT^3 + 30cT^4 + 40a\theta T^3 + 15b\theta T^4 + 12c\theta T^5}{120}\right) \\ + (1-\gamma)p\left(\dfrac{a\theta T^2}{2} + \dfrac{b\theta T^3}{3} + \dfrac{c\theta T^4}{4} - \dfrac{bT^2}{2} - \dfrac{cT^3}{3}\right) \\ - SI_e\left[aMT + bMT^2 + cMT^3 - \dfrac{aT^2}{2} - \dfrac{2bT^3}{3} - \dfrac{3cT^4}{4}\right] \end{pmatrix} \tag{16}$$

Since our object is to minimize the total cost $K_2(T)$ per unit time, the necessary condition for the total cost to be minimum is $\therefore \dfrac{\partial}{\partial T}K_2(T) = 0$ i.e.,

$$\frac{\partial}{\partial T}K_2(T) = -\frac{1}{T}(Y_1 + Y_2 - Y_3) - \frac{1}{T^2}(Y_4 + Y_5 + Y_6) \tag{17}$$

where

$$Y_1 = (1-\gamma)p\left(a\theta T - Tb - cT^2 + b\theta T^2 + c\theta T^3\right)$$

$$Y_2 = h\left(\frac{120bT^2 + 120cT^3 + 120aT + 120a\theta T^2 + 60b\theta T^3 + 60c\theta T^4}{120}\right)$$

$$Y_3 = SI_e\left[aM - 2bT^2 - 3cT^3 - aT + 2bMT + 3cMT^2\right]$$

$$Y_4 = A + h\left(\frac{60aT^2 + 40bT^3 + 30cT^4 + 40a\theta T^3 + 15b\theta T^4 + 12c\theta T^5}{120}\right)$$

$$Y_5 = (1-\gamma)p\left(\frac{a\theta T^2}{2} + \frac{b\theta T^3}{3} + \frac{c\theta T^4}{4} - \frac{bT^2}{2} - \frac{cT^3}{3}\right)$$

$$Y_6 = SI_e\left[aMT + bMT^2 + cMT^3 - \frac{aT^2}{2} - \frac{2bT^3}{3} - \frac{3cT^4}{4}\right]$$

Now from equation (17),

$$T(Y_1 + Y_2 - Y_3) + (Y_4 + Y_5 + Y_6) = 0$$

$$i.e.,\quad \begin{cases} T\begin{pmatrix} (1-\gamma)p\left(a\theta T - Tb - cT^2 + b\theta T^2 + c\theta T^3\right) \\ + h\left(\dfrac{120bT^2 + 120cT^3 + 120aT + 120a\theta T^2 + 60b\theta T^3 + 60c\theta T^4}{120}\right) \\ - SI_e\left[aM - 2bT^2 - 3cT^3 - aT + 2bMT + 3cMT^2\right] \end{pmatrix} \\ + \begin{pmatrix} \left(A + h\left(\dfrac{60aT^2 + 40bT^3 + 30cT^4 + 40a\theta T^3 + 15b\theta T^4 + 12c\theta T^5}{120}\right)\right) \\ + (1-\gamma)p\left(\dfrac{a\theta T^2}{2} + \dfrac{b\theta T^3}{3} + \dfrac{c\theta T^4}{4} - \dfrac{bT^2}{2} - \dfrac{cT^3}{3}\right) \\ + SI_e\left[aMT + bMT^2 + cMT^3 - \dfrac{aT^2}{2} - \dfrac{2bT^3}{3} - \dfrac{3cT^4}{4}\right] \end{pmatrix} \end{cases} = 0 \tag{18}$$

which minimises the $K_2(T)$ only if $\dfrac{\partial^2 K_2(T)}{\partial T^2} > 0$ for all values of T.

3.2.1 Numerical Example

Once again we consider the values of the parameters as given in 3.1.1. For these values, the output is presented in Table-5 through Table-8. It can be observed that the behaviour of these models, in the case of M > T, is quite similar to the results obtained as in the case of M < T. It is also observed that the total cost $K_2(T)$ is less than $K_1(T)$ when the delay period is increased from 15 days to 60 days. Thus it can be concluded that the total cost in both the cases is almost same when the delay period increases from 15 days to 60 days.

For T = M, we have

$$K_1(M) = K_2(M) = \frac{1}{M}(Z_1 - Z_2 - Z_3)$$

where

$$Z_1 = A + h\left(\frac{60aM^2 + 40bM^3 + 30cM^4 + 40a\theta M^3 + 15b\theta M^4 + 12c\theta M^5}{120}\right)$$

$$Z_2 = (1-\gamma)p\left(\frac{a\theta M^2}{2} + \frac{b\theta M^3}{3} + \frac{c\theta M^4}{4} - \frac{bM^2}{2} - \frac{cM^3}{3}\right)$$

$$Z_3 = SI_e\left[\frac{aM^2}{2} + \frac{bM^3}{3} + \frac{cM^4}{4}\right].$$

IV. Sensitivity Analysis

(*a* > 0, *b* > 0 and *c* > 0 i.e., accelerated growth model)

We now study the sensitivity of the models developed in 3.1.1 and 3.2.1 to examine the implications of underestimating and overestimating the parameters a, b, c, Ic , Ie , h and p on optimal value of cycle time and total cost of the system. Here we have taken the deterioration rate as θ=0.05 and the delay period is 30 days. The sensitive analysis is performed by changing each of the parameter by -20%, -10%, +10% and +20% taking one parameter at a time and keeping the remaining parameters are unchanged. The results are shown in Table-9 and Table-10.

The following interesting observations are made from the above tables:

   ### Case-1($M \leq T$)

(i)   Increase (decrease) in parameters *a, I_c , h* and *p* decreases (increases) the cycle time where as the total cost increases (decreases) with the increase (decrease) in these parameters. However the rate of increase/decrease is more pronounced in case of the changes made in the parameters 'a' and 'h' which indicate that the optimal values of cycle time and the total cost are less sensitive to 'I_c' and 'p' .
(ii) The effect of the parameters b, c and I_e on the optimum value of the cycle time and the total cost is similar but the rate of change is insignificant.
(iii) The salvage value of deteriorated items is not shown much effect on the optimal total cost of the system.

Case-2($M > T$)

(iv) Increase (decrease) in parameters *a, h* and *p* decreases (increases) the cycle time where as the total cost increases (decreases) with the increase (decrease) in these parameters. However the rate of increase/decrease is more pronounced in case of the changes made in the parameters 'a' and 'h' and less sensitive to the changes in 'p'
(v)   T and $K_2(T)$ are less sensitive to the changes made in the parameter 'b' and moderately sensitive to I_e.
(vi) The effect of salvage value is not so significant on optimal policies.

V. Conclusions

The main objective of this study is the formulation of a deterministic inventory model for items which have constant deterioration rate and follows time dependent quadratic demand rate when supplier offers a specific credit period. The total cost of the system is calculated when shortages are not allowed. Salvage value is considered while calculating the total cost of the system. Sensitivity of the models is also discussed.

Table-5: a > 0, b > 0 and c > 0 (i.e., accelerated growth model)

S.No	θ	M=15 days		M=30 days		M=45 days		M=60 days	
		T	$K_2(T)$	T	$K_2(T)$	T	$K_2(T)$	T	$K_2(T)$
1	0.05	0.29	1297.63	0.29	1223.44	0.29	1149.25	0.29	1075.06
2	0.06	0.29	1311.65	0.29	1237.46	0.29	1163.27	0.29	1089.09
3	0.07	0.28	1325.51	0.29	1251.32	0.29	1177.14	0.29	1102.95
4	0.08	0.28	1339.22	0.28	1265.04	0.28	1190.86	0.28	1116.67
5	0.09	0.28	1352.79	0.28	1278.61	0.28	1204.43	0.28	1130.25
6	0.10	0.28	1366.22	0.28	1292.05	0.28	1217.87	0.28	1143.69

Table-6: a > 0, b < 0 and c > 0 (i.e., retarded growth model)

S.No.	θ	M=15 days		M=30 days		M=45 days		M=60 days	
		T	$K_2(T)$	T	$K_2(T)$	T	$K_2(T)$	T	$K_2(T)$
1	0.05	0.29	1320.95	0.29	1247.19	0.29	1173.43	0.29	1099.66
2	0.06	0.28	1334.71	0.28	1260.95	0.28	1187.18	0.28	1113.42
3	0.07	0.28	1348.32	0.28	1274.56	0.28	1200.79	0.28	1127.03
4	0.08	0.28	1361.80	0.28	1288.03	0.28	1214.26	0.28	1140.49
5	0.09	0.28	1375.14	0.28	1301.36	0.28	1227.59	0.28	1153.82
6	0.10	0.27	1388.34	0.27	1314.57	0.27	1240.80	0.27	1167.03

Table-7: a > 0, b < 0 and c < 0 (i.e., accelerated decline model)

S.No.	θ	M=15 days		M=30 days		M=45 days		M=60 days	
		T	$K_2(T)$	T	$K_2(T)$	T	$K_2(T)$	T	$K_2(T)$
1	0.05	0.29	1321.03	0.29	1247.27	0.29	1173.51	0.29	1099.75
2	0.06	0.28	1334.79	0.28	1261.03	0.28	1187.27	0.28	1113.51
3	0.07	0.28	1348.40	0.28	1274.64	0.28	1200.88	0.28	1127.11
4	0.08	0.28	1361.87	0.28	1288.11	0.28	1214.34	0.28	1140.58
5	0.09	0.28	1375.21	0.28	1301.44	0.28	1227.68	0.28	1153.91
6	0.10	0.27	1388.42	0.27	1314.65	0.27	1240.88	0.27	1167.11

Table-8: a > 0, b > 0 and c < 0 (i.e., retarded decline model)

S.No.	θ	M=15 days		M=30 days		M=45 days		M=60 days	
		T	$K_2(T)$	T	$K_2(T)$	T	$K_2(T)$	T	$K_2(T)$
1	0.05	0.29	1297.72	0.29	1223.53	0.29	1149.34	0.29	1075.16
2	0.06	0.29	1311.73	0.29	1237.55	0.29	1163.36	0.29	1089.18
3	0.07	0.28	1325.59	0.29	1251.41	0.29	1177.23	0.29	1103.04
4	0.08	0.28	1339.30	0.28	1265.12	0.28	1190.94	0.28	1116.76
5	0.09	0.28	1352.87	0.28	1278.69	0.28	1204.51	0.28	1130.34
6	0.10	0.28	1366.30	0.28	1292.13	0.28	1217.95	0.28	1143.77

Case-1($M \le T$): Table-9

S.No	Parameter	% Change	% Change in T	% Change in $K_2(T)$
1	a	-20%	11.6838	-9.5847
		-10%	5.1546	-4.6231
		10%	-4.8110	4.3345
		20%	-8.9347	8.4197
2	b	-20%	-0.3436	0.1950
		-10%	-0.3436	0.0975
		10%	0.0000	-0.0978
		20%	0.0000	-0.1955
3	c	-20%	-0.3436	0.1958
		-10%	-0.3436	0.1954
		10%	-0.3436	0.1947
		20%	-0.3436	0.1943
4	I_c	-20%	-0.3436	0.1950
		-10%	-0.3436	0.1950
		10%	-0.3436	0.1950
		20%	-0.3436	0.1950
5	I_e	-20%	3.7801	-1.7468
		-10%	1.7182	-0.7544
		10%	-2.0619	1.1039
		20%	-3.7801	1.9745
6	h	-20%	5.4983	-5.9713
		-10%	2.4055	-2.8441
		10%	-2.7491	3.1532
		20%	-5.1546	6.0364
7	p	-20%	0.3436	-0.7257
		-10%	0.0000	-0.2644
		10%	-0.6873	0.6527
		20%	-1.0309	1.1085
8	γ	-20%	-0.3436	0.2747
		-10%	-0.3436	0.2349
		10%	-0.3436	0.1551
		20%	-0.3436	0.1153

Case-2($M > T$): Table-10

S.No	Parameter	% Change	% Change in T	% Change in $K_1(T)$
1	a	-20%	11.4695	-9.4032
		-10%	5.3763	-4.5309
		10%	-4.6595	4.2404
		20%	-8.9606	8.2299
2	b	-20%	-0.3584	0.1865
		-10%	-0.3584	0.0933
		10%	0.0000	-0.0935
		20%	0.0000	-0.1869
3	c	-20%	0.0000	-0.2381
		-10%	0.0000	0.0004
		10%	0.0000	-0.0003
		20%	0.0000	-0.0006
4	I_c	-20%	3.9427	-2.5888
		-10%	1.7921	-1.2700
		10%	-2.1505	1.2244
		20%	-3.9427	2.4064
5	I_e	-20%	0.0000	0.3472
		-10%	0.0000	0.1736
		10%	-0.3584	-0.1740
		20%	-0.3584	-0.3483
6	h	-20%	5.0179	-5.7520
		-10%	2.5090	-2.8386
		10%	-2.5090	2.7693
		20%	-4.6595	5.4743
7	p	-20%	0.7168	-0.8201
		-10%	0.3584	-0.4094
		10%	-0.3584	0.4079
		20%	-0.7168	0.8144
8	γ	-20%	-0.3584	0.0711
		-10%	-0.3584	0.0356
		10%	0.0000	-0.0356
		20%	0.0000	-0.0712

REFERENCES

[1]   Halley, C. G. & Higgins, R. C., (1973). Inventory Policy and Trade Credit Financing. Management Science. 20, 464 – 471.

[2]   Chapman, C. B., Ward, S. C., Cooper, D. F. & Page, M. J., (1984). Credit Policy and Inventory Control. Journal of the Operational Research Society. 35, 1055 – 1065.

[3]   Davis, R. A. & Gaither, N. (1985). Optimal Ordering Policies Under Conditions of Extended Payment Privileges, Management Sciences. 31, 499-509.

[4]   Goyal, S. K. (1985). Economic Order Quantity Under Conditions of Permissible Delay in Payment. Journal of the Operational Research Society. 36, 335–338.

[5]   Shah, V. R., Patel, H. C. & Shah. Y. K., (1988). Economic Ordering Quantity when Delay in Payments of Orders and Shortages are Permitted. Gujarat Statistical Review. 15, 51 – 56.126

[6]   Mandal, B. N. & Phaujdar, S. (1989a). Some EOQ Models Under Permissible Delay in Payments. International Journal of Managements Science, 5 (2), 99–108.

[7]   Mandal, B.N. & Phaujdar, S. (1989b). An Inventory Model f or Deteriorating Items and Stock Dependent Consumption Rate. Journal of Operational Research Society. 40, 483–488.

[8] Carlson, M.L. & Rousseau, J.J. (1989). EOQ under Date-Terms Supplier Credit. Journal of the Operational Research Society. 40 (5), 451–460.

[9] Chung, K.J. & Huang, Y.F. (2003). The Optimal Cycle Time for EPQ Inventory Model Under Permissible Delay in Payments. International Journal of Production Economics. 84 (3), 307–318.

[10] Daellenbach, H. G., (1986). Inventory Control and Trade Credit. Journal of the Operational Research Society, 37, 525 – 528.

[11] Daellenbach, H. G., (1988): Inventory Control and Trade Credit – a rejoinder. Journal of the Operational Research Society. 39, 218 – 219.

[12] Ward, S. C. & Chapman, C. B., (1987). Inventory Control and Trade Credit –a reply to Daellenbach. Journal of Operational the Research Society. 32, 1081 – 1084.

[13] Chapman, C. B. & Ward, S. C., (1988): Inventory Control and Trade Credit –A Future Reply. Journal Of Operational Research Society, 39, 219 – 220.

[14] Chung, K. J., (1998). A Theorem on the Deterioration of Economic Order Quantity Under Conditions of Permissible Delay in Payments. Computers and Operations Research. 25,49 – 52.

[15] Jamal, A. M. M., Sarker, B. R & Wang, S. (2000). Optimal Payment Time for a Retailer Under Permitted Delay of Payment by the Wholesaler. International Journal of Production Economics. 66, 59 - 66.

[16] Sarker, B. R., Jamal, A. M. M. & Wang, S., (2001). Optimal Payment Time Under Permissible Delay for Production with Deterioration. Production Planning and Control. 11, 380 – 390.

[17] Abad, P.L. & Jaggi, C.K. (2003). A Joint Approach for Setting Unit Price and the Length of the Credit Period for a Seller when End Demand is Price Sensitive. International Journal of Production Economics. 83 (2), 115–122.

[18] Shinn, S. W. & Hwang, H., (2003). Retailer's Pricing and Lot – Sizing Policy for Exponentially Deteriorating Products under the Conditions of Permissible Delay in Payments. Computers and Industrial Engineering. 24(6), 539 – 547.

[19] Chung, K.J., Goyal, S.K. & Huang, Yung-Fu (2005). The Optimal Inventory Policies Under Permissible Delay in Payments Depending on the Ordering Quantity. International Journal of Production Economics. 95(2), 203–213.

[20] Huang, Y.F. (2007). Optimal Retailer's Replenishment Decisions in the EPQ Model under Two Levels of Trade Credit Policy. European Journal of Operational Research. 176 (2), 911–924.

[21] Teng, J.T., Chang, C.T., Chern, M.S. & Chan, Y.L. (2007). Retailer's Optimal Ordering Policies with Trade Credit Financing. International Journal of System Science. 38 (3), 269–278.

[22] Khanra, S. & Chaudhuri. K.S. (2003). A Note on Order-Level Inventory Model for a Deteriorating Item with Time-Dependent Quadratic Demand. Computers and Operations Research. Vol.30, 1901-1916.

[23] Bhandari, R.M. & Sharma, P.K. (2000). A Single Period Inventory Problem with Quadratic Demand Distribution under the Influence of Market Policies. Eng. Science 12(2) 117-127.

[24] Shibshankar Sana & Chaudhary, K.S. (2004). A Stock-Review EOQ Model with Stock-Dependent Demand, Quadratic Deterioration Rate'. Advanced Modelling and Optimization. 6(2), 25-32.

[25] Ghosh, S.K. & Chaudhuri, K.S. (2004). An Order Level Inventory Model for a Deteriorating Item with Weibull Deterioration, Time-Quadratic Demand and Shortages. Advanced Modelling and Optimization. 6(1), 21-35.

[26] Venkateswarlu, R & Mohan.R.(2011). Inventory Models for Deteriorating Items with Time Dependent Quadratic Demand and Salvage Value. International Journal of Applied Mathematical Sciences. 5(1-2), 11-18.

[27] Venkateswarlu,R. & Mohan,R. (2013). An Inventory Model for Time Varying Deterioration and Price Dependent Quadratic Demand with Salvage Value. Journal of Computational and Applied Mathematics. 1(1):21-27.

Energy Based Analysis of a Thermal Power Station for Energy Efficiency Improvement

Dr. Mohammed Yunus[1], Mohammed Asadullah[2], Dr. Hamza A. Ghulman[3], Dr. J. Fazlur Rahman[4], Mohammed Irfan[5]

[1,2,4,5] *Department of Mechanical Engineering, H.K.B.K.College of Engineering/ Visvesvaraiah Technological University, India*
[3]*Department of Mechanical Engineering, Ummul Qura University, Mekkah, Kingdom of Saudi Arabia*

ABSTRACT: *Despite of growth of renewable energy stations installations like wind, solar, Tidal power, the energy for the world depends heavily on fossil fuels for electricity generation. It is also expected to continue the dependence on fossil fuels for next few decades. Therefore, given the continued reliance on the fossil fuels for some time, it is important to note these plants must reduce their environmental impact by operating fossil fuels more efficiently. Two types of analysis namely, energy and exergy analysis can be developed for the system. Energy analysis based on first law of thermodynamics cannot be applied as it cannot justify the real useful energy loss because it does not differentiate between the quality and quantity of energy within the system. Whereas, exergy analysis will characterize the work potential of a system based on the second law of thermodynamics and the maximum work that can be obtained from the system when its state is brought to the reference or dead state (standard atmospheric conditions).This technical paper presents the results of exergy and energy analysis carried out on 62 MW coal-based thermal power plant to evaluate the performance. The performance of the plant was estimated by a component-wise modeling followed by a system simulation. A parametric study is conducted for the thermal plant under various operating conditions, including different operating condenser pressures, temperatures and flow rates of cooling water across the condenser etc, in order to determine which parameter that maximizes plant performance. Energy loss distribution to find out the amount and source of irreversibilities generated in boiler and turbine in a plant so that any process in the system having largest energy destruction can be identified and that helps the designer to re design the system components.*
Keywords: *Exergy Analysis, Energy analysis, Coal based Thermal Power station, Fossil fuels, Irreversibility, Second Law of Thermodynamics.*

I.   Introduction

Despite of growth of renewable energy stations installations like wind, solar and tidal power, the energy for the world depends heavily on fossil fuels for electricity generation. It is also expected to continue the dependence on fossil fuels for decades. Therefore, given the continued reliance on the fossil fuels for some time, it is important that fossil fuel plants reduce their environmental impact by operating more efficiently. The heavy dependence on fossil fuels is expected to continue for decades. Despite the depletion of fossil fuel reserves and environmental concerns such as climate change, the growth in oil demand is expected to be 60% between 2014 and 2035, 94% for natural gas and 96% for coal [24]. Since it is very clean process, it is continued to reliance on the fossil fuels for some more time. Therefore, it is important that fossil fuel plants should reduce their environmental impact by operating more efficiently.

There are two types of analysis used for thermal power plants, namely, energy and exergy analysis can be developed for the system. Energy analysis based on first law of thermodynamics cannot be applied as it cannot justify the real useful energy loss because it does not differentiate between the quality and quantity of energy within the system and also does not characterize the irreversibility of processes within the system. Whereas, exergy analysis will characterize the work potential of a system based on the second law of thermodynamics and the maximum work that can be obtained from the system when its state is brought to the reference or dead state (standard atmospheric conditions). Exergy analysis is based on the second law of thermodynamics. Past exergy studies have evaluated the performance of power plants, as a means to optimize the performance and turbine power output.

Using exergy and energy analysis, the performance of 400MW capacity coal-fired and nuclear power plants carried out successfully by Habib et. al.and Zubair et.al [17] conducted a second law analysis of regenerative Rankine power plants with reheating. Sengupta et al. [19] conducted an exergy analysis of a 210 MW thermal power plant in India. Rosen et.al.[13], [16], [20], [21] and [22] performed exergy analysis of power plants that operate on various fuels. They have also investigated capital costs involved and thermodynamic

losses. Most common size of power plants in India are 100/110/200/210 MW [6]. The exergy analysis is not so popular among industries especially in India and it needs much more attention and application so that the irreversibilities can be minimized and thus the systems can be operated at much higher efficiency. The present work is to show the application of energy and exergy based analysis. The performance of the plant was estimated by a component-wise modeling followed by a system simulation (computer program) and detailed break-up of exergy losses are evaluated. For the low performance of plant, the various parameters responsible for the plant are mismatching of equipments/ components, improper maintenance, over a period of time, low performance due to deteriorated equipments, inadequate instrumentation, mismatching of equipments etc. [3].

The power plant is designed to utilize an air cooled condenser to condense the exhaust steam. This paper will identify major sources of losses and energy destruction in the power plant. It will provide ways and means to improve the system performance and reduce environment impact. Finally, it will perform a parametric study to determine how the system performance varies with different operating parameters. he introduction of the paper should explain the nature of the problem, previous work, purpose, and the contribution of the paper. The contents of each section may be provided to understand easily about the paper.

II. Experimental Methodology

A detailed process flow-sheet of a Thermal Power Station consists of a unit employs regenerative feed water heating system which is carried out in two stages of low pressure heaters and high pressure heaters along with one open de-aerating heat exchanger. Saturated steam from the boiler drum is fed to the super heater to heat it up to 500°C at a pressure of 85 bars.
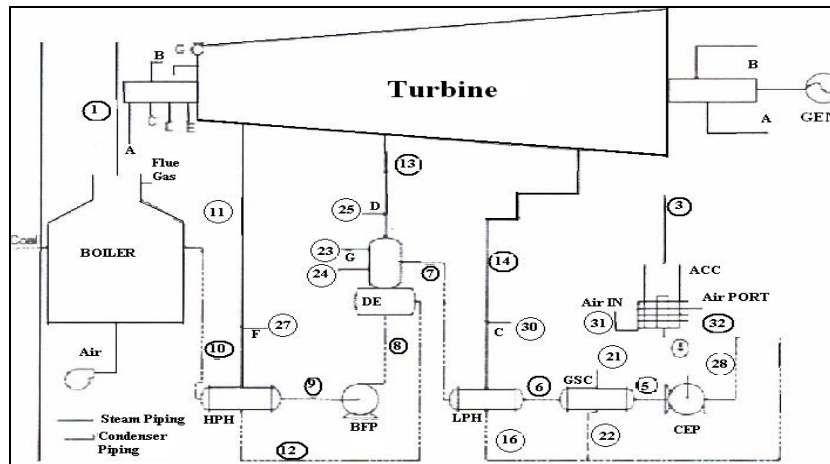
Fig. 1. Process flow diagram: ACC - air cooled condenser, BFP - boiler feed pump, CEP condensate extraction pump, DE - deaerator, GEN - generator, GSC gland steam condenser, HPH - high pressure heater, LPH - low pressure heater.

The condenser pressure is taken as 10 kPa. The extraction pressures of steams from the turbine varies at High Pressure Heater of fist stage of 30 bars to High Pressure Heater of stage of 16 bars , De-aerator of 6 bars and Low Pressure Heater of fist stage of 2.8 bars to Low Pressure Heater of 2 stage of 0.8 bar.

2.1 Composition Details

Coal available in India is the supply fuel of the power plant with the following components and the compositions of it used for coal fired thermal power plant are shown in table 1. Calorific value of Indian coal supplied to Raichur Thermal Power station has 15.5 MJ/kg.

Table 1.Composition of typical Indian coal

Components	Mass in percentage
Moisture	10
Ash	40
Hydrogen	2.68
Nitrogen	0.8
Sulphur	0.65
Oxygen	7
Carbon	38.87

2.2 Assumptions to be made for using flow sheet program method of analysis.
1. Reference temperature for water / steam is at 25^0C and incoming fuel temperature is also 25^0C.
2. Neglect the potential and kinetic exergies.
3. Environment model to calculate exergy has reference pressure and temperature are 1.013 bar and 25^0C and the composition of environment(% mole)for CO_2, H_2O, N_2, O_2, are 0.03, 3.12, 76, 21.
4. Excess air is 20%.
5. Generator efficiency is 95%.
6. Isentropic efficiency of pumps / fans and turbine are 70% and 80% respectively.

The present study has been performed using a flow-sheet program, which is a well-structured program for the thermodynamic analysis of energy systems. The ash content of Indian coal, as already mentioned is around 40 - 50% as against 5 - 10% in the coal being used in the western countries. This is one of the important factors contributing to the lower overall efficiency of the plant. Being a tropical country, the cooling water temperature in majority of the parts in India throughout the year is around 25^0C. In Europe and other western countries the cooling water temperatures are lower in the range of $5 – 10^0$C, which enables the operation of the condenser at much lower vacuum pressures (5 kPa), thus resulting in higher operating efficiencies. Since, both the above factors are nature's limitation; though coal can be beneficiated to a small extent, designer's / plant operator's focus should shift to other major sites of potential improvement. Thus, the goal of this paper is to identify such sites so that the overall efficiency of the system can be improved.

III. Results and Discussion

Parametric study has been carried out in order to account the performance of the over the parameters such as gain in cooling water temperature across the condenser, Steam temperature, steam pressure, inlet air temperature, and the condenser pressure. Fig 2. shows that the reference temperature does not have an effect on the energy efficiency, but it affects then exergy efficiency. The performance of the system depends on the surroundings of the system i.e. inlet air temperature. Fig. 4. shows the variation of efficiencies (both exergy and energy) with the increase in cooling water temperature across the condenser and it is found about $0.15 – 0.20\%$ for the temperature variation of 5^0C. As this power plant uses an air cooled condenser to condense the exhaust steam of the turbine and mainly the improvement that can be achieved by lowering the condenser pressure as shown in fig.3 due to the higher expansion of steam through the turbine, resulting in higher power output.
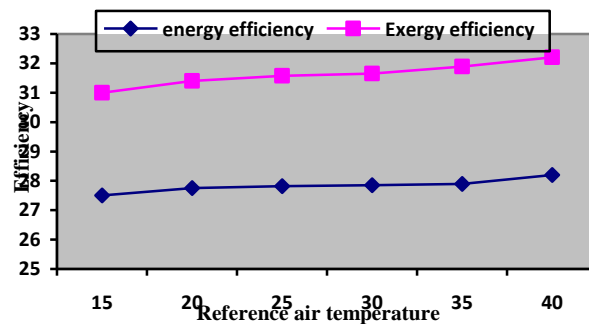
Fig.2. Variation of efficiencies v/s Reference air temperature
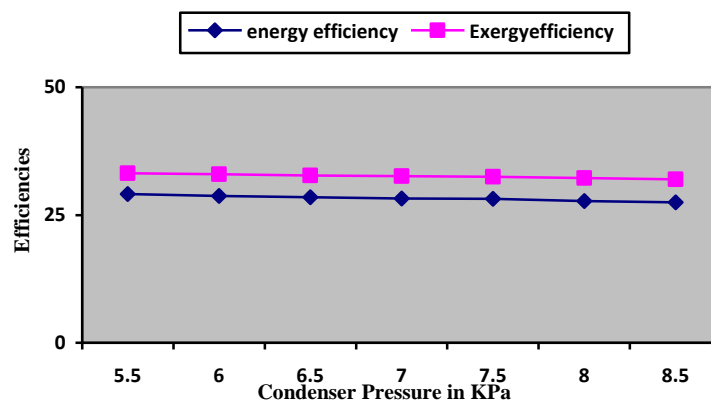
Fig. 3. Variation of efficiency vs. condenser pressure

In case of water cooled condensers, where the temperature of water can be easily controlled, but not in an air cooled condenser, the temperature at which the steam to be condensed cannot be reduced.
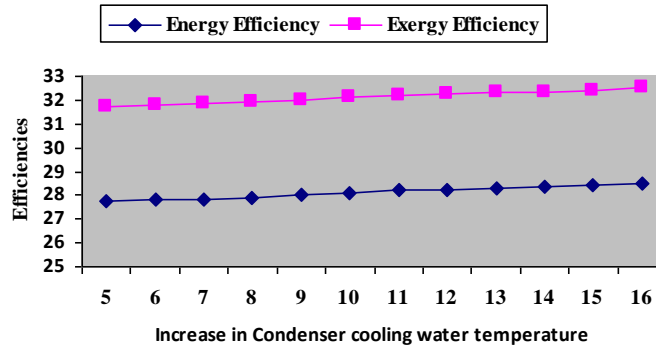
Fig. 4. Variation of efficiencies with increase in condenser cooling water temperature.

It is seen that the efficiency rises with an increase in the superheated steam parameters as presented in fig. 5. Show the effects of the steam temperature on the cycle performance. It is evident the increasing the cycle steam temperature will result in a higher power output for the same mass flow rate of steam and fuel input into the boiler. Therefore steam has higher energy/exergy content, resulting in higher work output of the turbine.
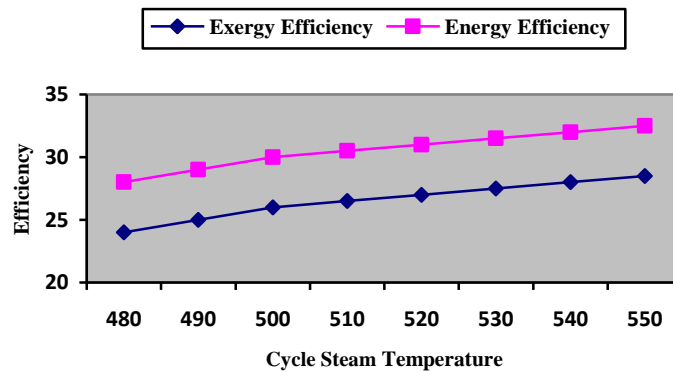
Fig.5.Illustrates the efficiency vs. Cycle steam pressure

It is seen that the efficiency rises with an increase in the superheated steam parameters as presented in fig. 5. Show the effects of the steam temperature on the cycle performance. It is evident the increasing the cycle steam temperature will result in a higher power output for the same mass flow rate of steam and fuel input into the boiler. Therefore steam has a higher energy/exergy content, resulting in higher work output of the turbine.
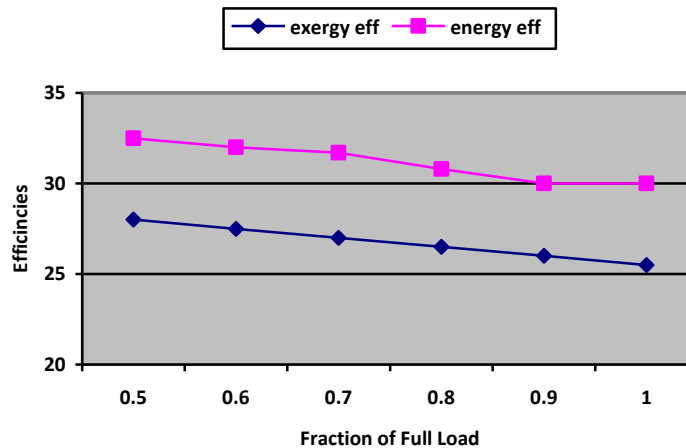
Fig. 6. Efficiency vs. Fraction of Full Load (% of generator output power)

It is evident from figs.6 and 7, that the variation of energy and exergy efficiencies with lower auxiliary power consumption, in terms of the percentage of generator output power which leads to higher system efficiencies. The operation of the plant below 50% of the designed capacity results in the significant increase of irreversibilities and indicates that when the plant is operated at its rated capacity would be more economical than operating at part loads. Figs.8 and 9 show the detailed energy and exergy balance of the considered system at the maximum operating load of 60 MW and difference in the composition of energy and exergy balances. It is noted that the exergy analysis has enabled the identification of the causes of process inefficiencies in detail when compared to the energy analysis.
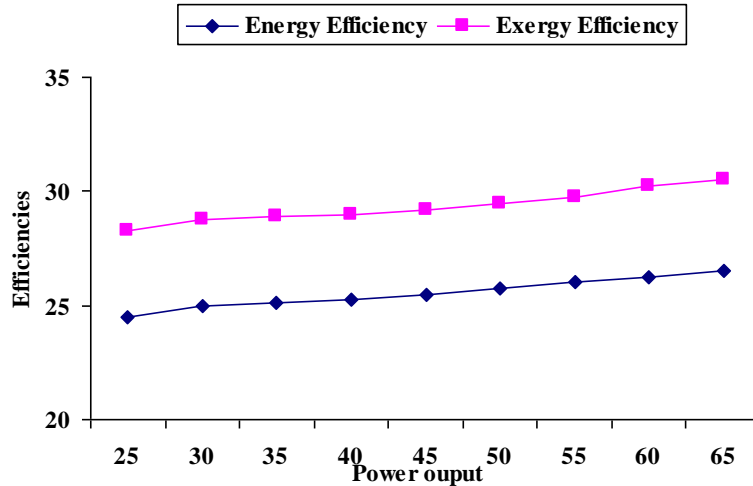
Fig.7. Variation of efficiencies vs. power output of Turbine
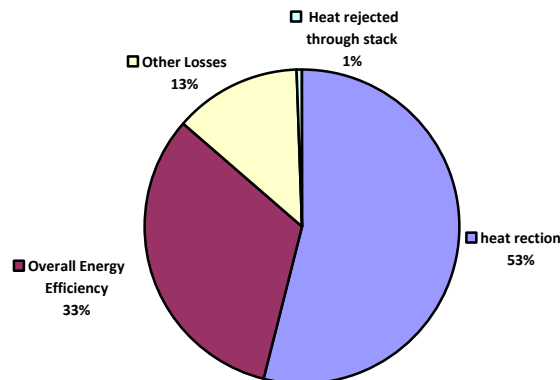
Fig. 8.Energy balance of 62 MW thermal power plant
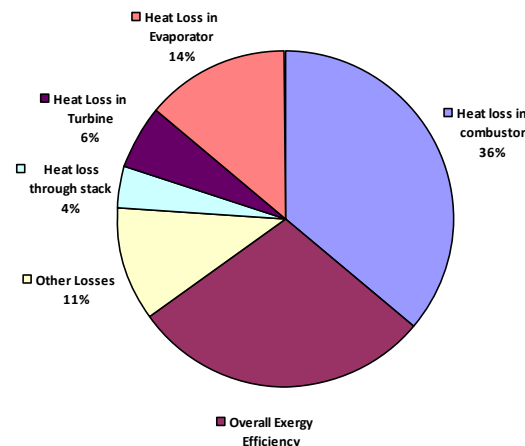
Fig. 9.Exergy balance of 62 MW thermal power plant

In order to utilize non-renewable sources more effectively like fossil fuels without damaging the environment, so that it can achieve better environmental sustainability. This will enable us to maximize its use of limited resources and make existing resources last longer. Fig. 10 shows the effect of exergy efficiency on the sustainability index.
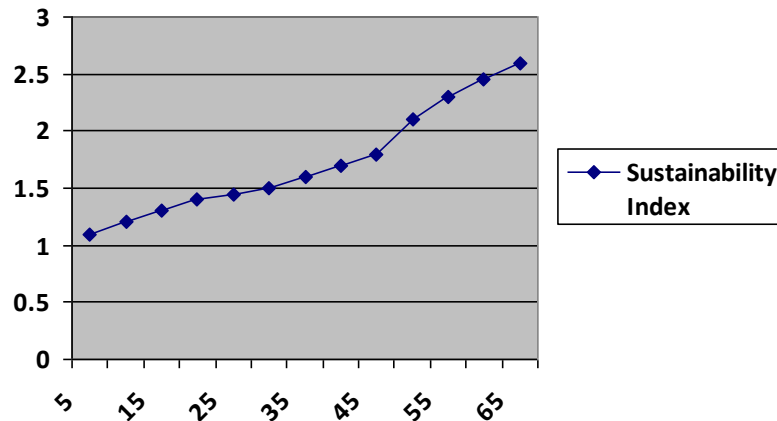
Fig.10. Sustainability index vs. exergy efficiency.

IV. Conclusion

Energy analysis of a thermal power plant based on a second law analysis has been presented and a detailed parametric study considering the effects of various parameters on the system performance has been performed to identify and quantify the sites having largest energy and exergy losses. The power plant's energy and energy efficiency is determined to be 32.5% and 27.5% for the gross generator output. The maximum exergy loss is found to occur in the boiler and turbine and if the performance of a boiler and turbine are improved, plant performance will also be improved. Hence the largest improvement the power plant efficiency. The exergy analysis of the plant showed that lost energy in the condenser is thermodynamically insignificant due to its low quality.

REFERENCES

[1]   T. J. Kotas, "Exergy Criteria of Performance for Thermal Plant: Second of Two Papers on Exergy Techniques in Thermal Plant Analysis," International Journal of Heat and Fluid yongping yang "comprehensive exergy based evaluation and parametric study of a coal fired ultra super critical power plant.

[2]   Mali Sanjay D, Dr. Mehta N S, " Easy Method Of Exergy Analysis For Thermal Power Plant", International Journal of Advanced Engineering Research and Studies,Vol. I, Issue III, April-June, 2012, PP-245-247

[3]   P Regulagadda "energy analysis of a thermal power plant with measured boiler and turbine losses" applied thermal engineering vol 30-[2010], PP.970-976.

[4]   T. Ganapathy, N. Alagumurthi, R. P. Gakkhar and K. Murugesan, "Exergy Analysis of Operating Lignite Fired Thermal Power Plant," Journal of Engineering Science and Technology Review, Vol. 2, No. 1, 2009, pp. 123-130.

[5]   S. C. Kamate and P. B. Gangavati, "Exergy Analysis of Cogeneration Power Plants in Sugar Industries," Applied Thermal Engineering, Vol. 29, No. 5-6, 2009, pp. 1187-1194.

[6]   A. Datta, S. Sengupta and S. Duttagupta, "Exergy Analysis of a Coal-Based 210 mw Thermal Power Plant," International Journal of Energy Research, Vol. 31, No. 1, 2007, pp. 14-28.

[7]   I. H. Aljundi, "Energy and Exergy Analysis of a Steam Power Plant in Jordan," Applied Thrmal Engineering, Vol. 29, No. 2-3, 2009, pp. 324-328.

[8]   Ankit patel "energy and exergy analysis of boiler with different fuels like Indian coal ,imported coal and L.H.H.S oil vol 8 oct 2012.

[9]   A. Rashad, and A. El Maihy, "Energy And Exergy Analysis Of A Steam Power Plant In Egypt" 13th International Conference on Aerospace Sciences & Aviation Technology, *ASAT- 13,* May 26 – 28, 2009.

[10]   Sarang j Gulhane, Prof. Amit Kumar Thakur, " Exergy Analysis of Boiler In cogeneration Thermal Power Plant", American Journal of Engineering Research (AJER), Volume-02, Issue-10, 2013, pp-385-392.

[11]   R saidur "energy and exergy economic analysis of industrial boiler" Vol 38(2010)2188-2197

[12]   R. Jyothu naik "exergy analysis of 120MWcoal based thermal power plant ''vol 2 4 apil 2013 issn 2278-0181.

[13]   M. A. Rosen, "Energy- and Exergy-Based Comparison of Coal-Fired and Nuclear Steam Power Plants," Exergy, Vol. 1, No. 3, 2001, pp. 180-192.

[14]   M.K. pal "energy and exergy analysis of boiler and turbine of a coal fired thermal power plant '' vol 2. Issue 6, June 2013.

[15]   H. Erdem, A. V. Akkaya., A. Dagdas, S. H. Sevilgen, B. Sahin, I. Tek, C. Gungor and S. Atas, "Comparative Energetic and Exergctic Performance Analyses for Coal-Fired Thermal Power Plants in Turkey." International Journal of Thermal Sciences, Vol. 48, No. 11, 2009, pp. 2179-2186.

[16]   M.A. Rosen, Energy and exergy-based comparison of coal-fired and nuclear steam power plants, Exergy - International Journal 1 (3) (2001) 180-192.

[17]   M.A. Habib, S.M. Zubair, 2nd-law-based thermodynamic analysis of regenerative-reheat Rankine-cycle power plants, Energy, vol. 17, Pergamon- Elsevier Science Ltd., 1992. pp. 295 301.

[18]   Tapan K. Ray, Amitava Datta, Amitava Gupta, Ranjan Ganguly, Exergy-based performance analysis for proper O&M decisions in a steam, Energy Conversion and Management 51 (2010) 1333–1344.

[19]   S. Sengupta, A. Datta, S. Duttagupta, Exergy analysis of a coal-based 21 OMW thermal power plant, International Journal of Energy Research 31 (2007) 14-28.

[20]   M.A. Rosen, 1. Dincer, Exergoeconomic analysis of power plants operating on various fuels, Applied Thermal Engineering 23 (2003) 643-658.

[21]   M.A. Rosen.. I. Dincer, On exergy and environmental impact, International Journal of Energy Research 21 (1997) 643-654.

[22]   M.A. Rosen. 1. Dincer, M. Kanoglu. Role of exergy in increasing efficiency and sustainability and reducing environmental impact, Energy Policy 36 (2008) 128-137.

[23]   M.J. Moran, H.N. Shapiro, Fundamentals of Engineering Thermodynamics, sixth ed., John Wiley & Sons, Inc., 2006.

[24]   S.C. Kaushika, V. Siva Reddya, S.K. Tyagib. Energy and exergy analyses of thermal power plants: A review, Renewable and Sustainable Energy Reviews 15(2011) 1857–1872.

Planning and Designing a Stand Alone Solar Power System for Multi-Building Organization

[1]Md. Ilyas, [2]J. K. Garg, [3]Anup Kumar Sinha

[1]*(Assistant Professor), Dept. of Electrical & Electronics Engg. Al-Falah School of Engg & Technology Faridabad, Haryana, India*
[2]*(Associate Professor), Dept. of Electrical & Electronics Engg. Al-Falah School of Engg & Technology Faridabad, Haryana, India*
[3]*(Student), Dept. of Electrical & Electronics Engg. Al-Falah School of Engg & Technology, Faridabad, Haryana, India*

Abstract: *The purpose of this project is to discover ways to produce energy with alternate sources. This presents current status, major achievements and future aspects of solar energy in India and evaluation of current energy policies for conquering the obstructions and implementing solar for the future is also been presented. Solar energy is expected to play a very significant role in the future especially in developing countries, but it has also potential prospects for developed countries. Solar radiation is an integral part of different renewable energy resources like PV power, solar thermal power, solar heater etc.*

This consists of Study of the Solar cell, Solar Photovoltaic Technology, ***Planning and Designing a Stand Alone Solar Power System for Multi Building in an Organization*** *where Solar energy plays an important role for the power supply in case of emergency by replacing Diesel Generator set i.e. DG Set.*

This gives a detail planning and designing of solar power system of 80KW demand per hour for Al-Falah School of engineering and technology, Brown hills college of engineering and technology, central canteen, masjid, Hostel as well as Al-Falah School of Training and Education.

Keywords: *MNRE, SP, DG Set.*

I. Introduction

A small solar electric or photovoltaic (PV) system can be a reliable and pollution-free producer of electricity for your home or office. Small PV systems also provide a cost-effective power supply in locations where it is expensive or impossible to send electricity through conventional power lines. A significant part of the large potential of solar energy in the country could be developed by promoting grid interactive solar

Photo voltaic power systems of varying sizes as per the need and affordability coupled with ensuring adequate return on investment. It has been proposed to set up a 80KW stand alone Power System plant on the roof top terrace of the north wing of Al-Falah Group of institution as a pilot project.

1.1   The SPV system at roof-top of Al-Falah Group of Institution, is estimated to provide annual Energy generation of 49290 KW/annum and operate at a capacity factor of 19%.

1.2   If I consider 265 days per annum sunshine days then the total load or backup power provided in this case/Thesis

Fig.1.1. Electricity generated by photovoltaic cell

1.3 The primary objective of the solar energy research enclave will be two-fold:-
a) Establishment of a solar power station that can supply 80 KW/hr power
b) Outline the research areas that will be explored for sustainable solar energy generation, storage and distribution.

The solar power station will be built in modular fashion such that different technologies can be utilized/tested for generating power. The modules will be designed not only as a demonstrator of existing technologies but also to explore cutting edge research Technologies that have potential for economic viability.

II. Background Related Work

To Study the various journal papers such as Elsevier, IEEE, Science direct, international & national conferences. Finally study the paper of solar power plant on rooftop connected status of solar energy in India and global, solar energy tariff, renewable energy policy of different states in India. About these papers short conclude and explanations are given below in the literature survey.

This chapter gives review of literature of different papers related our search. In this section the study of various papers and thoughts authors regarding **"A Stand Alone Power System for Al-Falah Group of Institution"** is proposed which helps in defining the objective.

The solar photovoltaic device systems for power generation had been deployed in the various parts in the country for electrification where the grid connectivity is either not feasible or not cost effective as also some times in conjunction with diesel based generating stations in isolated places, communication transmitters at remote locations. With the downward trend in the cost of solar energy and appreciation for the need for development of solar power, solar power projects have recently been implemented. A significant part of the large potential of solar energy in the country could be developed by promoting grid interactive solar photovoltaic power systems of varying sizes as per the need and affordability coupled with ensuring adequate return on investment.

III. Presentation Of The Main Contribution Of The Paper/ Scope Of Research

SOLAR power has always had a reputation for being expensive, but not for much longer. In India, electricity from solar is now cheaper than that from diesel generators. The news - which will boost India's "Solar Mission" to install 20,000 megawatts of solar power by 2022 - could have implications for other developing nations too.

Recent figures from market analysts Bloomberg New Energy Finance (BNEF)show that the price of solar panels fell by almost 50 per cent in 2011. They are now just one-quarter of what they were in 2008. That makes them a cost-effective option for many people in developing countries.

A quarter of people in India do not have access to electricity, according to the International Energy Agency's 2011 World Energy Outlook report. Those who are connected to the national grid experience frequent blackouts. To cope, many homes and factories install diesel generators. But this comes at a cost. Not only does burning diesel produce carbon dioxide, contributing to climate change, the fumes produced have been linked to health problems from respiratory and heart disease to cancer.

Now the generators could be on their way out. In India, electricity from solar supplied to the grid has fallen to just 8.78 rupees per kilowatt-hour compared with 17 rupees for diesel. The drop has little to do with improvements in the notoriously poor efficiency of solar panels: industrial panels still only convert15 to 18 per cent of the energy they receive into electricity. But they are now much cheaper to produce, so inefficiency is no longer a major sticking point.

The one thing stopping households buying a solar panel is the initial cost, says Amit Kumar, director of energy-environment technology development at The Energy and Resources Institute in New Delhi, India. Buying a solar panel is more expensive than buying a diesel generator, but according to Chase's calculations solar becomes cheaper than diesel after seven years. The panels last 25years.

3.1 The primary objective of the solar energy research enclave will be two-fold:-
a) Establishment of a solar power station that can supply 80 KW/hr power.
b) Outline the research areas that will be explored for sustainable solar energy generation, storage and distribution.

The solar power station will be built in modular fashion such that different technologies can be utilized/tested for generating power. The modules will be designed not only as a demonstrator of existing technologies but also to explore cutting edge research technologies that have potential for economic viability.

IV.   Proposed Methodology And   Discussion

	PV Crystalline	PV - Concentrators	PV – Thin Film	Total
Capacity (kW)	300	100	100	500
Expected Power Generation per year #	443644	184723	147880	776247
Value if consumed by IITK (per year)	443644*3.3 =Rs. 13.31 Lakh	184723*3.3 = Rs. 6.1 Lakh	147880*3.3 = Rs. 4.44 Lakh	Rs. 23.85 Lakh
Value if sold to Grid (per year)@	443644*11.4 Rs. 50.6 Lakh	184723*11.4 Rs. 21.06 Lakh	147880*11.4 = Rs. 16.86 Lakh	Rs. 88.49 Lakh
	Table no.4.1 Pricing			
Additional Benefits due to CDM Credits				

Basic Principles to Follow When Designing a Quality PV System

- Select a packaged system that meets the owner's needs. Customer criteria for a system may include reduction in monthly electricity bill, environmental benefits, desire for backup power, initial budget constraints, etc. Size and orient the PV array to provide the expected electrical power and energy.
- Ensure the roof area or other installation site is capable of handling the desired system size.
- Specify sunlight and weather resistant materials for all outdoor equipment.
- Locate the array to minimize shading from foliage, vent pipes, and adjacent structures.
- Design the system in compliance with all applicable building and electrical codes.
- Design the system with a minimum of electrical losses due to wiring, fuses, switches, and inverters.
- Properly house and manage the battery system, should batteries be required.
- Ensure the design meets local utility interconnection requirements.

Basic Steps to Follow When Installing a PV System

- Ensure the roof area or other installation site is capable of handling the desired system size.
- If roof mounted, verify that the roof is capable of handling additional weight of PV system. Augment roof structure as necessary.
- Properly seal any roof penetrations with roofing industry approved sealing methods.
- Install equipment according to manufacturer's specifications, using installation requirements and procedures from the manufacturers' specifications.
- Properly ground the system parts to reduce the threat of shock hazards and induced surges.
- Check for proper PV system operation by following the checkout procedures on the PV System Installation Checklist.
- Ensure the design meets local utility interconnection requirements
- Have final inspections completed by the Authority Having Jurisdiction (AHJ) and the utility (if required).

V.   Result

80 kW Solar Power Plant with the optimum quality components and the latest Computer/Mobile data monitoring system would cost a total of Rs. 88,00,000/- approximately.

The main components and accessories covered within the cost are mentioned as under:
1. PV modules: 350 Nos. approx. of 250W each
2. Inverters with total capacity of 100 KVA approx.
3. G.I. mounting structures and frames for modules.
4. Isolation Transformer.
5. Mobile phone/Computer data monitoring system.
6. MCBs.
7. SPDs (Surge Protection Devices).
8. Energy Meter.
9. Distribution boxes.
10. Lightening arrestors.

11. Cables, Wires and other accessories.
12. Supply, Installation, Testing and Commissioning.
13. Free Maintenance for a period of one year after commissioning.

A. Total cost of project:- Rs 88,00,000/ approx.
B. Subsidiary provided by Govt. of India under JNNSM @ 30% of total project cost then it become:- Rs 2640000/approx.
C. Total budget of the project became:- (A-B)= 6160000/approx
   5.1 COST FEASIBILITY OF EXITING DG SET

Al-Falah Group of Institution has already set-up three DG set the detail are as following:-

Sl. no	Company name	Rating in KVA	Cost in Rs
01	Cummins	82.50	4,40,000
02	Kirloskar	180	5,40,000
03	Caterpillar	320	10,00,000
	Total		19,80,000

5.2 Equation become:-
(i)   Fuel consumption @75% load with   Radiator & Fan= 51.1 ltr/hr @ 320 KVA
(ii) Cost of Fuel per KVA became= 51.1/320 = 0.159 ltr/KVA 0.16 ltr/KVA
(iii) Now we have to design the load of 80 KW emergency load i.e. (100 KVA)
(iv) Cost for 8 hrs will become= 0.16*100

= 16 ltr *Rs 53 per ltr.
= Rs 6800/day (8 hrs)

The Annual cost of diesel from the above system
become= Rs 24,48,000
The cost of Solar power system for 100 KVA calculated= Rs 61,60,000

Pay Back Period
The Annual cost of diesel from the above system become= Rs 24,48,000
The cost of Solar power system for 100 KVA calculated= Rs 61,60,000

Rs 6160000/2448000= 2 years 6 month and 6 days

Life cycle of the system is up to 25 Year
The cost of the installation of solar system will be recover in Two an half Years and after that there will be relief/saving of Rs 2448000. If the maintence is also included in the system, certainly the amount will be recovered in three year in all respect. If there is no power failure from the utility or in the night hour, the use of solar system can be done frequently after shunting of utility supply.

VI. Conclusions
Solar power is a good alternative energy source. It has many advantages over fossil fuels. One is that the sunlight is free of cost and does not have to be bought like other fuels. It also doesn't hurt the environment and it is a renewable energy source. There are a few drawbacks to solar power. One is that it can be expensive to installation/Setup and can be hard to use on cloudy days. Solar power is also difficult and expensive to store. Another demerit is that silicon material be use for manufacturing of solar cell is not readily available.
At the last, the project or thesis able to find out whether the planning and designing of solar power system is economical. This is very unfortunate because solar power would be far more advanced with more funding. 30 per cent central government able to provide subsidiary. Out of total cost of installation. One of the most important thing is eco-friendly and pollution free. Once installed upto 25 years.

REFERANCES

[1]   http://energy.gov/energysaver/articles/small-solar-electric-systems
[2]   Solar radiant Energy over India," 2009 India Meteorological Department, Ministry of Earth Sciences, Government of India. NREL, http://www.nrel.gov/international/ra_india.html, 2010.
[3]   MNRE, Jawaharlal Nehru National Solar Mission (JNNSM), Ministry of New and Renewable Energy (MNRE), Government of India, New Delhi, India, 2010, http://www.mnre.gov.in/file-manager/UserFiles/mission_document_JNNSM.pdf.
[4]   A. Singh, 2009 "A market for renewable energy credits in the Indian power sector," Renewable and Sustainable Energy Reviews, vol. 13, no. 3, pp. 643–652,
[5]   (6) EIA: Inernational Energy Outlook 2011 [Online], Available from:http://www.eia.gov/forecasts/ieo/pdf/0484(2011).pdf (2011).
[6]   EERE: 2010 Annual Progress Report, Energy Storage R&D [On-line], Available from: http://www1.eere.energy.gov/vehiclesandfuels/pdfs/program/2010 energy storage.pdf (2010).
[7]   Bikramjit sinha and Kriti joshi 2012"Analysis of india's solar photovoltaics research output" Annals of Library and Information studies vol. 59,June.
[8]   George ZHOU vol. 14, Aug 2011 "Using Multi-Agent Simulation to Design a Solar Energy Distribution System", www.springer.com
[9]   S. Rao Peddada, October 2012 "National Solar Mission & Solar Technology Deployment in India" Surya Power,.
[10]   J.Zuboy, S. Sczepanski, S. Moon, D. Gwinner, and R. Nahan, May 2010. "DOE Solar Energy
[11]   Technologies Program: Overview and Highlights," US Department Of Energy (DOE)
[12]   Narsi, September 2010 "Benchmark Capital Cost Norms for Solar PV Power Projects and Solar Thermal Power Projects,".
[13]   K. Ro and S. Rahman, Sep. 2008.
[14]   "Two loop Controller for Maximizing Performance of a
[15]   Grid Connected Photovoltaic- Fuel Cell Hybrid power plant," lEEE Trans.on Energy
[16]   Conversion, vol 13, Issue: 3, pp. 276 - 281, (14) G. M. Tina and F. Pappalardo, (SAE-2009) "Grid-Connected Photovoltaic System with Battery
[17]   Storage System into Market Perspective," IEEE Sustainable Alternative Energy pp.1-7.
[18]   S.G. Petoussis, A.G. Petoussis, G.E. Georghiou, X.-P. Zhang and K.R. Godfrey, "Grid-Connected Photovoltaic Power Plants: The Effect on the Electricity Market.

Solar-Thermoelectric Hybrid Powergenerator

[1]Syed Sharin Hameed, [2]Dr. P. V. Walke

[1*]*Student IV Semester, M. Tech. Heat Power Engineering, G.H.Raisoni College of Engineering, Nagpur-440016, India*
[2] *Professor Mechanical Engineering Department, G.H.Raisoni College of Engineering, Nagpur-440016, India*

Abstract: *Hybrid Photovoltaic and thermoelectric systems more effectively converts solar energy into electrical energy. Two sources of energy are used one of the energy is solar,that converts radiant light into electrical energy and heat energy which will convert heat into electricity.Photovoltaic cells and thermoelectric modules are used to capture and convert the energy into electricity.Furthermore solar-thermoelectric hybrid system is environmental friendly and has no harmful emissions.Solar-thermoelectric hybrid system increases the overall reliability without sacrificing the quality of power generated.In this paper an overview of the previous research and development of technological advancement in the solar-thermoelectric hybrid systems is presented.*

I. Introduction

Today the world daily oil consumption is 85million barrels of crude oil,and this is expected to increase to 123 million barrel per day by the year 2025[1].With this ever increasing oil consumption and growing concern on environmental protection ,there is pressing need to develop green energy sources.[2].With the known consequences of fossil fuel combustion on the environment there is urgent need to develop green energy sources.Solar energy is the largest and most abundantly available renewable energy resource on the planet,and is environmental friendly.Hybrid systems for solar energy utilization have gained considerable attention from the researchers and engineers during the last decade because of their higher efficiency and stability of performance in comparison to individual solar devices.

II. Solar Photovoltaic

Photovoltaic effect was discovered in selenium way back in 1839. The photovoltaic process converts sunlight directly into electricity. A Photovoltaic cell consists of two or more thin layers of semiconducting material,most commonly silicon. When the silicon is exposed to light ,electrical charges are generated andthis can be conducted away by metal contacts as direct current. Electrical output from single cell is small, so multiple cell are connected together and encapsulated to form a module also called as panel. The PV panel is the principle building block of a PV system and any number of panels can be connected together to give the desired electrical output. PV cell are made of various semiconductors, which are materials that are only moderately good conductors of electricity.These cells are packed into modules which produce a specific voltage and current when illuminated. PV modules are connected in series/parallel arrangement to meet voltage/current requirements. PV equipment has no moving parts and as a result requires minimal maintenance and has a long life. It generates electricity without producing emissions of greenhouse or any other gases, and its operation is virtually silent.[3].

III. Thermoelectric Generator

Thermoelectric phenomena were first observe about 180 years ago, the manufacturing of thermoelectric generators only emerged in early 1960's .The thermoelectric generators are based on the principle of seebeck effect; if appropriated semiconductors are connected thermally in parallel and electrically in series, a voltage potential is established. The cause is a statistical process in the semiconductor. Heat is converted into electricity, with a low efficiency value ,but silently, without moving parts and thus without mechanical wear. A Thermoelectric generator typically consists of several hundred thermoelectric elements, a heat source and convection cooling, which is usually passive. The heat source is normally a gas or petrol burner; however for extraterrestrial applications or special tasks with long running times radio isotopes are also used.
The discovery of high ZT(~1) thermoelectric semiconductors(e.g. PbTe and SiGe) and the availability of isotopic and nuclear heat sources made it possible to fabricate relatively efficient thermoelectric generator. The advances in technnology created a new market for long life, high reliability and low maintenance power

sources.Over the following decade various radioisotope thermoelectric generators and fossil fuelled thermoelectric generators have been developed.

The discovery of high figure of merit materials and a sustained market demand provided a foundation for the development of thermoelectric power industry.

IV.   Literature Review

Benson and Jaydev et al [4] presented the idea of using thermoelectric generators in very large scale installations to produce useful amounts of electricity from low grade heat sources. One possibility was to use thermoelectric generators in an ocean Thermal Energy Conversion system. The proposed temperature difference was 5-25°C. It was shown that some commercially available thermoelectric materials have an acceptable figure of merit in this temperature range. It was assumed that performance of 20% of Carnot efficiency could be achieved from the thermoelectric devices. Other potential sources of energy that were discussed included geothermally heated ocean water(85°C),solar ponds(50°C),natural lake thermoclines (10-20°C),and utility power plant waste heat(15C°C). Long term capital costs were taken into account in the discussion.

Lamley et al [5] presented an unusual application of a thermoelectric generator designed to produce power from the long wave infrared radiation leaving the surface of the earth. This project involved generation power for a high altitude, long duration communication platform. Energy would be collected by radiation from the earth's surface, and rejected by radiation into space. A thin-film thermoelectric device configuration was devised and tested. A total temperature difference of 58°C was used in the design.

Benson and Tracy et al [6].Discussed the development and use of thin-film thermoelectric generators for use with low grade thermal energy applications such as those discussed in Benson and Jayadev[4].

Chen, J. [7]. Performed the thermodynamic analysis of a thermoelectric generator powered by direct solar radiation. Four classes of important irreversibility's were identified and their effects were included in the analysis. These irreversibility's included: Finite rate heat transfer between the device and the surroundings. Heat leaks internal to the device, Ohmic heat production, and heat losses in the solar collector. The main conclusions of the analysis established performance limits for solar powered thermoelectric devices.

A.Steinhuser et al [8].Presented extensive investigations and have shown that there is still considerable potential for optimization, particularly concerning the gas burner and the connection of the thermoelectric modules to the heat source, and given the example that the total efficiency value and, in particular, the exhaust emission of the thermoelectric converter can be improved by using a large area burner or a catalytic burner.The Proposed system can also be used as the power supply for other facilities remote from the grid, such as environmental measurement stations, aviation safety equipment and traffic guiding systems. The economics of the proposed plant has been investigated in details.Analysis of all cost relevant parameters of the reference hybrid system shows that the thermoelectric generator size needs to be reduced as much as possible. Also the reference system has been compared with all relevant supply alternatives; PV battery system is always the cheapest solution for a small load, if site is located in tropical areas, but not in temperate zones. The fossil fuelled generators are too expensive due to their O&M costs.It is proved that the proposed hybrid system is cost competitive with pure thermoelectric generators, and the system also guarantees an higher reliability and avoids 2.4T CO2 annually.

NarongVatcharasathien et al. [9]Developed a design methodology for solar-thermoelectric power generation using TRYNSYS software which is an extremely powerful tool. The result do not show high system performance however, they demonstrate well the feasibility of this concept for power generation in Thailand. The result derived lay a foundation for further investigation of solar-thermoelectric power generation at large scale.

W.G.J.H.M. Van Sark [10] Developed a model to determine the combined efficiency of photovoltaic and thermoelectric converter. The result show that adding a TE converter to the backside of a PV module can lead 8-23% increase in efficiency, depending on the type of module integration, and assuming TE material with afigure of merit value of Z=0.004K-1. The efficiency increase depends on the assumption that the backside is sufficiently cooled and is at ambient temperature.

M.M.M. Daud et al[11]. Developed a prototype panel which utilizes solar radiation and heat from the sun to generate electricity, by using PV cells and TE modules. It is shown that the efficiency of PV thermal can be increased   upto 0.79% without cooling system and 1.84% with integration of cooling system from tradiational PV panel at 600w/m2 of solar radiation.Result also show that at 868 w/m2 solar radiations, the prototype panel with liquid cooling can improve efficiency up to 3%. Also with the use of high efficiency of SiGe QW or PbTe QD TE module could contribute to electricity with overall higher efficiency.

V. Discussion and Conclusion

The various conclusions emerging out of this study are presented below.

1) Improved performance can be gained by development work on semiconductor material,which will lead to increased figure of merit.
2) Improve manufacturing techniques will lead to reduction in cost of fabrication of semiconductor material and improved quality.
3) PV-TEG hybrids have proven to be an ideal alternative power source at sites where; high reliability is an important factor, winter solar insolation vales are low and shelter heating is required.
4) The PV-TEG innovation has no emission and requires less maintenance.
5) Many applications have been reported on TEG, such as the aerospace industry, automobile, waste incineration plants, centralheating's systems in cold city and stove-top generators in remote country areas, where the PVG can also be used.
6) Future work should be focus to improve the efficiency of hybrid power system and its cost reduction so as to make it more competitive.

Acknowledgments

REFERENCES

[1]. www.worldwatch.org.
[2]. J.Yang, "Potential applications of thermoelectric waste heat recovery in the automotive industry", International conference on Thermoelectrics, June 2005, pp. 155-159.
[3]. R.Nagaraj "Renewable Energy Based Small Hybrid Power System for Desalination Application in Remote Locations", Desalination 2012;978-4673-0934-9/12.
[4]. Benson, D.K. and Jaydev,T.S.,1980 "Thermoelectric Energy Conversion,Economical Electric Power from Low Grade Heat," Proceedings of the Third International Conference on Thermoelectric Energy Convrsion, Arlington,TX, March 12-14, 1980,publ. by IEEE, New York, NY,pp.27-56.
[5]. Lamley, L.W., 1980, "A Radiation Thermoelectric Power Converter",Proceedings of the Third International Conference on Thermoelectric Energy Conversion,Arlington,TX,March 12-14,1980.publ. by IEEE, New York, NY,pp. 20-26.
[6]. Benson, D.K. and Tracy, C.E., 1982, "Design and Fabrication of Thin Film Thermoelectric Generators", Proceeding of the Fourth International Conference on Thermoelectric Energy Conversion,Arlington, TX, March 10-12, 1982, publ. by IEEE, New York, NY, pp. 11-14.
[7]. Chen, J., 1979,"Thermodynamic Analysis of a Solar driven Thermoelectric Generator," Journal of Applied Physics, v 79 n 5, pp.2717-2721.
[8]. A.Steinhuser, G.Hille, R.Kugele, W.Roth, W.Schulz., 1996. "Reliable Power Supply with Photovoltaic-Thermoelectric Hybrid Systems". Fraunhofer Institute of Solar Energy System ISE Oltmannsstr. 5, D-79100 Freiburg, Germany.
[9]. Narong,Vatcharasathien,JosephKhedari,JongjitHirunlabh, and Michel Daguener.,2003, "A Computer Tool for Designing Solar-Thermoelectric Power Generation System" 22nd International Conference on Theroelectrics(2003).
[10]. W.G.J.H.M van Sark., 2011. "Feasibility of Photovoltaic-Thermoelectric Hybrid Modules". Journal of Applied Energy 88920110 2785-2790.
[11]. M.M.M. Daud, Nusyarizal Bin Mohd Nor, Taib Ibrahim.,2012, "Novel Hybrid Photovoltaic and Thermoelectric Panel". 2012 IEEE International Power Engineering and optimization Conference (PEOCO2012), Meleka Malaysia 6-7 June 2012.

A New Bi-level Program Based on Unblocked Reliability for a Continuous Road Network Design

Naoki Maruyama, Shujun Hou, Masafumi Hirota, Yaowateera Achawangkul

Department of Mechanical Engineering, Graduate School of Engineering, Mie University, Japan

ABSTRACT: *With increasing demands for better and more reliable service, developing a method for designing a highly-reliability road network has become a critical issue. A Network Design Problem is used to determine a set of design parameters leading to the creation of an optimal road network. Moreover, the performance of an Origin-Destination pair with high traffic demands is a top priority in the optimizing process. A bi-level programming technique, that is upper-level and lower-level programs, can be used to formulate the Continuous Network Design Problem. This study establishes a new type of bi-level program based on unblocked reliability. The proposed bi-level program is applied to analyze a real local road network that has 22 nodes and 62 links. A set of link capacity expansions is determined by solving the proposed bi-level program using the Hooke-Jeeves algorithm. This kind of capacity expansion results in optimization by maximizing the balance between the unblocked reliability of the entire road network and the road network expansion ratio. The new, proposed bi-level program can comply with the various limits on environment and financial resources.*

Keywords: Bi-level Program, Continuous Network Design Problem, Link capacity expansion, Unblocked Reliability, User Equilibrium

I. INTRODUCTION

The Network Design Problem (NDP) is used to determine a set of design parameters that leads the road network to an optimal state. Typically, the design parameters are link capacity expansions. There are two forms of the problem, the Continuous Network Design Problem (CNDP) and the Discrete Network Design Problem (DNDP). The CNDP takes the network topology as given and is concerned with the parameterization of the network. The DNDP is concerned with the topology of the network, such as the construction of a new road, bridge, tunnel or bypass.

The CNDP can be formulated as a bi-level program[1]. Planners and managers in the upper level determine the parameters of the road network, and travelers in the lower level respond to the change in the road network. The upper-level program expresses the expectation of the planners and managers, that is the minimization of the total cost function. In general, the total cost is the sum of the total travel cost in the network and investment cost of link capacity expansions for fixed traffic demands. A User Equilibrium (UE) can be formulated as an equivalent minimization problem, which is considered as a lower-level program in the CNDP[2]. The UE describes a stable state when all drivers attempt to minimize the respective travel time. In other words, the drivers' route choice behavior is voluntary rather than controlled by managers of the road network system.

With increasing demands for better and more reliable service, the road network system has incorporated a reliability analysis as an integral part of its planning, design and operation. Then, it is necessary to introduce a reliability index of road network system performance to the CNDP. There are several reliability concepts in the road network system, such as connectivity reliability[3], travel time reliability[4], capacity reliability[5], and unblocked reliability. Unblocked reliability is the probability during one day of the road unit or system's ability to maintain an unblocked state at peak hours in which the highest traffic volumes are observed. The length of the road was regarded as a factor affecting route choice behavior when unblocked reliability was applied to analyze the investment optimization of the road network.

This paper proposes a new model of the bi-level program based on unblocked reliability for solving the CNDP in order to supply a set of optimal link capacity expansions, which improve the road network to a higher reliability level. The upper-level program that consists of the unblocked reliability index and cost, which is expressed as the road network expansion ratio, is described. The UE traffic assignment is regarded as the lower-level program. The Hooke-Jeeves (HJ) algorithm[6] is applied to solve the proposed bi-level program. Then, the proposed bi-level program is tested by a local road network, which has 22 nodes and 62 links.

II. Basic Idea Of Bi-Level Programming Based On Reliability Index

The CNDP can be formulated as a bi-level program. Planners and managers can influence the drivers' route choice behavior by changing a road network, but they cannot control their route choice behavior. When the Origin-Destination (OD) demand is inelastic, the objective function of the upper-level program is the system cost and the investment cost. Generally, system cost is expressed by travel times of the total network, and minimum travel time is expected. In this paper, the optimization objective is obtained by subtracting the investment cost from the unblocked reliability when the performance of a road network is indexed by unblocked reliability. The maximum value of unblocked reliability is expected.

If the link flows, x, is fixed, optimization objective is maximized, where $x = (x_1, \cdots, x_a, \cdots, x_G)$ is a vector and G is the total number of links in a road network. When the solution of link capacity expansions, y, is given, where $y = (y_1, \cdots, y_a, \cdots, y_G)$ is a vector, an assignment algorithm can be performed to obtain new link flows, x. This forms the basis of the iterative design-assignment bi-level programming algorithm [7].

Upper-level program: Solve the network design problem for y given x. Proceed to the lower-level program.
Lower-level program: Given y find new x. Return to the upper-level program.

Only one variable's optimization failed to optimize the entire system performance, which reflects the essence of the bi-level programming.

III. Upper-Level Program Based On Unblocked Reliability

Objective function F of the upper-level program is expressed as follows:

$$\max F(y) = R - d\lambda\phi \tag{1}$$

where,

$$\phi = \sum_{a \in A}(L_a y_a) \tag{2}$$

From the viewpoint of a planner, the first term on the right-hand side of Eq. (1), R, is the entire network unblocked reliability that represents the performance of the road network system, and R is a function of link flows. The link flows are obtained by solving the lower-level program when a set of link capacity expansions is fixed. The second term on the right-hand side of Eq. (1) presents the cost associated with improving the road network. The second term consists of a product of three parts, such as a control factor of the road network expansion scale, d, unit conversion factor, λ, sum of the product of each link's length, L_a, and link capacity expansion, y_a, and, ϕ, which indicates the road network expansion scale. The ratio of the road network expansion scale to the existing network scale, $\lambda\phi$, equals the road network expansion ratio.

3.1 Model of unblocked reliability

Nodes and links are the elements composing a road network. A node is a junction of two or more links and a link connects two nodes. A link may be regarded as a conduit for the flow between two nodes; all links referred to in this paper are directed. A road network is aggregated as several associated levels depending on classification and viewpoint. A governor considers the performance of the whole network, whereas a driver focuses his attention on the performance of an OD pair. A path is a sequence of nodes connected by links in one direction so that a movement is feasible from the origin to a given destination. For a fundamental analysis of traffic network, the capacity of a node is regarded as infinite. When either queue behavior or turning movement is of interest, the extra nodes are introduced to represent each explicit direction. The problem of node capacity will be a transformed link capacity problem between extra nodes. Along these lines, a four-level model of the road network unblocked reliability (link, path, OD pair and the entire network) is introduced[8, 9]. Here, the unblocked reliabilities of the link, the path m connecting origin i and destination j, the OD pair connecting origin i and destination j, and the entire network are presented by R_a, R_{ij}^m, R_{ij}, and R, respectively.

3.2 Cost Associated with Improving Road Network

The second term on the right-hand side of Eq. (1), $d\lambda\phi$, is called the penalty term. The conversion factor for physical dimension, λ, is formulated as follows:

$$\lambda = \frac{1}{\sum_{a \in A}(L_a C_a)} \tag{3}$$

The physical meaning of a denominator of Eq. (3), which is the sum of the product of each link's length and capacity, is an index of an existing road network scale. For a given road network, λ is a constant. Then, the penalty term in the objective function of upper-level program, $d\lambda\phi$, becomes a dimensionless factor. This penalty term ensures the network can be expanded to a reasonable degree. Also, the road network expansion will reach the optimal degree when the bi-level program has been solved.

IV. Lower-Level Program

The lower-level model of the bi-level program for the CNDP based on unblocked reliability is a fixed demand UE problem in this paper. UE is the state in which there is no motivation to change the system. UE means that travel times are identical along any used routes connecting an OD pair and less than or equal to the travel time on all unused routes, if every traveler attempts to choose the path with the shortest travel time[10]. The UE assignment problem is to find the link flows that satisfy the UE criterion when all OD entries have been appropriately assigned.

This link flow pattern can be obtained by solving the following mathematical problem[8, 11]. The objective function of the lower-level program is given by $Z(x)$, where $x = (x_1, \cdots, x_a \cdots, x_G)$ is a vector variable of link flows.

$$\min Z(x) = \sum_{a \in A} \int_0^{x_a} t_a(\omega, y_a) d\omega \tag{4}$$

The objective function is the sum of the integrals of the link travel time functions for a given link capacity expansion, y. The link travel time, $t_a(x_a)$, which represents the relationship between the flow and the travel time for link a, is calculated using the standard Bureau of Public Roads function[12]. Of course, the total capacity of each link is composed of the link capacity expansion and the existing link capacity when travel time, t_a, is calculated by Eq. (5).

$$t_a(x_a) = t_a^e \left[1 + 0.15(x_a/C_a)^4\right] \tag{5}$$

The Frank-Wolfe (FW) algorithm is used to solve the mathematical problem[13]. This algorithm is an iteration process to find the feasible flows that can reduce the value of the objective function[8].

V. Using Hooke-Jeeves Algorithm To Solve The Continuous Network Design Problem Based On Un-Blocked Reliability Model

The Hooke-Jeeves (HJ) algorithm is a fundamental algorithm for solving the Continuous Network Design Problem (CNDP)[6]. It was used first to solve the CNDP by Abdulaal and LeBlanc as a direct search method in the road network[14].

Consider the problem of maximizing the objective function of the upper-level program without constraints. The HJ algorithm proceeds by a sequence of exploratory and pattern moves. If an exploratory move leads to an increase in the value of the objective function of the upper-level program, it is called a success; otherwise it is called a failure. The purpose of solving the proposed bi-level program is to find a set of link capacity expansions to maximize the objective function of the upper-level program. The flow chart of the Hooke-Jeeves algorithm employed in this paper is shown in Appendix A.

Reviewing the exploratory move procedure, the capacity change of a link will be accepted only when the increase in the penalty term is smaller than that of the entire road network unblocked reliability. After the total links have been tested, if the current objective function value of the upper-level program is greater than the corresponding objective function value of the upper-level program of success link capacity expansions, the new success link capacity expansions are obtained. The purpose of the pattern move is to speed up the process of road network expansion through multiplying a coefficient with the capacity expansion of every improving link; this coefficient is greater than unity.

The bi-level program that is used to describe the CNDP is a non-convexity program. Even the solution of the bi-level program can be found, although it is usually a local optimum, not a global optimum. Hence, the HJ algorithm, as one of the traditional heuristic algorithms for solving a bi-level program, also has a similar local optimum for a solution. There are four parameters, such as the initial step length of exploratory move, s, the

reduction factor of the step length of exploratory move, θ, the convergence step length of exploratory move, η, and the step length of pattern move, v, in the HJ algorithm. They will mainly influence the iteration times, but hardly influence the objective function of the upper-level program when the four parameters fall within a reasonable range. Even though it is possible to obtain a large objective function value of an upper-level program for a given road network using certain parameters in the HJ algorithm, these parameters do not have any universality. The four parameters provided for the case study in this paper are empirically defined as 1,000, 0.5, 100, and 2, respectively.

VI.   Case Study Of A Real Local Road Network

6.1. Features of existing road network

A trunk road network in a local area is being employed as a case study. This road network was constructed based on an actual road network belonging to the author's province. Congestion often occurs at peak hours in the morning on this road network. First, the actual road network was expressed by a graph consisting of nodes and links; a code expresses a node, and a link is denoted by codes of two adjacent nodes. The topology and distance of the existing road network is shown in Fig. 1. There are a national road and a parallel motorway in the north-south direction, as well as some national roads and some access roads. The access roads provide access to and from the motorway. There are 22 nodes and 62 links in the local road network. A traffic zone is the unit of geography most commonly used in road network planning models. It is represented with a single point from the graph theory viewpoint and regarded as the area of the origins and destinations of trips. The 1st to 11th nodes express traffic zones that are the cities in this area. The 12th to the 21st nodes express the interchange of the motorway. The 22nd node is an important intersection between two national roads. The two side-by-side links have the same parameters including length, free-flow travel time and capacity between each node pair in the existing road network. The link capacity on the motorway is 4,600 pcu/h. For a national road, the capacity of each link between node pairs such as (5, 16), (8, 16), (6, 8), (6, 18), (7, 20) and (9, 20), is 1,600 pcu/h, and between other node pairs is 3800 pcu/h. For the access road, the capacity of each link between node pairs such as (1, 12), (2, 13) and (3, 14) is 3,800 pcu/h, while that between other node pairs is 1,600 pcu/h.

An OD matrix shows the sources and objectives of traffic flows in a road network. The Ministry of Land, Infrastructure, Transport and Tourism of Japan (MLIT) conducts a nationwide traffic census. The OD matrix of a local area trunk road network is shown in Table 1, which was calculated according to the traffic census data provided by MLIT. The OD matrix is regarded as a fixed demand for traffic assignment in the local area of the trunk road network.
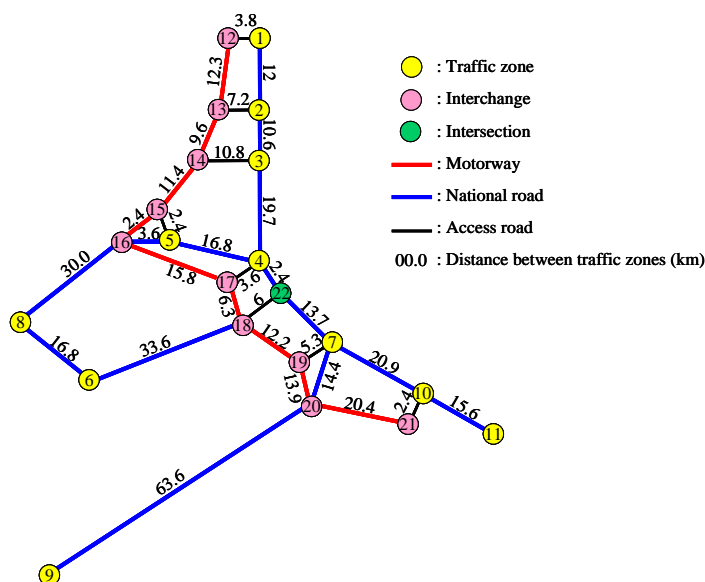
Fig. 1 Road network of a local area

Table 1 Origin-Destination matrix of traffic zones

Unit: pcu/h

Origin	Destination											
	1	2	3	4	5	6	7	8	9	10	11	Sum.
1	-	195	239	1,184	1,842	0	357	0	245	141	136	4,339
2	1,600	-	0	5	0	0	1	0	0	0	0	1,606
3	1,608	0	-	0	0	357	0	0	0	0	0	1,965
4	165	0	0	-	2,540	71	0	59	0	0	0	2,835
5	1,254	0	52	1,405	-	0	425	0	0	168	162	3,466
6	0	0	29	290	0	-	0	1,035	0	0	0	1,354
7	15	0	0	0	251	0	-	278	0	0	0	544
8	0	0	0	586	0	804	243	-	0	97	91	1,821
9	613	0	0	0	0	0	0	0	-	167	158	938
10	0	1,144	1,286	0	0	0	0	0	0	-	0	2,430
11	7	0	0	0	137	0	0	152	227	0	-	523
Sum.	5,262	1,339	1,606	3,470	4,770	1,232	1,026	1,524	472	573	547	21,821

6.2. Used path of existing road network

The used paths under the UE state can be obtained when the OD matrix is assigned to the road network by the lower-level program based on the FW algorithm. The travel time of any possible path can be calculated by the link travel times shown in Table 2. The link travel times of two directions may not be the same since the link flows in the two directions are not in balance. For example, here the travel time of path from 4 to 9 is estimated. The travel time of path 4-22-7-20-9 is 1.90 hour, which is greater than the travel time of the used path, 4-17-18-19-20-9, between the OD pair 4-9 as shown in Fig. 2. The travel times of other paths are also greater than the travel time of the used path, 4-17-18-19-20-9. This case study has verified that the lower-level program can determine the used paths in accord with the UE criterion. Of course, the link flows have also been calculated. Then, unblocked reliability in the upper-level program can be calculated by the proposed model.

Table 2 Link travel time in existing road network

Unit: h

Origin	Destination																					
	1	2	3	4	5	6	7	8	9	10	11	12	13	14	15	16	17	18	19	20	21	22
1		0.20										0.10										
2	0.22		0.18										0.18									
3		0.19		0.34										0.27								
4			0.34		0.29												0.09					0.04
5				0.28											0.10	0.09						
6								0.43										0.84				
7										0.35									0.13	0.36		0.24
8						0.42										0.61						
9																				1.29		
10							0.36				0.39										0.06	
11										0.39												
12	0.10												0.15									
13		0.18										0.15		0.12								
14			0.27										0.12		0.11							
15					0.11									0.11		0.06						
16						0.09			0.60						0.06		0.16					
17				0.09												0.16		0.06				
18						0.84											0.06		0.12			0.15
19							0.13											0.12		0.17		
20							0.36		1.27										0.17		0.29	
21										0.06										0.29		
22				0.04			0.23											0.15				
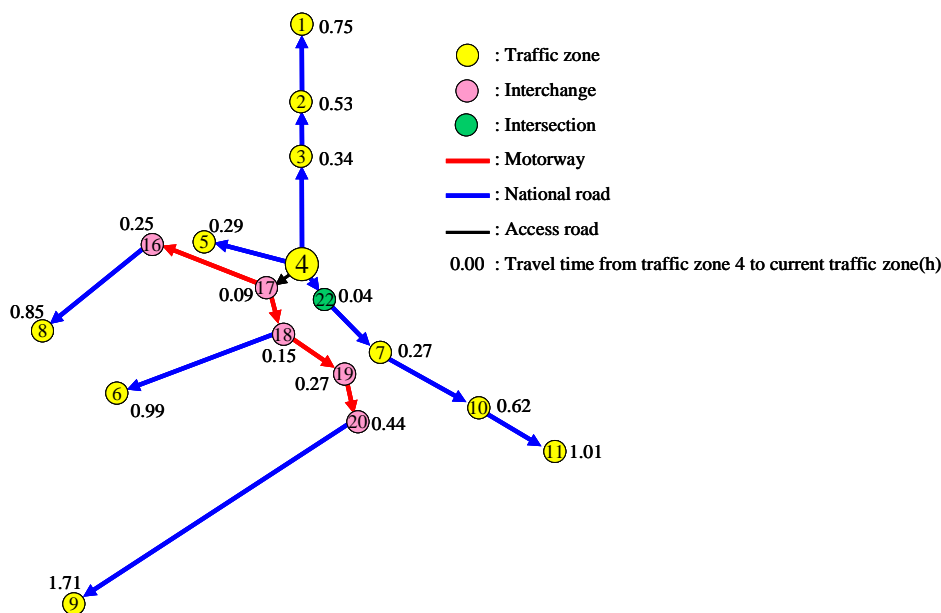
Fig. 2 Tree of used paths of traffic zone 4 originating in existing road network

6.3. Optimization result

Iteratively solving the lower-level and upper-level program in the HJ algorithm can optimize the road network in our case study. When the special constraints of the environment and financial resources are not considered, the controllable factor $d = 1$. The initial solution, $y^0 = 0$, is given initially. Then, the HJ algorithm is applied, and the result is a set of most worthy links and their capacity expansions as shown in Fig. 3. In Fig. 3, only links that will be improved are shown, and the other link capacities are not changed in the planning. The network expansion ratio, $\lambda\phi$, equals 7.9% in the existing road network scale by applying the HJ algorithm to solve the proposed bi-level program when the objective function of the upper-level program reaches maximum.

The links have been graded according to the unblocked reliability, as shown in Fig. 4. The brown, pink, blue and green arrows express the grade of reliability from low to high, corresponding to $R_a < 25\%$, $25\% \leq R_a < 50\%$, $50\% \leq R_a < 75\%$ and $75\% \leq R_a$, respectively. In the existing road network, the links of the four grades are 4, 15, 21, and 22, respectively. In the improved road network, the group of most unreliable links disappeared and all of the brown links were promoted to blue links; and six pink links were also promoted to blue links. No links were promoted to 75% or more because it would be too costly to improve links to an excessively high level of unblocked reliability. The proposed bi-level program can avoid this kind of unreasonable proposal. Therefore, in the improved road network, the links of four grades were 0, 9, 31, and 22. This case shows that the links of lower reliability were improved.

Fig. 3 Link capacity expansions
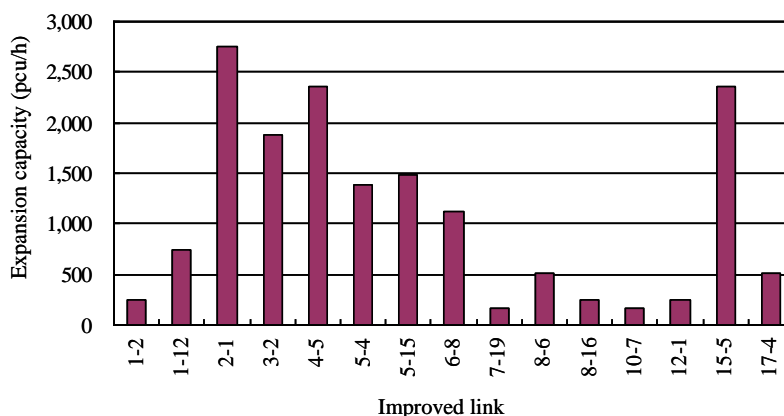
(a) Existing road network   (b) Improved road network
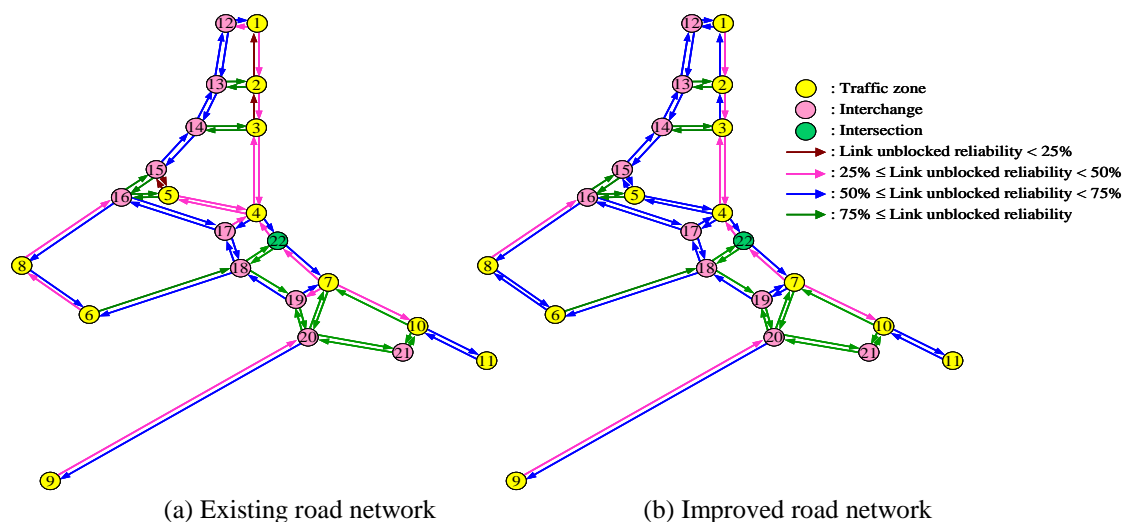
Fig. 4 Grading links by unblocked reliability

The OD pair's unblocked reliabilities of the existing road network and the improved road network are shown in Fig. 5. In Fig. 5, only 44 contributing OD pairs are displayed, which have positive OD flows in Table 2. The unblocked reliability of the entire road network, R, is the weighted mean of the contributing OD pair's unblocked reliability, since the other OD pair's weight is zero. Here, the weight is the proportion of the OD flow to the total traffic demand. There is a distinct improvement in the unblocked reliability of the entire road network from 35.1% of the existing network to 53.4% of the improved network.

For studying the influence of improvement planning, the arithmetic mean of the unblocked reliability of the contributing OD pairs was also calculated. The arithmetic mean is the sum of the contributing OD pair's unblocked reliability divided by the number of items. The arithmetic mean reports the central tendency. In the existing road network, the number of OD pairs, in which each unblocked reliability is less than the arithmetic mean, is 21, and the traffic demands account for 78.2% of the total. This case indicates that the unblocked reliabilities of OD pairs with high traffic demands, which have high weight, are at a lower level. Hence, the arithmetic mean and the weighted mean, 47.6% and 35.1%, respectively, show an extraordinary disparity in the existing road network. For the improved road network, the unblocked reliability of 21 OD pairs accounting for 52.9% of all traffic demands was greater than the arithmetic mean. In the improved road network, the arithmetic mean and weighted mean became 54.6% and 53.4%, respectively, obviously close to each other. These results showed that the performance of an OD pair with high traffic demands has been considered in the proposed model of the bi-level program since the increased scale of the weighted mean was greater than the arithmetic mean.
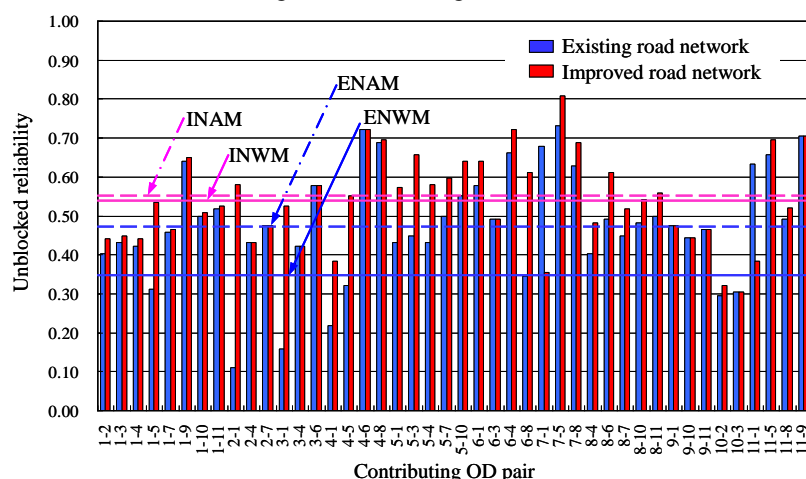
INAM: Improved network arithmetic mean   INWM: Improved network weighted mean
ENAM: Existing network arithmetic mean   ENWM: Existing network weighted mean

Fig. 5 Unblocked reliability of OD pair in improved network contrasts with existing network

6.4. Significant influence on objective function of upper-level program from control factor of road network expansion scale

        The trend in the objective function of the upper-level program with changes in the control factor of the road network expansion scale is shown in Fig. 6. The abscissa indicates the control factor of the road network expansion scale, *d*, and the ordinate expresses the three dimensionless values whose relationship is formulated by Eq. (1). When *d* increases, the results of the bi-level program in different simulation processes show the reducing objective function value of the upper-level program, lower unblocked reliability and network expansion ratio. The curve of the road network expansion ratio is steeper with a decrease in *d*, which signifies a reduction in the contribution of more network expansions to the road network performance improvement. In other words, the proposed bi-level program reflected the nature of road network improvement that satisfies a law of diminishing marginal utility. If *d* approaches zero, the expansion ratio will approach infinity, and the unblocked reliability will approach unity. When *d* is given a sufficiently large value, no link is expanded and the unblocked reliability is also unchanged.
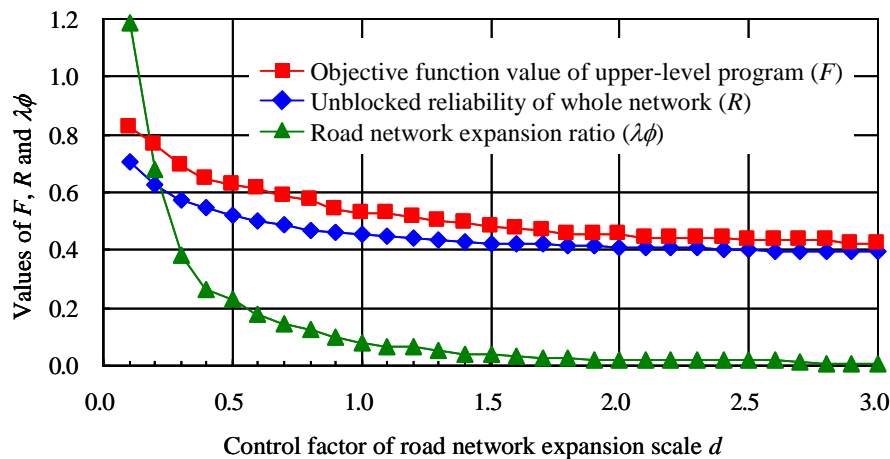
Fig. 6 Trend of objective function of upper-level program with changing control factor of road network expansion scale

VII.   Conclusion

        In this paper, a new bi-level program model based on the unblocked reliability for solving the continuous network design problem was proposed. A set of link capacity expansions that can best improve the road network was found using the Hooke-Jeeves algorithm to solve the proposed bi-level program. These link capacity expansions reach an optimization result by maximizing the surplus of the unblocked reliability of the entire road network minus the road network expansion ratio, where the user equilibrium is followed. Also, the performance of an Origin-Destination pair with high traffic demands is a top priority. The penalty term on improvement costs is established to ensure that the road network expansion reaches a reasonable scale and only the links that can greatly improve unblocked reliability of the entire road network will be selected when using the Hooke-Jeeves algorithm. The control factor of the road network expansion scale is introduced in the objective function of the upper-level program. When planners and managers set the control factor to different degrees, the proposed bi-level program can comply with various limits of environmental and financial resources. The proposed bi-level program is a useful tool for design of a high-reliability road network system with optimization link capacity expansions.

Nomenclature
A: set of links in network
a: link in network, $a \in A$
C: capacity of a link, pcu/h
d: control factor of road network expansion scale
F: objective function of upper-level program
g: counter for exploratory move in Hooke-Jeeves algorithm
G: total number of links in road network
h: counter for pattern move in Hooke-Jeeves algorithm
I: set of all origin nodes
J: set of all destination nodes

$L:$ length of a link, km

$M:$ set of used routes between Origin-Destination pair

$m:$ used path between Origin-Destination pair, $m \in M$

$R:$ unblocked reliability index

$s:$ step length of exploratory move for link capacity expansion in Hooke-Jeeves algorithm, pcu/h

$t:$ travel time, h

$v:$ step length of pattern move in Hooke-Jeeves algorithm

$x:$ link flow, pcu/h

$y:$ link capacity expansion, pcu/h

$Z:$ objective function of lower-level program

$\beta:$ direction factor in Hooke-Jeeves algorithm, $\beta = 1$ for positive capacity expansion, and $\beta = -1$ for negative capacity expansion

$\eta:$ convergence step length of exploratory move for link capacity expansion in Hooke-Jeeves algorithm, pcu/h

$\theta:$ reduction factor of step length of exploratory move in Hooke-Jeeves algorithm

$\lambda:$ conversion factor for physical dimension, h/(km·pcu)

$\mu:$ expansion direction in Hooke-Jeeves algorithm

$\phi:$ road network expansion scale

$\omega:$ variable of integration in objective function of User Equilibrium problem

Superscripts

  e: free-flow state

Subscripts

  i: origin node, $i \in I$

  j: destination node, $j \in J$

Abbreviations

  CNDP: Continuous Network Design Problem

  DNDP: Discrete Network Design Problem

  FW: Frank-Wolfe

  HJ: Hooke-Jeeves

  NDP: Network Design Problem

  OD: Origin-Destination

  UE: User Equilibrium

REFERENCES

[1] S. Chiou, Bilevel programming for the continuous transport network design problem, *Transportation Research Part B*, *39*, 2005, 361-383.

[2] J. Magnus and P. Michael, Sensitivity analysis of separable traffic equilibrium equilibria with application to bilevel optimization in network design, *Transportation Research Part B*, *41*, 2007, 4-31.

[3] Y. Iida and H. Wakabayashi, An Approximation Method of Terminal Reliability of Road Network Using Partial Minimal Path and Cut Sets, *Proc. of the Fifth World Conference on Transport Research*, *4*, 1989, 367-380.

[4] Y. Iida, Basic Concepts and Future Directions of Road Network Reliability Analysis, *Journal of Advanced Transportation*, *33(2)*, 1999, 125-134.

[5] A. Chen, H. Yang, H. K. Lo and W. H. Tang, A Capacity Related Reliability for Transportation Networks, *Journal of Advanced Transportation*, *33(2)*, 1999, 183-200.

[6] R. Hooke and T. A. Jeeves, Direct Search Solution of Numerical and Statistical Problems, *Journal of the Association for Computing Machinery*, *8(2)*, 1961, 212-229.

[7] M. G. H. Bell and Y. Iida, *Transportation Network Analysis*, (John Wiley & Sons, 1997), 193-204.

[8] S. Hou, N. Maruyama and S. Kato, New Methodology to Calculate Unblocked Reliability to Assess Road Network Operation Performance, *Journal of Mechanical Systems for Transportation and Logistics*, *1(3)*, 2008, 240-251.

[9] S. Hou, N. Maruyama, M. Hirota and S. Kato, Optimization Framework for Road Network Directed by Unblocked Reliability for Given Network Topology and Inelastic Demand with Stochastic User Equilibrium, *WSEAS Transactions on Business and Economics*, *6(6)*, 2009, 292-301.

[10] J. G. Wardrop, Some Theoretical Aspects of Road Traffic Research, *Proc. of the Institution of Civil Engineers*, Part II, *1(1)*, 1952, 325-362.

[11]   M. Beckmann, C. B. McGuire and C. B. Winsten, *Studies in the Economics of Transportation*, 3, (Yale University Press, 1956), 59-79.
[12]   A. Chen, H. Yang, H. K. Lo and W. H. Tang, Capacity reliability of a road network: an assessment methodology and numerical results, *Transportation Research Part B*, *36*, 2002, 225-252.
[13]   Y. Sheffi, *Urban Transportation Networks: Equilibrium Analysis with Mathematical Programming Methods*, (Prentice-Hall, 1984), 95-107 and 116-122.
[14]   M. Abdulaal and L. J. LeBlanc, Continuous equilibrium network design models, *Transportation Research part B*, *13* 1979, 19-32.

Appendix A

The Hooke-Jeeves (HJ) algorithm is a fundamental algorithm for solving the Continuous Network Design Problem (CNDP)[6, 14]. The HJ algorithm proceeds by a sequence of exploratory and pattern moves. The flow chart of the HJ algorithm is shown in Fig. A1.

In order to express different values of capacity expansion in the iteration process, three vectors are named, including the test link capacity expansion, $\hat{y}$, benchmark link capacity expansion, $\bar{y}$, and the success link capacity expansion, y^h. The implementation steps for solving a bi-level program based on unblocked reliability are given as follows:

Step 0: Initialization.

Given an initial solution of y^0, solve the lower-level program with y^0. That is, the current capacity is the sum of the initial capacity expansion, y^0, and the capacity of the existing road network. Calculate the objective function of the upper level to obtain $F(y^0)$. Set $\bar{y} = y^0$ and $F(\bar{y}) = F(y^0)$. Give the step length of exploratory move, s, reduction the factor of the step length of exploratory move, θ, convergence step length of exploratory move, η, and step length of pattern move, v. Set direction factor, $\beta = 1$, counter, $g = 1$ (from first link), for exploratory move and counter, $h = 0$, for the pattern move.

Step 1: Exploratory moves.
   Step 1-1: If $g > G$, each link has been tested, so go to step 2. Let μ_g be a vector that contains a '1' in the gth position and '0' elsewhere.
   Step 1-2: Set $\hat{y} = \bar{y} + \beta s \mu_g$. Solve the lower-level program with $\bar{y}$. Calculate the objective function of the upper level to obtain $F(\bar{y})$.
   Step 1-3: If $F(\hat{y}) > F(\bar{y})$ renew the benchmark link capacity expansions and objective function of the upper level, $\bar{y} = \hat{y}$ and $F(\bar{y}) = F(\hat{y})$, respectively. Then, set $g = g+1$ and go to step 1-1. Otherwise perform the next step.
   Step 1-4: If $\beta = 1$, set $\beta = -1$ and go to step 1-2; otherwise $g = g+1$, $\beta = 1$ and go to Step 1-1.

Step 2: Pattern moves.
   Step 2-1: If $F(\bar{y}) > F(y^h)$, renew the success solution and objective function value of the upper-level program to $y^{h+1} = \bar{y}$ and $F(y^{h+1}) = F(\bar{y})$, respectively. Perform pattern move, $\bar{y} = y^h + v(y^{h+1} - y^h)$. Solve the lower-level program with $\bar{y}$. Calculate the objective function of the upper level to obtain $F(\bar{y})$. Set $h = h+1$, $g = 1$ and go to step 1. Otherwise, perform the next step.
   Step 2-2: If the convergence criterion, $s < \eta$, is met, stop (the current solution, y^h, is the optimal link capacity expansion); otherwise, reduce the step length of exploratory, $s = \theta s$, return to the success solution and objective function value of the upper-level program, $\bar{y} = y^h$ and $F(\bar{y}) = F(y^h)$, respectively. Then, set $g = 1$ and go to step 1.

Start

$y^0,\ s,\ \theta,\ \eta,\ \nu,\ \beta = 1,\ g = 1,$
$h = 0,\ \bar{y} = y^0,\ F(\bar{y}) = F(y^0)$

$g > G$ — Yes

$g = g + 1$

No

$\hat{y} = \bar{y} + \beta s \mu_g$

Lower-level program

Upper-level program

$F(\hat{y}) > F(\bar{y})$ — No

Yes

$\bar{y} = \hat{y},\ F(\bar{y}) = F(\hat{y})$

No

$\beta = 1$

Yes

$\beta = -1$

$g = 1$
$h = h + 1$

No — $F(\bar{y}) > F(y^h)$

Yes

$y^{h+1} = \bar{y},\ F(y^{h+1}) = F(\bar{y})$

$\bar{y} = y^h + \nu(y^{h+1} - y^h)$

Lower-level program

Upper-level program

$s < \eta$

No — $s = \theta s,\ g = 1,$
$\bar{y} = y^h,\ F(\bar{y}) = F(y^h)$

Yes

End
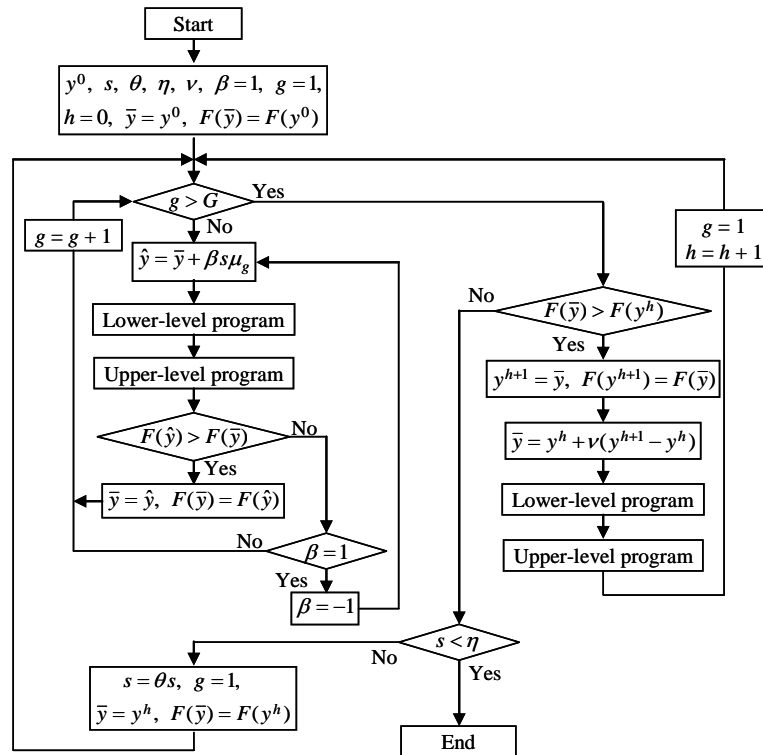
Fig. A1 Flowchart of Hooke-Jeeves algorithm to solve bi-level program with unblocked reliability.

Finite Element Analysis of Human RIB Cage

Prof. ROSHAN P. GHODKHANDE. (Author), Prof. NILESH D DHOTE, Prof. ANIL C GAWANDE

Asst Prof. Department Of Mechanical Engg.
[1,] *Datta Meghe Institute Of Engineering Technology & research wardha, Maharashtra, India*
Asst Prof. Department Of Mechanical Engg.
[2,] *Datta Meghe Institute Of Engineering Technology & research wardha, Maharashtra, India*
Asst Prof. Department Of Mechanical Engg.
[3,] *Datta Meghe Institute Of Engineering Technology & research wardha, Maharashtra, India*

ABSTRACT : *This paper of finite element analysis of the rib cage model is applied to recognize stress distributions and to determine the rate of bone fractures(especially for pathologically changed bones). Also to determine the load and stress to occurs on the human rib cage at any accident. Also find the maximum load sustain capacity of human rib cage and according to the load sustain capacity of the human rib cage by finite element analysis and search a material as like a bone cement and it take on a rib fracture and see the result . This paper is only of to nullify the rib fracture as present medical treatment give the elastic belt but due to respiration, the human ribs are contract and relax that's the rib fracture are only minimize not a nullify. The human models are considered in between age 15 to 40 year. The Simulation result shows a good agreement with the cadaver test data.*
Key Word: *Finite element model, thorax, rib cage, bone.*

I. Introduction

It is correctly said by Mr. DEVID STARR JORDAN "Wisdom knows what to do, skill is knowing how to do it and virtue is doing it." Following saying I started my project titled "FINITE ELEMENT ANALYSIS OF HUMAN RIB CAGE."Along with the analysisthis gives a plenty of option to the designers, manufactures and to the businessman. This project consists of some biological relation to understand as to know how wholeanatomy in a mankind can be correlated with machine. Everyone in world in a impression that man is nothing but a machines. So like any part in the machine one can renewed, repaired and replaced in the human anatomy. Along with the analysisthis gives a plenty of option to the designers, manufacturers and to the businessmen.

II. Mechanical Analysis

A mechanical analysis is nothing but making a model of the entity and using different finite element methods find the different properties of that element.Along with the analysisthis gives a plenty of option to the designers, manufacturers and to the businessmen. This project consists of some biological relation to understand as to know how whole anatomy in a mankind can be correlated with machine. Everyone in the world in a impression that man is nothing but a machine. So like any part in the machine one can renew, repaired and replaced in the human anatomy.And for this one must understand the relation between Biology and Mechanical Engineering.

III. Biomechanics

Biomechanics is the theory of how tissue, cells, muscles, bones, organs and the of them and how their form and function are regulated by basic mechanical properties. The purpose of this study is to illustrate the potential that a combination of knowledge fro biology and engineering from biology and engineering can have on the understanding of the development, maintenance and repair of the skeleton and on the clinical management of bone diseases.The mechanical loading of the environment and the circumstances of life have a huge impact on developmentand the evolution of our skeleton and the constituents of our body.

IV. Construction Of Human Rib Cage
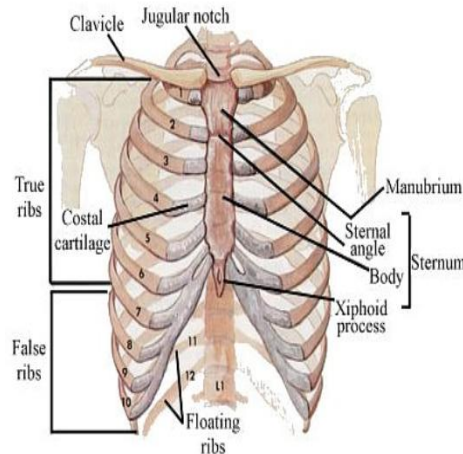
Fig 1: Human Rib Cage

The ribs are thin, flat, curved bones that form a protective cage around the organs in the upper body. They are comprised 24 bones arranged in 12 pairs.

These bones are divided into three categories:

1) The first seven bones are called the true ribs. These bones are connected to the spine (the backbone) in back. In the front, the true ribs are connected directly to the breastbone or sternum by a strips of cartilage called the costal cartilage.
2) The next three pairs of bones are called false ribs. These bones are slightly shorter than the true ribs and are connected to the spine in back. However, instead of being attached directly to the sternum in front, the false ribs are attached to the lowest true rib.
3) The last two sets of rib bones are called floating ribs. Floating ribs are smaller than both the true ribs and the false ribs. They are attached to the spine at the back, but are not connected to anything in the front.

V. Standard Properties of Bone

Human bone should be hard one.

Bone should able to sustain compressive strength between 50 MPato 70 MPa for normal human being.

The bone material should be flexible having a elastic value between 0.008mm to 0.031mm for the rib cage.

VI. Problem & Remedies with the Bone

Problem occurs when any accident is happen and in that accident the fracture or cracks are occurs in rib so due to how much load the rib is fracture is don't know and what is the load sustainable capacity of human rib is also don't know. Therefore, Finite Element Method is to calculate the mechanical properties of Human Ribs i.e. stress, deformation and sustainable capacity of human ribs. Finite Element method calculates the mechanical properties of human rib and that property is beneficial to Biomechanical Engineering to manufacture the artificial bone material.

VII. Boundary & Loading Condition Of Human Rib Cage

We are considering the human rib cage model between the age group 14 to 40.

According to age group,all the conditions are change.

1st boundary condition:-

Normal weight carrying capacity of human body 40kg.

2nd boundary condition:-

Maximum weight carrying capacity of human body = 1.5 times it's own weight

i.e. normal human weight = 60kg, then weight carrying capacity is 90kg.
3rd boundary condition:-
If more than 1000kg then this impact occur is in accidental condition.
        If more than Normal & maximum weight carrying capacity of human body then this impact is of accidental condition so 3rd boundary condition is 100kg
1stBoundary condition:- 40kg(normal condition)
2ndBoundary condition:- 60kg(1.5times its own weight)
3rdBoundary condition:- 100kg(accidental condition).

VIII. Static Analysis

        In static analysis the moment is applied at the rib cage as the rib cage bone are fixed at the backside of rib cage (nearer to backbone). The result obtained as maximum stress and deformation of rib cage. FE analysis shows the maximum stress and deformation occurred at the red zone.
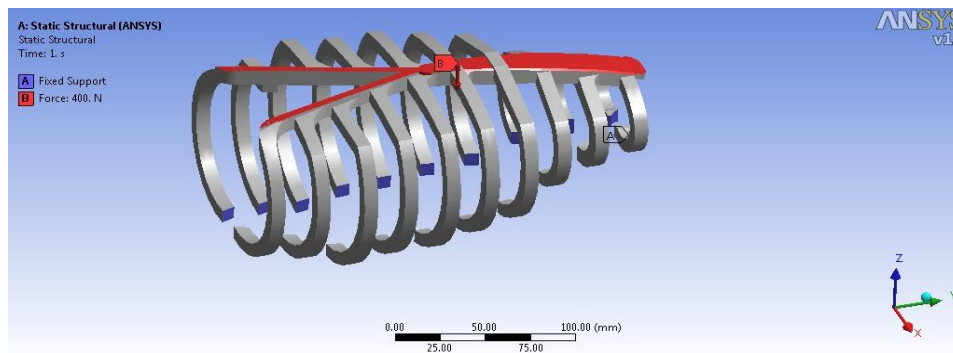
Fig 2A: Boundary condition by applying tangential load & axial load on human rib cage
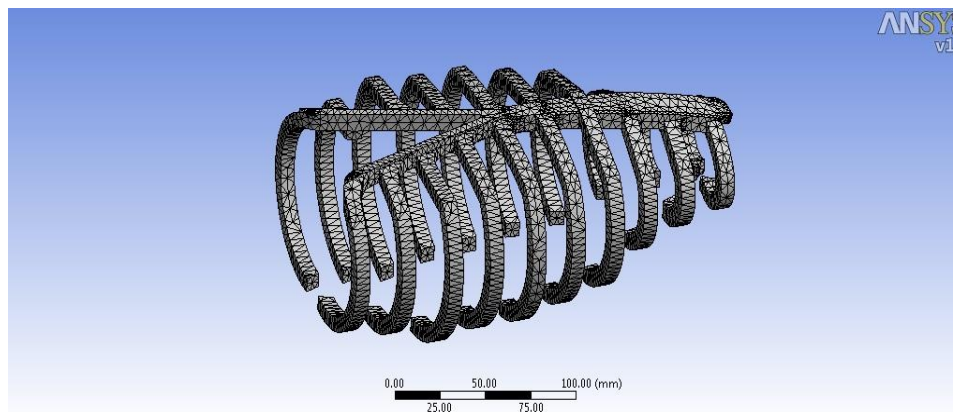
Fig 2B: Meshing of Human Rib cage assembly Fig 2C: Equivalent Stress σ = 10.338MPa

Fig 2D: Max deformation of Human Rib CageTable 1:FEM Results of Human Rib Cage

Loading	Ribs	Stresses(Mpa)	Deformation(mm)
400N	1-3	17.081	0.011
	4-6	21.644	0.047
	7-10	26.143	0.102
	Combine	10.338	0.034
600N	1-3	23.51	0.0144
	4-6	32.46	0.0711
	7-10	39.214	0.1541
	Combine	15.537	0.0515
1000N	1-3	39.183	0.024
	4-6	54.109	0.118
	7-10	65.35	0.2576

	Combine	25.895	0.086

IX.   Result & Discussion

The FEA and Analytical result shows the stress is increasing when load goes on increase and deformation are varying when load goes on increasing. As this FEA and Analytical result is compare to allowable limit of stress and deformation, if given result is within allowable limit of stress and deformation then rib cage can sustain this load. If stress and deformation value goes on increase over the allowable limit then rib cage can break or fracture in any accidental condition.

The following table shows FEA and analytical result of stress and deformation when load are apply on the human rib cage.

Table 2: Stresses& Deformation obtain by FEA & Analytical method

Sr No	Loading Condition	FEA Result		Analytically Result		Allowable Limit	
		Stress(Mpa)	Deformation(mm)	Stress(Mpa)	Deforma tion(mm)	Stress(Mpa)	Deformat ion(mm)
1	400N	10.338	0.034	0.8	-3.409	50-70	0.5-5.44
2	600N	15.537	0.0575	12	-5.11		
3	1000N	39.183	0.024	2	8.522		

X.   Conclusion

It is observed that the experimental analysis carried out in a forensic lab and FEA analysis value are very different. Still we can consider FEA analysis is a good tool for find out the mechanical properties of Bone material. With reference to the discussion with orthopedic surgeons this study can be helpful for them while inserting any kind of artificial bone material in human rib in case of accidents. Further one can make the study of bio-chemical of bone material and use this data for the medical research.

REFERENCES

[1.]   Art of Human Anatomy: Frank H. Netter MDPublisher: Saunders,Published: 2010-05-03ASIN: 1416059512
[2.]   The finite element method in engineering:-S.S. Rao,Butterworth Heinemann, 1999
[3.]   Introduction to finite elements in engineering:-Tirupathi R. Chanrupatla& Ashok D. Belegundu,Prentice Hall, 2002. Regular Contact with Dr. Ravi Dashputra(Orthopedic Surgeon)
[4.]   Będziński R., 1997, Engineers Biomechanics, Technical University of Wroclaw Press, Wroclaw [in Polish]
[5.]   Hacek S.1999,Introduction to the Finite Element Method ANSYS, Technical University of Krakow [in Polish].
[6.]   Harrigan T.P., Hamilton J.J., 1994, Necessary and sufficient conditions for global stability and uniqueness in finite element simulations of adaptive bone,Int. J. Solids Structures, 31, 1, 97-107.
[7.]   Oshita F., Omori K., Nakahira Y., Miki K., 2001, Development of a finite element model of the human body, 7-th International a LS-DYNA Users Conference.The Finite Element Model Of The Human Rib Cage. JAN AWERJCEWILZ, BARTOZ LUEZAK.
[8.]   Microstructural and Mechanical Properties Of Human Ribs ., JOSEPH MICHAEL CARMIER.
[9.]   A Finite Element Model Study On The Role Of Trunk Muscles In Generating Intra Abdominal Pressure., NAVID ARJMAND, ABOULFAZL SHIRAZI-ADL, MAHAMAD PARNIANPOUR.

Micro-Electromechanical Systems (Mems)

R. U. Sonje[1], S. V. Borde[2]

[1, 2]*Mechanical Department, Govt. Polytechnic, Nashik, Nashik, Maharashtra (India)*

Abstract: *Micro-electro-mechanical systems (MEMS) have been identified as one of the most promising technologies and will continue to revolutionize the industry as well as the industrial and consumer products by combining silicon-based microelectronics with micro-machining technology. All the spheres of industrial application including robots conception and development will be impacted by this new technology. If semiconductor microfabrication was contemplated to be the first micro-manufacturing revolution, MEMS is the second revolution. The paper reflects the results of a study about the state of the art of this technology and its future influence in the development of the construction industry. The interdisciplinary nature of MEMS utilizes design, engineering and manufacturing expertise from a wide and diverse range of technical areas including integrated circuit fabrication technology, mechanical engineering, materials science, electrical engineering, chemistry and chemical engineering, as well as fluid engineering, optics, instrumentation and packaging.*
Keywords: *MEMS, Electronics, Construction, Sensors, Automation*

I. Introduction

MEMS is a process technology used to create tiny integrated devices or systems that combine mechanical and electonic components. They are fabricated using integrated circuit (IC) batch processing techniques and can range in size from a few micrometers to millimetres. These devices (or systems) have the ability to sense, control and actuate on the micro scale, and generate effects on the macro scale. MEMS can be found in systems ranging across automotive, medical, electronic, communication and defence applications. Current MEMS devices include accelerometers for airbag sensors, inkjet printer heads, computer disk drive read/write heads, projection display chips, blood pressure sensors, optical switches, microvalves, biosensors and many other products that are all manufactured and shipped in high commercial volumes.

II. What Is Mems?

Micro electromechanical Systems (MEMS) is the integration of mechanical elements, sensors, actuators and electronics on a common silicon substrate through micro fabrication technology (Semiconductor chip)**.**These devices (or systems) have the ability to sense, control and actuate on the micro scale, and generate effects on the macro scale.
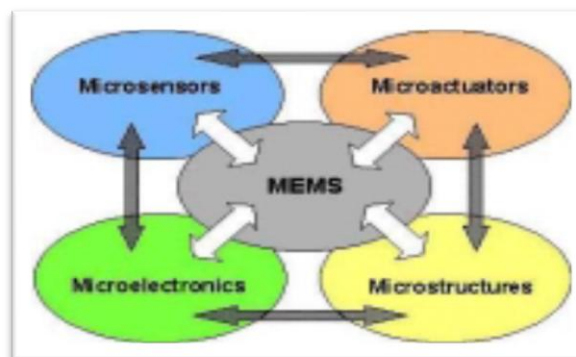
Fig.(1):Components of MEMS

III. Components In Mems

3.1Transducer

A transducer is a device that transforms one form of signal or energy into another form. The term transducer can therefore be used to include both sensors and actuators and is the most generic and widely used term in MEMS.

3.2 Sensor

A sensor is a device that measures information from a surrounding environment and provides an electrical output signal in response to the parameter it measured. These energy domains include:

➢ Mechanical - force, pressure, velocity, acceleration, position.
➢ Thermal - temperature, entropy, heat, heat flow.
➢ Chemical - concentration, composition, reaction rate.
➢ Radiant - electromagnetic wave intensity, phase, wavelength, polarization reflectance.
➢ Magnetic - field intensity, flux density, magnetic moment, permeability.
➢ Electrical - voltage, current, charge, resistance, capacitance, polarization.

3.3Actuator

An actuator is a device that converts an electrical signal into an action. It can create a force to manipulate itself, other mechanical devices, or the surrounding environment to perform some useful function.

IV. Classification Of MEMS

4.1 Bio MEMS

An area of particular interest in home-based medical applications where patients can use devices to monitor their own conditions, such as blood and urine analysis.
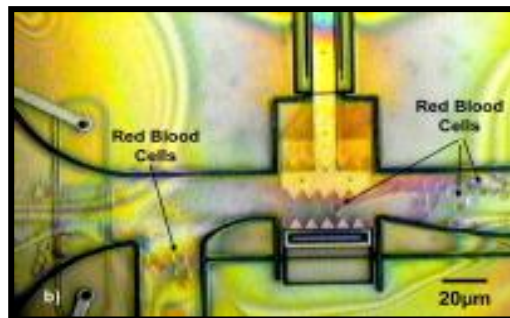
Fig.(2) A Bio MEMS device

A Bio MEMS device is actuated with 'micro teeth' to trap, hold and release single red blood cells (unharmed). The little balls in the channels are red blood cells.

4.2 MOEMS

MEMS-based devices make them a perfect solution to the problems of the control and switching of optical signals in telephone networks.

Fig(3) A. MEMS optical cross connect

A MEMS optical cross connect consists of an array of microscopic mirrors, each the size of a pin head and able to tilt in various directions to steer.

4.3 RF MEMS

RF MEMS is one of the fastest growing areas in commercial MEMS technology. RF MEMS are designed specifically for electronics in mobile phones and other wireless communication applications such as radar, global positioning satellite systems (GPS) and steerable antennae. MEMS has enabled the performance, reliability and function of these devices to be increased while driving down their size and cost at the same time.
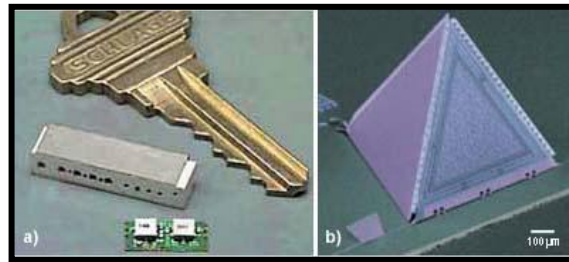
Fig(4) A

A miniature acoustic resonator, shown in the foreground, is one-fifth the size of a traditional component used in mobile phones and other wireless communications devices, and (b) on-chip micro-microphones may make it possible to build radios on a chip.The technology includes circuit tuning elements (capacitors/inductors, resonators, filters, microphones and switches). These low-loss ultra-miniature and highly integrative RF functions can and will eventually replace classical RF elements and enable a new generation of RF devices. As it can be seen today, if RF MEMS components continue to replace traditional components in today's mobile phones, then phones could become extremely small (the size of wristwatch is not too far away), require little battery power and may even be cheaper.

V. Materials Used To Fabricate MEMS

Silicon substrate (single crystal or polycrystalline)is preferable because; Homogeneous structure gives desirable electrical & mechanical properties. silicon's ability to be deposited in thin films is very suitable to MEMS. Provides high definition and reproduction of device shapes using photolithography. silicon microelectronics circuits are batch fabricated (a silicon wafer contains hundreds of identical chips not just one).

VI. Manufacturing Processes Of MEMS

The technique used for manufacturing MEMS and Microsystems components is called as Micromachining.
There are four methods of Micromachining.
1. Bulk Micromachining
2. Surface Micromachining
3. LIGA Process
4. Laser micromachining

6.1 Bulk Micromachining

Bulk micromachining involves the removal of part of the bulk substrate. It is a subtractive process that uses wet anisotropic etching or a dry etching method such as reactive ion etching (RIE), to create large pits, grooves and channels. Materials typically used for wet etching include silicon and quartz, while dry etching is typically used with silicon, metals, plastic and ceramics.

6.2 Surface Manufacturing

This method is used for production of microactuators.(Substrate: Silicon, Silicon Carbide).The material is deposited i.e. layer by layer (1 to 100µm thick) on top of substrate Phosposilicate Glass (PSG) sacrificial layer is deposited.Wet etching is used to remove sacrificial layer(HF or HCl is used as etchants)Structural layer of Polysilicon is deposited.

6.3 LIGA(Lithography, Galvanoformung, Abformung)

LIGA is an important tooling and replication method for high-aspect-ratio microstructures. The technique employs X-ray synchrotron radiation to expose thick acrylic resist of PMMA under a lithographic mask (see Figure 24 below).

The exposed areas are chemically dissolved and, in areas where the material is removed, metal is electroformed, thereby defining the tool insert for the succeeding moulding step. LIGA is capable of creating very finely defined microstructures up to 1000 µm high. LIGA is limited by the need to have access to an X-ray synchrotron facility.

6.4 Laser Micromachining

Most laser micromachining processes are not parallel and hence not fast enough for effective MEMS fabrication. Nonetheless, they have utility in specialty micromachining or making moulds. Excimer laser

micromachining is used particularly for the micromachining of organic materials (plastics, polymers etc.) as material is not removed by burning or vaporization. Hence, material adjacent to the machined area is not melted or distorted by heating effects. Lasers have found other applications in MEMS but only in a limited capacity; laser drilling, laser annealing and etching are the most common forms.

VII.   Conclusions

The development of MEMS is demanding higher levels of electrical-mechanical interaction, as well as a higher level of knowledge of the physical world. Their use increases the systems' properties like reliability and level of integration. The development of microdevices in which are embedded the electronic circuits, sensors, actuators and engines, open new ways of solving industrial problems at lower cost and increased quality. MEMS sensors utilization permit to avoid the necessity of point-to-point wiring, realizing a digital output format, and obtaining greater precision. Embedded sensors in different type of structures permits the creation of what is called "smart structures", which can be used in civil and mechanical engineering projects.

VIII.   The Future Of Mems

A. Industry Challenges
  Some of the major challenges facing the MEMS industry include:
i) Access to Foundries:
MEMS companies today have very limited access to MEMS fabrication facilities, or foundries, for prototype and device manufacture. In addition, the majority of the organizations expected to benefit from this technology currently do not have the required capabilities and competencies to support MEMS fabrication. For example, telecommunication companies do not currently maintain micromachining facilities for the fabrication of optical switches. Affordable and receptive access to MEMS fabrication facilities is crucial for the commercialization of MEMS.
ii) Design, Simulation and Modeling:
Due to the highly integrated and interdisciplinary nature of MEMS, it is difficult to separate device design from the complexities of fabrication. Consequently, a high level of manufacturing and fabrication knowledge is necessary to design a MEMS device. Furthermore, considerable time and expense is spent during this development and subsequent prototype stage. In order to increase innovation and creativity, and reduce unnecessary 'time-to-market' costs, an interface should be created to separate design and fabrication. As successful device development also necessitates modeling and simulation, it is important that MEMS designers have access to adequate analytical tools. Currently, MEMS devices use older design tools and are fabricated on a 'trial and error' basis. Therefore, more powerful and advanced simulation and modeling tools are necessary for accurate prediction of MEMS device behavior.
iii) Packaging and Testing:
The packaging and testing of devices is probably the greatest challenge facing the MEMS industry. As previously described, MEMS packaging presents unique problems compared to traditional IC packaging in that a MEMS package typically must provide protection from an operating environment as well as enable access to it. Currently, there is no generic MEMS packaging solution, with each device requiring a specialized format. Consequently, packaging is the most expensive fabrication step and often makes up 90% (or more) of the final cost of a MEMS device.

REFERENCES
[1.] [Vittorio 2001]. Vittorio, Salvatore A.. Micro-Electromechanical Systems (MEMS), Cambridge scientific abstracts. October 2001.www.csa.com/hottopics/mems/oview.html
[2.] [Singer 2002]. Singer, Peter. MEMS Diversity and Advance Semiconductor International. October 1st, 2002.
[3.] [Silicon Microstructures, Inc]. Silicon Microstructures, Inc. Simplified Description in the Process to Fabricate Piezoresistive Pressure Sensors.www.simicro.com/pdffiles/PressureFab.pdf.
[4.] [Carrillo]. Carrillo, Daniela. MEMS Sensor Technology: Present and Future.Frost.com. www.frost.com/prod/news.nsf/0/2C5351EB5F6D414A86256CBE005C5ED4
[5.] [Atto-Okine 2002], Attoh-Okine Nii O. MEMS Application in Pavement Condition Monitoring-Challenges. Proceedings of the 19th International Symposium on Automation and Robotics in Construction (ISARC) 2002, pp. 387-392. Gaithersburg, USA.

A Detailed Review on Artificial Roughness Geometries for Optimizing Thermo-Hydraulic Performance of Solar Air Heater

Surendra Agrawal[1], J.L. Bhagoria[2] , Rupesh Kumar Malviya[3]

[1]*Deparment of Mechanical Engineering, Surabhi & Satyam Group, Bhopal (MP), India*
[2]*Deparment of Mechanical Engineering, M.A.N.I.T., Bhopal (MP), India*
[3]*Deparment of Mechanical Engineering, Bansal College of Engineering., Bhopal (MP), India*

Abstract: *It is well known fact that the heat transfer coefficient between the absorber surface of solar air collector & flowing fluid i.e. air can be improved by providing artificial roughness geometry on heat transfer surface (absorber surface).In this way the Thermal efficiency is increased. But at the same time due to roughness geometry pumping power of solar air collector in increased due to fictional losses in duct. So it necessary to examine the shape, size & flow pattern of various roughness elements to get maximum efficiency with minimum frictional losses. Therefore the selection of roughness geometry has to be based on the parameter that takes into account both Thermal & Hydraulic (friction) performance i.e. Thermo-hydraulic Performance of Solar air collector. Number of roughness elements has been investigated on heat transfer & friction characteristics of solar air collectors. In this paper, reviews of various artificial roughness elements used as passive heat transfer techniques, in order to improve Thermo-hydraulic performance of solar air collectors is reviewed & presented. Correlations developed by various researchers with the help of experimental results for heat transfer & friction factor for solar air collector by taking different roughness geometries are given & these correlations are useful to predict the Thermo-hydraulic performance of solar air collector having roughened ducts. The objective of this paper is also the awareness of effect of various types' roughness geometries on heat transfer & friction characteristics of solar air collectors for future researchers in simplified form.*

Keywords: *Artificial roughness, solar air heater, roughness geometry, Nusselt number, thermo hydraulic performance, Reynolds number, heat transfer coefficients, friction factor, aspect ratio.*

I. Introduction

Due to fast growing population & advance-ment in technology in each & every field such as Industrial, Agriculture & Research, energy is the prime requirement & the same trend will be increasing day by day. Conventional energy sources are exhaustible and are depleting fast. The present energy con-sumption is about 0.3 to 0.5 Q/Yr (1Q=1018 kJ) [1, 2], while as availability in the form of conventional energy resources such as coal, oil and natural gas is less. Conventional energy sources are not sufficient to meet the energy demands for very long. Besides, there is fear of possible environmental risks associated with the conventional fuels and nuclear energy. In early seventies the awareness of the limited nature of the reserves of fossil fuels resulted in sharp rise in the prices of these fuels. This came to be known as energy crisis. [3].This requires an urgent search of an alternate source of energy. Out of many alternatives, solar energy is most promising source due to

1. Free of cost
2. Pollution free
3. Presence on everywhere
4. Non exhaustive nature.

The drawback is it is location & time dependent. It requires efficient collection & storage systems for economical utilization point of view. Solar air heaters are the simplest & economical systems, which converts solar energy into the useful thermal energy & utilizes for various heating, cooling & drying applications. But the basic problems with solar air heaters are low thermal efficiency due to low heat transfer coefficient between absorber surfaces to air in the duct. There are various Active & passive methods to increase heat transfer coefficients. Using artificial roughness geometry on absorber surface exposed to air side in one of passive technique used by various researchers.

II.   HISTORY OF ARTIFICIAL ROUGHNESS

The concept of artificial roughness was first applied by Joule [4] to enhance heat transfer coefficients for in-tube condensation of steam. Webb and Eckert [5] conducted experiential study of turbulent air flow in tubes roughened with rectangular repeated ribs and deduced heat transfer and friction factor correlations based on the law of wall similarity and application of the heat-momentum transfer analogy. Lewis [6] introduced new efficiency para-meter for optimizing thermohydraulic performance of roughened surfaces with respect to smooth surfaces. The experimental study carried out by Han [7-10] in search of the effect of rib shape, angle of attack, pitch to height ratio and spacing in square duct with two opposite rib roughened wall revealed that the maximum value of heat transfer and friction factor occurs for the ribs oriented at 45° angle with a relative roughness pitch of 10. Ravigururajan and Bergles [11] developed general statistical correlations for heat transfer and pressure drop for single-phase turbulent flow in tubes roughened with semicircular, circular, rectangular and triangular shape ribs. Liou and Hwang [12] conducted experimental study on heat transfer and friction for turbulent flow through channel with two opposite walls roughened with semicircular, square and triangular shape ribs. Zhang et al. and Kiml et al. [13, 14] reported that the thermal per-formance of V-shaped ribs with 60o angle of attack is better than that of 45° angle for the same range of flow parameters. Lau et al. [15] observed that the replacement of continuous transverse ribs by inclined ribs in a square duct results in higher turbulence near the roughened wall due to interaction of the primary and secondary flows which goes in favor of better thermal performance. Lau et al. [16, 17] studied the heat transfer and friction characteristics of fully developed flow in a square duct with transverse and inclined discrete ribs. Taslim et al. [18] and Olssom & Sunden [19] investigated the effect of V-shaped ribs in square channel and found fair enhancement in heat transfer as compared to inclined and transverse ribs. They observed that V-shaped ribs pointing downward have a much higher heat transfer coefficient because the warm air being pumped toward the rib leading region increases the apex region heat transfer coefficients as compared to that of the leading end region. Gao and Sunden [20] also reported that V-shaped ribs pointing downward perform better than the ribs pointing upward in rectangular ducts. A study by Hu and Shen [21] presented the effect of inclined discrete ribs with and without groove and revealed that the performance of inclined discrete rib without groove has been found best arrangement. In a recent study, Cho et al. [22] investigated the effect of a gap in inclined ribs on heat transfer for a fluid flow through square duct and reported that a gap in the inclined rib accelerates the flow and enhances the local turbulence, which results in an increase in the heat transfer.

They reported that the inclined rib with a downstream gap shows significant enhancement in heat transfer compared to that of continuous inclined rib arrangement. Moon et al. [23] investigated effect of channel height on heat transfer in a rectangular duct with a dimpled surface and observed enhancement in heat transfer by about 2.1 times regardless of channel height and friction factor of 1.6 - 2.0 times that of smooth channel. Mahmood and Ligrani [24, 25] measured local heat transfer on opposite walls with dimple type roughness with various temperature ratios having ratio of channel height to dimple print diameter of 0.5. They observed that the vortex structures augment local Nusselt number near downstream rim of each dimple. Burgess et al. [26] conducted an experimental study to investigate effect of dimple depth on heat transfer with aspect ratio of 8 and for Reynolds number range of 12000-70000 and reported that Nusselt number increases with increase in dimple depth. Sang et al. [27] investigated heat transfer with dimple/protrusion arrays in a rectangular duct with low Reynolds number range and observed heat transfer enhancement of 14 and 7 times for double protrusion wall and double dimpled wall at Reynolds number of 1000.

However at high Reynolds number of 10000, enhancement level observed was from 2 to 3. Chang et al. [28] examined heat transfer characteristics for four sets of dimpled channels with Reynolds number ranging from 1500 to 11000 and determined effect of dimpled arrangement, fin length to channel hydraulic diameter ratio and Reynolds number on heat transfer over the dimpled fin channel. Prasad and Mullick [29] were the first who introduced the application of artificial roughness in the form of small diameter wire attached on the underside of absorber plate to improve the thermal performance of solar air heater for drying purposes. Varun et al. [30], Hans et al. [31] , Bhushan et al. [32] ,A.K. Patil et al. [33], Pranab Kanti Roy [34] & Thakur Sanjay Kumar & NS Thakur [35] presented a review on roughness geometries used in solar air heaters wherein they discussed the outcomes of different studies concerning with heat transfer enhancement by the use of artificial roughness. Nikuradse (1950) [36] investigated the effect of roughness on the friction factor and velocity distribution in pipes which was roughened by sand blasting. Nunner (1958) [37] and Dippery and Sabersky (1963) [38] developed a friction similarity law and a heat momentum analogy for flow in sand grain roughened tubes. Donne and Meyer (1977) [39], Meyer (1982) [40], Wilkie (1966) [41], Sheriff and Gumley (1966) [42], Gomelauri (1964) [43], Wilkie and Mantle (1979) [44] & Vilemas and Simonis (1985) [45] investigated regular geometric roughness which can be produced in the form of cavities and ribs.

III. METHODOLOGY OF ARTIFICIAL ROUGHNESS

Whenever air flows over a heated surface, a very thin layer exists below the core turbulent region in which the flow remains predominantly laminar due to viscous effects called 'laminar sub layer'. Due to this viscous sub layer, the heat transfer rate from absorber surface to air is very low. Therefore the application of artificial roughness is to break that sub layer & creates local wall turbulence due to separation & reattachment of flow between two consecutive roughness elements. Thus turbulence created by various roughness elements significant enhances the heat transfer rates between the absorber surface & flowing fluid i.e. air.
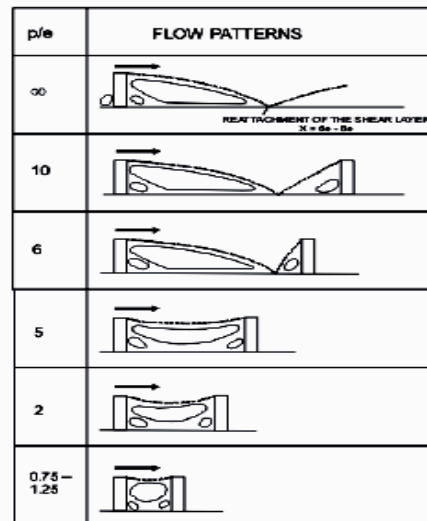
Fig. 1 Flow patterns downstream of wires with the roughness as a function of (p/e)
Source: Prasad & Saini (1988)

IV. ROUGHNESS PARAMETERS

1. Relative roughness height (e/D_H): It is the ratio of rib height (e) to equivalent diameter (D_H) of air passage.
2. Relative roughness pitch (p/e): It is the ration of distance between two consecutive ribs (p), height of rib (e).
3. Angle of attack (□): It is the inclination of the rib with the direction of air flow in the duct.
4. Aspect ratio: It is the ratio of duct width (W) to duct height (H).

V. EFFECT OF ROUGHNESS PARAMETERS

The effect of various roughness parameters & roughness geometry on heat transfer & friction factor is given below.

1. Effect of Reynolds Number

With the increases of Reynolds number, friction factor decreases due to the suppression of viscous sub-layer, whereas the Nusselt number increases with increases In Reynolds numbers because it is nothing but the ratio of conductive resistance to convective resistance of heat flow and as Reynolds member increases thickness of boundary layer decreases & hence convective resistance decreases which in turn increases the Nusselt number.

2. Effect of rib

The effect of rib is the most important that produced on the flow pattern; it generates two separate regions of the flow, one on each side of the rib. The turbulence occurs by the generation of the vortices and hence the enhancement in heat transfers as well as in the friction losses takes place.

3. Angle of attack (□)

Various researchers have investigated exp-erimentally, the effect of angle of attack (α) on the flow pattern. Besides the relative roughness height (e/D_H) & relative roughness pitch (p/e), the most important parameter is angle of attack (α) with respect to rib position. The inclined ribs gives a higher heat transfer rate that the transverse rib because of the secondary flow induced by the rib, in addition to breaking the viscous sub layer and producing local wall turbulence.

4. Effect of Relative roughness height (e/D$_H$)

Fig. 1 (Prasad & Saini, 1988) & Fig. 2 (Prasad & Saini, 1991) [47] depict the flow pattern downstream of a rib & effect on the laminar sub layer as the rib height is changed respectively. Breakage of viscous sub layer due to repeated ribs increases the rate of heat transfer by creating local wall turbulence. If the ribs protrude beyond the viscous sub layer, they would increase the heat transfer rate, but also causes much higher frictional losses. Optimal thermo -hydraulic performance conditions are obtained when the roughness height is slightly higher than the transition sub layer thickness (Prasad & Saini, 1991). Table 1 shows the values of Relative roughness height (e/D$_H$) for a maximum value of heat transfer coefficient.
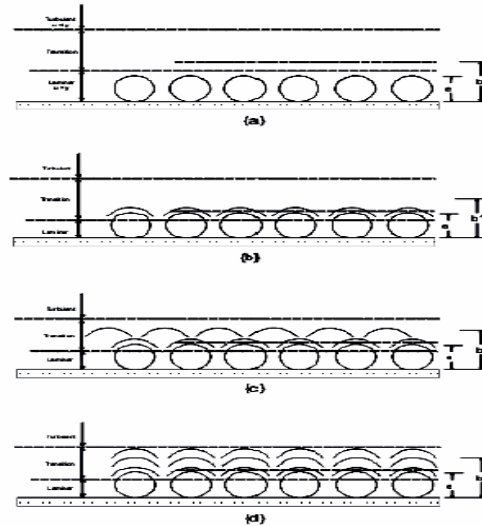
Fig. 2 Roughness heights with respect to laminar sub layer
Source: Prasad & Saini (1991)

5. Effect of Relative roughness pitch (p/e)

Various researchers have shown the effect of a relative roughness pitch (p/e) on the flow pattern i.e. heat transfer coefficient & fiction factor. Table 2 shows the values of relative roughness pitch (p/e) for a maximum value of heat transfer coefficients for different types of artificial roughness. Fig. 3 (Prasad & Saini, 1988) depicts the flow pattern downstream from a rib as a function of a relative roughness pitch (p/e). Due to separation at the rib, reattachment of the free shear layer does not occur for a relative roughness pitch (p/e) less than about 8 to 10. The maximum heat transfer coefficient occurs in the vicinity of the reattachment point. For relative roughness height (p/e) less than 8 to 10, reattachment will not occur, which results in the decrease of heat transfer rate. The rate of increase in friction factor will increase with the decrease of pitch. However, an increase in the relative roughness pitch (p/e) beyond 10 resulted in the decrease of heat transfer enhancement.

Fig. 3 Flow patterns downstream of ribs with the roughness as a function of (e/D$_H$)
Source: Prasad & Saini (1988)

VI.   Vi. EXPERIMENTAL APPROACH

An experimental investigation has been planned to generate data on heat transfer coefficient and friction factor that can be utilized to develop heat transfer and friction factor correlations. It is proposed to collect data on heat transfer coefficient and friction factor as function of roughness parameters (relative roughness height), aspect ratio of duct and Reynolds number of flow. Experimental data have also been collected on a smooth duct under similar geometrical and flow conditions in order to have a direct comparison of the performance of the roughened duct with that of a conventional smooth rectangular duct flow with respect to heat transfer and fluid flow characteristics. And to ensure the reliability of experimental data it is necessary to perform experimentation on validated experimental set as per guidelines of ASHARE standards 93-77 [46] under standard test conditions.

TABLE 1: VALUES OF RELATIVE ROUGHNESS HEIGHT (e/D_H) FOR A MAXIMUM VALUE OF HEAT TRANSFER COEFFICIENT FOR DIFFERENT ROUGHNESS GEOMETRIES USED IN SOLAR AIR HEATER DUCT

S. N	Investigators	Roughness geometry	Value of (e/D_H) for max heat transfer coeff.
1	Prasad & Saini (1988)	Wire	0.033
2	Karwa et al. (2001)	Chamfered rib	0.0441
3	Momin et.al. (2002)	V-Shaped rib	0.034
4	Bhagoria et.al. (2002)	Transverse wedge	0.033
5	Jaurker et.al. (2006)	Transverse rib-grooved	0.036
6	Karmare & Tikekarv (2007)	Metal grit rib roughness	0.044
7	Layek et.ala.(2007)	Transverse chamfered rib grooved	0.04
8	Saini & Verma (2008)	Dimple shape roughness	0.0379
9	Saini & Saini (2008)	Arc shaped wire	0.0422

TABLE 2: VALUES OF RELATIVE ROUGHNESS PITCH (p/e) FOR A MAXIMUM VALUE OF HEAT TRANSFER COEFFICIENT FOR DIFFERENT ROUGHNESS GEOMETRIES USED IN SOLAR AIR HEATER DUCT

S. N	Investigators	Roughness geometry	Value of (p/e) for max heat transfer coeff.
1	Prasad & Saini (1988)	Wire	10
2	Karwa et al. (2001)	Chamfered rib	7.09
3	Bhagoria et.al. (2002)	Transverse wedge	7.57
4	Sahu & Bhagoria (2005)	90^0 broken transverse	13.33
5	Jaurker et.al. (2006)	Transverse rib-grooved	6
6	Karmare & Tikekarv (2007)	Metal grit rib roughness	17.5
7	Layek et.ala.(2007)	Transverse chamfered rib grooved	6
8	Varun et.al.(2008)	Combination of inclined & transverse ribs	8
9	Saini & Verma (2008)	Dimple shape roughness	10

VII.   Main Elements Of Experimental Setup

The main elements of Experimental set up comprises of insulated rectangular duct with metallic artificially roughened absorber plate. Uniform heat flux in supplied over the top surface of the plate by means of electric heater and bottom surface is modified by providing artificial roughness elements. The duct has inlet section, test section & exit section. The test section consists of a micro manometer to measurement of Pressure drop. The duct is connected to a circular pipe which includes flow measurement device (inclined U tube manometer) & flow control valve. The other end of the pipe is connected to the suction side of a centrifugal blower which exhales the air to the surroundings thus forming an open loop system.

VIII.   Experimental Procedure

All components of the experimental setup and the instruments have been checked for proper operation.
The blower is then switched on and the joints of the setup are checked for air leakage with soap bubble technique. Micro manometer and inclined U-tube manometer are properly leveled. Blower is switched on and the flow control valve is adjusted to give a predetermined rate of airflow to the test section. The test runs to collect relevant heat transfer and flow friction data were conducted under quasi-steady state conditions. The quasi-steady state condition is assumed to have been reached when the temperature at a point does not change for about 10-12 minutes. When a change in the operating conditions is made, it takes about 30-40 minutes to reach such a quasi-steady state. After each change of flow rate, the system was allowed to attain a steady state before the data were recorded. In order to reduce the effect of inaccuracy in the measurement of temperature, this strongly affects the accuracy of the calculation of the heat transfer coefficient, the temperature of the air through the duct has been maintained greater than $10^{o}C$ and the temperature difference between the heated plate and the bulk air temperature has been kept above $20^{0}C$. During the experimentation the temperature of air entering the duct ranges between.

.
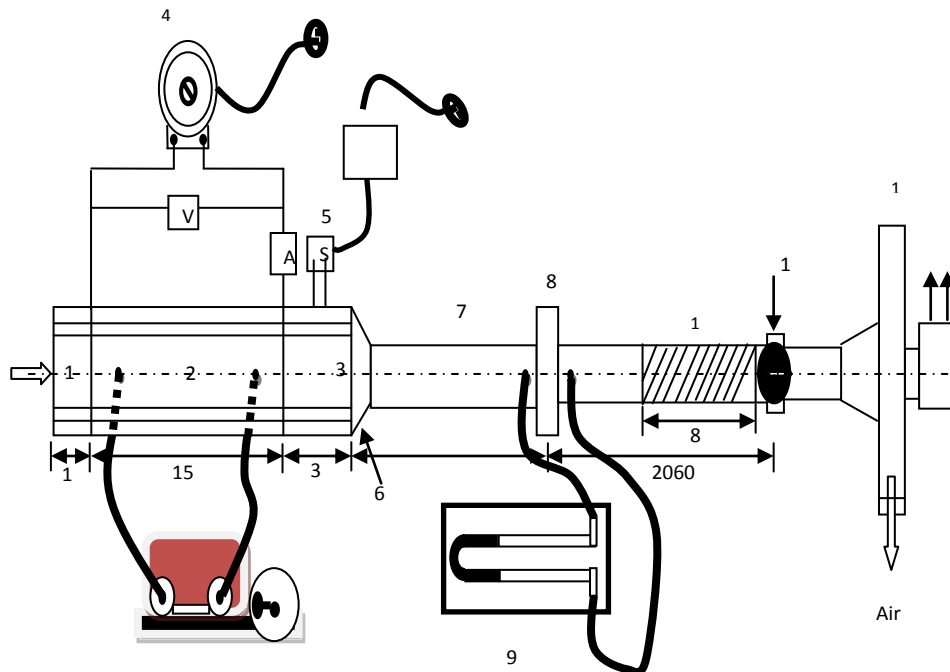
Fig. 4 Schematic diagrams showing top view of Indoor experimental Setup

(1) Air inlet section (2) Test section (3) Air outlet section (4) Variac (5) Selector switches (6) Mixing section (7) G.I. pipe (8) Orifice plate (9) Inclined U tube (10) Micro manometer (11) Flow control (12) Flexible pipe (13) Blower

30°C to 40°C according to the local atmospheric conditions. The temperature of the air at the outlet of the test section ranges between about 40°C to 65°C. All readings have been noted under steady state condition which was assumed to have been obtained when the plate and air outlet temperature did not deviate over a 15 min. period. After the steady state has reached, the heater assembly voltage and current, the plate temperatures, the inlet and exit air temperatures and the pressure drop across the duct and across the orifice plate have been recorded. For each rib configuration 6 runs have been conducted at air-flow rates corresponding to the flow Reynolds numbers between 3000 and 15000. The following parameters were measured during the experiments.

1. Pressure drop across the orifice plate & duct by inclined U- tube & micro manometer
2. Inlet air temperature of collectors by using digital multimeter and thermocouples.
3. Outlet air temperature of collectors
4. Temperature of plate

IX. Various Roughness Geometries Used in Solar Air heater

1. Transverse ribs in the form of small diameter wires

Prasad & Saini [48] investigated the effect of protrusions from underside of absorber surface in the form of small diameter wires on heat transfer & friction factor for fully developed turbulent flow in a solar air heater duct. As shown in Fig.5.

Range of Parameters:
1. p/e ---10, 15, 20
2. e/D_H---0.020,0.027,0.033

Results: Both Nusselt number & Friction factor increases with e/D_H, but the rate of heat transfer enhancement diminishes with increase in e/D_H, while the rate of increase of friction factor was found to be nearly constant. The maximum value of Nusselt number & Friction factor were reported to be 2.38 & 4.25 respectively at the p/e = 10.
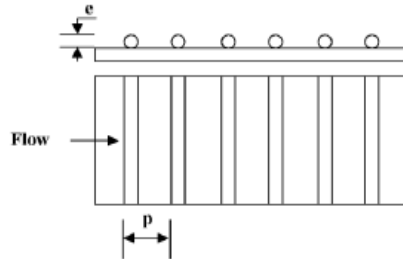
Fig. 5 Transverse ribs

2. Transverse & inclined ribs in the form of small diameter wires

Gupta et al. (1993) [49] investigated the effect of transverse & inclined wire roughness on fluid flow characteristics & heat transfer & friction factor for solar air heater. As shown in Fig.6.

Range of Parameters:
1. p/e:7.5 & 10
2. e/D_H:0.020-0.053
3. α: 30^0-90^0
4. Re: 5000-30000

Results: It was found that the heat transfer coefficient in roughened duct could be improved by a factor up to 1.8 & the friction factor had been found to increase by a factor of 2.7 times of smooth duct. The maximum heat transfer coefficient & friction factor were found at an angle of attack of 60^0 & 70^0 respectively in the range of parameters investigated. The thermo-hydraulic performance of roughened surface has been found best corresponding e/D_H = 0.033 & the Reynolds number corresponding to the best thermo-hydraulic performance were around 14000 in the range of parameters investigated. The investigation emphasized that the secondary flow rolling along the inclined rib is responsible for higher heat transfer rates.
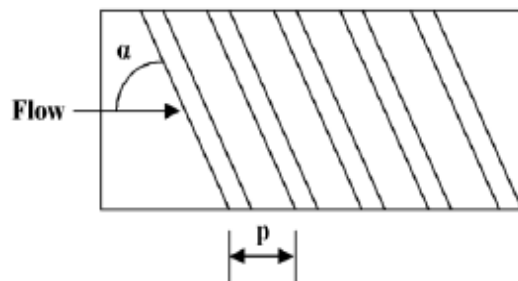
Fig. 6 Inclined ribs

3. Broken transverse rib roughness

Sahu & Bhagoria [50] varied the pitch for 90^0 broken transverse rib roughness & examined its effect on thermal performance of solar air heater. As shown in Fig.7.

Range of Parameters:
1. Re:3000-12000
2. p: 10-30 mm
3. e: 1.5 mm
4. W/H: 8

Results: The Nu increases sharply at low Re & remains constant for higher Re. The maximum enhancement of heat transfer was reported at the p=20 mm. It has been highlighted that smooth duct performs better than the roughened duct at Re below 5000. Experimental results revealed that roughened absorber plates increases the heat transfer coefficient 1.25-1.4 times as compared to smooth rectangular duct & maximum efficiency of roughened solar air heater lying in the range of 51-83.5%, depending upon the flow conditions.
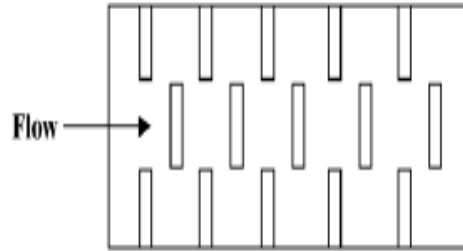
Fig. 7 Broken transverse ribs

4. Inclined broken rib roughness

Aharwal et al. [51] experimentally studied the heat transfer and friction factor of a rectangular duct roughened with repeated ribs with a gap & at an inclination with respect to the flow direction. As shown in Fig.8.

Range of Parameters:-
1. Re:3000-18000
2. Relative gap position: 0.16-0.5
3. Relative gap width: 0.5-2
4. W/H: 5.84
5. p/e:4-10
6. e/D_H:0.018-0.037
7. α: 30^0-90^0

Results: Maximum enhancement in Nu, f & thermo-hydraulic performance are 2.83, 2.89 & 1.97 times respectively as compared to smooth duct in the range of parameters investigated. The Nu & f were found to be highest corresponding to a relative gap position of 0.25 & a relative gap width of 1. It was found that below & beyond the relative gap width of value 1 reduces the heat transfer rates. It was found that due to gap in inclined rib the secondary flow along the rib joins the main flow through gap accelerating the flow field behind the rib, which energies the retarded boundary layer flow along the surface & enhances the heat transfer rates.
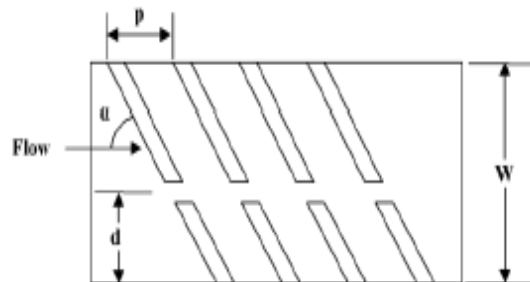
Fig.8 Inclined broken ribs

5. Combined inclined & transverse rib roughness

Varun et al. [52] experimentally investigated the combined inclined & transverse rib roughness geometry and studied its effect on the thermal performance. As shown in Fig.9.

Range of Parameters:-
1. Re:2000-14000
2. p/e: 3-8
3. e/D_H: 0.03
4. W/H: 10

Results: -It is found that the maximum thermal efficiency occurs at relative roughness pitch (p/e) of 8.
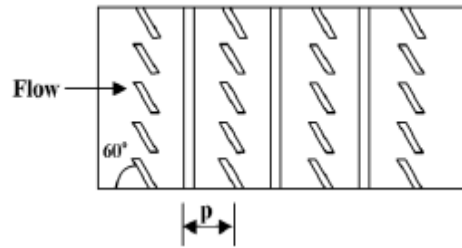
Fig. 9 Combined inclined & transverse ribs

6. Rib grooved roughness
Jaurker et al. [53] experimentally generated the friction & heat transfer data for turbulent flow through a rectangular duct with rib-grooved transverse repeated rib roughness produced on one broad heated wall. As shown in Fig.10.
Range of Parameters:-
1. Re:3000-21000
2. p/e: 4.5-10
3. e/D_H: 0.0181-0.0363
4. g/p: 0.3-0.7

Results: - Nu & friction factor increases up to 2.7 & 3.6 times as compared to smooth surface in the range of parameters investigated. The maximum heat transfer &friction factor were observed at p/e =10 & relative groove position of 0.4.The additional vortices in & around the grooves were found to be responsible for the higher turbulence intensity between the ribs results in higher heat transfer rates.
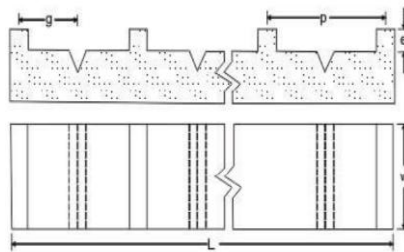
Fig. 10 Rib grooved roughness

7. Repeated chamfered rib roughness
Karwa et al. (1999) [54] experimentally found the effect of rib head chamfer angle (Φ) & duct aspect ratio heat transfer & friction factor in a rectangular duct roughened with integral chamfered ribs. As shown in Fig.11.
Range of Parameters:-
1. Re:3000-20000
2. p/e: 4.5,5.8,7,8.5
3. e/D_H: 0.014-0.0328
4. W/H: 4.8,6.1,7.8,9.66,12
5. Φ: $-15^0,0^0,10^0,15^0,18^0$
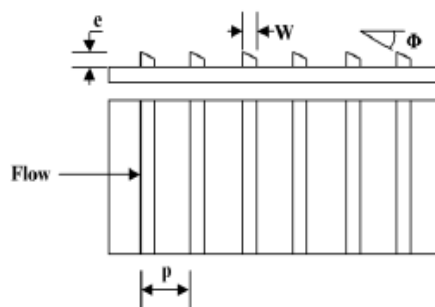
Fig. 11 Repeated chamfered ribs

Results: - As compared to smooth plate 2 & 3 times Stanton number & friction factor increases respectively in the range of parameters investigated. The highest heat transfer & friction factor exists for a chamfer angle (Φ) of 15^0. The minima of heat transfer function occur at roughness Reynolds number of about 20. The heat transfer function increases with the increase in the aspect ratio from 4.65-9.66 & the roughness function decreases with the increase in the aspect ratio from 4.65-7.75 & therefore both the functions attain nearly a constant value. It has been pointed out that positive chamfer encourages the frequent shedding of vortices causing greater heat removal from the surface & higher frictional losses while in case of negative chamfer.

8. V shaped rib roughness

Momin et al. (2002) [55] experimentally in-vestigated the effect of V shaped ribs on heat transfer & fluid flow characteristics in rectangular duct of solar air heater. As shown in Fig.12.
Range of Parameters:-
1. Re:2500-18000
2. p/e: 10
3. e/D_H: 0.02-0.034
4. α: 30^0-90

Results: - Friction factor increases more rapidly than Nu with the increase of Re because the reattachment of free shear layer might not occur at higher Reynolds number. The maximum enhancement in Nu & Friction factor had been found 2.3 & 2.83 times respectively as compared to smooth surface for an angle of attack of 60^0.It was also found that for e/D_H=0.034 & α=60^0, the V shaped ribs enhances the value of Nu by 1.14 & 2.3 times over inclined ribs & smooth plate respectively. It was concluded that V shaped ribs gave better heat transfer performance than the inclined ribs for similar operating conditions.
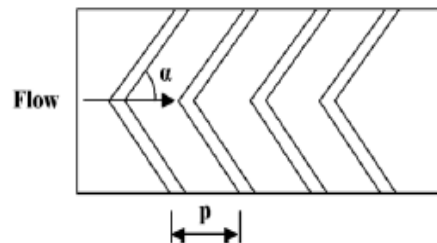
Fig.12 V shaped ribs

9. Staggered discrete V apex up & down rib roughness

Muluwork et al. (1998) [56] compared the thermal performance of staggered discrete V apex up & down with corresponding transverse staggered discrete ribs. The relative roughness length ratio had been considered as dimensionless geometric parameters of roughness element to compare three distinct configurations. As shown in Fig.13.
Range of Parameters:-
1. Re:2000-15500
2. B/S: 3-9
3. e/D_H: 0.02
4. α: 60^0

Results: -The Stanton number & friction factor increases with the increase of relative roughness length ratio. The Stanton number for V down discrete ribs was higher than the corresponding V up & transverse discrete ribs. The Stanton number ratio enhancement was found 1.32-2.47 in the range of parameters investigated. Further for Stanton number, it was seen that the ribbed surface friction factor for V down discrete ribs was highest among the three configurations investigated.
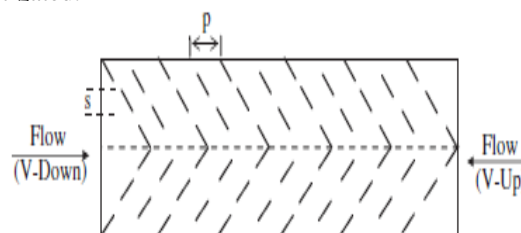
Fig. 13 Staggered discrete V apex up & down ribs

10. Transverse, Inclined, V-continuous & V-discrete rib roughness

Karwa [57] experimentally investigated heat transfer & friction factor in a high aspect ratio duct with transverse, Inclined, V-up & down continuous, V-up & down discrete ribs. As shown in Fig.14.

Range of Parameters:-
1. p/e: 10
2. B/S: 3
3. e/D_H: 0.0467-0.05
4. α: 60^0-90^0
5. W/H: 7.19-7.75

Results: -The enhancement in Stanton number of transverse, Inclined, V-up continuous, V- down continuous, V-up discrete & V-down discrete ribs over smooth duct was found to be 65-90%, 87-112%, 102-137%, 110-147%, 93-134%, 102-142% respectively. Study reveals that the V-down discrete ribs secured the best thermal performance for the same power consumption. The study also emphasized that discrete ribs have lower friction losses as compared to continuous ribs due to change in flow behavior.
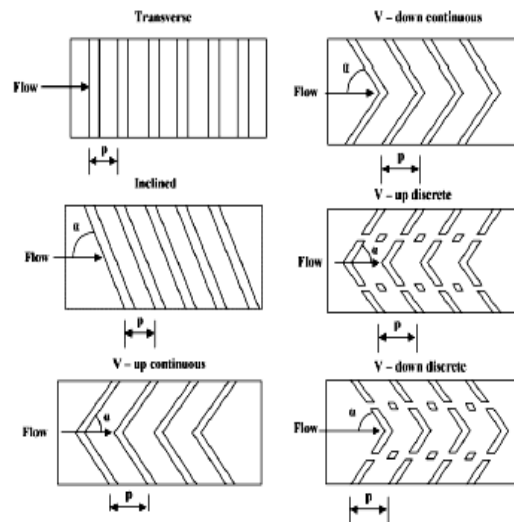
Fig. 14 transverse, Inclined, V-up continuous, V- down continuous,
V-up discrete & V-down discrete ribs

11. Multi V rib roughness

Hans et al. [58] recently experimentally studied the heat transfer& friction factor characteristics in a multi V rib roughened roughness. As shown in Fig.15.

Range of Parameters:-
1. Re:2000-20000
2. p/e: 6-12
3. e/D_H: 0.019-0.043
4. α: 30^0-75^0
5. W/w: 1-10

Results: -Maximum enhancement in Nu & f has found to be 6 &5 times respectively in comparison to smooth duct. The maximum value of heat transfer & friction factor has been found at relative roughness width (W/w) of 6 & 10 respectively. Beyond that heat transfer decreases & friction factor again increases both due to separation of flow. Also found that maximum Nu & f occurs at α=60^0.
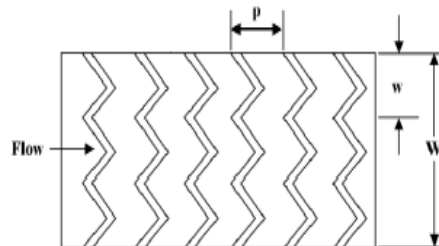
Fig. 15 Multi V rib roughness

12. Discrete W-shape rib roughness

Kumar et al. [59] investigated the heat transfer friction characteristics of W shape discrete ribs in solar air heater. As shown in Fig.16.

Range of Parameters:-
1. Re:3000-15000
2. p/e: 10
3. e/D_H: 0.0168-0.0338
4. α: 30^0-75^0

Results: - The maximum enhancement of Nu & f was found reported as 2.16 & 2.75 times respectively that of smooth duct for $\alpha=60^0$ & $e/D_H=0.0338$.Studied shows that the enhancement of V shape ribs is based on observation of the creation of secondary flow cell due to inclination of rib resulting in a region of high heat transfer near the leading edge & one trailing edge, & thus develops a region of almost double heat transfer rate. Therefore W shape roughness gives better performance than the V shape roughness since its leading is more than trailing edge.
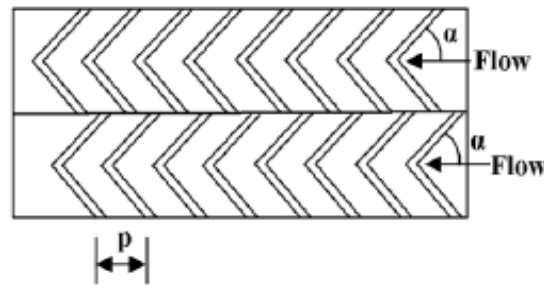
Fig. 16 Discrete W shape rib roughness

13. W-up & W-down rib roughness

Lanjewar et al. [60] reported the heat transfer & friction characteristics with W-shape ribs pointing downstream & upstream. As shown in Fig. 17 & 18.

Range of Parameters:-
1. Re:2300-14000
2. p/e: 10
3. e/D_H: 0.033
4. α: 45^0
5. W/H: 8
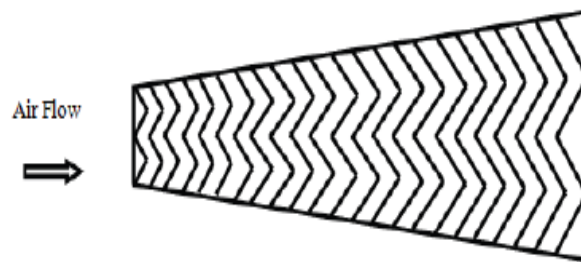
Fig. 17 W-down rib roughness
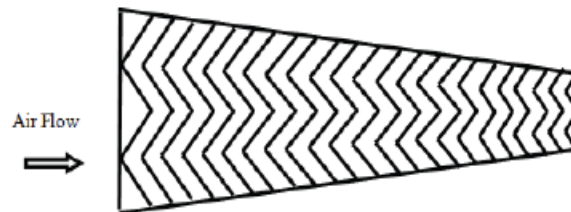
Fig. 18 W-up rib roughness

Results: -The enhancement of heat transfer by providing W-shape ribs is 2.39 for W-down & 2.21 for W-up than the smooth duct. Also found that W-down ribs give better thermo-hydraulic performance than W-up & V ribs. The maximum thermo-hydraulic performance for W-down ribs is 1.98 while it is 1.81 for W-up ribs in the range of parameters investigated.

14. Arc shape rib roughness

Saini & Saini [61] investigated the heat transfer & fluid characteristics of arc shape roughness of a solar air heater duct. As shown in Fig.19.

Range of Parameters:-
1. Re:2000-17000
2. p/e: 10
3. e/D_H: 0.0213-0.0422
4. relative angle of attack ($\alpha/90$): 0.333-0.666
5. W/H: 12

Results: - The maximum enhancement in Nu has been obtained as 3.80 times that of smooth duct for relative angle of attack ($\alpha/90$) of 0.333 & relative roughness height e/D_H of 0.0422. However the increment in friction factor corresponding to these parameters has been observed 1.75 times only.
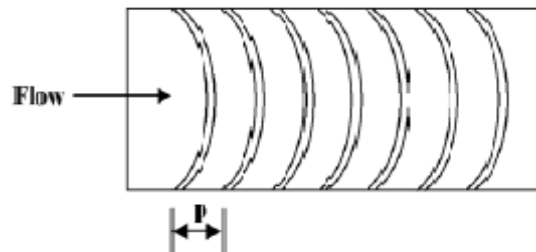
Fig. 19 Arc shape rib roughness

15. Wedge shape rib roughness

Bhagoria et al. [62] experimentally studied the heat transfer & fluid flow characteristics of transverse wedge shape ribs. As shown in Fig.20.

Range of Parameters:-
1. Re:3000-18000
2. p/e: 5.67,7.57,10,12.1
3. e/D_H: 0.015-0.033
4. α: 90^0
5. ø: 8,10,12,15

Results: - The maximum heat transfer occurs at a wedge angle (ø) of about 10, while on either side of this angle, Nu decreases. The friction factor increases as the wedge angle increases. The heat transfer & friction factor are 2.4 & 5.3 times of smooth duct at p/e of about 7.57. Studied shows that wedge shape ribs showed significant enhancement in heat transfer over square & chamfered ribs due to relatively lesser chances of eddy formation downstream of ribs.
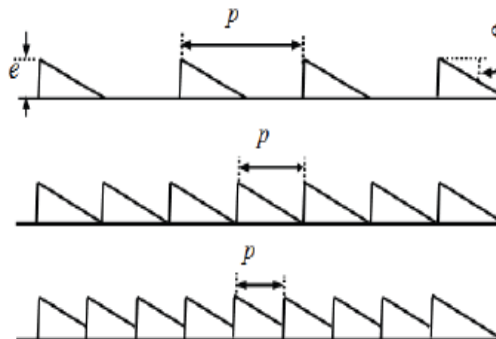
Fig.20 Wedge shape rib roughness

16. Dimple shape rib roughness

Saini & Verma [63] studied experimentally the effect of protrusion dimple shape of heat transfer & fluid flow characteristics. As shown in Fig.21.

Range of Parameters:-
1. Re:2000-12000
2. p/e: 8-12
3. e/D_H: 0.018-0.037
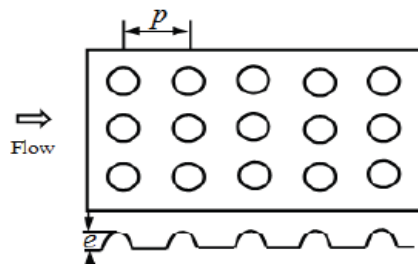
Fig. 21 Dimple shape rib roughness

Results: - The maximum heat transfer occurs at relative roughness height of 0.0379 & relative roughness pitch of 10.The friction factor is minimum corresponding to relative roughness height of 0.0289 & relative roughness pitch of 10.

17. Chamfered rib grooved roughness
Layek et al. [64] investigate experimentally the heat transfer & friction characteristics with repeated integral transverse chamfered rib with groove. As shown in Figure 22.
Range of Parameters:-
1. Re:3000-21000
2. p/e: 4.5-10
3. e/D_H: 0.022- 0.04
4. relative grove position(g/p):0.3-0.6
5. chamfer angle (ϕ): 5^0-30^0

Results: -For p/e=6,g/p=0.4, ϕ =18^0 & e/D_H=0.04 the enhancement in Nu is 3.24 times the smooth duct at Re=21000 while friction factor is of 3.78 times.
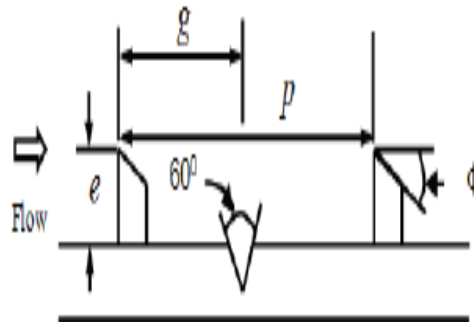
Fig.22 Chamfered ribs with groove roughness

18. Expanded metal mesh roughness
Saini & Saini [65] investigated experimentally the heat transfer & fiction characteristics for flow inside a large aspect ratio duct n the form of expanded metal mesh. As shown in Fig.23.
Range of Parameters:-
1. Re:1900-13000
2. L/e: 25-71.87
3. S/e: 15.62-46.87
4. e/D_H: 0.012- 0.039
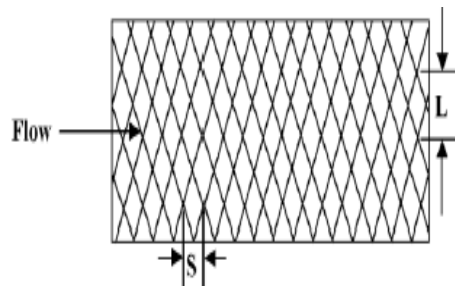
Fig. 23 Wire mesh roughness

Results: -The average Nusselt number attains maximum value at the relative longway length of mesh (L/e) of 46.87 & relative shortway length (S/e) of 25 at $\alpha= 72^0$ for relative longway length of 71.87 & relative shortway length of 15.62. The maximum enhancements in Nu & friction factor were found to be 4 & 5 times to the smooth plate respectively.

19. Metal grit ribs roughness

Karmare & Tikekar et al. [66] experimentally investigated the thermal performance of solar air duct with metal grit ribs roughness. As shown in Fig.24.

Range of Parameters:-
1. Re:4000-17000
2. Relative roughness height of grid(e/D_H): 0.035-0.044
3. Relative roughness pitch of grid (p/e): 12.5-36
4. Relative length of metal grit (l/s):1-1.72
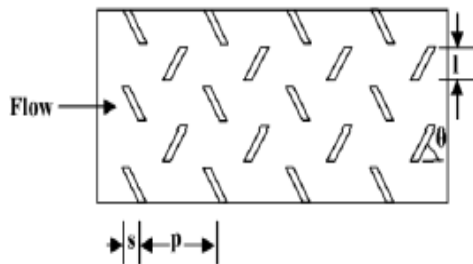
Fig. 24 Metal grit rib roughness

Results: -The enhancement in Nusselt number & friction factor was observed about (187%-200%) & (213%-300%) respectively as compared to smooth. The maximum heat transfer rate & optimum thermal hydraulic performance occurred for l/s=1.72, e/D_H =0.044 & p/e= 17.5.Similarly the maximum friction factor occurred for l/s=1.72, e/D_H =0.044 & p/e= 12.5.

20. Inverted U shape turbulators roughness

Bopche & Tandale [67] investigated experimentally the heat transfer & friction factor characteristics for inverted U shape turbulators in solar air heater. As shown in Fig.25.

Range of Parameters:-
1. Re:3800-18000
2. (e/D_H): 0.0186-0.03986
3. Turbulator pitch to height (p/e): 6.67-57.14
4. α: 90^0
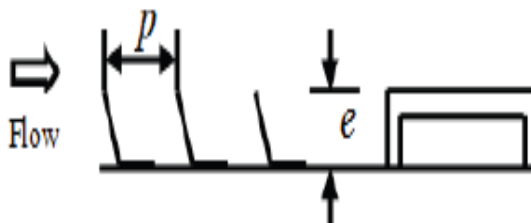
Fig. 25 Inverted U shaped turbulators

Results: -The inverted U shape turbulators showed appreciable heat transfer enhancement even at low Reynolds number (Re< 5000) where ribs were inefficient. The maximum enhancement in Nusselt number & friction factor compared to smooth duct were of the order of 2.82 & 3.72 respectively. Studied shows that turbulence generated only in the viscous sub layer region of the boundary layer resulted in better thermo-hydraulic performance i.e. maximum heat transfer enhancement at an affordable friction penalty.

References

[1]   Hsieh, J.S., Solar Energy Engineering, Prenticed Hall Inc., New Jersey, 1986
[2]   Veziroghu, T.N., Solar Energy International Progress, Pergamon Press, 1,167-173, 1980
[3]   Sukhatme S.P., "Solar Energy: Principles of Thermal Collections and Storage", Tata McGraw-Hill, New Delhi 1994.

[4] Joule J.P., "On the surface condensation of steam", Philos Trans R Soc Lond, 151, 133-160, 1861.
[5] Webb R.L., Eckert E.R.G. and Goldstein R. J., "Heat transfer and friction in tubes with repeated rib roughness", International journal of Heat mass transfer, 14, 601-617, 1971.
[6] Lewis M.J., "Optimizing the thermohydraulic performance of rough surfaces". International journal of Heat mass transfer, 18, 1243-1248, 1975.
[7] Han J.C., Glicksman L.R., Rohsenow W.M., "Heat transfer and friction for rib roughened surfaces", International journal of Heat mass transfer, 21, 1143-1156, 1978.
[8] Han J.C., "Heat transfer and friction in channels with opposite rib roughened walls", Trans. ASME Journal of Heat Transfer, 106, 774-781, 1984.
[9] Han J.C., Park J.S., "Developing heat transfer in a rectangular channel with rib turbulators", Trans. ASME Journal of Heat Transfer, 31, 183-195, 1988.
[10] Han, J.C., Park, J.S., Lei, C.K., "Augmented heat transfer in rectangular channel of narrow aspect ratios with rib turbulators", International journal of Heat mass transfer, 32/9, 1619-1630, 1989.
[11] Ravigururajan T.S., Bergles A.E., "General correlations for pressure drop and heat transfer for single-phase turbulent flow in internally ribbed tubes", J. ASME, 52, 9-20, 1985.
[12] Liou T.M., Hwang J.J., "Effect of ridge shapes on turbulent heat transfer and friction in a rectangular channel", International Journal of Heat and Mass Transfer, 36, 931−940, 1993.
[13] Han J.C., Zhang Y.M., "High performance heat transfers ducts with parallel broken and V- shaped broken ribs", International journal of Heat mass transfer, 35(2), 513-523, 1992.
[14] Kiml R., Mochizuki S., Murata A., "Effects of rib arrangements on heat transfer and flow behavior in a rectangular rib roughened passage", International Journal of Heat and mass transfer, 123, 675-681, 2001.
[15] Lau S.C., McMillin R.D., Han J.C., "Turbulent heat transfer and friction in a square channel with discrete rib turbulators", Trans. ASME Journal of Turbo machinery, 113, 360-366, 1991.
[16] Lau S.C., McMillin R.D., Han J.C., "Heat transfer characteristics of turbulent flow in a square channel with angled rib", Trans. ASME Journal of Turbo machinery, 113, 367-374, 1991.
[17] Lau S.C., Kukreja R.T., McMillin R.D., "Effects of V shaped rib arrays on turbulent heat transfer and friction of fully developed flow in a square channel", International Journal of Heat and mass transfer, 34,1605-1616, 1991.
[18] Taslim M.E., Li T., Kercher D.M., "Experimental heat transfer and friction in channels roughened with angled, V-shaped and discrete ribs on two opposite walls", Trans. ASME Journal of Turbo machinery, 118, 20-28, 1996.
[19] Olsson C.O., Sunden B., "Thermal and hydraulic performance of a rectangular duct with multiple V-shaped ribs", Trans. ASME, 120, 1072-1077, 1998.
[20] Gao X., Sunden B., "Heat transfer and pressure drop measurements in rib roughened rectangular ducts", Exp. Thermal Fluid Sci., 24, 25-34, 2001.
[21] Hu Z., Shen J., "Heat transfer enhancement in a converging passage with discrete ribs", International Journal of Heat and mass transfer, 39(8), 1719-1727, 1996.
[22] Cho H.H., Kim Y.Y., Rhee D.H., Lee S.Y., Wu S.J., "The effect of gap position in discrete ribs on local heat/mass transfer in a square duct", Journal of Enhanced Heat Transfer, 10(3),287-300, 2003.
[23] Moon H.K., O'Connell T., Glezer B., "Channel height effect on heat transfer and friction in a dimpled passage", ASME Journal Eng. Gas Turbines Power, 122(2), 307-313, 2000.
[24] Mahmood G.I., Hill M.L., Nelson D.L., Ligrani P.M., Moon H.K., Glezer B., "Local heat transfer and flow structure on and above a dimpled surface in a channel", Trans. ASME Journal of Turbo machinery, 123, 115, 2001.
[25] Mahmood G.I., Ligrani P.M., "Heat transfer in a dimpled channel: combined influences of aspect ratio, temperature ratio, Reynolds number and flow structure", International Journal of Heat and mass transfer, 45, 2011-2020, 2002.
[26] Burgess N.K., Oliveira M.M., Ligrani P.M., "Nusselt number behavior on deep dimpled surfaces within a channel", Journal of Heat Transfer, 125, 11-18, 2003.
[27] Sang D.H., Hyun G.K., Hyung H.C., "Heat transfer with dimple/protrusion arrays in a rectangular duct with low Reynolds number range", Int J Heat Fluid Flow, 29,916-926, 2008.
[28] Chang S.W., Chiang K.F., Yang T.L., Huang C.C., "Heat transfer and pressure drop in dimpled fin channels", Experimental thermal and fluid science, 33(1),23-40, 2008 .
[29] Prasad K., Mullick S.C., "Heat transfer characteristics of a solar air heater used for drying purposes", App. Energy, 13(2), 83-93, 1983.
[30] Varun, Saini R.P., Singal S.K., "A review on roughness geometry used in solar air heaters", Solar Energy, 81, 1340-1350, 2007.
[31] Hans V.S., Saini, R.P., Saini, J.S., "Performance of artificially roughened solar air heaters-A review", Renewable and Sustainable Energy Reviews, 13, 1854-1869, 2009.
[32] Bhushan B., Singh R., "A review on methodology of artificial roughness used in duct of solar air heaters", Energy, 35, 202-212, 2010.
[33] A.K. Patil, J.S. Saini, K. Kumar," A Comprehensive Review on Roughness Geometries and Investigation Techniques Used in Artificially Roughened Solar Air Heaters",IJRER,Vol.2, No.1, 2012.
[34] Pranab Kanti Roy & Kisalaya Chakrabarti, "A review on Heat transfer & friction factor characteristics of artificial roughened solar air heater duct", Asian Journal of Science and Technology Vol. 4, Issue 07, pp. 045-056, July, 2013
[35] Thakur Sanjay Kumar, N S Thakur, Anoop Kumar, Vijay Mittal," A review on use of artificial roughness to enhance heat transfer in solar air heaters", Journal of Energy in Southern Africa • Vol 21 No 1 • February 2010
[36] Nikuradse, J., 1950.Laws of flow in rough pipes. NACA, Technical Memorandum 1292. Nov 1950.

[37] Nunner, W, 1958 [A5]. Heat transfer and pressure drop in rough tubes. VDI Forch 445-B 5-39 (1956); AERE Lib Trans. 786.

[38] Dippery, D.F., Sabersky, R.H., 1963. Heat and momentum transfer in smooth and rough tubes at various Prandtl number. International Journal Heat and Mass Transfer 6, 329–353.

[39] Donne, D., Meyer, L., 1977.Turbulent convective heat transfer from rough surfaces with two dimensional rectangular ribs. International Journal of Heat and Mass Transfer 20, 582–620.

[40] Meyer, L., 1982.Thermohydraulic characteristics of single rods with three dimensional roughness. International Journal of Heat and Mass Transfer 25, 1043–1058.

[41] Wilkie, D., 1966. Forced convection heat transfer from surfaces roughened by transverse ribs. In: Proceedings of the 2nd International Heat Transfer Conference, Vol. 1, and AICHE New York.

[42] Sheriff, N., Gumley, P., 1966.Heat transfer and friction properties of surfaces with discrete roughness. International Journal of Heat and Mass Transfer 9, 1297–1320.

[43] Gomelauri, V, 1964. Influence of two-dimensional artificial roughness on convective heat transfer. International Journal of Heat and Mass Transfer 7, 653–663.

[44] Wilkie, D., Mantle, P.L., 1979. Multi-start helically ribbed fuel pins for CAGR. Nuclear Energy 18, 277–282.

[45] Vilemas, J.V., Simonis, V.M., 1985. Heat transfer and friction of rough ducts carrying gas flow with variable physical properties. International Journal of Heat and Mass Transfer 28, 59–68.

[46]   ASHRAE Standard 93-97, Method of Testing to Determine the Thermal Performance of Solar Collector, 1977.

[47] Prasad, B.N. and Saini, J.S., (1991).Optimal thermo-hydraulic performance of artificial roughness solar air heater, Solar Energy, 47, pp 91 – 96.

[48] Prasad, B.N., Saini J.S., "Effect of artificial roughness on heat transfer and friction factor in a solar air heater", Sol Energy, 41(6), 555-560, 1988.

[49] Gupta D., Solanki S.C., Saini J.S., "Heat and fluid flow in rectangular solar air heater ducts having transverse rib roughness on absorber plates", Solar Energy 51, 31-37, 1993.

[50] Sahu M.M., Bhagoria J.L., "Augmentation of heat transfer coefficient by using 90o broken transverse ribs on absorber plate of solar air heater", Renewable Energy, 30, 2057-2063, 2005.

[51] Aharwal K.R., Gandhi B.K., Saini J.S., "Experimental investigation on heat-transfer enhancement due to a gap in an inclined continuous rib arrangement in a rectangular duct of solar air heater", Renew Energy, 33, 585-596, 2008.

[52] Varun, Saini R.P., Singal S.K., "Investigation of thermal performance of solar air heater having roughness elements as a combination of inclined and transverse ribs on the absorber plate", Renew Energy, 33, 1398-1405, 2008.

[53] Jaurker A.R., Saini J.S., Gandhi B.K., "Heat transfer and friction characteristics of rectangular solar air heater duct using rib-grooved artificial roughness", Solar Energy, 80 (8), 895-907, 2006.

[54] Karwa R., Solanki S.C., Saini J.S., "Heat transfer coefficient and friction factor correlations for the transitional flow regime in rib-roughened rectangular ducts", Int J Heat Mass Transf, 42, 1597-1615, 1999.

[55] Momin A.M.E., Saini J.S., Solanki S.C., "Heat transfer and friction in solar air heater duct with V-shaped rib roughness on absorber plate", Int J Heat Mass Transfer, 45, 3383-3396, 2002.

[56] Muluwork, K.B., Saini, J.S., Solanki, S.C., 1998. Studies on discrete RIB roughened solar air heaters. In: Proceedings of National Solar Energy Convention, Roorkee; pp. 75–84.

[57] Karwa R., "Experimental studies of augmented heat transfer and friction in asymmetrically heated rectangular ducts with ribs on the heated wall in transverse, inclined, v-continuous and v-discrete pattern", Int Conf Heat Mass Transfer, 30(2), 241-250, 2003.

[58] Hans V.S., Saini R.P., Saini J.S., "Heat transfer and friction factor correlations for a solar air heater duct roughened artificially with multiple v-ribs", Solar Energy, 84, 898-911, (2010).

[59] Kumar A., Bhagoria J.L., Sarviya R.M., "Heat transfer enhancement in channel of solar air collector by using discrete w-shaped artificial roughened absorber", in 19th National & 8th ISHMT-ASME Heat and Mass Transfer Conference, 2008.

[60] Lanjewar A.M. Bhagoria J.L., Sarviya R.M. Indian Journal of science and Technology 2010; Vol. 3 No.8 pp. 908-910.

[61] Saini S.K., Saini R.P., "Development of correlations for Nusselt number and friction factor for solar air heater with roughened duct having arc-shaped wire as artificial roughness", Sol Energy, 82,1118-1130, 2008.

[62] Bhagoria J.L., Saini J.S., Solanki S.C., "Heat transfer coefficient and friction factor correlations for rectangular solar air heater duct having transverse wedge shaped rib roughness on the absorber plate", Renew Energy, 25, 341-369, 2002.

[63] Saini R.P., Verma J., "Heat transfer and friction factor correlations for a duct having dimple-shape artificial roughness for solar air heaters", Energy, 33, 1277-1287, 2008.

[64] Layek A., Saini J.S., Solanki S.C., "Effect of chamfering on heat transfer and friction characteristics of solar air heater having absorber plate roughened with compound turbulators", Renewable Energy, 34, 1292-1298, 2009.

[65] Saini R.P., Saini J.S., "Heat transfer and friction factor correlations for artificially roughened ducts with expended metal mesh as roughness element", Int J Heat Mass Transfer, 40(4), 973-986, 1997.

[66] Karmare S.V., Tikekar A.N., "Heat transfer and friction factor correlation for artificially roughened duct with metal grit ribs", Int. Journal Heat Mass Transfer, 50, 4342-4351, 2007.

[67] Bopche SB, Tandale MS, Experimental Investigation on Heat Transfer and Friction Characteristics of a turbulators Roughened Solar Air Heater Duct, Int. Journal of Heat and Mass Transfer, Vol.52,pp.2834-2848,2009.

Comparison of Different Absorbing Boundary Conditions for GPR Simulation by the Time Domain Finite Element Method

ZhiyongZhang[1,2], Man Li[1]

1,(School of Geosciences and Info-Physics, Central South University)
2, (School of Nuclear Engineering and Geophysics, East China Institute of Technology)

Abstract:*This paper compares three boundary conditions, i.e. transmitting boundary condition, Sarma absorbing boundary condition and the uniaxial complete matched layerabsorbing boundary condition for simulation of ground penetrating radar (GPR) by the time domain finite element (FEM) method. The formulations of the three boundary conditions for the FEM method are described. Their effectiveness in absorbing the incident electromagnetic waves are evaluated by the reflection coefficient on the boundary of a simple GPR model.The results demonstrate that UPML boundary condition can yield a reflection coefficient smaller than -50 dB, which is -20 dB smaller than other two boundary conditions.*

Keywords:*Ground penetrating radar (GPR);uniaxial complete matched layer absorbing boundary condition; Sarma boundary condition, transmitting boundary condition; finite element method*

I. Introduction

Ground penetrating radar (GPR) has been widely applied in many fields. Numerical simulation plays a great role in the interpretation of GPR data and the inversion of physical parameters. Finite element method (FEM) is widely used due to its easy adaption to a complex subsurface dielectric model with a triangle mesh. Shen et al [9]have performed a 2D forward GPR modeling by substituting the electromagnetic wave transmitting equation with the sound wave equation; Di and Wang [10] introduces the complex dielectric permittivity into the finite element equation using the Galerkin method. Tiao et al [11]perform a GPR numerical simulation on dispersive media using a discrete time-domain method. Arias et al [12] applies the GPR finite element technique to the imaging of archaeological remains. For GPR numerical simulation, absorbing boundary condition is indispensable for eliminating the undesired boundary reflection. An effective absorbing boundary condition is critical for improvement of the accuracy of GPR numerical simulation. Many research efforts have been paid to the absorbing boundary conditions for the GPR forward modelling using the finite different time domain (FDTD) algorithm. There are several absorbing boundary conditions working with different Attenuation mechanisms. For an example, the radiant boundary condition (Bayliss and Turkel E. 2009) and absorbing boundary condition are based on the separate wave equation(Engquist and Majda. 1977); ultra-absorbing boundary condition (Mei. 1992), and complete matched layer(Gedney et al. 2001; Berenger. 1994,) absorbing boundary condition have been applied. For the GPR simulation by the FEM method, Di and Wang (2005) use a transmitting absorbing boundary condition; Sarma absorbing condition has been used in GPR 2D numerical simulation by Feng (2013). UPML absorbing boundary condition also has applied in GPR 2D dispersive medium numerical simulation (Tiao L, 2006). In this paper, the principle and the formulations of the transmission absorbing, Sarma absorbing and UPML absorbing boundary conditions are going to be presented. Their performances while applied to the FEM simulation are tested.

II. Fem Applied To Wave Equation Of Gap

The electric field radiated by a GPR source is governed by wave equation, as expressed by (Di, et al., 1999)

$$\frac{\partial^2 \boldsymbol{E}}{\partial t^2} - \frac{\nabla^2 \boldsymbol{E}}{\mu\varepsilon} + \frac{\sigma}{\varepsilon}\partial \boldsymbol{E} / \partial t = \boldsymbol{S}_E \qquad (1)$$

where ε is the dielectric permittivity, μ is the magnetic permeability, σ is the electrical conductivity, $\boldsymbol{E}$ is electric-field intensity and $\boldsymbol{S}_E$ is the electric field source. We divide the 2D region into rectangular elements and let $\boldsymbol{E}$ be a linear function of position coordinates in each element, as given by

$$\boldsymbol{E} = \boldsymbol{N}^T \boldsymbol{E}_e \quad (2)$$

where $\boldsymbol{N}$ is the shape function for linear interpolation and $\boldsymbol{E}_e$ is the column vector whose components are $\boldsymbol{E}_i$ at the node i of the element where $i = 1, 2, 3, 4$. Using the Galerkin method, the general 2D finite-element

equation in time and spatial domain can be expressed as

$$M\ddot{E} + K'\dot{E} + KE = S_E \quad (3)$$

where M is the mass matrix, K' is the damping matrix, K is the stiffness matrix, $\dot{E}$ and $\ddot{E}$ are the first- and second-order derivatives of electric field, respectively.We can adopt the central difference method in time domain to solve the Eq. (3).

III. Absorbing Boundary Conditions

In this section, we apply the transmitting boundary condition, sarmaboundary condition and UPML absorbing boundary condition to the FEM simulation of GPR data.

3.1 Transmitting boundary condition

The transmitting boundary condition is established by directly simulating the common kinematic properties of various one-way waves. The principle is that the one-way waves are transmitted through the boundary interface at one point on the artificial boundary. This means that the one-way waves can be expressed as the superposition of a series of outgoing plane waves, because there is no specific limit to the speed at which these plane waves transmit along the artificial boundary, nor any limitation on their shapes. Assuming that all the one-way waves are transmitted along artificialboundary at the same velocity, we obtain a formula for the transmitting boundary condition[24-25].
Suppose

$$LE = \frac{\partial^2 E}{\partial t^2} - \frac{1}{\mu\varepsilon}\nabla^2 E + \frac{\sigma}{\varepsilon}\frac{\partial E}{\partial t} = S_E \ . \quad (4)$$

At each element, the electrical field E can be expressed as

$$E = \sum_{i=1}^{4} N_i E_i \ , \quad (5)$$

where E_i and N_i refer to the electric field and the shape function of the node i in each element. The residual quantity R can be expressed as

$$R = LE - S_E \ . \quad (6)$$

According to the Galerkinfinite element method, the 2D finite element equation can be expressed as

$$\sum_e \int_\Omega N^T r dx dy = 0 \ , \quad (7)$$

where Ω refers to the area of the element and r is the vector expression of R .According to the paraxial approximation deduced by Clear.bout[26], the down-going, up-going, left-going, right-going wave equations in a homogeneous isotropic medium, arerespectively expressed as

$$\frac{\partial E}{\partial t} = \frac{1}{v}\frac{\partial E}{\partial y}, \frac{\partial E}{\partial t} = -\frac{1}{v}\frac{\partial E}{\partial y}, \frac{\partial E}{\partial t} = -\frac{1}{v}\frac{\partial E}{\partial x}, \frac{\partial E}{\partial t} = \frac{1}{v}\frac{\partial E}{\partial x}, \quad (8)$$

According to the definition of the normal derivative, we know that

$$\frac{\partial}{\partial n} = \frac{\partial}{\partial x}n_x + \frac{\partial}{\partial y}n_y \ , \quad (9)$$

where n_x and n_y refer to the direction cosines of the boundary external normal.By importing Eq. (5) and (6) into Eq. (7) and applying Gauss theory, we can obtained

$$\sum_e \int_\Omega \frac{\partial}{\partial x}\left(\frac{\partial E^T}{\partial x}N\right)dxdy = \int_{\Gamma_l}\frac{\partial E^T}{\partial n}Nd\Gamma + \int_{\Gamma_d}\frac{\partial E^T}{\partial n}Nd\Gamma + \int_{\Gamma_r}\frac{\partial E^T}{\partial n}Nd\Gamma \int_{\Gamma_u}\frac{\partial E^T}{\partial n}Nd\Gamma \ , \quad (10)$$

where $\Gamma_l, \Gamma_r, \Gamma_d, \Gamma_u$ representthe left, right, bottom, upper boundary respectively. Importing the boundary conditions of Eq. (9) into Eq. (10) we can obtained

$$\int_{\Gamma_l} \frac{\partial \boldsymbol{E}^T}{\partial n} N d\Gamma + \int_{\Gamma_d} \frac{\partial \boldsymbol{E}^T}{\partial n} N d\Gamma + \int_{\Gamma_r} \frac{\partial \boldsymbol{E}^T}{\partial n} N d\Gamma + \int_{\Gamma_u} \frac{\partial \boldsymbol{E}^T}{\partial n} N d\Gamma$$

$$= v\dot{\boldsymbol{E}} \times \left(\begin{array}{c} \int_{\Gamma_l} N_1 N_2 \left(n_x + n_y \right) d\Gamma + \int_{\Gamma_d} N_2 N_3 \left(n_x + n_y \right) d\Gamma \\ + \int_{\Gamma_r} N_3 N_4 \left(n_x + n_y \right) d\Gamma + \int_{\Gamma_u} N_1 N_4 \left(n_x + n_y \right) d\Gamma \end{array} \right) \quad (11)$$

where $\dot{\boldsymbol{E}}$ is the first-order derivative of the electric field in time, and v refers to the transmission velocity of electromagnetic waves of medium. Therefore, the damping matrix of the boundary $\boldsymbol{F}$ can be expressed as

$$\boldsymbol{F} = \sum_{\Omega} \boldsymbol{F}_e = \sum_{\Omega} (\int_{\Gamma_l} \frac{\partial \boldsymbol{E}^T}{\partial n} N d\Gamma + \int_{\Gamma_d} \frac{\partial \boldsymbol{E}^T}{\partial n} N d\Gamma + \int_{\Gamma_r} \frac{\partial \boldsymbol{E}^T}{\partial n} N d\Gamma + \int_{\Gamma_u} \frac{\partial \boldsymbol{E}^T}{\partial n} N d\Gamma) . (12)$$

By importing boundary damping matrix into the GPR finite element equation, we can obtained

$$M\ddot{\boldsymbol{E}} + \left(K' + F \right) \dot{\boldsymbol{E}} + KE = S_E . \quad (13)$$

3.2 Sarma absorbing boundary

The Sarma absorbing boundary is a kind of attenuating absorbing layer. The basic principle is that an absorbing layer is added the boundaries of the simulation model to absorb the incident GPR waves. The medium of the absorbing layer is a kind of high attenuation characteristic media. The attenuation coefficient of the absorbing layer should be built on reasonable physical theory, and expressed as function of media parameters. Sarma (Sarma et al., 1998) proposed an absorbing boundary condition by adding an attenuating layer of a certain thickness around the boundaries area according to the material property to estimate the constant proportion coefficient. Figure 1(a) shows a sketch of the Sarma boundary condition. Rayleigh gives a classic method to calculate the damping matrix $\boldsymbol{F}$. This method uses the whole mass matrix $\boldsymbol{M}$ and total stiffness matrix $\boldsymbol{K}$ to calculate damping matrix $\boldsymbol{F}$. The matrix $\boldsymbol{F}$ can be expressed as

$$\left[F \right] = a_0 \left[M \right] + a_1 \left[K \right], (14)$$

where a_0, a_1 can be expressed as

$$a_0 = \frac{2\omega_i \omega_j \left(\xi_i \omega_j - \xi_j \omega_i \right)}{\omega_j^2 - \omega_i^2}, \quad a_1 = \frac{2 \left(\xi_j \omega_j - \xi_i \omega_i \right)}{\omega_j^2 - \omega_i^2}, (15)$$

The quantities, ω_i and ω_j are the inherent radiosfrequency of the i and j media, and ξ_i and ξ_j are the corresponding damping ratios, respectively. We apply the Sarma absorbing boundary to process the reflected wave. We substitute the matrix $\boldsymbol{F}$ into equation (3).Then EFM equation in the absorbing boundary area can be obtained as

$$M\ddot{\boldsymbol{E}} + \left(K' + F \right) \dot{\boldsymbol{E}} + KE = S, \quad (16)$$

In the absorbing layers areas, the proportionality coefficient a_0 and a_1 can be calculated according to equation (15).

3.3 UPML absorbing boundary condition

According to the electromagnetic theory, Maxwell equations in a UPML medium can be expressed as

$$\nabla \times \boldsymbol{E} = -j\omega\mu\bar{S} \cdot \boldsymbol{H} \quad (17)$$

$$\nabla \times \boldsymbol{H} = j\omega\varepsilon\bar{S} \cdot \boldsymbol{E} \quad (18)$$

where $\bar{S}$ is a parameter which expresses the characteristic of an anisotropic medium. It can be expressed as follows in two dimensions.

$$\bar{S} = \begin{bmatrix} s_y / s_x & 0 & 0 \\ 0 & s_x / s_y & 0 \\ 0 & 0 & s_x s_y \end{bmatrix} (19)$$

where $s_i = 1 + \sigma_i / (j\omega\varepsilon_0), \quad i = x, y$

To solve rotation on both sides of Eq. (17), and put Eq. (18) into it, we can obtain

$$\frac{1}{\mu} \bar{S}^{-1} \nabla \times \nabla \times \boldsymbol{E} = \omega^2 \varepsilon \bar{S} \cdot \boldsymbol{E} \quad (20)$$

Substitute Eq. (19) into Eq. (20) and we obtain

$$\frac{1}{\mu}\begin{bmatrix} (1+\sigma_x/(j\omega\varepsilon))^2 & 0 & 0 \\ 0 & (1+\sigma_y/(j\omega\varepsilon))^2 & 0 \\ 0 & 0 & 1 \end{bmatrix}\nabla\times\nabla\times\boldsymbol{E}=$$

$$\omega^2\varepsilon\cdot\begin{bmatrix} (1+\sigma_y/(j\omega\varepsilon))^2 & 0 & 0 \\ 0 & (1+\sigma_x/(j\omega\varepsilon))^2 & 0 \\ 0 & 0 & (1+\sigma_x/(j\omega\varepsilon))^2(1+\sigma_y/(j\omega\varepsilon))^2 \end{bmatrix}\cdot\boldsymbol{E} \tag{21}$$

Apply Fourier transform to the above equation, and we can obtain

$$\frac{1}{\mu}\nabla\times\nabla\times\boldsymbol{E}+\frac{2}{\mu\varepsilon_0}\boldsymbol{I}\frac{\partial\nabla\times\nabla\times\boldsymbol{E}}{\partial t}+\frac{1}{\mu\varepsilon_0^2}\boldsymbol{I}^2\frac{\partial\nabla\times\nabla\times\boldsymbol{E}}{\partial t^2}$$

$$=-\varepsilon\cdot\frac{\partial\boldsymbol{E}}{\partial t^2}-\frac{2\varepsilon}{\varepsilon_0}(\boldsymbol{J}+\boldsymbol{K})\cdot\frac{\partial\boldsymbol{E}}{\partial t}-\frac{\varepsilon}{\varepsilon_0^2}(\boldsymbol{J}^2+\boldsymbol{K}^2+2\cdot\boldsymbol{H})\cdot\boldsymbol{E}-\frac{2\varepsilon}{\varepsilon_0^3}\boldsymbol{K}\cdot\boldsymbol{H}\int_0^t\boldsymbol{E}\mathrm{d}t-\frac{\varepsilon}{\varepsilon_0^4}\boldsymbol{H}\cdot\int_0^t\int_0^t\boldsymbol{E}\mathrm{d}t\mathrm{d}t \tag{22}$$

Applying theGalerkin method [15] to Eq. (22), the FEM equation in a UPML medium can be expressed as

$$M\ddot{\boldsymbol{E}}+M_1\dot{\boldsymbol{E}}+M_2\boldsymbol{E}+M_3\int_0^t\boldsymbol{E}\mathrm{d}t+M_4\int_0^t\int_0^t\boldsymbol{E}\mathrm{d}t\mathrm{d}t-K\boldsymbol{E}-K_1\dot{\boldsymbol{E}}-K_2\ddot{\boldsymbol{E}}=S \tag{23}$$

The express of the matrixes in Eq. (23) is as follows

$$\begin{cases} \boldsymbol{M}=\int_e \boldsymbol{N}^{\mathrm{T}}N\mathrm{d}\Omega \\ \boldsymbol{K}=\frac{1}{\mu\varepsilon}\int_e\left(\frac{\partial\boldsymbol{N}}{\partial x}\left(\frac{\partial\boldsymbol{N}}{\partial x}\right)^{\mathrm{T}}+\frac{\partial\boldsymbol{N}}{\partial y}\left(\frac{\partial\boldsymbol{N}}{\partial y}\right)^{\mathrm{T}}\right)\mathrm{d}\Omega \end{cases} \qquad \begin{cases} \boldsymbol{M}_1=\frac{2}{\varepsilon_0}(\boldsymbol{J}+\boldsymbol{K})\int_e \boldsymbol{N}^{\mathrm{T}}N\mathrm{d}\Omega \\ \boldsymbol{K}_1=\frac{2}{\mu\varepsilon_0\varepsilon}\boldsymbol{I}\int_e\left(\frac{\partial\boldsymbol{N}}{\partial x}\left(\frac{\partial\boldsymbol{N}}{\partial x}\right)^{\mathrm{T}}+\frac{\partial\boldsymbol{N}}{\partial y}\left(\frac{\partial\boldsymbol{N}}{\partial y}\right)^{\mathrm{T}}\right)\mathrm{d}\Omega \end{cases}$$

$$\begin{cases} \boldsymbol{M}_2=\frac{1}{\varepsilon_0^2}(\boldsymbol{J}^2+\boldsymbol{K}^2+2\cdot\boldsymbol{H})\int_e \boldsymbol{N}^{\mathrm{T}}N\mathrm{d}\Omega \\ \boldsymbol{K}_2=\frac{1}{\mu\varepsilon_0^2\varepsilon}\boldsymbol{I}^2\int_e\left(\frac{\partial\boldsymbol{N}}{\partial x}\left(\frac{\partial\boldsymbol{N}}{\partial x}\right)^{\mathrm{T}}+\frac{\partial\boldsymbol{N}}{\partial y}\left(\frac{\partial\boldsymbol{N}}{\partial y}\right)^{\mathrm{T}}\right)\mathrm{d}\Omega \end{cases} \qquad \begin{cases} \boldsymbol{M}_3=\frac{2}{\varepsilon_0^3}\boldsymbol{K}\cdot\boldsymbol{H}\int_e \boldsymbol{N}^{\mathrm{T}}N\mathrm{d}\Omega \\ \boldsymbol{M}_4=\frac{1}{\varepsilon_0^4}\boldsymbol{H}\int_e \boldsymbol{N}^{\mathrm{T}}N\mathrm{d}\Omega \end{cases}$$

$$\boldsymbol{I}=\begin{bmatrix} \sigma_x & 0 & 0 \\ 0 & \sigma_y & 0 \\ 0 & 0 & 0 \end{bmatrix}, \boldsymbol{J}=\begin{bmatrix} \sigma_y & 0 & 0 \\ 0 & \sigma_x & 0 \\ 0 & 0 & 0 \end{bmatrix}, \boldsymbol{K}=\begin{bmatrix} 0 & 0 & 0 \\ 0 & 0 & 0 \\ 0 & 0 & \sigma_x+\sigma_y \end{bmatrix}, \boldsymbol{H}=\begin{bmatrix} 0 & 0 & 0 \\ 0 & 0 & 0 \\ 0 & 0 & \sigma_x\cdot\sigma_y \end{bmatrix}.$$

IV. Comparison test and results

To illustrate absorption effectson the incident waves at the artificially truncated boundary using different absorbing boundary condition, a 10 m × 10 m homogeneous model was established, with a pulse excitation source located at the center of the simulation area, as shown in Fig. 1. The wavelte of the GPR pulse excitation source is $f(t)=t^2e^{-\alpha t}\sin\omega_0 t$, where ω_0 is the central frequency of the transmitting antenna (in this example, ω_0=100 MHz). The attenuation velocity is governed by the coefficient α , which in this case equals to $0.93\omega_0$.

The sampling interval time is 0.1 ns. The dielectric constant of the medium is $\varepsilon=6.5$, the conductivity $\sigma=0.002$ S/m, and the mesh element size = 0.0025 m^2. Absorption effects resulting from different absorbing boundary conditions were observed by wave-field snapshots at various times. Fig.2. Fig. 3 and Fig. 4 show the snapshots of wave-field surrounded by transmitting boundary condition, Sarma boundary condition and UPML boundary condition respectively. In Fig. 2, we can see that the GPR wave reaches the edge of the area at 32 ns, and the reflected wave begins to form at the artificial truncated boundary. In the snapshot at 38 ns, we can see the GPR wave energy reflected strongly by the artificial truncated boundary, greatly affecting the target area. This also indicates the necessity for effective processing of artificial truncated boundaries. Fig. 3 and Fig. 4 show wave field snapshots at 12, 32 and 38 ns by using the transmitting boundary condition and Sarmaboundary condition respectively. As seen in the figures, wave energy again reaches the boundary area at 32 ns. By 38 ns, however, the majority of the electromagnetic wave energy has been transmitted through the boundary, with only a small portion reflected back. By comparison to the energy of the strongly reflected wave on the truncated

boundary at the same time (Fig. 5(c)), we see that the transmitting boundary condition and Sarmaboundary condition has a remarkable effect. However, wave field snapshot of 32 ns shows that there is still some reflected energy from the truncated boundary. Compared with Fig. 3 and Fig. 4, wave filed snapshots of 32 ns in Fig. 5 which is by using UPML absorbing boundary condition have perfectly absorbing effect, the reflected wave are nearly absorbing.

Fig. 6.showsthe recorded signal and their envelope at point A in Fig. 1 under different absorbing boundary conditions. The recorded signal contains the transmission signal and the reflected signal from the boundary. From these figures we can see that under the UPML boundary condition, the reflected energy is least. The refection efficient of no absorbing boundary condition，transmitting boundary condition, sarmaboundary condition and UPML boundary condition calculated after a spreading correction ofthe wave front are -9.68 dB, -24.8 dB, -34.7 dB,-55.8 dB respectively. Compared with other two absorbing boundary conditions, the UPML boundary condition has best absorbing effect.
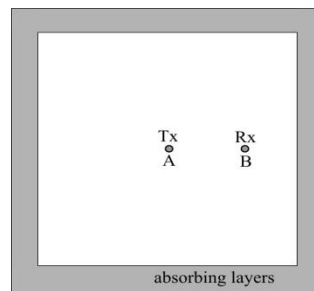
Fig.1. Sketch drawing of the Sarma boundary condition model
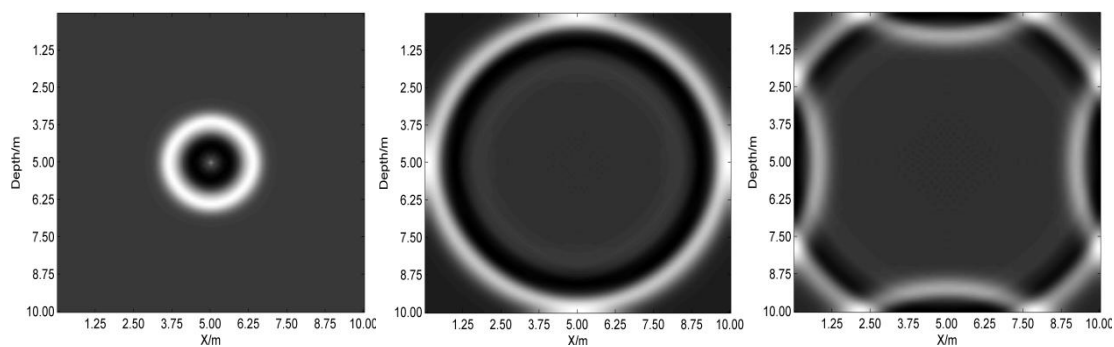
(a) 12 ns snapshot(b) 32 ns snapshot (c)38 ns snapshot
Fig.2.Snapshots of wave field without boundary conditions
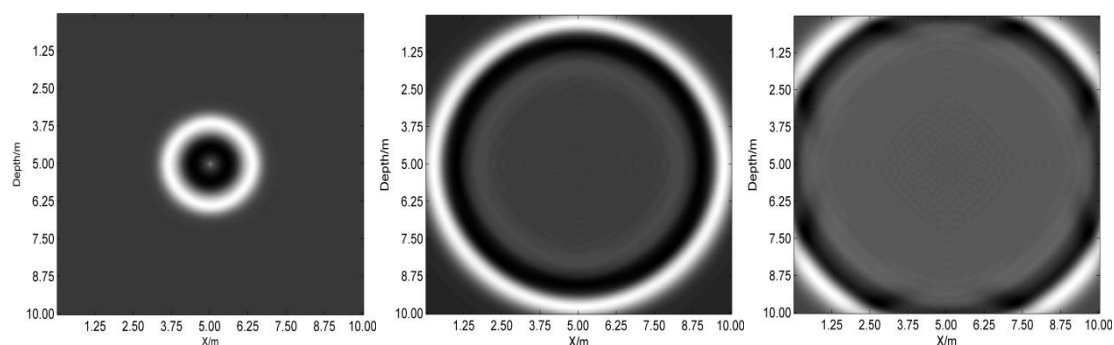
(a)12 ns snapshot (b) 32 ns snapshot(c) 38 ns snapshot
Fig.3. Snapshots of wave field with the transmitting boundary condi
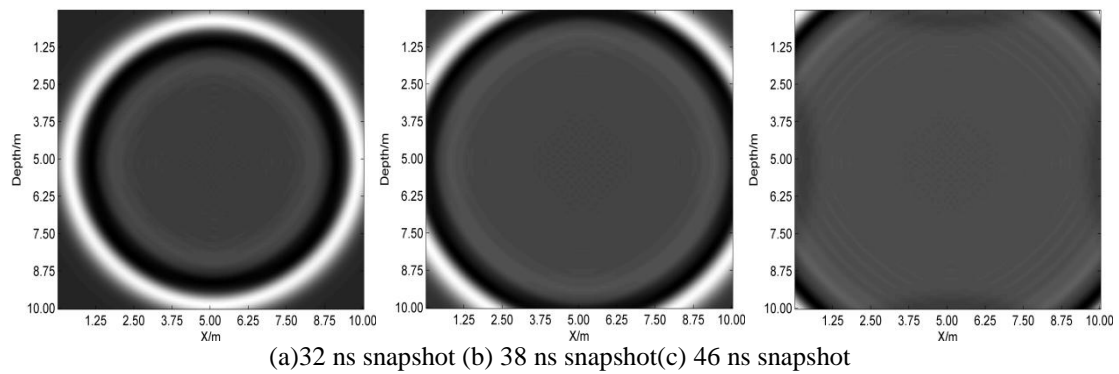
(a)32 ns snapshot (b) 38 ns snapshot(c) 46 ns snapshot
Fig.4. Snapshots of wave field with Sarma absorbing boundary condition
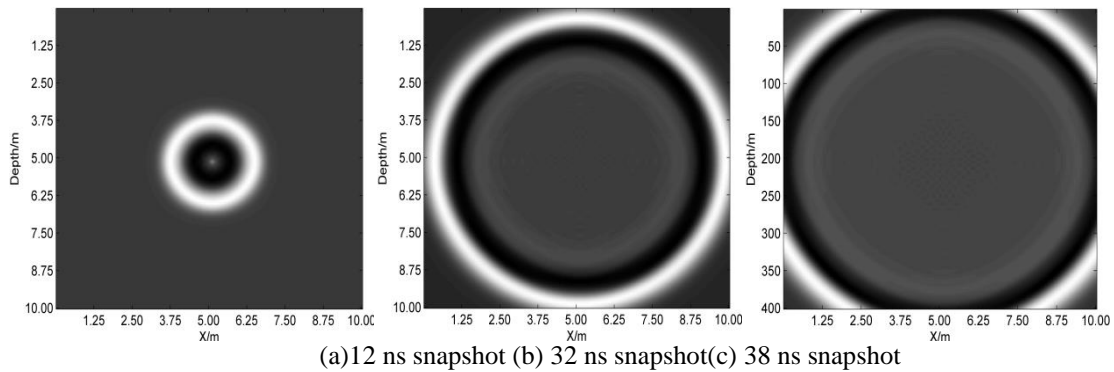
(a)12 ns snapshot (b) 32 ns snapshot(c) 38 ns snapshot
Fig.5. Snapshots of wave field ts with the UPML boundary condition

(a)

(b)

(c)

(d)
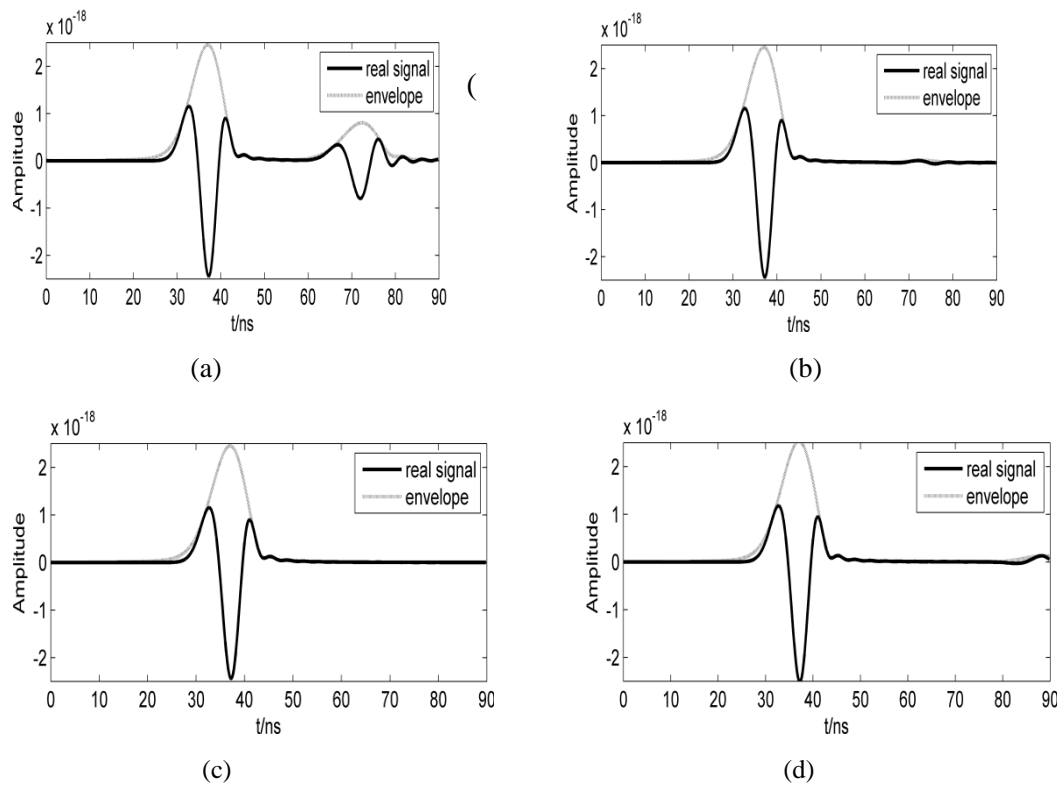
Fig.6. Incident and reflected signal from different absorbing boundary. (a) No absorbing boundary condition;(b) Transmitting boundary condition; (c) Sarma absorbing boundary condition and (d) UPML absorbing boundary condition.

IV. Conclusion

Transmitting boundary condition, Sarma absorbing boundary condition and UPML absorbing boundary condition for simulation of ground penetrating radar (GPR) by the time domain finite element (FEM) method are described and compared by the reflection coefficient.The results demonstrated that UPML boundary condition can yield a reflection coefficient smaller than -50 dB, which -20 dB smaller than other two boundary conditions.

Acknowledgments

REFERENCES

[1.] B.Shen,Study of radar wave equation and its forward modeling. Geophysical and Geochemical computation technology, 16(1,)1994,29-33.(in Chinese)

[2.] Q.Y. Di, and M.Y.Wang, 2D finite element modeling for radar wave. Chinese Journal of Geophysics, 42(6), 1999, 818-825. (in Chinese)

[3.] L. Tiao, W. Cai, and P.W. Zhang, Discontinuous Galerkin Time-Domain Method forGPR Simulation in Dispersive Media. IEEE Transactions on Geoscience and Remote Sensing, 43(1), 2005, 72-80.

[4.] P. Arias, J. Armesto, and D. Capua, Digital photogrammetry, GPR and computational analysis of structural damages in a mediaeval bridge. Engineering Failure Analysis, 14(8), 2007,1444-1457.

[5.] A Bayliss,and E.Turkel, Boundary conditions for the helmholtz equation in duct-like geometries. IntAssoc for Mathematics & Computers in Simulation, 1982, 455-458.

[6.] B Engquist, and A.MajdaAbsorbing boundary conditions for numerical simulation of waves. Proc.Conf. on the National Academy of Sciences, America, 1977, 1765-1766.

[7.] K. K. Mei,and Jiayuan.Fang,Superabsorption - A method to improve absorbing boundary conditions. IEEE Transactions on Antennas and Propagation, 40(9, 1992, 1001-1010.

[8.] S. D. Gedney, G.Liu, and J. A.Roden, Perfectly Matched Layer Media With CFS For An Unconditionally Stable ADI-FDTD Method.IEEE Transactions on Antennas and Propagation, 49 (11), 2001, 1554-1559.

[9.] J P.Berenger, A perfectly matched layer for the absorption of electromagnetic waves.Journal ofComputational Physics, 114 (2), 1994, 185-200.

[10.] G.Mur, Absorbing boundary conditions for the finite-difference approximation of the time-domain electromagnetic-field equations, IEEE Transactions on Electromagnetic Compatibility, 23(4), 1981, 377-382.

[11.] Q Y. Di, M G. Zhang, and M Y. Wang, Migration of groundpenetrating radar data with a finiteelement method that considers attenuation and dispersion, geophysics, 69(2), 2005, 472-477.

[12.] D S. Feng, C S. Chen, and H H. Wang, Finite element method GPR forward simulation based on mixed boundary condition. Chinese journal of geophysics, 55(11), 2012, 3773-3785.

[13.] S Z. Xu, Finite element method for geophysics.(Science Press,1994).

[14.] C. Cerjan, D. Kosloff, and M. Reshef, A nonreflecting boundary condition for discrete acoustic and elastic wave equation. Geophysics, 50, 1985, 705-708.

[15.] D C. Xu, S X. Wang, and S J.Jiao, Wave equation finite-element modeling including rugged topography and complicated medium. Progress in Geophysics, 22(2), 2007, 522-529.

[16.] J F.Claerbout, Imaging the Earth's Interior, (Blackwell Scientific Publications, 1985).

[17.] G S. Sarma, K. Mallick, and V R. Gadhinglajkar, Nonreflectingboundary condition in finite element formulation for an elastic wave equation. Geophysics, 63(3),1998, 1006-1016

[18.] J F. Semblat, A. Gandomzadeh, and L. Lenti, A simple numerical absorbing layer method in elastodynamics, ComptesRendusMecanique, 338, 2010, 24-32

[19.] D S. Feng,and Q w. Dai, GPR numerical simulation of full wave field based on UPML boundarycondition of ADI-FDTD. NDT&E International,44(6), 2011, 495-504.

[20.] J. Li, Z F. Zeng,L. Huang, and F S.Liu, GPRsimulation based on complex frequency shifted recursiveintegration PML boundary of 3D high order FDTD, Computers and Geosciences, 49,2012, 121-130.

Taguchi Analysis of Erosion Wear Maize Husk Based Polymer Composite

Prof. Manish Verma[1], Prof. Rupesh Kumar Malviya[2], Gunwant Sahu[3],
Mr. Prof. Ashish Khandelwal[4]

[1]*Assistant Professor and, Faculty of CEC Bilaspur (CG)*
[2]*Assistant Professor and, Faculty of BCE Mandideep Bhopal (MP)*
[3]*Student of M.E. (Pro. Engg) CEC Bilaspur, CG*

Abstract: *Amids the growing concern on environmental issues, science is seeking various alternatives to replace the synthetic and non degradable fibers composites with environment friendly biocomposites of comparable characteristics and performance. Visualizing the importance of polymer composites and owing to issue of ecological concerns, this experiment is an attempt to further investigate possibility of bio composites (Particularly maize husk) as an alternative of available synthetic polymer composites. Taking one leap forward the experiment also approximate qualities the effect of individual parameters on erosion by the application of Taguchi Technique. Experimental system were devised and designed to study the erosion rate of maize husk fiber Reinforced Polymer composites at various impingement angles, with profound variables such as particle velocity, fiber content, and particle size (erodent size) To cast the composite epoxy Resin LY 556 with corresponding hardener HY 551 was used. The erodent size was in range of it irregular shape. The tribological performance of sheets was investigated in respect to set of various variable parameters as suggested by L16 series of Taguchi Techniques. The morphological feature before and after the experiments were studies using SEM.*

Keywords: *Biocomposites, erosive wear rate, brittle fracture Taguchi Technique, impingement angle, erodent size.*

I. Introduction

Composites

A typical composite material is a system of materials composing of two or more materials (mixed and bonded) on a macroscopic scale. **Van Suchetclan [5]** explains composite materials as heterogeneous materials consisting of two or more solid phases, which are in intimate contact with each other on a microscopic scale. They can be also considered as homogeneous materials on a microscopic scale in the sense that any portion of it will have the same physical property.

Classification of composites

a) Metal Matrix Composites (MMC)
b) Ceramic Matrix Composites (CMC)
c) Polymer Matrix Composites (PMC)

Maize husk (MH) is one of the major agricultural residues produced as a by-product during maize processing. Usually it has been a problem for maize farmers due to its resistance to decomposition in the ground, difficult digestion and low nutritional value for animals. According to researches the lignin and hemicelluloses contents of maize husk are lower than wood whereas the cellulose content is similar. For this reason MHF can be processed at higher temperatures than wood. Therefore, the use of maize husk in the manufacturing of polymer composites is attracting much attention.

II. Literature Review

Particulate filled polymer composites have been used extensively in various fields due to their low production costs and the ease of manufacturing. Besides, they behave isotropically and are not as sensitive as long fiber composites to the mismatch of thermal expansion between the matrix and the reinforcement **[6-9]**.

The mechanical properties of particulate filled polymer composites depend strongly on the particle size, particle-matrix interface adhesion and particle loading. Smaller particle size yields higher fracture toughness for calcium carbonate filled high density polyethylene (HDPE) [**10-12**]. Many research articles have been published to justify the utility and to establish advantageous features of such natural fibers **[17].** Natural fibers under investigation include flax, hemp, jute, sisal, kenaf, coir, kapok, banana, henequen and many others **[18].** The various advantages of natural fibers over man-made glass and carbon fibers are reported to be low cost, low

density, comparable specific tensile properties, non-abrasive nature, non-allergic to the skin, reduced energy consumption, less health risk, renewability, recyclability and bio-degradability **[19-21].**
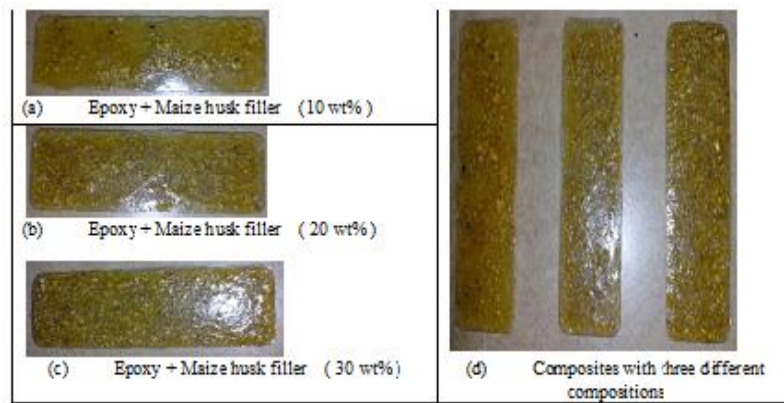
Maize husk which has become environmentally problematic waste is now being converted into useful industrial materials **[22].** Maize stalk has therefore demonstrated its potential to be used to reinforce natural rubber for shoe sole production **[23].** In the present work, the maize husk has been taken as a particulate filler and epoxy as matrix to prepare a bio-composite, and finding the various properties.

III. Methodology

Matrix materials are of different types like metals, ceramics and polymers. Polymer matrices are most commonly used because of cost efficiency, ease of fabricating complex parts with less tooling cost and they also have excellent room temperature properties when compared to metal and ceramic matrices. In the present research work, maize husk (collected from Rajaram Maize product, Rajnandgaon,C.G.,India) is used as filler material polymer matrix composites.

Table:1. **List of particulate filled composites fabricated by hand-lay-up technique**

Sample	Composition (Maize husk as filler material)
1	Epoxy + Maize husk filler (0 wt%)
2	Epoxy + Maize husk filler (5 wt%)
3	Epoxy + Maize husk filler (10 wt%)
4	Epoxy + Maize husk filler (15 wt%)
5	Epoxy + Maize husk filler (20 wt%)
6	Epoxy + Maize husk filler (25 wt%)
7	Epoxy + Maize husk filler (30 wt%)

Fig.1. Fabricated Composite for three different compositions

1. Density and Void Fraction

The theoretical density of composite materials in terms of weight fractions of different constituents can easily be obtained as per the following equations given by **Agarwal and Broutman [40].**

$$\rho_{ct} = \frac{1}{\left(W_f / \rho_f\right) + \left(W_m / \rho_m\right)} \tag{1}$$

Where, W and ρ represent the weight fraction and density respectively. The suffix f, m and ct stand for the fiber, matrix and the composite sample respectively. The actual density (ρ_{ce}) of the composite, however, can be determined experimentally by simple water immersion technique. The volume fraction of voids (V_v) in the composites is calculated using the following equation:

$$V_v = \frac{\rho_{ct} - \rho_{ce}}{\rho_{ct}} \tag{2}$$

2. Mechanical characterization
2.1 Tensile test

The standard test method according to ASTM D3039-76 has been used; gauge length of the test specimen used is 50 mm. The tensile test has been performed in universal testing machine INSTRON H10KS .The test was conducted with a cross head speed of 5mm/min. For each test, composite of three samples were tested and

---

average value was taken for analysis the Machine used for the test and the sample in loading condition. Tensile strength & Young's modulus were found out using the following formula.

$$\sigma = \frac{P}{A} \qquad (3)$$

and

$$E = \frac{\sigma L}{\delta} \qquad (4)$$

Where, "σ" is tensile strength, "P" is the load applied, "A" is the cross sectional area, "E" is Young's modulus, "L" is span length of the specimen and "δ" is the deflection recorded.

2.2 Flexural strength.

Three point bend test was carried out in an UTM 201 machine in accordance with ASTM D2344-84 to measure the flexural strength of the composites. The loading arrangement for the specimen and the photograph of the machine used .All the specimens (composites) were of rectangular shape having length varied from 100-110 mm, breadth of 50-60 mm and thickness of 2.5-3.5 mm. A span of 100 mm was employed maintaining a cross head speed of 5mm/min. The flexural strength in a three point bending test is found out by using equation (3). The flexural strength of composites was found out using the following equation:

$$FS = \frac{3PL}{2bt^2} \qquad (5)$$

Where, 'b' is breadth, 't' is thickness and 'y' is extension of the specimen during experiment.

3. Micro-hardness measurement

Micro-hardness measurement is done using a Leitz micro-hardness tester. A diamond indenter, in the form of a right pyramid with a square base and an angle 1360 between opposite faces, is forced into the material under a load F. The two diagonals X and Y of the indentation left on the surface of the material after removal of the load are measured and their arithmetic mean L is calculated. In the present study, the load considered is $F = 0.245$ N and Vickers hardness number is calculated using the following equation.

$$H_v = 0.1889 \frac{F}{L^2} \qquad (6)$$
$$and \quad L = \frac{X+Y}{2}$$

Where, F is the applied load (N), L is the diagonal of square impression (mm), X is the horizontal length (mm) and Y is the vertical length (mm).

4. Scanning electron microscopy

The surfaces of the maize husk filled epoxy composites are examined by JEOL JSM-6480LV . The specimens are cleaned thoroughly, air dried before being observed under SEM at 20 kV. The composite samples are mounted on stubs with silver paste. To enhance the conductivity of the samples, a thin film (100 Å thicknesses) of platinum is coated onto them in JEOL sputter ion coater before the photomicrographs are taken.

5. Tribological characterization
5.1 Solid particle erosion test

The set up for the solid particle erosion wear test used in this study is capable of creating reproducible erosive situations for assessing erosion wear resistance of the prepared composite samples. The test rig consists of an air compressor, an air drying unit, a particle feeder and an air particle mixing and accelerating chamber. In the present study, dry silica sand of four different mean particle sizes (40μm, 60μm, 80 μm and 100μm) are used as erodent.

5.2 Taguchi experimental design

From a scientific viewpoint, these experiments are either one or a series of tests to either confirm a hypothesis or to understand a process in further detail. In order to achieve a meaningful end result, several experiments are usually carried out. The experimenter needs to know the factors involved, the range these factors are varied between, the levels assigned to each factor as well as a method to calculate and quantify the response of each factor. This one-factor-at-a-time approach will provide the most favorable level for each factor but not the optimum combination of all the interacting factors involved. Thus, experimentation in this scenario can be considered as an iterative process. Although it will provide a result, such methods are neither time nor cost effective. But the design-of-experiments (DOE) is a scientific approach to effectively plan and perform

experiments using statistics. In such designs, the combination of each factor at every level is studied to determine the combination that would yield the best result.

Table 2: Parameter settings for erosion test

Command factors	Abbreviation	Constant Parameters	
Impact velocity	Factor A	Erodent	Silica sand
Maize husk content	Factor B	Erodent feed rate (g/min)	10.0 + 1.0
Impingement angle	Factor C	Nozzle Diameter (mm)	2.5 mm
Erodent size	Factor D	Standoff distance	150 mm

Table 3: Control factors and their selected levels

Command factors	Level				
	I	II	III	IV	Units
Factor A : Impact velocity	30	40	50	60	m/sec
Factor B : Maize husk content	0	10	20	30	wt. %
Factor C : Impingement angle	45	60	75	90	Degree
Factor D : Erodent size	25	50	75	100	Micron

Table 4: Taguchi orthogonal array design (L16)

Test run	Factor A Impact velocity	Factor B Maize husk content	Factor C Impingement angle	Factor D Erodent size
1	1	1	1	1
2	1	2	2	2
3	1	3	3	3
4	1	4	4	4
5	2	1	2	3
6	2	2	1	4
7	2	3	4	1
8	2	4	3	2
9	3	1	3	4
10	3	2	4	3
11	3	3	1	2
12	3	4	2	1
13	4	1	4	2
14	4	2	3	1
15	4	3	2	4
16	4	4	1	3

The impact of these four parameters on the erosion wear rate of these maize husk filled epoxy composites is therefore studied in this work using Taguchi's L16 orthogonal array design. The control factors and the parameter settings for erosion test are given in Table 2. and Table 3 presents the selected levels for various control factors. The tests are conducted as per the L16 experimental design given in Table 4.

The experimental observations are further transformed into signal-to-noise (S/N) ratios. There are several S/N ratios available depending on the type of characteristics as given by following equations:

'Smaller- the- better' characteristic:
$$\frac{S}{N} = -10\log\frac{1}{n}\left(\sum y^2\right) \qquad (7)$$

'Nominal- the- better' characteristics:
$$\frac{S}{N} = -10\log\frac{1}{n}\left(\sum \frac{\overline{Y}}{S_y^2}\right) \qquad (8)$$

'Larger- the- better' characteristics:
$$\frac{S}{N} = -10\log\frac{1}{n}\left(\sum \frac{1}{y^2}\right) \qquad (9)$$

Where, 'n' is the number of observations and 'y' is the observed data. The S/N ratio for minimum wear rate (both for erosion as well as sliding) comes under 'smaller is better' characteristic, which can be calculated as logarithmic transformation of the loss function by using Equation (7).

IV. Results And Discussion

1. Physical characterization
Density and Void Fraction

Density is a material property which is of prime importance in several weight sensitive applications. The theoretical and experimentally measured densities of epoxy composites reinforced with maize husk, along with the corresponding volume fraction of voids are presented in Table 5.

Table 5: Density values along with the void fractions of the maize husk filled epoxy composites

S.No.	Filler Content (wt %)	Measured density (gm/cm³)	Theoretical density (gm/cm³)	Voids contents (%)
1	0	1.1	1.1	-----
2	5	0.885	0.916	3.38
3	10	0.736	0.785	6.24
4	15	0.622	0.687	9.46
5	20	0.532	0.611	12.92
6	25	0.459	0.551	16.69
7	30	0.394	0.498	20.88

2. Mechanical characterization
Tensile properties

The variation of tensile strength of the natural filler polymer composite is presented in Figure 6.
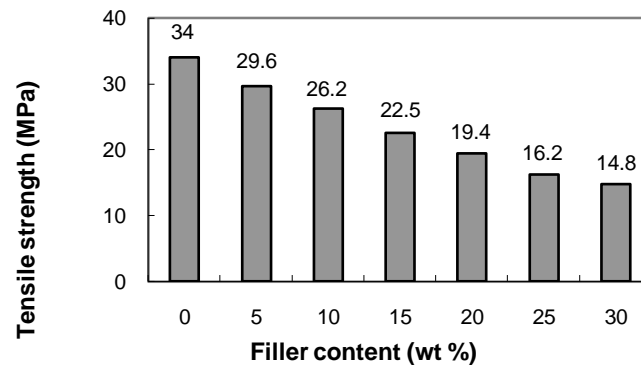
Fig. 6. Effect of maize husk content on tensile strength of epoxy composites
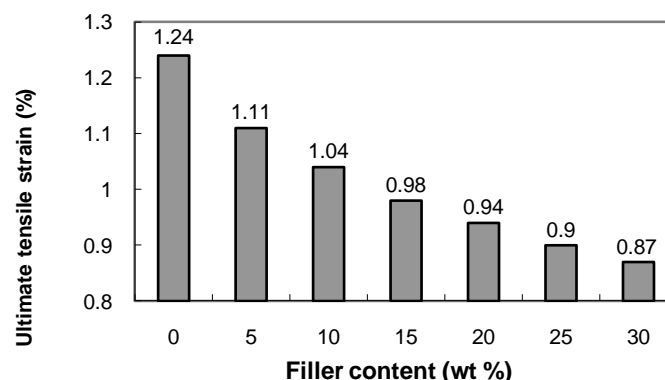
Fig. 7. Effect of maize husk content on ultimate tensile strain of epoxy composites

2.2 Flexural strength

Composite materials are subjected to bending and shear in many engineering applications. Therefore, it is essential to study the flexural characteristics of the developed new composites.
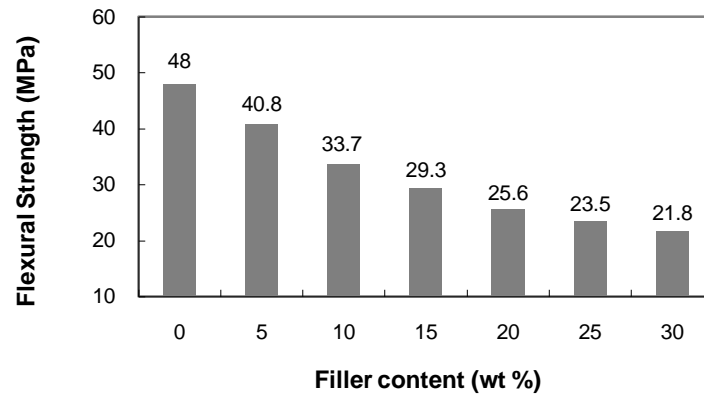
Fig. 8.Effect of maize husk content on flexural strength of epoxy composites

2.3 Micro-hardness

Hardness of is considered as one of the important factor which governs the wear resistance of any material. In the present investigation, micro-hardness values of the epoxy composites with maize husk filled in different proportions have been measured and the variation of micro-hardness with the maize husk content in the composites is shown in Figure 9.
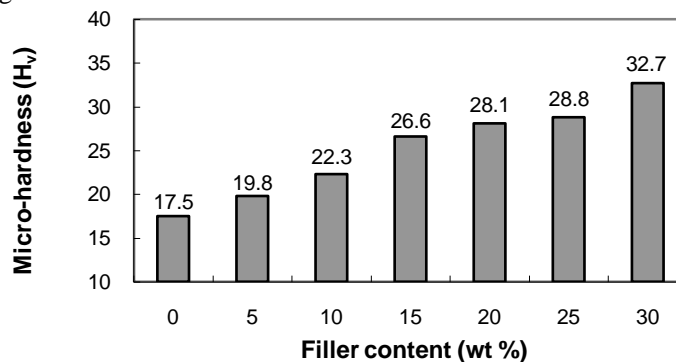
Fig. 9. Effect of maize husk content on micro-hardness of epoxy composite

2.4 Morphological Behaviour

It is clear from the image that the maize husk particles are not of regular shape and similar size which is obvious because the particle used in present investigation are generated by grinding process and no grinding process is as accurate to develop particles of similar shape and size.

(a)

(b)

(c)
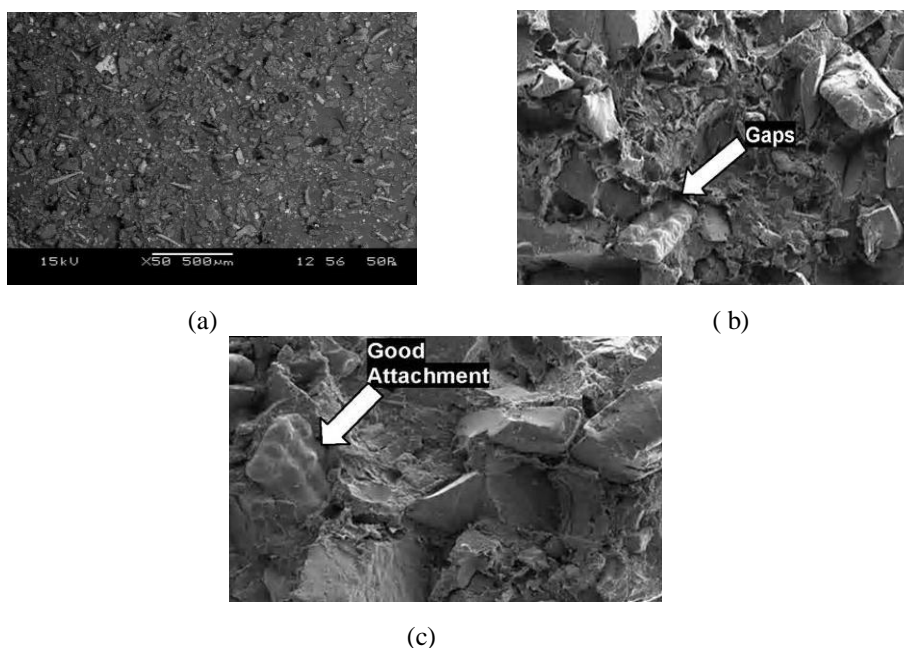
Fig. 10. SEM micrograph of maize husk particulate filled epoxy composites

3. Tribological characterization
Scanning electron micrograph of un-eroded and eroded composites
Fig. 11. SEM micrograph of un-eroded maize husk/epoxy composites

(a) (b)
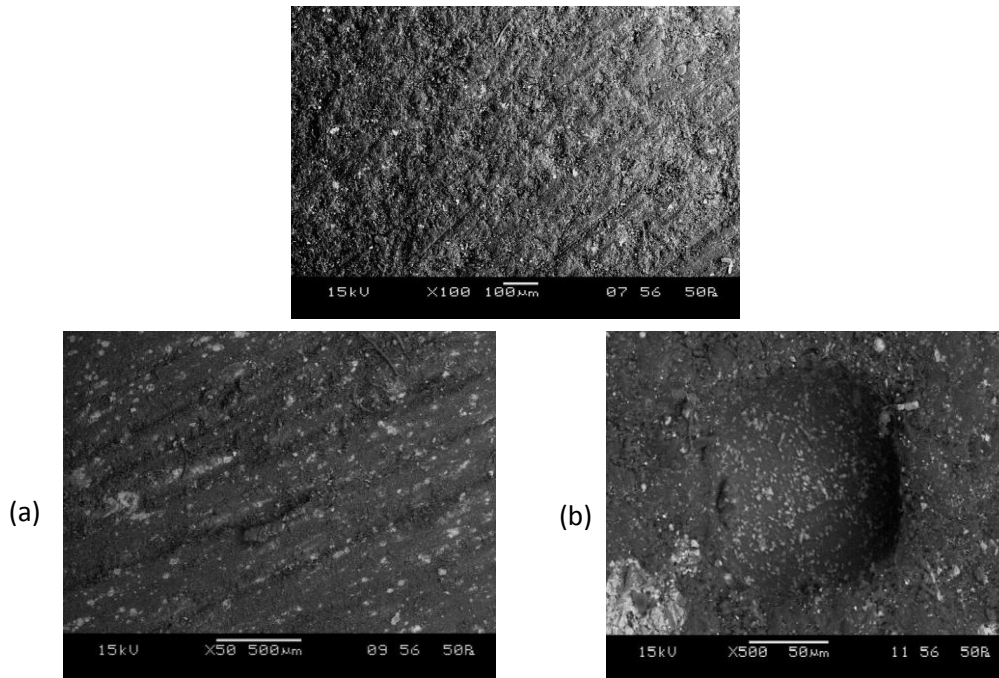
Fig. 12. SEM micrograph of eroded maize husk/epoxy composites

4. Erosion wear and Taguchi analysis

Table 6. shows the solid particle erosion wear rates of maize husk filled epoxy composites under various test conditions. The weight of the composite is taken before the erosion test, later after the erosion test again the weight of the composite under study is taken and the difference in their weight is calculated. The weight of the composite after erosion is always less than that of before erosion. The difference in their weight is called mass or weight loss of the sample due to solid particle impact. The ratio of this mass loss to the mass of the eroding particles causing the loss is then computed as the erosion rate. The erosion rate is thus defined as the mass loss of the specimen due to erosion divided by the mass of the erodent causing the loss.

Table 6: **Erosion wear test result with corresponding S/N ratios**

Test run	Factor A Impact velocity (m/sec)	Factor B Maize husk content (wt %)	Factor C Impingement angle (degree)	Factor D Erodent size (microns)	E_r Erosion rate (mg/kg)	S/N ratio (db)
1	30	0	45	25	88.92	-38.980
2	30	10	60	50	77.26	-37.759
3	30	20	75	75	64.58	-36.202
4	30	30	90	100	49.34	-33.864
5	40	0	60	75	97.46	-39.776
6	40	10	45	100	86.08	-38.698
7	40	20	90	25	70.87	-37.009
8	40	30	75	50	54.13	-34.669
9	50	0	75	100	118.42	-41.468
10	50	10	90	75	105.89	-40.497
11	50	20	45	50	88.51	-38.940
12	50	30	60	25	72.24	-37.176
13	60	0	90	50	134.73	-42.589
14	60	10	75	25	117.48	-41.399
15	60	20	60	100	106.83	-40.574
16	60	30	45	75	87.57	-38.847

These experimental observations are then transformed into a signal-to-noise (S/N) ratios which is represented in Table . Among various S/N ratios, smaller-is-better is used in present case for minimum erosion rate:

$$\frac{S}{N} = -10 \log \frac{1}{n} \left(\sum y^2 \right)$$

where, *'n'* the number of observations, and *'y'* the observed data.
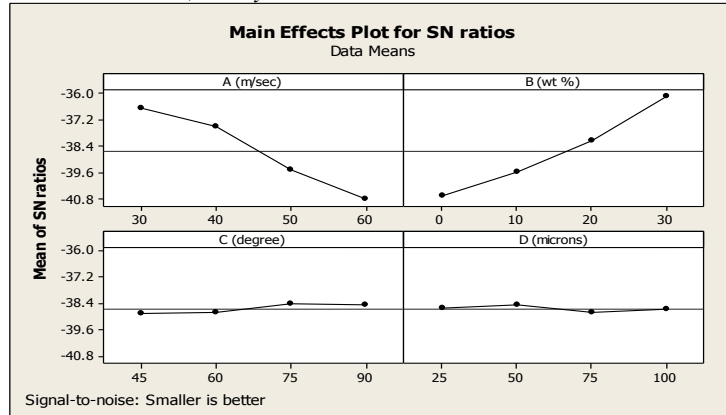
Fig. 13. Effects of control factors on erosion rate of fabricated composites

The analysis is made using the popular software specifically used for design of experiment applications known as MINITAB 14.

This present investigation on particulate filled maize husk/ epoxy composites has led to the following conclusions:

1) Maize husk possesses reinforcing potential to be used as a filler material in polymer matrix composites.
2) Successful fabrication of epoxy matrix composites reinforced with maize husk particles is possible by simple hand-lay-up technique.
3) The density of the fabricated composites decreases with increase in weight fraction and it also possesses low void content; even it is prepared by hand lay-up technique.
4) The tensile strength and flexural strength of these composites decreases with filler content because of poor mechanical properties of maize husk.
5) By surface morphology it is clear that there is good adhesion between the matrix phase and filler phase and very less gap is visible between them which results in low amount of porosity.
6) The micro-hardness of this natural filler based composite increases invariably with filler loading and provides improved impact resistance.
7) This study reveals that maize husk possesses good filler characteristics as it improves the erosion wear resistance of the epoxy resin.
8) Erosion characteristics of these composites can also be successfully analysed using Taguchi experimental design scheme. Taguchi method provides a simple, systematic and efficient methodology for the optimization of the control factors.

REFERENCES

[1] Stolarski T.A., "Tribology in machine design", Heiman Newnes, UK. (1990).
[2] Paivi Kivikyto-Reponen, "Correlation of material characteristics and wear of powder metallurgical metal matrix composites, doctoral theses in materials and earth sciences", Helsinki University of Technology, Laboratory of Materials Science, Espoo, (2006).
[3] Budinski K.G., "Surface engineering for wear resistance", Prentice Hall, New Jersey, (1998).
[4] Robinowicz E., "Friction and wear of materials", John Willey, New York, USA (1965).
[5] Suchtelen Van J., "Product properties: a new application of composite materials", Philips Res. Reports, Vol. 27, pp. 28, (1972).
[6] Ranganath S., "A Review on Particulate-reinforced titanium matrix composites", Journal of Materials Science, Vol. 32(1), pp. 1-16, (1997).
[7] Sawyer W. G., Freudenberg K. D., Praveen B. and Schadler L. S., "A study on the friction and wear behavior of PTFE filled with alumina nanoparticles", Wear, Vol. 254(5-6), pp. 573-580, (2003).
[8] Kim J., Kang P. H. and Nho Y.C., "Positive temperature coefficient behavior of polymer composites having a high melting temperature", Journal of Applied Polymer Science, Vol. 92(1), pp. 394-401, (2004).
[9] Nielsen L. E. and Landel R. F., "Mechanical properties of polymers and composites", 2nd ed. New York: Marcel Dekker, pp. 557, (1994).

[10]   Bartczak Z., Argon A. S., Cohen R. E. and Weinberg M., "Toughness mechanism in semi-crystalline polymer blends: II. High-density polyethylene toughened with calcium carbonate filler particles", Polymer, Vol. 40(9), pp. 2347-2365, (1999).

[11]   Young R. J. and Beaumont P. W. R., "Failure of brittle polymers by slow crack growth Part 3 Effect of composition upon the fracture of silica particle-filled epoxy resin composites", Journal of Materials Science, Vol. 12(4), pp. 684-692,(1977).

[12]   Kinloch A. J., Maxwell D. L. and Young R. J., "The fracture of hybrid particulate composites", Journal of Materials Science, Vol. 20(11), pp. 4169-4184, (1985).

[13]   Nakamura Y., Yamaguchi M., Kitayama A., Okubo M. and Matsumoto T., "Effect of particle size on fracture toughness of epoxy resin filled with angular-shaped silica", Polymer, Vol. 32(12), pp. 2221-2229, (1991).

[14]   Nakamura Y., Yamaguchi M., Okubo M. and Matsumoto T., "Effect of particle size on impact properties of epoxy resin filled with angular shaped silica particles", Polymer, Vol. 32(16), pp. 2976-2979, (1991).

[15]   Pukanszky B. and Voros G., "Mechanism of interfacial interactions in particulate filled composite", Composite Interfaces, Vol. 1(5), pp. 411-427, (1993).

[16]   Nicolais L. and Nicodemo L., "The Effect of particles shape on tensile properties of glassy thermoplastic composites", International Journal of Polymeric Materials, Vol. 3(3), pp. 229-243, (1974).

[17]   Nabi Saheb D. and Jog J. P., "Natural fiber polymer composites: a review", Adv Polym Technol, Vol.18, pp. 351–63, (1999).

[18]   Li X., Tabil L.G., Panigrahi S. and Crerar W.J., "The influence of fiber content on properties of injection molded flax fiber-HDPE biocomposites", Can BiosystEng., Vol. 08(148), pp. 1–10, (2009).

[19]   Malkapuram R., Kumar V., and Yuvraj S. N., "Recent development in natural fiber reinforced polypropylene composites", J Reinf Plast Compos, Vol. 28, pp. 1169–89, (2008).

[20]   Wambua P., Ivens J. and Verpoest I., "Natural fibers: can they replace glass in fiber reinforced plastics", Compos Sci Technol, Vol. 63, pp. 1259–64, (2003).

[21]   Ahmad I., Baharum A. and Abdullah I., "Effect of extrusion rate and fiber loading on mechanical properties of Twaron fiber-thermoplastic natural rubber (TPNR) composites", J Reinf Plast Compos, Vol. 25, pp. 957–65, (2006).

[22]   Crespo J. E., Sanchez L., Gracia D. and Lopez J., "Study of mechanical and morphological properties of plasticized PVC composites containing rice husk fillers", Journal of Reinforced Plastics and Composites, 27, pp.229- 42, (2008).

[23]   Yang H. S., Kim H. J., Son J., Park H. J., Lee B. J. and Hwang T. S., "Rice husk flour filled polypropylene composites; mechanical and morphological study", Composite Structures, 63, pp. 305- 12, (2004).

International Journal of Modern Engineering Research (IJMER)

Contents :

Greedy – based Heuristic for OSC problems in Wireless Sensor Networks

[1]S. Somasundaram, [2]Dr. T. Ravichandran

1Research Scholar, Karpagam University, Coimbatore, Tamil Nadu-641 021 India
2Hindusthan Institute of Technology, Coimbatore, Tamil Nadu-641 032 India

Abstract*: This paper contains optimize set coverage problem in wireless sensor networks with adaptable sensing range. Communication and sensing consume energy, so efficient power management can extended the network lifetime. In this paper we consider a enormous number of sensors with adaptable sensing range that are randomly positioned to monitor a number of targets. Every single target may be redundantly covered by various sensors. For preserving energy resources we organize sensors in sets stimulated successively. In this paper we introduce the Optimize Set Coverage (OSC) problem that has in unbiased finding with an extreme number of set covers in which every sensor node to be activated is connected to the base station. A sensor can be participated in various sensor sets, but the overall energy consumed in all groups is forced by the primary energy reserves. We show that the OSC problem is NP-complete and we propose the solutions: an integer programming for OSC problem, a linear programming for OSC problem with greedy approach, and a distributed and localized heuristic. Simulation results are presented and validated to our approaches.*

I. Introduction

A Wireless Sensor Networks (WSNs) are composed of low cost sensor nodes, which can be used for a wide range of applications. WSNs are consisting of a large number of low cost devices to gather information from various kinds of remote sensing applications. WSNs enabling technology for various applications it involve long-term and low-cost monitoring, such as battlefield reconnaissance, building inspection, security surveillance, etc. A goal in most WSN applications is to reconstruct the underlying physical phenomenon, e.g., temperature, based on sensor measurements. The networks may be composed by hundreds or thousands independent devices, therefore is called sensor node.

The sensor nodes in a WSN have typically short battery life. Most WSN applications are however expected to run autonomously for months or years. An important issue in sensor networks is power scarcity it's driven in part by battery size and weight limitations. Between the functional components of a sensor node the radio consumes a major portion of the energy. The several techniques are been proposed to minimize its energy consumption. Here we ponder the network lifetime optimization issues in the WSN, the energy saving techniques can normally be classified in two types, scheduling the sensor nodes to alternate between active and sleep mode, and adjusting the transmission or sensing range of the wireless nodes.

In this paper we give a lecture for aim to coverage problem. The goal is to maximize the network lifetime to an energy consuming of WSNs for monitoring the coverage area. We have to consider a large number of sensor nodes are randomly circulated and send information by central processing node. Then the all sensing data from each node are not necessary to users, and data redundancy can be expected in a densely distributed sensor network. The way used to extend the network's lifetime is to organize the sensors into a number of sets, such that all the targets are monitored continuously. Also the energy constraints for each sensor and BS connectivity of each sensor set must be satisfied. Besides reducing the energy consumed, this method lowers the density of active nodes is less, then reducing contention of MAC layer. The contributions of this paper are:

1. Introduce the Optimize Set Coverage (OSC) problem and prove its NP- completeness.
2. The model of OSC problem using Integer Programming.
3. The model of OSC problem using linear Programming.
4. Greedy-based heuristic for OSC.
5. Design a distributed and localized heuristic for the OSC.
6. Analyze the performance of these algorithms through simulations.

7.

II.   Related Work

In this paper we address the sensor coverage problem. As pointed out in, the coverage concept is a measure of the quality of service of the sensing function and is subject to a wide range of interpretations due to a large variety of sensors and applications. The goal is to have each location in the physical space of interest within the sensing range of at least one sensor.

III.   Optimization Of Network Lifetime

We consider a number of sensor nodes that circulate continuously and target with known locators. We also consider a central data collector node; it will be referring to the base station (BS). The sensing data are been process by the sensors in the BS.

We assuming the number of sensors deployed are larger than to needed to process the task. The sensing nodes are been alternate between the active states and sleep states. The sensing node contains the sleep mode at the time sensing tasks.

a) Aim to coverage the lifetime problem

We consider the sensors for the energy consume WSN will randomly circulate and the location, the sensing nodes are observed continuously for network lifetime optimized.

1.   The sensing node is accomplished as follows:
2.   The BS collects the location information of the sensing nodes.
3.   The BS executes the sensor scheduling algorithm and broadcast it when the node is in active.
4.   The sensing node take breaks by own for active are to sleep.

In this paper we consider the designing the scheduling mechanisms of node and do not address the problem by selecting which protocol is used for data gathering or node synchronization.

b) Energy consuming in transmitting data

The energy is delivering from a node to another node as one bit message within transmission range in one hop communication is combined with the transmission energy to transmit a bit at the sending node and the energy needed to receive a bit at the receiving node.

A small sensor nodes are contains the limitations for battery storage is containing only the small transmission ranges and may not be able to communicate directly with the sink nodes; hence the concept of multi-hop communication is needed.

In the multi-hop communication model, it is assumed that considerable energy savings can be achieved by the use of multiple short range transmissions as opposed to one large hop transmission. The distance from the source to the destination is communicates, and the transmission range for the multi-hop communication, the required consumption energy.

IV.   Optimize Set Coverage Problem

In this section we optimize the covered problem and prove it completely

a)   Definition of optimize set coverage

Here we assume the given area to be covered by WSN, each of which will collect data periodically. Then, lifetime optimization of the wireless sensor network is assigning the different transmission power of nodes to balance their battery usage to avoid energy wastage at the time network coverage. The main goal of this paper is to decide the communication between the each node.

We assume that the sensor s1, s2….sn and the randomly circulate and covers the aimed location range r1, r2…rn. The base station has the coordinates of the sensor nodes and the aimed location. It is able to compute the each sensor node which is covers the locations.

The method is to assume that the sensors are covers the aimed locations, if the distance between the sensor and the location is small or same with the predefined sensing range.

(a)   (b)
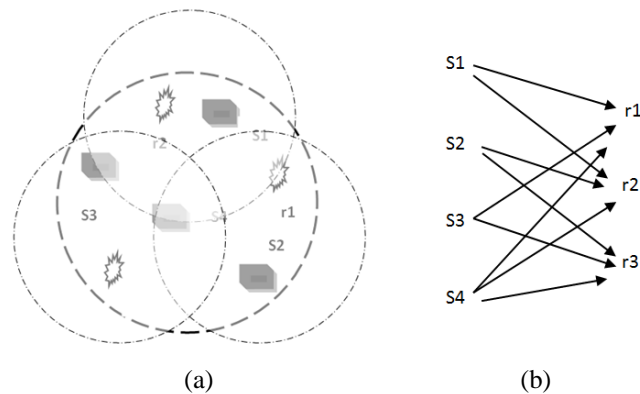
Figure: Example with four sensor nodes (s1, s2, s3, s4) and three location range (r1, r2, r3)

Above figure shows an example with four sensor nodes s1, s2, s3, s4 and three location range r1, r2, r3. In this example we assume that the each sensor can be active for a unit time of 1. That is, if all sensors are stored continuously, then the network lifetime is 1.

In this brief, we are improving the scheduling scheme by allowing every sensor to be part of more than one set, at by allowing the sets to be operational for different time intervals.

b) Optimize set coverage problem solution

In this section we first define the decision of optimize problem and then prove the problem.
A decision problem contains the collection of subsets of a finite sets and a number does it exist a family of set covers s1,……sn and the range r1,……rn and for each subset of collection and a is appear in s1,…..sn and the weight at most l, where l is the lifetime of each sensor.

c) Lifetime of network

The work of the WSN is collecting the data in the sensing applications. The wireless sensor network lifetime is generally determined by the last active node.

d) Sensing node

In the WSN the sensor nodes must maintain the coverage area and network connection. They determine the quality of service in the sensor network. The problem in data collecting from sensor network is how they monitored the coverage area and notice the each and every action from the wireless sensor network. It senses the coverage area to a wide-ranging of analyses in line for a large variety of sensors and applications. The goal is every location in the physical space of interest surrounded by the sensing range of at least on sensor.

The interrupts occurs at connectivity are robustness and reachable throughput of the communication link in a wireless sensor network. The wireless sensor network must also provide connectivity satisfaction; therefore every node is used for data collecting.

e) Energy model

Assume sensor nodes can adjust their transmission power to control the transmission range. The energy consumed by sensor to reliably transmit a b-bit message to sensor j.

$$c(b) = c \cdot b \cdot d_{i,j}^{\alpha}$$

Where is a system constant denoting the energy required by a transmitter amplifier to transmit 1-bit one meter, is the path loss exponent depending on the medium properties, and di,j is the distance between sensor i and sensor j.

V. Solution For Optimize Set Coverage

In this section we present the two heuristics for OSC problem. First we process the problem in integer programming. Second we process the linear programming. Then we process the greed based for OSC and finally we process the distributed and localized for OSC are given for computing the set covers.

The consolidated heuristics are implemented at the BS. When the sensors are placed, they send their synchronization to the BS. The BS calculates and broadcasts back the sensor lists. In the distributed and limited algorithm, each sensor node regulates its schedule created on communication with one-hop neighbors.

a) Integer programming for OSC problem
In this section we formulate the OSC problem using the integer programming

Given:
- Set N sensor nodes s1,s2,….sN
- Set L location range r1,r2,….rL
- The coefficient showing the relationship between the sensor nodes and ranges, therefore each sensor node is covers the aimed location. This is modeled as having each element in s is represented as a subset of the finite set r.
- Set E for initialize energy

Let us define sN = i|sensor si covers range rk

Variables:
- x_{ij}, Boolean variable, for i=1…n and j=1…p; x_{ij}=1 if sensor si is in the set cover sj,otherwise w_{ij}=0.
- tj $\in$ R, 0$\leq$ tj $\leq$ 1, for j=1…p, represents the time allocated for the set cover Sj.

Maximize t1 + … +tp

Subject to
$\sum_{j=1}^{p} x_{ij}t_j \leq 1$ for all $s_i \in C$

$\sum_{i \in C_k} x_{ij} \geq 1$ for all $r_k \in R, j = 1, .., p$

Where
$x_{ij} = 0, 1$ $(x_{ij} = 1$ if and only if $s_i \in S_j)$

Remarks:
The first constraint, $\sum_{j=1}^{p} x_{ij}t_j \leq 1$ for all si $\in$ N guarantees that the time allocated for each sensor s1,across all set covers, is not larger than 1,which is the life time of each sensor.

The second constraint, $\sum_{i \in C_k} x_{ij} \geq 1$ for all rk $\in$ L, j=1…p, and Nk= i|si covers range rk, guarantees that each target rk is covered by at least one sensor si in each set cover sj.

We notice that the term xijtj is not linear. Therefore we set yij = xijtj, and reformulate the problem as:

Maximize t1 + … +tp

Subject to
$\sum_{j=1}^{p} y_{ij} \leq 1$ for all $s_i \in C$

$\sum_{i \in C_k} y_{ij} \geq t_j$ for all $r_k \in R, j = 1, .., p$

Where
$y_{ij} = 0$ or t_j and $y_{ij} \leq 1$

b) Linear programming for OSC problem
In this section we formulate the problem using linear programming, before that we have apply the relax technique.

Maximize t1 + … +tp

Subject to
$\sum_{j=1}^{p} y_{ij} \leq 1$ for all $s_i \in C$

$\sum_{i \in C_k} y_{ij} \geq t_j$ for all $r_k \in R, j = 1, .., p$

Where
$0 \leq y_{ij} \leq t_j \leq 1$

Linear programming based heuristic:

1. Solve the LP and get the optimal solution *xikp* and *ck*
2. Set x'ikp = 0 and c'k = 0 for all i=1…N,k=1…K,p=1…P
3. Sort ck in non-increasing order c1,c2,…ck
4. for all variable *ck* taken from the list in non-increasing order do
5. if ck > 0 then
6. sort xikp, *i = 1..N, p = 1..P* in non-increasing order
7. for all *xikp* do
8. if *xikp* covers new targets and sensor *i* has at least
9. *ep* energy at the beginning of setting up the cover
10. *ck* then
11. *set up the range of sensor i to rp, xikp = 1*
12. else
13. *xikp = 0*
14. else if
15. else for
16. if all targets are covered by *xikp* having value 1 then
17. /∗ we formed a valid set cover ∗/
18. set c_k = 1
19. update residual energy of any sensor *i* with range
20. *rp* in *ck*: *Ei = Ei – ep*
21. *set ck = 0 and reset xikp = 0 for any i = 1..N and p = 1..P*
22. end if
23. end if
24. end for

The heuristic begins in line 1 by solving the relaxed LP that outputs the optimal solution *xikp* and *ck*. We round this solution in order to get a feasible solution *xikp* and *ck* for the IP. We use a greedy approach, by giving priority to the set covers with a larger *ck*. When adding sensors to a cover *ck*, priority is given to the sensors with larger *xikp*. We sort values *ck* in the non-increasing order.

We add sensors to the current set cover *k*, by adding first the sensors with higher *xikp* values. If, later, the same sensor with a larger range is encountered, the new range setting is used if new targets are covered and if the sensor has sufficient energy resources for this setting. If all the targets are covered by the selected sensors in this set cover, then we set *ck* = 1. Otherwise, forming the current set cover was unsuccessful, *ck* = 0, and all of set *k*'s members are removed (*xikp* = 0 for any   *i* = 1..*N* and *p* = 1..*P*).

The complication of this procedure is controlled by the linear programming solver, where *n* is the number of variables. In our case *n* = *K* (1 + *NP*), where *P* usually a small number.

c) Greedy-based heuristic for OSC

The Greedy-based heuristic for OSC is executed by the base station. When the sensors are arranged, they send their coordinates to the BS, it computes the connected set-covers and broadcasts back to the scheduling sensors.

Greed based OSC:

1.Set residual energy of each sensor u to E′u ← E
2: SENSORS ← {(s1,E′1), . . . , (sN,E′N)}
3: h ← 0
4: while the sensors in SENSORS are connected and cover all the targets do
5: /* a new set Ch will be formed */
6: h ← h + 1; Sh ← _; Rh ← _
7: TARGETS ← {r1, r2, . . . , rM}
8: while TARGETS 6= 0 do
9: /* more targets have to be covered */
10: find a critical target rcritical ∈ TARGETS
11: select a sensor su ∈ SENSORS with greatest contribution that covers r critical and has Eu ≥ E1 + E2
12: Sh ← Sh ∪ {su}
13: for all targets rj ∈ TARGETS do
14: if rj is covered by su then
15: TARGETS ← TARGETS − rj

16: end if
17: end for
18: end while
19: apply Breadth-First Search (BFS) algorithm starting from the BS
20: the BFS tree such that to sustain paths from the BS to each sensor in Sh
21: for all sensors su in the resulted BFS subtree with su /∈ Sh do
22: Rh ← Rh ∪ {su}
23: end for
24: for all sensors su ∈ Sh ∪ Rh do
25: if su ∈ Sh then
26: E′u ← E′u − (E1 + E2)
27: end if
28: if su ∈ Rh then
29: E′u ← E′u − E2
30: end if
31: if E′u < E2 then
32: SENSORS ← SENSORS − su
33: end if
34: end for
35: end while
36: return h-number of connected set covers and the connected set-covers (S1,R1), (S2,R2), . . . , (Sh,Rh).

The set covers build by the heuristic recursive, in lines 4 to 34. The enduring energy of every single sensor is set initially to E. Everyone connected set cover relates to a round that will be active for and thus an active sensing sensor consumes E1 + E2 energy, although a relay sensor consumes E2 energy per round. The set SENSORS maintain the set of sensors that must be at least E2 energy left, and can therefore contribute in additional set covers.

As like with OSC, we note with Sh (Rh) the set containing the sensing sensors in the current set-cover h. We first build the sensing sensor set Sh, in lines 8 to 18 and then the relay sensor set Rh in lines 19 to 23. The set TARGETS contain the targets that still have to be covered by the current set h. At all step, a critical target is selected, in line 10, to be covered.

This is an example for the target most densely covered, both in terms of number of sensors as well as with regard to the enduring energy of those sensors. The sensors considered for sensing have to be in the set SENSORS and to have at least E1+E2 residual energy. Once the critical target has been selected, the heuristic selects the sensor with the maximum contribution that covers the critical target. Various sensor contribution functions can be defined. For example we can consider a sensor to have greater contribution if it covers a larger number of uncovered targets and if it has more residual energy available. Once a sensor has been selected, it is added to the current set cover in line 12, and all additionally covered targets are removed from the TARGETS set. After all the targets have been covered, we need to guarantee BS connectivity.

d) Distributed and localized heuristic for OSC

In this section we process the distributed and localized for OSC, we discuss to a resolution process at each node that makes use of only data for a neighborhood within a constant number of hops. A distributed and localized algorithm is desirable in wireless sensor networks since it adapts better to dynamic and large topologies. The distributed greedy algorithm goes in rounds. Every round initiates with an initialization phase, in which sensors checks whether they will be in an active or sleep mode throughout the current round. The initialization phases proceeds W time, where W is far less than the duration of a round.

Every sensor sustains a waiting time, after that it decides its status (sleep or active) and its sensing range, and then it broadcasts the list of targets it covers to its one-hop neighbors. The waiting time of each sensor si depends on si's contribution, and is set up initially to $Wi = (1 − BiP/Bmax) × W$ where $Bmax$ is the largest possible contribution, defined as $Bmax = M/e1$, where M is the number of targets. The waiting time can change during the initialization phase, when broadcast messages are received from neighbors.

If a sensor si gets a broadcast message from one of its neighbors, at that time si updates the set of uncovered targets TiP and sets up its sensing range to the smallest value ru needed to cover this set of targets. The sensor contribution value is also updated to Biu. If all si's targets are already covered by its neighbors, then si sets up its sensing range to $r0 = 0$. The waiting time Wi of the sensor si is as well updated to $(1 − Biu/Bmax) × W$. At the end of its waiting time, a sensor broadcasts its status (active or sleep) as well as the list of targets it covers.

If a sensing range is $r0$ then this sensor node will be in the sleep mode, otherwise it will be active during this round. As unlike sensors have dissimilar waiting times, this serializes the sensors broadcasts in their local neighborhood and contributes priority to the sensors with advanced contribution. These sensors decide their status and broadcast their target coverage information first. In this algorithm we use a distinct time window, where the length of the time slot is d. Therefore, the time window W has $W\, d$ time units. The waiting timing of the two sensor si and sj are too close, i.e. $/Wi - Wj\,/ < d$, then the sensors neighbors to both si and sj cannot tell from whom the message was received, thus they will not update their uncovered target set. We assume sensor nodes are synchronized and the protocol starts by having the base station (BS) broadcast a start message. If, after the initialization phase, a sensor si cannot cover one of the targets in the set TiP and its waiting time reached the value zero, then si sends this failure information to BS. In our algorithm, we measure the network lifetime as the time until BS detects the first failure. Next we present the Distributed Initialization, that is run by each sensor si, $i = 1...N$ during the initialization phase

Distributed Initialization:
  1: compute the waiting time Wi and start timer t
  2: while $t \leq Wi$ and $TiP \_= \emptyset$ do
  3: if message from neighbor sensor is received then
  4: update TiP and set-up the sensing range to the smallest value ru needed to cover TiP
  5: if $TiP == 0$ then
  6: set si's sensing range to $r0$
  7: break
  8: end if
  9: update si's contribution to Biu
  10: update the waiting time Wi to $(1 – Biu/Bmax) \times W$
  11: end if
  12: end while
  13: /* assume si's sensing range was set up to ru */
  14: if $ru == r0$ then
  15: si broadcasts its sleep state decision
  16: return
  17: end if
  18: if $Ei < eu$ then
  19: si reports failure to BS, indicating the targets it cannot cover due to the energy constraints
  20: end if
  21: si broadcasts information about the set of targets Tiu it will monitor during this round
  22: return

The complexity of the Distributed Initialization procedure is $O\ (Wd/\ NMP)$. This corresponds to the case when si receives messages from N neighbors, each d time. The updates for each message take $O(MP)$.

VI. Simulation Results
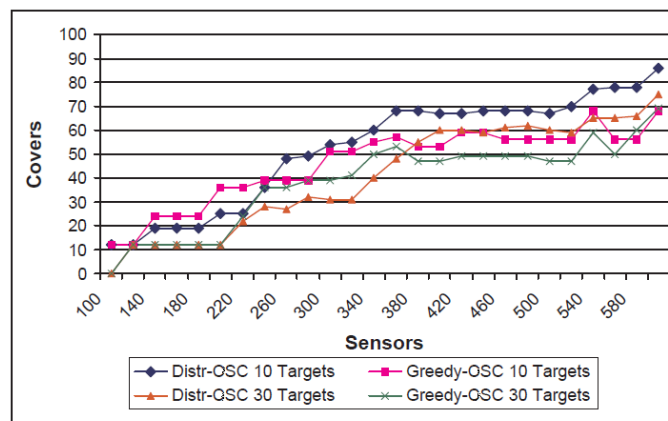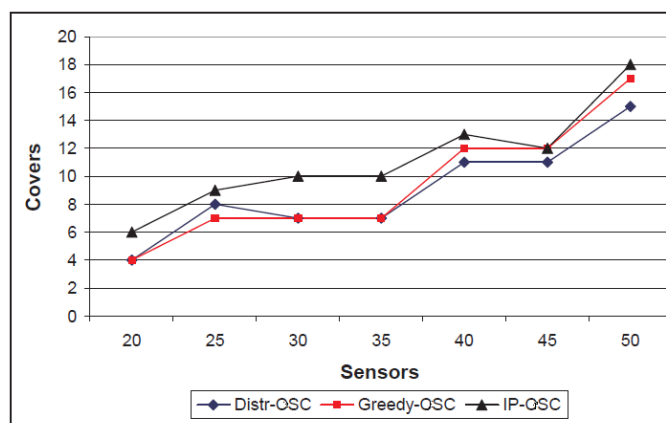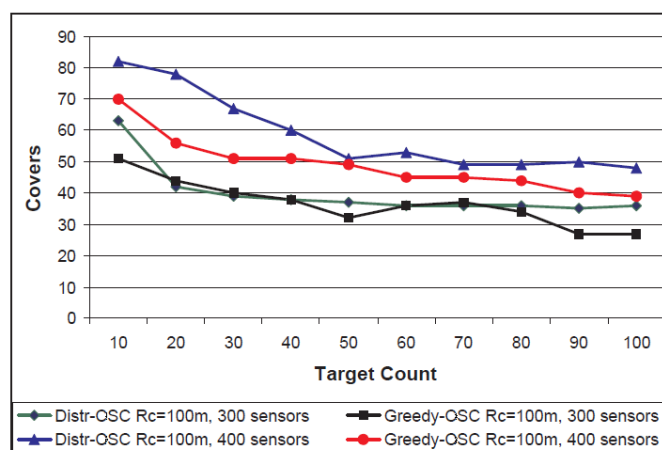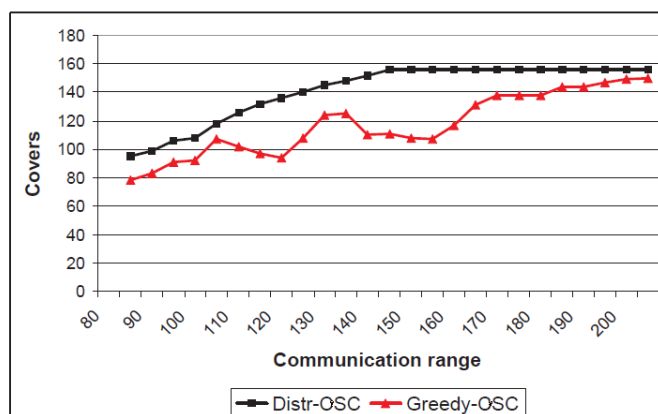
REFERENCES

[1]   Martin Gruber and G¨unther R. Raidl ”Cluster- Based (Meta-)Heuristics for the Euclidean Bounded Diameter Minimum Spanning Tree Problem”, Institute of Computer Graphics and Algorithms Vienna University of Technology, Vienna, Austria, 2012.

[2]   C. Joncour(1,3), S. Michel (2), R. Sadykov (3,1), D. Sverdlov (3), F. Vanderbeck (1,3) “Column Generation based Primal Heuristics”, (1) Institut de Mathmatiques, Universit Bordeaux 1, France (2) Institut suprieur d’tudes logistiques, Universit du Havre, France (3) Team RealOpt, INRIA Bordeaux-Sud-Ouest, France.

[3]   N. Lesh, M. Mitzenmacher “BubbleSearch: A Simple Heuristic for Improving Priority-based Greedy Algorithms”, TR2005-114 December 2005.

[4]   Orestis A. Telelis “Set Covering and Network Optimization: Dynamic and Approximation Algorithms”, Department of Informatics and Telecommunications National and Kapodistrian University of Athens, Hellas.

[5]   Belma Yelbay, S¸. ˙Ilker Birbil and Kerem B¨ulb¨ul ” The Set Covering Problem Revisited: An Empirical Study of the Value of Dual Information”, Sabancı University, Manufacturing Systems and Industrial Engineering, Orhanlı-Tuzla, 34956 Istanbul, Turkey.

[6]   Rong-chii Duh, Martin F¨urer "Approximation of k-Set Cover by Semi-Local Optimization", Dept. of Computer Science and Engineering Pennsylvania State University University Park, PA16802.

[7]   Shunji Umetani, Mutsunori Yagiura "RELAXATION HEURISTICS FOR THE SET COVERING PROBLEM", University of Electro-Communications, Nagoya University.

[8]   Robert P.D. Vanderkama, Yolanda F. Wiersmab , Douglas J. Kingc " Heuristic algorithms vs. linear programs for designing efficient conservation reserve networks: Evaluation of solution optimality and processing time", a Canadian Wildlife Service, Environment Canada, 351 St. Joseph Blvd., Gatineau, QC, Canada K1A 0H3.

[9]   S K SEN and A RAMFUL "A direct heuristic algorithm for linear programming", Supercomputer Education and Research Centre, Indian Institute of Science, Bangalore.

[10]   Krishnan Srinivasan, Karam S. Chatha "Integer linear programming and heuristic techniques for system-level low power scheduling on multiprocessor architectures under throughput constraints", Department of CSE, PO BOX 875406, Arizona State University, Tempe, AZ 85287-5406, USA.

OPEN ACCESS

Internal Model Based Vector Control of Induction Motor

P. Ram Kishore Kumar Reddy

Associate Professor, Department of EEE, MGIT, Hyderabad, India

ABSTRACT: *This paper deals with the design of PID and Internal Model Controllers (IMC) in adjusting the speed of induction machine under disturbances and set point changes. The performance of PID controller is compared with IMC. The internal model control is an alternative to the classic feedback structure. Internal model control is composed of an inverse model connected in series with the plant and a forward model connected in parallel with the plant, this structure allows the error feedback to reflect the effect of disturbances and plant mismodelling resulting in a robust control loop. The IMC provides good performance and robustness against the disturbances in system when compared with the PID controller. A simulation study of these methods is presented using MATLAB/SIMULINK.*

Keywords: Indirect Vector control, Internal Model control, PID controller, Ziegler-Nichols rules, Induction motor.

I. Introduction

The induction motor is widely used in industry because of its reliability and low cost. However, since the dynamical model of induction motor is strongly nonlinear, the control of induction motor is a challenging problem and has attracted much attention. Many control methods like Field-oriented control (FOC), Direct torque control (DTC) [1]-[3]   have been proposed.

FOC or vector control of an induction machine achieves decoupled torque and flux dynamics leading to independent control of the torque and flux as for a separately excited DC motor. FOC methods are attractive but suffer from one major disadvantage: they are sensitive to motor parameter variations and sufferers from an incorrect flux measurement.   The advent of vector control techniques has partially solved induction motor control problems. Consequently performance deteriorates and a controller is required to meet the desired specifications.

In this paper the design controllers such as PID [4], [5] and Internal Model Control (IMC) [6] are used along with indirect vector control to maintain satisfactory performance under set point changes and load disturbances.

The remainder of the paper is organized as follows: Section 2 introduces the model of induction motor. Section 3, 4 describes the design control schemes such as PID and IMC controllers. Section 5 presents simulation results. Section 6 concludes the paper

II. Model Of Induction Motor

The d-q axis dynamic equations for the squirrel cage induction motor with the reference frame fixed to the stator are given by following equations [7].

Voltage Equations

$$v_{qs}^s = r_s i_{qs}^s + \frac{1}{\omega_b}\frac{d}{dt}\psi_{qs}^s \qquad v_{qr}^{'s} = r'_r i_{qr}^{'s} + \frac{1}{\omega_b}\frac{d}{dt}\psi_{qr}^{'s} - \frac{\omega_r}{\omega_b}\psi_{dr}^{'s}$$

$$v_{ds}^s = r_s i_{ds}^s + \frac{1}{\omega_b}\frac{d}{dt}\psi_{ds}^s \quad v_{dr}^{'s} = r'_r i_{dr}^{'s} + \frac{1}{\omega_b}\frac{d}{dt}\psi_{qr}^{'s} - \frac{\omega_r}{\omega_b}\psi_{dr}^{'s} \qquad (1)$$

$$v_{0s}^s = r_s i_{0s}^s + \frac{1}{\omega_b}\frac{d}{dt}\psi_{0s}^s \quad v_{0r}^{'r} = r'_r i_{0r}^{''r} + \frac{1}{\omega_b}\frac{d}{dt}\psi_{0r}^{'r}$$

Flux linkage Equations

$$\begin{bmatrix} \psi_{qs} \\ \psi_{ds} \\ \psi_{0s} \\ \psi_{qr}^{'} \\ \psi_{dr}^{'} \\ \psi_{0r}^{'} \end{bmatrix} = \begin{bmatrix} x_{ls}+x_m & 0 & 0 & x_m & 0 & 0 \\ 0 & x_{ls}+x_m & 0 & 0 & x_m & 0 \\ 0 & 0 & x_{ls} & 0 & 0 & 0 \\ x_m & 0 & 0 & x_{lr}^{'}+x_m & 0 & 0 \\ 0 & x_m & 0 & 0 & x_{lr}^{'}+x_m & 0 \\ 0 & 0 & 0 & 0 & 0 & x_{lr}^{'} \end{bmatrix} \begin{bmatrix} i_{qs}^s \\ i_{ds}^s \\ i_{0s}^s \\ i_{qr}^{'} \\ i_{dr}^{'} \\ i_{0r}^{'} \end{bmatrix} \qquad (2)$$

Torque Equation

$$T_e = \frac{P_m}{\omega_m} = \frac{3}{2}\left(\frac{p}{2\omega_b}\right)(\psi_{ds}^s i_{qs}^s - \psi_{qs}^s i_{ds}^s) \qquad (3)$$

$[i_{qs}^s \quad i_{ds}^s]$ d- and q-axis stator currents

$[i_{qr}^s \quad i_{dr}^s]$ d- and q-axis rotor currents

$[v_{qs}^s \quad v_{ds}^s]$ d- and q-axis stator voltages

$[v_{qr}^s \quad v_{dr}^s]$ d- and q-axis rotor voltages

The field orientation principle is based on the following conditions which are expressed in the synchronous reference frame .The resultant rotor flux linkage, λ_r, is assumed to be on the direct axis to reduce the number of variables in the equations by one. Hence, rotor flux phasor is aligned along with d-axis yields

$$\lambda_r = \lambda_{dr}^e \qquad \lambda_{qr}^e = 0 \qquad (4)$$

Under these conditions, the induction machine is transformed into a linear current/torque converter:

$$T_e = K_{te}\lambda_r i_T \qquad (5)$$

where $\quad K_{te} = \frac{3}{2}\frac{P}{2}\frac{L_m}{L_r}$

The equations ensuring the indirect field orientation are expressed as

$$i_f = i_{ds} = \frac{1}{L_m}[1+T_r\frac{d}{dt}]\psi_{dr} \qquad (6)$$

$$\omega = \omega_r + \omega_{s1} = \omega_r + \frac{i_T}{i_f}\left(\frac{R_r}{L_r}\right) \qquad (7)$$

$$\theta_s = \int(\omega_r + \omega_{sl})dt \qquad (8)$$

$$\theta_f = \theta_s = \theta_r + \theta_{sl} \qquad (9)$$

where $i_f = i_{ds}^e$

$$i_T = i_{qs}^e$$

The field-oriented control block receives the computed torque/current from the speed controller and the flux from the field weakening block. In the look-up table used for field-weakening, the flux is assumed to be constant when the motor operates below the rated speed, and beyond the rated speed the flux speed product is held constant. The overall block diagram of a current controlled induction motor with indirect field orientation is given in Figure.1.
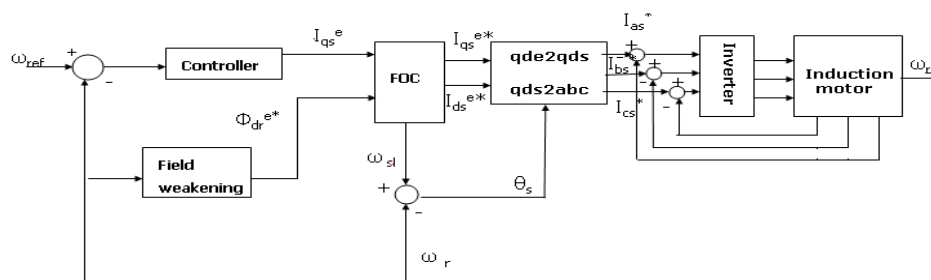
Figure.1 Speed control of current regulated indirect field oriented induction motor

The FOC block performs the slip calculation and generates i_{ds}^{e*} and i_{qs}^{e*}. Inside the qde to the abc transformation block, the following transformations are performed:

qde to qds
$$i_{qs}^{s*} = i_{qs}^{e*} \cos\theta_s + i_{ds}^{e*} \sin\theta_s$$
$$i_{ds}^{s*} = -i_{qs}^{e*} \sin\theta_s + i_{ds}^{e*} \cos\theta_s$$
(10)

qds to abc
$$i_{as}^* = i_{qs}^{s*}$$
$$i_{bs}^* = -\frac{1}{2} i_{qs}^{s*} - \frac{\sqrt{3}}{2} i_{ds}^{s*}$$
$$i_{cs}^* = -\frac{1}{2} i_{qs}^{s*} + \frac{\sqrt{3}}{2} i_{ds}^{s*}$$
(11)

Here θ_s represents the sum of slip and rotor angles.

A sinusoidal current source of variable magnitude and frequency is used to represent the fundamental component of the actual inverter waveform. This avoids lengthy simulation times caused by the inverter switching.

III.   PID Control

In feedback control system, the control device is made of the controller only as shown in Figure. 1
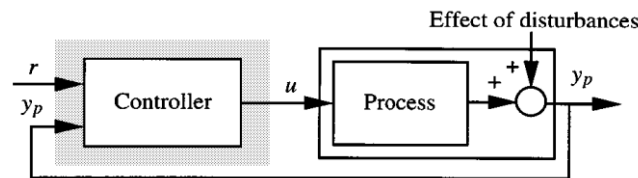
Figure.2 Feedback control system

The family of PID controllers is constructed from various combinations of the proportional, integral and derivative terms as required to meet specific performance requirements.

The formula for the basic parallel PID controller is

$$G_C(s) = \left[K_P + K_I \frac{1}{s} + K_D s \right] E(s)$$
(12)

Time constant form of eq.(12) is of the form

$$G_C(s) = K_P \left[1 + \frac{1}{s\tau_i} + \tau_d s \right] E(s)$$
(13)

where $\tau_i = \dfrac{K_I}{K_P}$ and $\tau_d = \dfrac{K_D}{K_P}$

Ziegler-Nichols Rules for Tuning of PID Controller

Ziegler-Nichols proposed rules for determining values of the proportional gain K_p, integral time T_i, and derivative time T_d based on the transient response characteristics of a given plant. The dynamics of a process can be determined from the response of a process to the step input [4]. From the transient response method a simple model of process is obtained. The model obtained is used for PID controller tuning.

The response of a plot for a unit step input is like an S-shaped curve as shown in Figure.3
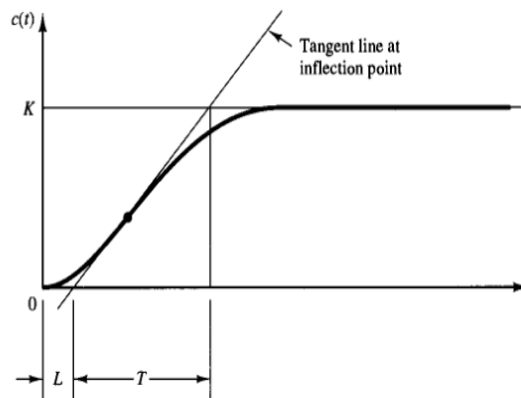
Figure.3 Step response of the process

The S-shaped curve is characterized by two constants delay time L and time constant T. L and T are determined by drawing a tangent line at the inflection point of S-shaped curve and determining the intersections of tangent line with time axis as shown in Fig 3.4. Ziegler-Nichols suggested setting the values of K_p, T_i and T_d according to the formula shown in table.1

Table.1.Tuning Parameters of PID Controller

	K_p	T_i	T_d
P	T/L	∞	0
PI	0.9T/L	L/0.3	0
PID	1.2T/L	2L	0.5L

Design of PID controller for Induction motor
In order to illustrate the performance of PID controller under disturbances let us consider the induction motor. The design of PID controller through Z-N method is based on the step response of the original system required [6]. Hence, let us consider the induction motor which is considered in section 2.11 for the design of PID controller.

The step response of the Induction motor is as shown in Figure.3.4. From the response the parameters delay time (L) and time constant (T) are determined by drawing a tangent line at the inflection point of S-shaped curve and determining the intersections of tangent line with time axis.
From Figure.4 the parameters L and T are as follows.
L=0.016
T=0.124
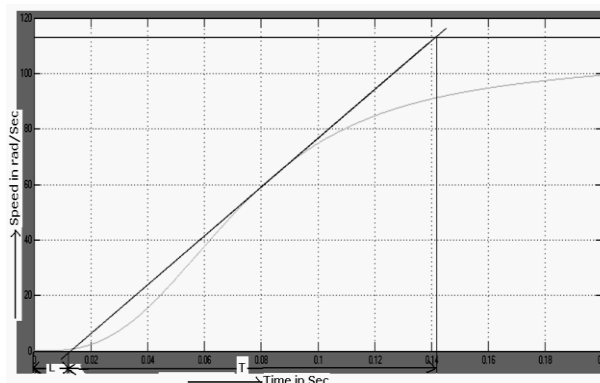
Figure.4 Step response of Induction Motor

From the Table.1 and Eq.3.6, the tuning parameters of PID controller for the Induction motor based on the Ziegler-Nicholes step response method is given as follows.
K_p= 9.3
K_i = 0.283
K_d =0.072

IV. Internal Model Control

The internal model control is an alternative to the classic feedback structure. Internal model control is composed of an inverse model connected in series with the plant and a forward model in parallel with the plant, this structure allows the error feedback to reflect the effect of disturbance and plant mismodelling resulting in a robust control loop [5].
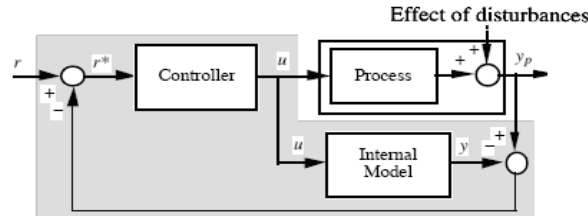
Figure.5 Internal model control system

It includes two blocks labeled controller and internal model. The control system has inputs as the set points and process output y_p and output as manipulated process input 'u' as shown in Figure.4.1. The internal model is connected in parallel to the process. It is also called process model. The effect of parallel path with the model is to subtract the effect of manipulated variables from the process output. If model is perfect representation of the process, then the feed back signal equal to the influence of disturbances and is not affected by the action of the manipulated variables. Thus the system is efficient open loop and the usual stability problems associated with feedback have disappeared the over all system is simply stable if and only if both the process and the IMC controller are stable.

The IMC design is followed by two step design procedure [5]. In step 1 controller is designed for optimal set point tracking i.e. disturbance rejection without regards for model uncertainty. In step 2 the controller is detuned for robust performance.

Procedure for design of IMC controller

Let us consider the following notations in internal model control: Input v ,Process model $\tilde{p}$, Inverse model $\tilde{q}$.

The IMC design procedure consists of the two steps

Step 1: Nominal Performance

Model inverse 'q' is selected to yield good system response for the inputs without regard for constraint and model uncertainty. The selection of 'q' is such that it is H_2 Optimal for a particular input v .Thus $\tilde{q}$ has to solve

$$\min_{\tilde{q}} \| e \|_2 = \min_{\tilde{q}} \| (1 - \tilde{p}\tilde{q})v \|_2 \qquad (14)$$

Subjected to constraint that $\tilde{q}$ is stable and causal. The Eq. (14) reaches to the absolute minimum for

$$\tilde{q} = \frac{1}{\tilde{p}} \qquad (15).$$

The model inverse is an acceptable solution for Minimum Phase systems.

Step 2: Robust stability and performance

$\tilde{q}$ is augmented with a low pass filter f to achieve robust stability and performance. That is

$$q = \tilde{q}f \qquad (16)$$

Internal model control algorithm

The internal model is summarized by following algorithm.

i. *Model design*: the process model is connected in parallel with the plant. Obtain the internal model or forward model of the plant based on the reduced model of the plant. The process model is considered as the Minimum Phase system i.e. there are no zeroes in the right half of the plane.

ii. *Inverse model design*: The inverse model must be connected in series with the plant. The model inverse is an acceptable solution for Minimum Phase systems. The inverse model is selected to yield good system response for the given input and the controller must be H_2 optimal.

iii. *IMC Filter design*: In general the inverse model exhibit undesirable behavior in response. For robustness inverse model has to be augmented by a low pass filter.

IMC design for Induction Motor
(a)Process model
Process model of the indirect vector controller induction motor drive **is** given by

$$\tilde{p} = \frac{\omega_r(s)}{I_T(s)} = \frac{K_m}{1+sT_m} \tag{17}$$

Where $K_m = \frac{P}{2}\frac{K_t}{B_t}$; $B_t = B + B_l$; $T_m = \frac{J}{B_t}$;

ω_r is the rotor speed

$I_T = I_{qs}$ is torque producing component of current

The process considered is a minimum phase system

(b)Inverse model
For the minimum phase system, the model inverse is given by Eq.15

$$\tilde{q} = \frac{I_T(s)}{\omega_r(s)} = \frac{1+sT_m}{K_m} \tag{18}$$

(c)IMC filter

The simplest form of filter is of the form

$$f(s) = \frac{1}{(\lambda s + 1)^n} \tag{19}$$

Filter parameter n is selected as 1 for Minimum phase system. Adjusting λ is equivalent to adjusting the speed of closed loop response.

In order to get robust stability IMC filter is augmented with inverse model as in Eq. (16). The controller q along with the model inverse and filter of induction motor is as shown.

$$q = (\frac{1+sT_m}{K_m})(\frac{1}{1+\lambda s}) \tag{20}$$

The block diagram of internal model control for induction motor is as shown in Figure.6.
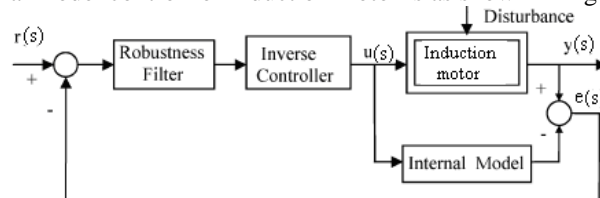
Figure.6 Block diagram of IMC for Induction motor

V. Simulation Results

In order to evaluate the performance of induction motor, the Simulink model for the given induction motor has been developed. Induction Motor with the following parameters has been considered:
3 phase, 20 hp, 220 V, 4-pole

Frequency:	60 Hz
Stator resistance (rs):	0.1062 ohm
Rotor resistance (rr′):	0.0764 ohm
Stator inductance (Ls):	0.01604H
Rotor inductance (Lr′):	0.01604H
Magnetizing inductance (Lm):	0.01547H

In simulation, Load variations are applied 0 to -80 N-m and 0 to 40 N-m at 0.5sec and 0.8 sec, respectively. Consider the set point changes at 0.2 sec and 0.4 sec. Due to the load variations and set point changes the IVC based induction motor undergoes large fluctuations in speed response as shown in Figure.7.it is not going to attain the reference speed.
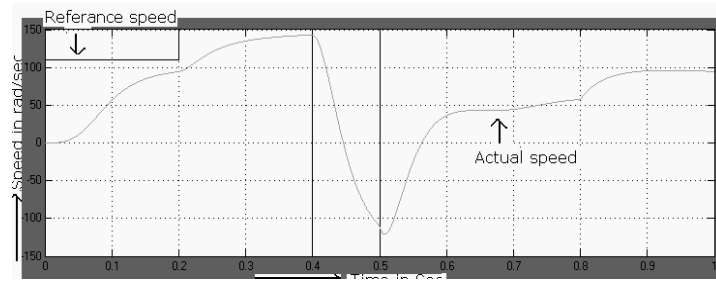
Figure.7 Speed response of IVC based   Induction motor without any controller.

The simulation results of PID control of IVC based induction motor are shown in Figure.8.
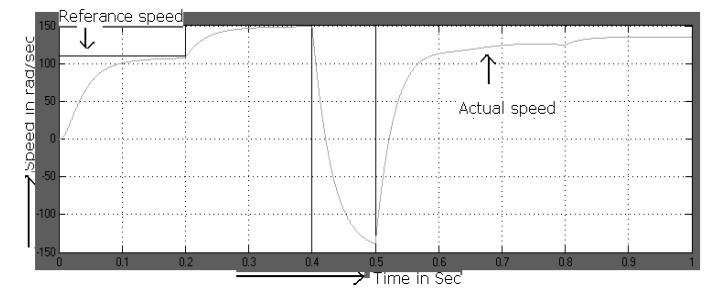
(a)Speed response
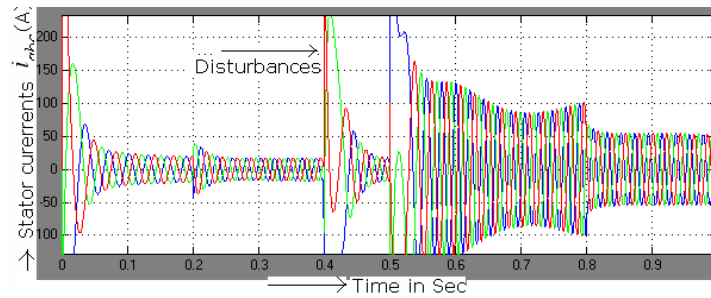
(b) Current response
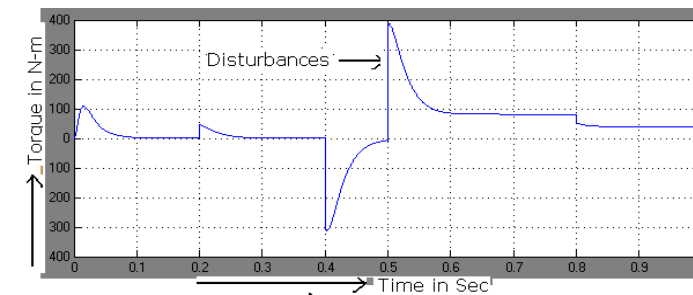
(c) Torque response
Figure.8 PID control of IVC based induction motor

The simulation results of internal model control of IVC based induction motor are shown in Figure.9.

(a)Speed response

(b) Current response
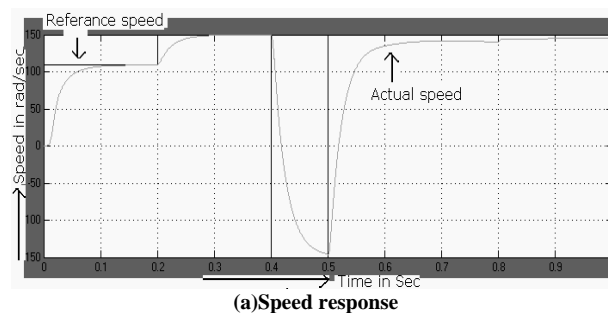
(c) Torque response
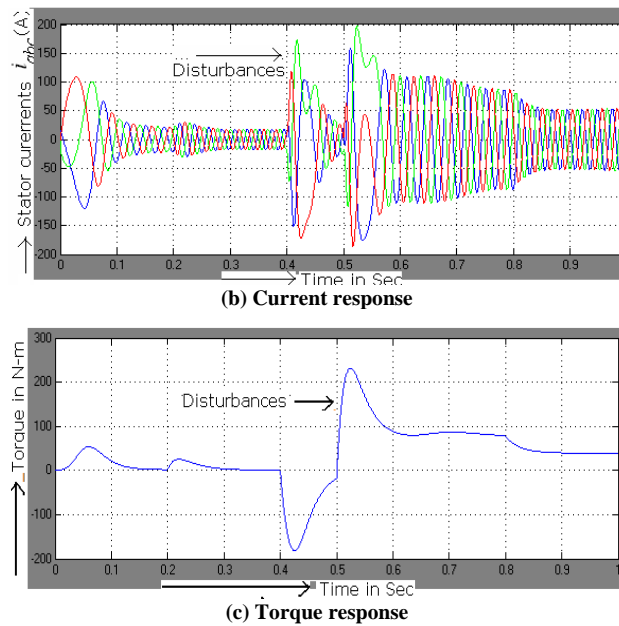
Figure.9 Internal model control of IVC based Induction Motor

In internal model control the disturbances are less when compared with PID controller. This is as shown in Figure.'s 8 and 9.

VI. Conclusions

The speed control of the induction motor through Z-N based PID controller and Internal Model Control (IMC) controller has been implemented. It has been observed that due to the load disturbances and set point changes the vector controlled induction motor undergoes large fluctuations in speed response. In order to overcome those fluctuations, the design of PID controller and internal model controller has been developed and applied to the induction motor. The results demonstrate the ability of controllers to produce the required response compensating the component of load variations in order to maintain a stable response. It has been observed that the speed control obtained with the internal model controller is smoother and better than that obtained through the PID controller. Hence it can be say that the internal model controller is better than the PID controller for the speed control of induction motor.

REFERANCES

[1]   R.Krishnan, Electric Motor Drives, Prentice Hall of India, 2002.
[2]   Bimal K. Bose, Modern Power Electronics and AC Drives, Prentice Hall, 2002.
[3]   Peter Vas, Vector control of AC Drives, Oxford university press, 1990.
[4]   K.J.Astrom and T.Hagglund, PID controllers, 2nd Edition, Instrument society of America, 1995.
[5]   M.Morari, E.Zafiriou, Robust process control, Prentice Hall, 1989.
[6]   K.Ogata, Modern Control Engineering, Prentice Hall, 2002.
[7]   V.Subramanyam, Thyristor control of Electric drives, Mc-Graw Hill, 2006.
[8]   Chee-Mun Ong, Dynamic Simulation of Electric Machinery, Prentice Hall, 1998.
[9]   I. Rivals and L. Personnaz, Nonlinear internal model control using neural networks: Application to processes with delay and design issues, IEEE Trans. Neural Networks, vol. 11, pp. 80–90, Jan. 2000.
[10]   M.A.Denai and S.A.Attia, Fuzzy and Neural control of an Induction motor, International Journal Applied Mathematics computer sciences, 2002, Vol.12, no.2, 221-233.

Some Common Fixed Point Theorems for Multivalued Mappings in Two Metric Spaces

[1]T. Veerapandi, [2]T. Thiripura Sundari, [3]J. Paulraj Joseph

[1] Professor and H.O.D of Science and Humanities, S.Veerasamy Chettiar College of Engineering and Technology, S.V.Nagar, Puliangudi, India
[2]Department of Mathematics, Sri K.G.S Arts College, Srivaikuntam, India
[3] Professor and H.O.D of Mathematics, Manonmaniam Sundaranar University, Tirunelveli, India

Abstract: *In this paper we prove some common fixed point theorems for multivalued mappings in two complete metric spaces.*
AMS Mathematics Subject Classification: 47H10, 54H25
Keywords: *complete metric space, fixed point, multivalued mapping.*

I. Introduction

In 1981, Fisher [1] initiated the study of fixed points on two metric spaces. In1991, Popa [2] proved some theorems on two metric spaces. After this many authors([3]-[7],[8],[9]-[11]) proved many fixed point theorems in two metric spaces. Using the Banach contraction mapping, Nadler [12] introduced the concept of multi-valued contraction mapping and he showed that a multi-valued contraction mapping gives a fixed point in the complete metric space. Later, some fixed points theorems for multifunctions on two complete metric spaces have been proved in [13], [14] and [15].The purpose of this paper is to give some common fixed point theorems for multi-valued mappings in two metric spaces.

Definition1.2 A sequence $\{x_n\}$ in a metric space (X, d) is said to be convergent to a point $x \in X$ if given $\in > 0$ there exists a positive integer n_0 such that $d(x_n, x) < \in$ for all $n \geq n_0$.

Definition1.3. A sequence $\{x_n\}$ in a metric space (X, d) is said to be a Cauchy sequence in X if given $\in > 0$ there exists a positive integer n_0 such that $d(x_m, x_n) < \in$ for all $m, n \geq n_0$.

Definition1.4. A metric space (X, d) is said to be complete if every Cauchy sequence in X converges to a point in X.

Definition1.5 Let X be a non-empty set and $f : X \rightarrow X$ be a map. An element x in X is called a fixed point of X if $f(x) = x$.

Definition1.6. Let X be a non-empty set and f , $g : X \rightarrow X$ be two maps. An element x in X is called a common fixed point of f and g if $f(x) = g(x) = x$.

Definition1.7. Let (X, d_1) and (Y, d_2) be complete metric spaces and B(X) and B(Y) be two families of all non-empty bounded subsets of X and Y respectively. The function $\delta_1(A, B)$ for A, B in B(X) and $\delta_2(C, D)$ for C,D in B (Y) are defined as follow

$\delta_1(A, B) = \sup\{ d_1(a, b): a \in A, b \in B \}$

$\delta_2(C, D) = \sup\{ d_2(c, d): c \in C, d \in D \}$

and $\delta(A) = \text{diameter}(A)$

If A consists of a single point a we write $\delta_1(A,B) = \delta_1(a,B)$. If B also consists of a single point b we write $\delta_1(A,B) = \delta_1(a,B) = \delta_1(a,b)$. It follows immediately that $\delta_1(A,B) = \delta_1(B,A) \geq 0$, and $\delta_1(A,B) \leq \delta_1(A,C) + \delta_1(C,B)$ for all A,B in B(X).

Definition1.8. If $\{A_n : n = 1,2,3\ldots\}$ is a sequence of sets in B(X), we say that it converges to the closed set A in B(X) if

(i)   Each point a in A is the limit of some convergent sequence $\{a_n \in A_n : n = 1,2,3\ldots\}$,

(ii)   For arbitrary $\in > 0$, there exists an integer N such that $A_n \subset A\in$ for $n > N$ where $A\in$ is the union of all open spheres with centres in A and radius $\in$.

The set A is then said to be the limit of the sequence $\{A_n\}$.

Definition1.9. Let f be a multivalued mapping of X into B(X). f is continuous at x in X if whenever $\{x_n\}$ is a sequence of points in X converging to x, the sequence $\{f(x_n)\}$ in B(X) converges to fx in B(X). If f is continuous at each point $x \in X$, then f is continuous mapping of X into B(X).

Definition1.10. Let T be a multifunction of X into B(X). z is a fixed point of T if Tz = {z}.

Lemma 1.11[16]. If {An} and {Bn} are sequences of bounded subsets of a complete metric space (X, d) which converges to the bounded subsets A and B, respectively, then the sequence {δ(An,Bn)} converges to δ(A,B).

II.   Main Results

Theorem 2.1: Let (X, d_1) and (Y, d_2) be two complete metric spaces. Let A, B be mappings of X into B(Y) and S, T be mappings of Y into B(X) satisfying the inequalities.

$$\delta_1(SAx, TBx') \leq \lambda \max\{ \delta_1(x,x'), \delta_1(x,SAx), \delta_1(x',TBx'),$$
$$\tfrac{1}{2}[\delta_1(x,TBx')+\delta_1(SAx, x')], \delta_2(Ax, Bx')\}$$

--------- (1)

$$\delta_2(BSy, ATy') \leq \lambda \max\{ \delta_2(y,y'), \delta_2(y,BSy), \delta_2(y',ATy'),$$
$$\tfrac{1}{2}[\delta_2(y,ATy')+\delta_2(BSy,y')], \delta_2(Sy,Ty')\}$$

---------- (2)

for all x, x' in X and y, y' in Y where $0< \lambda < 1$. If one of the mappings A, B, S and T is continuous, then SA and TB have a unique common fixed point z in X and BS and AT have a unique common fixed point w in Y. Further, Az = Bz = {w} and Sw = Tw = {z}.

Proof: From (1) and (2) we have

$$\delta_1(SAC, TBD) \leq \lambda \max\{ \delta_1(C,D), \delta_1(C,SAC), \delta_1(D,TBD),$$
$$\tfrac{1}{2}[\delta_1(C,TBD)+\delta_1(SAC,D)], \delta_2(AC,BD)\} \quad \text{--------- (3)}$$

$$\delta_2(BSE, ATF) \leq \lambda \max\{ \delta_2(E,F), \delta_2(E,BSE), \delta_2(F,ATF),$$
$$\tfrac{1}{2}[\delta_2(E, ATF)+\delta_2(BSE,F)], \delta_1(SE,TF) \} \quad \text{---------- (4)}$$

$$\forall C,D \in B(X) \text{ and } E,F \in B(Y)$$

Let x_0 be an arbitrary point in X. Then $y_1 \in A(x_0)$ since A: X $\rightarrow$ B(Y), $x_1 \in S(y_1)$ since S : Y $\rightarrow$ B(X) , $y_2 \in B(x_1)$ since B: X $\rightarrow$ B(Y) and $x_2 \in T(y_2)$ since T : Y $\rightarrow$ B(X). Continuing in this way we get for $n \geq 1$, $y_{2n-1} \in A(x_{2n-2})$, $x_{2n-1} \in S(y_{2n-1})$, $y_{2n} \in B(x_{2n-1})$ and $x_{2n} \in T(y_{2n})$. We define the sequences $\{x_n\}$ in B(X) and $\{y_n\}$ in B(Y) by choosing a point $x_{2n-1} \in (SATB)^{n-1}SAx = X_{2n-1}$, $x_{2n} \in (TBSA)^n x = X_{2n}$, $y_{2n-1} \in A(TBSA)^{n-1}x = Y_{2n-1}$ and $y_{2n} \in B(SATB)^{n-1}SAx = Y_{2n}$ $\forall$ n = 1.2,3, ...

Now from (3) we have

$$\delta_1(X_{2n+1}, X_{2n}) = \delta_1(SAX_{2n}, TBX_{2n-1})$$

$$\leq \lambda . \max\{ \delta_1 (X_{2n}, X_{2n-1}), \ \delta_1 (X_{2n}, SAX_{2n}), \ \delta_1 (X_{2n-1}, TBX_{2n-1}),$$
$$\frac{1}{2}[\delta_1 (X_{2n}, TBX_{2n-1}) + \delta_1 (SAX_{2n}, X_{2n-1})], \delta_2 (AX_{2n}, BX_{2n-1}) \}$$
$$= \lambda . \max\{ \delta_1 (X_{2n}, X_{2n-1}), \ \delta_1 (X_{2n}, X_{2n+1}), \ \delta_1 (X_{2n-1}, X_{2n}),$$
$$\frac{1}{2}[\delta_1 (X_{2n}, X_{2n}) + \delta_1 (X_{2n+1}, X_{2n-1})], \ \delta_2 (Y_{2n+1}, Y_{2n}) \}$$
$$= \lambda . \max\{ \delta_1 (X_{2n}, X_{2n-1}), \ \delta_1 (X_{2n}, X_{2n+1}), \ \delta_1 (X_{2n-1}, X_{2n}),$$
$$\frac{1}{2}. \delta_1 (X_{2n+1}, X_{2n-1}), \ \delta_2 (Y_{2n+1}, Y_{2n}) \}$$
$$\leq \lambda . \max\{ \delta_1 (X_{2n}, X_{2n-1}), \ \delta_1 (X_{2n}, X_{2n+1}), \frac{1}{2}. \delta_1 (X_{2n+1}, X_{2n}) + \delta_1 (X_{2n}, X_{2n-1}),$$
$$\delta_2 (Y_{2n+1}, Y_{2n}) \}$$

Hence
$$\delta_1 (X_{2n+1}, X_{2n}) \leq \lambda . \max\{ \delta_1 (X_{2n}, X_{2n-1}), \ \delta_2 (Y_{2n+1}, Y_{2n}) \} \qquad \text{-------------- (5)}$$
Now from (4) we have
$$\delta_2 (Y_{2n+1}, Y_{2n}) = \delta_2 (BSY_{2n-1}, ATY_{2n})$$
$$\leq \lambda . \max\{ \delta_2 (Y_{2n}, Y_{2n-1}), \ \delta_2 (Y_{2n-1}, BSY_{2n-1}), \ \delta_2 (Y_{2n}, ATY_{2n}),$$
$$\frac{1}{2}[\delta_2 (Y_{2n-1}, ATY_{2n}) + \delta_2 (Y_{2n}, BSY_{2n-1})], \ \delta_1 (SY_{2n-1}, TY_{2n})\}$$
$$\leq \lambda . \max\{ \delta_2 (Y_{2n-1}, Y_{2n}), \ \delta_1 (X_{2n-1}, X_{2n})\}$$
Similarly we have
$$\delta_1 (X_{2n}, X_{2n-1}) \leq \lambda . \max\{ \delta_1 (X_{2n-2}, X_{2n-1}), \ \delta_2 (Y_{2n-1}, Y_{2n})\} \qquad \text{---------------- (6)}$$
$$\delta_2 (Y_{2n}, Y_{2n-1}) \leq \lambda . \max\{ \delta_2 (Y_{2n-2}, Y_{2n-1}), \ \delta_1 (X_{2n-1}, X_{2n-2})\}$$
from inequalities (5) and (6), we have
$$\delta_1 (X_{n+1}, X_n) \leq \lambda \max\{ \delta_1 (X_n, X_{n-1}), \ \delta_2 (Y_{n+1}, Y_n) \}$$
$$\vdots$$
$$\leq \lambda^n. \max\{ \delta_1 (X_1, x_0), \ \delta_2 (Y_2, Y_1) \} \rightarrow 0 \text{ as n} \rightarrow \infty$$
Also $\delta_1 (x_{n+1}, x_n) \leq \delta_1 (X_{n+1}, X_n)$

which implies $\delta_1 (x_{n+1}, x_n) \rightarrow 0$ as n$\rightarrow \infty$

Thus $\{x_n\}$ is a Cauchy sequence in X. Since X is complete, it converges to a point z in X.
Further
$$\delta_1 (z, X_n) \leq \delta_1 (z, x_n) + \delta_1 (x_n, X_n)$$
$$\leq \delta_1 (z, x_n) + 2 \delta_1 (X_n, X_{n+1})$$
$$\Rightarrow \delta_1 (z, X_n) \rightarrow 0 \text{ as n} \rightarrow \infty$$

Similarly $\{y_n\}$ is a Cauchy sequence in Y and it converges to a point w in Y and $\delta_2 (w, Y_n) \rightarrow 0$
as n$\rightarrow \infty$.
Now
$$\delta_1 (SAx_{2n}, z) \leq \delta_1 (SAx_{2n}, x_{2n}) + \delta_1 (x_{2n}, z)$$
$$\leq \delta_1 (SAx_{2n}, TBx_{2n-1}) + \delta_1 (x_{2n}, z)$$
$$\leq \lambda . \max\{ \delta_1 (x_{2n}, x_{2n-1}), \ \delta_1 (z, SAx_{2n}), \ \delta_1 (x_{2n}, TBz),$$
$$\frac{1}{2}[\delta_1 (x_{2n}, TBx_{2n-1}) + \delta_1 (x_{2n-1}, SAx_{2n})], \delta_2 (Ax_{2n}, B x_{2n-1}) \}$$
$$+ \delta_1 (x_{2n}, z) \rightarrow 0 \text{ as n} \rightarrow \infty.$$

Thus $\lim_{n\rightarrow\infty} SAx_{2n} = \{z\} = \lim_{n\rightarrow\infty} Sy_{2n+1}$
Similarly we prove
$$\lim_{n\rightarrow\infty} TBx_{2n-1} = \{z\} = \lim_{n\rightarrow\infty} Ty_{2n}$$
$$\lim_{n\rightarrow\infty} BSy_{2n-1} = \{w\} = \lim_{n\rightarrow\infty} Bx_{2n-1}$$

$$\lim_{n \to \infty} ATy_{2n} = \{w\} = \lim_{n \to \infty} Ax_{2n}$$

Suppose A is continuous, then

$$\lim_{n \to \infty} Ax_{2n} = Az = \{w\}.$$

we prove SAz = {z}.

We have

$$\delta_1 (SAz, z) = \lim_{n \to \infty} \delta_1 (SAz, TBx_{2n-1})$$

$$\leq \lim_{n \to \infty} \lambda .\max\{ \delta_1 (z, x_{2n-1}),\ \delta_1 (z, SAz),\ \delta_1 (x_{2n-1}, TBx_{2n-1}),$$

$$\tfrac{1}{2}[\delta_1 (z, TBx_{2n-1}) + \delta_1 (x_{2n-1}, SAz)],\ \delta_2 (Az, Bx_{2n-1})\}$$

$$< \delta_1 (z, SAz)\ \text{(since } \lambda <1)$$

Thus SAz = {z}.

Hence Sw = {z}. (Since Az = {w})

Now we prove BSw = {w}.

We have

$$\delta_2 (BSw, w) = \lim_{n \to \infty} \delta_2 (BSw, ATy_{2n})$$

$$\leq \lim_{n \to \infty} \lambda .\max\{ \delta_2 (w, y_{2n}),\ \delta_2 (w, BSw),\ \delta_2 (y_{2n}, ATy_{2n}),$$

$$\tfrac{1}{2}[\delta_2 (w, ATy_{2n}) + \delta_2 (y_{2n}, BSw)],\ \delta_1 (Sw, Ty_{2n})\}$$

$$< \delta_2 (w, BSw)\ \text{(Since } \lambda < 1)$$

Thus BSw = {w}.

Hence Bz = {w}. (Since Sw = z)

Now we prove TBz = {z}.

We have

$$\delta_1 (z, TBz) = \lim_{n \to \infty} \delta_1 (SAx_{2n}, TBz)$$

$$\leq \lim_{n \to \infty} \lambda .\max\{ \delta_1 (x_{2n}, z),\ \delta_1 (x_{2n}, SAx_{2n}),\ \delta_1 (z, TBz),$$

$$\tfrac{1}{2}[\delta_1 (x_{2n}, TBz) + \delta_1 (z, SAx_{2n})],\ \delta_2 (Ax_{2n}, Bz)\}$$

$$< \delta_1 (z, TBz)\ \text{(Since } \lambda < 1)$$

Thus TBz = { z }.

Hence Tw = {z}.   (Since Bz = {w})

Now we prove ATw = {w}.

We have

$$\delta_2 (w, ATw) = \lim_{n \to \infty} \delta_2 (BSy_{2n-1}, ATw)$$

$$\leq \lim_{n \to \infty} \lambda .\max\{ \delta_2 (y_{2n-1}, w),\ \delta_2 (y_{2n-1}, BSy_{2n-1}),\ \delta_2 (w, ATw),$$

$$\tfrac{1}{2}[\delta_2 (y_{2n-1}, ATw) + \delta_2 (w, BSy_{2n-1})],\ \delta_1 (Sy_{2n-1}, Tw)\}$$

$$< \delta_2 (w, ATw)\ \text{(Since } \lambda < 1)$$

Thus ATw = {w}.

The same results hold if one of the mappings B, S and T is continuous.

Uniqueness: Let z′ be another common fixed point of SA and TB so that z′ is in SAz′ and TBz′.

Using inequalities (1) and (2) we have

$$\max\{ \delta_1 (SAz',\ z'),\ \delta_1 (z',\ TB\ z')\}$$

$$\leq \delta_1 (SAz',\ TBz')$$

$$\leq \lambda .\max\{ \delta_1 (z', z'),\ \delta_1 (z', SAz'),\ \delta_1 (z', TBz'),$$

$$\tfrac{1}{2}[\delta_1 (z', TBz') + \delta_1 (z', SAz')],\ \delta_2 (Az', Bz')\}$$

$$< \lambda . \delta_2 (Az', Bz')$$

$$\leq \lambda . \max\{ \delta_2 (ATBz', Bz'), \ \delta_2 (Az', BSAz')\}$$

$$\leq \lambda . \delta_2 (BSAz', ATBz')$$

$$\leq \lambda^2. \max\{ \delta_2 (Az', Bz'), \delta_2 (Az', BSAz'), \ \delta_2 (Bz', AT Bz'),$$

$$\tfrac{1}{2}[\delta_2 (Az', ATBz') + \delta_2 (BSAz', Bz')], \delta_1 (SAz', TBz') \}$$

$$< \lambda^2. \ \delta_1 (SAz', TBz')$$

$$\Rightarrow \quad SAz' = TBz' \quad (\text{since } \lambda < 1)$$

$$\Rightarrow \quad SAz' = TBz' = \{z'\} \text{ and } Az' = Bz' = \{w'\}$$

Thus $SAz' = TBz' = Sw' = Tw' = \{z'\}$ and

$$BSw' = ATw' = Az' = Bz' = \{w'\}$$

We have

$$\delta_1 (z, z') = \delta_1 (SAz, TBz')$$

$$\leq \lambda . \max\{ \ \delta_1 (z,z'), \ \delta_1 (z,SAz), \ \delta_1 (z',TBz'),$$

$$\tfrac{1}{2}[\delta_1 (z,TBz') + \delta_1 (z',SAz)], \delta_2 (Az,Bz')\}$$

$$< \delta_2 (w, w')$$

$$\delta_2 (w, w') = \delta_2 (BSw, ATw')$$

$$\leq \lambda . \max \{ \delta_2 (w,w'), \ \delta_2 (w,BSw), \ \delta_2 (w',ATw'),$$

$$\tfrac{1}{2}[\delta_2 (w,ATw') + \delta_2 (w',BSw)], \ \delta_1 (Sw,Tw') \}$$

$$< \delta_1 (z, z')$$

Hence $\delta_1 (z, z') < \delta_2 (w, w') < \delta_1 (z, z')$

Thus $z = z'$.

So the point z is the unique common fixed point of SA and TB. Similarly we prove w is a unique common fixed point of BS and AT.

Remark :2.2 : If we put A = B, S = T in the above theorem 2.1, we get the following corollary.

Corollory 2.3 : Let (X, d_1) and (Y, d_2) be two complete metric spaces. Let A be a mapping of X into B(Y) and T be a mapping of Y into B(X) satisfying the inequalities.

$$\delta_1 (TAx, TAx') \leq \lambda \max \{ \ \delta_1 (x,x'), \ \delta_1 (x,TAx), \ \delta_1 (x',TAx'),$$

$$\tfrac{1}{2}[\delta_1 (x,TAx') + \delta_1 (x',TAx)], \ \delta_2 (Ax,Ax') \}$$

$$\delta_2 (ATy, ATy') \leq \lambda \max \{ \ \delta_2 (y,y'), \ \delta_2 (y,ATy), \ \delta_2 (y',ATy'),$$

$$\tfrac{1}{2}[\delta_2 (y,ATy') + \delta_2 (y',ATy)], \ \delta_1 (Ty,Ty')\}$$

for all x, x' in X and y, y' in Y where $0 < \lambda < 1$. If one of the mappings A and T is continuous, then TA has a unique fixed point z in X and AT has a unique fixed point w in Y. Further,
Az = Bz = {w} and Sw = Tw = {z}.

Theorem 2.4: Let (X, d_1) and (Y, d_2) be two complete metric spaces. Let A, B be mappings of X into B(Y) and S, T be mappings of Y into B(X) satisfying the inequalities.

$$\delta_1 (SAx, TBx') \leq \lambda \ \max\{ \delta_1 (x,x'), \ \delta_1 (x',TBx'), \ \delta_2 (Ax,Bx'), \tfrac{1}{2}[\delta_1 (x,TBx') + \delta_1 (SAx,x')],$$

$$[\delta_1 (x,SAx). \delta_1 (x',TBx')] / \delta_1 (x,x')\}$$

$$--------- (1)$$

$$\delta_2 (BSy, ATy') \leq \lambda \ \max\{ \delta_2 (y,y'), \ \delta_2 (y',ATy'), \ \delta_2 (Sy,Ty'), \tfrac{1}{2}[\delta_2 (y,ATy') + \delta_2 (BSy,y')],$$

$$[\delta_2 (y,BSy). \delta_2 (y',ATy')] / \delta_2 (y,y')\}$$

$$------- (2)$$

for all x, x′ in X and y, y′ in Y where $0 < \lambda < 1$. If one of the mappings A, B, S and T is continuous, then SA and TB have a unique common fixed point z in X and BS and AT have a unique common fixed point w in Y. Further, Az = Bz = {w} and Sw = Tw = {z}.

Proof:

From (1) and (2) we have

δ_1(SAC, TBD) $\leq \lambda$ max{ δ_1(C,D), δ_1(D,TBD), δ_2(AC,BD),

$\frac{1}{2}$[δ_1(C,TBD)+ δ_1(SAC,D)], [δ_1(C,SAC). δ_1(D,TBD)] / δ_1(C,D)}

--------- (3)

δ_2(BSE, ATF) $\leq \lambda$ max{ δ_2(E,F), δ_2(F,ATF), δ_1(*SE,TF*),

$\frac{1}{2}$[δ_2(E,ATF)+ δ_2(BSE,F)], [δ_2(E,BSE). δ_2(F,ATF)] / δ_2(E,F)}

---------- (4)

$$\forall \ C,D \in B(X) \ and \ E,F \in B(Y)$$

Let x_0 be an arbitrary point in X. Then $y_1 \in A(x_0)$ since A: X $\rightarrow$ B(Y) , $x_1 \in$ S(y_1) since S : Y $\rightarrow$ B(X) , $y_2 \in$ B(x_1) since B: X $\rightarrow$ B(Y) and $x_2 \in$ T(y_2) since T : Y $\rightarrow$ B(X). Continuing in this way we get for n $\geq$ 1, $y_{2n-1} \in A(x_{2n-2})$, $x_{2n-1} \in S(y_{2n-1})$, $y_{2n} \in B(x_{2n-1})$ and $x_{2n} \in T(y_{2n})$. We define the sequences {x_n} in B(X) and {y_n} in B(Y) by choosing a point $x_{2n-1} \in$ (SATB)$^{n-1}$SAx = X_{2n-1}, $x_{2n} \in$ (TBSA)^{n}x = X_{2n}, $y_{2n-1} \in$ A (TBSA)$^{n-1}$x = Y_{2n-1} and $y_{2n} \in$ B(SATB)$^{n-1}$SAx = Y_{2n} $\forall$ n = 1.2,3, ...

Now from (3) we have

δ_1(X_{2n+1}, X_{2n}) = δ_1(SAX$_{2n}$, TBX$_{2n-1}$)

$\leq \lambda$. max{ δ_1(X_{2n}, X_{2n-1}), δ_1(X_{2n-1},TBX$_{2n-1}$), δ_2(AX$_{2n}$,BX$_{2n-1}$),

$\frac{1}{2}$[δ_1(X_{2n},TBX$_{2n-1}$)+ δ_1(SAX$_{2n}$,X$_{2n-1}$)],

[δ_1(X_{2n},SAX$_{2n}$). δ_1(X_{2n-1},TBX$_{2n-1}$)] / δ_1(X_{2n}, X_{2n-1})}

= λ .max{ δ_1(X_{2n}, X_{2n-1}), δ_1(X_{2n-1},X_{2n}), δ_2(Y_{2n+1},Y_{2n}),

$\frac{1}{2}$[δ_1(X_{2n},X_{2n})+ δ_1(X_{2n+1},X_{2n-1})],

δ_1(X_{2n}, X_{2n+1}). δ_1(X_{2n-1}, X_{2n})] / δ_1(X_{2n}, X_{2n-1})}

= λ .max{ δ_1(X_{2n}, X_{2n-1}), δ_2(Y_{2n+1},Y_{2n}), 1/2[δ_1(X_{2n+1},X_{2n})+ δ_1(X_{2n}, X_{2n-1})],

δ_1(X_{2n},X_{2n+1})}

$\leq \lambda$ .max{ δ_1(X_{2n}, X_{2n-1}), δ_2(Y_{2n+1},Y_{2n})}------------------------------------ (5)

Now from (4) we have

δ_2(Y_{2n}, Y_{2n+1}) = δ_2(BSY$_{2n-1}$, ATY$_{2n}$)

$\leq \lambda$. max{ δ_2(Y_{2n-1}, Y_{2n}), δ_2(Y_{2n},ATY$_{2n}$), δ_1 (SY$_{2n-1}$, TY$_{2n}$),

1/2[δ_2(Y_{2n-1},ATY$_{2n}$)+ δ_2(BSY$_{2n-1}$, Y$_{2n}$)] ,

δ_2(Y_{2n-1},BSY$_{2n-1}$). δ_2(Y_{2n},ATY$_{2n}$) / δ_2(Y_{2n-1}, Y_{2n})}

$\leq \lambda$. max { δ_2(Y_{2n-1}, Y_{2n}), δ_1(X_{2n-1}, X_{2n})}

Similarly

δ_1(X_{2n}, X_{2n-1}) $\leq \lambda$. max{ δ_1(X_{2n-2},X_{2n-1}), δ_2(Y_{2n-1},Y_{2n})}-------------------------------- (6)

δ_2(Y_{2n},Y_{2n-1}) $\leq \lambda$. max { δ_2(Y_{2n-1}, Y_{2n-2}), δ_1(X_{2n-1}, X_{2n-2})}

from inequalities (5) and (6), we have

δ_1(X_{n+1},X_n) $\leq \lambda$ max { δ_1(X_n, X_{n-1}) , δ_2(Y_{n+1}, Y_n) }

$\vdots$

$\leq \lambda^n$.max { δ_1(X_1, x_0) , δ_2(Y_2, Y_1) } $\rightarrow$ 0 as n→∞

Also δ_1(x_n, x_{n+1}) $\leq$ δ_1(X_n, X_{n+1})

$\Rightarrow$ δ_1(x_n, x_{n+1}) $\rightarrow$ 0 as n $\rightarrow \infty$

Thus $\{x_n\}$ is a Cauchy sequences in X. Since X is complete, $\{x_n\}$ converges to a point z in X. Further

$\delta_1(z, X_n) \leq \delta_1(z, x_n) + \delta_1(x_n, X_n)$

$\qquad \leq \delta_1(z, x_n) + 2\delta_1(X_n, X_{n+1})$

$\Rightarrow \delta_1(z, X_n) \to 0$ as $n \to \infty$

Similarly $\{y_n\}$ is a Cauchy sequence in Y and it converges to a point w in Y and $\delta_2(w, Y_n) \to 0$ as $n \to \infty$.

Now

$\delta_1(SAx_{2n}, z) \leq \delta_1(SAx_{2n}, x_{2n}) + \delta_1(x_{2n}, z)$

$\qquad \leq \delta_1(SAx_{2n}, TBx_{2n-1}) + \delta_1(x_{2n}, z)$

$\qquad \leq \lambda . \max \{ \delta_1(x_{2n}, x_{2n-1}), \delta_1(x_{2n-1}, TBx_{2n-1}), \delta_2(Ax_{2n}, Bx_{2n-1}),$

$\qquad\qquad\qquad \frac{1}{2}[\delta_1(x_{2n}, TBx_{2n-1}) + \delta_1(SAx_{2n}, x_{2n-1})],$

$\qquad\qquad\qquad [\delta_1(x_{2n}, SAx_{2n}). \delta_1(x_{2n-1}, TBx_{2n-1})] / \delta_1(x_{2n}, x_{2n-1})\}$

$\qquad\qquad\qquad\qquad + \delta_1(x_{2n}, z) \to 0$ as $n \to \infty$.

Thus $\lim\limits_{n\to\infty} SAx_{2n} = \{z\} = \lim\limits_{n\to\infty} Sy_{2n+1}$

Similarly we prove

$\qquad \lim\limits_{n\to\infty} TBx_{2n-1} = \{z\} = \lim\limits_{n\to\infty} Ty_{2n}$

$\qquad \lim\limits_{n\to\infty} BSy_{2n-1} = \{w\} = \lim\limits_{n\to\infty} Bx_{2n-1}$

$\qquad \lim\limits_{n\to\infty} ATy_{2n} = \{w\} = \lim\limits_{n\to\infty} Ax_{2n}$

Suppose A is continuous, then

$\qquad \lim\limits_{n\to\infty} Ax_{2n} = Az = \{w\}$.

Now we prove $SAz = \{z\}$

We have

$\quad \delta_1(SAz, z) \leq \lim\limits_{n\to\infty} \delta_1(SAz, TBx_{2n-1})$

$\qquad\qquad \leq \lim\limits_{n\to\infty} \lambda . \max \{ \delta_1(z, x_{2n-1}), \delta_1(x_{2n-1}, TB x_{2n-1}), \delta_2(Az, Bx_{2n-1}),$

$\qquad\qquad\qquad\qquad \frac{1}{2}[\delta_1(z, TBx_{2n-1}) + \delta_1(SAz, x_{2n-1})],$

$\qquad\qquad\qquad\qquad \delta_1(z, SAz), \delta_1(x_{2n-1}, TB x_{2n-1}) / \delta_1(z, x_{2n-1})\}$

$\qquad\qquad < \delta_1(z, SAz)$ (Since $\lambda < 1$)

Thus $SAz = \{z\} = Sw$

Now we prove $BSw = w$.

We have

$\quad \delta_2(BSw, w) \leq \lim\limits_{n\to\infty} \delta_2(BSw, ATy_{2n})$

$\qquad\qquad \leq \lim\limits_{n\to\infty} \lambda . \max \{ \delta_2(w, y_{2n}), \delta_2(y_{2n}, ATy_{2n}), \delta_1(Sw, Ty_{2n}),$

$\qquad\qquad\qquad\qquad \frac{1}{2}[\delta_2(w, ATy_{2n}) + \delta_2(BSw, y_{2n})],$

$\qquad\qquad\qquad\qquad \delta_2(w, BSw). \delta_2(y_{2n}, ATy_{2n}) / \delta_2(w, y_{2n})\}$

$\qquad\qquad < \delta_2(w, BSw)$ (Since $\lambda < 1$)

Thus $BSw = \{w\} = Bz$.

Now we prove $TBz = \{z\}$.

$\quad \delta_1(z, TBz) \leq \lim\limits_{n\to\infty} \delta_1(SAx_{2n}, TBz)$

$\qquad\qquad \leq \lim\limits_{n\to\infty} \lambda . \max \{ \delta_1(x_{2n}, z), \delta_1(z, TBz), \delta_2(Ax_{2n}, Bz),$

$$\tfrac{1}{2}[\ \delta_1(x_{2n},TBz) + \delta_1(SAx_{2n},z)],$$

$$\delta_1(x_{2n},SAx_{2n}).\ \delta_1(z,TBz)\ /\ \delta_1(x_{2n},z)\}$$

$$< \delta_1(z,TBz)\quad (\text{Since } \lambda < 1)$$

Thus $TBz = \{z\} = Tw$.

Now we prove $ATw = \{w\}$.

$$\delta_2(w, ATw) \ \le\ \lim_{n\to\infty} \delta_2(BSy_{2n-1}, ATw)$$

$$\le\ \lim_{n\to\infty} \lambda\,.\max\{\ \delta_2(y_{2n-1}, w),\ \delta_2(w,ATw),\ \delta_1(Sy_{2n-1}, Tw),$$

$$\tfrac{1}{2}[\ \delta_2(y_{2n-1}, ATw) + \delta_2(BSy_{2n-1}, w)],$$

$$\delta_2(y_{2n-1}, BSy_{2n-1}).\ \delta_2(w,ATw)\ /\ \delta_2(y_{2n-1}, w)\ \}$$

$$< \delta_2(w,ATw)\quad (\text{Since } \lambda < 1)$$

Thus $ATw = \{w\}$.

The same results hold if one of the mappings B, S and T is continuous.

Uniqueness: Let z' be another common fixed point of SA and TB so that z' is in SAz' and TBz'.

Using inequalities (1) and (2) we have

$$\max\{\ \delta_1(SAz',z'),\ \delta_1(z',TBz')\}$$

$$\le\ \delta_1(SAz',TBz')$$

$$\le\ \lambda\,.\max\{\ \delta_1(z',z'),\ \delta_1(z',TBz'),\ \delta_2(Az',Bz'),$$

$$\tfrac{1}{2}[\ \delta_1(z',TBz') + \delta_1(SAz',z')],\ [\ \delta_1(z',SAz').\ \delta_1(z',TBz')]\ /\ \delta_1(z',z')\}$$

$$\le\ \lambda\,.\ \delta_2(Az',Bz')$$

$$\le\ \lambda\,.\max\{\ \delta_2(ATBz',Bz'),\ \delta_2(Az',BSAz')\}$$

$$\le\ \lambda\,.\ \delta_2(BSAz',ATBz')$$

$$\le\ \lambda^2.\max\{\ \delta_2(Az',Bz')\,,\ \delta_2(Bz', ATBz'),\ \delta_1(SAz',TBz')$$

$$\tfrac{1}{2}[\ \delta_2(z',BSAz') + \delta_2(ATBz', z')],$$

$$\delta_2(z',BSAz').\ \delta_2(z',ATBz')/\ \delta_2(z',z')\ \}$$

$$\le\ \lambda^2\ \delta_1(SAz',TBz')$$

$$\Rightarrow\quad SAz' = TBz'\quad (\text{since } \lambda < 1)$$

$$\Rightarrow\quad SAz' = TBz' = \{z'\}\ \text{ and } Az' = Bz' = \{w'\}$$

Thus $\quad SAz' = TBz' = Sw' = Tw' = \{z'\}$ and

$$BSw' = ATw' = Az' = Bz' = \{w'\}$$

We have

$$\delta_1(z, z') = \delta_1(SAz, TBz')$$

$$\le\ \lambda\,.\max\{\ \delta_1(z, z'),\ \delta_1(z', TBz'),\ \delta_2(Az,Bz'),$$

$$\tfrac{1}{2}[\ \delta_1(z, TBz') + \delta_1(SAz, z')],\ \delta_1(z, SAz)\,.\ \delta_1(z', TBz')\ /\ \delta_1(z, z')\ \}$$

$$<\ \delta_2(w, w')\quad (\text{Since } \lambda < 1)$$

Now

$$\delta_2(w, w') = \delta_2(BSw, ATw')$$

$$\le\ \lambda\,.\max\{\ \delta_2(w, w'),\ \delta_2(w', ATw'),\ \delta_1(Sw,Tw'),$$

$$\tfrac{1}{2}[\ \delta_2(w, ATw') + \delta_2(BSw, w')],\ \delta_2(w, BSw)\,.\ \delta_2(w', ATw')\ /\ \delta_2(w, w')\}$$

$$<\ \delta_1(z, z')$$

Hence $\delta_1(z, z') < \delta_2(w, w') < \delta_1(z, z')$

$$\Rightarrow z = z'.$$

So the point z is the unique common fixed point of SA and TB. Similarly we prove w is a unique common fixed point of BS and AT.

Remark: 2.5 : If we put A = B, S = T in the above theorem 2.4, we get the following corollary.

Corollory 2.6 : Let (X, d_1) and (Y, d_2) be two complete metric spaces. Let A be a mapping of X into B(Y) and T be a mapping of Y into B(X) satisfying the inequalities.

$$\delta_1 (TAx, TAx') \leq \lambda \ \max\{ \delta_1 (x,x'), \ \delta_1 (x',TAx'), \ \delta_2 (Ax,Ax'), \ ½[\delta_1 (x,TAx')+ \delta_1 (TAx,x')],$$
$$[\delta_1 (x,TAx). \delta_1 (x',TAx')] \ / \ \delta_1 (x,x')\}$$

$$\delta_2 (ATy, ATy') \leq \lambda \ \max\{ \delta_2 (y,y'), \ \delta_2 (y',ATy'), \ \delta_2 (Ty,Ty'), ½[\delta_2 (y,ATy')+ \delta_2 (ATy,y')],$$
$$[\delta_2 (y,ATy). \delta_2 (y',ATy')] \ / \ \delta_2 (y,y')\}$$

for all x, x′ in X and y, y′ in Y where $0< \lambda < 1$. If one of the mappings A and T is continuous, then TA has a unique fixed point z in X and AT has a unique fixed point w in Y. Further, $Az = Bz = \{w\}$ and
$Sw = Tw = \{z\}$.

Theorem 2.7: Let (X, d_1) and (Y, d_2) be complete metric spaces. Let A, B be mappings of X into B(Y) and S, T be mappings of Y into B(X) satisfying the inequalities.

$$\delta_1 (SAx, TBx') \leq \lambda . \max\{ \delta_1 (x,x'), \ \delta_1 (x,SAx), \ \delta_1 (x',TBx'), \ \delta_2 (Ax,Bx'),$$
$$\frac{\delta_1 (x,TBx')}{2}, \frac{\delta_1 (SAx, x')}{2} \} \text{ ------- (1)}$$

$$\delta_2 (BSy, ATy') \leq \lambda . \max\{ \ \delta_2 (y,y'), \ \delta_2 (y,BSy), \ \delta_2 (y',ATy'), \ \delta_1 (Sy,Ty'),$$
$$\frac{\delta_2 (y, ATy')}{2}, \frac{\delta_2 (BSy, y')}{2} \} \text{ ---------(2)}$$

for all x, x′ in X and y,y′ in Y where $0 \leq \lambda < 1$. If one of the mappings A, B, S and T is continuous , then SA and TB have a unique common fixed point z in X and BS and AT have a unique common fixed point w in Y. Further, $Az = Bz = \{w\}$ and $Sw = Tw = \{z\}$.

Proof: From (1) and (2) we have

$$\delta_1 (SAC, TBD) \leq \lambda \ \max\{ \delta_1 (C,D), \ \delta_1 (C,SAC), \ \delta_1 (D,TBD), \ \delta_2 (AC,BD),$$
$$\frac{\delta_1 (C,TBD)}{2} , \frac{\delta_1 (SAC,D)}{2} \} \text{ --------- (3)}$$

$$\delta_2 (BSE, ATF) \leq \lambda \ \max\{ \delta_2 (E,F), \ \delta_2 (E,BSE), \ \delta_2 (F,ATF), \ \delta_1 (SE,TF),$$
$$\frac{\delta_2 (E, ATF)}{2} , \frac{\delta_2 (BSE, F)}{2} \} \text{ ---------- (4)}$$
$$\forall \ C,D \in B(X) \text{ and } E,F \in B(Y)$$

Let x_0 be an arbitrary point in X. Then $y_1 \in A(x_0)$ since $A: X \to B(Y)$, $x_1 \in S(y_1)$ since $S : Y \to B(X)$, $y_2 \in B(x_1)$ since $B: X \to B(Y)$ and $x_2 \in T(y_2)$ since $T : Y \to B(X)$. continuing in this way we get for $n \geq 1$, $y_{2n-1} \in A(x_{2n-2})$, $x_{2n-1} \in S(y_{2n-1})$, $y_{2n} \in B(x_{2n-1})$ and $x_{2n} \in T(y_{2n})$. We define the sequences $\{x_n\}$ in B(X) and $\{y_n\}$ in B(Y) by choosing a point $x_{2n-1} \in (SATB)^{n-1}SAx = X_{2n-1,}$ $x_{2n} \in (TBSA)^{n}x = X_{2n,}$
$y_{2n-1} \in A (TBSA)^{n-1}x = Y_{2n-1}$ and $y_{2n} \in B(SATB)^{n-1}SAx = Y_{2n} \ \forall \ n = 1.2,3, _{....}$
Now from (3) we have

$$\delta_1 (X_{2n+1}, X_{2n}) \leq \delta_1 (SAX_{2n,} TBX_{2n-1})$$

$$\leq \lambda .\max\{ \delta_1 (X_{2n}, X_{2n-1}), \ \delta_1 (X_{2n},SAX_{2n}), \ \delta_1 (X_{2n-1}, TBX_{2n-1}), \ \delta_2 (AX_{2n},BX_{2n-1}),$$
$$\frac{\delta_1 (X_{2n},TBX_{2n-1})}{2}, \frac{\delta_1 (SAX_{2n}, X_{2n-1})}{2} \}$$

$$= \lambda \, . \max\{ \, \delta_1(X_{2n}, X_{2n-1}), \ \delta_1(X_{2n}, X_{2n+1}), \ \delta_1(X_{2n-1}, X_{2n}), \ \delta_2(Y_{2n+1}, Y_{2n}),$$
$$\frac{\delta_1(X_{2n}, X_{2n})}{2}, \frac{\delta_1(X_{2n+1}, X_{2n-1})}{2} \, \}$$

$$\leq \lambda \, . \max\{ \, \delta_1(X_{2n}, X_{2n-1}), \ \delta_1(X_{2n}, X_{2n+1}), \ \delta_1(X_{2n-1}, X_{2n}), \ \delta_2(Y_{2n+1}, Y_{2n}),$$
$$\frac{\delta_1(X_{2n+1}, X_{2n}) + \delta_1(X_{2n}, X_{2n-1})}{2} \, \}$$

$$\leq \lambda \, . \max\{ \, \delta_1(X_{2n-1}, X_{2n}), \ \delta_2(Y_{2n+1}, Y_{2n})\} \qquad \text{-------------------------- (5)}$$

Now from (4) we have

$$\delta_2(Y_{2n}, Y_{2n+1}) \leq \delta_2(BSY_{2n-1}, ATY_{2n})$$
$$\leq \lambda \, . \max\{ \, \delta_2(Y_{2n-1}, Y_{2n}), \ \delta_2(Y_{2n-1}, BSY_{2n-1}), \ \delta_2(Y_{2n}, ATY_{2n}),$$
$$\delta_1(SY_{2n-1}, TY_{2n}), \frac{\delta_2(Y_{2n-1}, ATY_{2n})}{2}, \frac{\delta_2(BSY_{2n-1}, Y_{2n})}{2} \, \}$$

$$\leq \lambda \, . \max\{ \, \delta_2(Y_{2n-1}, Y_{2n}), \ \delta_1(X_{2n-1}, X_{2n})\}$$

Similarly

$$\delta_1(X_{2n}, X_{2n-1}) \leq \lambda \, . \max\{ \, \delta_1(X_{2n-2}, X_{2n-1}), \ \delta_2(Y_{2n-1}, Y_{2n})\} \text{----------------------------- (6)}$$

$$\delta_2(Y_{2n}, Y_{2n-1}) \leq \lambda \, . \max \{ \, \delta_2(Y_{2n-1}, Y_{2n-2}), \ \delta_1(X_{2n-1}, X_{2n-2})\}$$

from inequalities (5) and (6), we have

$$\delta_1(X_n, X_{n+1}) \leq \lambda \, \max \{ \, \delta_1(X_n, X_{n-1}), \ \delta_2(Y_{n+1}, Y_n) \}$$
$$\vdots$$
$$\leq \lambda^n . \max \{ \, \delta_1(x_0, X_1), \ \delta_2(Y_1, Y_2) \} \to 0 \text{ as } n \to \infty$$

Also $\delta_1(x_n, x_{n+1}) \leq \delta_1(X_n, X_{n+1})$

$$\Rightarrow \delta_1(x_n, x_{n+1}) \to 0 \text{ as } n \to \infty$$

Thus $\{x_n\}$ is a Cauchy sequence in X. Since X is complete, $\{x_n\}$ converges to a point z in X. Further

$$\delta_1(z, X_n) \leq \delta_1(z, x_n) + \delta_1(x_n, X_n)$$
$$\leq \delta_1(z, x_n) + 2\delta_1(X_n, X_{n+1})$$

$$\Rightarrow \delta_1(z, X_n) \to 0 \text{ as } n \to \infty$$

Similarly $\{y_n\}$ is a Cauchy sequence in Y and it converges to a point w in Y and

$\delta_2(w, Y_n) \to 0 \text{ as } n \to \infty$.

Now

$$\delta_1(SAx_{2n}, z) \leq \delta_1(SAx_{2n}, x_{2n}) + \delta_1(x_{2n}, z)$$
$$\leq \delta_1(SAx_{2n}, TBx_{2n-1}) + \delta_1(x_{2n}, z)$$
$$\leq \lambda \, . \max\{ \, \delta_1(x_{2n}, x_{2n-1}), \ \delta_1(x_{2n}, SAx_{2n}), \ \delta_1(x_{2n-1}, TBx_{2n-1}), \ \delta_2(Ax_{2n}, Bx_{2n-1}),$$
$$\frac{\delta_1(x_{2n}, TBx_{2n-1})}{2}, \frac{\delta_1(SAx_{2n}, x_{2n-1})}{2} \, \}$$
$$+ \delta_1(x_{2n}, z) \to 0 \text{ as } n \to \infty$$

Thus $\lim\limits_{n\to\infty} SAx_{2n} = \{z\} = \lim\limits_{n\to\infty} Sy_{2n+1}$

Similarly we prove

$$\lim\limits_{n\to\infty} TBx_{2n-1} = \{z\} = \lim\limits_{n\to\infty} Ty_{2n}$$

$$\lim\limits_{n\to\infty} BSy_{2n-1} = \{w\} = \lim\limits_{n\to\infty} Bx_{2n-1}$$

$$\lim_{n\to\infty} ATy_{2n} = \{w\} = \lim_{n\to\infty} Ax_{2n}$$

Suppose A is continuous, then

$$\lim_{n\to\infty} Ax_{2n} = Az = \{w\}.$$

Now we prove SAz = {z}

We have

$$\delta_1(SAz,z) = \lim_{n\to\infty} \delta_1(SAz, TBx_{2n-1})$$

$$\leq \lim_{n\to\infty} \lambda \cdot \max\{ \delta_1(z, x_{2n-1}),\ \delta_1(z,SAz),\ \delta_1(x_{2n-1},TB\,x_{2n-1}),\ \delta_2(Az, Bx_{2n-1}),$$

$$\frac{\delta_1(z,TBx_{2n-1})}{2},\ \frac{\delta_1(SAz, x_{2n-1})}{2} \}$$

$$< \delta_1(z,SAz) \quad (\text{Since } \lambda < 1)$$

Thus SAz = {z}.

Hence Sw = {z}. (Since Az = {w})

Now we prove BSw = {w}.

We have

$$\delta_2(BSw, w) = \lim_{n\to\infty} \delta_2(BSw, ATy_{2n})$$

$$\leq \lim_{n\to\infty} \lambda \cdot \max\{ \delta_2(w, y_{2n}),\ \delta_2(w, BSw),\ \delta_2(y_{2n}, ATy_{2n}),\ \delta_1(Sw, Ty_{2n}),$$

$$\frac{\delta_2(w, ATy_{2n})}{2},\ \frac{\delta_2(BSw, y_{2n})}{2} \}$$

$$< \delta_2(w,BSw) \quad (\text{Since } \lambda < 1)$$

Thus BSw = {w}.

Hence Bz = {w}. (Since Sw = {z})

Now we prove TBz = {z}

$$\delta_1(z,TBz) = \lim_{n\to\infty} \delta_1(SAx_{2n}, TBz)$$

$$\leq \lim_{n\to\infty} \lambda \cdot \max\{ \delta_1(x_{2n},z),\ \delta_1(x_{2n},SAx_{2n}),\ \delta_1(z, TBz),\ \delta_2(Ax_{2n}, Bz),$$

$$\frac{\delta_1(x_{2n},TBz)}{2},\ \frac{\delta_1(SAx_{2n}, z)}{2} \}$$

$$< \delta_1(z, TBz) \quad (\text{Since } \lambda < 1)$$

Thus TBz = {z}.

Hence Tw = {z}. (Since Bz = {w})

Now we prove ATw = {w}.

$$\delta_2(w, ATw) = \lim_{n\to\infty} \delta_2(BSy_{2n-1}, ATw)$$

$$\leq \lim_{n\to\infty} \lambda \cdot \max\{ \delta_2(y_{2n-1}, w),\ \delta_2(y_{2n-1}, BSy_{2n-1}),\ \delta_2(w, ATw),\ \delta_1(Sy_{2n-1}, Tw),$$

$$\frac{\delta_2(y_{2n-1}, ATw)}{2},\ \frac{\delta_2(BSy_{2n-1}, w)}{2} \}$$

$$< \delta_2(w, ATw) \quad (\text{Since } \lambda < 1)$$

Thus ATw = {w}.

The same results hold if one of the mappings B, S and T is continuous.

Uniqueness: Let z′ be another common fixed point of SA and TB so that z′ is in SAz′ and TBz′.

Using inequalities (1) and (2) we have

$$\max\{ \delta_1(SAz′, z′),\ \delta_1(z′, TB\,z′)\}$$

$$\leq \delta_1 (SAz', TBz')$$

$$\leq \lambda \cdot \max\{ \delta_1 (z', z'), \delta_1 (z', SA z'), \delta_1 (z', TB z'), \delta_2 (A z', B z'),$$

$$\frac{\delta_1 (z', TBz')}{2}, \frac{\delta_1 (SAz', z')}{2} \}$$

$$\leq \lambda \cdot \delta_2 (Az', Bz')$$

$$\leq \lambda \cdot \max\{ \delta_2 (ATBz', Bz'), \delta_2 (Az', BSAz')\}$$

$$\leq \lambda \cdot \delta_2 (BSAz', ATBz')$$

$$\leq \lambda^2 \cdot \max\{ \delta_2 (Az', Bz'), \delta_2 (Az', BSAz'), \delta_2 (Bz', ATBz'),$$

$$\delta_1 (SAz', TBz'), \frac{\delta_2 (Az', ATBz')}{2}, \frac{\delta_2 (BSAz', Bz')}{2} \}$$

$$\leq \lambda^2 \delta_1 (SAz', TBz')$$

$$\Rightarrow \quad SAz' = TBz' \quad (\text{since } \lambda < 1)$$

$$\Rightarrow \quad SAz' = TBz' = \{z'\} \text{ and } Az' = Bz' = \{w'\}$$

Thus $SAz' = TBz' = Sw' = Tw' = \{z'\}$ and

  $BSw' = ATw' = Az' = Bz' = \{w'\}$

We have

$$\delta_1 (z, z') = \delta_1 (SAz, TBz')$$

$$\leq \lambda \cdot \max\{ \delta_1 (z, z'), \delta_1 (z, SAz), \delta_1 (z', TBz'), \delta_2 (Az, Bz'),$$

$$\frac{\delta_1 (z, TBz')}{2}, \frac{\delta_1 (SAz, z')}{2} \}$$

$$< \delta_2 (w, w') \quad (\text{since } \lambda < 1)$$

$$\delta_2 (w, w') = \delta_2 (BSw, ATw')$$

$$\leq \lambda \cdot \max\{ \delta_2 (w, w'), \delta_2 (w, BSw), \delta_2 (w', ATw'), \delta_1 (Sw, Tw'),$$

$$\frac{\delta_2 (w, ATw')}{2}, \frac{\delta_2 (BSw, w')}{2} \}$$

$$< \delta_1 (z, z') \quad (\text{since } \lambda < 1)$$

Hence $\delta_1 (z, z') < \delta_2 (w, w') < \delta_1 (z, z')$

Thus z = z'.

So the point z is the unique common fixed point of SA and TB. Similarly we prove w is a unique common fixed point of BS and AT.

Remark 2.8: If we put A = B, S = T in the above theorem 2.7, we get the following corollary.

Corollary 2.9: Let (X, d_1) and (Y, d_2) be two complete metric spaces. Let A be a mapping of X into Y and T be a mapping of Y into X satisfying the inequalities.

$$\delta_1 (TAx, TAx') \leq \lambda \cdot \max\{ \delta_1 (x, x'), \delta_1 (x, TAx), \delta_1 (x', TAx'), \delta_2 (Ax, Ax'), \frac{\delta_1 (x, TAx')}{2}, \frac{\delta_1 (TAx, x')}{2} \}$$

$$\delta_2 (ATy, ATy') \leq \lambda \cdot \max\{ \delta_2 (y, y'), \delta_2 (y, ATy), \delta_2 (y', ATy'), \delta_1 (Ty, Ty'), \frac{\delta_2 (y, ATy')}{2}, \frac{\delta_2 (ATy, y')}{2} \}$$

for all x, x' in X and y, y' in Y where $0 \leq \lambda < 1$. If one of the mappings A and T is continuous, then TA has a unique fixed point z in X and AT has a unique fixed point w in Y. Further,

Az = Bz = {w} and Sw = Tw = {z}.

Theorem 2.10: Let (X, d_1) and (Y, d_2) be complete metric spaces. Let A, B be mappings of X into B(Y) and S, T be mappings of Y into B(X) satisfying the inequalities.

$$\delta_1 (SAx, TBx') \leq \lambda . \max\{ \delta_1(x,x'), \delta_1(x,SAx), \delta_2(Ax,Bx'), \frac{\delta_1(x,TBx')}{2}, \frac{\delta_1(SAx,x')}{2}$$

$$[\delta_1(x,SAx).\delta_1(x',TBx')] / \delta_1(x,x') \} \text{ ------- (1)}$$

$$\delta_2 (BSy, ATy') \leq \lambda . \max\{ \delta_2(y,y'), \delta_2(y,BSy), \delta_1(Sy,Ty'), \frac{\delta_2(y,ATy')}{2}, \frac{\delta_2(BSy,y')}{2}$$

$$[\delta_2(y,BSy).\delta_2(y',ATy')] / \delta_2(y,y') \} \text{ --------(2)}$$

for all x, x′ in X and y,y′ in Y where $0 \leq \lambda < 1$. If one of the mappings A, B, S and T is continuous , then SA and TB have a unique common fixed point z in X and BS and AT have a unique common fixed point w in Y. Further, $Az = Bz = \{w\}$ and $Sw = Tw = \{z\}$.

Proof: From (1) and (2) we have

$$\delta_1 (SAC, TBD) \leq \lambda \max\{ \delta_1(C,D), \delta_1(C,SAC), \delta_2(AC,BD), \frac{\delta_1(C,TBD)}{2}, \frac{\delta_1(SAC,D)}{2}$$

$$[\delta_1(C,SAC).\delta_1(D,TBD)] / \delta_1(C,D) \} \text{ --------- (3)}$$

$$\delta_2 (BSE, ATF) \leq \lambda \max\{ \delta_2(E,F), \delta_2(E,BSE), \delta_1(SE,TF), \frac{\delta_2(E,ATF)}{2}, \frac{\delta_2(BSE,F)}{2}$$

$$[\delta_2(E,BSE).\delta_2(F',ATF)] / \delta_2(E,F)\} \text{ ---------- (4)}$$
$$\forall C,D \in B(X) \text{ and } E,F \in B(Y)$$

Let x_0 be an arbitrary point in X. Then $y_1 \in A(x_0)$ since $A: X \to B(Y)$, $x_1 \in S(y_1)$ since $S : Y \to B(X)$, $y_2 \in B(x_1)$ since $B: X \to B(Y)$ and $x_2 \in T(y_2)$ since $T : Y \to B(X)$. Continuing in this way we get for $n \geq 1$, $y_{2n-1} \in A(x_{2n-2})$, $x_{2n-1} \in S(y_{2n-1})$, $y_{2n} \in B(x_{2n-1})$ and $x_{2n} \in T(y_{2n})$. We define the sequences $\{x_n\}$ in B(X) and $\{y_n\}$ in B(Y) by choosing a point $x_{2n-1} \in (SATB)^{n-1}SAx = X_{2n-1}$, $x_{2n} \in (TBSA)^n x = X_{2n}$, $y_{2n-1} \in A (TBSA)^{n-1}x = Y_{2n-1}$ and $y_{2n} \in B(SATB)^{n-1}SAx = Y_{2n}$ $\forall$ n = 1.2,3, ...

Now from (3) we have
$$\delta_1 (X_{2n+1}, X_{2n}) \leq \delta_1 (SAX_{2n}, TBX_{2n-1})$$

$$\leq \lambda .\max\{ \delta_1(X_{2n}, X_{2n-1}), \delta_1(X_{2n},SAX_{2n}), \delta_2(AX_{2n},BX_{2n-1}), \frac{\delta_1(X_{2n},TBX_{2n-1})}{2},$$

$$\frac{\delta_1(SAX_{2n}, X_{2n-1})}{2}, [\delta_1(X_{2n},SAX_{2n}).\delta_1(X_{2n-1}, TBX_{2n-1})] / \delta_1(X_{2n}, X_{2n-1})\}$$

$$= \lambda . \max\{ \delta_1(X_{2n}, X_{2n-1}), \delta_1(X_{2n}, X_{2n+1}), \delta_2(Y_{2n+1},Y_{2n}), \frac{\delta_1(X_{2n}, X_{2n})}{2},$$

$$\frac{\delta_1(X_{2n+1}, X_{2n-1})}{2},[\delta_1(X_{2n},X_{2n+1}).\delta_1(X_{2n-1},X_{2n})] / \delta_1(X_{2n}, X_{2n-1}) \}$$

$$\leq \lambda . \max\{ \delta_1(X_{2n}, X_{2n-1}), \delta_1(X_{2n}, X_{2n+1}), \delta_2(Y_{2n+1},Y_{2n}), 0,$$

$$\frac{\delta_1(X_{2n+1}, X_{2n}) + \delta_1(X_{2n}, X_{2n-1})}{2}, \delta_1(X_{2n},X_{2n+1}) \}$$

$$\leq \lambda . \max\{ \delta_1(X_{2n-1}, X_{2n}), \delta_2(Y_{2n+1}, Y_{2n})\} \text{ ------------------------- (5)}$$
Now from (4) we have
$$\delta_2 (Y_{2n}, Y_{2n+1}) \leq \delta_2 (BSY_{2n-1}, ATY_{2n})$$

$$\leq \lambda \max\{ \delta_2(Y_{2n-1}, Y_{2n}), \delta_2(Y_{2n-1}, BSY_{2n-1}), \delta_1(SY_{2n-1}, TY_{2n}), \frac{\delta_2(Y_{2n-1}, ATY_{2n})}{2},$$

$$\frac{\delta_2(BSY_{2n-1}, Y_{2n})}{2}, [\,\delta_2(Y_{2n-1}, BSY_{2n-1}).\,\delta_2(Y_{2n}, ATY_{2n}) \,/\, \delta_2(Y_{2n-1}, Y_{2n})\,\}$$

$$\le \lambda . \max\{\ \delta_2(Y_{2n-1}, Y_{2n}),\ \delta_1(X_{2n-1}, X_{2n})\}$$

Similarly

$$\delta_1(X_{2n}, X_{2n-1}) \le \lambda . \max\{\ \delta_1(X_{2n-2}, X_{2n-1}),\ \delta_2(Y_{2n-1}, Y_{2n})\} \text{-----------------------------} (6)$$

$$\delta_2(Y_{2n}, Y_{2n-1}) \le \lambda . \max\{\ \delta_2(Y_{2n-1}, Y_{2n-2}),\ \delta_1(X_{2n-1}, X_{2n-2})\}$$

from inequalities (5) and (6) we have

$$\delta_1(X_n, X_{n+1}) \le \lambda \ \max\{\ \delta_1(X_n, X_{n-1}),\ \delta_2(Y_{n+1}, Y_n)\}$$
$$\vdots$$
$$\le \lambda^n. \max\{\ \delta_1(x_0, X_1),\ \delta_2(Y_1, Y_2)\} \to 0 \text{ as } n \to \infty$$

Also $\delta_1(x_n, x_{n+1}) \le \delta_1(X_n, X_{n+1})$

$\Rightarrow \delta_1(x_n, x_{n+1}) \to 0$ as $n \to \infty$

Thus $\{x_n\}$ is a Cauchy sequence in X. Since X is complete, $\{x_n\}$ converges to a point z in X. Further

$$\delta_1(z, X_n) \le \delta_1(z, x_n) + \delta_1(x_n, X_n)$$
$$\le \delta_1(z, x_n) + 2\delta_1(X_n, X_{n+1})$$

$\Rightarrow \delta_1(z, X_n) \to 0$ as $n \to \infty$

Similarly $\{y_n\}$ is a Cauchy sequence in Y and it converges to a point w in Y and

$\delta_2(w, Y_n) \to 0$ as $n \to \infty$.

Now

$$\delta_1(SAx_{2n}, z) \le \delta_1(SAx_{2n}, x_{2n}) + \delta_1(x_{2n}, z)$$
$$\le \delta_1(SAx_{2n}, TBx_{2n-1}) + \delta_1(x_{2n}, z)$$
$$\le c.\max\{\ \delta_1(x_{2n}, x_{2n-1}),\ \delta_1(x_{2n}, SAx_{2n}),\ \delta_2(Ax_{2n}, Bx_{2n-1}),\ \frac{\delta_1(x_{2n}, TBx_{2n-1})}{2},$$
$$\frac{\delta_1(SAx_{2n}, x_{2n-1})}{2}, [\,\delta_1(x_{2n}, SAx_{2n}).\,\delta_1(x_{2n-1}, TBx_{2n-1})\,] \,/\, \delta_1(x_{2n}, x_{2n-1})\,\}$$
$$+ \delta_1(x_{2n}, z) \to 0 \text{ as } n \to \infty$$

Thus $\displaystyle\lim_{n\to\infty} SAx_{2n} = \{z\} = \lim_{n\to\infty} Sy_{2n+1}$

Similarly we prove

$$\lim_{n\to\infty} TBx_{2n-1} = \{z\} = \lim_{n\to\infty} Ty_{2n}$$
$$\lim_{n\to\infty} BSy_{2n-1} = \{w\} = \lim_{n\to\infty} Bx_{2n-1}$$
$$\lim_{n\to\infty} ATy_{2n} = \{w\} = \lim_{n\to\infty} Ax_{2n}$$

Suppose A is continuous, then

$$\lim_{n\to\infty} Ax_{2n} = Az = \{w\}.$$

Now we prove $SAz = \{z\}$

We have

$$\delta_1(SAz, z) = \lim_{n\to\infty} \delta_1(SAz, TBx_{2n-1})$$

$$\le \lim_{n\to\infty} \lambda . \max\{\ \delta_1(z, x_{2n-1}),\ \delta_1(z, SAz),\ \delta_2(Az, Bx_{2n-1}),\ \frac{\delta_1(z, TBx_{2n-1})}{2},$$
$$\frac{\delta_1(SAz, x_{2n-1})}{2}, \delta_1(z, SAz),\ \delta_1(x_{2n-1}, TBx_{2n-1}) \,/\, \delta_1(z, x_{2n-1})\,\}$$

$$< \delta_1 (z, SAz) \quad (\text{Since } \lambda < 1)$$

Thus $SAz = \{z\}$.
Hence $Sw = \{z\}$. (Since $Az = \{w\}$)
Now we prove $BSw = \{w\}$.
We have

$$\delta_2 (BSw, w) = \lim_{n \to \infty} \delta_2 (BSw, ATy_{2n})$$

$$\leq \lim_{n \to \infty} \lambda \max \{ \delta_2 (w, y_{2n}), \delta_2 (w, BSw), \delta_1 (Sw, Ty_{2n}), \frac{\delta_2 (w, ATy_{2n})}{2},$$

$$\frac{\delta_2 (BSw, y_{2n})}{2}, \delta_2 (w, BSw) . \delta_2 (y_{2n}, ATy_{2n}) / \delta_2 (w, y_{2n}) \}$$

$$< \delta_2 (w, BSw) \quad (\text{Since } \lambda < 1)$$

Thus $BSw = \{w\}$.
Hence $Bz = \{w\}$. (Since $Sw = \{z\}$)
Now we prove $TBz = \{z\}$

$$\delta_1 (z, TBz) = \lim_{n \to \infty} \delta_1 (SAx_{2n}, TBz)$$

$$\leq \lim_{n \to \infty} \lambda . \max \{ \delta_1 (x_{2n}, z), \delta_1 (x_{2n}, SAx_{2n}), \delta_2 (Ax_{2n}, Bz), \frac{\delta_1 (x_{2n}, TBz)}{2},$$

$$\frac{\delta_1 (SAx_{2n}, z)}{2}, \delta_1 (x_{2n}, SAx_{2n}) . \delta_1 (z, TBz) / \delta_1 (x_{2n}, z) \}$$

$$< \delta_1 (z, TBz) \quad (\text{Since } \lambda < 1)$$

Thus $TBz = \{z\}$.
Hence $Tw = \{z\}$. (Since $Bz = \{w\}$)
Now we prove $ATw = \{w\}$.

$$\delta_2 (w, ATw) = \lim_{n \to \infty} \delta_2 (BSy_{2n-1}, ATw)$$

$$\leq \lim_{n \to \infty} \lambda . \max \{ \delta_2 (y_{2n-1}, w), \delta_2 (y_{2n-1}, BSy_{2n-1}), \delta_1 (Sy_{2n-1}, Tw), \frac{\delta_2 (y_{2n-1}, ATw)}{2},$$

$$\frac{\delta_2 (BSy_{2n-1}, w)}{2}, \delta_2 (y_{2n-1}, BSy_{2n-1}) . \delta_2 (w, ATw) / \delta_2 (y_{2n-1}, w) \}$$

$$< \delta_2 (w, ATw) \quad (\text{Since } \lambda < 1)$$

Thus $ATw = \{w\}$.
The same results hold if one of the mappings B, S and T is continuous.

Uniqueness: Let z′ be another common fixed point of SA and TB so that z′ is in SAz′ and TBz′.
Using inequalities (1) and (2) we have

$$\max \{ \delta_1 (SAz', z'), \delta_1 (z', TBz') \}$$

$$\leq \delta_1 (SAz', TBz')$$

$$\leq \lambda . \max \{ \delta_1 (z', z'), \delta_1 (z', SAz'), \delta_2 (Az', Bz'), \frac{\delta_1 (z', TBz')}{2},$$

$$\frac{\delta_1 (SAz', z')}{2}, [\delta_1 (z', SAz') . \delta_1 (z', TBz')] / \delta_1 (z', z') \}$$

$$\leq \lambda . \delta_2 (Az', Bz')$$

$$\leq \lambda . \max \{ \delta_2 (ATBz', Bz'), \delta_2 (Az', BSAz') \}$$

$$\leq \lambda . \delta_2 (BSAz', ATBz')$$

$$\leq \lambda^2 . \max\{ \delta_2(Az', Bz'), \delta_2(Az', BSAz'), \delta_1(SAz', TBz'), \frac{\delta_2(Az', ATBz')}{2},$$

$$\frac{\delta_2(BSAz', Bz')}{2}, \delta_2(z', BSAz').\delta_2(z', ATBz')/ \delta_2(z', z')\}$$

$$\leq \lambda^2 \delta_1(SAz', TBz')$$

$\Rightarrow \quad SAz' = TBz' \quad (\text{since } \lambda < 1)$

$\Rightarrow \quad SAz' = TBz' = \{z'\} \text{ and } Az' = Bz' = \{w'\}$

Thus $\quad SAz' = TBz' = Sw' = Tw' = \{z'\}$ and

$\qquad BSw' = ATw' = Az' = Bz' = \{w'\}$

We have

$$\delta_1(z, z') = \delta_1(SAz, TBz')$$

$$\leq \lambda . \max\{ \delta_1(z, z'), \delta_1(z, SAz), \delta_2(Az, Bz'), \frac{\delta_1(z, TBz')}{2},$$

$$\frac{\delta_1(SAz, z')}{2}, \delta_1(z, SAz).\delta_1(z', TBz')/ \delta_1(z, z')\}$$

$$< \delta_2(w, w') \quad (\text{since } \lambda < 1)$$

$$\delta_2(w, w') = \delta_2(BSw, ATw')$$

$$\leq \lambda . \max\{ \delta_2(w, w'), \delta_2(w, BSw), \delta_1(Sw, Tw'), \frac{\delta_2(w, ATw')}{2},$$

$$\frac{\delta_2(BSw, w')}{2}, \delta_2(w, BSw).\delta_2(w', ATw')/ \delta_2(w, w')\}$$

$$< \delta_1(z, z') \quad (\text{since } \lambda < 1)$$

Hence $\delta_1(z, z') < \delta_2(w, w') < \delta_1(z, z')$

Thus $z = z'$.

So the point z is the unique common fixed point of SA and TB. Similarly we prove w is a unique common fixed point of BS and AT.

Remark :2.11 : If we put A = B, S = T in the above theorem 2.10, we get the following corollary.

Corollary 2.12: Let (X, d_1) and (Y, d_2) be two complete metric spaces. Let A, B be mappings of X into B(Y) and S, T be mappings of Y into B(X) satisfying the inequalities.

$$\delta_1(TAx, TAx') \leq \lambda . \max\{ \delta_1(x, x'), \delta_1(x, TAx), \delta_2(Ax, Ax'), \frac{\delta_1(x, TAx')}{2}, \frac{\delta_1(TAx, x')}{2}$$

$$[\delta_1(x, TAx).\delta_1(x', TAx')]/ \delta_1(x, x') \}$$

$$\delta_2(ATy, ATy') \leq \lambda . \max\{ \delta_2(y, y'), \delta_2(y, ATy), \delta_1(Ty, Ty'), \frac{\delta_2(y, ATy')}{2}, \frac{\delta_2(ATy, y')}{2}$$

$$[\delta_2(y, ATy).\delta_2(y', ATy')]/ \delta_2(y, y') \}$$

for all x, x′ in X and y, y′ in Y where $0 \leq \lambda < 1$. If one of the mappings A and T is continuous, then TA has a unique fixed point z in X and AT has a unique fixed point w in Y. Further,
Az = Bz = {w} and Sw = Tw = {z}.

REFERENCES

[1]   B. Fisher, Fixed point on two metric spaces, *Glasnik Mate., 16(36),* (1981), 333-337.

[2]   V. Popa , Fixed points on two complete metric spaces,.Rad.Prirod.Mat.FizSer.Mat.Univ.*Novom Sadu, 21*(1991),83–93.

[3]   Abdulkrim Aliouche, Brain Fisher, A related fixed point theorem for two pairs of mappings on two complete metric spaces, *Hacettepe Journal of Mathematics and Statistics 34,(*2005), 39-45.

[4]   Y.J. Cho , S.M. Kang , S.S. Kim , Fixed points in two metric spaces, *NoviSad J.Math., 29(1),*(1999), 47-53.

[5]   Y.J Cho, Fixed points for compatible mappings of type *Japonica, 38(3),* (1993), 497- 508.

[6]   A. Constantin , Common fixed points of weakly commuting Mappings in 2- metric spaces, *Math. Japonica, 36(3),* (1991), 507-514

[7]   A. Constantin , On fixed points in noncomposite metric spaces, *Publ. Math. Debrecen, 40(3-4),* (1992), 297-302.

[8]   B. Fisher , Related fixed point on two metric spaces, *Math. Seminor Notes, Kobe Univ.,10* (1982), 17-26.

[9]   T. Veerapandi , T.Thiripura Sundari , Paulraj Joseph J., Some fixed point theorems in two complete metric spaces, International Journal of mathematical archive, 3(3), (2012), 826- 837.

[10]   T. Veerapandi , T. Thiripura Sundari , J. Paulraj Joseph , Some common fixed point theorems in two complete metric spaces, *International Journal of mathematical archive, 4(5),* (2013), 251- 273.

[11]   Xianjiu Huang, Chuanxi Zhu, Xi Wen, Fixed point theorem on two complete cone metric Spaces, *Ann Univ Ferrara 57,* (2011), 431-352.

[12]   S. B. Nadler, Jr., Multi-valued contraction mapping*, Pacific J. Math., vol. 30,* 1969, 475– 488.

[13]   B. Fisher, and D. Turkoglu , Related fixed point for set valued mappings on two metric spaces, *Internat. J.Math.Math.Sci. 23*(2000), 205–210.

[14]   Z. Liu , Q. Liu , Stationary points for set-valued mappings on two metric spaces, *Rostok Math. Kolloq. 55*(2001), 23–29.

[15]   V.Popa , Stationary Points for Multifunctions on Two Complete Metric Spaces, *Mathematica Moravica,8(1),* (2004), 33–38

[16]   B. Fisher, Common fixed points of mappings and set valued mappings, *Rostok Kolloq.8*(1981), 68–77.

Transformer less Boost Converter Topologies with Improved Voltage Gain Operating In Continuous Conduction Mode

Meera Balaraman[1], Jyothi G. K.[2]

[1](Student, Department of Electrical and Electronics, FISAT, MG University, Kerala, India)
[2](Assistant professor, Department of Electrical and Electronics, FISAT, MG University, Kerala,India)

ABSTRACT: *In this project, a new step up converter proposed in a recent work is analyzed, designed, simulated with MATLAB Simulink. Conventional dc–dc boost converters are unable to provide high step-up voltage gains due to the effect of power switches, rectifier diodes, and the equivalent series resistance of inductors and capacitors. This paper proposes transformer less dc–dc converters to achieve high step-up voltage gain without an extremely high duty ratio. In the proposed converters, two inductors with the same level of inductance are charged in parallel during the switch-on period and are discharged in series during the switch-off period. The structures of the proposed converters are very simple.*

Keywords: *DC-DC boost converter, high step up voltage gain*, *DC–DC boost converter, high step-up voltage gain.*

I. Introduction

Power electronics is:" The technology associated with the efficient conversion, control and conditioning of electric power by static means from its available input form into the desired electrical output form." The goal of power electronics is to realize power conversion from an electrical source to an electrical load in a highly efficient, highly reliable and cost-effective way.

The application of power electronics includes a variety of fields such as energy storage, transmission and distribution, pollution avoidance, communication, computer systems, propulsion and transportation .Power electronics modules are key units in power electronics system. As the integration of power switches, device gating, sensors, controls and actuators, power modules can be used to perform energy transfer, storage and conditioning. According to the type of the input and output power, power conversion systems can be classified into four main categories, namely:
 AC to DC (rectification)
 DC to AC (inversion)
 AC to AC(cycloconversion)
 DC to DC(chopping)

A DC-to-DC converter is a device that accepts a DC input voltage and produces a DC output voltage which is-typically- at a different voltage level than the input. Apart from voltage level conversion, DC-to-DC converters are used to provide noise isolation, power bus regulation. The typical usage of DC-DC converters is to convert unregulated dc voltage to regulated or variable dc voltage at the output. The output voltage in DC-DC converters is generally controlled using a switching concept. In fact, early DC-DC converters were known as choppers with silicon-controlled rectifiers (SCRs) used as the switching mechanism.

Modern DC-DC converters employ insulated gate bipolar transistors (IGBTs) and metal oxide silicon field effect transistors (MOSFETs) as they possess attractive switching capabilities, especially in terms of switching frequency and power ratings. Based on their performances, DC-DC converters are subcategorized into three general types; Buck Converters which convert from a voltage level to a relatively lower voltage level. Conversely, Boost Converters transform to higher voltage level. The third one is buck-boost converter which can either be a buck or a boost converter based on its control signals.

A DC–DC converter with a high step-up voltage gain is used for many applications, such as high-intensity discharge lamp ballasts for automobile headlamps, fuel-cell energy conversion systems, solar-cell energy conversion systems, and battery backup systems for uninterruptible power supplies. Theoretically, a dc–dc boost converter can achieve a high step up voltage gain with an extremely high duty ratio. However, in practice, the step-up voltage gain is limited due to the effect of power switches, rectifier diodes, and the equivalent series resistance (ESR) of inductors and capacitors. Moreover, the extremely high duty-ratio

operation will result in a serious reverse-recovery problem. Many topologies have been presented to provide a high step-up voltage gain without an extremely high duty ratio.

A dc–dc flyback converter is a very simple structure with a high step-up voltage gain and an electrical isolation, but the active switch of this converter will suffer a high voltage stress due to the leakage inductance of the transformer. For recycling the energy of the leakage inductance and minimizing the voltage stress on the active switch, some energy-regeneration techniques have been proposed to clamp the voltage stress on the active switch and to recycle the leakage-inductance energy.

For recycling the energy of the leakage inductance and minimizing the voltage stress on the active switch, some energy-regeneration techniques have been proposed toclamp the voltage stress on the active switch and to recycle the leakage-inductance energy. The coupled-inductor techniques provide solutions to achieve a high voltage gain, a low voltage stress on the active switch, and a high efficiency without the penalty of high duty ratio
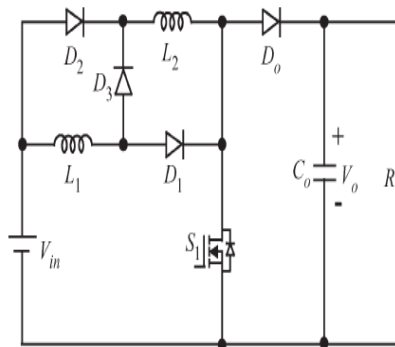
Figure. 1. Transformerless dc–dc high step-up converter.

The modified boost type with switched-inductor technique is shown in Fig. 1 The structure of this converter is very simple. Only one power stage is used in this converter. However, this converter has two issues:

1). Three power devices exist in the current-flow path during the switch-on period, and two power devices exist in the currentflow path during the switch-off period, and
2). The voltage stress on the active switch is equal to the output voltage.

II. Proposed Converters

Figure 2 shows the three proposed topologies. These three proposed dc–dc converters utilize the switched inductor technique, in which two inductors with same level of inductance are charged in parallel during the switch-on period and are discharged in series during the switch-off period, to achieve high step-up voltage gain without the extremely high duty ratio. The operating principles and steady-state analysis are discussed in the following sections. To analyze the steadystate characteristics of the proposed converters, some conditions are assumed as follows:

1) All components are ideal—the ON-state resistance RDS(ON) of the active switches, the forward voltage drop of the diodes, and the ESRs of the inductors and capacitors are ignored
2) all capacitors are sufficiently large, and the voltages across the capacitors can be treated as Constant

(a)
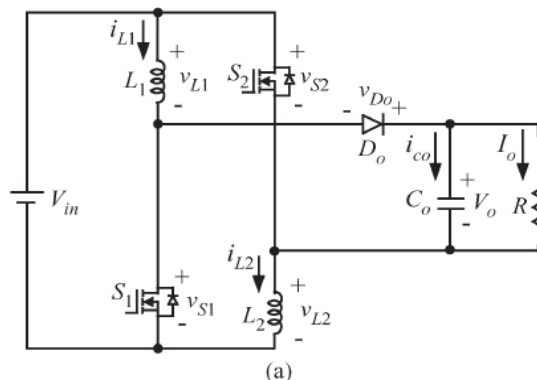
Figure 2(a) proposed converter 1
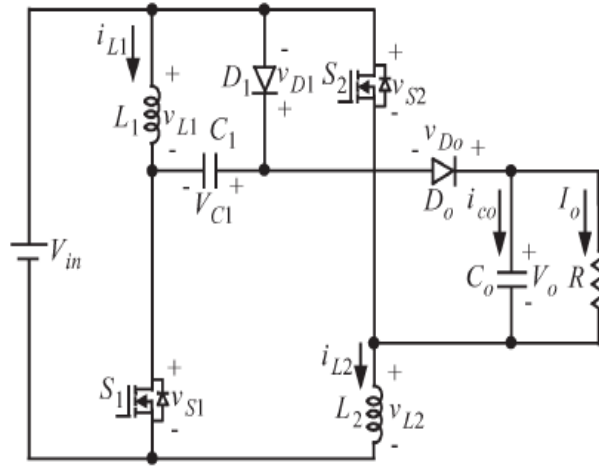
Figure 2(b) proposed converter 2
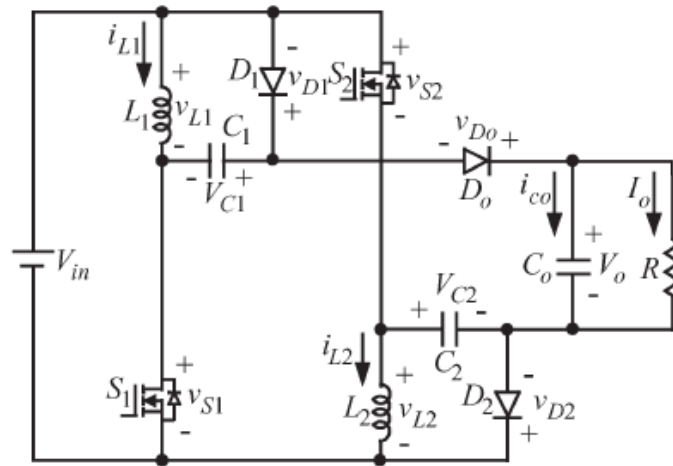
Figure 2(c) proposed converter 3

2.1 PROPOSED CONVERTER 1

Figure 2(a) shows the circuit configuration of the proposed converter I, which consists of two active switches ($S1$ and $S2$), two inductors ($L1$ and $L2$) that have the same level of inductance, one output diode Do, and one output capacitor Co. Switches $S1$ and $S2$ are controlled simultaneously by using one control signal. Figure 3 shows some typical waveforms obtained during continuous conduction mode (CCM)
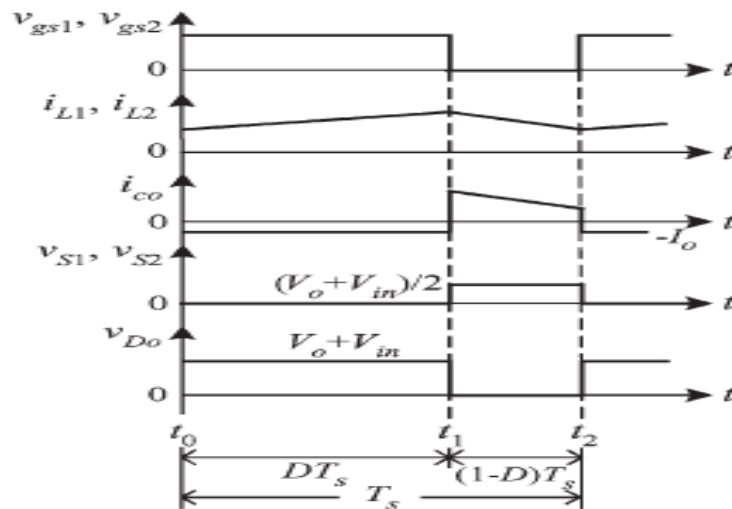
Figure 3 waveforms of converter 1

2.1 A. CCM Operation

The operating modes can be divided into two modes, defined as modes 1 and 2. Figure 3 Some typical waveforms for the proposed converter I.CCM operation.

1) Mode 1 [$t0$, $t1$]. During this time interval, switches $S1$ and $S2$ are turned on. The equivalent circuit is shown in Fig. 4(a). Inductors $L1$ and $L2$ are charged in parallel from the dc source, and the energy stored in the output capacitor Co is released to the load. Thus, the voltages across $L1$ and $L2$ are given as

$$vL1 = vL2 = Vin \ldots\ldots\ldots\ldots\ldots\ldots\ldots\ldots\ldots (3.1.1)$$

2) Mode 2 [$t1$, $t2$]. During this time interval, $S1$ and $S2$ are turned off. The equivalent circuit is shown in Figure. 4(b). The dc source, $L1$, and $L2$ are series connected to transfer the energies to Co and the load. Thus, the voltages across $L1$ and $L2$ are derived as

$$vL1 = vL2 = Vin - Vo/2 \ldots\ldots\ldots\ldots\ldots\ldots(3.1.2)$$

By using the volt–second balance principle on $L1$ and $L2$, the following equation can be obtained:

$$\int_{0}^{DTs} Vin \; dt + \int_{DTs}^{Ts} \frac{Vin-Vo}{2} \; dt = 0 \ldots\ldots\ldots\ldots\ldots\ldots\ldots\ldots\ldots(3.1.3)$$

By simplifying (3), the voltage gain is given by

$$\frac{Vo}{Vin} = \frac{1+D}{1-D} \ldots\ldots\ldots\ldots\ldots\ldots\ldots..\ldots\ldots\ldots\ldots\ldots\ldots\ldots..(3.1.4)$$

Voltage across s1 and s2 and diode is given by:

$$Vs1 = Vs2 = VD1 = \frac{V0}{2} \ldots\ldots\ldots\ldots\ldots\ldots\ldots\ldots\ldots..\ldots\ldots.(3.1.5)$$
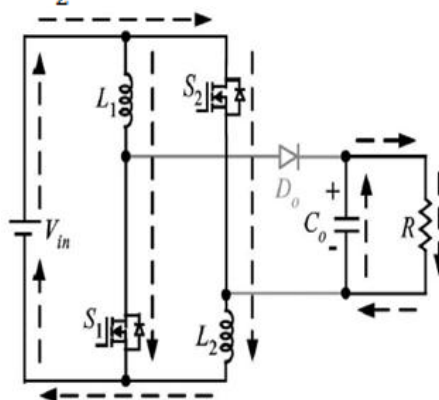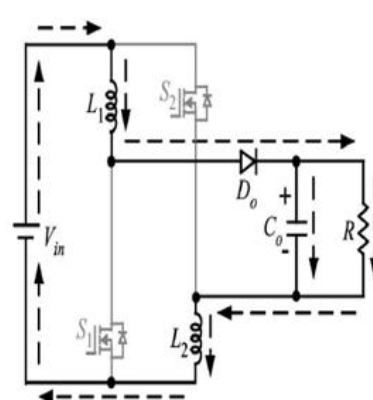
Figure 4(a); mode 1   Figure 4(b): mode 2

2.2 PROPOSED CONVERTER 2

Figure 2(b) shows the circuit configuration of the proposed converter II, which is the proposed converter I with one voltage-lift circuit.Thus, two inductors ($L1$ and $L2$) with the same level of inductance are also adopted in this converter. Switches $S1$ and $S2$ are controlled simultaneously by one control signal.
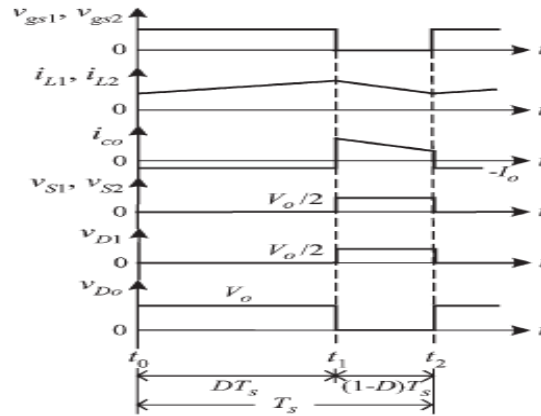
Figure 5 typical waveforms of proposed converter operating in CCM

2.2 A. CCM Operation

The operating modes can be divided into two modes, defined as modes 1 and 2.

1) **Mode 1 [*t0, t1*].**

   During this time interval, *S*1 and *S*2 are turned on. The equivalent circuit is shown in Fig. 6(a). *L*1 and *L*2 are charged in parallel from the dc source, and the energy stored in *Co* is released to the load. Moreover, capacitor *C*1 is charged from the dc source. Thus, the voltages across *L*1, *L*2, and *C*1 are given as

   $$vL1 = vL2 = VC1 = Vin.$$

2) **Mode 2 [*t1, t2*].**

   During this time interval, *S*1 and *S*2 are turned off. The equivalent circuit is shown in Fig.6(b). The dc source, *L*1, *C*1, and *L*2 are series connected to transfer the energies to *Co* and the load. Thus, the voltages across *L*1 and *L*2 are derived as

$$VL1 = VL2 = \frac{Vin+Vc1-V0}{2} = \frac{2Vin-Vo}{2} \dots\dots\dots\dots\dots\dots\dots\dots\dots\dots\dots\dots(3.2.6)$$

By using the volt–second balance principle on *L*1 and *L*2, the following can be obtained:

$$\int_0^{DTs} Vin\, dt + \int_{DTs}^{Ts} \frac{2Vin-V0}{2}\, dt =0 \dots\dots\dots\dots\dots\dots\dots\dots\dots\dots\dots\dots\dots\dots\dots\dots(3.2.7)$$

So the voltage gain is given by

$$\frac{V0}{Vin} = \frac{2}{1-D} \dots\dots\dots\dots\dots\dots\dots\dots\dots\dots\dots\dots\dots\dots\dots\dots\dots\dots\dots\dots(3.2.8)$$

The voltage stress on switches and diodes is given by:

$$VS1 = VS2 = VD1 = \frac{Vo}{2} \quad \dots\dots\Big\}\dots\dots\dots (3.2.9)$$
$$VDo = Vo$$
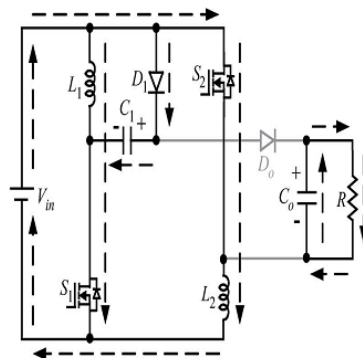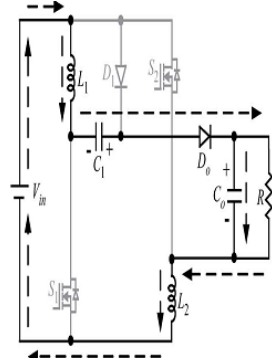
Figure 6(a): mode1   Figure 6(b): mode 2

2.3 PROPOSED CONVERTER 3

Figure. 2(c) shows the circuit configuration of the proposed converter III, which is the proposed converter I with two voltage lift circuits. Thus, two inductors (*L1* and *L2*) with the same level of inductance are also adopted in this converter. Switches *S1* and *S2* are controlled simultaneously by one control signal.
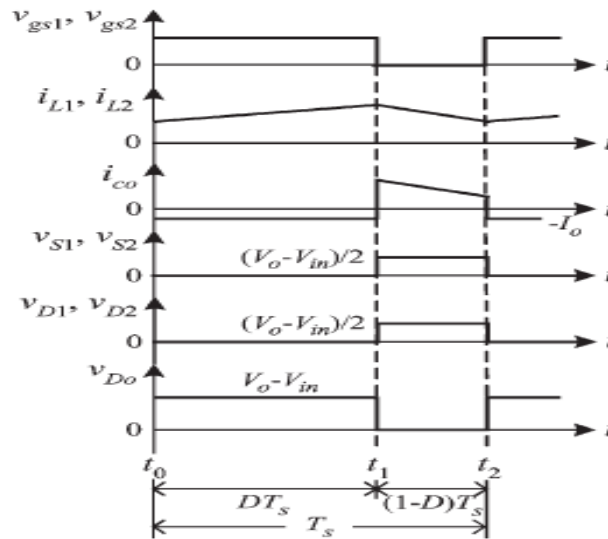
Figure 7: typical wave forms of proposed converter3 operating in CCM

2.3 A. CCM Operation

The operating modes can be divided into two modes, defined as modes 1 and 2.

1) **Mode 1 [*t0, t1*].**
    During this time interval, *S1* and *S2* are turned on. The equivalent circuit is shown in Fig. 8(a). *L1* and *L2* are charged in parallel from the dc source, and the energy stored in *Co* is released to the load.

Moreover, capacitors *C1* and *C2* are charged from the dc source. Thus, the voltages across *L1*, *L2*, *C1*, and *C2* are given as

$$vL1 = vL2 = VC1 = VC2 = Vin \dots\dots\dots\dots\dots\dots\dots\dots\dots\dots(3.3.10)$$

2) **Mode 2 [*t1, t2*].**
    During this time interval, *S1* and *S2* are turned off. The equivalent circuit is shown in Fig. 8(b). The dc source, *L1*, *C1*, *C2*, and *L2* are series connected to transfer the energies to *Co* and the load. Thus, the voltages across *L1* and *L2* are derived as

$$VL1 = VL2 = \frac{Vin + Vc1 + Vc2 - Vo}{2} = \frac{3Vin - Vo}{2} \dots\dots\dots\dots\dots\dots\dots\dots(3.3.11)$$

By using the volt–second balance principle on *L1* and *L2*, the following can be obtained:

$$\int_0^{DTs} Vin \, dt + \int_{DTs}^{Ts} \frac{3Vin - V0}{2} = 0 \dots\dots\dots\dots\dots\dots\dots\dots\dots\dots(3.3.12)$$

Voltage gain of the circuit is given by

$$\frac{Vo}{Vin} = \frac{3 - D}{1 - D} \dots\dots\dots\dots\dots\dots\dots\dots\dots\dots\dots\dots\dots\dots(3.3.13)$$

Voltage stress across switches and diodes is given by:

$$VS1 = VS2 = VD1 = VD2 = \frac{Vo - Vin}{2} \dots \left\} \dots\dots\dots\dots\dots\dots\dots\dots(3.3.14)$$

$$VD0 = V0 - Vin$$
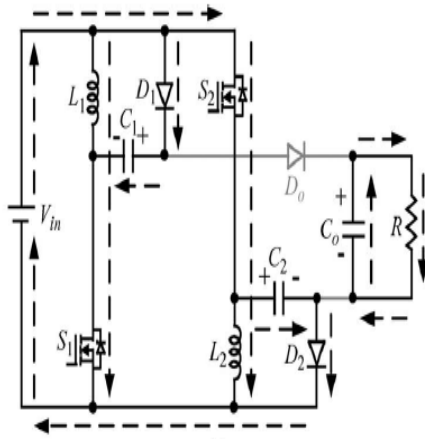
Figure 8(a): mode 1
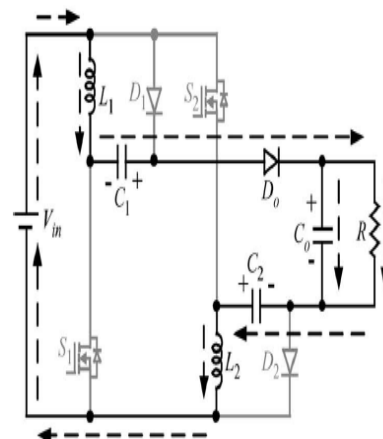
Figure 8(b):mode 2

III. Comparison of Proposed Converter and Boost Converter

The voltage stresses on the active switch and the voltage gains of the boost converter and the proposed converters are summarized in Table 4.1. The voltage stresses on the active switch of the three proposed converters are less than the voltage stress on the active switch of the boost converter, and thus, the active switches with low voltage ratings can be selected. Moreover, the curves of the voltage gain of the boost converter and the proposed converters

Table4.1: Comparison of Voltage Gain and Voltage Stress on Active Switch for Boost Converter and Three Proposed Converters

	GAIN	VOLTAGE STRESS
Boost converter	$\dfrac{1}{1-D}$	$V0$
Proposed converter 1	$\dfrac{1+D}{1-D}$	$\dfrac{V0+Vin}{2}$
Proposed converter 2	$\dfrac{2}{1-D}$	$\dfrac{V0}{2}$
Proposed converter 3	$\dfrac{3-D}{1-D}$	$\dfrac{V0-Vin}{2}$

IV. Simulation Results

This section carry simulation result of the improved topology by using MATLAB Simulink the parameter values that are used are

- L1= L2=100μH
- Fs(switching frequency)=100kHZ
- Co=33μF
- C1=C2=47μF
- Ro=250
- VO/Vin = (1+D)/(1-D) = 100/12
  . ' . D= 78.57%

4.1 PROPOSED CONVERTER1
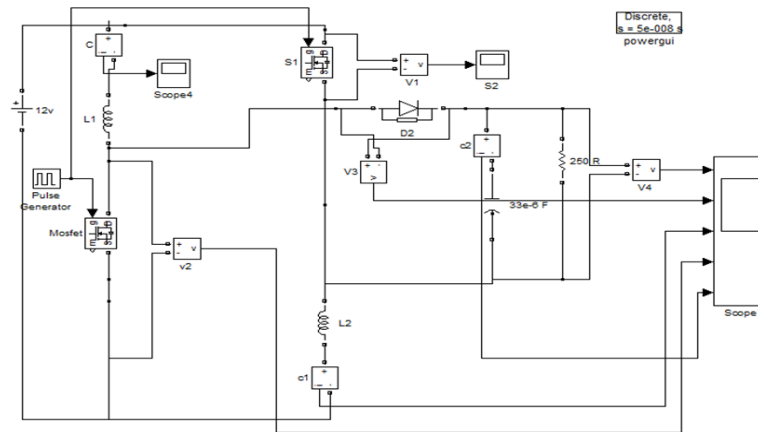
Figure 4.1.1 Simulation block diagram
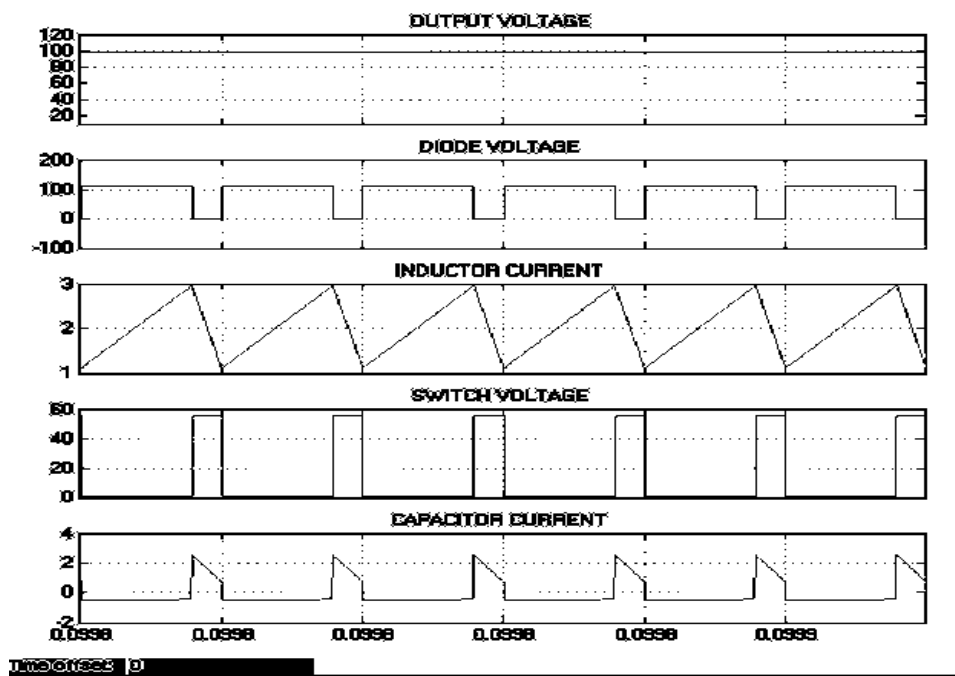
Figure 4.1.2 Output waveforms

4.2. PROPOSED CONVERTER 2
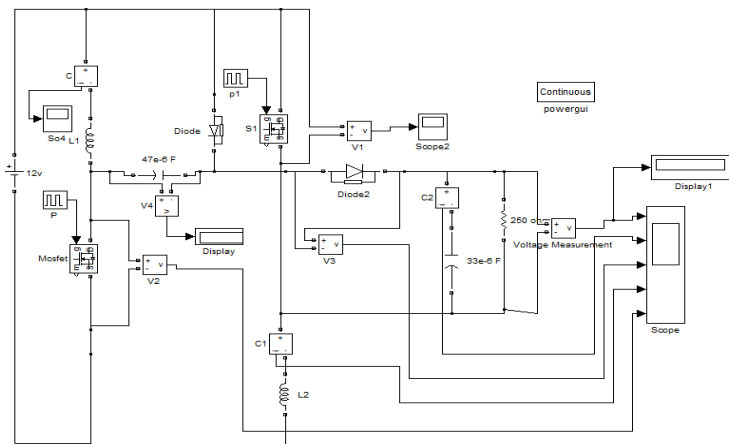
Figure 5.2.1: simulation block diagram

Figure 4.2.2 output waveforms

4.3 PROPOSED CONVERTER 3

Figure 4.3.1: simulation block diagram

Figure 4.3.2:0utput waveforms
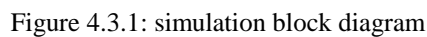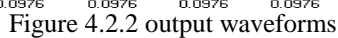
4.4 BASIC CONVERTER
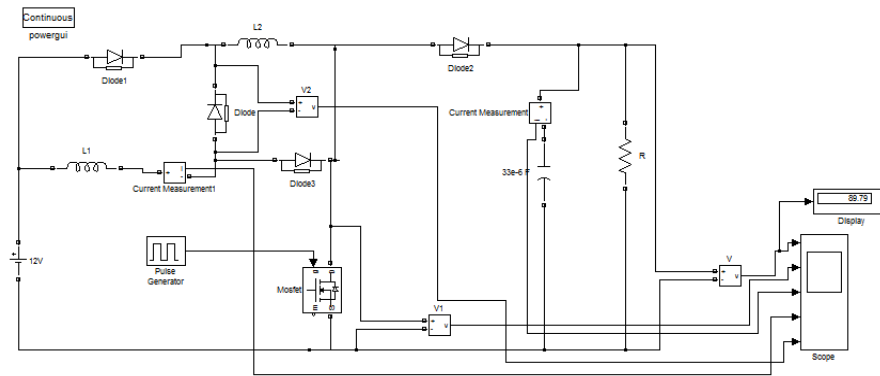
Figure 4.4.1: simulation block diagram
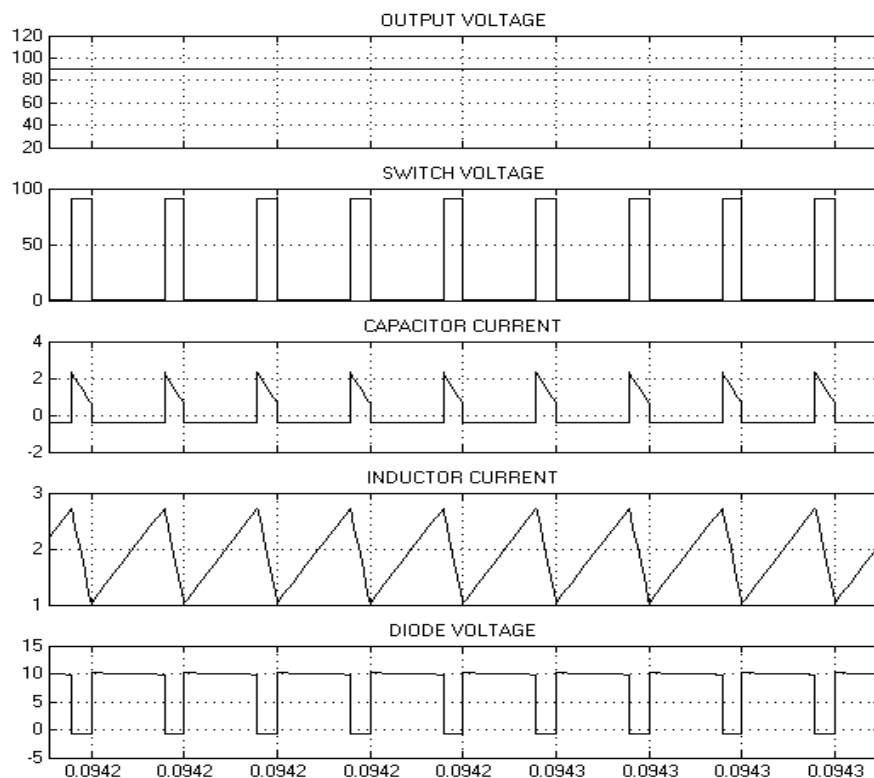
Figure 4.4.2: output waveforms

V. Conclusion

DC-DC converters employ insulated gate bipolar transistors (IGBTs) and metal oxide silicon field effect transistors (MOSFETs) as they possess attractive switching capabilities, especially in terms of switching frequency and power ratings. DC- DC switching converters are becoming popular in industrial area and these converters suitable for applications where the output DC voltage needs to be larger than the DC input and can offer technical advantages economic.

This project has studied three Transformerless topologies with simple structures to reduce the power losses by decrease the switch voltage stress. The structures of the proposed converters are very simple. Since the voltage stresses on the active switches are low.

REFERENCES

[1]   B. Bryant and M. K. Kazimierczuk, "Voltage-loop power-stage transfer functions with MOSFET delay for boost PWM converter operating in CCM," IEEE Trans. Ind. Electron., vol. 54, no. 1, pp. 347–353, Feb. 2007.

[2]   X. Wu, J. Zhang, X. Ye, and Z. Qian, "Analysis and derivations for a family ZVS converter based on a new active clamp ZVS cell," IEEE Trans. Ind. Electron., vol. 55, no. 2, pp. 773–781, Feb. 2008.

[3]   D. C. Lu, K. W. Cheng, and Y. S. Lee, "A single-switch continuousconduction- mode boost converter with reduced reverse-recovery and switching losses," IEEE Trans. Ind. Electron., vol. 50, no. 4, pp. 767–776, Aug. 2003.

[4]   N. P. Papanikolaou and E. C. Tatakis, "Active voltage clamp in flyback converters operating in CCM mode under wide load variation," IEEE Trans. Ind. Electron., vol. 51, no. 3, pp. 632–640, Jun. 2004.

[5]   B. R. Lin and F. Y. Hsieh, "Soft-switching zeta–flyback converter with a buck–boost type of active clamp," IEEE Trans. Ind. Electron., vol. 54, no. 5, pp. 2813–2822, Oct. 2007.

[6]   C. M. Wang, "A novel ZCS-PWM flyback converter with a simple ZCSPWM commutation cell," IEEE Trans. Ind. Electron., vol. 55, no. 2, pp. 749–757, Feb. 2008.

[7]   T. F. Wu, Y. S. Lai, J. C. Hung, and Y. M. Chen, "Boost converter with coupled inductors and buck–boost type of active clamp," IEEE Trans. Ind. Electron., vol. 55, no. 1, pp. 154–162, Jan. 2008.

[8]   K. C. Tseng and T. J. Liang, "Novel high-efficiency step-up converter," Proc. Inst. Elect. Eng. —Elect. Power Appl., vol. 151, no. 2, pp. 182–190,Mar. 2004.

[9]   R. J. Wai, C. Y. Lin, R. Y. Duan, and Y. R. Chang, "High-efficiency DC–DC converter with high voltage gain and reduced switch stress," IEEE Trans. Ind. Electron., vol. 54, no. 1, pp. 354–364, Feb. 2007.

[10] J. W. Baek, M. H. Ryoo, T. J. Kim, D. W. Yoo, and J. S. Kim, "High boost converter using voltage multiplier," in Proc. IEEE IECON, 2005, pp. 567–572.

[11] Q. Zhao and F. C. Lee, "High-efficiency, high step-up DC–DC converters," IEEE Trans. Power Electron., vol. 18, no. 1, pp. 65–73, Jan. 2003.

[12] R. J. Wai and R. Y. Duan, "High-efficiency DC/DC converter with high voltage gain," Proc. Inst. Elect. Eng.—Elect. Power Appl., vol. 152, no. 4,

[13] G. A. L. Henn, L. H. S. C. Barreto, D. S. Oliveira, Jr., and E. A. S. Silva, "A novel bidirectional interleaved boost converter with high voltage gain," in Proc. IEEE APEC, 2008, pp. 1589–1594.

[14] G. V. T. Bascope, R. P. T. Bascope, D. S. Oliveira, Jr., S. A. Vasconcelos, F. L. M. Antunes, and C. G. C. Branco, "A high step-up DC–DC converter based on three-state switching cell," in Proc. IEEE ISIE, 2006, pp. 998–1003.

[15] L. Huber and M. M. Jovanovic, "A design approach for server power supplies for networking applications," in Proc. IEEE APEC, 2000, pp. 1163–1169.

[16] L. H. Barreto, E. A. Coelhp, V. J. Farias, J. C. Oliveira, L. C. Freitas, and J. B. Vieira, "A quasi-resonant quadratic boost converter using a single resonant network," IEEE Trans. Ind. Electron., vol. 52, no. 2, pp. 552– 557, Apr. 2005.

[17] F. L. Luo and H. Ye, "Positive output multiple-lift push–pull switchedcapacitor Luo converters," IEEE Trans. Ind. Electron., vol. 51, no. 3, pp. 594–602, Jun. 2004.

[18] F. L. Luo, "Six self-lift DC–DC converters, voltage lift technique," IEEE Trans. Ind. Electron., vol. 48, no. 6, pp. 1268–1272, Dec. 2001.

[19] R. Gules, L. L. Pfitscher, and L. C. Franco, "An interleaved boost DC–DC converter with large conversion ratio," in Proc. IEEE ISIE, 2003, pp. 411–416.

[20] D. Zhou, A. Pietkiewicz, and S. Cuk, "A three-switch high-voltage converter," IEEE Trans. Power Electron., vol. 14, no. 1, pp. 177–183, Jan. 1999.

Numerical (CFD) Analysis of Thermal Spray Coating Process

T. Raja jayasingh[1], T. Raja jeyaseelan[2], C. Kannan[3], M. Ganesh Karthikeyan[4]

[1, 3, 4] *(Assistant Professors Mechanical Department, TRP Engineering College, Trichy, India)*
[2] *(Assistant Professor Mechanical Department, the Rajas Engineering College Vadakkankulam)*

ABSTRACT: *numerical study of Thermal spraying process is required for optimizing performance and gun design for spraying various materials. Cold spray process is a new technique of thermal spray process which is used in industries and very limited data is available. This paper presents an investigation on the powder stream characteristics in cold spray supersonic nozzles. This work describes a detailed study of the various parameters, namely applied gas pressure, gas temperature, size of particles, outlet gas velocity, dimensions of the nozzle on the outlet velocity of the particles. A model of a two-dimensional axisymmetric nozzle was used to generate the flow field of particles (copper or tin) with the help of a carrier gas (compressed) stream like nitrogen or helium flowing at supersonic speed. Particles are dragged by the carrier gas up to high velocity magnitudes, resulting in severe plastic deformation processes upon impact with a solid substrate positioned at the distance SoD (Standoff Distance).*

Keywords: Carrier gas, Cold spray, Critical velocity, Substrate, Stand- off distance, FLUENT.

I. Introduction

Over the past few years new spraying techniques for coating purposes have been experimentally and computationally analyzed for better understanding of the thermo-mechanical processes involved. Cold spray technology is attracting the researchers and industries worldwide because of its advantages over the other spraying methods [1]. The cold spray dynamic technology is a new technique for coating metals with very small metal powder particles using compressed gas stream propulsion. This technology was developed with the aim of producing pore free and non oxidized coatings which were not possible with other conventional coating techniques like HVOF, Plasma spraying and arc spraying. Due to the high velocity of particles, this process gives a highly bonded coating with good adhesion between particles and substrate, low friction coefficient, high thermal and electrical conductivity, and excellent corrosion and oxidation resistance [2].

Many companies and researchers worldwide are working on cold spray. In USA, research on cold spray technology was first undertaken by a consortium formed under the auspices of the National Centre for Manufacturing Sciences (NCMS). After that many research centers became interested in this technology e.g. the Institute of Theoretical and Applied Mechanics of the Russian Academy of Science, Sandia National Laboratories and Pennsylvania State University [3]. Sandia National Lab had funded companies like ASB Industries, Ford, K-Tech, Pratt & Whitney to a value of 0.5 million U.S. dollars a year for 3 years to do R&D and develop this technology. Pennsylvania State University have received grants from the U.S. Navy to do R&D on the cold spray process and develop an anti skid coating [4].

1.1 Thermal Spraying

Thermal spray is the process in which a metal or alloy in molten or semi molten state is used to make a layer on a substrate. The thermal spray technique was first used in the early 1900s when Dr Schoop (refer to the Master patent of Schoop technology) [5] used a flame as a heat source. Initially it was practiced on metals with low melting point and after that it was progressively extended to metals with high melting point [5]. For making the deposit in thermal spraying a stream of molten metal particles strike a substrate, become flattened and then undergo rapid solidification and quenching. Every droplet spreads to make its own layer and these layers join to make a deposit of thermally sprayed material. In this process voids are formed in the deposit mainly because of incomplete filling or incomplete wetting of the molten metal and during the quenching of brittle materials micro cracks are formed after the solidification of molten material. These affect the mechanical properties like elastic modulus and stress at failure and physical properties like thermal conductivity [6].

1.1.1 Cold Spray Process

The phenomenon of cold spray was discovered during an aeronautical investigation in the 1980's. When dusty gases were used in shock tube experiments, the particles were observed to stick on the substrate. This process was undesirable but was recognized to be useful because particles of ductile metals or alloys could be bonded onto metal surfaces, glass or ceramics at impact velocities ranging from 400 to 1200 m/s. This is how coatings are made on work pieces [15]
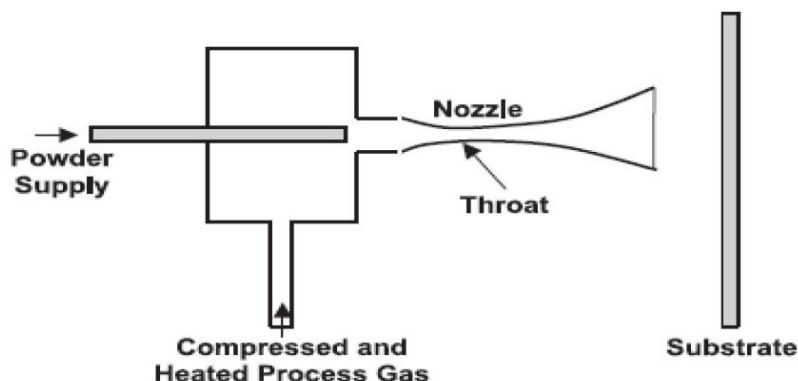

Figure 1.1: Schematic diagram of cold spraying system

The cold spray process or cold gas-dynamic process is a coating process utilizing high speed metal or alloy particles ranging from 1 to 50 μm in size, with a supersonic jet of compressed gas with a velocity ranging from 300 to 1200 m/s on the surface of the work piece is shown in Fig.1.1. The coating formed by this process depends upon a combination of factors like particle velocity, temperature and size. The powder particles in this process are accelerated by a supersonic gas jet at a temperature lower than its melting point, thus reducing many effects which occur in high temperature spraying like oxidation at high temperature, melting of the substrate or spray particles, crystallization, evaporation, stress generation, gas release and other related problems [16].

Studies on cold spraying shows that the most important parameter is the velocity of the particles before they strike the substrate. For making a successful coating the particles should strike the substrate at a higher velocity than a critical velocity [17].
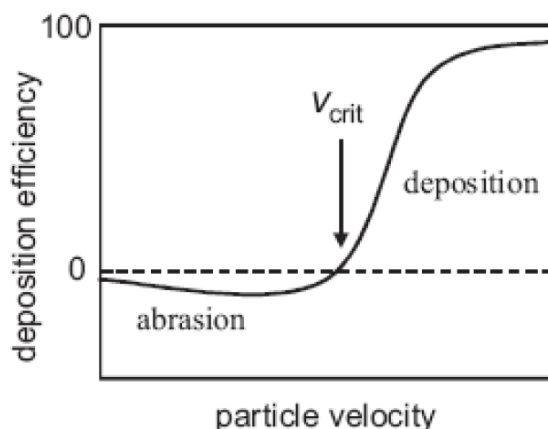
Figure 1.2: Correlation between the particle velocity and deposition efficiency

If the particles strike the substrate at a velocity lower than the critical velocity then the particles will just scratch the surface of the substrate as they do in grit blasting. By increasing the particle velocity the deposition efficiency reaches saturation point which is nearer to 100%. Most of the research related to cold spray is focused on achieving high particle velocity by making new designs of the nozzle used for spraying [17].

1.1.1.1 Reason for Doing Cold Spraying

In the cold spray process, particles ranging in size from 5 to 50μm are used to make a coating by number of layers. The cold spray process is relatively better for making thicker coatings than thermal spraying because there are no thermal stresses involved in it [18]. A most important consideration in introducing new

process to industry is a reduction in the manufacturing cost of components. Most components in industry are fabricated by casting which is the initial step in the production line. The Pratt & Whitney Company as a part of the US Air Force forging supplier has developed a model called value stream analysis which shows that reduction in cost cannot be achieved by reducing the cost of one area in a production line. Pratt & Whitney also developed a model for Laser Powder Deposition of titanium and this model has been extended to model the cold spray process for titanium [4].

1.1.1.2 Equipment Used in Sprayin
A block diagram of cold spray equipment with a powder heater installed is shown in fig.1.3
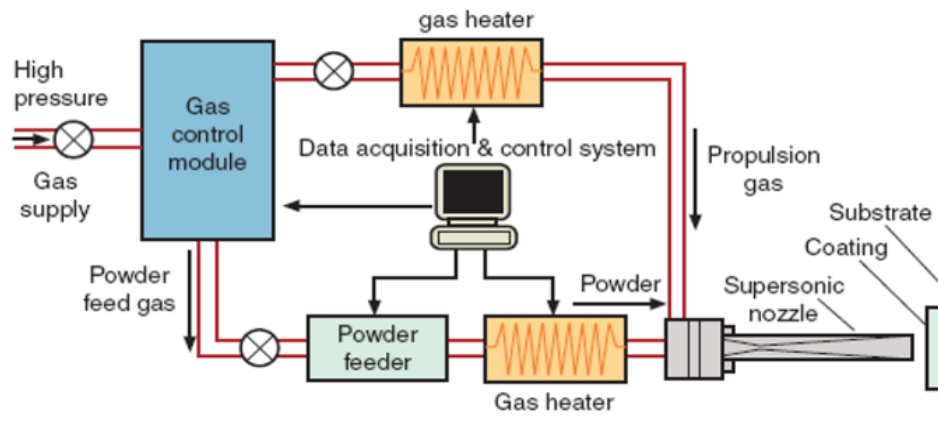
Figure 1.3: The block diagram of cold spraying system

The main parts of the cold spray system involves
1) A gas control module which contains the working gases such as helium, nitrogen, argon, and mixes of these gases and which enter the nozzle at higher pressure.
2) A data acquisition and control system for controlling the gas pressure from the compressor, the powder feed rate into the nozzle and the gas heater that maintains the proper temperature of the gas.[20]
3) A powder feeder which delivers powder in a continuous flow at a mass flow rate of 5 to 10 kg/h to make a uniform coating and improve reliability for measuring deposition efficiency. The powder feeders currently available with features like low maintenance, uniform and accurate powder feeding, low powder wastage, minimal pulsing and easy cleaning.[16]
4) A gas heater is used to heat the gas up to a temperature ranging from 300° to 650°C before it enters the nozzle. Heating the gas eventually increases the powder particles temperature and velocity and hence ensures plastic deformation after they strike a substrate. However the gas temperature at the inlet of the nozzle is below melting point which means particles do not melt during the process.[21]
5) In the coating process, nozzle is the main component for depositing solid-state particles. In the cold spray process, a convergent-divergent De Laval type nozzle is used to accelerate the particles at supersonic speed by the gas flow. After leaving the nozzle at high velocity, the particles impinge on the work piece and undergo plastic deformation because of collision and bonding with the work piece surface and other particles to make a coating. Studies show [22] that better injection through the nozzle gives the following benefits in coating formation:-
    a) It enables the use of an increased gas temperature for the cold spray process.
    b) The dwell time of the sprayed particles can be increased before they enter the convergent divergent nozzle and heat the particle.
    c) More powder gas flow can be used without clogging the nozzle hence increasing the effective temperature of propellant gas [22].

1.1.1.3 Factors Affecting the Cold Spray Process
Recent research on the cold spray process shows that successful coating formation on a substrate depends upon the velocity of the particles exiting the nozzle and striking the surface of work piece. The velocity further depends upon factors such as gas temperature, gas pressure, type of gas used [23], the size of the particles used for spraying and the nozzle design which includes the throat diameter, inlet diameter, outlet diameter, convergent and divergent length of the nozzle [24].

1.1.1.3.1 Effect of Gas Temperature

Previous studies have found that if the temperature of the carrier gas is increased then it directly affects the velocity of the particles [21] [22] [25] and it also results in higher deposition efficiency of the particles on the substrate. Compressed gas enters the convergent divergent nozzle with an inlet pressure of around 27-35 bar to get the supersonic velocity. The solid powder particles are introduced in the nozzle upstream (convergent portion) and are accelerated by the rapidly expanding gas in the divergent part of the nozzle. The carrier gas is often preheated to get high gas flow velocities through the nozzle. In the cold spray process the gas is first heated to a temperature ranging from 300 K to 900 K. Particles when introduced into a hot gas stream, are in contact with the gas for a shorter time, so that when the gas expands in the divergent part its temperature decreases. In this process the temperature of the particles remains below their melting temperature [26].The main gases which are used for cold spraying are helium and nitrogen because of their lower molecular weight and larger specific heat ratio.

The main consideration arising from increasing the temperature of the gas is the robustness of the nozzle material, which results in getting limited particle velocity and temperature. The German company CGT commercially manufactured a tungsten carbide MOC-nozzle which can spray copper particles at 600° C at a pressure of 30 bars without plugging and erosion of the nozzle material [25].The main advantage of a high impact temperature is that it decreases the critical velocity of the spray material because of thermal softening. The deposition efficiency also depends upon the temperature of the carrier gas. It was found that when nitrogen is used to spray titanium particles the critical temperature is 155 °C, below this temperature no particle deposition took place. When the temperature was further increased from this critical temperature, the deposition efficiency also increased rapidly, especially when the temperature of nitrogen exceeded 215 °C.

1.1.1.3.2 Effect of Gas Pressure

In an experiment performed by M. Fukumoto*et al* [27] the effect of the gas inlet pressure on the deposition efficiency was investigated and the results showed that deposition efficiency increases with increase in the gas pressure.

Cold spray systems are subdivided into two categories high pressure systems and low pressure systems on the basis of gas pressure. Fig.1.4 shows the higher pressure system. A separate gas compressor is required in these systems andgases such as helium is used in this system because of its low molecular weight to achieve very high particle velocity.Fig.1.5 shows the lower pressure system. In a low pressure system a powder stream is injected into the nozzle at the point where gas has expanded to low pressure. Since no pressurized feeder is required in this system, it is often used in portable cold spray systems.
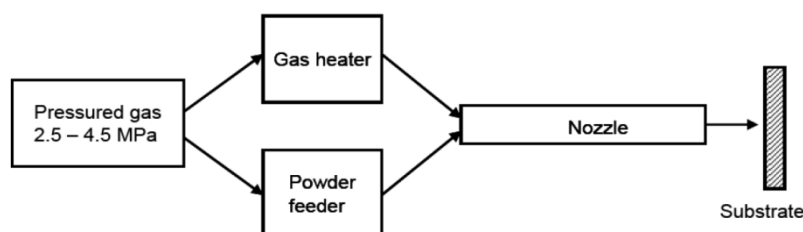
Figure 1.4: High pressure system
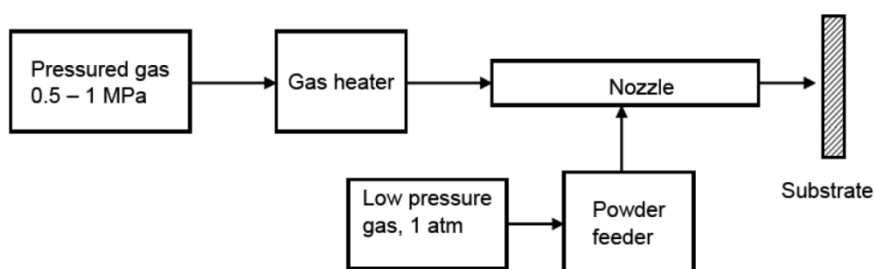
Figure 1.5: Low pressure system

1.1.1.3.3 The Effect of the Type of Gas

In cold spray processes the type of gas used to spray powder particles plays an important role in the acceleration of particles. In most cases nitrogen, helium, air or the mixture of air and helium or air and nitrogen are used as carrier gasses because of their lower molecular weight [28].

Initially experiments using helium as a carrier gas were very successful in achieving high adhesion and corrosion resistant coatings. Cold spray process parameters were also developed with nitrogen to reduce the costs while maintaining satisfactory coating performance [29]. In one-dimensional flow theory the Mach number at the throat is assumed to be unity and the velocity of gas can be calculated from:

$$V = \sqrt{\gamma R T}$$

Where γ is specific heat ratio, T is temperature of gas and R is the specific gas constant (the universal gas constant is divided by the gas molecular weight). The above equation shows why it is often found that helium makes a better carrier gas for cold spraying. It has a smaller molecular weight and higher specific heat ratio [23]. The specific heat ratios of nitrogen and helium are 1.4 and 1.66 respectively. The specific gas constants for nitrogen and helium are 296.8 J/Kg K and 2,077 J/Kg K respectively. According to the above equation the velocity of nitrogen will be lower than the velocity of helium, and when the temperature of the gas is increased the gas velocity increases. Subsequently the particle velocity also increases. The drag force on particles increases when gas pressure is increased because higher gas pressure increases the density of the gas [24].

1.1.1.3.4 The Effect of Particle Size

Previous study shows that the powder particles used for spraying have a wide size distribution range [28][29][30]. The powder is fed into a gas stream flowing through the nozzle. The acceleration of each particle depends upon its size. Particles cannot make a coating if they are very small in size or light in weight, because then they will follow the flow where as if the powder particles are very heavy or large in size they will not get the kinetic energy from the carrier gas to strike the substrate [30]. Small particles achieve high acceleration and large particles achieve less acceleration. For making a successful powder deposit only the particles with a velocity greater than a critical velocity can contribute to the coating. Hence it is very important to consider the particle size before carrying out cold spraying. The particles size distribution can be expressed by the following Rosin-Rammler formula:

$$Y_d = e^{-\left(\frac{d}{\bar{d}}\right)^n}$$

Where Y_d is the mass fraction and 'n' is the size distribution At high temperatures more plastic deformation occurs in particles when they strike a substrate and this improves deposition efficiency [31]. A previous study shows that the particle temperature reaches maximum value when the diameter of the particle is 10μm. This behaviour is determined by the particle and gas phase heat transfer. There is a maximum temperature profile for the smaller particles because the heat transfer rate is faster for smaller particles. In larger particles, the temperature increases slowly [32].

II. Numerical Methodology

2.1 Geometry
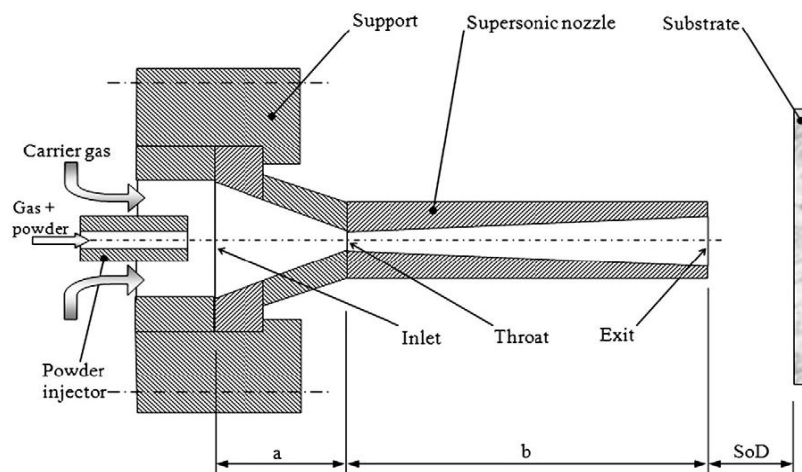
Figure 2.1: Schematic of the Nozzle

A schematic diagram of the cold spray system is shown infig.2.1. The spraying gun of the system comprises a supersonic converging– diverging nozzle and a powder injector. The injector outlet is located near the convergent part of the nozzle because it is a high pressure system. In low pressure system the injector outlet is located after the throat(low pressure area) of the nozzle. A pressurized carrier gas fed through a number of ports enters the nozzle inlet zone of length a. At the same time, a mixture of gas and powder is delivered from a powder feeder to the powder injector shown in the figure. The carrier gas will therefore expand up to atmospheric pressure and accelerate throughout the main nozzle total length (a+b), giving sonic velocity at the throat and supersonic velocity at the exit. Particles are dragged by the carrier gas up to high velocity magnitudes, resulting in severe plastic deformation processes upon impact with a solid substrate positioned at the distance SoD (Standoff Distance). As a consequence, bonding with the substrate can occur and the coating process can be initiated. The substrate is connected to a CNC table which moves the substrate inX and Y directions at an imposed speed.

2.1 Introduction to CFD

Euler-Lagrange (Two way coupling) Discrete Phase Modeling (DPM) algorithm implemented in Fluent 13 was used in this study. In this approach the fluid phase is treated as a continuum by solving the Navier-Stokes equations, while the dispersed phase is solved by tracking a large number of particles through the calculated flow field. The dispersed phase can exchange momentum, mass, and energy with the fluid phase. The physical properties of all fluid flow are governed by the following three fundamental equations:

The general continuity equation is written as follows:

$$\frac{\partial \rho}{\partial t} + \frac{\partial}{\partial x_i}(\rho u_i) = 0$$

Here $\rho$is the density

The momentum equation that is solved in this study is:

$$\frac{\partial}{\partial t}(\rho u_i) + \frac{\partial}{\partial x_j}(\rho u_i u_j) = -\frac{\partial p}{\partial x_i} + \frac{\partial \tau_{ij}}{\partial x_j} + \rho g_i + F_i$$

Where $p$is static pressure, $\boldsymbol{\tau_{ij}}$is the stress tensor, $\boldsymbol{\rho g_i}$is the body force due to gravity and $\boldsymbol{F_i}$is the external body force. As we are dealing with supersonic flow, $\boldsymbol{\rho g_i}$is very small compared to external body forces, so it is neglected in this study.
The energy equation is written as follows:

$$\frac{\partial}{\partial t}(\rho E) + \frac{\partial}{\partial x_i}\big(u_i(\rho E + P)\big) = \frac{\partial}{\partial x_i}\left[k\frac{\partial T}{\partial x_i} - \sum_j h_j J_j + u_j \tau_{ij}\right] + S_h$$

Where E is the total energy per unit mass, k is the conductivity, $\boldsymbol{J_j}$is the diffusion flux of species j and $\boldsymbol{S_h}$is the source term which refers to any heat source.

These basic principles for a flowing fluid can be written mathematically in the form of partial differential equations. Basically Computational Fluid Dynamics (CFD) replaces the governing differential equations with numbers to represent the fluid flow, and these numbers are put in three-dimensional space with a time interval to get the desired flow field in numerical form. The final outcome of the CFD is a group of numbers in closed form which represent a flow field analytically. The application of CFD for more complex and sophisticated cases depends mostly upon the computational resources like storage capacity and computational speed (RAM) [40].

2.2 Introduction to Ansys FLUENT

AnsysFluent is one of the major commercially available computational fluid dynamics (CFD) software. For doing Computational Fluid Dynamics AnsysFLUENT uses computer as a tool for analyzing and designing models. Fluent is computer software used for making models of flowing fluid and heat transfer. In fluent geometry of very complex models can be formed by using different type of meshes for solving the problems related to fluid flow. It also allows the mesh refining or coarsening depends on the solution required [40].

2.3 Numerical Procedure

To attain supersonic velocity of the gas stream, it is necessary to construct the geometry of aConvergent-divergent de-Laval nozzle [41]. ICEM CFD is used to create the geometry and mesh used in this study. The simulation can be used to determine the various flow parameters like the pressure and temperature of

the gas phase, velocity of the copper particles used in this spray, etc. It can also be used to determine the optimum operating parameters needed for achieve a good quality cold spray. For analyzing the flow parameters, 3D model & 2D axisymmetric model of the nozzle was created, because 3D model will predict the turbulence accurately. The reasons for making axisymmetric were:

- It reduces the computational effort required to solve the problem, and therefore it takes less time to get a converged solution.
- Flow field and geometry were symmetrical.
- Zero normal velocity at the plane of symmetry.
- Zero normal gradients of all variables at plane of symmetry.

The plane of symmetry was specified as the axis in boundary specifications and the nozzle model was defined such that flow, pressure gradient and temperature were zero along this specified edge of the domain. Using an axisymmetric model reduces computational effort but it does not affect the outcome of the simulation. Y. Li *et al.* [42] who investigated both the axisymmetric nozzle and two-dimensional full nozzle, found good agreement with the experimental results.

2.3.1 Model Parameters
The nozzle for cold spraying of copper particles was simulated by commercial code AnsysFLUENT 13 using the 2D double precision density solver to see the effects of the different parameters on the velocity of the copper particles, and how changing different parameters like temperature, pressure and size of the particles affects their velocity. From the literature[42], it was found that the velocity of the particles could be influenced by the nozzle expansion ratio (i.e. ratio of area of exit of nozzle to the area of throat). The coupled implicit density-based solver along with the Green-Gauss Cell Based gradient method was used to simulate the flow field inside the nozzle. The flow, turbulent kinetic energy, and turbulent dissipation rate were modelled using second order upwind accuracy.

2.3.2 Second Order Scheme
In the second order scheme, the values of cells are computed by using a multidimensional linear reconstruction approach. This approach was used for obtaining higher order accuracy and is achieved at cell faces by a Taylor series expansion of the cell centred solution of the cell centroid. The face value $\emptyset f$ is computed using the following expression:

$$\emptyset f = \emptyset + \nabla\emptyset.\Delta s$$

Where $\emptyset$ and $\nabla\emptyset$ are the cell centred values and their gradient in the upstream cell, and Δs is the displacement vector from the upstream cell centroid to the face centroid. This formulation requires the determination of the gradient $\nabla\emptyset$ in each cell. This gradient is computed by using the divergence theorem, which in discrete form is written as:

$$\Delta\emptyset \ = \ \frac{1}{V}\sum_{f}^{N_{faces}} \emptyset_f A$$

Here the face values $\emptyset f$ are computed by averaging $\emptyset$ from the two cells adjacent to the face. Finally, the gradient $\nabla\emptyset$ is limited so that no new maxima or minima are introduced.

2.4 Turbulence Modelling
The fluid flowing through the nozzle had a very high Reynolds number (more than 50,000), so the flow can be said to be fully turbulent. Different turbulence models adopt different approaches for tackling turbulence but choosing the right model ensures the accuracy of the final solution. Modelling turbulence is very complex and a highly technical field, and the selection of a turbulence model depends on factors including accuracy, computational time, resources available, and application. In this work Realizable k-ε turbulence model is used.

2.4.1 Realizable k-$\square$ Turbulence Model
The realizable k-ε model is a relatively recent development and differs from the standard k-ε model in two important ways:

- The realizable k-ε model contains a new formulation for the turbulent viscosity.
- A new transport equation for the dissipation rate,ε has been derived from an exact equation for the transport of the mean-square vorticity fluctuation.

The term "realizable" means that the model satisfies certain mathematical constraints on the Reynolds stresses, consistent with the physics of turbulent flows. The standard k-ε model or its variants like the RNG k-ε are realizable. An immediate benefit of the realizable k-ε model is that it more accurately predicts the

spreading rate of both planar and round jets. It is also likely to provide superior performance for flows involving rotation, boundary layers under strong adverse pressure gradients, separation, and recirculation. To understand the mathematics behind the realizable k-ε model, consider combining the Boussinesq relationship and the eddy viscosity definition to obtain the following expression for the normal Reynolds stress in an incompressible strained mean flow:

$$\overline{u}^2 \;=\; \frac{2}{3}k - 2\vartheta_t \frac{\partial U}{\partial x}$$

Using $\vartheta_t \equiv \frac{\mu_t}{\rho}$ one obtains the result that the normal stress, $\overline{u}^2$, which by definition is a positive quantity, becomes negative, i.e., "non-realizable", whenthe strain is large enough to satisfy

$$\frac{k}{\varepsilon}\frac{\partial U}{\partial x} > \frac{1}{3C_\mu} \approx 3.7$$

Both the realizable and RNG k-ε models have shown substantial improvements over the standard k-ε model where the flow features include strong streamline curvature, vortices, and rotation. Studies have shown that the realizable model provides superior performance compared to other variants of k-εmodel for separated flows and flows with complex secondary flow features. One of the weaknesses of the standard k-εmodel or other traditional k-ε models lies with the modeled equation for the dissipation rate (ε). The well-known round-jet anomaly is considered to be mainly due to the modeled dissipation equation.The realizable k-ε was intended to address thesedeficiencies of traditional k-εmodels by adopting the following:

- Eddy-viscosity formula involving a variable C_μ originally proposed by Reynolds.
- dissipation(ε) is modelledbased on the dynamic equation of the mean-square vorticity fluctuation.

2.5 Discrete Phase Modelling
AnsysFluent provides a model that is specially developed for spray simulations, or more general suspended particle trajectory simulations. This is the Discrete Phase Model (DPM) and it is based on the so-called Euler-Lagrange method. In the computational domain there are two separate phases present, namely the continuous and the discrete phase (particles). The transport equations from the previous section are solved for the continuous phase only and the motion of particles is dealt with particle trajectory calculations. Through an iterative solution procedure the mass, momentum and energy interaction between both phases can be realized. Some important aspects of the DPM model are presented in this section.

2.5.1 The Euler- Lagrange Approach
The discrete phase modelling follows the Euler-Lagrange approach. In this approach the fluid phase is treated as a continuum by solving the Navier-Stokes equations, while the dispersed phase is solved by tracking a large number of particles through the calculated flow field. The dispersed phase can exchange momentum, mass, and energy with the fluid phase. A fundamental assumption made in this model is that the dispersed second phase occupies a low volume fraction, even though high mass loading ($\dot{m}_{particles} \geq \dot{m}_{fluid}$) is acceptable. The particle or droplet trajectories are computed individually at specified intervals during the fluid phase calculation. This makes the model appropriate for the modeling of spray dryers, coal and liquid fuel combustion, and some particle-laden flows.

2.5.2 Particle Motion
The trajectory calculation of a discrete phase particle is done by integrating the force balance on the particle, which is written in a Lagrangian referenceframe. This force balance equates the particle inertia with the forces acting on the particle, and can be written (for the x direction in Cartesian coordinates) as

$$\frac{du_p}{dt} \;=\; F_D\big(u - u_p\big) + \frac{g_x(\rho_p - \rho)}{\rho_p} + F_x$$

where the left hand term is the acceleration of the particle, F_x is an additional acceleration due to external force field and the term with $F_D$is the drag force on the particle. $F_D$is defined as:

$$F_D \;=\; \frac{18\mu}{\rho_p d_p{}^2}\frac{C_D R_e}{24}$$

where u is the fluid phase velocity, u_p is the particle velocity, μ is the molecular viscosity of the fluid, ρ is the fluid density, ρ_p is the density of the particle, d_p is the particle diameter and R_e is the relative Reynolds number.

2.5.3 Turbulent Dispersion of Particles

The dispersion of particles due to turbulence in the fluid phase can be predicted using the stochastic tracking model or the particle cloud model. The stochastic tracking (random walk) model includes the effect of instantaneous turbulent velocity fluctuations on the particle trajectories through the use of stochastic methods. The particle cloud model tracks the statistical evolution of a cloud of particles about a mean trajectory. The concentration of particles within the cloud is represented by a Gaussian probability density function (PDF) about the mean trajectory. For stochastic tracking a model is available to account for the generation or dissipation of turbulence in the continuous phase. Turbulent dispersion of particles cannot be included if the Spalart-Allmaras turbulence model is used.

2.5.3.1 Stochastic Tracking

When the flow is turbulent, AnsysFLUENT will predict the trajectories of particles using the mean fluid phase velocity, $\overline{u}$, and the fluctuating velocity $u^{'}$

$$u = \overline{u} + u^{'}$$

In the stochastic tracking approach, AnsysFLUENT predicts the turbulent dispersion of particles by integrating the trajectory equations for individual particles, using the instantaneous fluid velocity, $\overline{u} + u^{'}(t)$, along the particle path during the integration. By computing the trajectory in this manner for a sufficient number of representative particles (termed the "number of tries"), the random effects of turbulence on the particle dispersion can be included. ANSYS FLUENT uses a stochastic method (random walk model) to determine the instantaneous gas velocity. In the discrete random walk (DRW) model, the fluctuating velocity components are discrete piecewise constant functions of time. Their random value is kept constant over an interval of time given by the characteristic lifetime of the eddies.

The DRW model may give nonphysical results in strongly nonhomogeneous diffusion-dominated flows, where small particles should become uniformly distributed. Instead, the DRW will show a tendency for such particles to concentrate in low-turbulence regions of the flow.

2.5.3.2 Particle Cloud Tracking

In particle cloud tracking, the turbulent dispersion of particles about a meantrajectory is calculated using statistical methods. The concentration of particles about the mean trajectory is represented by a Gaussian probability density function (PDF) whose variance is based on the degree of particle dispersion due to turbulent fluctuations. The mean trajectory is obtained by solving the ensemble-averaged equations of motion for all particles represented by the cloud. The cloud enters the domain either as a point source or with an initial diameter. The cloud expands due to turbulent dispersion as it is transported through the domain until it exits. As mentioned before, the distribution of particles in the cloud is defined by a probability density function (PDF) based on the position in the cloud relative to the cloud center. The value of the PDF represents the probability of finding particles represented by that cloud with residence time t.

2.5.4 Phase Coupling

While the discrete particle phase is always influenced by the continuous phase solution (one-way coupling). However, when the particle influences the flow characteristics of the continuous phase, then it is called two way coupling. In the one-way coupling case the continuous phase is solved first thereafter the particle trajectory calculation is performed. When two-way coupling is applied an iterative procedure is followed. Then, after the particle trajectory calculation the continuous flow field is solved again with updated source terms until convergence is reached.

2.5.5 Discrete Phase Boundary Conditions

The copper particles of varying sizes were used in the simulation to see their effect on the outlet velocity. The varying sizes of copper particles were used with an initial velocity of 30 m/s and an initial temperature of 300 K. The powder mass flow rate used for particle tracking was 10-15% less than the gas mass flow rate so that it would not disturb the gas flow field.

The following assumptions were made for DPM:
1) The copper particles were spherical in shape.
2) The particles introduced in the axial direction of the nozzle.
3) The particles were accelerated by the drag force of the gas used.
4) The temperature inside the copper particle was uniform.

For powder size distribution Rosin-Rammler diameter distribution method is used. If the size distribution is of the Rosin-Rammler type, the mass fraction of particles of diameter greater than d is given by:

$$Y_d = e^{-\left(\frac{d}{\bar{d}}\right)^n}$$

Where 'n' is the size distribution parameter and $\bar{d}$ is the mean diameter of a particle.

III.   Results and Discussions

3.1 Geometry
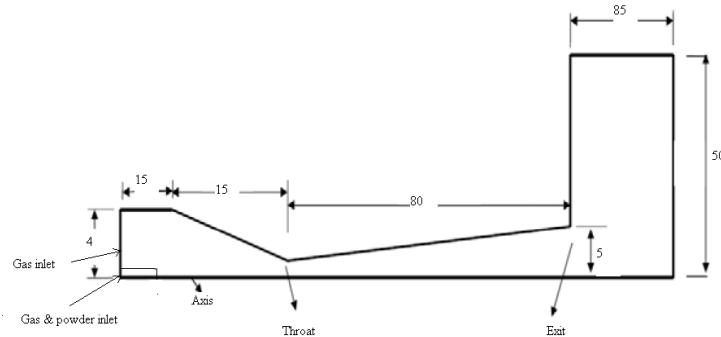
Figure 3.1: Geometry used for simulation

The 3.1 shows the dimensions of cold spray nozzle used for the simulation. The main aim of selecting this convergent-divergent nozzle is to attain the supersonic velocity of gas in the exit. A high pressure gas is preheated and led into a converging-diverging nozzle through the gas inlet. The cold spray copper powder is fed axially and centrally into the nozzle. In the divergent section, gas and powder particles are accelerated to supersonic velocity.

3.2 Meshing
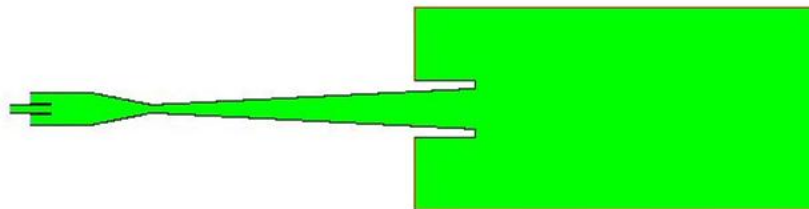
Figure 3.2: Computational Domain of Spray Gun created in ICEM-CFD

Meshing is the first and foremost step for the simulation process. It includes finding the dimensions for the sprat gun and discretizing the domain into finite volume cells. Meshing has significant impact on rate of convergence, solution accuracy and CPU time.

3.2.1 Meshing Procedure
Modelling has been done with the above dimensions and used the meshing tool of AnsysICEM CFD. After meshing the mesh was subjected to an quality testing and following results were obtained.
Mesh quality   : 0.9784 (it ranges from 0 to 1, close to zero as low quality)
Maximum aspect ratio   : 3.858
Number of cells   : 54000 (after analyzing mesh independence)

3.3 Boundary Conditions for Base Case
Carrier Gas inlet   : Pressure inlet
Gas & powder inlet   : Pressure inlet
Gas outlet   : pressure outlet
Carrier Gas inlet pressure   : 21 bar
Outlet pressure   : atmospheric pressure
Carrier gas inlet temperature : 473 K
Type of carrier gas used   : Helium
Injector & nozzle wall   : Adiabatic
Spray gun material   : Steel

Particle injection type	: Surface injection
Particle inlet temperature	: 300 K
Particle velocity at inlet	: 30m/s
Particle type	: Inert
Particle Material	: Copper
Diameter distribution	: Rosin-Rammler

3.5 Validation

It is important to validate the computational values before implementing them into the practical work and assessing their usefulness. Validation was performed by comparing the present CFD results with previously published experimental [43] results. Different applications require a different degree of accuracy in the It is important to validate the computational values before implementing them into the practical work and assessing their usefulness. Validation was performed by comparing the present CFD results with previously published experimental [43] results. Different applications require a different degree of accuracy in the validation, so the validation process is flexible to allow for different degree of accuracy.

3.6 Velocity & Pressure Contours (Base Case)
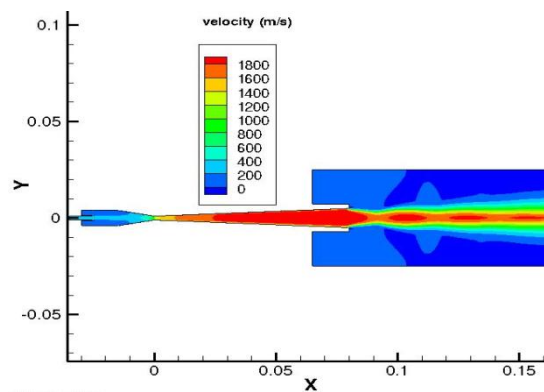
Figure 3.3: Velocity contour plot using helium as a carrier gas

Fig.3.3 shows contour plot of velocity magnitude between the inlet and outletregions. The injection portpressure was set to 31.69 bar, to generate a mass flow rate of approximately20% of the main gas (carrier gas inlet) flow. This condition falls within theoptimum range for the current Cold Spray system to generate a consistentpowder flow from the feeder. The gas phase maximum velocity is 1800 m/s, which corresponds to a Mach number of 3.5. The nozzle is shown to be over-expanded and thereforeoblique shock waves develop at the exit.

Fig.3.4 shows the changes in pressure along the length of the nozzle. The pressure of the gas is high till the throat of the nozzle, After that the gas starts expanding in the divergent part of the nozzle and therefore the pressure decreases. At the exit of the nozzle the gauge pressure becomes nearly zero, Due to over expansion of the gas phase at the nozzle exit, Shock waves are formed and therefore pressure fluctuations are seen. The changes in pressure and velocity due to shock waves are clearly shown in fig.3.6. Several oblique shock waves are seen after the exit of the convergent- divergent nozzle due to the expansion of the supersonic gas as seen in fig.3.5.
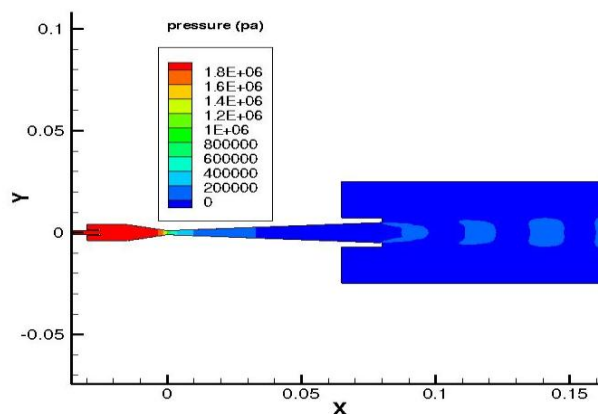
Figure 3.4: pressure contours
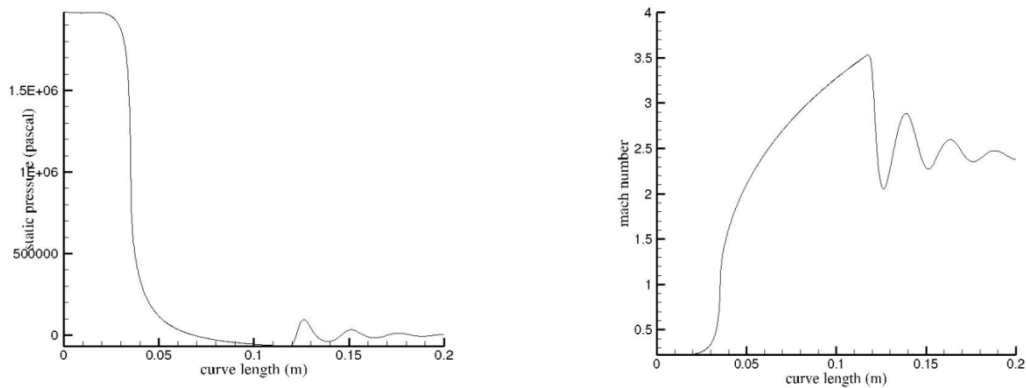
Figure 3.5: Profile of static pressure and Mach number distribution along the nozzle axis

3.7 Effects Various Carrier Gases on Particle Velocity

In this case only changing the type of gas used for the simulation and keep all other conditions are same as in the base case. Three types of gases were used in the simulation to see their effect on the velocity on copper particles through the nozzle.

The three different gases used for the simulation are helium, nitrogen and argon. Out of three gases, helium is the lightest gas because its molecular weight is lowest compared to the other two gases. The molecular weight of helium, nitrogen and argon are 4, 28 and 39.948 respectively. Because of the lower molecular weight, helium gas attains almost three times the velocity of nitrogen and argon at the exit of the spray gun is shown in fig.3.6.
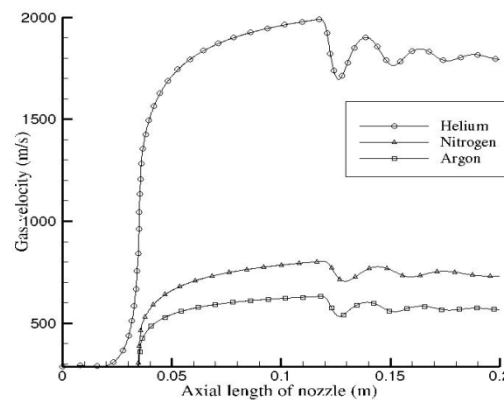
Figure 3.6: Velocity Variation of three Different Gases

Figs 3.7-3.9 shows the velocity profile along the axial length for different particle sizes when helium, nitrogen and argon are used as carrier gas. When helium is used it imparts the highest particle velocity compared to nitrogen and argon. It can be seen that there is an increase in particle velocity upto 200 m/s in the case of helium as compared to nitrogen.
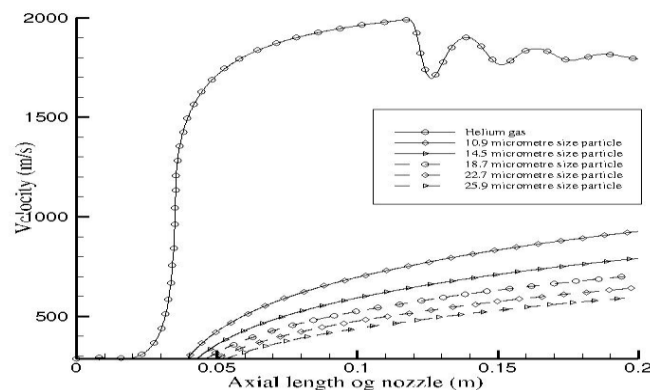
Figure 3.7: Velocity Variation of Particles by Using Helium as a Carrier Gas
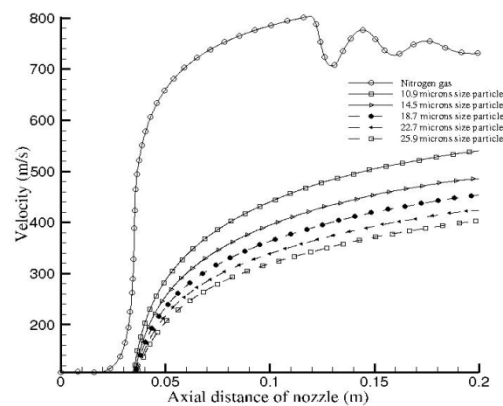
Figure 3.8: Velocity Variation of Particles by Using Nitrogen as a Carrier Gas

The Figs 3.7-3.9 shows that the particles reach approximately 42% of the gas velocity when helium is used, 60% of gas velocity when nitrogen is used and 70% when argon is used. Since the drag imparted to the particle improves with increasing molecular weight of the carrier gas, however, particles in helium has the highest velocity as the carrier gas has the highest velocity. Because of higher particle velocity by using by using helium results in a deposition efficiency of 75% as compared to 30 to 35% when using nitrogen or argon as a carrier gas.
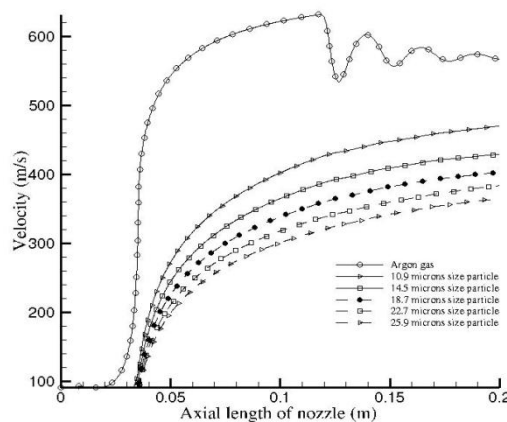
Figure 3.9: Velocity Variation of Particles by Using Argon as a carrier Gas

Fig.3.10 shows the mean particle velocity by using various carrier gases. In that curve clearly shows the particles achieve very high velocity by using helium as a carrier gas as compared to nitrogen and argon.The figs 3.7-3.9 Show that the particles of different sizes have different velocities. Velocities of the particles decrease with increase in particle size because acceleration due to drag on the particles depends on mass of the particles. So the lighter particles travel with higher velocity as compared to heavier particles.
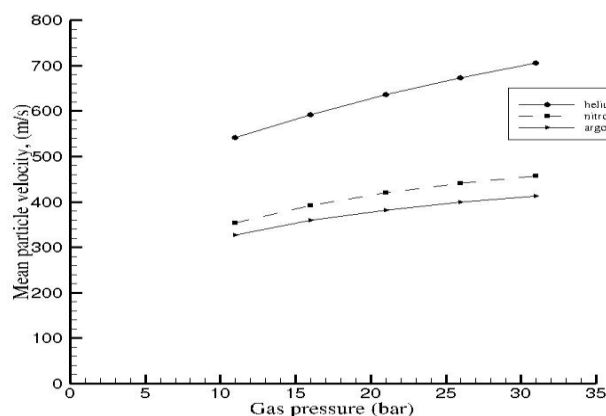
Figure 3.10: Effect of Carrier Gases on Mean Particle Velocity

3.8 Effect of Gas Temperature on Particle Velocity

In this case only changing the temperature of gas used for the simulation and keep all other conditions are same as in the base case.
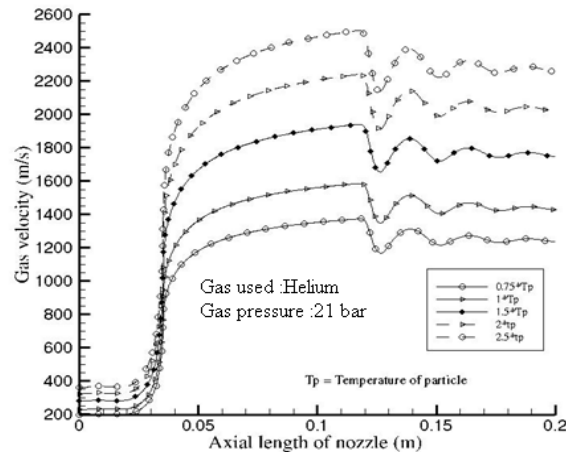
Figure 3.11: Effect of Gas Temperature on Gas Velocity

The deposition efficiency of particles depends upon the temperature of the carrier gas. It was reported earlier [25] that when nitrogen is used to spray titanium particles the critical temperature is 155 °C, below this temperature no particle deposition took place. When the temperature was further increased, the deposition efficiency also increased rapidly, especially when the temperature of nitrogen exceeded 215 °C. The reason behind the above statement is the critical velocity is a function of the temperature of carrier gas. Fig.3.11 shows the increase in carrier gas velocity by changing the carrier gas temperature. As the temperature of carrier gas is increased the velocity of particles also increase and it should result in higher deposition efficiency of the particles on the substrate.

Fig3.12 shows the variation in particle velocity at the outlet with varying gas temperature. As discussed earlier, switching from a carrier gas with higher molecular weight to one with lower molecular weight like helium results in increase in the mean particle velocity. In the same manner increase in gas inlet temperature results in decrease in gas density, therefore the overall drag on the particles increases.
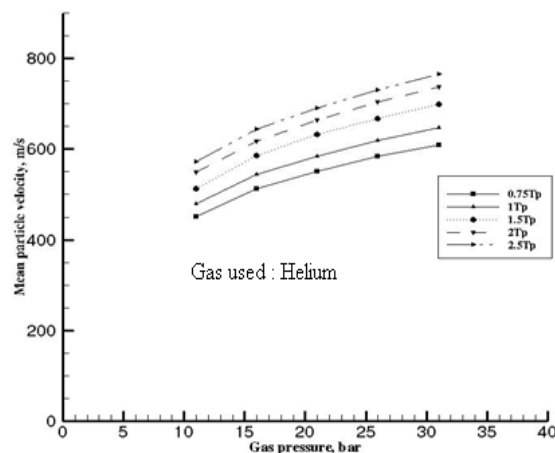
Figure 3.12: Effect of Carrier Gas Temperature on Mean Particle Velocity

3.9 Effect of Gas Pressure on Mean Particle Velocity

In this case only changing the inlet pressure of carrier gas used for the simulation and keep all other conditions are same as in the base case. The fig 3.13 shows the effect of changing the inlet pressure of carrier gas used for simulation. The variation in outlet gas velocity by changing the inlet carrier gas pressure is less as compared to changing carrier gas inlet temperature. But the particle velocity in the outlet increases, because increasing the inlet carrier gas increase the density of gas, so the drag on the particle increases.
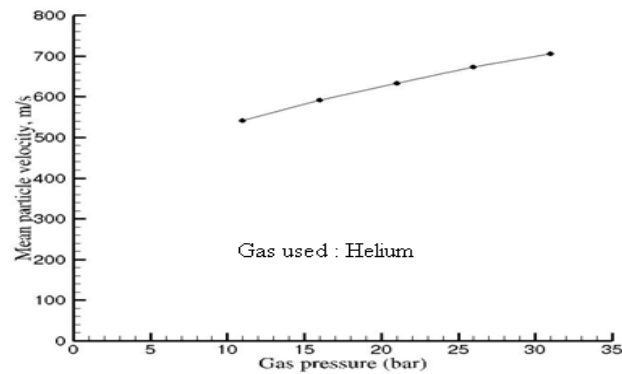
Figure 3.13: Effect Gas Pressure on Mean Particle Velocity

3.10 Effect of Particle Size on Mean Particle Velocity
    The Rosin-Rammler distribution function is used for calculating the size distribution of particles. In Rosin-Rammler distribution the parameter 'n' called the spread parameter, by changing this parameter 'n' and finding various size distributions. If the parameter 'n' is increased, it will increase the difference between the diameter range of particles, and if the parameter 'n' is decreased the difference is increased is shown in fig.3.14
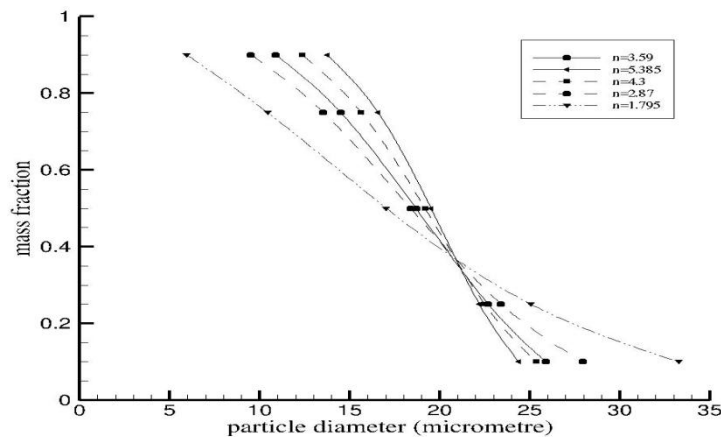
Figure 3.14: Various Particle Size Distribution

    Fig.3.15 shows the particle velocity in outlet by using various size distribution of particles. If the size distribution parameter 'n' is decreased, then the particle distribution have smaller particles as well as larger particles but the smaller particles have larger in number, this is the reason for increasing the mean velocity of particles in the outlet. If the parameter 'n' is increased, the particle velocity in the outlet was decreased.
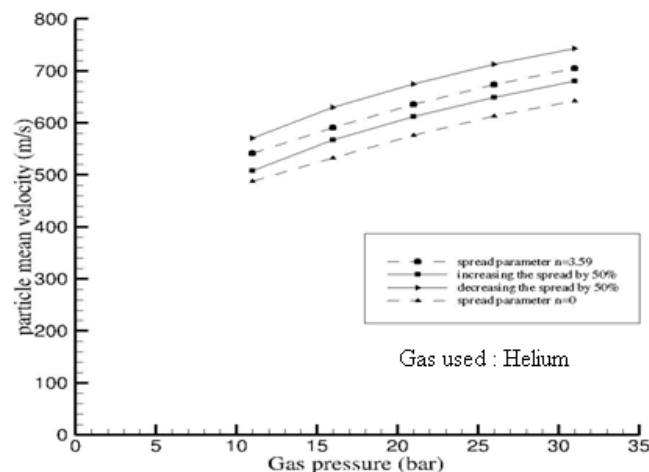
Figure 3.15: Effect Particle Size Distribution on Mean Particle Velocity

IV. Conclusion

The velocity of copper particles achieved in a cold spray nozzle were analysed with different particle size distributions, different gases, different gas pressure & temperature, one way & two way couplings and different turbulence models using CFD simulations. The simulation results showed that:

- The Mach number of the gas increases with a decrease in pressure along the axis of the nozzle. This results in greater gas velocity toward the nozzle exit.
- The results show that by increasing the gas temperature increases the gas velocity more significantly than the gas pressure, which shows that the gas velocity is a function of gas temperature and not the gas pressure.
- The results shows the particle size distribution plays a major role in the particle exit velocity i.e. lighter particles travels much faster than heavier particles.
- In the simulation argon, nitrogen and helium were used for spraying copper particles. Results show that helium is a far better carrier gas because particles achieve much higher velocity when helium is used for spraying.
- The temperature of the gas influences the velocity of copper particles because the density of gas decreases with increasing gas temperature and hence there is a greater gas velocity to accelerate the copper particles.
- Increasing the applied gas pressure increase the density of the gas which results in more drag on the particles. Increasing gas pressure does not affect the velocity of gas.
- The 2d analysis does not shows any difference between one way & two way coupling but the 3d analysis shows some difference in particle velocity.
- The turbulence analysis shows the turbulent activity is high at the starting time of the flow after that it will be reduced and the flow becomes stable.
- The turbulence analysis also shows the production of turbulent kinetic energy is high in area where large velocity gradient.

REFERENCES

[1]   Tobias Schmidt, Hamid Assadi, Frank Gartner, Horst Richter, Thorsten Stoltenhoff, Heinrich Kreye, and Thomas Klassen, From Particle Acceleration to Impact and Bonding in Cold Spraying, Journal of Thermal Spray Technology, JTTEE 18, 2009, p. 794-808

[2]   TizianaMarrocco, Cold Spray Technology from TWI, TWI Technology Centre (Yorkshire), 2007

[3]   V.F. Kosarev, S.V. Klinkov, A.P. Alkhimov, and A.N. Papyrin, On some aspects of gas dynamic of the cold spray process, ASM international,2003, JTTEE5 12:265-281

[4]   J. Karthikeyan, Cold spray technology: International status and USA efforts, ASB Industries, Inc., december 2004

[5]   P. Fauchais, A. Vardelle, and B. Dussoubs, Quo Vadis Thermal Spraying, ASM International, JTTEE 10, 2001, p. 44-66

[6]   C.-J. Li and A. Ohmori, Relationships Between the Microstructure and Properties of Thermally Sprayed Deposits, Journal of Thermal Spray Technology, JTTEE5 11, 2002, p. 365-374

[7]   Cast steel: Advances in Thermal Spray Technology, http://www.keytometals.com/Articles/Art138.htm, 2010, p. 1-2

[8]   Jin Kawakita a,□, Hiroshi Katanoda b, Makoto Watanabe a, Kensuke Yokoyama a, Seiji Kuroda a, Warm Spraying: An improved spray processto deposit novel coatings, Surface & Coating Technology, 202, 2008, p. 4369-4373

[9]   Thermal spray products, file:///F:/27April/thermalsprayprocesses.html, Metallisation

[10]   J. Karthikeyan, Evolution of cold spray technology, http://www.entrepreneur.com/tradejournals/article/print/146546589.html, 2010

[11]   G. D. Davis*, G. B. Groff, R. A. Zatorski, Plasma Spray Coatings as Treatments for Aluminum, Titanium and Steel Adherends, Surface andInterface Analysis, VOL. 25, 1997, p. 366-373

[12]   Rainer Gadow, Andreas Killinger, and Johannes Rauch, Introduction to High-Velocity Suspension Flame Spraying (HVSFS), Journal of ThermalSpray Technology, JTTEE5 17, 2008, p. 655-661

[13]   Mingheng Li, PanagiotisD.Christofides, Multi-scale modelling and analysis of an industrial HVOF thermal spray process, Journal of chemical Engineering Science, 60, 2005, p.3649-3669.

[14]   J. Rauch, G. Bolelli, A. Killinger, R. Gadow, V. Cannillo, L. Lusvarghi, Advances in High Velocity Suspension Flame Spraying (HVSFS), Journal of thermal spray technology, JTTEE 15,203, 2009, 2131-2138

[15]   Sergei VladimirovichKlinkov, Vladimir FedorovichKosarev, Martin Rein, Cold spray deposition: Significance of particle impact phenomena,Journal of Thermal spray technology, JTTEE, 9, 2005, p. 582-591

[16]   AnatoliiPapyrin, Vladimir Kosarev, Sergey Klinkov, AnatoliiAlkhimov, VasilyFomin, Cold Spray Technology, JTTEE 12, 2007

[17]   F. Gärtner, T. Schmidt, T. Stoltenhoff and H. Kreye, Recent Developments and Potential Applications of Cold Spraying, Wiley Inter Science, 8 no.7,2006, 611-618

[18]   Frank Gaertner, Tobias Schmidt, Heinrich Kreye, Present Status and Future Prospects of Cold Spraying, Trans Tech Publications, Switzerland,vols. 534-536, 2007, p. 433-436

[19]   R.E. Blose, B.H. Walker, R.M. Walker, S.H. Jroes, New opportunities to use cold spray process for applying additive features to titanium alloys, ASME, 2006, p. 30-37

[20] Vladimir F. Kosarev*, Sergey V. Klinkov and Aleksey A. Sova, Recently Patented Facilities and Applications in Cold Spray Engineering, BenthamScience Publishers Ltd, 2007, p. 35-42

[21] T. Stoltenhoff, H. Kreye, and H.J. Richter, An Analysis of the Cold Spray Process and Its Coatings, Journal of Thermal Spray Technology, JTTEE511, 2002, p. 542-550

[22] T. Han, B.A. Gillispie, and Z.B. Zhao, An Investigation on Powder Injection in the High-Pressure Cold Spray Process, Journal of Thermal Spray Technology, JTTEE5 18, 2009, p. 320-330

[23] Saden H. Zahiri, William Yang, and MahnazJahedi, Characterization of cold spray titanium supersonic jet, Journal of Thermal Spray Technology,JTTEE5 18, 2009, 110-117

[24] Wen-Ya Li and Chang-Jiu Li, Optimal design of a novel cold spray gun nozzle at a limited space, Journal of Thermal Spray Technology, JTTEE514, 2005, 391-396

[25] T. Schmidt, F. Gaertner, and H. Kreye, New Development in Cold Spray Based on Higher Gas and Particle Temperature, Journal of Thermal SprayTechnology, JTTEE5 15, 2006, 488-494

[26] M Grujicic, W S DeRosset and D Helfritch, Flow analysis and nozzleshape optimization for the cold-gas dynamic-spray process, ProQuest Science Journals, 217 part B, 2003, p. 1603-1613

[27] M. Fukumoto, M. Mashiko, M. Yamada, and E. Yamaguchi, Deposition Behavior of Copper Fine Particles onto Flat Substrate Surface in Cold Spraying, Journal of Thermal Spray Technology, JTTEE5 19, 2010, 89-94

[28] T. Van Steenkiste and J.R. Smith, Evaluation of Coatings Produced via Kinetic and Cold Spray Processes, Journal of Thermal Spray Technology,JTTEE5 13, 2004, p. 274-282

[29] Victor K. Champagne, The Repair of Magnesium Rotorcraft Components by Cold Spray, ASME, 2008, p. 164-175

[30] V. Shukla, G.S. Elliott, and B.H. Kear, Nanopowder Deposition by Supersonic Rectangular Jet Impingement, Journal of Thermal Spray Technology, JTTEE 59, 2000, p. 394-398

[31] J.G. Legoux, E. Irissou, and C. Moreau, Effect of Substrate Temperature on the Formation Mechanism of Cold-Sprayed Aluminum, Zinc and Tin Coatings, Journal of Thermal Spray Technology, JTTEE5 16, 2007, p.619-627

[32] X. Luo · G. Wang · H. Olivier, Parametric investigation of particle acceleration in high enthalpy conical nozzle flows for coating applications, ASME, 2008, 351-362

[33] John D. Anderson, Modern Compressible Flow, Third Edition, McGraw- Hill Companies, Inc., p. 228-229

[34] C. S. JOG, Fluid Dynamics, Second Edition, volume-2, Alpha Science International Ltd., p. 412-414

[35] B. Jodoin, Cold Spray Nozzle Mach Number Limitation, Journal of Thermal Spray Technology, JTTEE5 11, 2002, p. 496-507

[36] Cold spray, file://E:\mass flow rate\mm_mp_ct_cs.html, Applied Research Laboratory at Penn State, 2010, p. 1-4

[37] M. Grujicic, J.R. Saylor, D.E. Beasley, W.S. DeRosset, D. Helfritch, Computational analysis of the interfacial bonding between feed-powder particles and the substrate in the cold-gas dynamic-spray process, JTTEE 41, 219, 200, p. 211-227

[38] R. Morgan*, P. Fox, J. Pattison, C. Sutcliffe, W. O‟Neill, Analysis of cold gas dynamically sprayed aluminium deposits, ASME, 58, 2004, p. 1317-1320

[39] Wen-Ya Li *, Hanlin Liao, G. Douchy, C. Coddet, Optimal design of a cold spray nozzle by numerical analysis of particle velocity and experimental validation with 316L stainless steel powder, Journal of thermal spray technology, JTTEE 7, 2007, p. 2129-2137

[40] Introduction to Fluent Inc., Chapter 2, 2006, 2-(1-2)

[41] B. Samareh, A. Dolatabadi, A Three-Dimensional Analysis of the Cold Spray Process: Effect of Substrate Location and Shape, ConcordiaUniversity, Montreal

[42] Y. Li, A. Kirkpatrick, C. Mitchell, B. Willson, Characteristics and Computational Fluid Dynamics Modelling of High-Pressure Gas Jet Injection, ASME, vol. 126, January 2004, p. 192-198

[43] R.Lupoi, W.O'Neill, Powder stream characteristics in cold spray nozzles, Surface and Coatings Technology, 206(2011), p. 1069-1076.

[44] D.L.Gilmore, R.C.Dykhuizen, R.A.Neiser, T.J.Roemer,andM.F.Smith, Particle velocity and deposition efficiency in the cold spray process, JTTEE5:576-582

Artificial Intelligence based optimization of weld bead geometry in laser welding of Al-Mg alloy sheet

Mr. Manoj Kumar[1], Mrs. Sony Tripathi[2]

[1](Assistant Professor, Department of Mechanical Engineering, Maharana Pratap Engineering College Kanpur, India)
[2](Department of Computer Science & Engg., Naraina College of Engineering & Technology, Kanpur)

ABSTRACT: *This paper reports on a modeling and optimization of laser welding of aluminum-magnesium alloy thickness of 1.7mm. Regression analysis is used for modeling and Genetic algorithm is used for optimize the process parameters.The input values for the regression methods is taken according the Taguchi based orthogonal array. A software named Computer aided Robust Parameter Genetic Algorithm CARPGA has been developed in MATLAB 2013 which combine all of these methodologies. This software has been validated with some published paper.*
Keywords: Genetic Algorithm, laser welding, orthogonal array.

I. Introduction

Due to the high efficiency, high energy density, low heat input, large ratio of weld penetration to width, less thermal distortion and easy controlling parameters, Laser Welding process is a promising technology to weld Aluminum based alloy and it has become the most favorable process in industry. LBW is a thermal process in which a high intensity laser beam interacts with the solid surface while resulting in phase change in the irradiated region and melting and evaporation takes place in the heated region.

The ability of Laser beam Welding (LBW) mainly depends on the optical and thermal properties of workpiece materials, and it offers difficulty in processing of materials having relatively high reflectivity and thermal conductivity, such as aluminum and its alloys. These materials are in high demand in various fields of engineering and technology that require complex shapes and geometries in sheet metal components. Also, Problems in dissimilar welding arise from the differences of physical and chemical properties between the welding counterparts and possible formation of intermetallic brittle phases resulting in the degradation of mechanical properties of welds [4].

Various author used the different techniques to optimize the process parameters for weld bead geometry. Vidyut Dey,*et al*. [5] used the Genetic Algorithm to minimize weldment area without sacrificing the quality of the weld.

Mingjun Zhang, Genyu Chen et al.[9] investigated the effect of the processing parameters on the weld appearance of stainless steel plates 12 mm thick using a 10 kW fiber laser and optimal parameters were evaluated. M. Mazar Atabaki et al.[10] used the hybrid laser arc welding for welding of Aluminum alloy sheet. They investigated the joint properties and characteristics of the bonds by the metallographic investigations of the bonds and micro hardness test. They showed that when the offset distance is within the critical distance the laser and arc share the molten pool and specific amount of penetration and dilution can be achieved. Experimental results were compared with simulation.

Taguchi's approach has become one of the most powerful methods of statistical design of experiment (DOE) techniques in recent years. The Taguchi methodology (TM) for robust design is a unique statistical experimental design technique which greatly improves the engineering productivity [7]. In Taguchi Methodology -based experimental studies carried out so far, the experimenters have optimized a single quality characteristic at a time. However, the performance of any manufacturing process depends on many quality characteristics and it is always desired to achieve an optimum parameter level that improves multiple quality characteristics (MQC) at the same time. Dubey A K and Yadava V [7] optimized the three-quality characteristics kerf width, kerf deviation and kerf taper simultaneously using the Taguchi method of Laser cutting process.

In this paper Genetic Algorithm has been applied to investigate the optimum parameter settings for welding of Aluminum-Magnesium alloy sheet (a difficult to laser cut material). The controllable factors taken are laser power, welding speed and wire feed whereas the quality characteristics analyzed are upper width U, lower width L and fusion zone area . Hybrid software named, Computer aided Robust Parameter Genetic Algorithm (CARPGA) software has been developed in MATLAB. This software has been used for selection of appropriate

experimental design matrix or orthogonal array (OA) and Multi-objective optimization of Laser welding process parameters. The experimental data is taken from the literature [6].

II.   Experimental planning method

The experimental data's were modified by taking different orthogonal arrays and then linear model were developed by using Regression analysis. And these equations were used as objective functions for genetic algorithm.

2.1 selection of orthogonal array

The selection of OA is based on the total degree of freedom (dof) of the process. The minimum number of experiment required for certain control factors is equal to the Degree of freedom. Mathematically, the dof can be computed as [7]:

DOF = (number of levels-1) for each control factor + (number of levels for P-1) × (number of levels for Q-1) for each interaction +1

Where P and Q are control factors.

2.2 Regression Analysis

Regression analysis is a statistical technique for investing and modelling the relationship between variables. If y is a single dependent variable or response and x_1, x_2, x_3,……., x_k are the independent or regressor variables, then a mathematical model that might describe this relationship is;

$$y_j = b_0 + \sum_{i=1}^{k} b_i x_i + \sum_{i=1}^{k} b_{ij} x_i^2 + \sum_i \sum_j b_{ij} x_i x_j$$

……(i)

Multivariable linear regression (MVLR) analysis was used here and these model equations were used in GA. In this case, there are three independent variables and three dependent variables.

2.2 Genetic Algorithm

Genetic algorithms are computerized search and optimization algorithms based on the mechanics of natural genetics & natural selection that can be used to obtain global and robust solution to optimization problems. GA produces ever-improving solutions based on the rule 'the best one survives'. For this purpose, it uses a fitness function that selects the best and operators like regeneration and mutation to produce new solutions.

GA's identify a set of solutions of a given problem that are close to the optimum solution. It can be employed linear as well as nonlinear optimization problems. Therefore, it can be used to find multiple optimal solutions simultaneously in multi-objective optimization problems [8].

In this research work, upper width U, lower width L and fusion zone area are the objective functions and all of three have been optimized simultaneously.

III.   Development of software & validation

Hybrid software named, Computer aided Robust Parameter Genetic Algorithm (CARPGA) software has been developed in MATLAB. This software automatically selects the orthogonal array, develop a mathematical model for output characteristics and optimize the process parameters simultaneously. This software was validated by some published paper [7,11]. Dubey, Yadava [7] developed a software named computer aided robust parameters design to optimize the kerf width and MRR of laser cutting process.

Table 1: Comparison between the published result and software result [7]:

	Input parameters				Output characteristics	
	Oxygen pressure (kg/cm^2)	Pulse width (ms)	Pulse frequency (HZ)	Cutting speed (mm/min)	Kerf Taper (degree)	MRR (mg/min)
Published result	4	1.2	28	7.5	0.2295	12.193
Software result	4.3	1.23	27.32	8.01	0.1795	13.01

Sharma et al.[11] used Taguchi and Grey relational analysis to optimize the laser cutting processes. Objective was to minimize the average kerf taper and average surface roughness. From table 2 It can be seen that on given input parameters, the output characteristics give better result.

Table 2: Comparison between the published result and software result [11]

	Input parameters				Output characteristics	
	Oxygen pressure (kg/cm^2)	Pulse width (ms)	Pulse frequency (HZ)	Cutting speed (mm/min)	Average kerf taper (degree)	Average surface roughness Ra (µm)
Paper result	6	1.8	10	8	0.1255	1.7
Software result	5.5	2.1	9.5	7.32	0.1001	1.45

From the above validations, it proved that the proposed developed software give the better result compares to published result. Therefore, this software can be used to our foregoing optimization problem.

IV. Multi objective optimization using Carpga

The original Taguchi method has been applied to develop L_{18} orthogonal array which is listed in table3. Because it gives the randomized values for process parameters to conduct the experiment [3].

Table 3: Experimental layout using L_{18} orthogonal array

Input Parameters			Corresponding output characteristics		
Laser power	Welding speed	Wire feed speed	Upper width	Lower width	Fusion zone area
2.4	1.5	2	4.32	3.76	6.79
2.4	1.5	5	3.79	2.35	6.37
2.4	1.5	8	3.57	3.21	6.78
2.4	2.1	2	3.76	3.41	5.27
2.4	2.1	5	4.76	1.7	7.42
2.4	2.1	8	4.45	1.34	7.48
2.4	3	2	3.75	2.52	4.98
2.4	3	5	3.76	2.49	6.54
2.4	3	8	4.27	3.1	5.67
2.6	1.5	2	4.19	3.41	6.72
2.6	1.5	5	5.7	1.75	6.66
2.6	1.5	8	5.43	1.34	6.67
2.6	2.1	2	4.32	2.3	6.78
2.6	2.1	5	3.17	2.34	5.92
2.6	2.1	8	3.21	2.31	7.27
2.6	3	2	3.25	2.23	7.78
2.6	3	5	3.23	3.1	4.78
2.6	3	8	4.23	3.2	6.58

4.2 Modeling

The mathematical model equations developed for upper width (U), lower width (L) and the Fusion zone Area (A) by the software are:

Upper width (U) = $4.4831+0.1667 \times A - 0.4785 \times B + 0.0436 \times C$ …..(ii)

Lower width (L) = $5.3326 - 1.0556 \times A + 0.1313 \times B - 0.0869 \times C$ …..(iii)

Fusion zone area = $4.5374 + 1.0333 \times A - 0.4303 \times B + 0.0592 \times C$ …..(iv)

Where A,B,C are laser power, welding speed and wire feed speed respectively.

4.3 Optimization

The developed equations for upper width (U), lower width (L) and the Fusion zone Area (A) were used as objective function in Genetic Algorithm. In the Genetic Algorithm optimization we get the some sets of optimized result. Among these we generally select the set of result according to our aim (i.e. objective is

maximization or minimization). Here our objective is to minimize the upper width, lower width and fusion zone area. Therefore, the objective functions and their constraints used are given below;

Minimize:

Upper width (U):

Fun(1) = 4.4831+0.1667×laser power − 0.4785 × welding speed + 0.0436 ×wire feed speed

Lower width (L):

Fun(2) = 5.3326 − 1.0556 × laser power + 0.1313× welding speed − 0.0869× wire feed speed

Fusion Size (F):

Fun(3) = 4.5374 + 1.0333 ×laser power − 0.4303×welding speed + 0.0592 × wire feed speed

Subjected to:

$2.4 \leq$ laser power ≤ 2.8

$1.5 \leq$ welding speed ≤ 3

$2 \leq$ wire feed speed ≤ 8

V. Results and discussions

The set of multi-objective optimization results obtained by CARPGA are shown in Table 4. The population size = 250, mutation rate = 0.5, and double point cross over were selected as genetic algorithm parameters. These parameters were chosen by trial and error method. The score diversity of three objectives are shown in fig.1.

In genetic algorithm we get a set of results. Actually our aim is to minimize the objectives, so we have selected the minimized value of upper width, lower width and fusion zone area are 3.2 mm, 2.89mm and 5.73 mm respectively. From the figure 2, we can say that the optimization is healthy since the value of pareto spread is very low.

Table 4. Optimum result of process parameters using CARPGA

Laser power(kW)	Welding Speed (m/min)	Wire feed speed (m/min)	Upper width (mm)	Lower width (mm)	Fusion zone size (mm)
2.4	2.998	6.170	3.716	2.656	6.092
2.4	2.992	3.8769	3.619	2.855	5.95
2.4	2.831	7.975	3.875	2.40	6.27
2.4	**2.99711**	**3.490**	**3.200**	**2.189**	**5.73**
2.4	1.6499	7.965	4.440	2.323	6.77
2.4	1.5736	7.976	4.477	2.312	6.81
2.4	2.9893	2.454	3.558	2.978	5.87
2.4	1.7650	7.973	4.385	2.337	6.72
2.4	2.7325	7.987	3.923	2.463	6.31
2.4	2.9996	3.731	3.609	2.868	5.94
2.4	1.7549	7.983	4.391	2.335	6.73
2.4	2.9970	3.083	3.582	2.924	5.91
2.4	2.9790	2.523	3.566	2.971	5.88
2.4	2.9893	4.117	3.631	2.833	5.97
2.4	1.5021	7.995	4.512	2.301	6.84
2.4	2.9975	7.833	3.789	2.511	6.19
2.4	2.8237	7.986	3.879	2.475	6.27
2.4	2.0652	7.987	4.242	2.376	6.60
2.4	2.9951	3.642	3.608	2.875	5.94
2.4	2.9793	7.933	3.802	2.500	6.20
2.4	2.6211	7.979	4.397	2.334	6.74
2.4	1.7419	7.983	4.292	2.362	6.64
2.4	1.9621	7.988	3.769	2.558	6.16
2.4	2.9899	7.283	4.482	2.309	6.81
2.4	1.5643	7.996	3.803	2.505	6.20
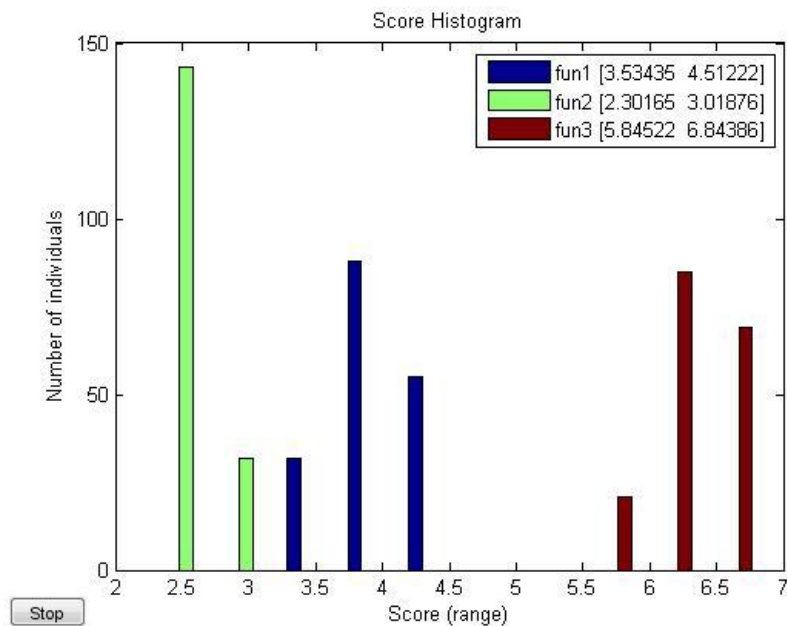
Fig.1. Score diversity of the upper width, lower width and fusion zone area
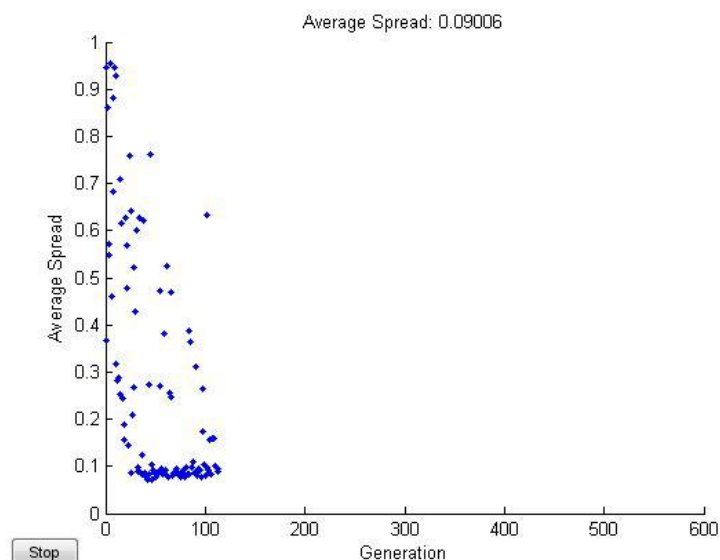
Fig.2. Variation of Avereage pareto spread with number of generations

VI. Conclusions

In this paper, hybrid software was developed and this was used to optimize the laser welding process. It was found that at laser power =2.4 kW, welding speed =2.9971m/min, and wire feed rate =3.49, the optimal values of upper width=3.2, lower width =2.189mm, and fusion zone area =5.73 mm respectively, which is agreed well with experimental result. It was also found that welding speed is most influent parameter. . It can be concluded that proposed CARPGA approach is efficient and gives the promising results. The heuristic is also found to give better solutions in shorter computational time

REFERENCES

[1]   Bekir Sami Yilbas, Sohail Akhtar, and Shahzada Zaman Shuja, Laser Forming and Welding Processes, Springer International Publishing Switzerland 2013

[2]   Phadke MS. Quality engineering using robust design. Englewood CL: Prentice-Hall; 1989.

[3]   Montgomery DC. Design and analysis of experiments. New York: Wiley; 1997.

[4]   Anawa EM, Olabi AG. Control of welding residual stress for dissimilar laser welded materials. J Mater Process Technol 2008; 204:22–33

[5]   Vidyut Dey, Dilip Kumar Pratihar,et.al.,Optimization of bead geometry in electron beam welding using a Genetic Algorithm, Journal of materials processing technology 2 0 9 (2 0 0 9) 1151–1157

[6]   Yang Dongxia, Li xiaoyan et al.Optimization of weld bead geometry in laser welding with filler wire process using Taguchi'sapproach, Optics & Laser Technology 44 (2012) 2020–2025.

[7]   Dubey, A. K. and Yadava, V., Robust parameter design and multiobjective optimization of laser beam cutting for aluminium alloy sheet, International Journal of Advanced Manufacturing Technology, Vol. 38, No. 3-4, pp. 268-277, 2008.

[8]   Kumar Sanjay, Dubey A.K., and Pandey A.K., computer-aided genetic algorithm-based multi-objective optimization of laser trepan Drilling, IJPEM, Vol. 14, No. 7, pp. 1119-1125, July 2013.

[9]   Mingjun Zhang, Genyu Chen, Yu Zhou, Shenghui Liao, Optimization of deep penetration laser welding of thick stainless steel with a 10 kW fiber laser, Materials and Design 53 (2014) 568–576

[10] M. Mazar Atabaki, M.Nikodinovski, P.Chenier, J.Ma, W.Liu , R.Kovacevic Experimental and numerical investigations of hybrid laser arc welding of aluminum alloys in the thick T-joint configuration, Optics &LaserTechnology59(2014)68–92

[11] Sharma Amit, Yadava Vinod, Modelling and optimization of cutquality during pulsed Nd:YA Glaser cutting of thin Al-alloy sheet for straight profile , Optics & Laser Technology 44 (2012) 159–168

New Topology for Transformer less Single Stage -Single Switch AC/DC Converter

Nirma Peter[1], Surya Natrajan[2]

[1](Student, Department of Electrical and Electronics, FISAT, MG University, Kerala, India)
[2](Assistant Professor, Department of Electrical and Electronics, FISAT, MG University, Kerala, India)

ABSTRACT : *This paper presents a transformer less single-stage single-switch ac/dc converter suitable for universal line applications (90–270 Vrms). The topology consists of a buck-type power-factor correction (PFC) cell with a buck–boost dc/dc cell and part of the input power is directly coupled to the output after the first power processing. With this direct power transfer and sharing capacitor voltages, the converter is able to achieve efficient power conversion, high power factor, low voltage stress on intermediate bus (less than 120 V) and low output voltage without a high step-down transformer. The absence of transformer reduces the size of the circuit , component counts and cost of the converter. Unlike most of the boost-type PFC cell, the main switch of the proposed converter only handles the peak inductor current of dc/dc cell rather than the superposition of both inductor currents. Tight voltage regulation is provided by using PID controller. Detailed analysis and design procedures and simulation of the proposed circuit are given .*

Keywords: *Direct power transfer (DPT), integrated buck– buck–boost converter (IBuBuBo), power-factor correction (PFC), single-stage (SS), transformer less.*

I. Introduction

The use of rectifiers in industrial applications started at the era of mercury converters with the electromechanical contact converter. DC machines are common in day to day use. But the supply that we get from power companies is AC. To use those machines AC supply has to be turned into DC supply by the use of a rectifier.The basic block diagram of AC/DC converter is shown in Figure 1.1. A rectifier is an electrical device that converts the incoming AC (alternating current) from a transformer or any other ac power source to pulsating DC (direct current). Rectifier may be made of diodes, solid states, vacuum tube, mercury arc valves and other components. Rectifiers are widely used in non linear loads which are connected with distribution systems which plays an important role in power system network (ex: UPS, discharge lamp, television, computer, fax machines, ferromagnetic devices, arc furnaces, energy savers etc).

The research on single-stage PFC ac/dc converters can be traced back to the early 1990s .Single-stage (ss) ac/dc converters have lot of applications because of its cost effectiveness, compact size, and simple control mechanism. Among existing SS converters, most of them are comprised of a boost power-factor correction (PFC) cell followed by a dc/dc cell. Dc/dc cell is used for output voltage regulation . Several such methods are shown in references [1]–[7] .But their intermediate bus voltage is usually greater than the line input voltage and goes beyond 450 V at high-line application. Also there are a lot of efforts to limit this bus voltage, it is still near or above the peak of the line voltage due to the nature of boost-type PFC cell. In addition, the other drawbacks of the boost-type PFC cell are that it cannot limit the input inrush current and provide output short-circuit protection[14] .
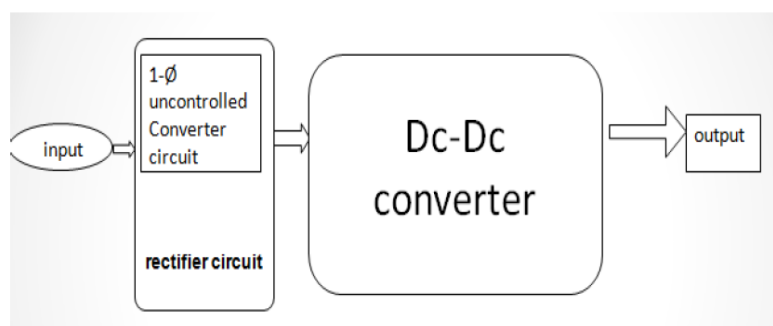
Figure1.1: Block Diagram Of AC/DC Converter

Some multistage power electronics system (e.g., in data center, electrochemical and petrochemical industries), the isolation has been done in the PFC stage, the second transformer in the dc/dc cell for the sake of isolation is considered as redundant. Hence, nonisolated ac/dc converter can be employed to reduce unnecessary or redundant isolation and enhance efficiency of the overall system. Besides, leakage inductance of the transformer causes high spike on the active switch and lower conversion efficiency. To protect the switch, snubber circuit is usually added resulting in more component counts[13]. For low voltage application (e.g.,≤48V), this high intermediate bus voltage increases components stresses on the dc/dc cell. This problem can be overcome by using a simple step-down dc/dc cell (i.e. buck or buck–boost converter).Extremely narrow duty cycle is needed for the conversion.This leads to poor circuit efficiency and limits the input voltage range for getting better performance.

Several methods were introduced to reduce the bus voltage much below the line input voltage during the years 2007-2011. Several such topologies have been reported in the references [9], [10], [13], [15]–[18]. Although the recently reported IBoBuBo converter in [13] is able to limit the bus voltage under 400 V, it cannot be applied to the low-voltage application directly due to the boost PFC cell. On the other hand, the converters in [9], [10], [15]–[18] employ different PFC cells to reduce the intermediate bus voltage. Among those converters in [9] and [15] use a transformer to achieve low output voltage either in PFC cell or dc/dc cell. Therefore, the leakage inductance is unavoidable. Converters in [10], [17], and [18], employ a buck–boost PFC cell resulting in negative polarity at the output terminal. In addition, the topologies in references [18] and [10] process power at least twice resulting in low power efficiency. Moreover, the reported converters, in [16], and [17], consist of two active switches leading to more complicated gate control. Apart from reducing the intermediate bus voltage, the converter in [19] employs resonant technique to further increase the step-down ratio based on a buck converter to eliminate the use of intermediate storage capacitor. The converter features with zero-current switching to reduce the switching loss. However, without the intermediate storage, the converter cannot provide hold-up time and presents substantial low-frequency ripples on its output voltage. Besides, the duty cycle of the converter for high-line input application is very narrow, i.e., < 10%. This greatly increases the difficulty in its implementation due to the minimum on-time of pulse-width-modulation (PWM) IC and rise/fall time of MOSFET.

To tackle the aforementioned problems, an intergrated buck–buck–boost (IBuBuBo) converter with low output voltage is proposed. This proposed circuit consists of a buck converter, used as PFC cell and a buck-boost converter as a dc/dc converter. This circuit is able to limit the bus voltage below the input voltage effectively.In addition, by In addition, by sharing voltages between the intermediate bus and output capacitors, further reduction of the bus voltage can be achieved. Therefore, a transformer is not needed to obtain the low output voltage. The converter is able to achieve:

1)low voltage stress on intermediate bus (less than 120 V) ;

2)high PF, compact size, Less cost;

3) low intermediate bus and output voltages in the absence of transformer;

4) simple control structure with a single-switch;

5) positive output voltage;

6) high conversion efficiency due to part of input power is processed once and

7) input surge current protection because of series connection of input source and switch.

II.   Direct Power Transfer

In a conventional two-stage or S PFC ac/dc converter, there are two functional cells, i.e., PFC cell and dc/dc cell. AC input power is first transferred into somewhat pulsating dc power stored on intermediate bulk capacitors by the PFC cell. The stored dc power on the bulk capacitors is processed again by the dc/dc cell to the desired dc output power. So the input power is processed twice to reach the output, as shown in Fig. 2.1(a). Assuming the PFC cell has unity input power factor, and the efficiency of the PFC cell and dc/dc cell η_1 and η_2 are and, respectively, we have output power

$$P_O = P_{in}\eta_1\eta_2 \qquad\qquad (1)$$

and the resultant efficiency of SS PFC ac/dc converter is

$$\eta = \eta_1\eta_2 \qquad\qquad (2)$$

From the above equations, we can see that the dual power processing approach means lower conversion efficiency since it is the product of the efficiency of each power conversion
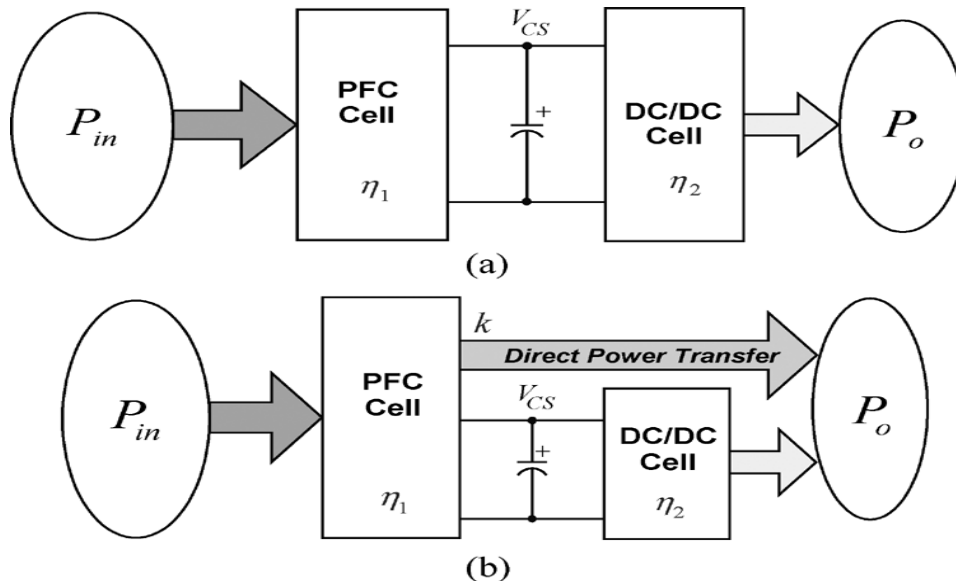
Figure. 2.1. Power transfer block diagrams of PFC ac/dc converters: (a) conventional power transfer and (b) proposed power transfer with DPT concept.

Direct power transfer approaches will allow a part of the input power to be processed only once and let the remaining input power to be processed twice while still achieving both high power factor and tight output

$$P_0 = P_{in}\eta_1 k + P_{in}\eta_1\eta_2(1-k) \qquad (3)$$

regulation. Those power transfer approaches provide a new way to achieve more efficient and higher power rating PFC converters than the conventional double power processing approach. A block diagram of the proposed power transfer approach with the DPT concept is expressed in Fig. 2 .1(b). In Fig. 2.1(b), (1-k) portion of the power from the PFC cell is directly transferred to the output, and the remaining power from PFC cell is stored in the intermediate bus capacitor and then processed by the dc/dc cell. Based on this concept, we have so the efficiency of this S PFC ac/dc converter is

$$\eta = \eta_1\eta_2 + k\eta_1(1-\eta_2) \qquad (4)$$

Comparing (2) with (4), it is clear that the converter with the DPT generally has higher efficiency than its counterpart without the DPT approach, simply because the converter with the DPT concept follows an inequality

$$\eta_1\eta_2 + k\eta_1(1-\eta_2) > \eta_1\eta_2$$
$$where \_ k < 1.\eta_1 < 1.and\eta_2 1. \qquad (5)$$

The above efficiency comparison enhances our understanding why the DPT concept will help build an inherently more efficient PFC converter

III. Single-Stage PFC Converter

Power factor correction (PFC) techniques have become increasingly important since several regulations that are used to limit harmonic injection to the power utilities have been enacted recently. There are two basic PFC approaches, namely, active PFC and passive PFC. Active PFC, classified by the system configurations, can be categorized into two-stage and single-stage SS schemes. A two-stage scheme results in high power factor and fast response output voltage regulation by using two independent controllers and optimized power stages, as shown in Fig. 3.1(a). The main drawbacks of this scheme are its relatively higher cost and larger size resulted from its complicated power stage topology and control circuits, particularly in low power applications.

An SS scheme combines the PFC cell and dc/dc power conversion cell into one stage, and typically uses only one controller and shares power switches, as shown in Fig. 3.1(b). It should be pointed out that from the viewpoint of functionality, in order to get high power factor and regulated output, an SS converter actually still needs to complete PFC and dc/dc regulating tasks as a two-stage converter. Usually, the high power factor of an SS PFC converter is guaranteed by operating the PFC cell in discontinuous current mode (DCM), while the fast response output regulation is achieved by the dc/dc cell. Although the single-stage scheme is especially

attractive in low cost and low power applications due to its simplified power stage and control circuit, major issues still exist, such as low efficiency and difficulty being moved to higher power level, and high as well as wide-range intermediate dc bus voltage stress.
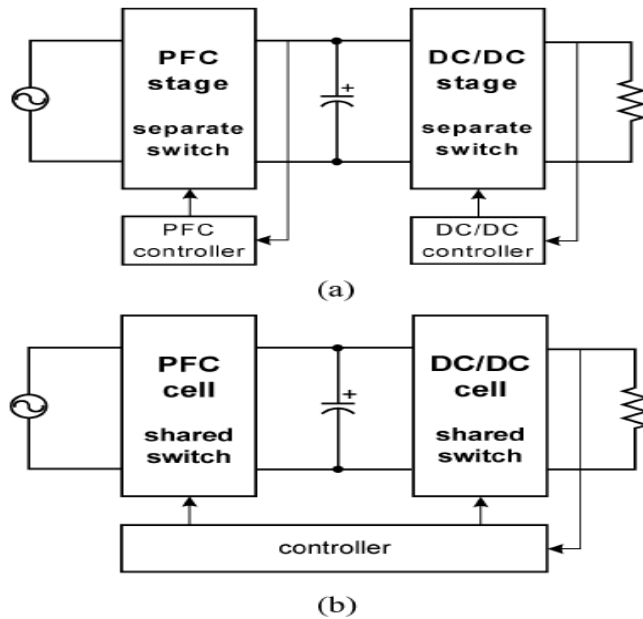
Figure. 3.1. Functional block diagram of PFC converters: (a) two-stage PFC converter and (b) typical single-stage PFC converter.

IV. Proposed Circuit and Its Operating Principle

The proposed I Bu Bu Bo converter, which consists of the merging of a buck PFC cell (L_1, S_1, D_1, C_O, C_B) and a buck–boost dc/dc cell ($L_2, S_2, D_2, D_3, C_O, C_B$) is illustrated in Fig. 4.1(a). Although L2 is on the return path of the buck PFC cell, does not contribute to the cell electrically. Thus, L2 is not considered as in the PFC cell. Moreover, both cells are operated in discontinuous conduction mode (DCM) so there are no currentsin both inductors L1 and L2 at the beginning of each switching cycle t0 . Due to the characteristic of buck PFC cell, there are two operating modes in the circuit.
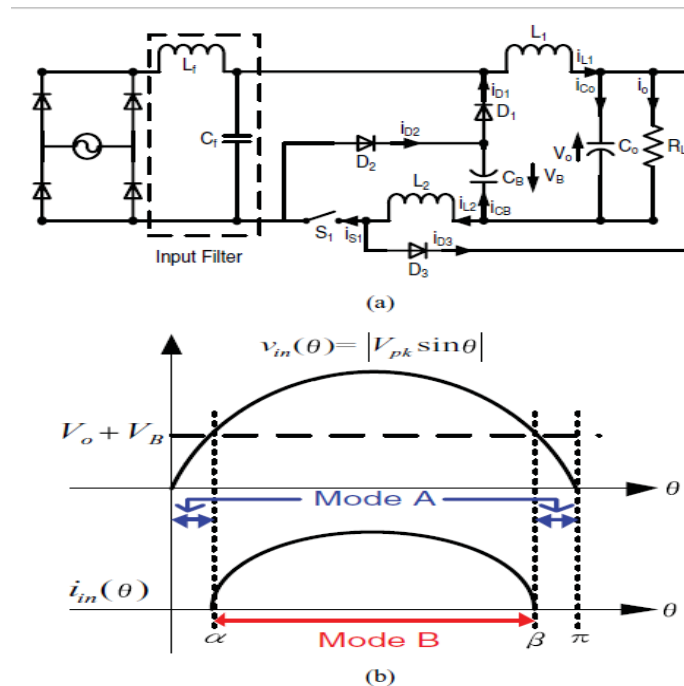
Figure 4.1: (a) Proposed IBuBuBo SS ac/dc converter. (b) Input voltage and current waveforms

ModeA(vin (θ)≤VB + Vo): When the input voltage vin (θ) is smaller than the sum of intermediate bus voltage VB , and output voltage Vo , the buck PFC cell becomes inactive and does not shape the line current around zero-crossing line voltage , owing to the reverse biased of the bridge rectifier. Only the buck–boost dc/dc cell sustains all the output power to the load. Therefore, two dead-angle zones are present in a half-line period and no input current is drawn as shown in Fig. 4.1(b). The circuit operation within a switching period can be divided into three stages and the corresponding sequence is Fig. 4.2(a),(b), and (f). Fig. 4.3(a) shows its key current waveforms.

1) Stage 1 (period d1Ts in Fig. 4.3) [see Fig. 4.2(a)]: When switch S1 is turned ON, inductor L2 is charged linearly by the bus voltage VB while diode D2 is conducting. Output capacitor Co delivers power to the load.
2) Stage 2 (period d2Ts in Fig. 4.3) [see Fig. 4.2(b)]: When switch S1 is switched OFF, diode D3 becomes forward biased and energy stored in L2 is released to Co and the load.
3) Stage 3 (period d3Ts - d4Ts in Fig. 4.3) [see Fig. 4.2(f)]: The inductor current iL2 is totally discharged and only Co sustains the load current.

Mode B (vin (θ) > VB + Vo): This mode occurs when the input voltage is greater than the sum of the bus voltage and output voltage. The circuit operation over a switching period can be divided into four stages and the corresponding sequence is Fig. 4.2(c), (d), (e), and (f). The key waveforms are shown in Fig. 4.3(b).

1) Stage 1   (period d1Ts in Fig. 4.3) [see Fig. 4.2(c)]: When switch S1 is turned ON, both inductors L1 and L2 are charged linearly by the input voltage minus the sum of the bus voltage and output voltage (vin (θ) − VB − Vo), while diode D2 is conducting.
2) Stage 2   (period d2Ts in Fig. 4.3) [see Fig. 4.2(d)]: When switch S1 is switched OFF, inductor current iL1 decreases linearly to charge CB and Co through diode D1 as well as transferring part of the input power to the load directly. Meanwhile, the energy stored in L2 is released to Co and the current is supplied to the load through diode D3. This stage ends once inductor L2 is fully discharged.
3) Stage 3   (period d3Ts in Fig. 4.3) [see Fig. 4.2(e)]: Inductor L1 continues to deliver current to Co and the load until its current reaches zero.
4) Stage 4   (period d4Ts in Fig.4.3) [see Fig. 4.2(f)]: Only Co delivers all the output power.
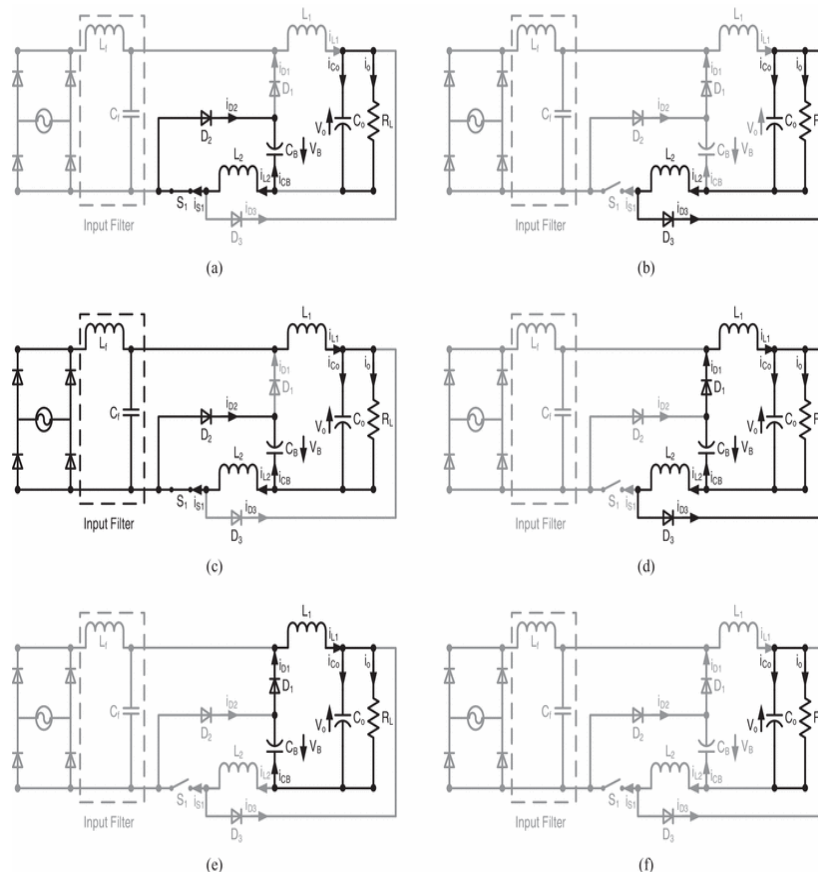
Figure. 4.2 Circuit operation stages of the proposed ac/dc converter.
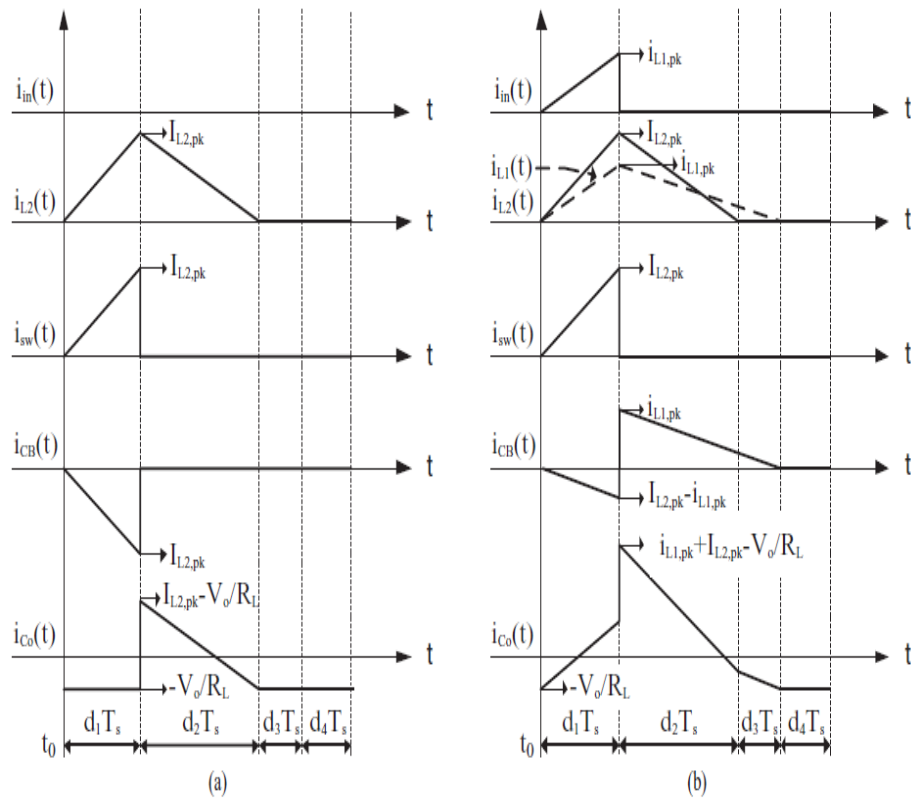
Figure. 4.3. Key waveforms of the proposed circuit

V. Design Consideration

To simplify the circuit analysis, some assumptions are made as follows:

1) all components are ideal;

2) line input source is pure sinusoidal, i.e. vin (θ) = Vpksin(θ) where Vpk and θ are denoted as its peak voltage and phase angle, respectively;

3) both capacitors CB and Co are sufficiently large such that they can be treated as constant DC voltage sources without any ripples;

4) the switching frequency fs is much higher than the line frequency such that the rectified line input voltage |vin (θ)| is constant within a switching period.

5.1. Circuit Characteristics

According to Fig.4.1 (b), there is no input current drawn from the source in Mode A, and the phase angles of the dead-time α and β can be expressed as

$$\alpha = \arcsin(\frac{V_T}{V_{pk}}) \qquad (6)$$

$$\beta = \pi - \alpha = \pi - \arcsin(\frac{V_T}{V_{pk}}) \qquad (7)$$

where VT is the sum of VB and Vo . Thus, the conduction angle of the converter is

$$\gamma = \beta - \alpha = \pi - 2\arcsin(\frac{V_T}{V_{pk}}) \qquad (8)$$

From the key waveforms (see Fig. 4.3), the peak currents of the two inductors are:

$$i_{L1\_pk} = \begin{cases} \dfrac{v_{in}(\theta) - V_T}{L_1} d_1 T_S, \alpha < \theta < \beta \\ 0, otherwise \end{cases} \qquad (10)$$

$$I_{L2\_pk} = \frac{V_B}{L_2} d_1 T_s \qquad (11)$$

where Ts (1/fs) is a switching period of the converter. In (10) and (11), the dependency of iL1 pk on θ has been omitted for clarity. It is noted that L2 does not contribute in equation (10) even though it is on the current return path of the PFC cell.

In addition, by considering volt–second balance of the L1 and L2 , respectively, the important duty ratio relationships can be expressed as follows

$$d_2 + d_3 = \begin{cases} \dfrac{v_{in}(\varTheta) - V_T}{V_T} d_1, \alpha < \theta < \beta \\ 0, otherwise \end{cases} \qquad (12)$$

$$d_2 = \frac{V_B}{V_O} d_1 \qquad (13)$$

By applying charge balance of CB over a half-line period, the bus voltage VB can be determined. From Fig. 4.3, the average current of CB over a switching and half-line periods are expressed as follows:

$$<i_{CB}>_{sw} = .5(i_{L1\_pk}(d_1 + d_2 + d_3) - I_{L2\_pk} d_1)$$

$$<i_{CB}>_{sw} = d_1{}^2 T_S \frac{[(v_{in}(\varTheta) - V_T)v_{in}(\varTheta)]}{L_1 V_T} - d_1{}^2 T_S \left[\frac{V_B}{L_2}\right] \qquad (14)$$

And

$$<i_{CB}>_\pi = \frac{1}{\pi} \int_0^\pi <i_{CB}>_{sw} d\theta$$

$$<i_{CB}>_\pi = \frac{d_1^2 T_S}{2\pi} \left[\frac{V_{pk}}{L_1} \left(\frac{V_{pk}}{V_T} \left(\frac{\gamma}{2} + \frac{A}{4} \right) - B \right) - \frac{\pi V_B}{L_2} \right] \qquad (15)$$

where the constants A and B are

$$A = \sin(2\alpha) - \sin(2\beta)$$
$$B = \cos(\alpha) - \cos(\beta) \qquad (16)$$

Putting equation (4.8) to zero due to the steady-state operation, this leads to

$$V_B = \frac{M V_{pk}^2}{2\pi(V_B + V_O)} \left[\pi - 2\arcsin(\frac{V_B + V_O}{V_{pk}}) - \frac{2(V_B + V_O)\sqrt{(V_{pk} + V_B + V_O)(V_{pk} - V_B - V_O)}}{V_{pk}^2} \right] \qquad (17)$$

where M is the inductance ratio L2/L1 .

As observed from equation(4.11), the bus voltage VB can be obtained easily by numerical method. It is noted that VB is independent on the load, but dependent on the inductance ratio M.. It is noted that the bus voltage is kept below 150 V at high-line input condition.

Similarly, the instantaneous and average input currents of the proposed circuit are

$$<i_{in}>_{sw} = \frac{i_{L1\_pk} d_1}{2} = \begin{cases} \dfrac{v_{in}(\varTheta) - V_T}{2L_1} d_1{}^2 T_S, \alpha < \theta < \beta \\ 0, otherwise \end{cases} \qquad (18)$$

And

$$I_{in} = \frac{1}{\pi} \int_\alpha^\beta <i_{in}>_{sw} d\theta$$

$$I_{in} = \frac{d_1{}^2 T_S}{2\pi L_1} \left[V_{pk} B - \gamma V_T \right] \qquad (19)$$

Using equation (18) and (19), the rms value of the input current, average input power and power factor are given by

$$I_{in\_rms} = \sqrt{\frac{1}{\pi}\int_{\alpha}^{\beta}(<i_{in}>_{sw})^2 \, d\Theta} \tag{20}$$

$$I_{in\_rms} = \frac{d_1^2 T_S}{2\sqrt{\pi}L_1}\sqrt{V_{pk}^2(\frac{\gamma}{2}+\frac{A}{4})-2V_{pk}V_T B + \gamma V_T^2}$$

$$P_{in} = \frac{1}{\pi}\int_{\alpha}^{\beta}v_{in}(\Theta)<i_{in}>_{sw} \, d\Theta \tag{21}$$

$$P_{in} = \frac{d_1^2 T_S V_{pk}}{2\pi L_1}\left[V_{pk}(\frac{\gamma}{2}+\frac{A}{4})-V_T B\right]$$

$$PF = \frac{\frac{1}{\pi}\int_{\alpha}^{\beta}v_{in}(\Theta)<i_{in}>_{sw} \, d\Theta}{\frac{V_{pk}}{\sqrt{2}}I_{in\_rms}} \tag{22}$$

$$PF = \sqrt{\frac{2}{\pi}}\,\frac{V_{pk}(\frac{\gamma}{2}+\frac{A}{4})-V_T B}{\sqrt{V_{pk}^2(\frac{\gamma}{2}+\frac{A}{4})-2V_{pk}V_T B + \gamma V_T^2}}$$

5.2 Condition for DCM

To ensure both cells working in DCM mode throughout the ac line period, we must determine their critical inductance first. To allow L1 working in DCM and from equation (12), we have the following inequalities

$$d_2 + d_3 \subseteq 1 - d_{1\_PFC} \tag{23}$$

$$d_{1\_PFC} <= \begin{cases} \frac{V_T}{v_{in}(\theta)}, \alpha < \theta < \beta \\ 0, otherwise \end{cases} \tag{24}$$

$$d_2 \subseteq 1 - d_{1\_DC/DC} \tag{25}$$

$$d_{1\_DC/DC} <= \frac{V_O}{V_O + V_B} = \frac{V_O}{V_T} \tag{26}$$

$$d_{1\_max} = \begin{cases} \min(d_{1\_PFC}, d_{1\_DC/DC}), \alpha < \theta < \beta \\ d_{1\_DC/DC}, otherwise \end{cases} \tag{27}$$

$$R_{L\_\_min} = \frac{V_O^2}{P_O} \tag{28}$$

where d1 PFC is the maximum d1 of the PFC cell.

By applying input–output power balance of the PFC cell and substituting in equation (27) into equation (21), the critical inductanceL1 crit is given by

$$L_{1\_crit} = \frac{R_{L\_min}T_s V_{pk}}{2\pi V_0^2}\left[V_{pk}(\frac{\gamma}{2}+\frac{\sin(2\alpha)-\sin(2\beta)}{4})+V_T(\cos(\beta)-\cos(\alpha))\right]d_{1\_max}^2 \tag{29}$$

where RL min is denoted as the minimum load resistance of the converter.

For the dc/dc cell sustaining all the power to the load under DCM operation in Mode A, the critical inductance L2 crit is the smallest. Under the input–output power balance of the dc/dc cell, the critical inductance L2 crit can be determined. The input power of the dc/dc cell in Mode A is given by

$$P_{in\_DC/DC} = \frac{V_B}{\pi}\int<i_{DC/DC}>_{sw}d\theta = \frac{V_B^2 T_s d_1^2}{2L_2} \tag{30}$$

where < idc/dc >sw is the instantaneous input current of dc/dc cell. Hence, by substituting (27) into (30), the critical inductance L2 crit is given by

$$L_{2\_crit} = \frac{R_{L\_min} V_B{}^2 T_S}{2V^2{}_0} d^2{}_{1\_max}$$

(31)

4.3. Capacitors Optimization

To determine the size of the intermediate bus capacitor CB , we can consider the hold-up time (thold up) of the circuit. The bus capacitor CB will sustain all the output power within t_hold up when the ac input source is removed. In normal practice, the hold-up time is one of the ac line cycle. In addition, the maximum capacitance of CB to meet this hold-up time requirement is determined under the low-line and full output load conditions. Thus, the size of CB is expressed as follows:

$$C_B = \frac{2P_O t_{hold\_up}}{V^2{}_{B\_nominal} - V^2{}_{B\_min}}$$

(32)

where hold up time is:

$$t_{hold\_up} = \frac{\alpha}{\omega} = \arcsin(\frac{V_B + V_O}{V_{pk}})$$

(33)

Apart from the size of CB, it is noted that the line frequency ripple on the output capacitor Co is inevitable since a portion of the input power is coupled to the load directly. However, this ripple can be reduced by increasing its capacitance.

VI.   Design of the Simulation Prototype

The performance of the proposed circuit is verified by using MATLAB/ Simulink. To ensure the converter working properly with constant output voltage, a simple voltage mode control is employed. To achieve high performance of the converter for universal line operation in terms of low bus voltage (< 150V) and high power factor (> 96%), the inductance ratio has to be optimized. The lower the bus voltage of the converter, the lower voltage rating capacitor (150 V) can be used.

6.1 Specifications
1) output power: 100 W;
2) output voltage: 19 Vdc
3) power factor: > 96%;
4) intermediate bus voltage: < 150V;
5) line input voltage: 90–270 Vrms/50 Hz;
6) switching frequency (fs): 20 kHz.
7) M =.4

6.2 Input filter

A low-pass filter is a filter that passes low-frequency signals and attenuates (reduces the amplitude of) signals with frequencies higher than the cutoff frequency. A low-pass filter is the opposite of a high-pass filter. A band-pass filter is a combination of a low-pass and a high-pass. Low-pass filters exist in many different forms, including electronic circuits (such as a hiss filter used in audio), anti-aliasing filters for conditioning signals prior to analog-to-digital conversion, digital filters for smoothing sets of data, acoustic barriers, blurring of images, and so on. The moving average operation used in fields such as finance is a particular kind of low-pass filter, and can be analyzed with the same signal processing techniques as are used for other low-pass filters. Low-pass filters provide a smoother form of a signal, removing the short-term fluctuations, and leaving the longer-term trend.

F_r as the resonance frequency

$$F_r = \frac{1}{(2\pi \sqrt{L_f C_f})}$$

(34)

Assume the value of L_f and find C_f

Here we take F_{cy} as 2500 Hz assume L_f as 2mH then, $= 2\mu F$

6.3 Intermediate bus voltage
Equation (17) is solved by using MATLAB.

```
m=.4;
vpk= 230*sqrt(2);
vo=19;
f=vb-(((m*vpk*vpk)/(2*pi*(vb+vo)))*((pi(2*asin((vb+vo)/vpk)))-(2*(vb+vo)*sqrt((vpk+vb+vo)*(vpk-vb-
vo))/(vpk*vpk))));
df = diff (f);
vb=1;
for    M=1:10
p=eval(f);
q=eval(df);
eval('vb=vb-(p/q)');
end
```

For input given is 230V ,intermediate voltage VB obtained is 98.73V.

It is noted that VB is independent on the load, but dependent on the inductance ratio M. Depicts the relationship among VB , rms value of the line voltage, and inductance ratio M. It is noted that the bus voltage is kept below 150 V at high-line input condition.

Table 2:different intermediate voltage as input varies

INPUT VOLTAGE	INTERMEDIATE VOLTAGE
90V	32V
230V	98.7V
270V	117.8V

6.4 Intermediate capacitor
$Let,$

$P_O = 100W, V_{B\_nominal} = 98.7V, ripple = 40\%V_O, V_{B\_min} = 98.5V, V_O = 19V$

$then,$

$V_{pk} = 230 * \sqrt{2}V = 325.26V$

$\alpha = .370 radians$

$\beta = 2.77 radians$

$\gamma = 2.40 radians$

$\omega = 2 * \pi * f = 314.15 radians/\sec$

Using equation (33)
t_holdup =1.17ms

   Assume ripple of about 40% of the output voltage
   Using equation (32) intermediate capacitor is:
   CB = 5mF

6.5 Buck and buck- boost inductor
Using equation (24) and (26)

$$d_{1\_PFC} = \begin{cases} .362, \alpha < \theta < \beta \\ 0, otherwise \end{cases}$$

$$d_{1\_DC/DC} <= \frac{V_O}{V_O + V_B} = \frac{V_O}{V_T} = .161$$

Using equation (27) d_max is choose as

$$d_{1\_max} = \begin{cases} .161, \alpha < \theta < \beta \\ .161, otherwise \end{cases}$$

$$R_{L\_\_min} = \frac{V_O{}^2}{P_O} = 3.61\Omega$$

where RL min is denoted as the minimum load resistance of the converter.

$$Let,$$
$$V_O = 19V$$
$$V_{pk} = 230 * \sqrt{2}V = 325.26V$$
$$\alpha = .370 radians$$
$$\beta = 2.77 radians$$
$$\gamma = 2.40 radians$$

Using equation (29) and (31)

$$L_{1\_crit} = 188\mu H$$
$$L_{2\_crit} = 63\mu H$$

6.6 Output capacitor filter
Output capacitor is used to eliminate the ripple in output voltage

$$C_O = \frac{1}{4fR_L}(1 + \frac{1}{\sqrt{2}R.F})$$ (35)

$$R.F = \frac{V_{ac}}{V_{dc}} = .27$$
$$C_O = 5mF$$

Table 3 circuit components

PARAMETERS	VALUES
Input Filter Inductor	2 mH
Input Filter Capacitor	2 μF
Inductor L1	188μH
Inductor L2	63μH
Capacitor CB	5mF
Capacitor CO	5mF

VII.   Simulation and Results
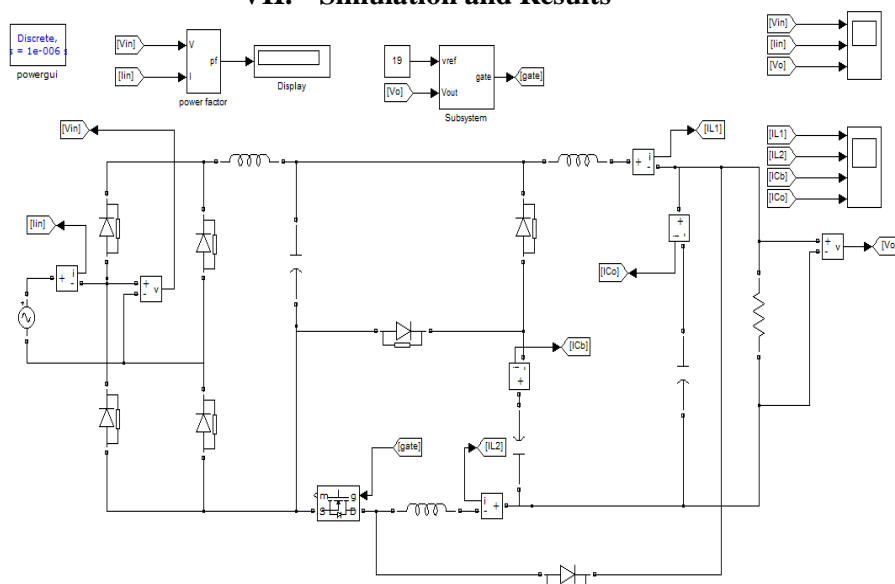
Fig 6.1: Proposed Circuit In MATLAB/Simulink

7.1 Subsystems

a) Pulse generating system
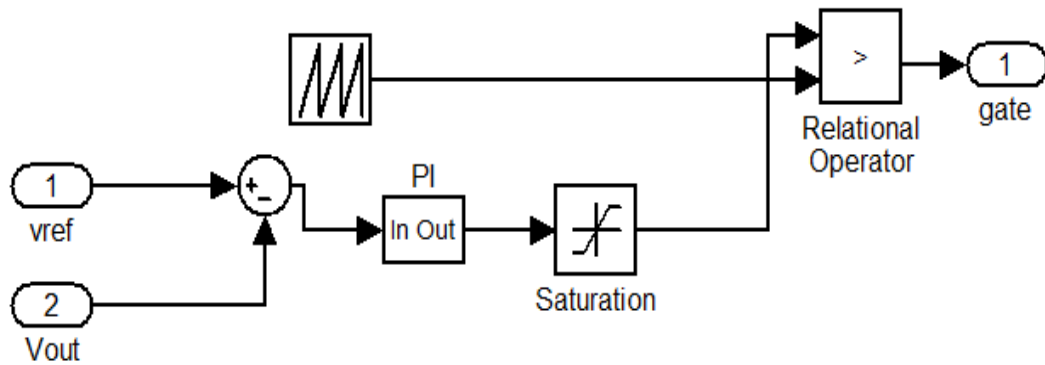
b) PI Controller
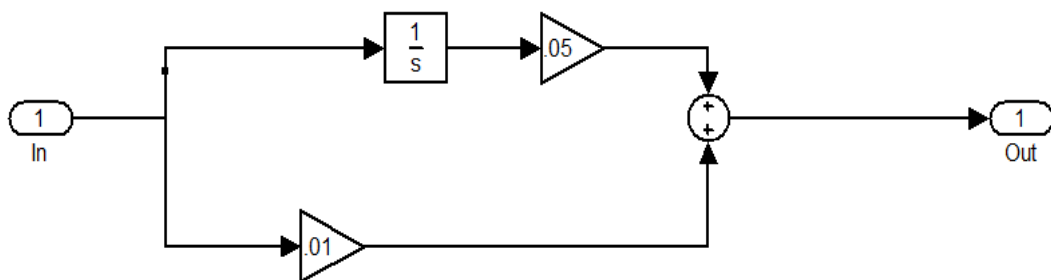
c) PF measurement
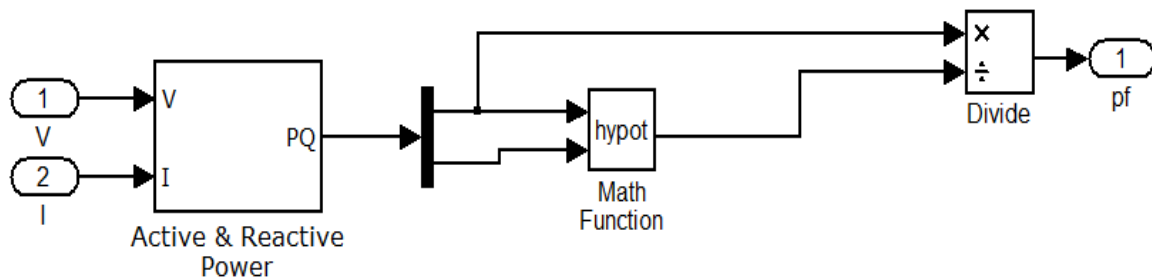
Fig 6.2 Different Subsystems used in Simulation

7.2 Results
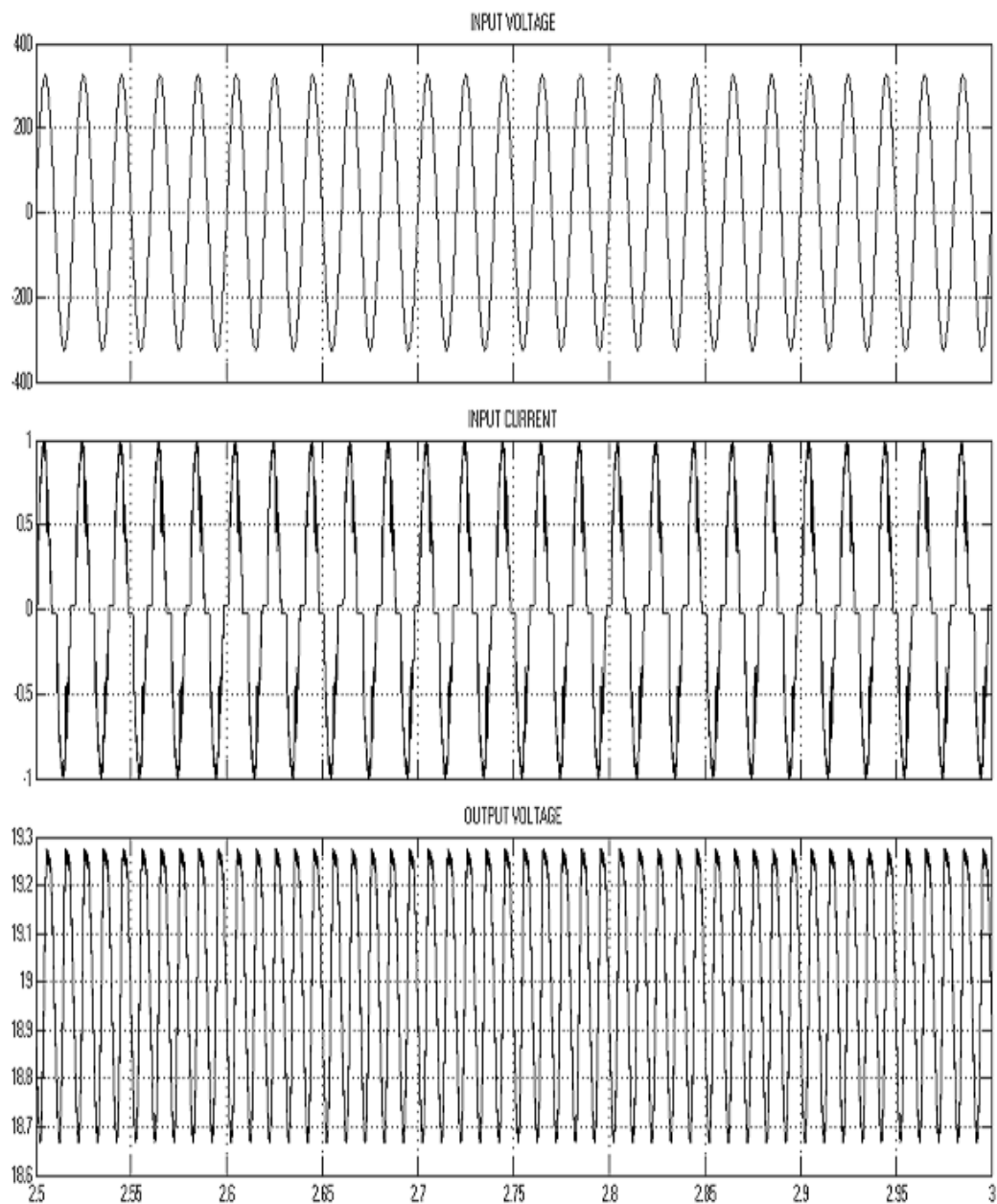
Fig 6.3 waveforms of input voltage, input current,output voltage
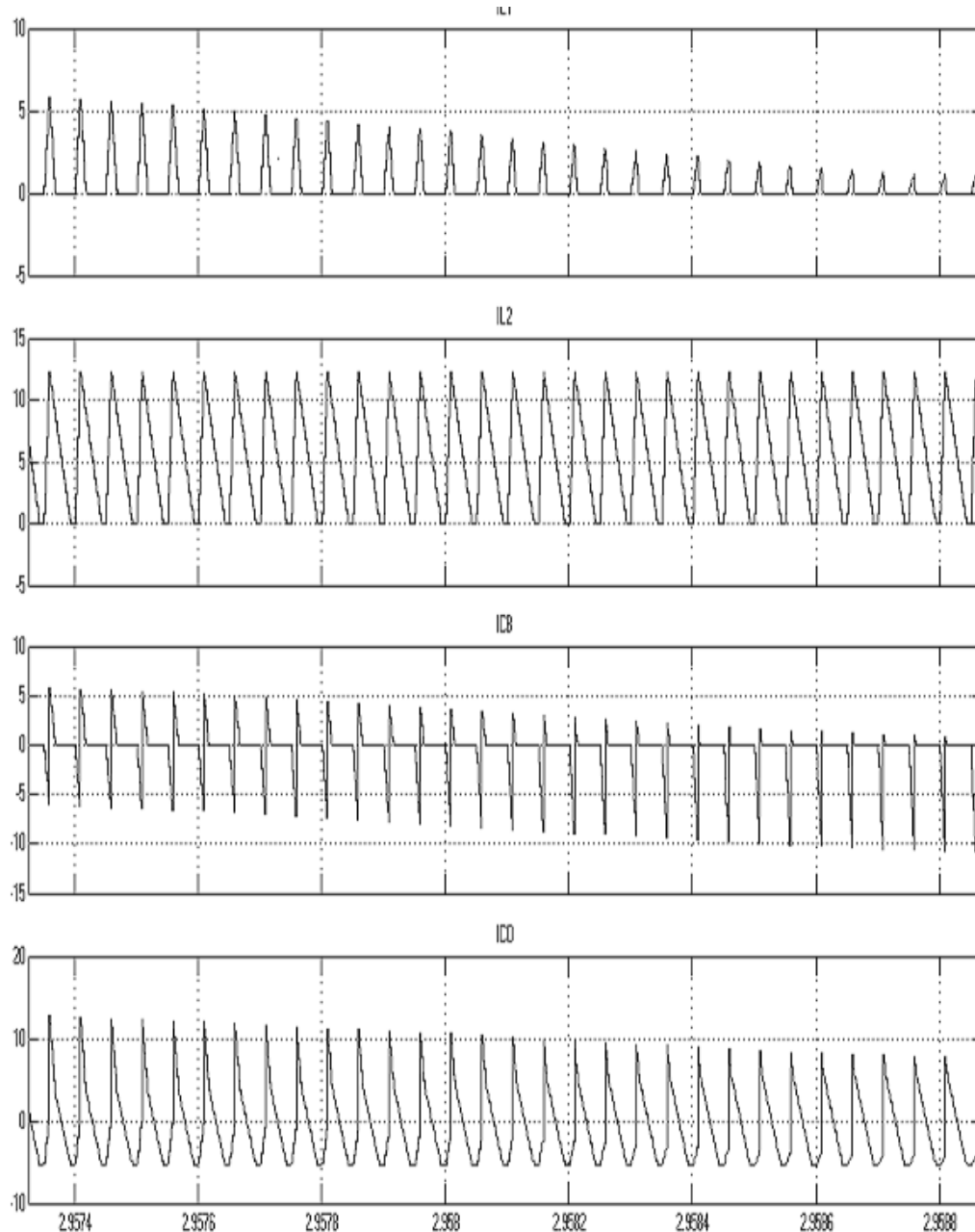
Fig 7.4: Waveforms of IL1, IL2, ICB, ICO

VIII.   Conclusion

The proposed AC/DC converter has been simulated, and the waveforms have been observed. The intermediate bus voltage of the circuit is able to keep low at all input and output conditions and is lower than that of the most reported converters. Thus, the lower voltage rating of capacitor can be used. Moreover, the topology is able to obtain low output voltage without high step-down transformer. Owing to the absence of transformer, the demagnetizing circuit, the associated circuit dealing with leakage inductance and the cost of the proposed circuit are reduced compared with the isolated counterparts. Because of the direct power transfer path in the proposed converter, it is able to achieve high efficiency.

REFERENCES

[1]   Q. Zhao, F. C. Lee, and F.-s. Tsai, "Voltage and current stress reduction in single-stage power-factor correction AC/DC converters with bulk capacitor voltage feedback," IEEE Trans. Power Electron., vol. 17, no. 4, pp. 477–484, Jul. 2002.

[2]   O. Garcia, J. A. Cobos, R. Prieto, P. Alou, and J. Uceda, "Single phase power factor correction: A survey," IEEE Trans. Power Electron., vol. 18, no. 3, pp. 749–755, May 2003.

[3]   S. Luo,W. Qiu,W.Wu, and I. Batarseh, "Flyboost power factor correction cell and a new family of single-stage AC/DC converters," IEEE Trans. Power Electron., vol. 20, no. 1, pp. 25–34, Jan. 2005.

[4]   D. D. C. Lu, H. H. C. Iu, and V. Pjevalica, "A Single-Stage AC/D converter with high power factor, regulated bus voltage, and output voltage," IEEE Trans. Power Electron., vol. 23, no. 1, pp. 218–228, Jan. 2008.

[5]   M. K. H. Cheung, M. H. L. Chow, and C. K. Tse, "Practical design and evaluation of a 1 kW PFC power supply based on reduced redundant power processing principle," IEEE Trans. Ind. Electron., vol. 55, no. 2, pp. 665–673, Feb. 2008.

[6]   D. D. C. Lu, H. H. C. Iu, and V. Pjevalica, "Single-Stage AC/DC Boost: Forward converter with high power factor and regulated bus and output voltages," IEEE Trans. Ind. Electron., vol. 56, no. 6, pp. 2128–2132, Jun. 2009.

[7]   H.-Y. Li and H.-C. Chen, "Dynamic modeling and controller design for a single-stage single-switch parallel boost-flyback–flyback converter," IEEE Trans. Power Electron., vol. 27, no. 2, pp. 816–827, Feb. 2012.

[8]   R. Redl and L. Balogh, "Design considerations for single-stage isolated power-factor-corrected power supplies with fast regulation of the output voltage," in Proc. IEEE Appl. Power Electron. Conf. Expo., 1995, vol. 1, pp. 454–458.

[9]   L. Antonio, B. Andrs, S. Marina, S. Vicente, and O. Emilio, "New power factor correction AC-DC converter with reduced storage capacitor voltage," IEEE Trans. Ind. Electron., vol. 54, no. 1, pp. 384–397, Feb. 2007.

[10] E. H. Ismail, A. J. Sabzali, and M. A. Al-Saffar, "Buck–boost-type unity power factor rectifier with extended voltage conversion ratio," IEEE Trans. Ind. Electron., vol. 55, no. 3, pp. 1123–1132, Mar. 2008.

[11] M. Ryu, J. Baek, J. Kim, S. Park, and H. Kim, "Electrolytic capacitor-less, nonisolated PFC converter for high-voltage LEDs driving," in Proc. IEEE Int. Conf. Power Electron. and ECCE Asia, 2011, pp. 499–506.

[12] A. A. Badin and I. Barbi, "Unity power factor isolated three-phase rectifier with two single-phase buck rectifiers based on the scott transformer," IEEE Trans. Power Electron., vol. 26, no. 9, pp. 2688–2696, Sep. 2011.

[13] S. K. Ki and D. D. C. Lu, "Implementation of an efficient transformerless single-stage single-switch ac/dc converter," IEEE Trans. Ind. Electron., vol. 57, no. 12, pp. 4095–4105, Dec. 2010.

[14] A. Abramovitz and K. M. Smedley, "Analysis and design of a tappedinductor buck–boost PFC rectifier with low bus voltage," IEEE Trans. Power Electron., vol. 26, no. 9, pp. 2637–2649, Sep. 2011.

[15] J. M. Alonso, M. A. Dalla Costa, and C. Ordiz, "Integrated buck-flyback converter as a high-power-factor off-line power supply," IEEE Trans. Ind. Electron., vol. 55, no. 3, pp. 1090–1100, Mar. 2008.

[16] K. Nishimura, K. Hirachi, S. Komiyama, and M. Nakaoka, "Two buck choppers built-in single phase one stage PFC converter with reduced DC voltage ripple and its specific control scheme," in Proc. IEEE Appl. Power Electron. Conf. Expo., 2008, pp. 1378–1383.

[17] T. J. Liang, L. S. Yang, and J. F. Chen, "Analysis and design of a single phase ac/dc step-down converter for universal input voltage," IET Electr. Power Appl., vol. 1, no. 5, pp. 778–784, Sep. 2007.

[18] M. A. Al-Saffar, E. H. Ismail, and A. J. Sabzali, "Integrated buck–boost–quadratic buck PFC rectifier for universal input applications," IEEE Trans. Power Electron., vol. 24, no. 12, pp. 2886–2896, Dec. 2009.

[19] X. Qu, S.-C. Wong, and C. K. Tse, "Resonance-assisted buck converter for offline driving of power LED replacement lamps," IEEE Trans. Power Electron., vol. 26, no. 2, pp. 532–540, Feb. 2011.

[20] Y. Jang and M. M. Jovanovic, "Bridgeless high-power-factor buck converter," IEEE Trans. Power Electron., vol. 26, no. 2, pp. 602–611, Feb. 2011.

[21] O. Garcia, J. A. Cobos, R. Prieto, P. Alou, and J. Uceda, "An alternative to supply DC voltages with high power factor," IEEE Trans. Ind. Electron.,vol. 46, no. 4, pp. 703–709, Aug. 1999.

A DC-DC Converter with Ripple Current Cancellation Based On Duty Cycle Selection

Janma Mohan[1], H. Sathish Kumar[2]

*(Student, Department of Electrical and Electronics Engineering, FISAT, MG university, Kerala, India)
** (Assistant Professor, Department of Electrical and Electronics Engineering, FISAT, MG university, Kerala, India)

Abstract: *In this paper a boost dc-dc converter is proposed based on the concept of ripple current cancellation. This proposed system has the novel capability of cancelling the input current ripple at an arbitrarily preselected duty cycle. This is accomplished without increasing the count of the number of components in contrast to other solutions available in the conventional system. In addition to this, the converter also features a high voltage gain without utilizing extreme values of duty cycle or boosting transformers. These features make the converter ideal to process electric power coming from low-voltage power-generating sources, such as renewables. This system also provides details on the principle of operation via topological considerations and a mathematical model. The key factor of reactive component sizing is also discussed in detail. The proposed boost dc-dc converter is evaluated by simulating in MATLAB/Simulink software.*

Keywords: *Boost converter, Complete charge interchange (CCI), Current ripple cancellation, Duty Cycle Selection, Switched capacitor (SC).*

I. Introduction

Dc – Dc converters are widely used in today's industrial or commercial electronic devices to manipulate a dc voltage source. As the name implies, dc – dc converters work exclusively to take a dc voltage input and convert it to output at a different level of dc voltage. They can either step-up or step-down the input dc voltage while maintaining minimal power loss during the process. There are many different topologies available for use such as Buck (step down), Boost (Step up), Fly back, Push-Pull, etc. This versatility is the reason that dc – dc converters are popular among many current electronic devices.

Owing to worldwide energy crisis and awareness of environmental protection in recent years, to seek for substitute energy has become an important issue. Among many substitute energies, solar energy, wind energy, hydroelectric power, biomass energy, and fuel cells are green energies with potential development.

A fuel Cell is a device that converts the chemical energy from a fuel into electricity through a chemical reaction with oxygen or another oxidizing agent. The fuel cell is one of the most promising power supplies and is drawing attention by many researchers. Due to high efficiency, high stability, low energy consumed and friendly to environment, this technology is in the progress to commercialize. Fuel cell has higher energy storage capability thus enhancing the range of operation for automobile. It is a source of clean energy, only water is produced after the reaction; hence, there is hardly any environmental pollution. Fuel cells as a source of power are usually applied to electric hybrid automobiles, distributed electric generation system, and portable and stationary power. In order to link the low output voltages of the fuel cells to an inverter or a load boost-type architecture with a large voltage gain is required.

The major challenge of designing a boost converter for high power application is how to handle the high current at the input and high voltage at the output. Another important requirement for a converter in renewable energy applications (for example, in fuel cells) is to drain a continuous current with minimum ripple. In boost converter designs, the input current-ripple is required to be a small percentage of the input dc current. It is well known that the current ripple is smaller as the input inductor becomes larger. This is a constraint since increasing the input inductor increases the size and cost of the converter. Several solutions have been proposed for addressing this drawback of the boost converter. In addition, a large inductor also slows down the open loop transient response of the converter. Therefore, converters combining these two features are expected to find many applications within the renewable-energy context.

Here, a boost converter topology is presented which combines two principles highly used in state of-the-art power converters:

- At the converter's input, two inductors are connected for canceling the input current ripple, and

- At the converter's output, an SC voltage multiplier is utilized to increase the voltage gain.

The SC stage has been improved by using a small resonant inductor to limit the peak current resulting from the switching process and hence preventing large current spikes. The presented converter does not require transformers or coupled inductors and is intended to be used along with fast-switching power semiconductors. Also, the topology presented herein is able to cancel the input current ripple. Furthermore, it combines a complete charge interchange- switched capacitor (CCI-SC) circuit with a boost converter into a single converter.

II. Literature Survey

In high voltage multilevel boost converter the leakage resistance in the inductor-charging loop limits the boost ratio. Because of this, a boost converter is not used when the required boost ratio is higher than four. A standard approach to overcome this issue is the use of small reactive components by increasing the converter's switching frequency for a given amount of acceptable ripple. In three switch and high voltage dc-dc converters, small reactive elements also feature a small leakage resistance. However, the finite switching time in actual power semiconductors limits the switching frequency when the duty ratio is too small or too high. A traditional solution to this is the employment of intermediate transformers to increase the voltage without using extreme values of duty cycles.

Several topologies have been proposed for overcoming the above challenges, including the use of coupled inductor and/or transformers. Moreover, the literature offers additional solutions based on the switched capacitor (SC) principle, with a combination of converters featuring coupled inductors with voltage multipliers or SC multipliers. Converters without coupled inductors based on pure SC circuits have found applications in low-power on-chip applications, but at larger power levels, solutions based on traditional converters have been preferred due to the number power semiconductors required, current spikes among capacitors, and high switching frequency limitations.

The interleaving of SC circuits has also been proposed as a solution for high voltage gain in switched capacitor based converters that already exist. A number of power converters for higher power application that eliminate the use of coupled inductors or transformers have been also proposed literatures. These topologies are expected to penetrate the market of high-gain dc–dc converter as silicon carbide and other wide-band gap fast-switching power semiconductors become available. This will make the switching frequency limitation in power converters to become a transformer issue, since transformers increase their losses when the frequency is too high.

In the paper of Gu et al. , of large gain hybrid dc-dc converter they use the SC principle with complete charge interchange (CCI) along with an additional pulse width modulated (PWM) boost converter for voltage regulation. As explained in the literature SC based resonant converter SC circuits with CCI are not utilized for voltage regulation, because this negatively affects the converter's efficiency. However, combining a CCI-SC circuit with a PWM controlled converter allows for optimizing the efficiency of both converters. In summary, converters with a high voltage gain which do not require a transformer, coupled inductors, or extreme duty cycle values are highly desirable given the quick penetration of low-voltage power-generating sources.

Different from coupled inductor based converters, the proposed converter does not require transformers or coupled inductors and is intended to be used along with fast-switching power semiconductors. Different from hybrid SC converter, the topology proposed herein is able to cancel the input current ripple. Furthermore, it combines a CCI-SC circuit with a boost converter into a single converter and is able to provide voltage regulation without sacrificing the converter's efficiency.

III. Presented Converter Topology

3.1 Novel Boost Converter Topology

The improved boost converter topology is shown in Figure 3.1 As the figure suggests, the topology contains two transistors (S_1 and S_2), three diodes (d_1, d_2, and d_3), three capacitors (C_1, C_2, and C_3), two inductors for energy storage (L_1 and L_2), and a small inductor (L_3) for current limiting through d_3. In practical implementation, L_3 is around 100 times smaller than L_2 and 50 times smaller than L_1. As a result of its reduced size, small-ripple approximations do not apply to $L3$, and hence, the selection of its inductance is based on the CCI between C_2 and C_3.
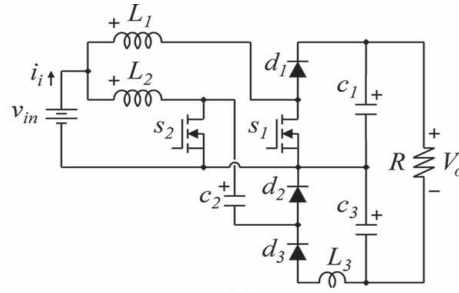
Figure 3.1: Circuit Schematic of the new topology

The transistors switch complementarily, i.e., when S_1 is closed, S_2 is open and vice versa. The operation of the converter may be explained considering the small-ripple approximation for the voltage across capacitors and continuous conduction mode for L_1 and L_2. The details on the circuit operation are conveniently introduced by employing several analytical waveforms. As shown in Figure 3.2 and 3.3, the converter has two equivalent circuits resulting from the switch action. When S_1 is on (and S_2 is off), the topology is represented by the equivalent circuit in Figure 3.2. During this time, the diode d_1 is reversely biased, blocking the voltage across C_1. Similarly, diode d_3 is reversely biased, blocking the voltage across C_3. The current through L_2 forces the diode d_2 to be closed since transistor S_2 is open.

The typical waveforms for the currents through L_1 and L_2, the input current, and the switching sequence for S_1 and S_2 are shown in Figure 3.4 from top to bottom. While S_1 is conducting, the current through L_1 rises with a slope of v_{in}/L_1, and L_2 discharges at a rate of $(v_{in} - v_{c2})/L_2$. biased, blocking the voltage across C_3. The current through L_2 forces the diode d_2 to be closed since transistor S_2 is open.
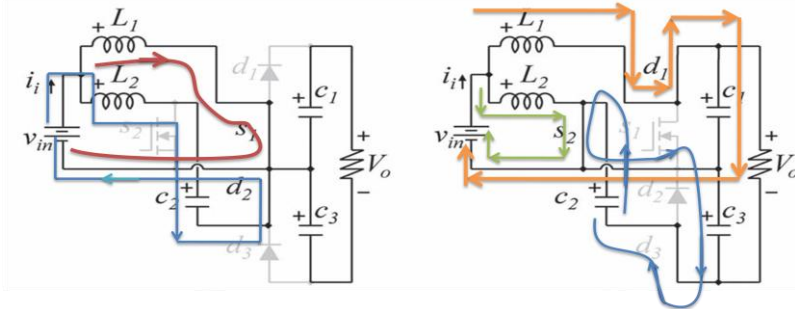
Figure 3.2: Equivalent circuit when S_1 is on   Figure 3.3: Equivalent circuit when S_2 is on

The typical waveforms for the currents through L_1 and L_2, the input current, and the switching sequence for S_1 and S_2 are shown in Figure 3.4 from top to bottom. While S_1 is conducting, the current through L_1 rises with a slope of v_{in}/L_1, and L_2 discharges at a rate of $(v_{in} - v_{c2})/L_2$.
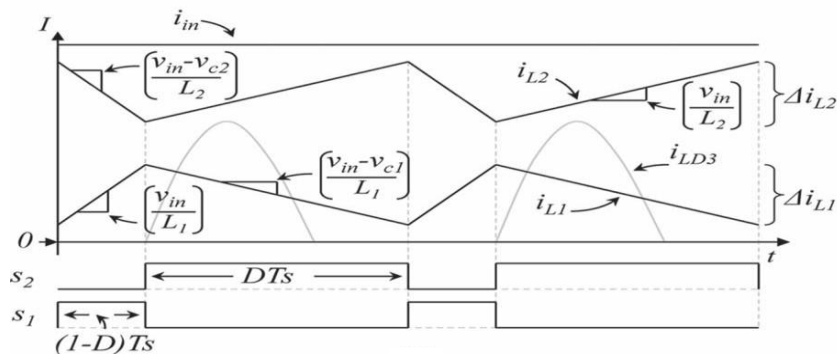
Figure 3.4: Waveforms of input current, current through input inductors, and switching sequence

On the other hand, while S_2 is on (and S_1 is off), the resulting equivalent circuit is as shown in Figure 3.3. During this time, the L_1 discharges with a slope that is equal to $(v_{in} - v_{C1})/L_1$, while L_2 charges at a rate of v_{in}/L_2. Furthermore, while S_2 is conducting, the capacitors C_2 and C_3 are connected in parallel, leading to an SC-type behavior. As a result of this, a small inductor (L_3) is needed in order to limit the peak current around this loop.

A typical waveform for the current through L_3 is also shown in Figure 3.4. A key feature of the boost converter topology can be observed in Figure 3.1 that is the converter's input current corresponds to the sum of the currents through L_1 and L_2. Since L_1 and L_2 charge/discharge in a complementary manner, one can size those two inductors such that the input current is ripple free for a selected value of the converter's duty cycle. The current waveforms shown in Figure 3.4 correspond to a converter that features a zero input current ripple at a duty cycle of $D = 75\%$. This is possible if both inductors are charged with the same voltage and $L_2 = 3L_1$.

3.2 Principle of Switched Capacitor
A switched capacitor is an electronic circuit element used for discrete time signal processing. It works by moving charges into and out of capacitors when switches are opened and closed. Usually, non-overlapping signals are used to control the switches, so that not all switches are closed simultaneously.
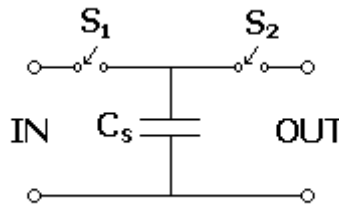
Figure 3.5: Circuit schematic of switched capacitor

The simplest switched capacitor (SC) circuit is the switched capacitor resistor, made of one capacitor C and two switches S_1 and S_2 which connect the capacitor with a given frequency alternately to the input and output of the SC. Each switching cycle transfers a charge q from the input to the output at the switching frequency f

IV. Analysis and Selection of Components
The architecture corresponds to an interleaving-type converter, combining features from a boost converter and a high-voltage converter. The topology features a small inductor for peak current limiting which has no effect on the basic operation of the converter for power transfer. In addition, the interleaving of two inductors allows current ripple cancelation at an arbitrary preselected duty cycle. Furthermore, as there are only two switches, the converter is controlled by a single duty cycle.

4.1 Voltage Gain Analysis
The dynamics of L_1, L_2, and C_1 may be conveniently analyzed considering their average behavior, as their state variables feature triangular waveforms similar to those in traditional dc/dc converters. On the other hand, C_2, C_3, and L_3 form a SC circuit, and therefore, their dynamic behavior has to be formulated with additional considerations. However, a number of the converter's features can be explained focusing on L_1, L_2, and C_1, where dynamic averaging applies. Under this assumption, switching functions may be readily replaced by their corresponding duty cycles. For the analysis hereinafter, the converter's duty ratio *d(t)* is defined as percentage of time over the switching period that the switch S_2 is on, i.e.,

$$d(t) = \frac{1}{T_s} \int_t^{t+T_s} q_2(\tau) d\tau \qquad (1)$$

Where T_S is the switching period and q_2 is the switching function of S_2 that is equal to one while S_2 is closed and zero otherwise. Under this assumption, and neglecting for now the inductors' equivalent series resistance (ESR), the equations that represent the average dynamics for inductors L_1 and L_2 are

$$L_1 \frac{di_{L1}}{dt} = d(v_{in} - v_{c1}) + (1 - d)v_{in} \tag{2}$$

$$L_2 \frac{di_{L2}}{dt} = d(v_{in}) + (1 - d)(v_{in} - v_{c2}) \tag{3}$$

In steady state, the average voltage across the inductors must be equal to zero. Thus, by zeroing the left-hand side of equations (1) and (2), the steady state voltage across C_1 and C_2 may be expressed as

$$V_{C1} = \frac{1}{D} V_{in} \tag{4}$$

$$V_{C2} = \frac{1}{1-D} V_{in} \tag{5}$$

In equations (4) and (5), capital letters denote steady-state quantities. It readily follows from equations (4) and (5) that the voltages across C_1 and C_2 are proportional to one another, i.e.

$$V_{C1} = \frac{1-D}{D} V_{C2} \tag{6}$$

$$V_{C2} = \frac{D}{1-D} V_{C1} \tag{7}$$

On the other hand, the equation that represents the average dynamics for C_1 is

$$C_1 \frac{dv_{C1}}{dt} = di_{L1} - \frac{v_{C1} + v_{C3}}{R} \tag{8}$$

In steady state, the average current through C_1 must be equal to zero, which leads to the following expressions for the current through L_1

$$I_{L1} = \frac{1}{D} \left(\frac{V_{C1} + V_{C3}}{R} \right) \tag{9}$$

As C_2 and C_3 form an SC circuit, average dynamic equations do not apply. However, the steady-state current through L_2 can be computed by input/output power balance considerations. It becomes

$$I_{L2} = \frac{1}{1-D} \left(\frac{V_{C1} + V_{C3}}{R} \right) \tag{10}$$

Furthermore, from figure 3.1, the output voltage is

$$V_0 = V_{C1} + V_{C2} \tag{11}$$

Thus combining equations (4), (5) and (9)-(11), the converter voltage gain becomes

$$\frac{V_0}{V_{in}} = \frac{1}{D(1-D)} \tag{12}$$

The improved circuit has an SC stage which maybe increased by including additional capacitors and diodes Capacitors C_2 and C_3 work in an SC way because C_2 clamps the voltage across C_3 while the switch S_2 is closed. This is because the energy stored in L_3 is negligible compared to other energy storage elements in the converter. Furthermore, in steady state, C_2 and C_3 feature the same average voltage.

$$V_{C2} = V_{C3} \tag{13}$$

The gain expressed by equation (12) corresponds to an ideal case as the inductor's ESR has been neglected. In a practical implementation, the leakage resistance in inductors greatly limits this gain. In order to quantify this, consider first rewriting equations (9) and (10) using (6) and (7) and (11).

$$I_{L1} = \left(1 + \frac{D}{1-D} \right) \frac{1}{D} \frac{V_{C1}}{R} = \frac{1}{D(1-D)} \frac{V_{C1}}{R} \tag{14}$$

$$I_{L2} = \left(1 + \frac{1-D}{D} \right) \frac{1}{1-D} \frac{V_{C2}}{R} = \frac{1}{D(1-D)} \frac{V_{C2}}{R} \tag{15}$$

Equations (14) and (15) simplify the inclusion of ESRs as the inductor currents have been expressed in terms of the voltages across the capacitors that they directly connect to. By including the ESR of L_1, equation (2) becomes

$$L_1 \frac{di_{L1}}{dt} = d(v_{in} - R_{L1} i_{L1} - v_{C1}) + (1 - d)(v_{in} - R_{L1} i_{L1}) \tag{16}$$

where R_{L1} is the ESR resistance of L_1. In steady state, the equation (16) becomes

$$0 = D(V_{in} - R_{L1} I_{L1} - V_{C1}) + (1 - D)(V_{in} - R_{L1} I_{L1})$$
$$= V_{in} - R_{L1} I_{L1} - DV_{C1} \tag{17}$$

By substituting (14) in (17), the ratio between the voltage across C_1 and the input voltage becomes,

$$\frac{V_{C1}}{V_{in}} = \frac{1}{D + \frac{R_{L1}}{D(1-D)R}} \tag{18}$$

Similarly, the inclusion of the ESR in L_1 (R_{L2}) leads to rewriting (3) as

$$L_2 \frac{di_{L2}}{dt} = d(v_{in} - R_{L2}i_{L2}) + (1-d)(v_{in} - R_{L2}i_{L2} - v_{C2}) \tag{19}$$

This in steady state becomes,

$$\begin{aligned} 0 &= D(V_{in} - R_{L2}I_{L2}) + (1-D)(V_{in} - R_{L2}I_{L2} - V_{C2}) \\ &= V_{in} - R_{L2}I_{L2} - DV_{C2} \end{aligned} \tag{20}$$

Moreover, substituting (15) in (20), the ratio between the voltage across C_2 and the input voltage becomes

$$\frac{V_{C2}}{V_{in}} = \frac{1}{(1-D) + \frac{R_{L2}}{D(1-D)R}} \tag{21}$$

Finally, using equations (3.11) and (3.13), the converter's practical gain is obtained by adding (3.18) and (3.21)

$$\frac{V_0}{V_{in}} = \frac{1}{D + \frac{R_{L1}}{D(1-D)R}} + \frac{1}{(1-D) + \frac{R_{L2}}{D(1-D)R}} \tag{22}$$

By construction, a smaller inductor features a smaller ESR. As explained earlier, the topology herein sizes the inductors to cancel the input current ripple at a given duty ratio. For example, if $L_2 = 3L_1$, the input current is ripple free at $D = 75\%$. As a first approximation, it may be assumed that the inductor's ESRs follow the same trend, i.e., $R_{L2} = 3R_{L1}$. Figure 3.1 shows the converter's voltage gain under this assumption for different values of the ratio between the load resistance (R) and R_{L2}. The figure is readily obtained by plotting equation (3.22). As the figure suggests, the minimum voltage gain is four and occurs at $D = 50\%$. If the duty cycle is smaller than 50%, the gain increases again, and therefore, the minimum gain that the converter can operate is around four. The operating range is selected to be at $D > 50\%$, which ensures that L_3 will have enough time to discharge.

As a result, the selection of the inductors has to be such that $L_2 > L_1$, in order to achieve ripple cancelation for the input current. Furthermore, $L_2 > L_1$ implies that $R_{L2} > R_{L1}$., and thus, larger voltage gains are obtained for $D < 10\%$, which can be observed in figure 3.1. This is a compromise between canceling the input current ripple and obtaining a larger voltage gain. However, in practical applications, dc/dc converters are operated at duty cycles of about $20\% < D < 80\%$.

It can be seen from the figure that, between that range, the voltage gain is practically symmetric, and hence, the voltage gain lost is minimal. It is noteworthy that selecting $D > 50\%$ as the operating range translates into having the SC part of the converter handling a larger amount of the converter's throughput power. The figure also suggests that, as in most dc/dc converter's topologies, the inductor's ESR limits the practical gain of the approach. Therefore, this topology is more suitable if a large switching frequency is employed as, in that case, reactive components (and, hence, ESRs) are very small.
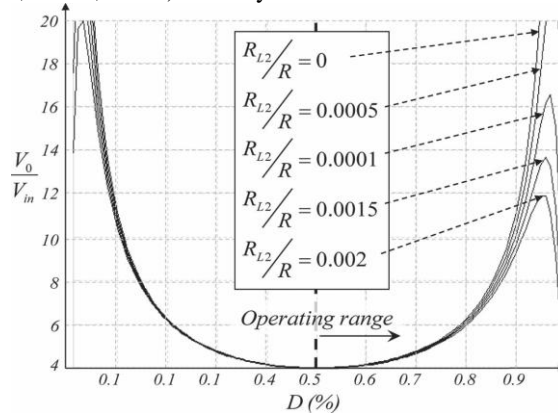
Figure 4.1: Voltage gain versus duty cycle considering inductor's ESR

4.2 Energy Storage Inductor Sizing
From figure 4, it readily follows that the current ripple on the inductor is given by

$$\Delta i_{L1} = \frac{V_{in}}{L_1} \frac{(1-D)}{F_S} \tag{23}$$

$$\Delta i_{L2} = \frac{V_{in}}{L_2} \frac{D}{F_S} \tag{24}$$

where $F_S = 1/T_S$ is the converter's switching frequency. The input current ripple, denoted by Δi_{in}, corresponds to the difference between each inductor's current ripples, i.e.,

$$\Delta i_{in} = \Delta i_{L2} - \Delta i_{L1} \tag{25}$$

$$\Delta i_{in} = \frac{V_{in}}{F_S} \left(\frac{D}{L_2} - \frac{1-D}{L_1} \right) \tag{26}$$

As it is evident from equation (26), the input current ripple can be eliminated by zeroing out the left-hand side of this equation. This leads to the following relationship:

$$L_2 = L_1 \frac{D}{1-D} \tag{27}$$

For example, if the expected input and output voltages are such that the duty cycle is equal to 75%, by sizing $L_2 = 3L_1$, the input current ripple is eliminated. Once the values of L_1 and L_2 are selected, equation (26) may be used to predict the input current ripple for the full operating range. Thus, if $L_2 = 3L_1$, (26) becomes

$$\Delta i_{in} = \frac{3V_{in}}{F_S L_2} \left(\frac{4D}{3} - 1 \right) \tag{28}$$

It is clear from the equation(28) that there is a linear dependence of the input current ripple with respect to the value of the duty cycle, and the assumption of ripple-free input current becomes weaker as the operating point departs from the selected duty ratio.

4.3 Peak -Current- Limiting Inductor Sizing

As mentioned earlier, the diode d_3 connects the capacitors C_2 and C_3 in parallel, and as a result, a peak- current-limiting inductor is needed. Moreover, the average current through the diode equals the load current, as it may be evident from Figure 4.1. However, the shape of the current through d_3 may be undesirable and, hence, the need to control it. In order to understand the phenomenon, consider the switching process at the time when S_2 turns off. As suggested by Figure 4.3, at that instant, capacitors C_2 and C_3 feature exactly the same voltage because they were connected in parallel. Call this voltage $V_{C.0}$. After S_2 opens, the circuit commutes into the topology in Fig. 1(b), and as a result of this, C_2 and C_3 are no longer connected. While S_2 is off (during $(1-D)T_S$ seconds), C_3 discharges following the load current while C_2 charges following the current through L_2. Call $V_{C3.1}$ and $V_{C3.1}$ the final voltages across capacitors C_2 and C_3, respectively. They can be expressed as

$$V_{C3.1} = V_{C.0} + \Delta v_{C2} = V_{C.0} + \frac{I_{L2}}{C_2}(1-D)T_S \tag{29}$$

$$V_{C3.1} = V_{C.0} - \Delta v_{C3} = V_{C.0} - \frac{I_0}{C_3}(1-D)T_S \tag{30}$$

At the end of $(1-D)T_S$, the voltage difference between them is given by

$$V_{diff} = \Delta v_{C2} + \Delta v_{C3} = \left(\frac{I_{L2}}{C_2} + \frac{I_0}{C_3} \right)(1-D)T_S \tag{31}$$

If there is no inductor in series with d_3, the peak current would be V_{diff} (some volts) over the resistance in this loop, given by the on-state resistance of S_2 and d_3, and the ESR of C_2 and C_3 (some tens of milliohms). Figure 4.2 shows a circuit schematic for the current loop where R_{eq} stands for the lumped resistance of the various elements around the loop. This may lead to a peak current that overpasses the peak current limit of the various devices in that loop.

At the time of design, this peak current can be computed using manufacturer datasheets, and thus, the inductor in series with d_3 may (or may not) be required. If the current overpasses the peak current limit of devices, the inductor is mandatory.

As shown in Figure 3.3, this current rises rapidly and may destroy power semiconductors if the inductor L_3 is not properly designed. From Figure 3.2, it is also evident that C_{eq} is the series connection of C_2 and C_3. Since L_3 stores a small amount of energy, it charges and discharges completely in a switching cycle, smoothing out the current among capacitors. However, it also produces a resonant current peak at a frequency of

$$f_0 = \frac{\omega_0}{2\pi} = \frac{1}{2\pi\sqrt{L_3 C_{eq}}} \qquad (32)$$
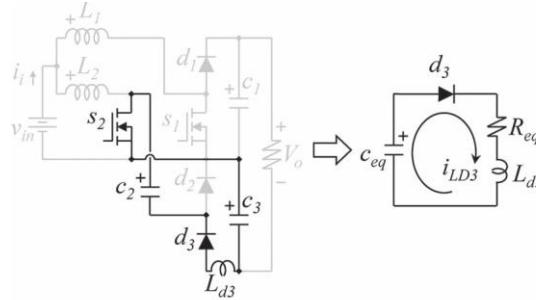
Figure 4.2: Equivalent circuit schematics
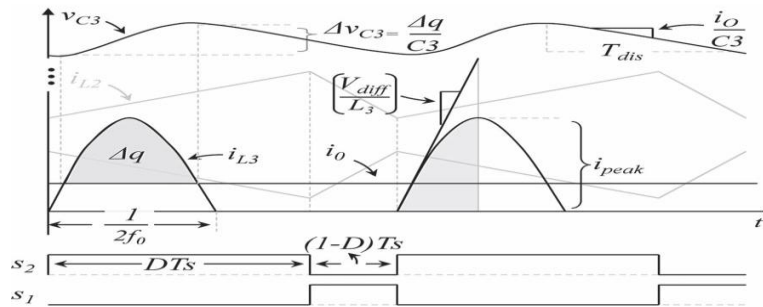
Figure 4.3: Waveforms for the reactive component selection

As mentioned above, the converter will operate at a duty cycle larger than 50%. Therefore, L_3 should be selected such that $f_0 > F_S$. This ensures that the inductor will complete the discharge process before the beginning of the next switching stage for all values of the duty cycle within the operating range. Furthermore, Figure 3.3 provides the basis for the calculation of the peak current around the loop. At the beginning of the charging period, the current starts rising at a rate of V_{diff}/L_3 . Hence, representing the current through the loop as $i_{L3}(t) = i_{L3}\sin(\omega_o t)$, its derivative at $t = 0$ can be computed and equated to V_{diff}/L_3. This allows solving for i_{L3}

$$i_{L3} = \frac{V_{diff}}{\omega_o L_3} \qquad (33)$$

4.4 Capacitor Sizing

The selection of the capacitance for C_1, C_2, and C_3 may be approached following a procedure analogous to that used in the sizing of the inductors L_1 and L_2. While S_1 is on, the current through C_1 follows the load current, and thus

$$\Delta v_{c1} = \frac{I_0}{C_1}(1 - D)T_S \qquad (34)$$

Also, while S_1 is closed, the capacitor C_2 charges following the current through L_2, and hence

$$\Delta v_{c2} = \frac{I_{L2}}{C_2}(1 - D)T_S \qquad (35)$$

Finally, C_3 may be selected recognizing that L_3 carries the same average current as the load. When the instantaneous value of current through this inductor overpasses the output current, the capacitor C_3 begins

charging, which leads to a voltage increase ΔV_{C3} given by $\Delta q/C_3$. This is graphically shown in Figure 3.3, where the shaded area represents the charge Δq. After L_3 has been selected, the time while C_3 is charging can be computed by finding the time at which $i_0 < i_{L3}(t)$,as suggested in Figure 3.3. Next, C_3 discharges through the remaining of the switching period, and hence

$$T_{dis} = T_S - \left(\frac{2}{\omega_0}\arcsin\left(\frac{i_0}{i_{L3}}\right)\right) \tag{36}$$

where T_{dis} corresponds to the time while C_3 discharges and arcsin represents the inverse of the sine function. Since, during this period, C_3 follows the load current, it is possible to state that

$$\Delta v_{c3} = \frac{I_0}{C_3}T_{dis} \tag{37}$$

which allows for the sizing of C_3.

V. Simulink Model and Simulation Results

The converter presented herein was simulated in MATLAB/Simulink software in order to validate its principle of operation. The simulation circuit is as shown by the Figure 5.1. The list of parameters i.e. values of each component in the circuit is shown in the TABLE 5.1

Parameters	Values
INPUT VOLTAGE	15 V
DUTY CYCLE	70 %
OUTPUT VOLTAGE	71 V
L_2	140 µH
L_1	330 µH
L_3	28 µH
C_1 , C_2 , C_3	10 µF
SWITCHING FREQUENCY F_S	25 kHz

Table 5.1: Parameter specification table

5.1 Simulink Model

5.1.1 Novel Boost Converter Topology

5.2 Simulation Results- Waveforms
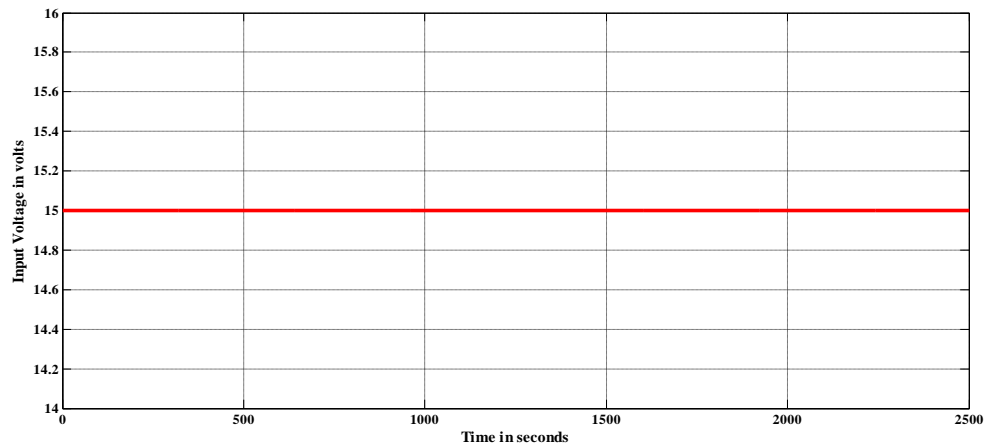
Figure 5.1: Waveform of input voltage
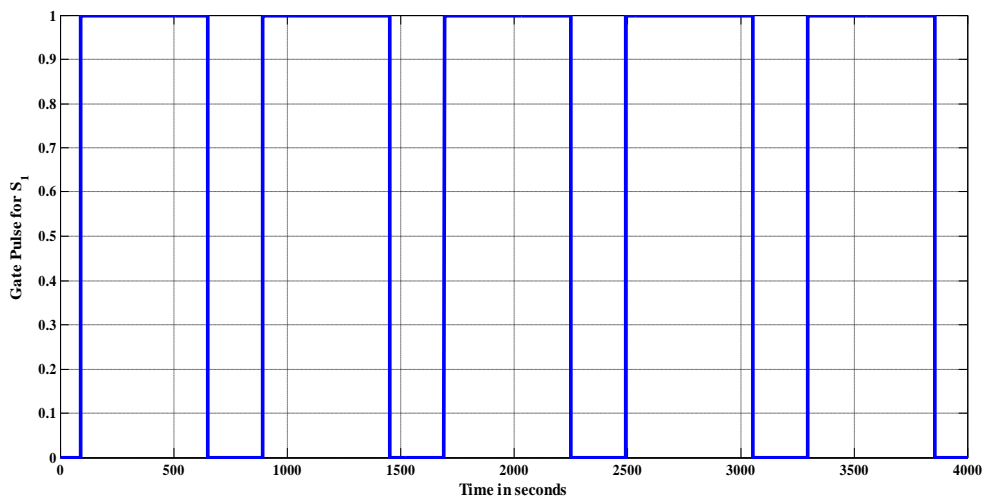
Figure 5.2: Gate pulse for switch S_1
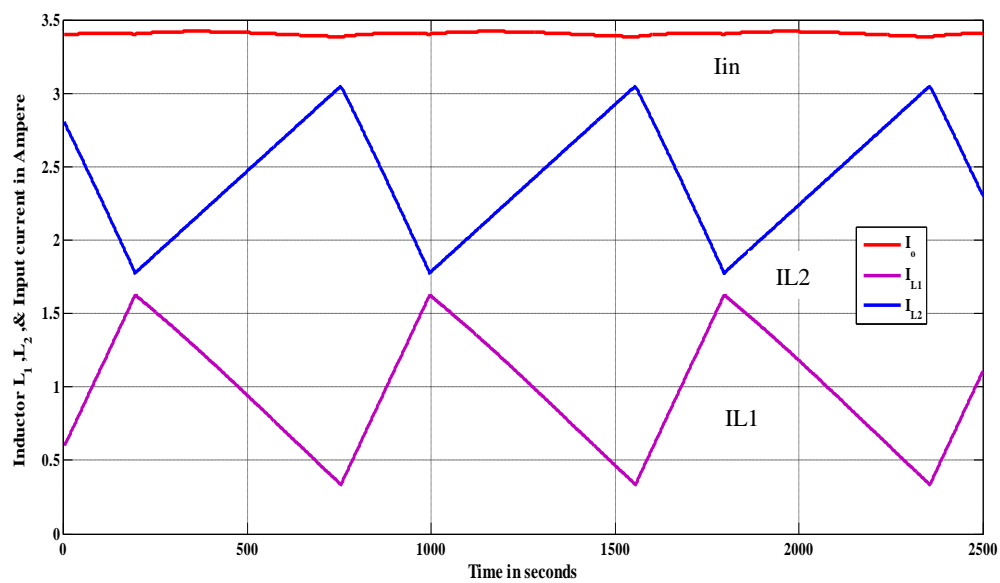
Figure 5.3: Waveforms of current through inductors and input current
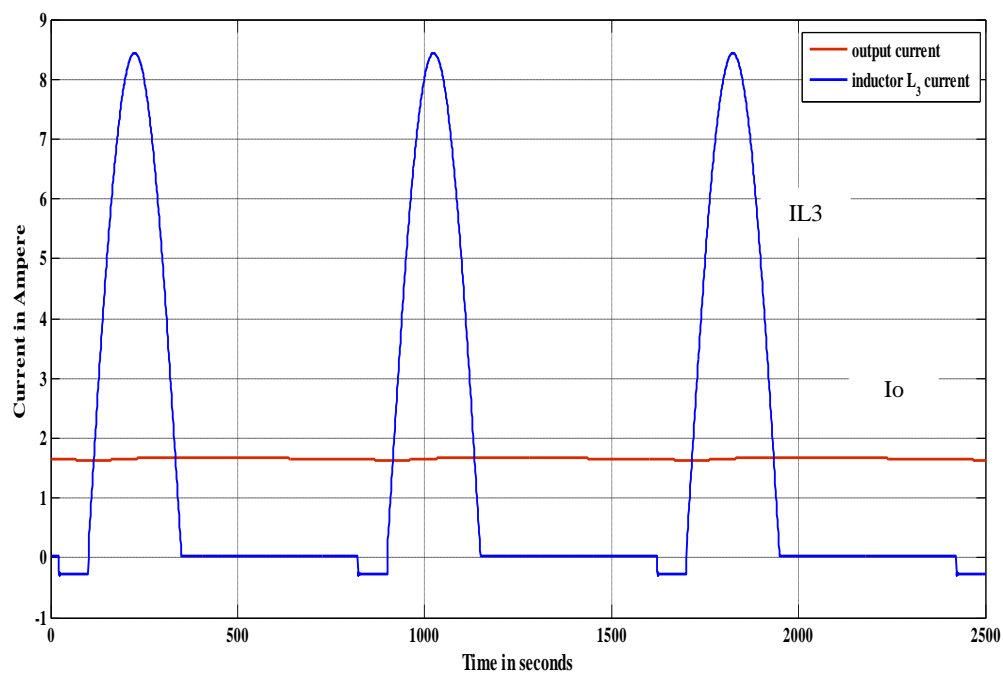
Figure 5.4: Waveforms of current through resonant inductor and output current
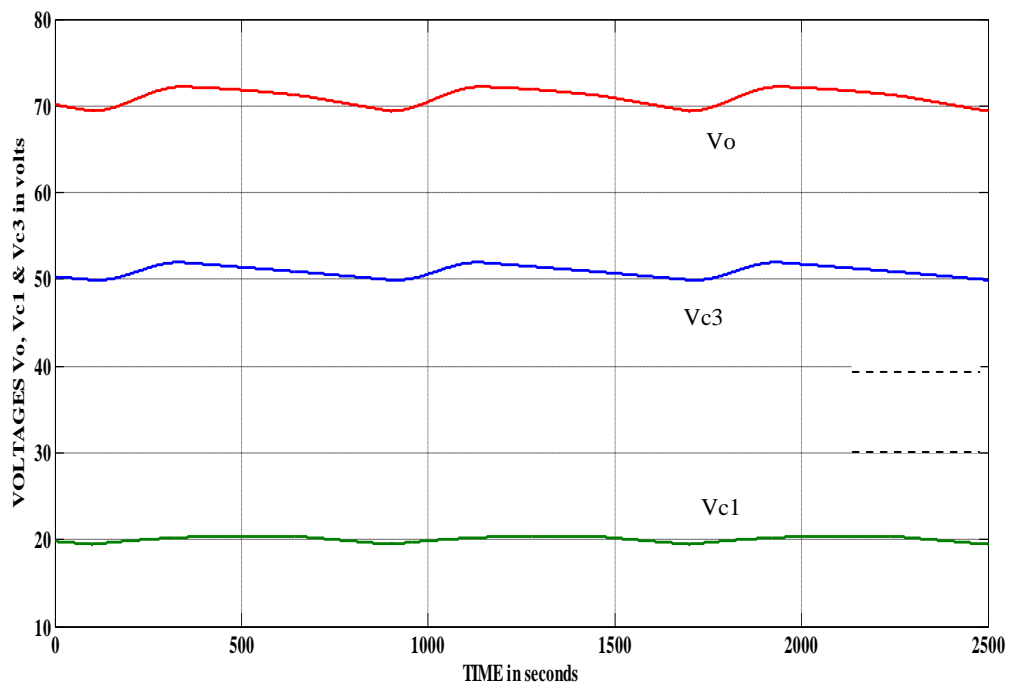
Figure 5.5: Waveforms of voltages through capacitors and output voltage

It is evident from the simulation results that the input current is almost ripple free. A closer examination of the measurements also suggests the simulation datas are consistent with the values obtained as per the design.

VI.   Conclusion

This paper has presented a boost dc–dc converter topology, with the novel capability of canceling the input current ripple at an arbitrarily preselected duty cycle. This is accomplished without increasing the count of the number of components. In addition, the converter features a high voltage gain without utilizing extreme values of duty cycle or boosting transformers. These features make the converter ideal to process electric power coming from low-voltage power-generating sources, such as renewable. The boost factor or voltage gain may be extended by utilizing diode-capacitor multipliers. Those features are highly desirable in fuel cell applications.

Moreover, the rapid development of silicon carbide and other wide-band gap fast-switching power semiconductors will enable the use of smaller reactive components and hence provide further advantages to the approach presented herein against transformer or coupled-inductor-based topologies. Simulation results are consistent with the analytical predictions of the various formulas developed through this paper, and hence, the approach may be considered definitely validated.

6.1 Scope for Future Work

The presented converter can be extended to a multiplier boost converter. An advantage of this topology is that helps to reduce the size of the input inductor and its corresponding series resistance. The converter presented is designed in such a way that both switches are operated alternatively. However, they can also be operated with the same duty cycle in an interleaving manner. In this particular case, both output capacitors would obtain the same voltage and thus output voltage can be doubled.

REFERENCES

[1]   J. C. Rosas-Caro, J. E. Valdez-Resendiz, J. C. Mayo-Maldonado, R. Salas- Cabrera, J. M. Ramirez-Arredondo, and J. Salome-Baylon, "Transformer-less High Gain Boost Converter with Input Current Ripple Cancellation At a Selectable Duty Cycle," *in IEEE Trans. Ind. Electron*, vol. 60, Oct. 2013.
[2]   D. Gu, D. Czarkowski, and A. Ioinovici, "A large DC-gain highly efficient hybrid switched-capacitor-boost converter for renewable energy systems," in *Proc. IEEE Energy Convers. Congr. Expo. ECCE*, Sep. 2011, pp. 2495–2500.
[3]   J. C. Rosas-Caro, J. C. Mayo-Maldonado, R. F. Vazquez-Bautista, A. Valderrabano-Gonzalez, R. Salas-Cabrera, and J. E. Valdez-Resendiz, "Hybrid voltage-multipliers based switching power converters," *IAENG Trans. Eng. Technol.*, vol. 1373, no. 1, pp. 29–43, Aug. 2011.
[4]   C. S. Leu, P. Y. Huang, and M. H. Li, "A novel dual-inductor boost converter with ripple cancellation for high-voltage-gain applications," *IEEE Trans. Ind. Electron.,* vol. 58, no. 4, pp. 1268–1273, Apr. 2011.
[5]   Y. Berkovich and B. Axelrod, "Switched-coupled inductor cell for DC–DC converters with very large conversion ratio," *IET Power Electron.*, vol. 4, no. 3, pp. 309–315, Mar. 2011.
[6]   S. C. Tan, S. Kiratipongvoot, S. Bronstein, A. Ioinovici, Y. M. Lai, and C. K. Tse, "Adaptive mixed on-time and switching frequency control of a system of interleaved switched-capacitor converters," *IEEE Trans. Power Electron.*, vol. 26, no. 2, pp. 364–380, Feb. 2011.

International Journal of Modern Engineering Research (IJMER)

Contents :

Single-Input Double Output High Efficient Boost Dc–Dc Converter

Thulasi V. S.[1], H. Satish kumar[2]

[1](Student, Department of Electrical and Electronics Engineering, FISAT, MG university, Kerala, India))
[2](Assistant Professor, Department of Electrical and Electronics Engineering, FISAT, MG university, Kerala, India)

ABSTRACT: *The aim of this project is to develop a high-efficiency single-input multiple-output (SIMO) dc–dc converter. The proposed converter can boost the voltage of a low-voltage input power source to a controllable high-voltage dc bus and middle-voltage output terminals. The high-voltage dc bus can take as the main power for a high-voltage dc load or the front terminal of a dc–ac inverter.Moreover, middle-voltage output terminals can supply powers for individual middle-voltage dc loads or for charging auxiliary power sources (e.g., battery modules). In this project, a coupled-inductor based dc–dc converter scheme utilizes only one power switch with the properties of voltage clamping and soft switching, and the corresponding device specifications are adequately designed. As a result, the objectives of high-efficiency power conversion, high step up ratio, and various output voltages with different levels can be obtained.*
Keywords: *Coupled inductor, high-efficiency power conversion, single-input multiple-output (SIMO) converter, soft switching, voltage clamping.*

I. Introduction

In order to protect the natural environment on the earth, the development of clean energy without pollution has the major representative role in the last decade. By dealing with the issue of global warning, clean energies, such as fuel cell (FC), photovoltaic, and wind energy, etc., have been rapidly promoted. Due to the electric characteristics of clean energy, the generated power is critically affected by the climate or has slow transient responses, and the output voltage is easily influenced by load variations.For example Photovoltaic (PV) sources are used today in many applications from satellite power systems to battery chargers and home appliances. The power produced by a solar panel depends on two factors;irradiation,and temperature. As irradiation and temperature levels change rapidly, the voltage produced fluctuates and becomes inconstant.

A converter is therefore required to produce a constant voltage that is matched to the requirements of the load and supplied efficiently. Therefore dc–dc converters with steep voltage ratio are usually required in many industrial applications. The conventional boost converters cannot provide such a high dc-voltage ratio due to the losses associated with the inductor, filter capacitor, main switch, and output diode.As a result, the conversion efficiency is degraded, and the electromagnetic interference (EMI) problem is severe under this situation.This study presents a newly designed SIMO converter(Boost converter) with a coupled inductor. Patra *et al*. presented "Single inductor multiple output switcher with Simultaneous Buck, Boost, and Inverted Outputs ".Which is capable of generating buck, boost, and inverted outputs simultaneously.However, over three switches for one output were required. This scheme is only suitable for the low output voltage and power application, and its power conversion is degenerated due to the operation of hard switching.

II. Literature Review

Nami et al. proposed "Multi-output DC–DC converters based on diode-clamped converters configuration topology and control strategy" a new dc–dc multi-output boost converter, which can share its total output between different series of output voltages for low- and high-power applications. Unfortunately, over two switches for one output were required, and its control scheme was complicated. Besides, the corresponding output power cannot supply for individual loads independently. Chen et al. "The Multiple-Output DC–DC Converter With Shared ZCS Lagging Leg" investigated a multiple-output dc–dc converter with shared zero-currentswitching (ZCS) lagging leg. Although this converter with the soft-switching property can reduce the switching losses, this combination scheme with three full-bridge converters is more complicated, so that the objective of high-efficiency power conversion is difficult to achieve, and its cost is inevitably increased.

This study presents a newly designed SIMO converter with a coupled inductor. The proposed converter uses one power switch to achieve the objectives of high-efficiency power conversion, high step-up ratio, and different output voltage levels. In the proposed SIMO converter, the techniques of soft switching and voltage

clamping are adopted to reduce the switching and conduction losses via the utilization of a low-voltage-rated power switch with a small $RDS(on)$. Because the slew rate of the current change in the coupled inductor can be restricted by the leakage inductor, the current transition time enables the power switch to turn ON with the ZCS property easily, and the effect of the leakage inductor can alleviate the losses caused by the reverse-recovery current. Additionally, the problems of the stray inductance energy and reverse-recovery currents within diodes in the conventional boost converter also can be solved, so that the high-efficiency power conversion can be achieved. The voltages of middle-voltage output terminals can be appropriately adjusted by the design of auxiliary inductors; the output voltage of the high-voltage dc bus can be stably controlled by a simple proportional-integral (PI) control.

III. Converter Design and Analyses

The system configuration of the proposed high-efficiency SIMO converter topology to generate two different voltage levels from a single-input power source is depicted in Fig. 2. This SIMO converter contains five parts including a low-voltage-side circuit (LVSC), a clamped circuit, a middle-voltage circuit, an auxiliary circuit, and a high-voltage-side circuit (HVSC). The major symbol representations are summarized as follows. $V_{FC}(I_{FC})$ and $V_{01}(I_{01})$ denote the voltages (currents) of the input power source and the output load at the LVSC and the auxiliary circuit, respectively; V_{02} and I_{02} are the output voltage and current in the HVSC. C_{FC}, C_{01}, and C_{02} are the filter capacitors at the LVSC, the auxiliary circuit, and the HVSC, respectively; C_1 and C_2 are the clamped and middle-voltage capacitors in the clamped and middle-voltage circuits, respectively. L_P and L_S represent individual inductors in the primary and secondary sides of the coupled inductor Tr, respectively, where the primary side is connected to the input power source; Laux is the auxiliary circuit inductor. The main switch is expressed as S_1 in the LVSC; the equivalent load in the auxiliary circuit is represented as R_{01}, and the output load is represented as R_{02} in the HVSC. The corresponding equivalent circuit given in Fig. 2 is used to define the voltage polarities and current directions. The coupled inductor in Fig. 1 can be modeled as an ideal transformer including the magnetizing inductor Lmp and the leakage inductor Lkp in Fig. 2. The turns ratio N and coupling coefficient k of this ideal transformer are defined as

$$N = \frac{N_2}{N_1} \tag{1}$$

$$K = \frac{L_{mp}}{L_{kp} + L_{mp}} = \frac{L_{mp}}{L_P} \tag{2}$$

where N1 and N2 are the winding turns in the primary and secondary sides of the coupled inductor Tr. Because the voltage gain is less sensitive to the coupling coefficient and the clamped capacitor $C1$ is appropriately selected to completely absorb the leakage inductor energy , the coupling coefficient could be simply set at one ($k = 1$) to obtain Lmp = LP via (2). In this study, the following assumptions are made to simplify the converter analyses: 1) The main switch including its body diode is assumed to be an ideal switching element; and 2) The conduction voltage drops of the switch and diodes are neglected.
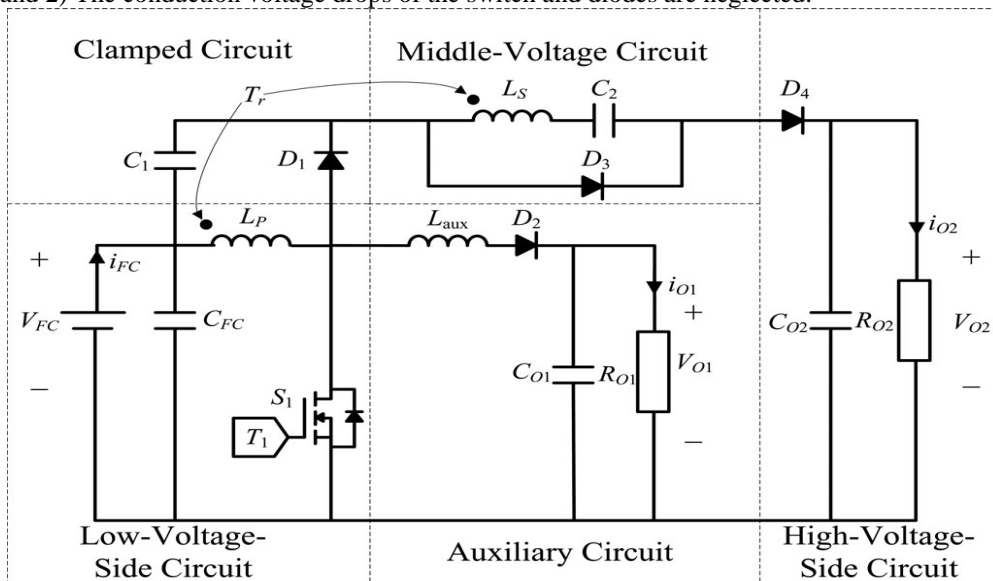
Figure 3.1: stem configuration of high-efficiency single-input multiple-output (SIMO) converter
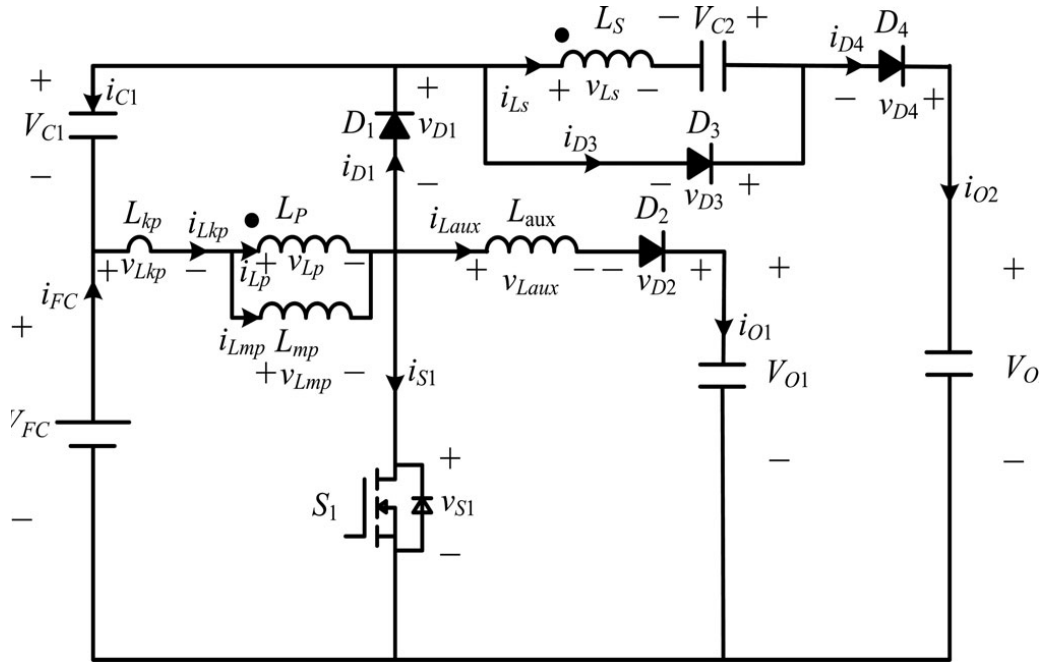
Figure 3.2: Equivalent circuit.

IV. OPERATION MODES

The characteristic waveforms are depicted in Fig. 3, and the topological modes in one switching cycle are illustrated in Fig.3.1

4.1 Mode 1

Mode 1 (t_0–t_1) [Fig. 3.1(a)]: In this mode, the main switch S1 was turned ON for a span, and the diode D_4 turned OFF. Because the polarity of the windings of the coupled inductor Tr is positive, the diode D_3 turns ON. The secondary current i_{L_S} reverses and charges to the middlevoltage capacitor C_2. When the auxiliary inductor L_{aux} releases its stored energy completely, and the diode D_2 turns OFF, this mode ends.

4.2 Mode 2

Mode 2 (t1 –t2) [Fig. 3.1(b)]: At time t = t_1 , the main switch s_1 is persistently turned ON. Because the primary inductor L_p is charged by the input power source, the magnetizing current $i_{L_{mp}}$ increases gradually in an approximately linear way. At the same time, the secondary voltage v_{L_S} charges the middle-voltage capacitor C_2 through the diode D_3 . Although the voltage $v_{L_{mp}}$ is equal to the input voltage v_{FC} both at modes 1 and 2, the ascendant slope of the leakage current of the coupled inductor (di_{Lkp} /dt) at modes 1 and 2 is different due to the path of the auxiliary circuit. Because the auxiliary inductor Laux releases its stored energy completely, and the diode D_2 turns OFF at the end of mode 1, it results in the reduction of di_{Lkp}/dt at mode 2.

4.3 Mode 3

Mode 3 (t_2 –t_3) [Fig. 3.1(c)]: At time t = t_2 , the main switch S1 is turned OFF. When the leakage energy still released from the secondary side of the coupled inductor, the diode D_3 persistently conducts and releases the leakage energy to the middle-voltage capacitor C_2 . When the voltage across the main switch v_{s1} is higher than the voltage across the clamped capacitor V_{c1} , the diode D_1 conducts to transmit the energy of the primary-side leakage inductor L_{kp} into the clamped capacitor C_1 .At the same time, partial energy of the primary-side leakage inductor L_{kp} is transmitted to the auxiliary inductor Laux, and the diode D_2 conducts. Thus, the current i_{Laux} passes through the diode D_2 to supply the power for the output load in the auxiliary circuit. When the secondary side of the coupled inductor releases its leakage energy completely, and the diode D_3 turns OFF, this mode ends.

4.4 Mode 4

Mode 4 (t_3–t_4) [Fig. 3.1(d)]: At time t = t_3 , the main switch S_1 is persistently turned OFF. When the leakage energy has released from the primary side of the coupled inductor, the secondary current i_{LS} is induced in reverse from the energy of the magnetizing inductor Lmp through the ideal transformer, and flows through the diode D_4 to the HVSC. At the same time, partial energy of the primary side leakage inductor L_{kp} is still persistently transmitted to the auxiliary inductor Laux, and the diode D_2 keeps to conduct. Moreover, the current i_{Laux} passes through the diode D_2 to supply the power for the output load in the auxiliary circuiti_{Laux} .

4.5 Mode 5

Mode 5 (t_4 –t_5) [Fig. 3.1(e)]: At time t = t_4, the main switch S_1 is persistently turned OFF, and the clamped diode D_1 turns OFF because the primary leakage current i_{Lkp} equals to the auxiliary inductor current i_{Laux} . In this mode, the input power source, the primary winding of the coupled inductor Tr , and the auxiliary inductor Laux connect in series to supply the power for the output load in the auxiliary circuit through the diode D_2 . At the same time, the input power source, the secondary winding of the coupled inductor Tr , the clamped capacitor C_1 , and the middlevoltage capacitor (C_2) connect in series to release the energy
into the HVSC through the diode D_4 .

4.6 Mode 6

Mode 6 (t_5 –t_6) [Fig. 3.1(f)]: At time t=t_5 , thismode begins when the main switch S_1 is triggered. The auxiliary inductor current i_{Laux} needs time to decay to zero, the diode D_2 persistently conducts. In this mode, the input power source, the clamped capacitor C_1 , the secondary winding of the coupled inductor Tr , and the middle-voltage capacitor C_2 still connect in series to release the energy into the HVSC through the diode D_4 . Since the clamped diode D_1 can be selected as a low-voltage Schottky diode, it will be cut off promptly without a reverse-recovery current. Moreover, the rising rate of the primary current i_{Lkp} is limited by the primary-side leakage inductor L_{kp} . Thus, one cannot derive any currents from the paths of the HVSC, the middle-voltage circuit, the auxiliary circuit, and the clamped circuit. As a result, the main switch S_1 is turned ON under the condition of ZCS and this soft-switching property is helpful for alleviating the switching loss. When the secondary current i_{Ls} decays to zero, this mode ends. After that, it begins the next switching cycle and repeats the operation in mode 1.

Remark 1: In general, a dc–dc converter operated at the continuous conduction mode (CCM) can provide a low ripple current for protecting the energy source. In the proposed SIMO converter, it is operated at the CCM due to the design of the auxiliary inductor. The coupled inductor is charged by the input power source when the main switch is turned ON, and the coupled inductor releases its energy to the auxiliary inductor when the main switch is turned OFF until the energy balance of the coupled inductor and the auxiliary inductor is established. As can be seen from Fig. 3, the primary current of the coupled inductor is positive during one switching cycle. This CCM operation is helpful to extend the lifetime of the input energy source.
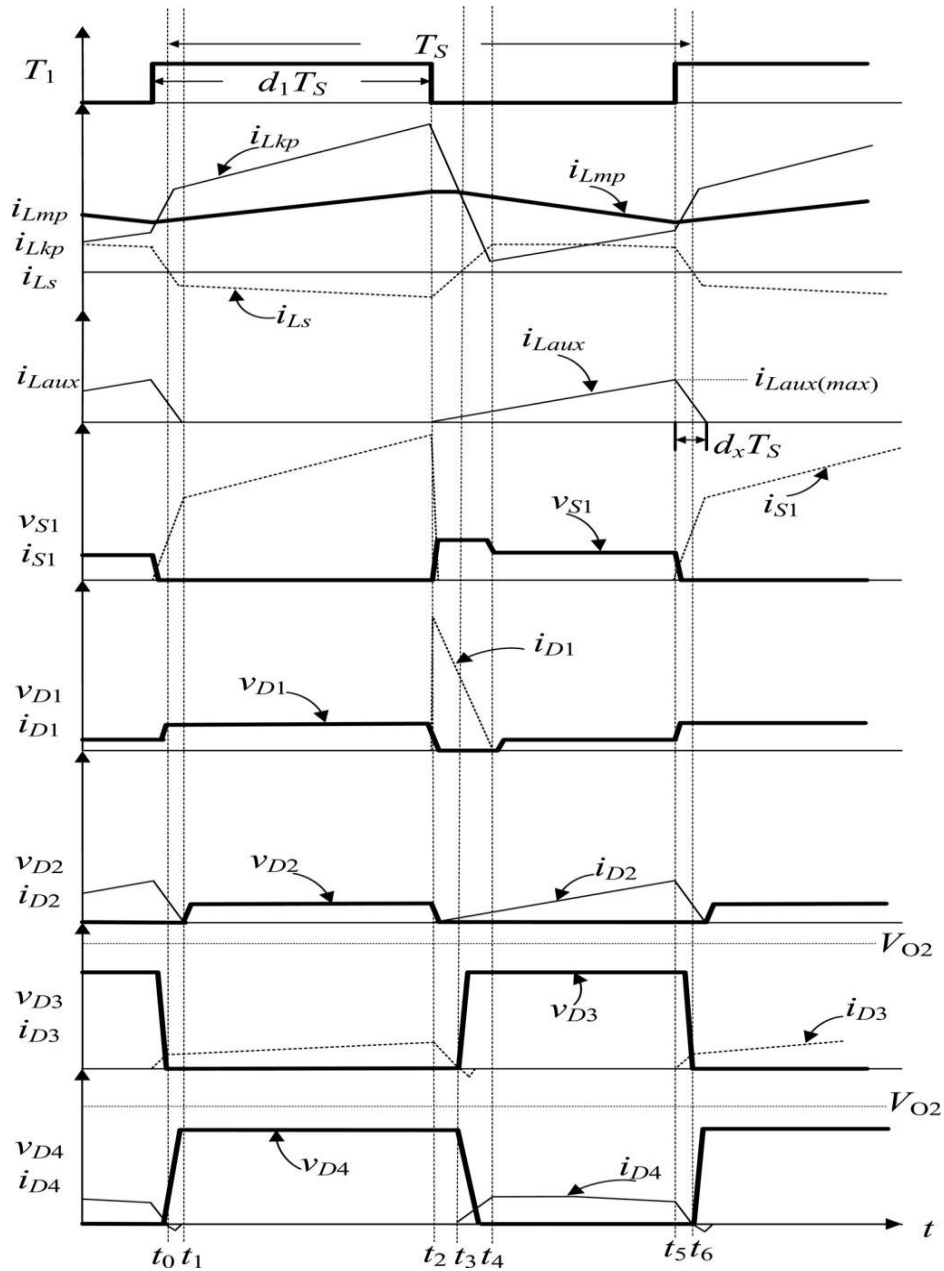
Figure 4.1: Characteristic waveforms of high-efficiency SIMO converter.
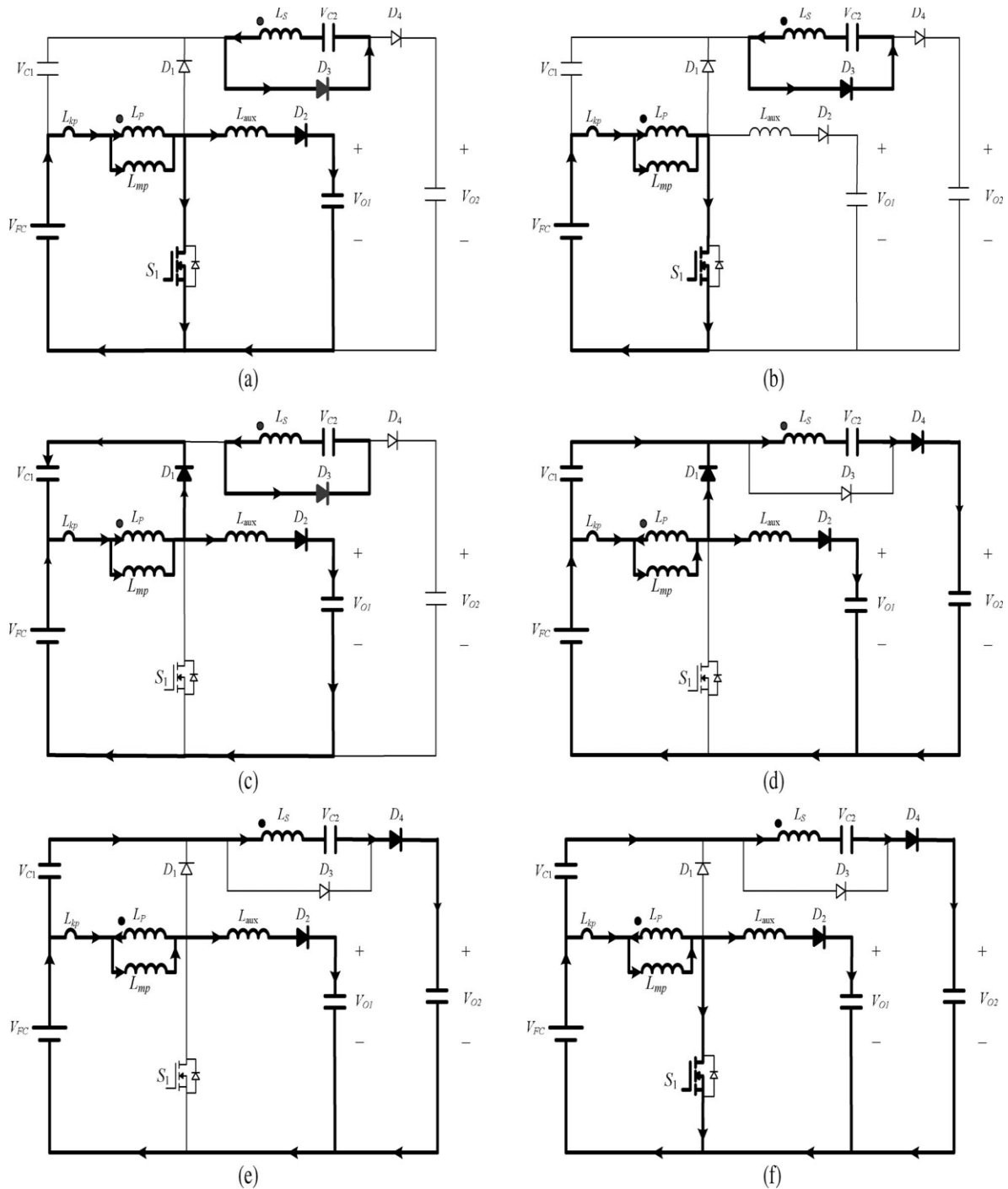
Figure4.2: Topological modes: (a) Mode 1 [$t0$–$t1$]; (b) Mode 2 [$t1$–$t2$]; (c) Mode 3 [$t2$–$t3$]; (d) Mode 4 [$t3$–$t4$]; (e) Mode 5 [$t4$–$t5$]; (f) Mode 6 [$t5$–$t6$].

V. Voltage Gain Derivation

Since the magnetizing inductor voltage v_{Lmp} is equal to the input power source V_{FC} at the mode 2, the voltage v_{Lmp} can be represented as

$$v_{Lmp} = V_{FC} \tag{3}$$

Due to the relation of $v_{LS} = N v_{LP} = V_{C2}$, the voltage V_{C2} can be represented as

$$V_{C2} = N V_{FC}. \tag{4}$$

By using the voltage-second balance , the relation of the average voltage across the magnetizing inductor L_{mp} of the coupled inductor Tr to be zero can be represented as

$$V_{FC} d_1 T_S + v_{Lmp} (1 - T_1) T_S = 0. \tag{5}$$

From (5), one can obtain

$$v_{Lmp} = [-d_1 /(1 - d_1)] V_{FC}. \tag{6}$$

Since the voltage of the clamped capacitor V_{C1} is equal to the negative voltage of magnetizing inductors voltage VC1 at modes 3 and 4, the voltage V_{C1} can be expressed via (6) as

$$V_{C1} = - v_{Lmp} = [d_1 (1 - d_1)] V_{FC} \tag{7}$$

According to Kirchhoff's voltage law, the output voltage V_{02} can be obtained as

$$V_{02} = V_{FC} + V_{C1} + V_{C2} - V_{LS} \tag{8}$$

By using the voltage-second balance , the relation of the average voltage across the secondary winding V_{LS} to be zero can be expressed by (4) and (8) as

$$(N V_{FC}) d_1 T_S + (V_{FC} + V_{C1} + V_{C2} - V_{02})(1 - d_1) T_S = 0 \tag{9}$$

From (4)–(9), the voltage gain G_{VH} of the proposed SIMO converter from the LVSC to the HVSC can be given as

$$G_{VH} = \frac{V_{02}}{V_{FC}} = \frac{N+1}{1-d_1} \tag{10}$$

For calculating the discharge time of the auxiliary inductor at modes 1 and 6, the corresponding time interval can be denoted as $d_x T_S = [(t_6 - t_5) + (t_1 - t_0)]$. By using the voltage-second balance , the relation of the average voltage across the auxiliary inductor L_{aux} to be zero can be represented as

$$(V_{FC} - v_{Lmp} - V_{01})(1 - d_1) T_S + (- V_{01}) d_x T_S = 0. \tag{11}$$

The voltage gain GVL of the proposed SIMO converter from the LVSC to the auxiliary circuit can be obtained by (6) and (11) as

$$G_{VL} = \frac{V_{01}}{V_{FC}} = \frac{1}{1-d_1+d_x} \tag{12}$$

Because the diode current i_{D2} is equal to the current i_{Laux} , the average value of the diode current i_{D2} can be calculated from the third graph in Fig. 3 as

$$i_{D2(avg)} = \left[\frac{1}{2} i_{Laux(MAX)}(1 - d_1)T_S + \frac{1}{2} i_{Laux(MAX)}d_x T_S\right] \tag{13}$$

where T_S is the converter switching cycle, $i_{Laux(MAX)}$ is the maximum current of the auxiliary inductor and can be expressed as

$$i_{Laux(MAX)} = (\frac{V_{01}}{L_{aux}})d_x T_S \tag{14}$$

By substituting (14) into (13), one can obtain

$$i_{D2(avg)} = \frac{V_{01}}{2L_{aux}}d_x T_S \quad (1 - d_1 + d_x) \tag{15}$$

Because the average current of the diode D_2 is equal to the current i_{01}, it yields

$$i_{D2(avg)} = \frac{V_{01}}{R_{01}} \tag{16}$$

From (15) and (16), the duty cycle d_x can be rewritten as

$$i_{D2(avg)} = \left[\frac{1}{2} i_{Laux(MAX)}(1 - d_1)T_S + \frac{1}{2} i_{Laux(MAX)}d_x T_S\right] \tag{17}$$

By substituting (17) into (12), the voltage gain G_{VL} of the proposed SIMO converter from the LVSC to the auxiliary circuit can be rearranged as

$$G_{VL} = \frac{V_{01}}{V_{FC}} = \frac{2}{(1-d_1)+\sqrt{(1-d_1)^2+\left[\frac{8L_{aux}}{R_{02}T_S}\right]}} \tag{18}$$

VI. Design Considerations

To verify the effectiveness of the proposed SIMO converter topology, a 12-V power supply *V*FC is taken as the input source to imitate a FC stack, and a 24-V battery module is utilized for the output load in the

auxiliary circuit. Moreover, the maximum battery floating charge voltage is set at 28 V, and the allowable charging power is 100 W (R_{01}= 7.84 Ω). In addition, the desired output voltage V_{02} is set at 200 V in the HVSC, and the maximum output power in the HVSC is 1.1 kW (R_{02}= 36.36 Ω). Define the minimum and maximum output powers in the auxiliary circuit and the HVSC as (P_{1min}, P_{1max}) and (P_{2min}, P_{2max},), respectively. In the case of resistive loads, one can, respectively, obtain the minimum and maximum resistances connected at the auxiliary circuit and the HVSC as

$$(R_{01min} = \frac{G_{vL}{}^2 V_{FC}{}^2}{P_{1max}}, R_{01max} = \frac{G_{vL}{}^2 V_{FC}{}^2}{P_{1min}}) and (R_{02min} = \frac{G_{VH}{}^2 V_{FC}{}^2}{P_{2max}}, R_{02max} = \frac{G_{VH}{}^2 V_{FC}{}^2}{P_{2min}})$$

according to (10) and (12). Furthermore, this converter is operated with a 100-kHz switching frequency (f_s= 100 kHz), and the coupling coefficient could be simply set at one ($k = 1$) because the proposed circuit has a good clamped effect.

By substituting N = 1– 7 into (10), the curve of the voltage gain G_{VH} with respect to different duty cycles d_1 is depicted in Fig. 5. Moreover, the curve of the voltage gain G_{vL} with respect to different duty cycles d_1 can be represented as Fig. 6.2 by substituting L_{aux} =1– 7µH, T_S = 10 µs, and R_{01}= = 7.84 Ω into (18). By analyzing Fig. 6.1, the turns ratio of the coupled inductor can be selected as N = 5 when the operational conditions are V_{02} =200V and V_{FC} = 12V (i.e., G_{VH}= 16.67), so that the corresponding duty cycle can be obtained as d_1 = 0.64. This value is reasonable in practical applications. As can be seen from Fig. 3, the relation of $d_x < d_1$ should be satisfied. According to (5.15), the limit for *L*aux can be calculated as *L*aux < 0.5 $d_1 R_{01} T_S$. By considering V_{FC} = 12V, V_{01} = 28 V, and d_1 =0.64, the value of the auxiliary inductor can be obtained as L_{aux} = 2 µH from Fig.6.2

Figure 6.1 Voltage gain *G*VH with respect to duty cycle *d*1 under different turns ratios.
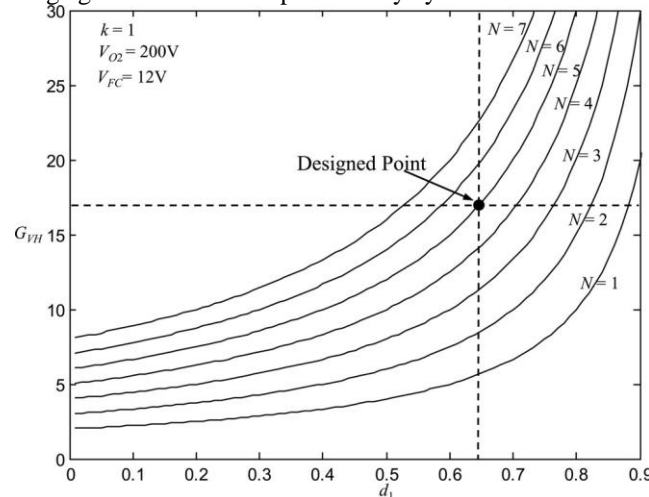
Figure.6.2. Voltage gain GVL with respect to duty cycle *d*1 under different auxiliary inductor values.
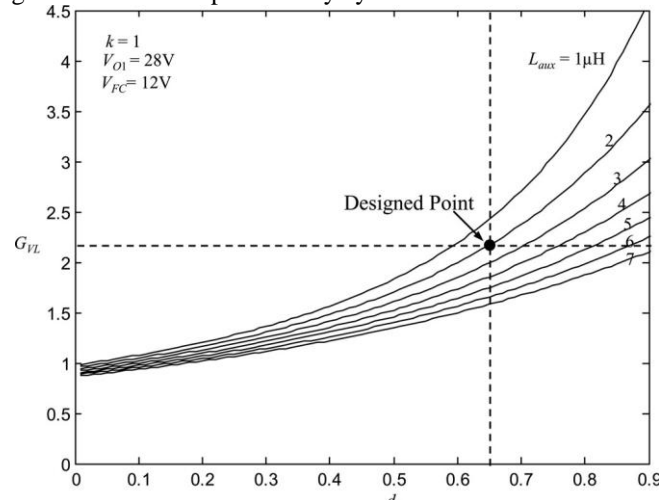
Because the voltage across the main switch S1 at the mode 3 can be represented as $v_{S1} = V_{C1} + V_{FC} = [1/(1 - d_1)] V_{FC}$, and the voltage relation between the LVSC and the HVSC according to (10) can be given by $V_{FC} = [(1 - d_1)/(N + 1)] V_{02}$, the voltage across the main switch S_1 can be rewritten as

$$v_{S1} = \frac{V_{02}}{N+1} \tag{19}$$

By analyzing (19), the switch voltage v_{S1} is not related to the input power source V_{FC} and the duty cycle d_1 if the values of the output voltage V_{02} and the turns ratio N are fixed. Thus, the switch voltage v_{S1} can be clamped at 33.3 V by substituting N = 5 and $V_{02} =$200V into (19). As long as the input voltage in the LVSC is not higher than the output voltage in the HVSC, the proposed SIMO converter can be applied well to the input power source with voltage variations. To consider the ring phenomena caused by the circuit stray inductance and the parasitic capacitance of the main switch S_1, the main switch S_1 with a 75-V voltage rating is selected in the proposed SIMO converter.

In this study, the clamped diode D_1 should be a fast conductive device. Because the clamped voltage of the diode D_1 is the same as the one of the main switch S_1, a low-voltage Schottky diode can be adopted to conduct promptly with lower conduction loss and reverse-recovery current. During the mode 2, the diode D_2 turns OFF, and its voltage can be represented by $v_{D2} = V_{01} + [L_{aux}(di_{D2}/d_t)]$. Since the ascendant slope of the diode current (di_{D2}/d_t) is equal to zero at the mode 2, the voltage v_{D2} can be rearranged as $v_{D2} = V_{01}$. According to $v_{01} = 28$ V, the voltage stress on the diode D_2 is smaller than 100V. Thus, a low-voltage Schottky diode also can be selected to reduce the conduction loss and the reverserecovery current. The voltage across the diodes D_3 and D_4, which can be expressed by $v_{D3D4} = v_{02} - (v_{C1} + v_{FC}) = [N/(N + 1)]v_{02}$, is 166.67 V by considering N = 5 and $v_{02} = 200$V. Thus, the diodes (D_3 and D_4) with 200 V voltage ratings can be selected.

When the main switch S_1 is turned ON during modes 1, 2, and 6, the voltage across the magnetizing inductor is $v_{Lmp} = V_{FC} = 12$V. Moreover, the relation between the current and voltage of the magnetizing inductor can be represented as $v_{Lmp} = L_P(d_i/d_t)$If the current range *di* is designed as 30 A and $d_t = d_1 T_s = 6.4 \mu s$, one can calculate the value of L_P as 2.56 µH. In order to manufacture the couple inductor easily, the number of winding turns in the primary side of the coupled inductor is $N_1 = 2$, and its measured inductor value is $L_P = 3$ µH. Because the ratio of the primary and secondary inductors in the coupled inductor is square proportional to the turns ratio (N = 5), the value of L_S can be determined as 75 µH, and the winding turns in the secondary side of the coupled inductor is $N_2 = 10$ in this study.

In this study, an EE-55 core with the magnetic flux density 390 mT, the maximum magnetic flux 138 μWb, the cross section area 354 mm^2, and the designed air gap 1.5 mm is adopted as the magnetic core of the coupled inductor. According to the magnetic circuit law, the air resistance can be calculated as 3.4 MΩ. By considering the maximum output power 1.1 Kw with the corresponding conversion efficiency 85%, the maximum input current is about 107.84 A, and the maximum magnetizing current is about 122.84 A. The produced magnetic flux can be obtained as 72.25 μWb by using the primary winding turns ($N_1 = 2$), maximum magnetizing current (122.84 A), and air resistance (3.4MΩ). Thus, the saturation phenomenon of the magnetizing current can be prevented by the designed magnetic core of the coupled inductor.

In the proposed SIMO converter, the electric charge variation $\Delta Q1$ of the filter capacitor for the auxiliary circuit can be represented as $\Delta Q_1 = (V_{01}/R_{01})(d_1 - d_x)T_S = C_{01}\Delta V_{01}$. By substituting $d_1 = 0.64$, $R_{01} = 7.84$ Ω, $T_s = 10$ µs, and $L_{aux} = 2$ µH into (17), the duty cycle dx can be calculated as 0.11. If one sets the voltage ripple of VO1 to be less than 1%, the value of CO1 should be selected over 67.6 µF by substituting $d_1 = 0.64$, $d_x = 0.11$, $R_{01} = 7.84$ Ω, $F_S = 100$ kHz, and $V_{01} = 28$ V into the function of $C_{01} = (d_1 - d_x)/[(R_{01}F_s)(\Delta V_{01}/V_{01})]$. Moreover, the electric charge variation of the filter capacitor $\Delta Q2$ for the HVSC can be expressed as $\Delta Q2 = (V_{02}/R_{02})d_1 T_S = C_{02} c\Delta V_{02}$. and the ripple of the output voltage V_{02} can be rearranged as $\Delta V_{02}/V_{02} = d_1/(R_{02}C_{02}F_s)$. By substituting $F_s = 100$ kHz, $d_1 = 0.64$, $R_{02} = 36.36$ Ω, and $V_{02} = 200$V into the function of $C_{02} = (d_1)/[(R_{02}F_s)(\Delta V_{02}/V_{02})]$, The value of C_{02} should be chosen over 17.6 μF with the constraint on the output voltage ripple to be less than 1%. According to the previous consideration, the values of $C_{01} = 100\mu$F and $C_{02} = 20$ μF are adopted in the experimental prototype.

Due to a high-switching frequency (F_s = 100 kHz) in the proposed SIMO converter, the factors of lower equivalent series resistance and faster dynamic response should be considered in the design of the clamped capacitor C_1 and the middle-voltage capacitor C_2 for reducing the capacitor voltage ripples. In this study, metalized-polyester film capacitors are adopted for C_1 and C_2 for satisfying the fast charge and discharge property.In order to further minimize the current and voltage ripples imposed to the main switch $S1$ and the diodes D_3 and D_4, the cutoff frequencies of the $L_P - C_1$ and $L_S - C_2$ filters are taken to be at least ten times smaller than the switching frequency. According to the previous consideration, the values of C_1 and C_2 are, respectively, chosen as 85 and 10 μF in theproposed SIMO converter so that the corresponding resonant frequencies are $F_{01} \equiv 1/\left(2\pi\sqrt{L_P C_1}\right) \cong 9.97$kHZ. and $F_{02} \equiv 1/\left(2\pi\sqrt{L_S C_2}\right) \cong 5.81$kHZ.

According to (6.1), the switch voltage v_{S1} can be effectively clamped at a predetermined value if the values of the output voltage V_{02} and the turns ratio N are fixed. As can be seen from Fig. 4.2(a) and (f), the action of the auxiliary circuit is helpful to share the switch current iS1 . For the proposed SIMO converter with larger output powers and more than two outputs, the increase of the input current will raise the current stress on the main switch. Fortunately, one can use the parallel MOSFET to reduce the conduction loss of the main switch.

VII. Simulation Results

Simulation is done on MATLAB/Simulink background
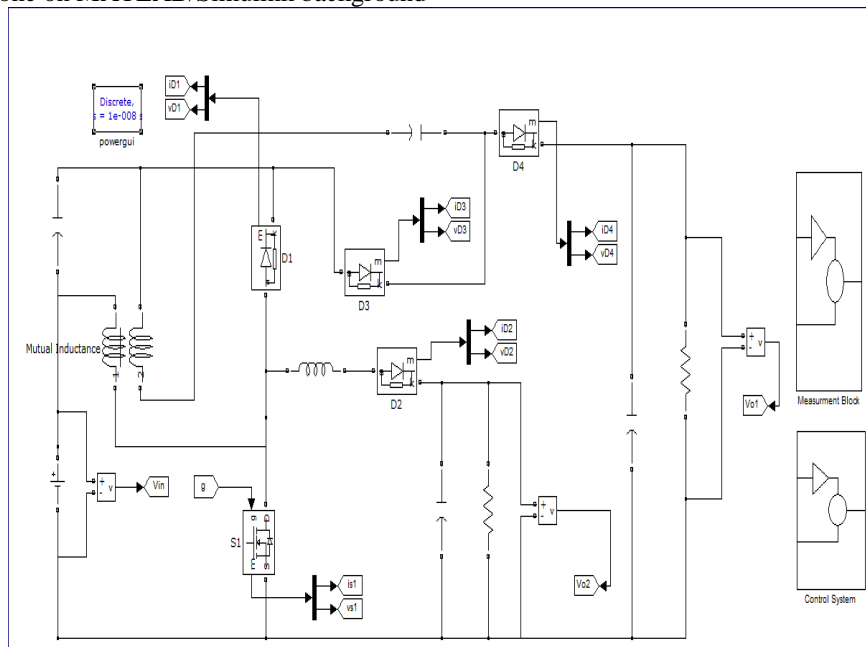
PI Controller
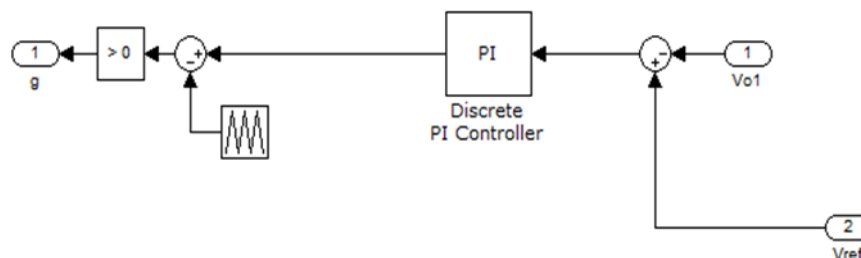
Simulation results of the circuit

7.1 voltage waveforms
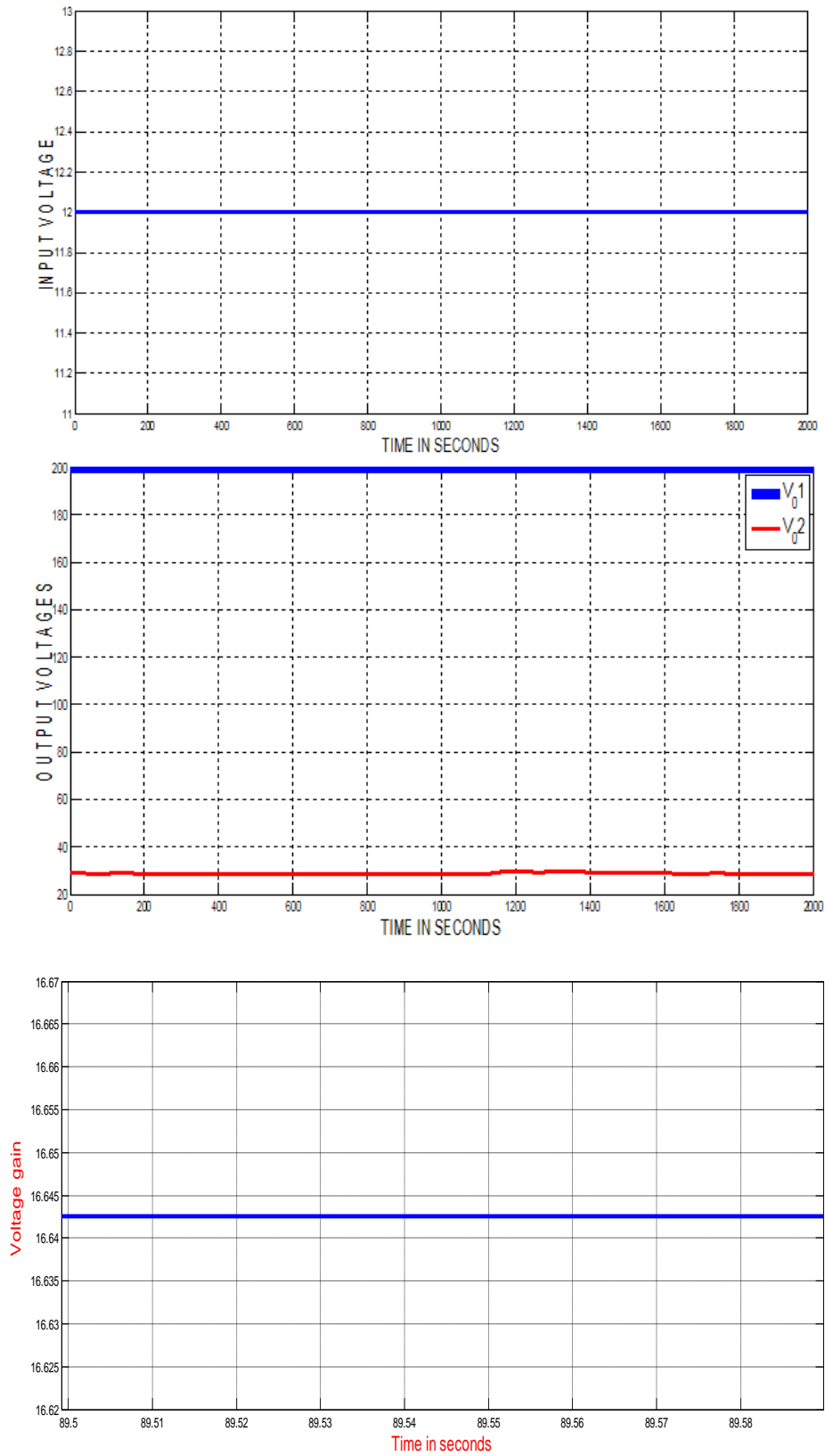
7.2 Voltage & current waveforms across diode
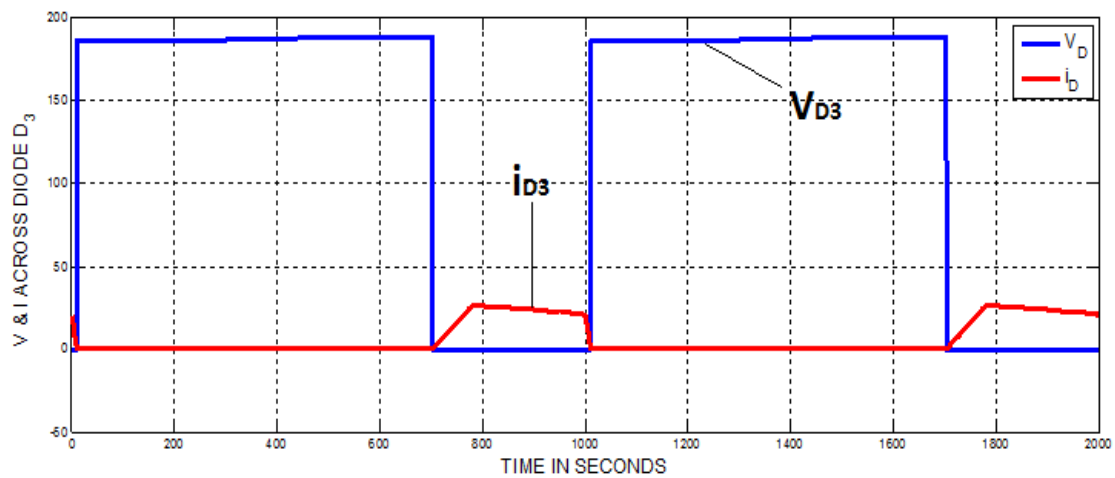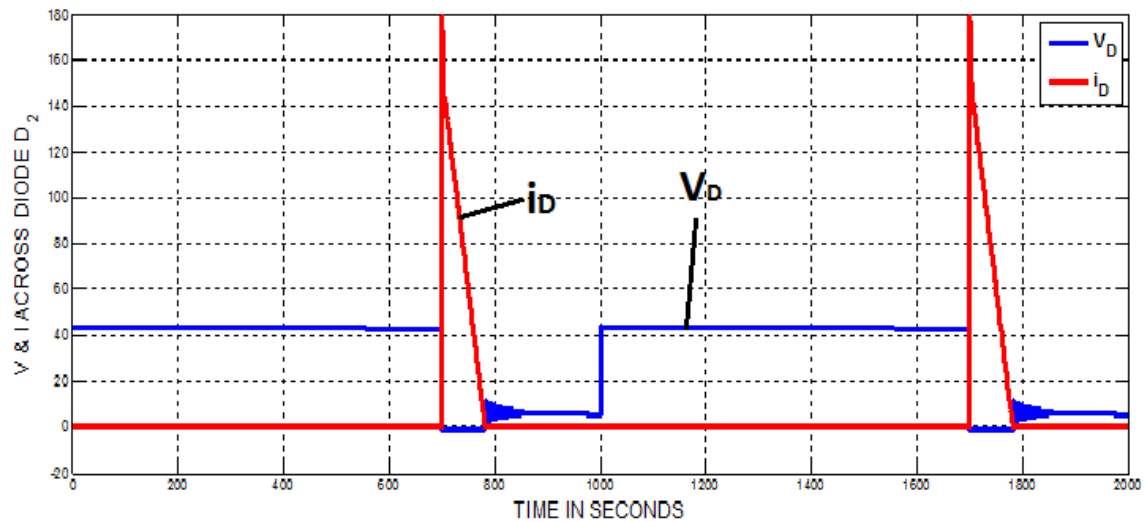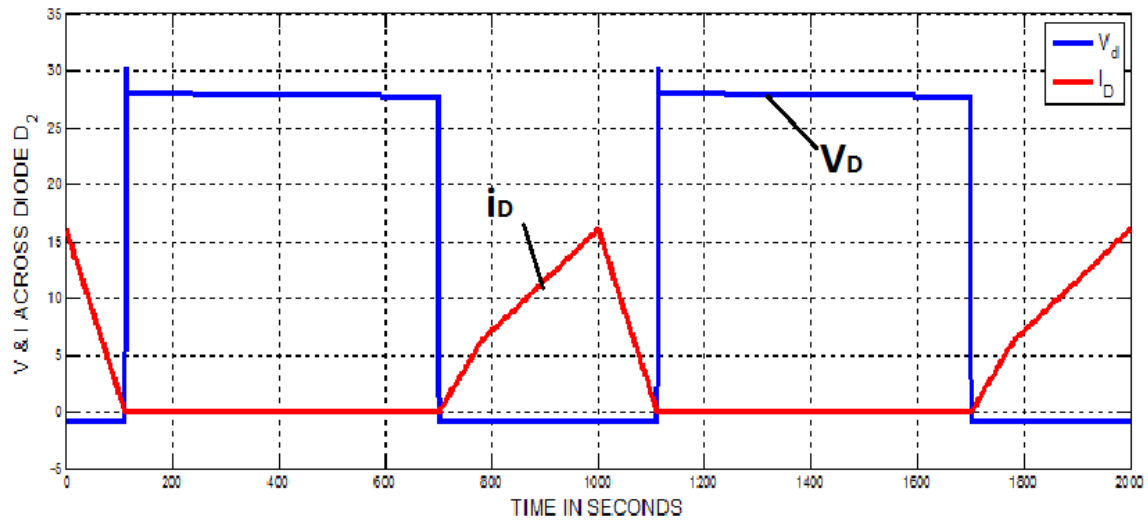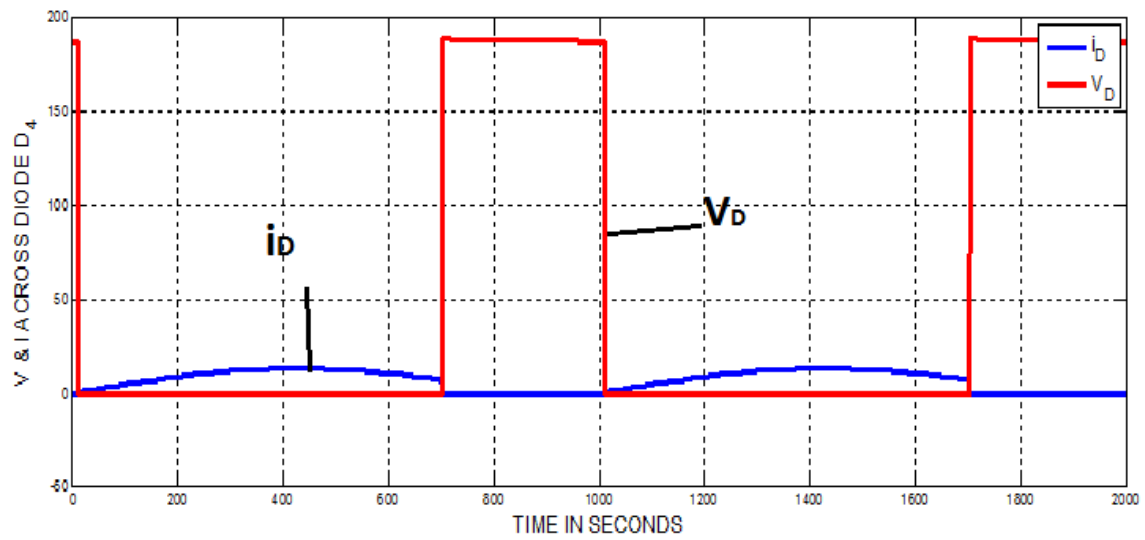
7.3 Voltage & current waveforms across switch
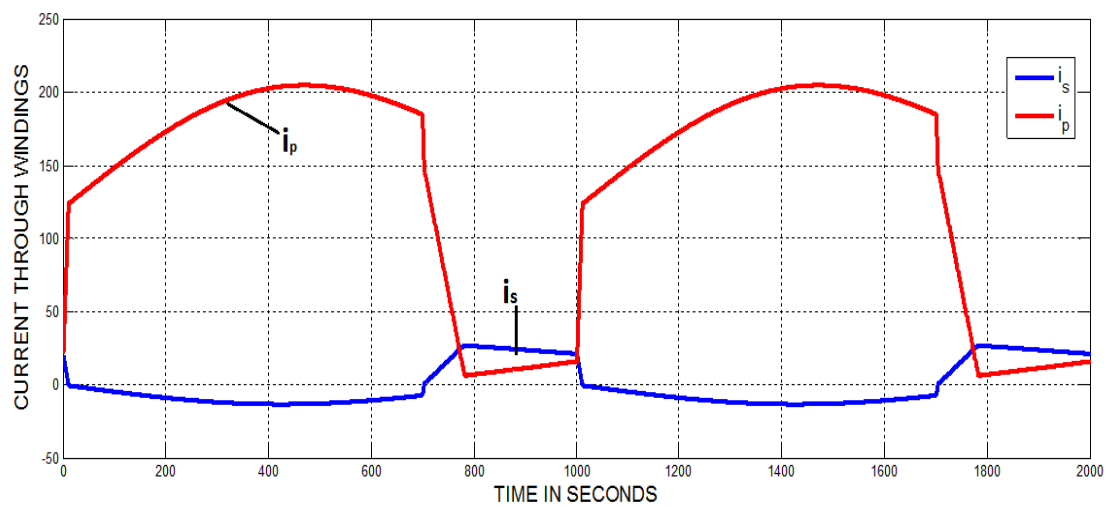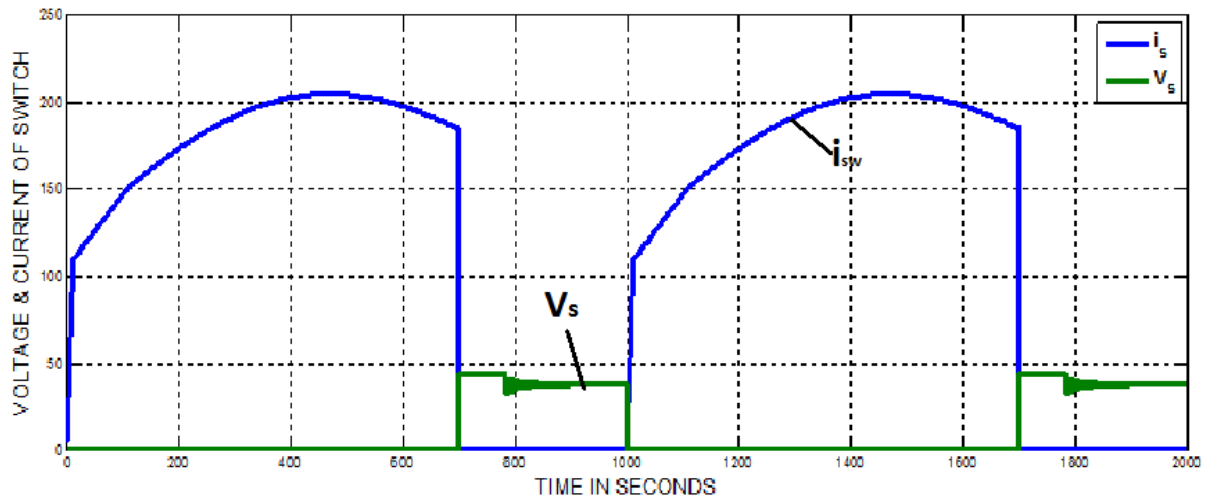
VIII. Conclusion

This study has successfully developed a high-efficiency SIMO dc–dc converter, and this coupled-inductor-based converter was applied well to a single-input power source plus two output terminals composed of an auxiliary battery module and a high-voltage dc bus. The experimental results reveal that the maximum efficiency was measured to exceed 95%, and the average conversion efficiency was measured over 91%. The proposed SIMO converter is suitable for the application required one common ground, which is preferred in most applications.However, it is not appropriate to be used as the active front for dc–ac multilevel inverters. This limitation is worthy to be investigated in the future research.The major scientific contributions of the proposed SIMO converter are recited as follows:

1) this topology adopts only one power switch to achieve the objective of high-efficiency SIMOpower conversion; 2) the voltage gain can be substantially increased by using a coupled inductor; 3) the stray energy can be recycled by a clamped capacitor into the auxiliary battery module or high-voltage dc bus to ensure the property of voltage clamping; 4) an auxiliary inductor is designed for providing the charge power to the auxiliary battery module and assisting the switch turned ON under the condition of ZCS; 5) the switch voltage stress is not related to the input voltage so that it is more suitable for a dc power conversion mechanism with different input voltage levels; and 6) the copper loss in the magnetic core can be greatly reduced as a full copper film with lower turns.

REFERENCE

[1]   Rong-Jong Wai, and Kun-Huai Jheng, "High-Efficiency Single-Input Multiple-Output DC–DConverter" EEE Trans.Power Electron., vol. 28, no. 2, pp. 3853–3864, Feb. 2013.

[2]   A. Nami, F. Zare, A. Ghosh, and F. Blaabjerg, "Multiple-output DC–DCconverters based on diode-clamped converters configuration: Topology and control strategy," IET Power Electron., vol. 3, no. 2, pp. 197–208, 2010.

[3]   M. Singh and A. Chandra, "Application of adaptive network-based fuzzy interference system for sensorless control of PMSG-based wind turbinewith nonlinear-load-compensation capabilities," IEEE Trans. Power Electron.,vol. 26, no. 1, pp. 165–175, Jan. 2011.

[4]   C. T. Pan,M. C. Cheng, and C.M. Lai, "A novel integrated dc/ac converter with high voltage gain capability for distributed energy resource systems,"IEEE Trans. Power Electron., vol. 27, no. 5, pp. 2385–2395, May 2012.

[5]   S. D. Gamini Jayasinghe, D. Mahinda Vilathgamuwa, and U. K. Madawala, "Diode-clamped three-level inverter-based battery/ supercapacitor direct integration scheme for renewable energy systems," IEEE Trans. Power Electron., vol. 26, no. 6, pp. 3720–3729, Dec.2011.

[6]   H.Wu, R. Chen, J. Zhang, Y. Xing, H. Hu, and H. Ge, "A family of threeport half-bridge converters for a stand-alone renewable power system," IEEE Trans. Power Electron., vol. 26, no. 9, pp. 2697–2706, Sep. 2012.

Simulation of Bridgeless SEPIC Converter with Modified Switching Pulse

Danly Elizabeth Mathew[1], Jyothi G. K.[2]

[1]*(Student, Department of Electrical and Electronics Engineering, FISAT, MG university, Kerala, India)*
[2]*(Assistant Professor, Department of Electrical and Electronics Engineering, FISAT, MG university, Kerala, India)*

ABSTRACT: *In this paper, a new bridgeless single-ended primary inductance converter(SEPIC) power-factor-correction(PFC) rectifier is introduced. The proposed circuit provides lower conduction losses with reduced components simultaneously. In conventional PFC converters(continuous-conduction-mode boost converter), a voltage loop and a current loop are required for PFC.Simulation is done on bridgeless SEPIC and full bridge SEPIC and found that by working both in DCM conduction losses is less for bridgeless. In the proposed converter, the control circuit is simplified, and no current loop is required while the converter operates in discontinuous conduction mode.*

Keywords: *Continuous Conduction Mode (CCM), Discontinuous Conduction Mode (DCM), Duty cycle (D), IPower factor correction (PFC), Single ended primary inductance converter(SEPIC).*

I. Introduction

Today's commercial, industrial, retail and even domestic premises are increasingly populated by electronic devices such as PCs, monitors, servers and photocopiers which are usually powered by switched mode power supplies (SMPS). If not properly designed, these can present non-linear loads which impose harmonic currents. Harmonics can damage cabling and equipment within this network, as well as other equipment connected to it. Problems include overheating and fire risk, high voltages and circulating currents, equipment malfunctions and component failures, and other possible consequences. A non-linear load is liable to generate these harmonics if it has a poor power factor. Today's standards like International Electro technical Commission (IEC) 61000-3-2 limit the harmonics produced by these devices. Therefore, to satisfy the standards, power-factor-correction (PFC) converters are used for ac–dc conversion. The conventional PFC converter is a boost converter, and thus, the output voltage must be greater than the input voltage. In spite of this problem, this converter is widely used because of its simplicity.

In large number of applications, like offline low-voltage power supplies, where it is preferred to have the PFC output voltage lower than the input ac voltage, a buck-type converter is required. However, the input current of buck converter is discontinuous, and to filter this current, another passive filter must be used at the buck converter input. This is the characteristic of all converters in which a buck converter is at its input, such as buck–boost, non-inverting buck–boost, fly back, etc.. To resolve this problem, boost–buck converters like single-ended primary-inductor converter (SEPIC) and C´uk converters must be used. SEPIC is a DC to DC converter and is capable of operating in either step up or step down mode and widely used in battery operated equipment by varying duty cycle of gate signal of MOSFET. We can step up or step down voltage .For duty cycle above 0.5 it will step up and below 0.5, it will step down the voltage to required value. Various conversion topologies like buck, boost, buck-boost are used to step up or step down voltage. Some limitation like pulsating input and output current, inverted output voltage, in case of buck converter floating switch make it unreliable for different application. So it is not easy for conventional power converter design to maintain high efficiency especially when it step or step down voltage. All these characteristics are obtained in SEPIC DC to DC power conversion . Consequently, the input current would be continuous and also the output voltage can be lower than the input voltage. All these converters can be used in either discontinuous conduction mode (DCM) or continuous conduction mode (CCM). In CCM, a control circuit is required, but in DCM, the converter can operate at a fixed duty cycle to correct the input power factor (PF). DCM operation of boost converter causes the input current to become discontinuous.

Therefore, extra passive filter is needed to shape the input current toward sinusoidal waveform. In case of SEPIC and C´uk converters, due to the existence of two inductors in each converter, the input current is continuous even when the converter is operating in DCM.

II.   Review of Literature and Statement of Problem

Conventional PFC converter is a rectifier followed by a boost converter as shown in Fig. 2.1. There are several disadvantages in this combination. At any given instant, three semiconductor devices exist in the power flow path. Also, special design of the dc-side inductor is necessary to carry the dc current as well as high-frequency ripple current. To overcome these problems, the bridgeless ac to dc rectifier is proposed as shown in Fig. 2.2.

Fig. 2.3 shows a conventional SEPIC PFC converter. In the literature, an interesting and novel bridgeless SEPIC PFC is introduced to minimize the conduction losses . This topology is similar to the bridgeless boost PFC rectifier .Despite the mentioned advantage, in comparison to the conventional SEPIC rectifier, this converter has three extra passive elements which contribute to the volume and weight of the converter. Another major problem with this converter is that it doubles the output voltage which considerably increases the size of output filter. To overcome these limitations, a new bridgeless SEPIC PFC is introduced in this paper. This converter has no extra (passive or active) elements in comparison to conventional SEPIC PFC. Also, in this converter, the conduction losses (number of active elements in the current path) are reduced in comparison to the conventional SEPIC PFC.
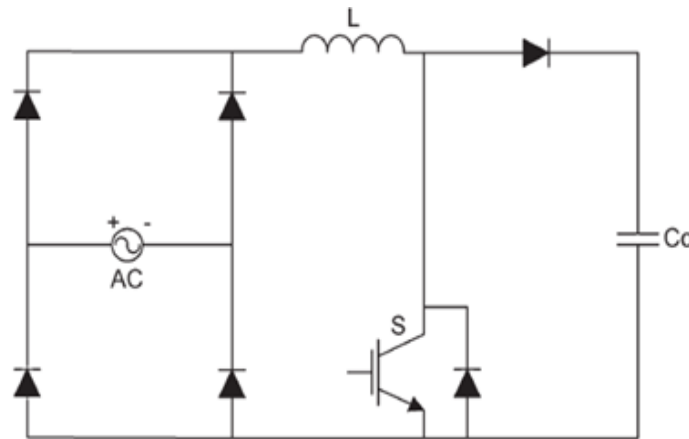
Figure. 2.1: Conventional PFC converter
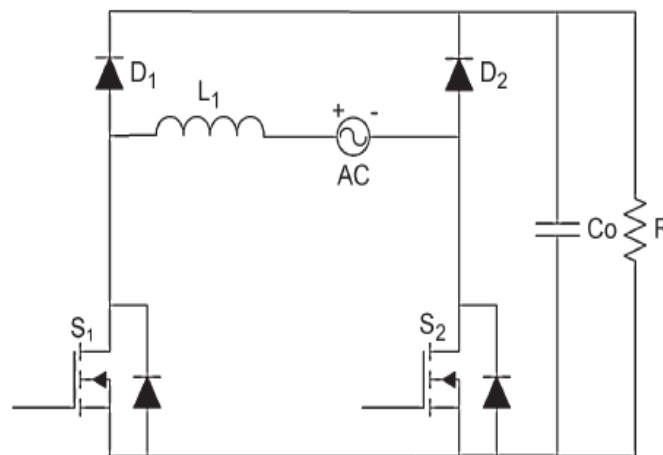
Figure 2.2: Conventional bridgeless boost PFC.
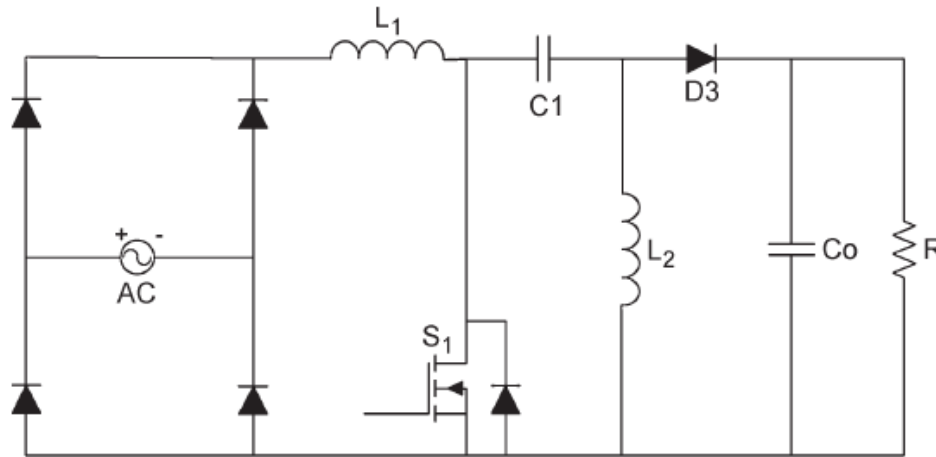
Figure 2.3 Conventional SEPIC PFC rectifier

III.   Modified Bridgeless PFC Circuit Operation

Fig. 3.1 shows the power stage of a bridgeless SEPIC PFC rectifier. In this circuit, the SEPIC converter is combined with the input rectifier and operates like a conventional SEPIC PFC converter. The operation of this converter is symmetrical in two half-line cycles of input voltage. Therefore, the converter operation is explained during one switching period in the positive half-line cycle of the input voltage. It is assumed that the converter operates in DCM. It means that the output diode turns off before the main switch is turned on. In order to simplify the analysis, it is supposed that the converter is operating at a steady state, and all circuit elements are ideal. In addition, the output capacitance is assumed sufficiently large to be considered as an ideal dc voltage source (V_0) as shown in Fig. 3.2. Also, the input voltage is assumed constant and equal to $V_{ac}(t_0)$ in a switching cycle.
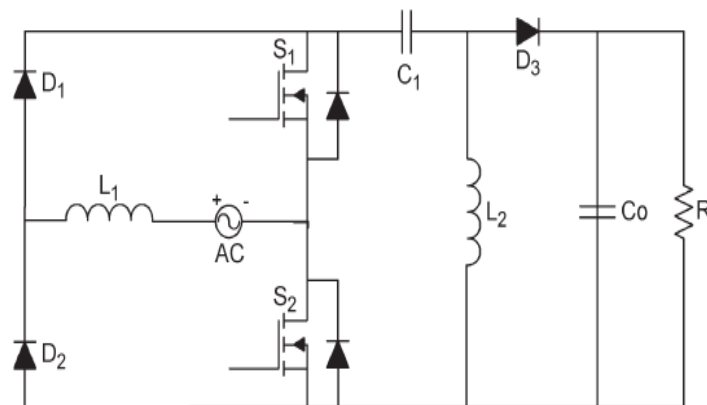
Figure 3.1: Proposed bridgeless SEPIC PFC
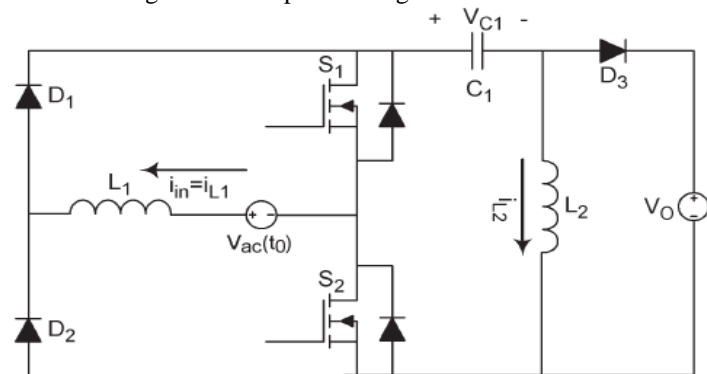
Figure 3.2: Equivalent circuit of the proposed bridgeless SEPIC PFC in a switching cycle.

Based on the aforementioned assumptions, the circuit operation in a switching cycle can be divided into three modes as shown by the equivalent circuits in Fig. 3.3. The theoretical waveforms are shown in Fig. 4.1. Before the first mode, it is assumed that the converter is in freewheeling mode. Therefore, D_1 and the body diode of S_2 are conducting, and all other semiconductor devices are off. Note that the voltage of C_1 follows the input voltage in DCM.

Mode 1: $[t_0 - t_1]$

This mode starts by turning S_1 and S_2 on. Input inductor current (L_1 current) starts to rise linearly by a slope of $V_{ac}(t_0)/L_1$. The voltage across L_2 is equal to the voltage of C_1 which follows the input voltage. Thus, i_{L_2} decreases linearly by a slope of $-V_{ac}(t_0)/L_2$. This mode ends by turning off $S1$. Based on the aforementioned operation, the following equations can be obtained:

$$i_{in}(t) = i_{L1}(t) = i_{fw} + \frac{V_{ac}(t_0)}{L_1}(t-t_0) \tag{1}$$

$$i_{L2}(t) = i_{fw} - \frac{V_{ac}(t_0)}{L_2}(t-t_0) \tag{2}$$

$$i_{sw1}(t) = i_{L1} - i_{L2} = (\frac{V_{ac}(t_0)}{L_1} + \frac{V_{ac}(t_0)}{L_2})t \tag{3}$$

where ifw is the freewheeling current which is equal to the input current. From (3), it can be concluded that $S1$ turns on under zero-current (ZC) switching condition.

Mode 2: $[t_1 - t_2]$

By turning S_1 and S_2 off, D_3 begins to conduct. Input inductor current decreases linearly by a slope of $-V_0/L_1$, and i_{L_2} increases linearly by a slope of V_0/L_2 until it reaches to i_{fw}. By substituting $t = t_1$ in (2), i_{L_2} is obtained as the following:

$$i_{L2}(t) = i_{L2}(t_1) + \frac{V_0}{L_2}(t-t_1) \tag{4}$$

Thus, the duration of this mode is

$$t_2 - t_1 = \frac{V_{ac}(t_0)}{V_0}(t_1 - t_0) \tag{5}$$

Mode 3: $[t_2 - t_3]$

This mode begins when D_3 turns off and the freewheeling mode starts. This mode ends by starting the next switching cycle at t_3. The current through inductors L_1 and L_2 are equal.
The duration of this mode is

$$t_3 - t_2 = T_s - (t_2 - t_0) \tag{6}$$
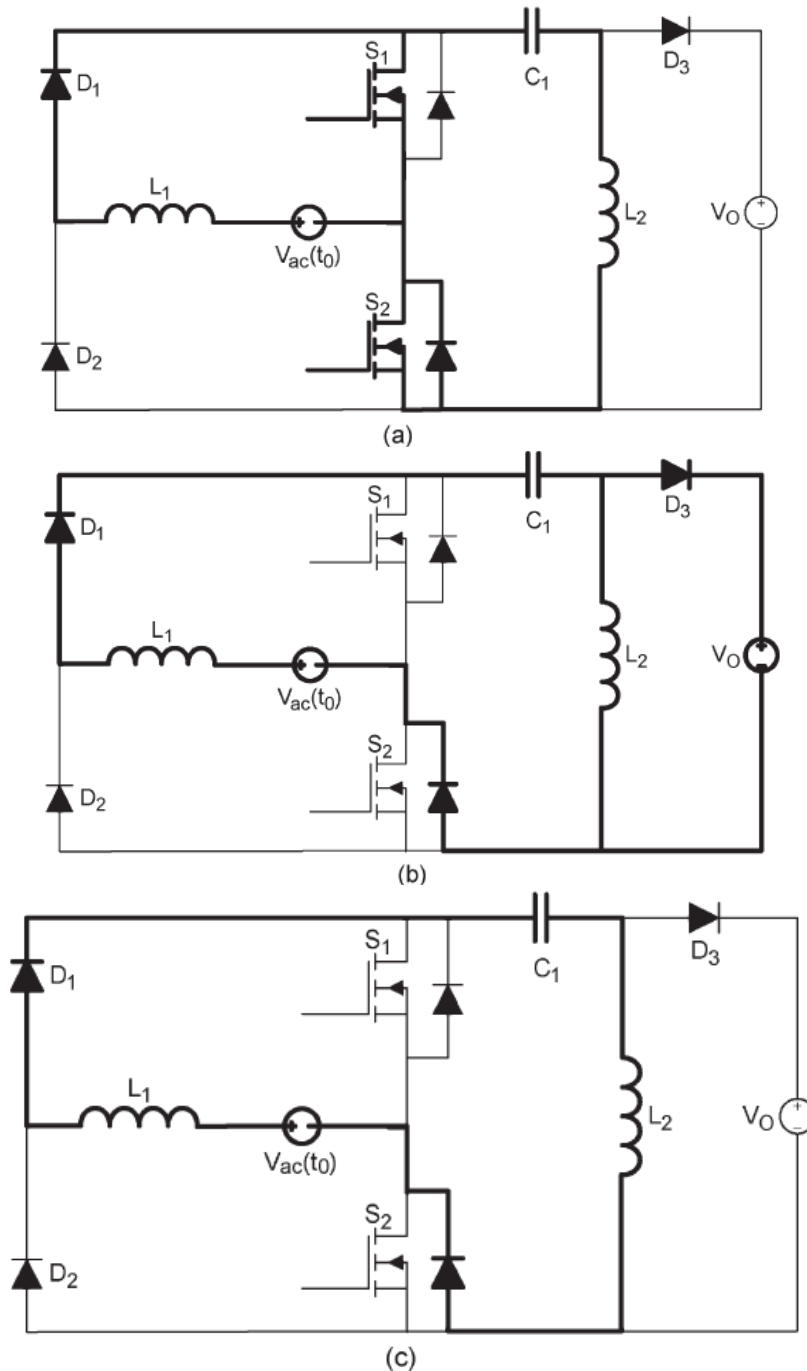
where Ts is the switching period.

Figure 3.3: Equivalent waveforms of different modes of operation

The above equivalent circuit holds if the switching pulse is as in Fig 3.6 .If the switching pulse is as in Fig 3.7 then instead of body diode the switch path is taken in Fig 3.3 (b) and (c) i.ethe current via an intrinsic body diode is forced to flow through the channel of the switch. It can reduce the conduction loss on the switch further and the efficiency can be improved.
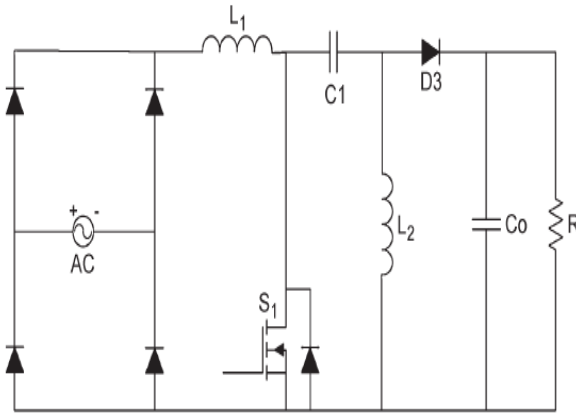
3.1 Comparison of Full Bridge and Bridgeless SEPIC Converter

Figure 3.4: Full bridge SEPIC converter   Figure 3.5: Bridgeless SEPIC converter
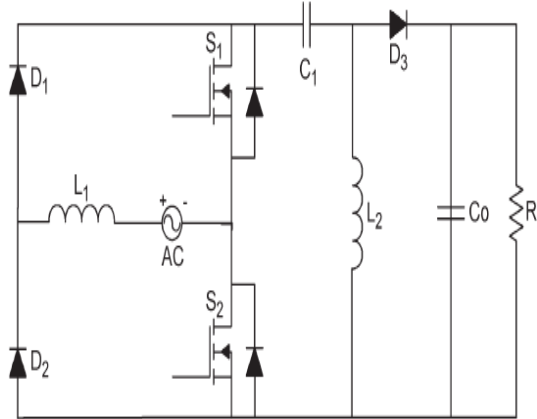
Conventional full bridge SEPIC converter is given PWM pulses and operated in switch on mode, switch off mode and freewheeling mode. Bridgeless SEPIC converter is given switching pulses such that one switch is continuously turned on during on half cycle with other switch is given PWM pulses, in the next half the switches are reversed. So in effect both switches off condition don't exist, so the conduction through the body diode can be omitted and thus reduce conduction losses and efficiency can be improved.
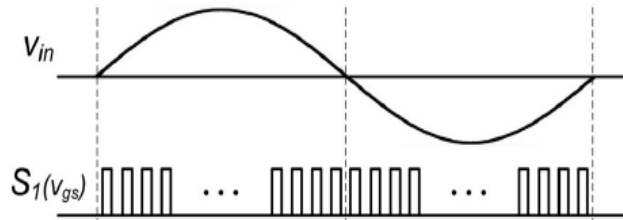
Figure 3.6: Switching pulses for full bridge SEPIC converter
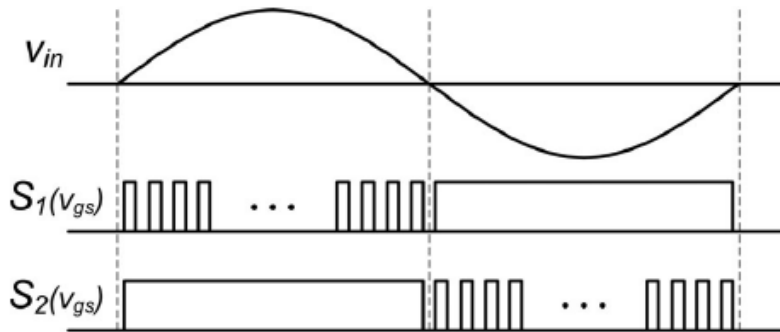
Figure 3.7:Switching pulses for Bridgeless SEPIC converter

IV. Design Procedure and Efficiency Improvement

Design procedure of this converter is similar to the conventional SEPIC PFC converter. Therefore, in this section, the design procedure is explained by an example. A converter with the following specifications is designed:

$V_{ac} = V_1 \sin(\omega t) = 180\sqrt{2} \sin(2\pi 50 t)$

$V_0 = 150 \pm 5$ Vdc

$P_0 = 150$ W

$f_s = 100$ kHz

$\Delta I_L = 20\%$ I_1

where V_{ac} is the input sinusoidal voltage, V_0 is the output dc voltage, P_0 is the output power, f_s is the switching frequency, ΔI_L is the input current ripple, and I_1 is the input current peak.

Step 1: Input Current
From the output power and converter efficiency, the following equation can be obtained:

$$I_{in} = I_1 \sin(\omega t) = \frac{2P_0}{V_1 \eta} \sin(\omega t) \tag{7}$$

if efficiency, (η) is set equal to 90%, then

$$I_{in} = 1.32\sin(2\pi 50 t), \quad \Delta I_L = 0.26\text{A} \tag{8}$$

Fig. 4 shows that input current ripple is

$$\Delta I_L = \frac{V_{ac}(t_0)d}{L_1 f_s} \tag{9}$$

Step 2: Output Current
The output current is the average current of $D3$. Therefore, the output average current in a switching cycle can be obtained from the following equation:

$$i_{0,avg} = \frac{i_{op} d_1}{2} \tag{10}$$

where d_1 is the duty ratio of diode D_3 and is the peak current of D_3 which can be obtained from the following relation:

$$i_{op} = i_{L1}(t_1) + i_{L2}(t_1) = \left(\frac{1}{L_1} + \frac{1}{L_2}\right) V_{ac}(t_0) d T_s \tag{11}$$

Assuming $1/L_e = (1/L_1) + (1/L_2)$, then, from (5), (10), and (11), the following can be deduced:

$$i_{0,avg} = \frac{Vac^2(t_0)d^2}{2L_e V_0} T_s \tag{12}$$

The average output current in one half of the line cycle becomes

$$I_{0,avg} = \frac{1}{\pi} \int_0^\pi i_{0,avg} \, d\omega t = \frac{V1^2 d^2}{4L_e V_0} T_s \tag{13}$$

Step 3: Ensuring DCM Operation
To operate at DCM, the following inequality must hold:

$$d_1 < 1\text{-d} \tag{14}$$

By substituting (5) in the previous equation, the following inequality is obtained. This ensures that the converter operates at DCM.

$$\text{d} \leq \frac{V_0}{V_{ac}(t_0) + V_0} \, 0.392 \tag{15}$$

Using (4.8) and selecting $d = 0.3$, thus

$$L_e = \frac{V1^2 d^2}{4V_0 f_s I_{o,avg}} = 147\mu\text{H} \tag{16}$$

From (9), *L* can be calculated as

$$L_1 = \frac{V_{ac}(t_0)d}{f_s I_{rip}} = 3.4\text{mH} \tag{17}$$

Therefore, L_2 can be calculated from the following equation:

$$\frac{1}{L_2} = \frac{1}{L_e} - \frac{1}{L_1}$$

(18)

Step 4: Output Capacitor (C_0)

Output ripple frequency is two times the input frequency, and at the worst case, the output current during the half period of ripple frequency must be provided by the output capacitor. Therefore, *CO* can be obtained from the following equation:

$$C_0 = \frac{P_0}{4f_1 V_0 \Delta V_0} = 1000\mu H$$

(19)

where f_1 is the input frequency and ΔV_0 is the output ripple.

Step 5: Maximum Ratings of Semiconductor Elements

The maximum switch voltage and current can be obtained from the following equations:

$$V_{D,max} = V_{SW,max} = V_1 + V_0 = 400V$$

(20)

$$I_{D,max} = I_{SW,max} \approx I_1 + \Delta I_L - I_{L2,min} = 7.68 \text{ A}$$

(21)

where V_1 and I_1 are the input voltage and current peaks, respectively.
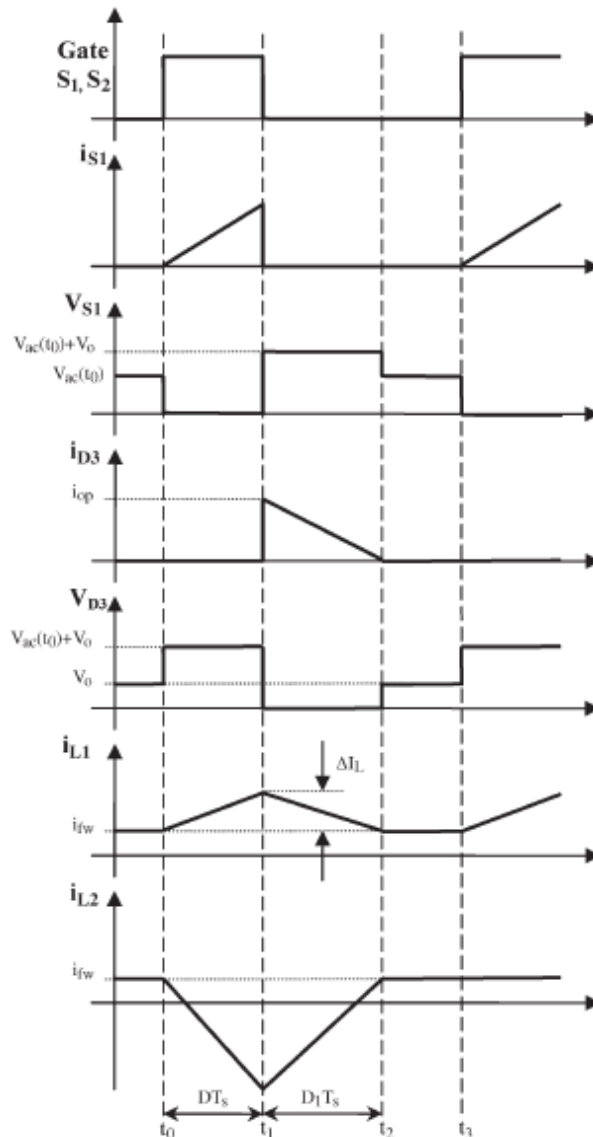
Figure 4.1: Theoretical waveform of proposed PFC converter

Step 6: Control Circuit

Based on the aforementioned operation of the proposed PFC circuit in DCM and the model given in for SEPIC PFC rectifier, the control circuit does not require a current loop to shape the input current. Therefore, any pulse width modulation IC can be used to control this PFC converter. The block diagram of the controller is shown in Fig. 4.1. It must be noted that, similar to conventional PFC, the voltage loop cannot compensate the 2*f*in output voltage ripple (*f*in is the input voltage frequency). Thus, the voltage loop must be designed so that the control circuit would neglect the 2*f*in ripple.

4.1 Efficiency Improvement

Based on circuit operation, it can be observed that one diode of rectifier is omitted in the current flow path and another diode is replaced by a switch. The voltage drop of a MOSFET is usually lower than a diode at low currents (In this application, the current is not so high). Therefore, it can be assumed that the losses of rectifier diodes are reduced from the total losses. By the following equations, the losses of these two diodes can be calculated

$$P_{D,avg} = \frac{1}{T}\int_0^T V_D I_D dt = \frac{1}{\pi}\int_0^\pi 1 * 1.3 \sin(\omega)\, d\omega \qquad (22)$$
$$P_{D,avg} = 0.83W$$

where $P_{D,avg}$ is the average power loss in one diode of the input rectifier. Thus, the efficiency improvement of 150-W converter can be calculated from the following equation:

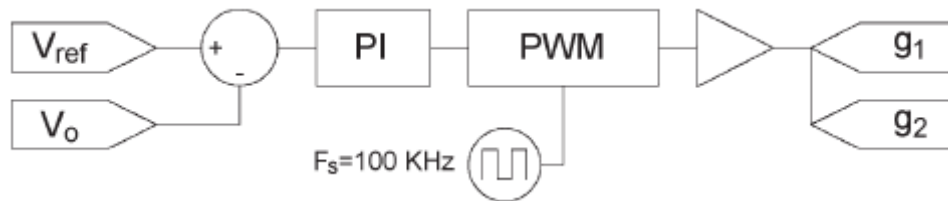$$\eta\text{improvement} = \frac{2P_{D,avg}}{150} = 1.11\%$$

Figure 4.2: Control circuit

V. Simulation Results

The proposed bridgeless SEPIC PFC is simulated by MATLAB when V_{ac} = 180 Vrms, V_0 = 150 ± 5 Vdc, ΔI_L = 20% I1, f_{sw} = 100 kHz and 150Woutput power. According to the aforementioned design considerations, the circuit elements are obtained as C_1 =1 μF, L_1 = 3.4 mH, L_2 = 100 μH, and C_0 = 1000 μF.Fig. 5.2,5.3 shows the input current and voltage at full load .Fig 5.1Output waveform without controller. It can be observed from this figure that input current is in phase with input voltage and is practically sinusoidal with low total harmonic distortion and high Power Factor. Current waveforms of *L*1 and *L*2 are shown in Fig. 5.4. The voltage of *C*1 is shown in Fig.5.3.Simulation was done on full bridge SEPIC converter also in discontinuous conduction mode and could see that the conduction losses is more for this than full bridge SEPIC.
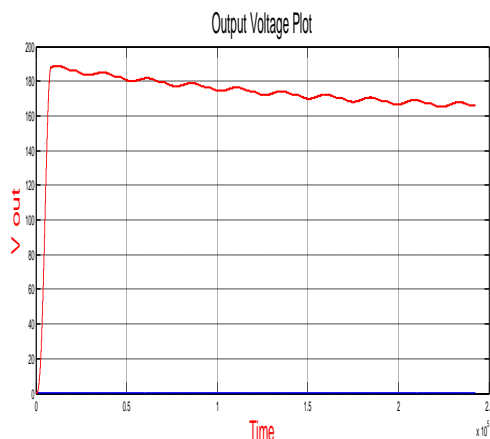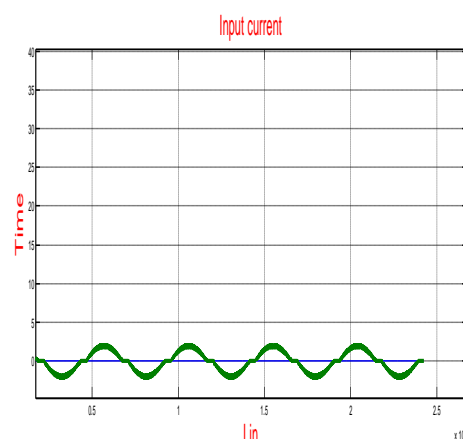

Figure. 5.1: Output
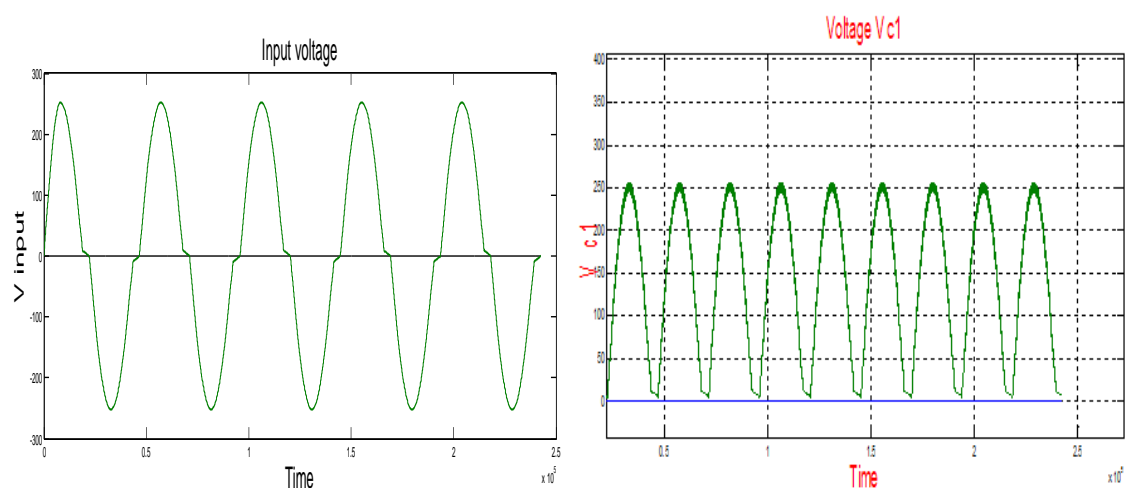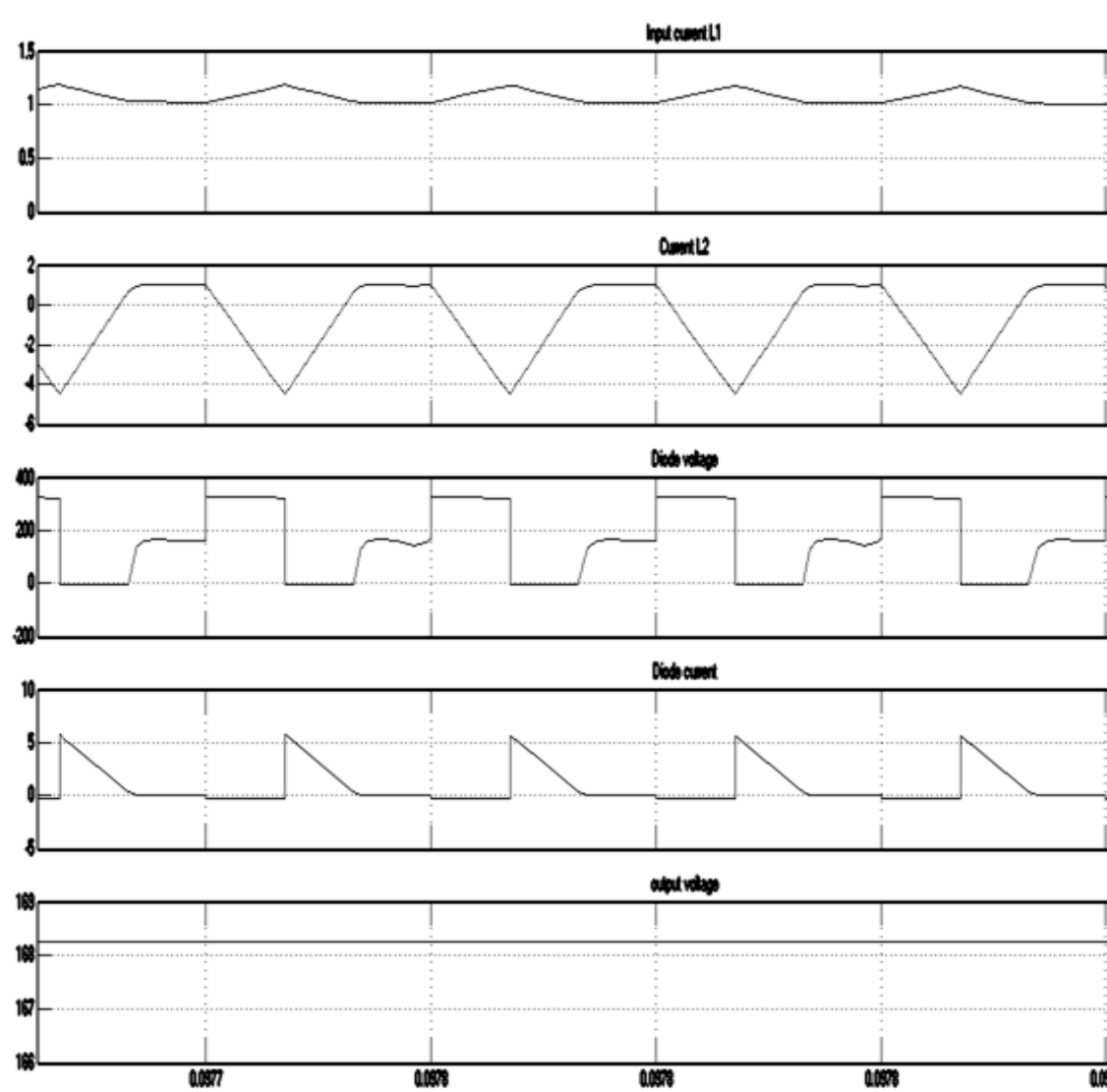

Figure 5.2: Input current

Figure 5.3: Input voltage Figure 5.4: capacitor

Time (sec)

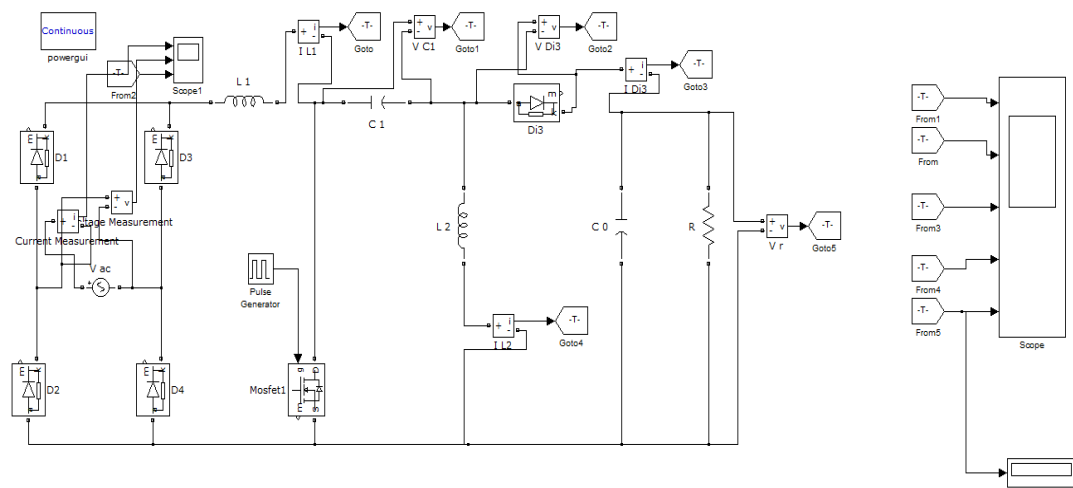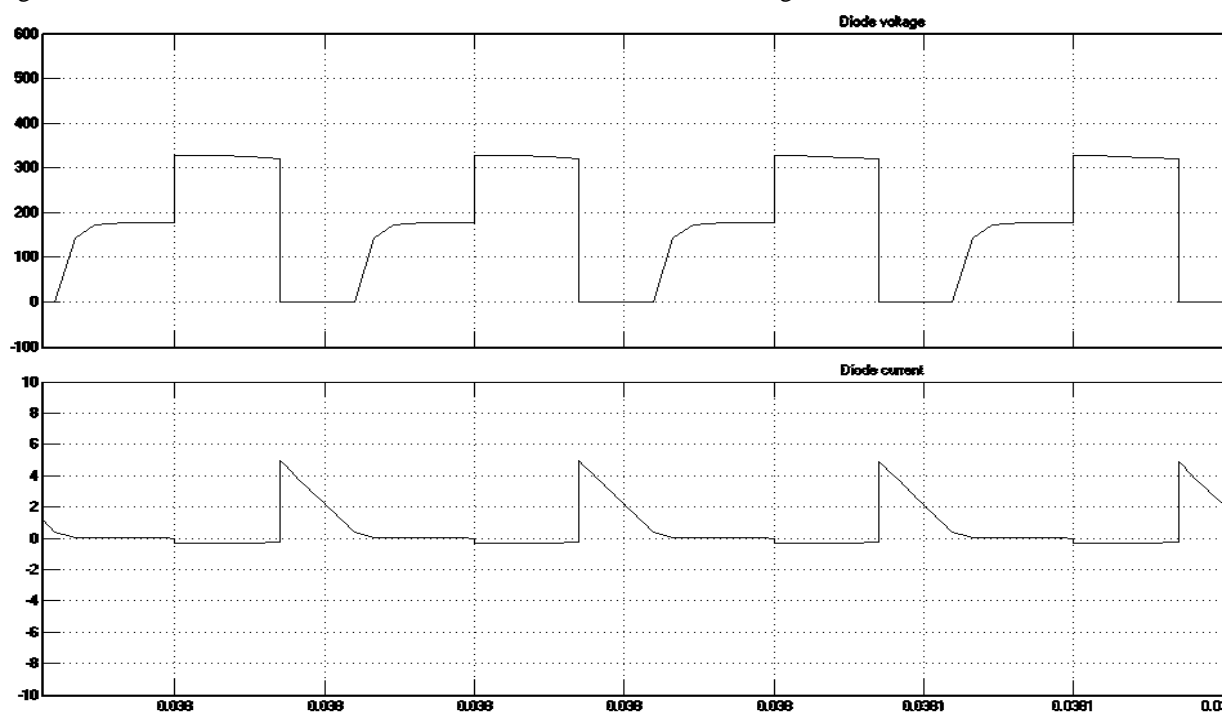Figure 5.5: waveforms of open loop fullbridge SEPIC

Figure 5.6: Simulink diagram of fullbridge SEPIC

Figures 5.1 ,5.2,5.3,5.4,5.5,5.6 shows the different waveforms of full bridge SEPIC converter.

Time(sec)

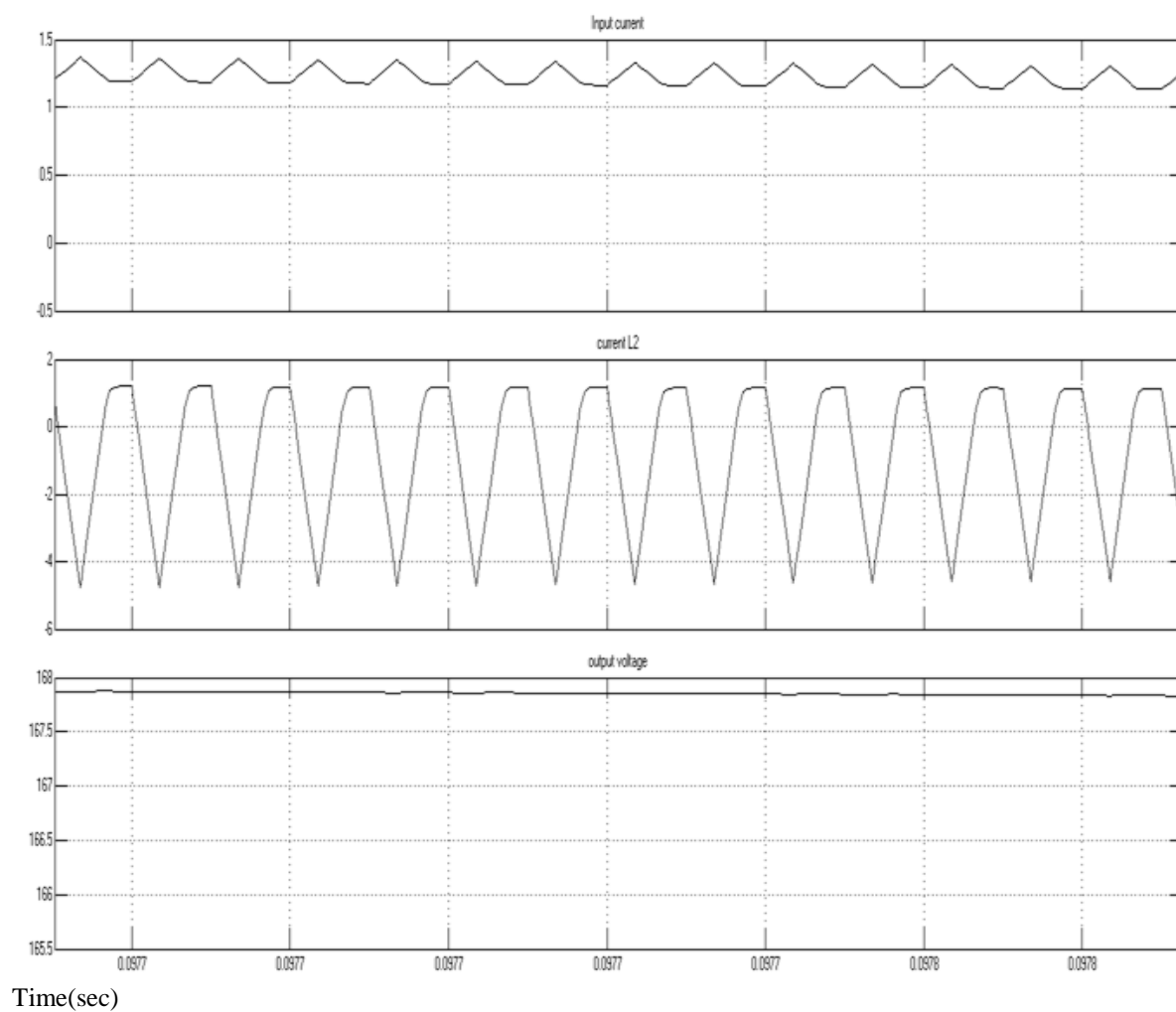Figure 5.7: Diode voltage and current of bridgeless SEPIC

Time(sec)
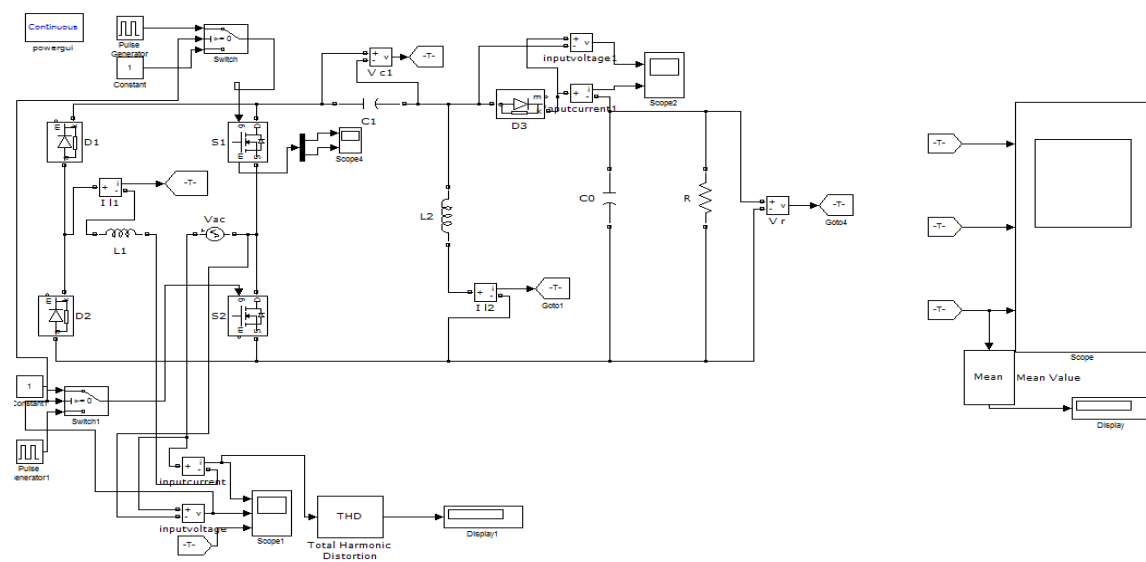
Figure 5.8: waveforms of bridgeless SEPIC converter
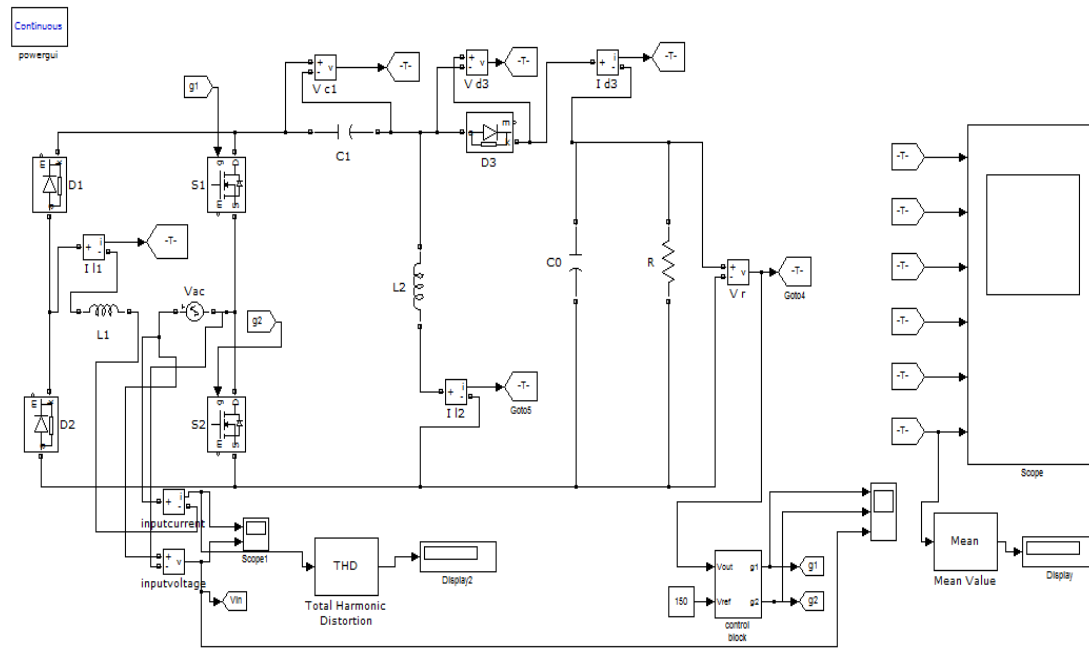

Figure 5.9: Simulink diagram of bridgeless SEPIC
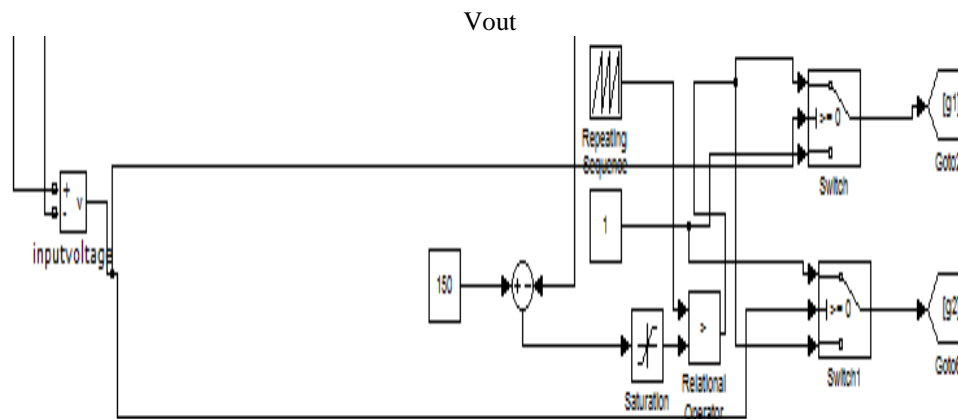
Figure 5.10: Closed loop SEPIC converter

Figure 5.11: Controller circuit

VIII. Conclusion

In this paper, a new bridgeless SEPIC PFC rectifier has been introduced. The proposed circuit provides lower conduction losses with reduced components simultaneously. Two diodes of input rectifier are substituted with two switches in order to use one switch for SEPIC converter. In conventional PFC converters (CCM boost converter), a voltage loop and a current loop are needed for PFC.Here conventional is operated in DCM and compared with the bridgeless SEPIC. By using DCM operation in the proposed converter, the control circuit is simplified, and the current loop is omitted. The main features of the proposed converters include high efficiency, low voltage stress on the semiconductor devices, and simplicity of design. These advantages are desirable features for low-voltage power-supply applications.

REFERENCE

[1]   Jae-Won Yang and Hyun-Lark Do, Bridgeless SEPIC Converter With a Ripple-Free Input Current IEEE Transactions On Power Electronics, Vol. 28, No. 7, July 2013
[2]   Y. Jang and M. M. Jovanovic, Bridgeless high-power-factor buck converter IEEE Trans. Power Electron., vol. 26, no. 2, Feb.2011.
[3]   M. Mahdavi and H. Farzanehfard, "Bridgeless SEPIC PFC rectifier withreduced components and conduction losses," *IEEE Trans. Ind. Electron.,*vol. 58, no. 9, Sep. 2011.
[4]   W.-Y. Choi, J.-M.Kwon, E.-H.Kim, J.-J.Lee, and B.-H. Kwon, Bridgeless boost rectifier with low conduction losses and reduced diode reverse recovery problemsIEEE Trans. Ind. Electron., vol. 54, no. 2Apr. 2007.

Application of Analytical HIERARACHY Process in Industries

Shashikant Tamrakar[1], Dr. Ajay Tiwari[2], Praveen Tandon[3]
[1](Mechanical Engineering Department, RCET /Dr. C.V. Raman University, INDIA)
[2](Principal, Rungta Engineering College / Dr. C.V. Raman University University, INDIA)
[3](Mechanical Engineering Department, RCET / Dr. C.V. Raman University University, INDIA)

ABSTRACT: *Analytic Hierarchy Process (AHP) is a multiple criteria decision-making(MCMD) tool that has been used in almost all the applications related with decision-making. It is used to derive ratio scales from both discrete and continuous comparison in pair wise. These comparisons may be taken from actual measurements or from a fundamental scale which reflects the relative strength of preferences and feelings. AHP being a powerful tool to make decisions which are accurate and fast in the engineering applications. In many situations, an accurate and correct decision need to be taken.*
Keywords: *AHP Analytic Hierarchy Process, Predictive Maintenance, Corrective Maintenance, Expert Choice.*

I. Introduction

With AHP technique, several aspects, which characterise each of the maintenance strategies, are arranged in a hierarchic structure and evaluated using only a series of pairwise judgements. To improve the effectiveness of the methodology AHP is coupled with a sensitivity analysis[1]. For example robot selection for a particular application in a given environment and also a robot performance in different work environment, although the method has been applied in the past new attributes and more demanding situations can be analyzed with AHP more effectively. Similarly vendor selection, selection of a person most suited for a job, resource allocation, conflict resolution, evaluation of technology, investment decision on any project, whether to apply flexible manufacturing system, layout design, automobile assembly line design, employee performance evaluation and best method of doing a job from among various alternatives can be effectively done with the help of software (Expert choice). The unique features of AHP is its flexibility to be integrated with useful and effective techniques like Linear Programming, Quality Function Deployment, Fuzzy Logic, etc.

II. Objective

The objective of present work is to make use of AHP to find easy and effective solution to what appears to be a complex set of problems. As maintenance management is taking on an important strategic role, numerous companies are expecting their maintenance to be performed effectively in order to leverage and transform the maintenance into competitive advantages. More importantly, the successful maintenance management starts with a proper maintenance system strategy produced through a robust evaluation method. However, the maintenance strategy selection is a kind of MCDM problem[2], which requires considering a large number of complex factors as multiple evaluation criteria.

III. Methodology

With the help of case studies and data survey the methodology along with software will be developed to solve the complex decision making problems in maintenance of the machine shop of steel plant to involve a number of options and constraints.

To carry out the proposed research work through data collection, maintenance history of the machines, interviews, group discussions, questionnaires, databases, seminars, conferences etc. to maintenance wing of steel plant and the analysis of data.
Take some case studies and validate them.

IV. Case Study

SELECTION OF ROBOT FOR WELDING OPERATION BY MULTIPLE ATTRIBUTE DECISION MAKING (MADM) APPROACH

4.1 Introduction

There has been rapid increase in the number of robot systems and robot manufacturers. Robots with vastly different capabilities and specifications are available for a wide range of applications. The selection of the robot to suit a particular application and production environment, from the large number of robots available in the market today has become a difficult task. Various considerations such as availability, management policies, production systems compatibility, and economics need to be considered before a suitable robot can be selected. The complexity of problem can be better appreciated when one realizes that there are over 75 attributes that have to be considered in the selection of robot for particular application. Moreover, many of them are conflicting in nature and have different units, which cannot be unified and compared as they are. The quantification and monitoring of the attribute magnitudes will help the manufacturer to control them closely so that he can fulfil the demand of the user precisely. Moreover, he can find out the market trend by observing the attributes magnitudes. This will help the manufacturer to modify his product to suit the future needs of the robot user. He can use the database to produce optimum robots in the minimum possible time. The robot manufacturer can also use these attributes for the SWOT (Strength–Weakness–Opportunity–Threat) analysis of his product. This identification of the attributes will help the user for the database storage and its retrieval. This will generate the computerized database, which can be used in different formats for different purposes by different people in the organization. It also will help the user to select the best possible robot for the particular application whenever it is required. The user will know exactly what are the physical characteristics and performance parameters of the robot. This will keep the user well informed about the capabilities of the robot while putting it to use.

4.2 PROCEDURE - TOPSIS (Technique for Order Preference by Similarity to Ideal Solution) Method

Selection of ROBOT using Multiple Attribute Decision Making -We take the example of robot selection for welding operation using MADM approach. Flow chart for Multiple attribute decision making is given below-
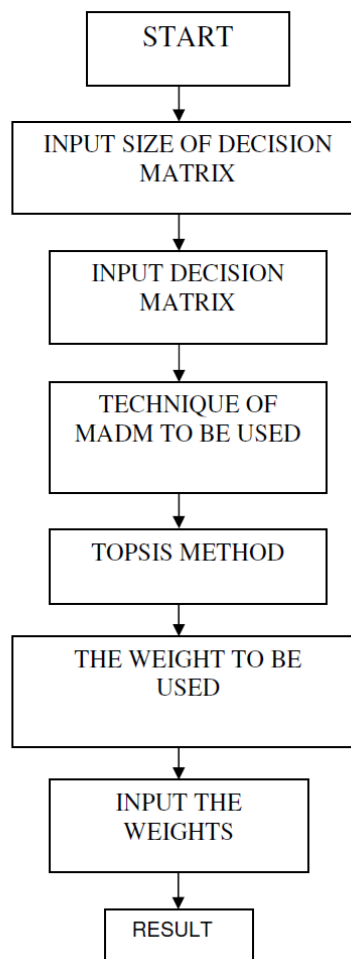
The minimum requirement for this application is as follows Table 1:

1. Load capacity	minimum 2 kg
2. Repeatability	0.5 mm
3. Maximum tip speed	at least 255 mm/s
4. Type of drives (actuators)	electrical only
5. Memory capacity	At least 250 points/steps
6. Manipulator reach	500 mm
7. Degree of freedom	at least 5

From the database generated, after 'elimination search' we can find out manageable number of candidate robots and their pertinent attributes.

Candidate robots are listed below in Table 2: -

No.	Name of Robot
A1	ABB–IRA1400M97
A2	Kawasaki F 545 N
A3	Mitshubishi Melfa CR
A4	Yaskawa Electric Motoman
A5	Fanuc Arcmate100 I
A6	Panasonic VR 006

Pertinent attributes are listed below Table 3: -

Attribute	No.
- Reach (mm)	X1
- Max. Tip Speed (mm/sec)	X2
- Memory Capacity (Points or Steps)	X3
- Load Capacity (kg)	X4
- Repeatability (mm)	X5
- Price (Rs.)	X6

Table shows the Attributes for the short-listed candidate robots is show in table 4:-

| Attribute Alternate	X1	X2	X3	X4	X5	X6
A1	1.40	1200	500	6	0.30	375000
A2	1.97	1450	3000	20	0.25	425000
A3	1.00	1000	800	5	0.08	100000
A4	0.92	850	1000	3	0.15	150000
A5	1.36	1600	2000	5	0.16	225000
A6	1.36	1740	1400	6	0.12	250000

The weighted normalized matrix V is used to obtain the +ve and -ve benchmark robots, where the both benchmark robots are hypothetical robots, which supposed to have best and worst possible attribute magnitudes. Hwang and Yoon developed TOPSIS based upon the concept that the chosen option (optimum) should have the shortest distance from the +ve benchmark robot (best possible robot) and be farthest from the -ve benchmark robot (worst possible robot). The measure ensures that the top ranked robot is closest to +ve benchmark robot and farthest from -ve benchmark robot.

The ranking obtained is shown below in table 5:-

Sl. No.	Alternative Robot	TOPSIS Ranking
1	ABB–IRA1400M97	5
2	Kawasaki F 545 N	4
3	Mitshubishi Melfa CR	6
4	Yaskawa Electric Motoman	1
5	Fanuc Arcmate100 I	2
6	Panasonic VR 006	3

V. Selection of Robots by Using AHP

By using AHP using software Expert choice the ranking obtained is shown
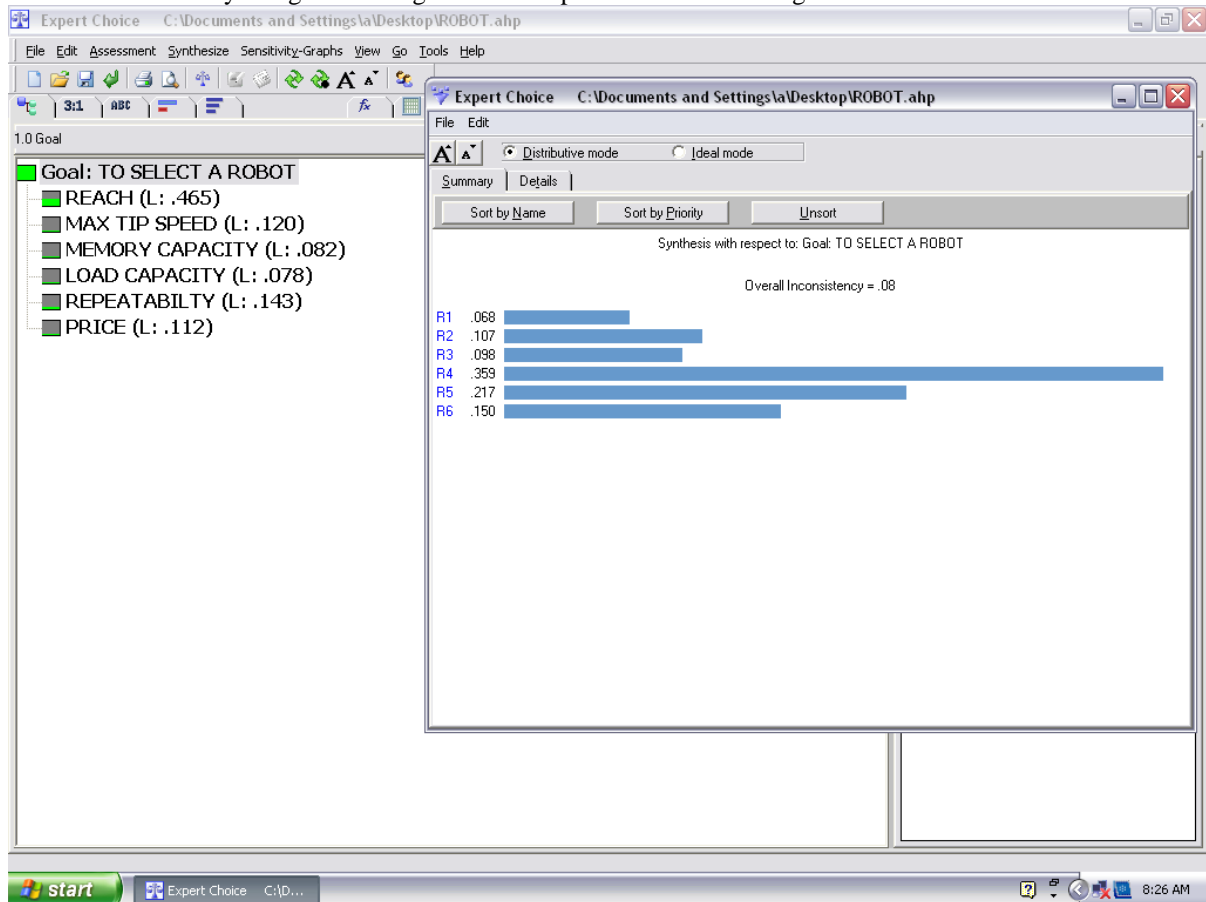
Sl. No.	Alternative Robot	TOPSIS Ranking	Ranking by AHP
1	ABB–IRA1400M97	5	6
2	Kawasaki F 545 N	4	4
3	Mitshubishi Melfa CR	6	5
4	Yaskawa Electric Motoman	1	1
5	Fanuc Arcmate100 I	2	2
6	Panasonic VR 006	3	3

The ranking of Robots obtained is similar to paper referred.

VI.   Conclusion

In this case study the raking is similar so this complex decision is solved by Analytical Hierarchy Process and is validated. So I am very much hopeful to apply this technique in making decision in different industrial applications. The AHP is an effective approach in dealing with day – to – day complex decision problems like machine shop maintenance strategy etc.

REFERENCES

[1]   Thomas L. Saaty, Decision making with the analytic hierarchy process , *Int. J. Services Sciences, Vol. 1, No. 1,* (2008)*,* 83-98 , Inderscience Enterprises Ltd.

[2]   Subhajyoti Ray, Analytical Hierarchy Approach to the Selecting a Doctoral Dissertation, International Journal of Doctoral Studies Volume 2, (2007)

[3]   Jiaqin Yang and Ping Shi, Applying Analytic Hierarchy Process in Firm's Overall Performance Evaluation, International Journal Of Business, 7(1), (2002) Issn:1083-4346

[4]   Maggie C.Y. Tama, V.M. Rao Tummalab, An application of the AHP in vendor selection of a telecommunications system , (2001) Elsevier Science Ltd., International Journal of Management Science Pg. 171-182.

[5]   A. P. Agalgaonkar, S. V. Kulkarni, and S. A. Khaparde, "Multi-attribute Decision Making Approach for Strategic Planning of DGs", publisher IEEE, Year 2005.

[6]   Abhishek Kumar and V.P. Agrawal, "Attribute based specification, comparison and selection of electroplating system using MADM approach", Expert Systems with Applications, Year 2009, Vol.-36, Issue 8, 10815-10827.

[7]   A.S. Milani, A. Shanian, R. Madoliat and J.A. Nemes, "The effect of normalization norms in multiple attribute decision making models: a case study in gear material selection", springer link journal article, Year 2004, vol.- 29, 312-318.

[8]   Cengiz Kahraman & Selçuk Çebı, "A new multi-attribute decision making method: Hierarchical fuzzy axiomatic design", Expert Systems with Applications: An International Journal, Year 2009, vol.-36, issue 3, 4848-4861.

[9]   Christer Carlsson and Robert Fuller, "Fuzzy multiple criteria decision making : Recent developments", Year 1996, vol.-78, issue 2, 139-153.

[10]   Chen, Jason C.H. ,Ma, Jian, "Multiple attribute decision making: approach integrating subjective and objective information", International journal of Manufacturing Technology and Management, Year 2003, vol.-5, 338-361.

[11]   Gin-Shuh Liang, "fuzzy multi-criteria decision making approach for robot selection", journal of Elsevier, Amsterdam, PAYS-BAS, Year 1993, vol.-10, 267-274.

[12]   Hsu-Shih Shih, "Incremental analysis for MCDM with an application to group TOPSIS" , European Journal of Operational Research 186 Year 2007, 720–734

[13]   Haymwantee P. Singh & Wilfred V. Huang, "A decision support system for robot selection", Elsevier Science Publishers B. V., Year 1991, vol.-7, issue 3, 273-283.

[14]   K. L. Poh, "knowledge-based guidance system for multi-attribute decision making", Science Direct, Year 1998, vol.-12, issue 3, 315-326.

[15]   Muh-Cherng Wu & Wen-Jen Chang. "A multiple criteria decision for trading capacity between two semiconductor fabs", Expert Systems with Applications: An International Journal, Year 2008, vol.-35, issue 3, 938-945.

[16]   Moutaz Khouja, "The use of data envelopment analysis for technology selection", Computers and Industrial Engineering, Year 1995, vol-28, issue 1, 123-132.

[17]   Piotr Jankowski, Natalia Andrienko and Gennady Andrienko. "Map-centred exploratory approach to multiple criteria spatial decision makes", International Journal of Geographical Information Science, Year 2001, vol.-15, 101-127.

[18]   Quan Zhang Zhi-Ping Fan, "A method for multiple attribute decision-making with the fuzzy preference relation on alternatives", science direct, Year 2004, vol. - 46, issue 2, 321-327.

Design and Implementation of wireless heart monitor for expectant mothers in their 3rd trimester

Niyan Marchon[1], Dr. Gourish Naik[2]

[1]*(Electronics and Telecommunication Department, Padre Conceicao College of Engineering, India)*
[2]*(Electronics Department, Goa University, India)*

ABSTRACT: *A low cost Maternal & Fetal Heart Rate (MFHR) monitor is introduced in an attempt to reduce or eliminate hypoxic episodes well before the development of fetal asphyxia. MFHR monitoring is sensitive and detects fetal hypoxia early in the evolution to acidosis. The abdominal electrocardiogram (AECG) is the recording of the cardiac activity of both the mother and the fetus. The main challenge is to extract the fetal ECG, which is strongly distorted by maternal component of dominating energy and artifacts like baseline wander and power-line interference which were effectively preprocessed and filtered by using a Kaiser FIR filter having a SNR ratio of 13.68 , filter order of 298 and a Notch filter (fc = 50 Hz) with a bandwidth of 2 Hz respectively. Our endeavor has been to design this MFHR monitoring device using a smartphone. This system continuously monitors the patient's AECG data especially in the 3rd trimester. For the ongoing research work the maternal AECG signals were taken from the Physionet non-invasive ECG database. The AECG file is transferred from the PC to a microcontroller ATMEGA32A which is interfaced to a Bluetooth module. Data is then transferred wirelessly via Bluetooth to the phone. The smartphone contains an application that displays data received from the Bluetooth module interfaced with a plotter application. This Bluetooth Plotter application plots the ECG waveforms of the content on the phone. Various inferences were effectively made based upon the ECG graphs produced on the phone, thus giving the doctors an alert about the patient's and Fetal ECG information. Further research will examine the real time patient's data from the hospital assigned to us.*

Keywords: *Maternal & Fetal Heart Rate (MFHR), asphyxia, Abdominal Electrocardiogram (AECG), baseline wander, power-line interference, Physionet, Bluetooth, smartphone.*

I.   Introduction

The intrapartum management of fetal distress is a challenge to obstetricians, compounded by difficulties in interpreting the fetal heart rate (FHR) pattern and confusion regarding the definition of asphyxia. Fetal asphyxia refers to acidosis resulting from progressive hypoxia in utero [1]. FHR monitoring is sensitive and can detect hypoxic episodes early in the evolution to acidosis. Electronic FHR monitoring was introduced in an attempt to reduce or eliminate the potentially disastrous consequences of fetal asphyxia. Enthusiasm for this new technology established the role of continuous FHR monitoring in labor before studies demonstrated its accuracy. Abnormal FHR patterns in the auscultation can be backed up by electronic fetal monitoring. Electronic FHR monitoring has other benefits over auscultation that are not always considered. These include an ability to understand the mechanism of developing hypoxia by pattern recognition and the ability to assess the fetal response to hypoxia by evaluating reactivity or variability. Reports shows in table I the total infant deaths occurred in the year 2012 in the medical hospitals in Goa, India, where 5 % of the infant deaths have occurred due to birth asphyxia.

TABLE I.   CAUSE OF DEATH IN INFANTS AT THE MEDICAL HOSPITALS IN GOA

Total deaths	Congential Anomalies	Low birth Weight	Sepsis	Birth Asphyyxia	Others
249	81	69	66	12	21

Newspaper report, Heraldo (Insight) Friday, May 17 2013

FHR monitoring has several disadvantages, however. The most important is, increased cesarean sections (CSs) associated with overreaction to, or misinterpretation of, FHR patterns and a large increase in medicolegal malpractice litigation.

The ideal goals of fetal assessment in labor should be: 1)   To detect and reverse hypoxia before it progresses. 2) Failing the ability to reverse hypoxia, monitoring should allow physicians to detect hypoxia and

determine when it leads to metabolic acidosis. 3) This allows for intervention by operative delivery before fetal death or damage occurs.

Electronic FHR monitoring is helpful in detecting hypoxia, but determining the precise point when metabolic acidosis occurs is difficult at best. The frequency of metabolic acidosis in labor is generally approximately 1% [1].

Despite disadvantages, the goal of protecting the fetus during this potentially dangerous 3ʳᵈ trimester should and does supersede all other considerations. A thorough understanding of abnormal FHR patterns not only allows physicians to direct resuscitative efforts and prevent hypoxic damage but also prevents unnecessary interventions.

II.   Procedure For Denoising AECG

The Non-invasive abdominal ECG (AECG) taken from the online Physionet database as shown in figure 1 is the recording of the cardiac activity of both the mother and the fetus when several leads are placed on the abdomen of the mother. The motivation for monitoring the fetal heart rate through pregnancy is to recognise pathologic conditions, typically asphyxia, with sufficient warning to enable intervention by the clinician before irreversible changes set in. Fetal ECG is strongly distorted by the maternal component having a dominating energy and other artifacts such as baseline wandering and power line interference. An efficient way to remove the baseline wander is to use FIR Kaiser High pass filter. It also exhibits the highest SNR ratio, while all the IIR filters displayed a poor SNR ratios [2].
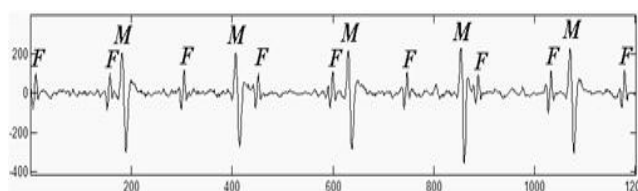

Fig 1 Composite Maternal Abdominal Signal; M- maternal QRS complex, F- fetal QRS complex

The Fast Fourier Transform (FFT) of the denoised signal shows that the 50 Hz frequency component has been effectively removed using the Notch filter. The combined methodology of using the Kaiser FIR high pass filter, Notch filter followed by the Savitzky Golay filter effectively denoises the abdominal Maternal ECG signal without destroying the fetal ECG information [2] as shown in figure 2.
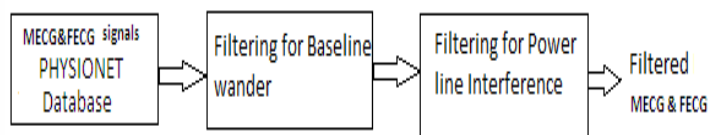

Fig 2 Combination method: Proposed Technique to filter AECG signals.

III.   Implementation Of The Wireless Heart Monitor

The wireless heart monitoring device consists of the Physionet non-invasive AECG database which is fed to the ATmega32 microcontroller, Bluetooth module and a smart phone as shown in figure 3. The physionet patient's recording was taken from a single subject between 21 to 40 weeks of pregnancy with a 10 second duration for each signal [3]. The signals sampled at a rate of 1 kHz, with 16 bit resolution which are sent to the Microcontroller via the HyperTerminal. The digital values are sent by the ATmega32 microcontroller to the smart phone via Bluetooth module as shown in figure 4. An Android application developed using the smart phone displays the ECG signal waveform using the digital values obtained from the Bluetooth module. The Android application also calculates the heart rate and checks whether it is above a threshold level. In case any abnormality is found the smart phone immediately sends a message to the doctor.

To test the proposed system, we imported data from Physionet and created our own database of three diseases for training the neural network. Each patient record, sampled at 1ms each contained 1000 values. This was further compressed using Debaushy's wavelet transform to 42 values. Three patient's records of each disease, of 10millisecond, were imported for each disease for training.
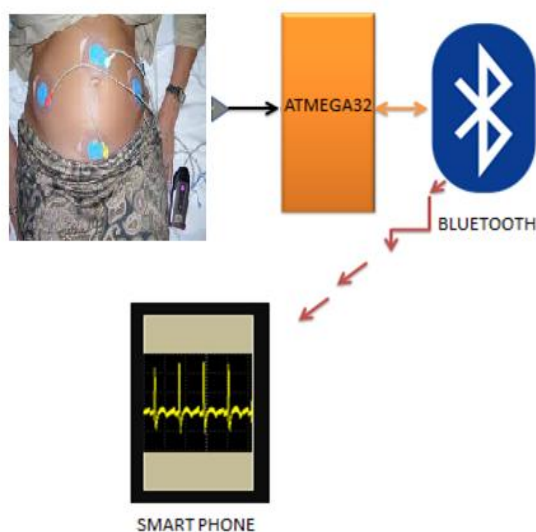
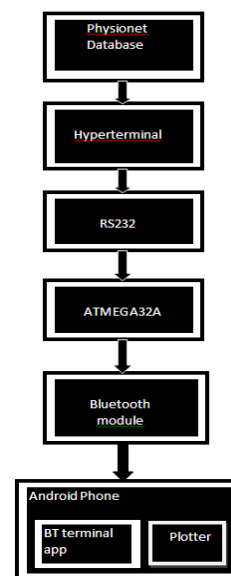Fig 4 Flowchart of the proposed Wireless Heart Monitor   Fig 3 Proposed system of a Wireless Heart Monitor

3.1 . Initialization and Sending/Receiving data
The ATmega32 is a low-power CMOS 8-bit microcontroller based on the AVR enhanced RISC architecture. By executing powerful instructions in a single clock cycle, theATmega32 achieves throughputs approaching 1 MIPS per MHz allowing the system designer to optimize power consumption versus processing speed.

3.1.1 Baud Rate: The microcontroller does not accept the baud rate value. Instead, this value is used to calculate a value called Baud Number which is stored in a 16 bit register. This number signifies that value from which the counter has to go to zero so as to get/send the next bit. Hence, choosing a value of F_CPU = 8 MHz and a Baud Rate of 9600 bps, we get Baud   Number = 51. Therefore, each time before sending / receiving a bit, the CPU counts from 51 to 0.

3.1.2 Enable the receiver and/or transmitter: This is done by writing a '1' to the RXEN and/or TXEN bits of the register UCSRB.

3.1.3 Selecting mode of operation: You can use USART in synchronous as well as asynchronous mode.That is done by altering the UMSEL bit in the UCSRC register. Asynchronous mode is generally used (which is the default selection).

3.1.4 Registers and bits involved in sending data: We have to simply write data to a register named UDR to send the data serially. But before that, we have to check if the register is actually ready to receive data. That is done by checking the status of a bit named UDRE. If its status is '1', it means that UDR is at your service and if it is 0, wait for it to become '1' because it is already busy serving you.

3.1.5 Register and bits involved in receiving data: In order to receive data, we have to simply transfer the contents of UDR into a variable. But before this, we have to check if we have received the entire byte. This is done by checking the status of RXC bit. If RXC is '1', then there is an unread byte in UDR which needs to be emptied so as to receive the next byte of data.

3.2 USB2.0 to RS232 converter
As the baud rate is 9600 bits per second, hence one bit takes 1/9600 seconds or 104 micro sec. Our AVR ATmega32A will communicate with the computer through the RS-232 protocol. On the computer side we need to use the terminal emulation program that can communicate through the RS-232 protocol. For this ongoing research work, we used the standard windows communication program called HyperTerminal.

3.3. Bluetooth Module:
Serial Bluetooth RF Transceiver Module Interface JY-MCU BT_BOARD V1.3 was used. The power supply input of the module is 3.6 ~ 6V, and should not be more than 7V.This Bluetooth Module Baseboard can be compatible with master mode, slave mode and both master-slave mode. The key interface on the baseboard is

the master mode button and can be controlled by high level from external MCU, then this module will search again automatically.

Fig.5 Bluetooth Module: JY-MCU BT_BOARD V1.3

3.4. Neutral Networks to classify the heart diseases:
We have used the concept of neural networks to train a network, through supervised learning, to help classify an ECG into different heart diseases. For our present network, we used Physionet database and created a database of different patient records (taken over a period of 10 seconds each, with readings at an interval of 1ms each) for three different types of heart diseases viz. Atrial Fibrillation, Congestive Heart Failure and Ventricular Malignancy. The network helps classify which of the above disease, the test ECG belongs to.

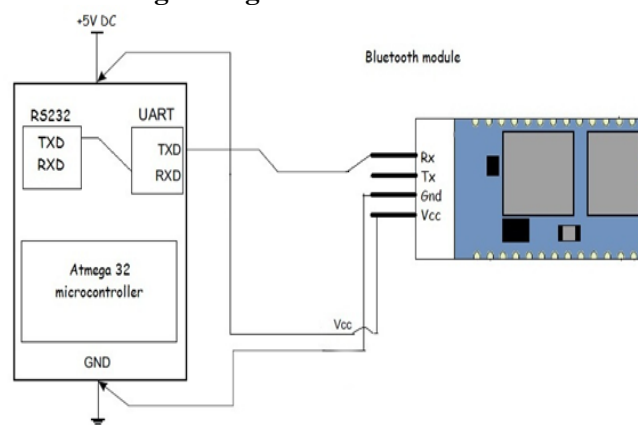## IV. Interfacing Atmega32 With The Bluetooth Module

Fig.6 Interfacing ATmega32 with the Bluetooth Module

For the interfacing, the TXD pin of Atmega32 is connected to the RX pin of the Bluetooth module. We have used 9600 bps as the baud rate for the serial communication and also for the communication between the Atmega32 and the Bluetooth module. By default the Bluetooth module transmits and receives at 9600/8/N/1.The power supply options are 3.6 to 5V.When powered up, the chip will blink red. Even after tethering, it will continue to blink. As soon as something initializes the connection by trying to send or get data, the light will switch to solid red.

V. Interfacing Atmega32 with the Bluetooth Module

An already present 'Bluetooth Terminal' application (that allows us to display the values received by a phone from another device, via Bluetooth, on the phone screen) and a coded application called 'Plotter' (that plots ECG graph) were interfaced with each other to provide our resultant application called, 'Bluetooth-Plotter'. It can be described as an Android application that asynchronously receives and plots graph data from an SPP (serial port profile) Bluetooth device using the RFCOMM protocol. The 'Bluetooth-Plotter' application consists of four codes: Bluetooth chat, Bluetooth chat service, Device list activity and the Graph view.

VI. Results

The physionet non-invasive AECG data was filtered and processed. The Bluetooth transmission module (JY-MCU BT_BOARD V1.3) was interfaced with the ATmega32 and successfully carried out the communication between them. The AECG was displayed on a smart phone using Android as shown in figure 7. The neural network correctly classified one of the three heart diseases which was fed to the module.
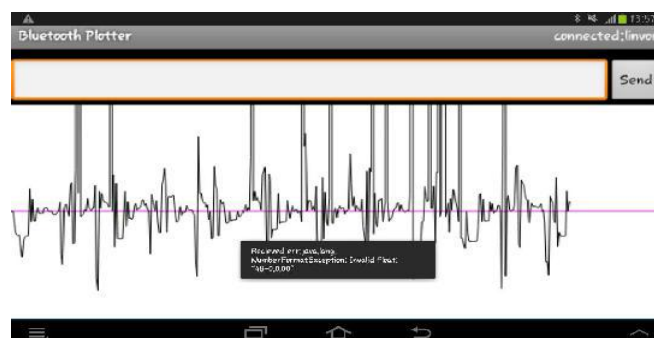
Figure 7: AECG plotted using Android application

VII. Conclusion

A low cost Maternal & Fetal Heart Rate (MFHR) monitor device using a smartphone was introduced in an attempt to eliminate hypoxic episodes well before the development of fetal asphyxia in the 3rd trimester. The AECG signals from the Physionet effectively filtered [2] the baseline wander and power-line interference using a Kaiser FIR filter having a SNR ratio of 13.68 , filter order of 298 and a Notch filter (fc = 50 Hz) with a bandwidth of 2 Hz respectively. The AECG file was transferred from the PC to a microcontroller ATMEGA32A which was interfaced to a Bluetooth module. Data was then effectively transferred wirelessly via Bluetooth to the phone. The Android smartphone's application 'Bluetooth plotter 'displayed the ECG waveform. Various inferences were effectively made based upon the ECG graphs produced on the phone, thus giving the doctors an alert about the patient's ECG information. Further research will examine the real time maternal and Fetal Heart rate to be alerted to the Hospital doctor.

Android being an open source allows future scope of adding enhanced functionality. GPS and GSM API's could be integrated in the application so that a patient's location could be tracked, and the doctor whose number has been already stored could be notified.

REFERENCES

[1] Stephanie Penning, DO , Thomas J. Garite, "Management of Fetal Distress" MD,Obstetrics and Gynecology Clinics Volume 26, Issue 2 , Pages 259-274, 1 June 1999
[2] Niyan Marchon , Dr Gourish Naik, "Denoising of Abdominal Maternal ECG signals" International Journal of Engineering Research & Industrial Applications (IJERIA) , vol.7,No.I, February 2014.
[3] Physionet website : www.Physionet.org
[4] Mahesh S. Chavan, R.A.Agarwala, M.D.Uplane, Comparative Study of Chebyshev I and Chebyshev II Filter used For Noise Reductionin ECG Signal, International Journal Of Circuits, Systems And Signal Processing Issue 1, Volume 2, 2008,pp1-17
[5] Mahesh S. Chavan, R.A.Aggarwala, M.D.Uplane, 'Suppression Of Baseline Wander And Power Line Interference in ECG Using Digital IIR Filter', International Journal of Circuits, Systems And Signal Processing, Issue 2, Volume 2, 2008,pp-356-65.
[6] C.Rodriguez, S. Borromeo, R. de la Prieta, J.A Hernández, N.Malpica "Wireless ECG based on Bluetooth protocol: design and implementation."
[7] Borromeo S, Rodriguez-Sanchez C, Machado F, Hernandez-Tamames JA, De la Prieta R "A Reconfigurable, Wearable, Wireless ECG System",. Proceedings of the 29th Annual International Conference of the IEEE EMBS Cité Internationale, Lyon, FranceAugust 23-26, 2007.
[8] Poonam T. Bedarkar, Shanti Swamy "Design and Implementation of Wireless Handheld Device For Android Cell Phone", Conference on Advances in Communication and Control Systems 2013 (CAC2S 2013)
[9] Poonam T. Bedarkar, Shanti Swamy,"BLUETOOTH BASED VISUALIZATION FOR REAL TIME ECG MONITORING" International Journal of Electrical, Electronics and Data Communication, ISSN (p): 2320-2084, Volume-1, Issue-2, April-2013.
[10] Veysel Aslantas, Rifat Kurban ,Tuba Caglikantar "A Low-Cost Wireless Healthcare Monitoring System And Communication To A Clinical Alarm Station", Erciyes University, Faculty Of Engineering, Department Of Computer Engineering, 38039, Kayseri, Turkey.
[11] R. Fensli, E. Gunnarson, O. Hejlesen, "A wireless ECG system for continuous event recording and communication to a clinical alarm station" , EMBC 2004, Vol. 1, (s):2208 – 2211

Simulation of a Two Stage High Power Factor Driver for White Power Led

Ambily Krishnadas[1], Rabiya Rasheed[2]

[1](Student, Department of Electrical and Electronics Engineering, FISAT, MG university, Kerala, India)
[2](Assistant Professor, Department of Electrical and Electronics Engineering, FISAT, MG university, Kerala, India)

ABSTRACT : *In this paper, an integrated double buck–boost (IDBB) converter is proposed as a high-power-factor offline power supply for power-LED lamps. The IDBB converter features just one controlled switch and two inductors and is able to supply a solid-state lamp from the mains, providing high power factor and good efficiency. In this paper, the IDBB converter is analyzed, and a design methodology is proposed. It is demonstrated that, with a careful design of the converter, the filter capacitances can be made small enough so that film capacitors may be used. In this way, the converter mean time between failures can be made as high as that of the solid-state lamp. A design example for a 70-W converter supplied from a 230 V/50 Hz mains for street lighting applications is shown. MATLAB is applied to execute the whole circuit simulations. Finally, simulation results demonstrate that the power factor of the closed-loop IDBB converter is 0.993 and the output voltage of the designed controller can be stably maintained at 200V.*
Keywords : *Continuous Conduction Mode (CCM), Discontinuous Conduction Mode (DCM), Duty cycle (D), Integrated double Buck–boost (IDBB), white power LED*

I. INTRODUCTION

Energy prices have skyrocketed in recent years owing to depleting renewable resources. In addition to seeking other energy sources, countries worldwide are also initiating energy-saving and carbon reduction programs. Due to the small size and high efficiency, semiconductor lighting has attracted researchers and manufacturers to develop new products using this technology. Nowadays the energy-inefficient incandescent lamps and mercury-based tubular and compact fluorescent lamps are replacing LED lamps. Although HB white LEDs are not the most efficient lighting systems in terms of lumens per watt for streetlight applications (indeed, they achieve a lower efficiency than low-pressure sodium vapor lamps), they are quite interesting compared to traditional solutions due to their longer operating life and their more pleasant light spectrum (sodium lights emit only in yellow color, thus providing a very poor Color Rendering Index, CRI). High Brightness-LEDs do not need neither warm up nor restart period, which do imply the use of specific circuitry.

Due to the high efficiency of the LEDs with maximum illumination, the utilization is 85%-90% of the input power into light energy, whereas the fluorescent lamps will produce only 77%. On the other hand global warming and increasing power demand etc. may be fulfilled by LEDs by implementing enhanced control technique (light dimming and preheating of filaments if possible). The recombination of electrons and holes can cause either photons (light) or phonons (heat). So the junction temperature of the LEDs increasing leads to the degradation of the luminous flux of LEDs [11]. The high efficacy of power LEDs is only maintained under strict operating conditions, which include low direct current and low junction temperature (Fig 1). All these mean that the development of power supplies that achieve correct driving of the LED-based lamp is an important topic of research [16]–[20].

White power LEDs are becoming an attractive light source, owing to their high reliability, long life, high color rendering index, and small size [1]. In addition, there are commercially available units that can reach light efficacies as high as 100 lm/W. All these features make white LEDs a good candidate to override fluorescent and other discharge lamps.

The main drawback of these LEDs is they need constant voltage as input and they need current limiter before the input of the LED. Therefore, some kind of current-limiting device must be used, similarly to the ballast used to limit the current through a discharge lamp. On the other hand, the high efficacy of power LEDs is only maintained under strict operating conditions, which include low direct current and low junction temperature.

A review of literature shows that a variety of LED power supplies and driver solutions, which can accurately control the current of the LED while achieving a near-unity input power factor, have been proposed

[8]–[10]. This drive is currently implemented with power electronic stages based on switch mode power supplies (SMPS). However, an electrolytic capacitor is required in these applications. Unfortunately, the operating life of such capacitors is by far shorter than the life of the HB LEDs, and usually are the shortest of all the devices in the power supply. Thus, removing the electrolytic capacitor would imply a remarkable increase in the operating life and reliability of the system [3],[4].

PFC converters can be classified into two types: two-stage and single-stage. Two-stage PFC converters consist of a PFC stage and a dc/dc stage. Single-stage PFC converters integrate the PFC stage and the dc/dc stage, leading to simple topology and low cost. They are suitable for low-power applications [7]. The simplest active PFC circuits are implemented with a single-stage that makes the power factor correction. The most common single-stage topology used is the flyback converter [5], [6] working in Discontinuous Conduction Mode (DCM), being called DCM flyback PFC converter. The main drawbacks of these pre-regulators are, by one hand, the high peak current stresses caused by the DCM and serious EMI problem [3] and, by the other, the poor dynamics that these converters perform due to the low-pass filter (10 Hz-20 Hz) needed to reduce the input line current total harmonic distortion (THD). Therefore, if dimming operation is required, which must be done at frequencies above 200 Hz, these single stage solutions are not feasible . Attending to the reasons exposed above, a two-stage is needed so the Power Factor Correction can be done properly and a fast enough output dynamics is obtained.

The numerous types of switching converter include boost, buck, buck-boost, and Cuk converters. Here an integrated double buck–boost converter is proposed to supply power-LED lamps from the line, providing high power factor, low LED current ripple, and high efficiency. The operation of the converter is equivalent to two buck–boost converters in cascade, in which the controlled switch is shared by the two stages. Thus, the proposed converter includes two inductors, two capacitors, three diodes, and one ground-referenced controlled switch, featuring affordable low cost and good reliability for this kind of applications.
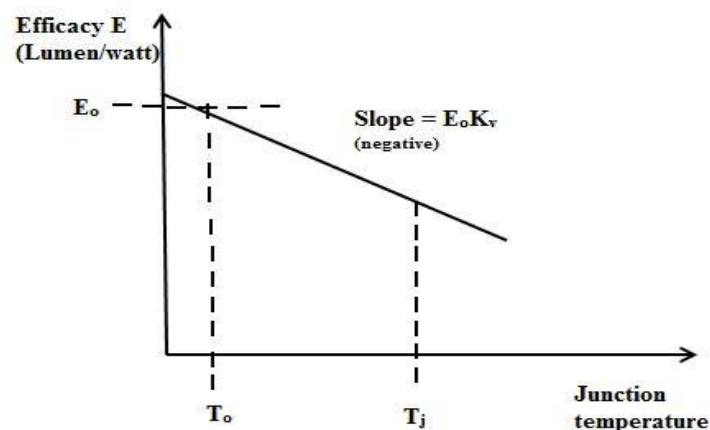

Figure 1.1: Efficacy versus junction temperature of LED.

II.   White Power Led

LEDs can be divided into three categories: indicative LEDs, high-brightness LEDs, and power LEDs. White power LEDs are becoming an attractive light source, owing to their high reliability, long life, high color rendering index, and small size [1]. In addition, there are commercially available units that can reach light efficacies as high as 100 lm/W. All these features make white LEDs a good candidate to override fluorescent and other discharge lamps in many applications, including street lighting, automotive lighting, and decorative applications.

There are two primary ways of producing white light-emitting diodes (WLEDs), LEDs that generate high-intensity white light. One is to use individual LEDs that emit three primary colors—red, green, and blue— and then mix all the colors to form white light. The other is to use a phosphor material to convert monochromatic light from a blue or UV LED to broad-spectrum white light, much in the same way a fluorescent light bulb works.

There are three main methods of mixing colors to produce white light from an LED:
   [1]   blue LED + green LED + red LED (color mixing; can be used as backlighting for displays)
   [2]   near-UV or UV LED + RGB phosphor (an LED producing light with a wavelength shorter than blue's is used to excite an RGB phosphor)

[3]   blue LED + yellow phosphor (two complementary colors combine to form white light; more efficient than first two methods and more commonly used)[79]

2.1 LED efficiency and efficacy:

In lighting design, "efficacy" refers to the amount of light (luminous flux) produced by a lamp (a lamp or other light source), usually measured in lumens, as a ratio of the amount of power consumed to produce it, usually measured in watts. This is not to be confused with efficiency which is always a dimensionless ratio of output divided by input which for lighting relates to the watts of visible power as a fraction of the power consumed in watts. The visible power can be approximated by the area under the Planck curve between 300 nm and 700 nm for a blackbody at the temperature of the filament as a ratio of the total power under the blackbody curve. Efficiency values for light from a heat source are typically less than two percent.

2.2 Advantages of LED over incandescent and fluorescent lamps

a. Efficiency: LEDs emit more lumens per watt than incandescent light bulbs.[115] The efficiency of LED lighting fixtures is not affected by shape and size, unlike fluorescent light bulbs or tubes.
b. Color: LEDs can emit light of an intended color without using any color filters as traditional lighting methods need. This is more efficient and can lower initial costs.
c. Size: LEDs can be very small (smaller than 2 mm) and are easily attached to printed circuit boards.
d. On/Off time: LEDs light up very quickly. A typical red indicator LED will achieve full brightness in under a microsecond.
e. Cycling: LEDs are ideal for uses subject to frequent on-off cycling, unlike fluorescent lamps that fail faster when cycled often, or HID lamps that require a long time before restarting.
f. Dimming: LEDs can very easily be dimmed either by pulse-width modulation or lowering the forward current.
g. Cool light: In contrast to most light sources, LEDs radiate very little heat in the form of IR that can cause damage to sensitive objects or fabrics. Wasted energy is dispersed as heat through the base of the LED.
h. Slow failure: LEDs mostly fail by dimming over time, rather than the abrupt failure of incandescent bulbs.
i. Lifetime: LEDs can have a relatively long useful life. One report estimates 35,000 to 50,000 hours of useful life, though time to complete failure may be longer. Fluorescent tubes typically are rated at about 10,000 to 15,000 hours, depending partly on the conditions of use, and incandescent light bulbs at 1,000 to 2,000 hours.
j. Shock resistance: LEDs, being solid-state components, are difficult to damage with external shock, unlike fluorescent and incandescent bulbs, which are fragile.
k. Focus: The solid package of the LED can be designed to focus its light. Incandescent and fluorescent sources often require an external reflector to collect light and direct it in a usable manner. For larger LED packages total internal reflection (TIR) lenses are often used to the same effect.

2.3 Disadvantages of LED

a. High initial price: LEDs are currently more expensive, price per lumen, on an initial capital cost basis, than most conventional lighting technologies. As of 2010, the cost per thousand lumens (kilolumen) was about $18. The price is expected to reach $2/kilolumen by 2015. The additional expense partially stems from the relatively low lumen output and the drive circuitry and power supplies needed.
b. Temperature dependence: LED performance largely depends on the ambient temperature of the operating environment – or "thermal management" properties. Over-driving an LED in high ambient temperatures may result in overheating the LED package, eventually leading to device failure. An adequate heat sink is needed to maintain long life. Toshiba has produced LEDs with an operating temperature range of -40 to 100°C, which suits the LEDs for both indoor and outdoor use in applications such as lamps, ceiling lighting, street lights, and floodlights.
c. Voltage sensitivity: LEDs must be supplied with the voltage above the threshold and a current below the rating. This can involve series resistors or current-regulated power supplies.
d. Light quality: Most cool-white LEDs have spectra that differ significantly from a black body radiator like the sun or an incandescent light. The spike at 460 nm and dip at 500 nm can cause the color of objects to be perceived differently under cool-white LED illumination than sunlight or incandescent sources, due to metamerism, red surfaces being rendered particularly badly by typical phosphor-based cool-white LEDs. However, the color rendering properties of common fluorescent lamps are often inferior to what is now available in state-of-art white LEDs.

e.   Area light source: Single LEDs do not approximate a point source of light giving a spherical light distribution, but rather a lambertian distribution. So LEDs are difficult to apply to uses needing a spherical light field, however different fields of light can be manipulated by the application of different optics or "lenses".

f.   Electrical polarity: Unlike incandescent light bulbs, which illuminate regardless of the electrical polarity, LEDs will only light with correct electrical polarity. To automatically match source polarity to LED devices, rectifiers can be used.

g.   Electric shock hazard: There have been LED recalls because faulty wiring that can cause electric shock, fire or burns.

h.   Blue hazard: There is a concern that blue LEDs and cool-white LEDs are now capable of exceeding safe limits of the so-called blue-light hazard as defined in eye safety specifications such as ANSI/IESNA RP-27.1–05: Recommended Practice for Photo biological Safety for Lamp and Lamp Systems.

i.   Blue pollution: Because cool-white LEDs with high color temperature emit proportionally more blue light than conventional outdoor light sources such as high-pressure sodium vapor lamps, the strong wavelength dependence of Rayleigh scattering means that cool-white LEDs can cause more light pollution than other light sources. The International Dark-Sky Association discourages using white light sources with correlated color temperature above 3,000 K.

j.   Efficiency droop: The luminous efficacy of LEDs decreases as the electrical current increases above tens of milliamps.

III.   Modeling Of Led

   HB-LEDs are usually low power devices, ranging from 1 W to 5 W at currents from 350 mA up to 2000 mA in the latest devices, while performing luminous efficiencies around 100 lm/W at 350 mA [8], [9]. The fact that they are low power devices means that many of them will be necessary for wide area lighting applications such as streetlights. The devices chosen for the first prototypes were the DragonTape from Osram [10], composed of six Golden Dragon LEDs in series attached to a flexible self-adhesive tape, achieving a luminous efficiency of 21 lm/W at 350 mA . Since as forward current rises the luminous flux decreases, and lifetime decreases too, the design is focused on providing the nominal current of 350 mA. The nominal power requirement for most LED streetlights ranges from 60 W to 150 W [1]. The load finally chosen is made of 10 DragonTapes run at 350 mA, composing a 60LEDs load emitting 1500 lumens at a nominal power of 72 W.

   The second step in the load design consists of its modeling. In a first step, the data obtained from the datasheet [11] are used. The simplest linear model takes in account only the equivalent resistance of the device at the nominal operating point. This is a valid method only if the load is going to work in a narrow range around the nominal point. Otherwise, this approximation yields to unacceptable errors due to the great difference between the equivalent resistance at the operating point and the dynamic resistance, much higher the former than the latter. Therefore, the most accurate approximation is the one consisting of a threshold voltage and a dynamic resistance in series, as shown in Fig 3. 1.

Then, the LED load I-V model would be the following:

$$Vd = Rd * Id + V\gamma$$

Where Vdi is the forward voltage drop of the LED, Rdi is the dynamic resistance, ID is the LED current and $V\gamma$ is the threshold voltage.
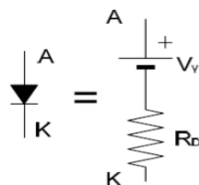

Figure 3.1: Equivalent circuit of diode: linear model

   The LED modeling process done in the lab consisted in obtaining the forward voltage for several current values, taking steps of approximately 50 mA during few seconds and letting the devices to cool down again, so the heating effects on the threshold voltage were negligible. The results extracted from the test, as well as the load threshold voltage and dynamic resistance obtained from a linear interpolation, are shown in Table 3.1, as well as in Fig 3.2.

TABLE 3.1: TEST FORWARD CURRENT AND VOLTAGE VALUES

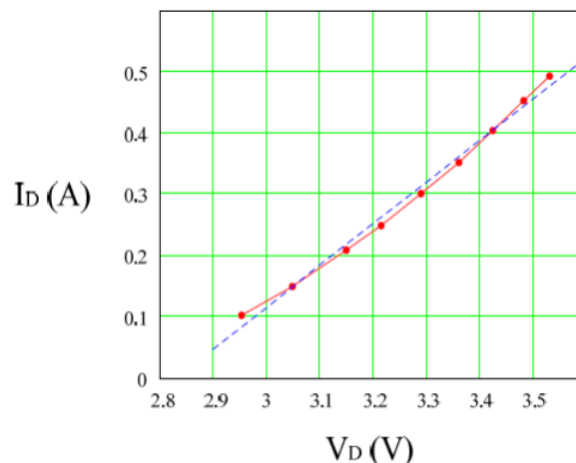| $I_D(A)$	$V_O(V)$	$R_D(\Omega)$	$V_\gamma(V)$
0.102	177.2		
0.150	182.9		
0.208	189.0		
0.249	192.9		
0.301	197.4	87.2	170.1
0.352	201.6		
0.403	205.4		
0.453	208.9		
0.492	211.8		

Figure 3.2: Forward current id and forward voltage vd values obtained from the led lamp built and tested in laboratory (dotted line) and linear model (dashed line)

IV. Modified Idbb Converter

This IDBB converter acts as two buck-boost converter in series. The input of the buck-boost converter is made by Li,D1,C, and S. similarly the output is L1,D2,D3,Co,ans S. The reversing polarity produced by the first converter in the capacitor CB is corrected by the second converter, given a positive output voltage with respect to ground. It will make the circuit simple for the measurement of the load current in the closed loop operation and it leads to reducing sensing circuit and cost.
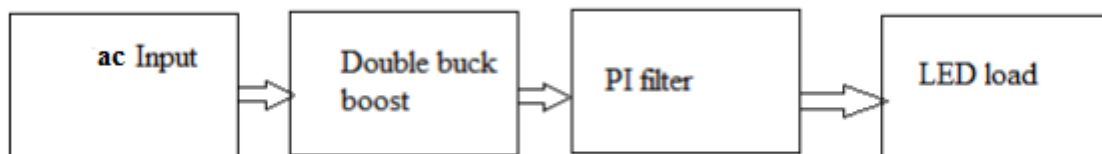

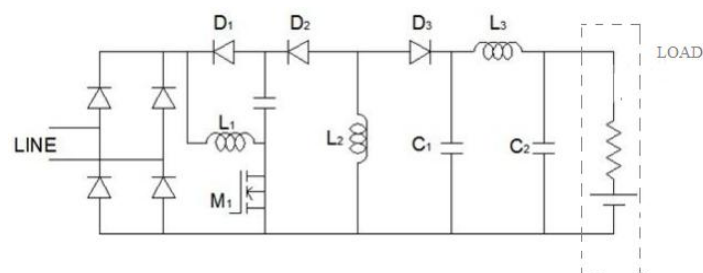Figure 4.1: Block Diagram of Circuit Diagram

Figure 4.2: Modified IDBB converter

By operating the input inductor Li in discontinuous conduction mode (DCM), the average current through the line will be proportional to the line voltage, therefore providing a near unity PF. On the other hand, the output inductance LO can be operated either in continuous conduction mode (CCM) or DCM. The operation in DCM has the advantage of providing a bus voltage across CB independent of the duty cycle and output power. However, it presents the disadvantage of requiring a higher value of the output capacitance to achieve low current ripple through the load. In order to have a reduced value for the output capacitance, the output inductance is operated in CCM, because the current ripple is lower in this operation mode. In addition, the operations of the second stage in CCM with a duty cycle lower than 0.5 reduces the low-frequency ripple voltage since it is multiplied by the buck–boost converter voltage ratio. In this way, it will be possible to use a film capacitor to implement the output capacitance, thus having a higher life rating and better efficiency than using electrolytic capacitors.

Moreover, with a careful design of the converter, the bus capacitor can also be made low enough to be implemented with film technology, thus avoiding the low-life-rating electrolytic capacitors in the whole converter. This implies the design of the converter so that it operates with a duty cycle lower than 0.5. In this manner, the output converter voltage ratio will be lower than one, thus reducing the low-frequency voltage ripple in the same amount. Under the exposed operation conditions, the equivalent circuits for the operation of the IDBB converter within a switching period are shown in Fig. 4.3. The main waveforms are shown in Fig. 4.4.
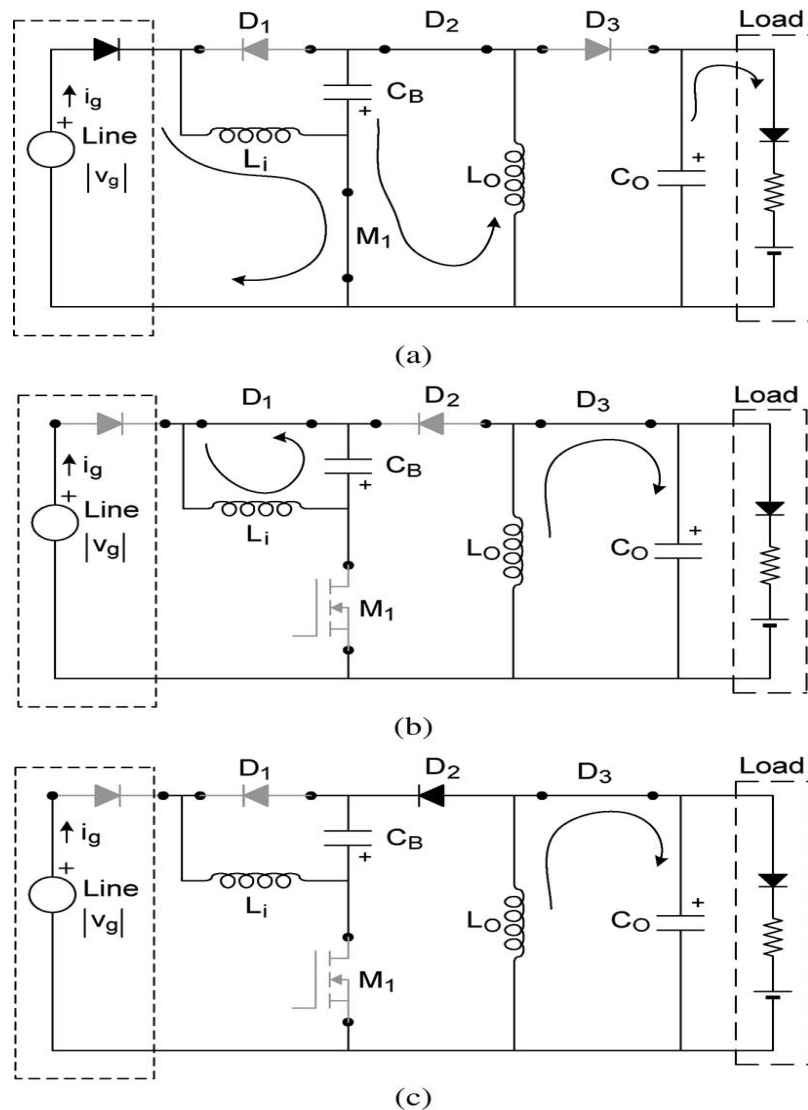

Figure 4.3: Equivalent circuits for the operation of the IDBB converter. (a) Interval
I: $0 < t < DTS$. (b) Interval II: $DTS < t < DTS + t1$. (c) Interval III:
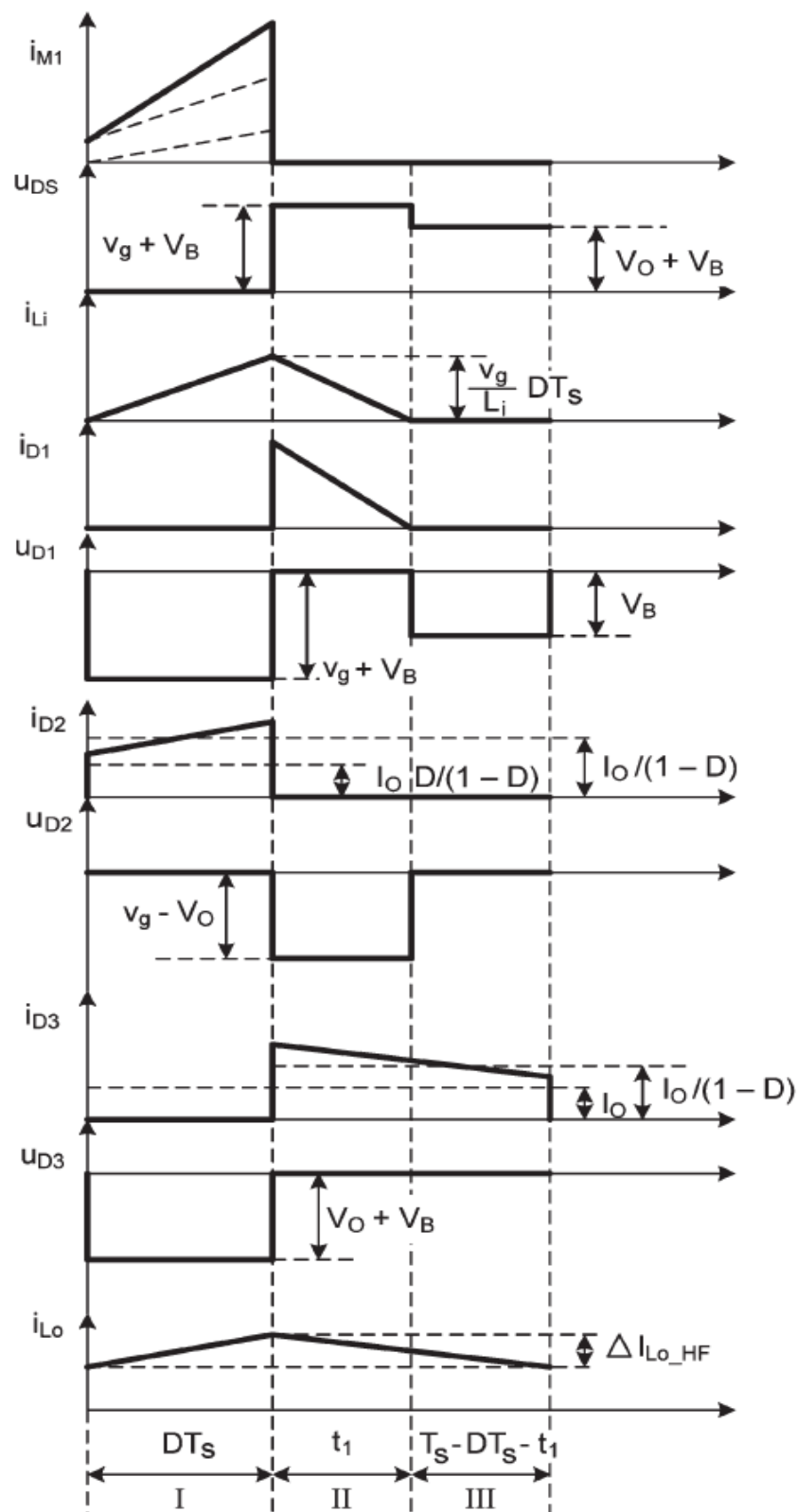$DTS + t1 < t < TS$.

Figure 4.4:Main waveforms of IDBB converter with a high frequency switching period around peak line voltage

V. Analysis of the Offline Idbb Converter

In this section, the IDBB converter is analyzed when operated from the main voltage, achieving a near-unity input PF and a low-ripple current through the power-LED load. It is assumed that the line voltage is a sinusoidal waveform given as

$$vg = Vg \sin \omega t \tag{1}$$

5.1 Line current and input power

The input current ig corresponds to the current through the inductance Li during the time interval 0 − DTS, where D is the transistor duty cycle and TS is the transistor switching period. Thus, the value of the input current averaged at line frequency can be calculated as follows

$$ig = \frac{1}{Ts}\frac{1}{2} ig_{peak}DTs = \frac{D^2 Vg}{2Lifs} \sin \omega L\ t \tag{2}$$

where ig_peak is the instantaneous peak current in each switching period, fS is the switching frequency, Vg is the peak line voltage, and ωL is the line angular frequency. As can be seen in figure 6.1, the averaged input current is a sinusoidal waveform that will provide an input PF close to unity once filtered by the input electromagnetic interference (EMI) filter. The mean input power Pg can now be calculated, taking into account that both input waveforms will be sinusoidal

$$Pg = \frac{1}{2} Vg < ig > peak = \frac{D^2 vg^2}{4Lifs} \tag{3}$$

where $\_ig\_peak$ is the peak value of the averaged input current.

Since the output stage corresponds to a buck–boost converter operating in CCM, the bus voltage VB can be calculated by using the voltage conversion ratio for this converter.

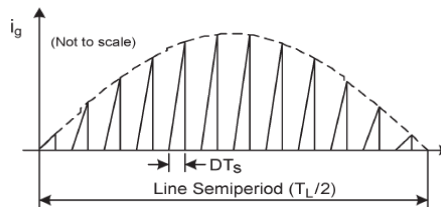
Figure 5.1: Input current waveform.

5.2 Output and Bus Voltages

The output voltage VO for the ideal converter can be obtained by equaling input and output powers. The output power is obtained as follows

$$Po = \frac{Vo^2}{R} \tag{4}$$

With R being the static equivalent resistance of the LED load, which can be obtained by the ratio between the dc values of LED voltage (VLED) and current (ILED) at each operating point.

$$R = \frac{V_{LED}}{I_{LED}} = \frac{(V\gamma + R\gamma I_{LED})}{I_{LED}} = \frac{V\gamma}{I_{LED}} + R\gamma \tag{5}$$

where $V\gamma$ and $R\gamma$ are the voltage and resistance parameters of the LED lamp equivalent circuit[29].

Then, assuming 100% efficiency, by equating equations (6.3) and (6.4), the output voltage is finally obtained

$$Vo = \frac{DVg}{2\sqrt{K}} \tag{6}$$

where K is a non dimensional factor given by

$$K = \frac{fsLi}{R} \tag{7}$$

Since the output stage corresponds to a buck–boost converter operating in CCM, the bus voltage VB can be calculated by using the voltage conversion ratio for this converter [29]

$$V_B = \frac{1-D}{D} = \frac{(1-D)Vg}{2\sqrt{K}} \tag{8}$$

When operating the input stage in DCM and the output stage in CCM, the bus and output voltages are reversely dependent on the duty cycle. For example, if the duty cycle increases, the output voltage increases, and the bus voltage decreases in the same amount.

It must be noted that the input stage must be operated in DCM under any load and input voltage conditions to assure high input PF. The limit duty cycle Dlimit can be obtained from the voltage conversion ratio in the DCM–CCM boundary

$$D_{limit} = \frac{1}{1+\frac{Vg}{V_B}} \tag{9}$$

As long as the actual duty cycle is lower than the limit value the input stage will operate in DCM.

5.3 Reactive Components

The input inductance *Li* can be calculated for a given output power using equation (6.6) and assuming 100% efficiency

$$Li = \frac{D^2 V g^2}{4 P o f s} \tag{10}$$

The bus capacitor C_B is calculated to limit the low-frequency ripple of the bus voltage, which is the voltage applied to the second stage. The current through this capacitor is given by the currents through diodes *D1* and *D2*. In these diodes, only the current through *D1* is modulated by a rectified line frequency, as shown in Figure. 6.2. In order to calculate the bus ripple, the low-frequency component of the current through *D1* must be obtained. Referring to Figure.6.2, the average current through *D1* can be calculated as follows:

$$< i_{D1} > = \frac{1}{Ts} \frac{i_{D1} \, peak \, t1}{2} \tag{11}$$

where $iD1\_peak$ is the peak current through *D1* in each switching period and *t1* is the time needed by this current to reach zero. Both values are changing after double the line frequency and have the following values:

$$i_{D1} peak = \frac{vg}{L_i} DTs \tag{12}$$

$$t1 = \frac{DvgTs}{V_B} \tag{13}$$

Using equations (11) and (12) in equation (10), the *D1* average current is calculated as

$$< i_{D1} > = \frac{D^2 V g^2}{4 V_B f s \, L_i} v_g^2 = \frac{D^2 V g^2}{4 V_B f s \, L_i} V g^2 \sin^2 wt \tag{14}$$

$$< i_{D1} > = \frac{D^2 V g^2}{2 V_B f s \, L_i} \left(\frac{1}{2} - \frac{1}{2} \cos 2wt \right) \tag{15}$$
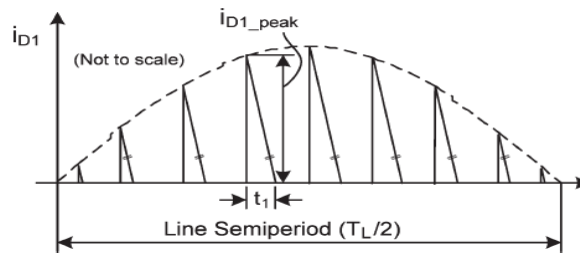

Figure. 5.2: Current waveform through diode *D1*.

Then, the low-frequency ac component circulating through *D1* and C_B is given by

$$< i_{D1} > ac = \frac{D^2 V g^2}{4 V_B f s \, L_i} \cos 2wt \tag{16}$$

Now, the low-frequency peak-to-peak ripple voltage across capacitor C_B, ΔV_{B_LF} can be obtained as

$$\Delta V_{B\,LF} = 2 < i_{D1} > ac_{peak} X_{C_B} \tag{17}$$

$$= \frac{2 D^2 V g^2}{4 V_b L_i f_s 2\pi (2f_L) C_B}$$

$$= \frac{D^2 V g^2}{8\pi V_B L_i f_s C_B f_L}$$

where $\_iD1\_ac\_peak$ is the peak value of the low-frequency current through diode *D1*, obtained from equation (16), and *fL* is the line frequency. The necessary bus capacitance for a given peak-to-peak ripple in the bus voltage is then calculated from equation (17) as follows:

$$C_B = \frac{D^2 V g^2}{8\pi V_B L_I \Delta V_{B\,LF} f_s f_L} \tag{18}$$

Since the output buck–boost converter operates in CCM, the low-frequency voltage ripple at the output will be given by

$$V_{O_{LF}} = \frac{D}{1-D} \Delta V_{B\,LF} \tag{19}$$

This ripple voltage will produce a low-frequency ripple current through the LED load that can be determined by the following:

$$\Delta I_{LED_{LF}} = \frac{\Delta V_{O_{LF}}}{R\gamma} \tag{20}$$

As long as the output buck–boost converter operates in CCM, the LED current ripple at low frequency depends only on the bus voltage ripple and, thus, on the bus capacitance C_B. The output capacitance C_O has no effect on this low frequency ripple.

Finally, the output inductance and capacitance L_O and C_O are obtained using the well-known expressions for a buck–boost converter operating in CCM [29]

Output voltage ripple,

$$\Delta Vo_{HF} = \frac{\Delta Q}{C_O} \tag{21}$$

$$\Delta Q = I * t$$
$$= IoDTs$$

$$C_o = \frac{I_o D}{\Delta Vo_{HF} fs} \tag{22}$$

Average current through Lo,

$$I_{L_o} = I_{D_2} + I_{D_3}$$

$$= \frac{I_o D}{1-D} + I_o = \frac{I_o}{1-D} \tag{23}$$

Taking average voltage across Lo=0

$$\frac{Lo\Delta I_{D2}}{DTs} = V_B$$

$$\frac{Lo\Delta I_{D3}}{t_{off}} = V_o$$

$$\Delta I_{L_{o\,HF}} = \Delta I_{D2} + \Delta I_{D3}$$

$$= \frac{2DV_B}{L_o f_s} \tag{24}$$

Output inductance, $\quad L_o = \frac{2DV_B}{\Delta I_{L_{o\,HF}} f_s}$ $\qquad\qquad$ (25)

where ΔILo_HF is the Lo high-frequency peak-to-peak current ripple, ΔV_{O-HF} is the high-frequency peak-to-peak output voltage ripple, and Io is the dc current through the LED load.

VI. Design of the Simulation Prototype

A simulation prototype for a street lighting application has been developed using MATLAB/SIMULINK. The lamp is formed by 60 LW W5SG power LEDs by Osram in a series array. The load rating current is 350 mA, with an output power of 70Wand a total luminous flux of 1500 lm. The load was tested at the laboratory, obtaining the following model parameters: $V\gamma = 170$ V and $R\gamma = 87\Omega$. The equivalent load resistance at nominal power is $R = 570$ Ω. The selected switching frequency is 50 kHz. The line voltage is 230 Vrms with a 50-Hz line frequency. The converter must admit at least • 10% line voltage variation, assuring constant current through the load.

Using equation (10) and selecting a 45% duty cycle for the nominal operating point, a value $Li = 1.7$ mH is calculated. Now, the operation of the Li in DCM for the whole line voltage range must be checked. Therefore Li is selected to be 0.5mH. The limit duty cycle for the DCM–CCM boundary is obtained from equation (9). As can be seen, DCM operation is maintained in the range 208–253 Vrms line voltage. For voltages lower than 202 Vrms, the required duty cycle will be higher than the limit duty, and the input stage will enter in CCM mode. The bus voltage varies from 240 to 366 V for DCM operation. This must be taken into consideration in selecting the bus capacitor C_B. The bus capacitance has been calculated using equation (18). The maximum bus ripple voltage appears at the lower value of the line voltage. The maximum bus peak-to-peak ripple voltage has been selected to be 5%; this is 15 Vpp approximately. Using equation (18), a value $C_B = 68$ μF is obtained. The low-frequency ripple voltage transferred to the LED load is obtained from equation (19).

In this case, giving a maximum ripple voltage of 4.2%, this is around 10 Vpp.The output inductance Lo is calculated for a 50% current ripple. Using equation (25), a value $Lo = 13.5$ mH is obtained. Finally, the output capacitance Co is designed to achieve a 0.2% high frequency current ripple through the LED load. It must be noted that the voltage and current ripples in the LED load ΔV_{LED} and ΔI_{LED}, respectively, are related by the dynamic resistance as follows:

$$\Delta V_{LED} = \Delta I_{LED}\, R\gamma \tag{26}$$

Then, by using equation (26) in (22), $Co = 52$ μF is obtained for a .2% current ripple at high frequency. However, the low-frequency current ripple is much higher. It can be calculated from (20), giving a value of 33%. This means a peak-to-peak current ripple of 110 mA p-p approximately for nominal operation, which is a current crest factor of only 1.16. In addition, both capacitances C_B and Co can be implemented using long-life film capacitors without excessive volume penalty.

VII. Simulation Results
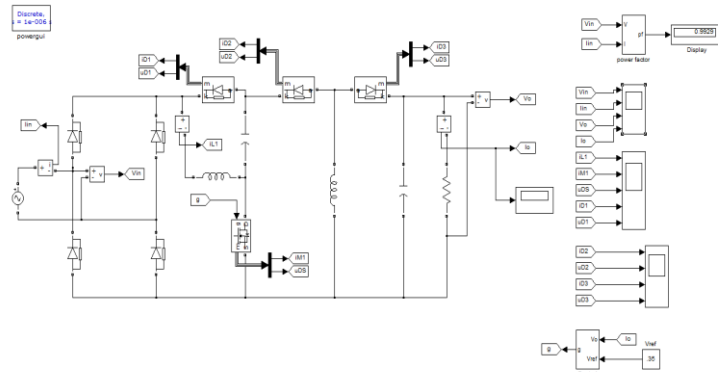
Simulation is done on MATLAB/Simulink background
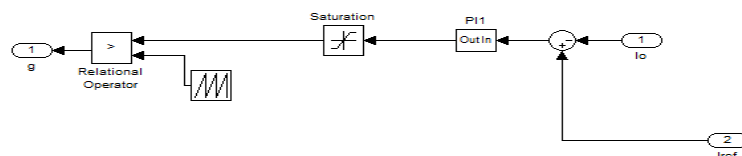

Figure 7.1: Simulated IDBB
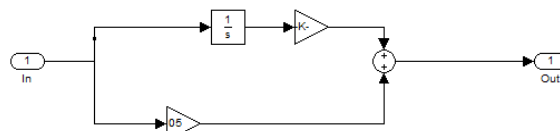

Figure 7.2: PWM signal generation subsystem

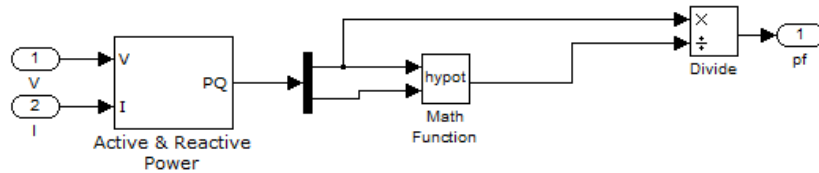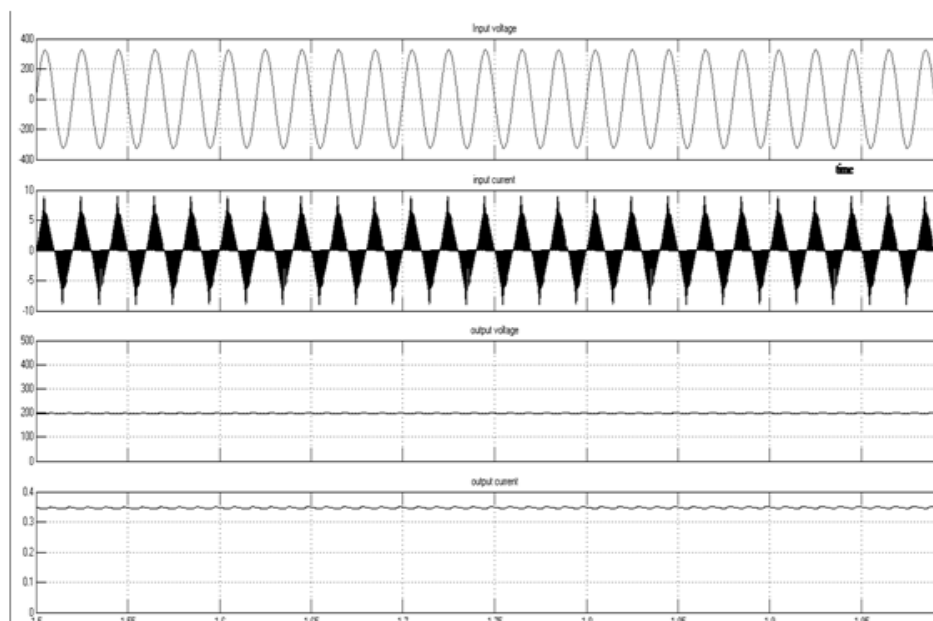Figure 7.3 PI controller subsystem

Figure 7.4: Power factor subsystem

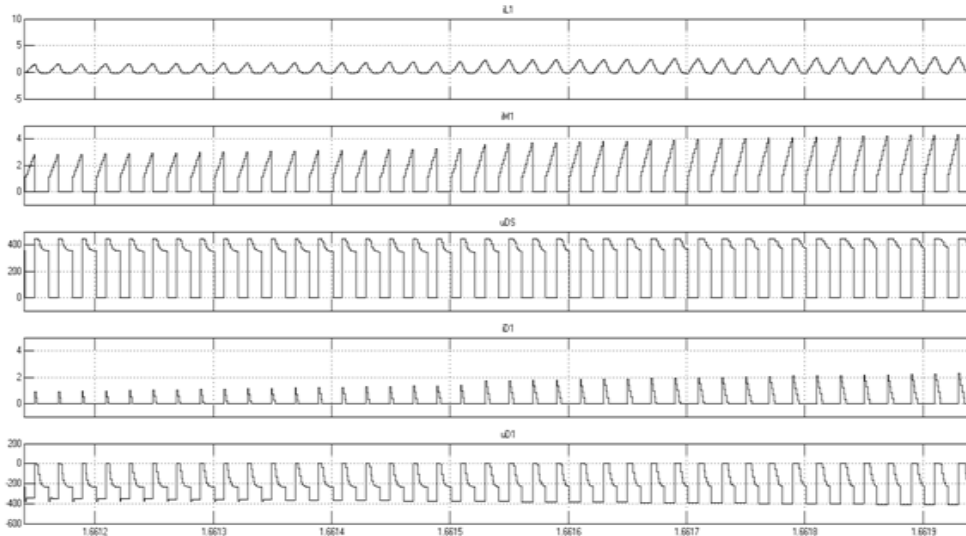Figure 7.5: (a) input voltage (b) input current (c) output voltage (d) output current

Figure 7.6: (a) current through inductor Li (b) current through switch (c) voltage through switch (d) current through diode D1 (e) voltage through diode D1
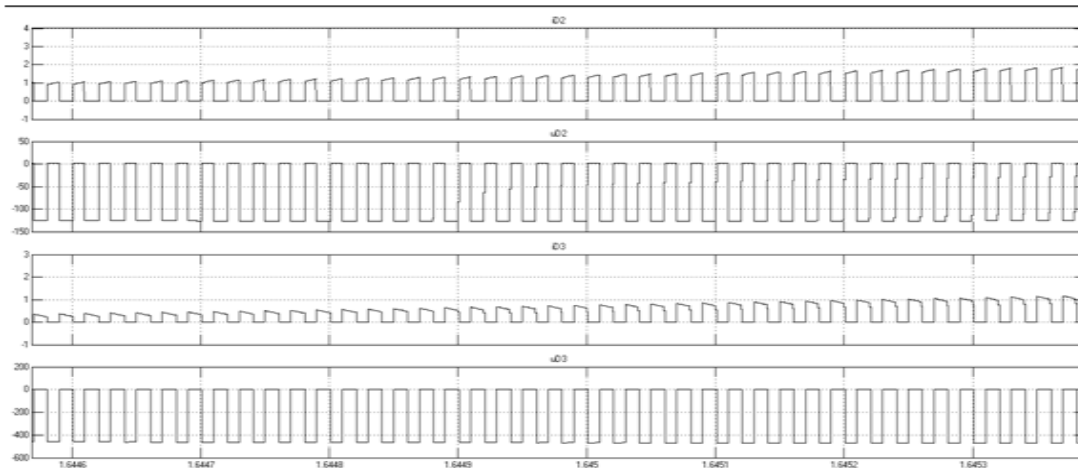

Figure 7.7:(a) current through diode D2 (b) voltage through diode D2 (c)current through diode D3 (d) voltage through diode D3

VIII. Conclusion

An IDBB converter has been investigated in this paper as a solution to implement a high-power-factor offline power supply for LED lighting applications. The topology features two buck–boost converters in cascade but using only one controlled switch. By operating the input converter in DCM, a high input PF can be obtained. On the other hand, the operation of the second stage in CCM assures a low-ripple current through the LED load without using a very high output capacitance. In this way, the converter can be implemented using only film capacitors, avoiding the use of electrolytic capacitors and increasing the converter mean time between failures.

A laboratory prototype for a 70-W solid-state lamp supplied from a 230-Vrms line voltage has been developed. Simulation results have shown that the proposed converter can provide high PF, good efficiency, and low cost.

8.1 Scope for Future Work

As a future scope, the low dimming level can be implemented by reducing the mean current through the LED lamp. It is proven that this method is more efficient compared with the PWM solution, because the LED efficiency increases for lower current values. Nevertheless, since the converter is formed by two stages integrated in a single one, its dynamics response can be made quite fast. Therefore, it is expected that a PWM dimming feature could be added for dimming frequencies up to 200–500 Hz. Also an EMI filter can be used to avoid high-frequency current circulating through the line.

In regard to galvanic isolation, the idea in this converter was to maintain it as simple as possible in order to reduce cost and achieve high efficiency. For these reasons, and taking into account that, at this moment, galvanic isolation is not required by the standards, the converter was designed without isolation. Nevertheless, it can be achieved very easily by simply including a secondary winding coupled to the output inductor. In this manner, the second stage will behave as a flyback converter instead of a buck–boost converter. The operation of the converter will be exactly the same, having just an extra design parameter given by the winding turn ratio.

REFERENCE

[1.] J. Marcos Alonso, Juan Viña, David Gacio Vaquero, Gilberto Martínez, and René Osorio, "Analysis and Design of the Integrated Double Buck–Boost Converter as a High-Power-Factor Driver for Power-LED Lamps," IEEE TRANSACTIONS ON INDUSTRIAL ELECTRONICS, VOL. 59, NO. 4, APRIL 2012

[2.] D. Gacio, J. M. Alonso, J. Garcia, L. Campa, M. Crespo, and M. Rico- Secades, "High frequency PWMdimming technique for high power factor converters in LED lighting," in Proc. 25th Annu. IEEE APEC, Feb. 21–25, 2010, pp. 743–749.

[3.] J. Garcia, A. J. Calleja, E. L. Corominas, D. Gacio, and J. Ribas, "Electronic driver without electrolytic capacitor for dimming high brightness LEDs," in Proc. 35th Annu. IEEE IECON, Nov. 3–5, 2009, pp. 3518–3523.

[4.] Y.X.Qin, H.S.H. Chung, D.Y.Lin, S.Y.R.hui, "Current Source Ballast for high Power Lighting Emitting Diodes without Electrolytic Capacitor", IEEE IECON 2008, 34th Industrial electronics Annual Conference, Proceedings of, pp. 1968- 1973, 10-13 Nov. 2008, Orlando, Florida, USA.

[5.] Hsiu-Ming Huang; Shih-Hsiung Twu; Shih-Jen Cheng; Huang-Jen Chiu, "A Single-Stage SEPIC PFC Converter for Multiple Lighting LED Lamps", *Electronic Design, Test and Applications, 2008. DELTA'08,* 23-25 January 2008, pp.15 – 19.

[6.] Pan TianFu; Chiu HuangJen; Cheng ShihJen; ChyngShihYen, "An Improved Single-Stage Flyback PFCConverter for High-Luminance Lighting LED Lamps", *Electronic Measurement and Instruments, 2007, ICEMI '07,* August 16 2007-July 18 2007, pp.4-212 - 4-215.

[7.] C. Qiao and K. M. Smedley, "A topology survey of single-stage power factor correction with a boost type input-current-shaper," in Proc. IEEE APEC 2000, pp. 460–467.

[8.] H. Broeck, G. Sauerländer, and M. Wendt, "Power driver topologies and control schemes for LEDs," in *Proc. IEEE APEC 2007*, pp. 1319–1325.

[9.] J. Sebasti´an, D. G. Lamar,M. Arias, M. Rodr´ıguez, andM.M. Hernando, "A very simple control strategy for power factor correctors driving high brightness light-emitting diodes," in *Proc. IEEE APEC 2008*, pp. 537–543.

[10.] W. Chang, D. Chen, H. Nien, and C. Chen, "A digital boost converter to drive white LEDs," in *Proc. IEEE APEC 2008*, pp. 558–564.

[11.] Z. Bo, Y. Xu, X. Ming, C. Qiaoliang, and W. Zhaoan, "Design of boost-flyback single-stage PFC converter for LED power supply without electrolytic capacitor for energy-storage," in Proc. 6th IEEE IPEMC, May 17–20, 2009, pp. 1668–1671.

[12.] K. I. Hwu, Y. T. Yau, and L.-L. Lee, "Powering LED using high-efficiency SR flyback converter," in Proc. 24th Annu. IEEE APEC, Feb. 15–19, 2009, pp. 563–569.

[13.] C. C. Chen, C. Y. Wu, Y. M. Chen, and T. F. Wu, "Sequential color LED backlight driving system for LCD panels," IEEE Trans. Power Electron., vol. 22, no. 3, pp. 919–925, May 2007.

[14.] K. Zhou, J. G. Zhang, S. Yuvarajan, and D. F. Weng, "Quasi-active power factor correction circuit for HBLED driver ," IEEE Trans. Power Electron., vol. 23, no. 3, pp. 1410–1415, May 2008.

[15.] "Luxeon LXK2 white LED datasheet, (2006). DS51," in [Online]. Available: http://www.lumileds.com [Online]. Available:

[16.] Y. Gu and N. Narendran, "A non-contact method for determining junction temperature of phosphor-converted white LEDs ," in Proc. SPIE 5187, 3rd Int. Conf. Solid State Lighting, 2004 , vol. 5187, pp. 107–114.

[17.] C. C. Lee and J. Park, " Temperature measurement of visible light-emitting diodes using nematic liquid crystal thermography with laser illumination," IEEE Photon. Technol. Lett., vol. 16, no. 7 , pp. 1706–1708, Jul. 2004 .

[18.] H.-J. Chiu, Y.-K. Lo, J.-T. Chen, S.-J. Cheng, C.-Y. Lin, and S.-C. Mou, "A high-efficiency dimmable LED driver for low-power lighting applications," IEEE Trans. Ind. Electron., vol. 57, no. 2, pp. 735–743, Feb. 2010.

[19.] H. J. Chiu and S. J. Cheng, "LED backlight driving system for large-scale LCD panels," IEEE Trans. Ind. Electron., vol. 54, no. 4, pp. 2751–2760, Oct. 2007.

[20.] C. C. Chen, C. Y. Wu, Y. M. Chen, and T. F. Wu, "Sequential color LED backlight driving system for LCD panels," IEEE Trans. Power Electron., vol. 22, no. 3, pp. 919–925, May 2007.

[21.] Kening Zhou, Jian Guo Zhang, S. Yuvarajan, and T.-F Da Feng Weng, "Quasi-active power factor correction circuit for hb led driver," IEEE Trans. Power Electron., vol. 23, no. 3, pp. 1410–1415, May 2008.

[22.] J. A Villarejo, J. Sebastián, F. Soto, and E. de Jódar, "Optimizing the design of single-stage power-factor correctors," IEEE Trans. Ind. Electron., vol. 54, no. 3, pp. 1472–1482, Jun. 2007.

[23.] J. J. Lee, J. M. Kwon, E. Ho Kim, W. Y. Choi, and B. H. Kwon, "Single stage single-switch PFC flyback converter using a synchronous rectifier," IEEE Trans. Ind. Electron., vol. 55, no. 3, pp. 1352–1365, Mar. 2008.

[24.] F. J. Azcondo, C. Branas, R. Casanueva, and S. Bracho, "Power-mode controlled power-factor corrector for electronic ballast," IEEE Trans. Ind. Electron., vol. 52, no. 1, pp. 56–65, Feb. 2005.

[25.]   P. TianFu, C. HuangJen, C. ShihJen, and C. ShihYen, "An improved single-stage flyback PFC converter for high-luminance lighting LED lamps," in Proc. ICEMI, Aug. 16–Jul. 18 2007, pp. 4-212–4-215.

[26.]   H. Wei, I. Batarseh, G. Zhu, and P. Kornetzky, "A single-switch AC-DC converter with power factor correction," IEEE Trans. Power Electron., vol. 15, no. 3, pp. 421–430, May 2000.

[27.]   K. Zhou, J. G. Zhang, and G. Meneghesso, "Quasi-active power factor correction circuit for HB LED driver," IEEE Trans. Power Electron., vol. 23, no. 3, pp. 1410–1415, May 2008.

[28.]   D. Fu, F. C. Lee, and M. Xu, "A novel driving scheme for synchronous rectifiers in LLC resonant converters," IEEE Trans. Power Electron., vol. 24, no. 5, pp. 1321–1329, May 2009.

[29.]   D. Gacio, J. M. Alonso, A. J. Calleja, J. Garcia, and M. Rico-Secades, "A universal-input single-stage high-power-factor power supply for HB-LEDs based on integrated buck-flyback converter," *IEEE Trans. Ind. Electron.*,

Under Water Image Enhancement by Fusion

T. Santosh kumar[1], V. Poojitha[2], S. Manisrinivas[3], D. Anilkumar[4],
B. Hemanth Nag

[1,2,3,4,]*(B.Tech), ECE, Lendi Institute of engg And Tech, Vizianagaram, India.*
M.Tech. Assistant Professor, ECE, Lendi Institute of Engg. And Tech., Vizianagaram, India.

Abstract: *This paper describes a strategic approach to enhance underwater images. The image gets degraded due to the absorption and scattering of light falling on the objects.This degraded version of the image is enhanced by fusion principles by deriving inputs and weight measures from it. Our strategy is very simple in which white balance and global contrast technologies are applied to the original image. This implementation is followed by taking these two processed outputs as inputs that are weighted by specific maps. This strategy provides better exposedness of the dark regions, improves contrast and the edges, preserved and enhanced significantly. This algorithm effectively enhances the underwater images which is clearly demonstrated in our experimental results of our images.*

I. Introduction

Underwater imaging is difficult due to the illumination properties existing in different environments. The underwater images degrades more than a normal image which have poor visibility due to the improper illumination and obstruction of the propagated light. Generally the light gets exponentially decreases with the distance and depth due to scattering and absorption of the light. The light direction gets affected which eventually blurs the image. The attenuation of light is not fixed in a particular direction. It instantly varies depending on the external conditions. This attenuation of light causes muddled appearance while the scattered light back vitiates the contrast. The objects in the sea water which are more than 10 meters are almost hazy with faded colours as their wavelengths are affected. Finally, these all factors results in an image with poor contrast which appear blurred and hazy.

There are several methods and strategies to restore the degraded image. The degraded image can be Enhanced by different complex techniques which are not much efficient. The image can be restored by using multiple images [1], specialized hardware [2] and by using polarization filters [3]. Though, these techniques have produced effective results on underwater images, they are not efficient concerned to practicability. The Hardware techniques like using camera can deal with dynamic scenes but it is trouble-some, expensive and complex. The multiple image methods requires many images in different environmental conditions while polarization requires several images that have different degrees of polarization.

Figure 1original image

In this paper, we introduce an efficient strategy that is able to enhance underwater images based on a single image. This approach is simple which is able to perform relatively fast on any hardware. This approach is fusion based approach which can be used in several applications such as image compositing [4], multispectral video enhancement [5], defogging [6] and HDR imaging [7]. The magnificence of this approach lies in its

requirement of just a single image. This approach does not require multiple images, only single image is enough which is processed by several enhancing techniques. These techniques consists of derivation of inputs and the weights only from the degraded image. Traditional enhancing techniques like white balance, colour correction, histogram equalization show strong limitations but the use of these techniques cumulatively elicits best results. The efficiency of fusion technique is highly dependent on the choice of inputs and the weights eventually a set of operators in order to get clear enhanced images in all underwater environments.

The undesired noise is supressed from the initially restored version. Our approach enhances the images by several weight maps. The weight maps of our algorithm gauge the several image qualities that specify the spatial pixel relationships. To improve the image quality, these weights assign higher values to pixels. This is a multi-resolution process which is robust to artifacts.

II. Our Enhancing Approach

In this approach we use a single image based approach built on fusion principle. This is a simple and fast approach that is able to increase the visibility of underwater images. The considered weights and specified inputs were carefully taken to overcome the limitation of such environments even though specialized optical models are not used. The original image is processed by using two inputs. First the image is processed and white balance is done. Then the weights are applied to this image followed by fusion of these resulting weighted images. In the same way image is processed by the second input. The two resultant images are further undergone fusion and the enhanced image is obtained.

Inputs:

We get the enhanced images using fusion algorithm, which involve in proper application of the inputs and weights to the images.so as to achieve the final image from the degraded image.

So, here we use few fusion techniques to enhance the underwater images. By combining several input images preserving the most significant features. Here we consider an appropriate feature in at least one of the input images. And the whole obtained images are then combined to form a fusion based image featuring those important features among them.so, we use here the fast and easiest techniques to achieve fusion process, so we use here a derived inputs to tackle this process. Due to the different wavelengths of light, like light Absorption and scattering cause part of the light of shorter Wavelength scattering, and the rest of the light of other length.

$$\mu_I = 0.5 + \Lambda \quad \square_{ref}$$

Wavelength will cross the medium. This will inevitably lead to the offset of the color. Simultaneously, Light Absorption will make the light intensity weaker .Therefore, we need an input methodology to handle this problem that is called white balancing method. This white balance is used to restore the natural light. Whereas global contrast enhancement is another e input methodology used because the global contrast of the image become weaker after the attenuation of the light. In order to get a clear image, we will be bound to improving a global contrast of the source image. Now after applying the input to the original image that is white balancing method we get an image (I1) and later when we apply global contrast enhancement methodology we get another input image (I2).
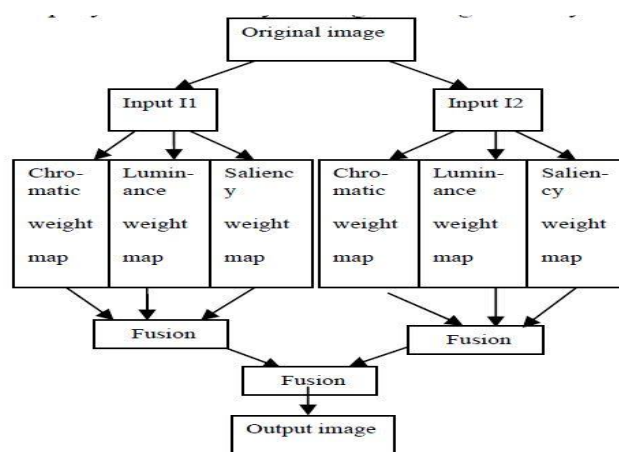
White balancing:

White balancing is a significant process that aims to enhance the image appearance by discarding unwanted color casts, due to various illuminants. In water deeper than 30 ft.White balancing suffers from noticeable effects since the absorbed colours are difficult to be restored.This White balance refers to no matter in any kind of the light source, it can revert the white objects to White in images. For the color cast while taking

pictures under certain light source, it will be compensated through the strengthening of the complementary color. White balance is an indicator which can describe the accuracy of the white color which is generate by mixing three primary colours red (R), green (G), blue (B) .So we use the white color as the standard to restore color offset. The brightness value of images will be normalized and compressed within the range of [0, 1].

μɪ = 0.5 + _μref

This step can effectively reduce the significant difference between the brightness values and prepare for the next step of image enhancement. As a result, we get the first input image I1.

Figure 2white balanced image

Global contrast enhancement:

To enhance the images using global contrast enhancement we use histogram stretching to increase the contrast. this can amplify the visibility in the regions of haze but yielding some degradation in the rest of the image.so for this we use certain enhancing operators like gamma correction etc. but to avoid the rest of degradation in the image we could apply better weight maps to the images and the output image obtained after applying global contrast enhancement technology to the original image gives the second input image (I2)

Weights:

We are considering weight maps because to recreate the original image back. Mainly any image is mutually related to colour appearance and as a result the measurable values such as salient features, local and global contrast or exposedness are difficult to integrate by naive per pixel blending, without risking to introduce artifacts.so we required higher values of weights because to get final and clear image.in RGB, generally to the image white balance and improving the image is the inception process. Actually the RGB model is not well adapted to explain the color for the human visual.While we trace the colour entity because to explain the hue, contrast, saturation and in this process we are using Weight maps like the luminance weight map、chromatic weight map and saliency weight map to measure and to find information from the input image. Then integrated into one image, we can get more accurate results. In this approach we have three weight maps they are:

Chromatic weight map: It is used here to control the saturation gain in the output image. Also it is used to explain the saturation of the of the image .the higher the saturation is, the more realistic the colour is to acquire the weight Map, so we are calculated the distance between saturation value S and the maximum of the saturation range using the gauss in curve:

$$d = exp\left(-\frac{(S - S_{max})^2}{2\sigma^2} \right)$$

Figure 3 Chromatic map

The standard deviation σ =0.3. Thus, weights close to zero are assigned to the pixels with smaller saturation while the most saturated pixels have weights close to one.

LUMINANCE WEIGHT MAP: This map come through the luminance gain in the output image. This map explain the standard deviation between every R, G, B colour channels and each pixel luminance L of the input. Here the two input images are regenerate from RGB HSV space, for the component of V is the component of luminance .the luminance weight map plays a key role of balancing the brightness.

Figure 4 luminance map

Saliency weight map: The main aim of the saliency weight map is identifies the property with respect to the neighbourhood regions. The main information of the image is concentrated in only a small number of critical areas. This map reflects the distinction between a particular region and its neighbouring areas. If the area's distinction become more understandable, it will be easier to attract people's attention, and it will have greater impact. Different with the method in enhancing the global contrast which was mentioned previously, saliency map can make the edge of the original image to be highlighted. After extracting the contours of the local area. We increase the equivalent weight value, so as to accomplish the result of image distinction enhanced. Here, we use a newer method to generate Saliency map. They propose a regional contrast based Saliency extraction algorithm, which simultaneously calculates global contrast differences and spatial Coherence. The proposed algorithm is simple, efficient, and yields full resolution saliency maps .this algorithm is consistently beat current saliency detection method, yielding higher precision and better recall rates. This algorithm can produce the full-resolution map. It is better than the previous method. The example for the weight map is show in Figure below,

Figure 5 saliency map

Laplacian contrast weight: We denoted it with (W_L) and it is mainly deals with global contrast simply by smearing a Laplacian filter on each input luminance channel and figuring the exact value of the filter result. It used in different applications such as tone mapping and extending depth by directly accomplishments naive blending results not related image. On the other hand, by employing the multi-scale approaches based on WLS filter and Laplacian pyramid yield significant improvements. As may be observed, the difference between WLS and Laplacian pyramid is negligible.

Local contrast weight (w_{LC}): In this approach each relation between each pixel of the image and neighbourhoods average were comprises. .by measuring this approach we reinforce the local contrast appearance, so this we can get a changes mainly in the highlighted and shadowed parts of the second input. The (W_{LC}) is calculated as the standard deviation between pixel luminance level and the local average of its surrounding region.

WLC(x, y) = ‖ Ik-Ik w hc‖

Where I^k represents the luminance channel of the input and the I^k_{hc} represents the low-passed version of it.

Figure 6contrast enhanced image

Image fusion: In the last step we have implemented a multi scale image fusion.Image fusion is a process in which the inputs are weighted by exact computed maps to preserve the most important perceived features. The main aim is just to combine the input weights various maps. In this approach we are combining the input data in a per pixel manner to minimize the loss of the image structure. Now we got two images as inputs, we have to extract the three weight maps for each individual image, they are :

wL _ 1，*wL _ 2*

（Luminance weight map）,

wC _ 1 ， *wC _ 2*

（chromatic weight map）and

wS _ 1 ， *wS _ 2*

（Saliency weight map).

In order to ease the consequent weighted fusion each weight map must first normalized.

The normalized luminance map of the input I1 is:

NwL _1 = wL _1 ⁄(wL _1 + wL _ 2)(3)

NwL _ 2 = wL _ 2 ⁄(wL _1 + wL _ 2) (4)

The same process is implemented for other values for 2I.

In the following step we use linear integration of the three weighted values.

W_i=a*NwL_i+b*NwC_i+c*NwS_i (5)

Where a,b,c are the weighted value of the coefficient. We have to set the a, b, c values to 1.

$$F^{(i,j)} = \sum m_k * W_k^{(i,j)} I_k^{(i,j)}$$

(6)

Where k,m are the coefficients of the two input images.Here every pixel image of the outputF is Calculated by adding the inputs Ik weight by consistent normalised weight maps kW.In our approach each and every input is decomposed.
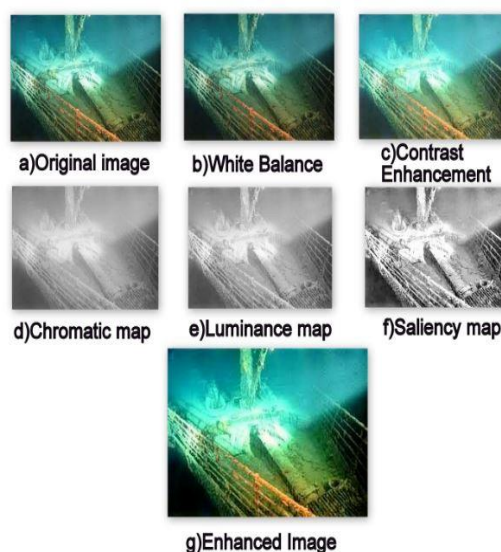
Into a pyramid by applying a operator at dissimilar scales, likewise for each and every normalised weight map Wa Gaussian pyramid is calculated.

Result: Here from the above discussion we are taking different under water images from different sources and process them by applying the corresponding weight maps we can get the final image as shown in the figure 7.At first we are white balancing the image so that we can avoid the unwanted colour casts during various illuminants. After that we are now applying the weights to our white balanced image. In our approach we can get a picture of an underwater image with good colour clear details of the background. When compared with other techniques the mail structural alteration to our method is the amplified contrast.Our approach emphasize details without disturbing the colour. This technique requires very less computational means and is wellappropriate for real time applications.Finally in our approach it shows a good strength to protect the consistency in the appearance of colour for various cameras.

Figure 7final result

More Results:

a)Original image b)White Balance c)Contrast Enhancement

d)Chromatic map e)Luminance map f)Saliency map

g)Enhanced Image

III. Conclusion

In this paper, we propose an efficient and low complexity underwater image enhancement method. The proposed approach contains two mainly procedures, the direct reflection of light from the object and the reflection from the particles of the medium. We have shown that by choosing appropriate weight maps and inputs, the fusion strategy can be used to effectively underwater images. Our technique has been tested for a large data set of underwater images. The method is faster than existing single image enhanced strategies yielding accurate results and the color contrast of the object in underwater. The experimental results show that the proposed approach can effectively enhance the underwater image. To future work we would like to test our method for videos.

References:

[1.] S. Narasimhan and S. Nayar. Contrast restoration of weather degraded images.IEEE Trans. on Pattern Analysis and Machine Intell, 2003.

[2.] D.-M. He and G. G. L. Seet. Divergent-beam lidar imaging in turbid water.Optics and Lasers in Engineering, 2004.

[3.] Y. Schechner and Y.Averbuch. Regularized image recovery in scattering media.IEEE Trans Pattern Anal Mach Intell, 2007.

[4.] M. Grundland, R. Vohra, G. P. Williams, and N. A. Dodgson. Cross dissolve Without cross fade. Computer Graphics Forum, 2006.

[5.] E. P. Bennett, J. L. Mason, and L. McMillan. Multispectral bilateral video Fusion. IEEE Trans. on Image Processing, 2007.

[6.] C. O. Ancuti, C. Ancuti, and P. Bekaert. Fusion-based restoration of the underwaterimages. In In IEEE ICIP, 2011.

[7.] T. Mertens, J. Kautz, and F. V. Reeth. Exposure fusion. Comp. Graph. Forum,12009.

[8.] Shuai Fang, Rong Deng and Yang Cao Effective Single Underwater Image Enhancement by Fusion

[9.] Cosmin Ancuti,Codruta Orniana Ancuti, Tom Haber and Philieppe Bekaert Enhancing Underwater images and videos by fusion

[10.] R.Achantay,S.Hemamiz,F.Estraday,andS.Susstrunky.Frequency-tuned salientregiondetection.IEEECVPR,2009

[11.] C.O.Ancuti,C.Ancuti,andP.Bekaert.Fusion-basedrestorationoftheunderwaterimages.InInIEEEICIP,2011.

[12.] C.O.Ancuti,C.Ancuti,C.Hermans,andP.Bekaert.Afastsemi-inverse, Aproach to detect and remove the haze from a single image. ACCV, 2010.

[13.] T.O.Aydin,R.Mantiuk,K.Myszkowski,andH.-S.Seidel.Dynamic range independent image quality assessment. In SIGGRAPH, 2008.

[14.] S.Bazeille,L.J.I.Quidu,andJ.P.Malkasse. Automatic under water image pre-processing.InProc.ofCMM,2006.

[15.] E.P.Bennett,J.L.Mason,and L.McMillan.Multispectralbilateral video fusion.IEEETrans.onImageProcessing,2007.

[16.] P.BurtandT.Adelson.The laplacianpyramidasa compact image code.IEEE TransactionsonCommunication,1983.

[17.] D.J.Jobson, Z.Rahman,andG.A.Woodell.Amultiscaleretinexforbridging the gap between color images and the human observation of scenes. IEEE Transactions on Image Processing,1997.

[18.] M.Ebner.ColorConstancy,Wiley1stedition.2007.

[19.] Z.Farbman,R.Fattal,D.Lischinski,andR.Szeliski.Edge-preservingdecompositionformulti-scale tone and detail manipulation. SIGGRAPH08.

[20.] R.Fattal.Singleimagedehazing.SIGGRAPH,2008.

[21.] G.D.FinlaysonandE.Trezzi.Shadesofgrayandcolourconstancy.IS&T/SID,welfthColorImagingConference:ColorScience,SystemsandApplications,SocietyforImagingScienceandTechnology,pages37–41,2004

Vibrational Analysis a Key for Pump Maintenance-Case Study

Aditya U. Ganapathy[1], K. Sainath[2]

1, 2, Student, Department of ME, Assistant Professor,
Sreyas Institute of Engineering and Technology, Jawaharlal Nehru Tech. University, India

Abstract: *The following case study is the result of the project work and research done by me at one of the major plant in AP. The case study is of a medium pressure water pump which had developed high vibrations. The causes of vibrations were identified using latest non destructive testing tools and corrective measures were implemented. The condition of the pump after the correction was checked and was found within acceptable healthy condition therefore pump was put to use.*
Keywords: *Bearing clearance, misalignment, unbalance.*

I. Introduction

The said pump was observed to be having undue vibrations during routine inspection of all the running equipments. The observation was recorded in the log book for conducting thorough condition monitoring before any major break down occurs. The preventive maintenance team requested for a shutdown of the said pump and subjected it to oil analysis, infrared analysis, oil particle analysis and vibrational analysis.

II. Identification Of Problem

The said pump was observed to be having undue vibrations during routine inspection of all the running equipments. The observation was recorded in the log book for conducting thorough condition monitoring before any major break down occurs. The preventive maintenance team requested for a shutdown of the said pump and subjected it to oil analysis, infrared analysis, oil particle analysis and vibrational analysis. But of all the techniques only vibrational analysis was able to give the answer. All the spectrum analysis of the pump with correction and without correction is given in the spectrum analysis section along with a table in case study section. Finally the paper will end with the spectrum of the healthy pump in running condition.
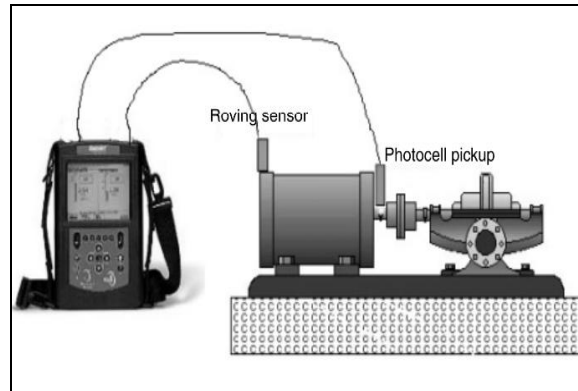

Centrifugal pump

Condition Monitoring System Implementation

TEST SETUP:

Vibration measurements should be taken at the inboard and outboard bearings of a pump and motor in axial, horizontal, and vertical directions. If a more intensive analysis is required, measurements also should be taken at several places on the pump base. Electronic probes or sensors can be attached at each of these locations, sending electronic signals to a vibration analyzer. Measurements should be taken at operating speed for constant-speed motors and at varying speeds for pumps operating on variable-speed drives.
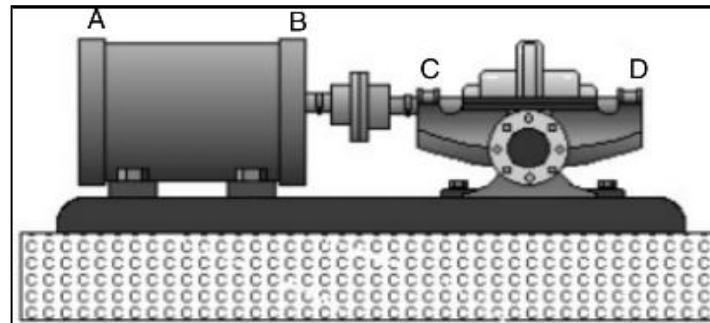
Motor non-drive end bearing – A
Motor drive end bearing – B
Pump outboard bearing (next to the coupling) – C
Pump inboard bearing (away from coupling) – D.
At all the above points the reading were taken and the values have been analyzed and included.

Case Study:

A motor with capacity of 200kw, 1490rpm is attached to a pump with 1853 rpm, suction pressure of 6 kg /cm2 , discharge pressure of 10 kg/cm2 ,flow rate of 600m3/hr was monitored regularly by CONDITION MONITORING.

The Layout is as given below:

Pump with Over-hung Impeller and Simply Supported V-Pulley
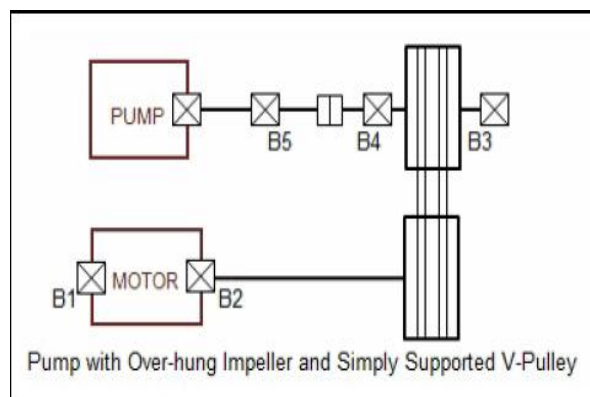
Location of the above layout:

Equipment: Cellar-8, Pump-1.
Utility: Supplies Water for Tempcore Cooling and for cooling of rolling stands
Equipment Details:
Motor:
Rating: 200KW
RPM: 1490
Pump:
Flow: 600m3/hr
Suction Pressure: 6Kg/cm2
Discharge Pressure: 10 Kg/cm2
RPM: 1853

Problem:
        It was found that one of plumber block bearing had indicated undue vibrations (9.8 mm /S2) in horizontal direction and generation of heat beyond acceptable limits.
 The misalignment was then measured using dial gauge and actual correction of the shaft carried out till accepted limits.
The unbalance was detected due to the undue vibrations reaching more than the recommended value.

Data collection: At points b1, b2, b3, b4, b5 the reading were taken. The following is one of them indicating some problems.

Vibration on 06/1/2014 in (mm/sec- rms)				
	MNDE	MDE	PB1	PB2	Pump
V	3.8	3	3.5	2.5	1.7
H	2.3	4.1	5.3	9.8	3.7
A	2.7	4.5	3.1	5.3	2.2

The Overall Vibration of PLUMMER BLOCK B3 and B4 were high.

The Horizontal vibration of PB2 reached to a very critical value of 9.8mm/sec

Plummer Block.

The threats found were:
Bearing Clearance
Misalignment
Unbalance

Corrections:

All the corrections made on the pump are based on the vibrational analysis. The peaks were keenly observed and accordingly the corrections were made to bring the machine back to normal working condition. Both the peaks (i.e) the damaged , corrected(machine in normal condition) are included below.

Bearing clearance:

Correction: The bearing was opened and the shaft clearances were measured using precision vernier calipers where it was observed that the clearance was more than the allowed norms. This was corrected by providing an exact size copper shim between the wearing ring and the bearing cover. The bearing clearance was reduced by using shims.
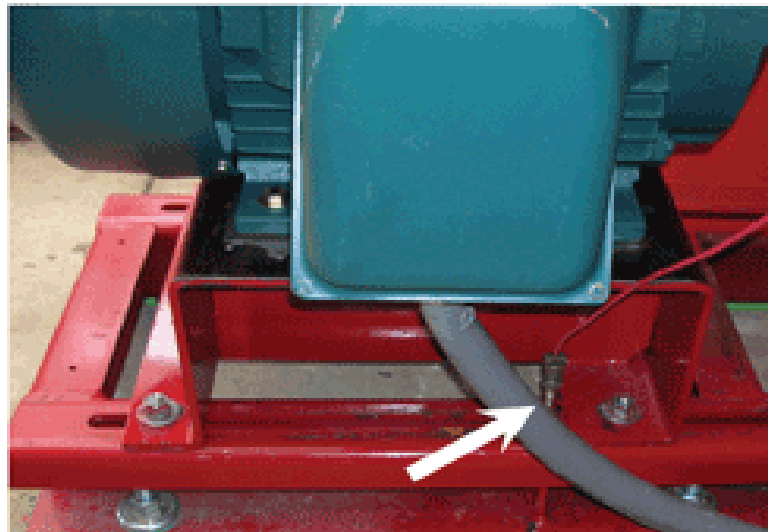

Misalignment:

Correction: Misalignment was corrected by correcting parallel misalignment. The pulley shaft was realigned with the pump shaft.
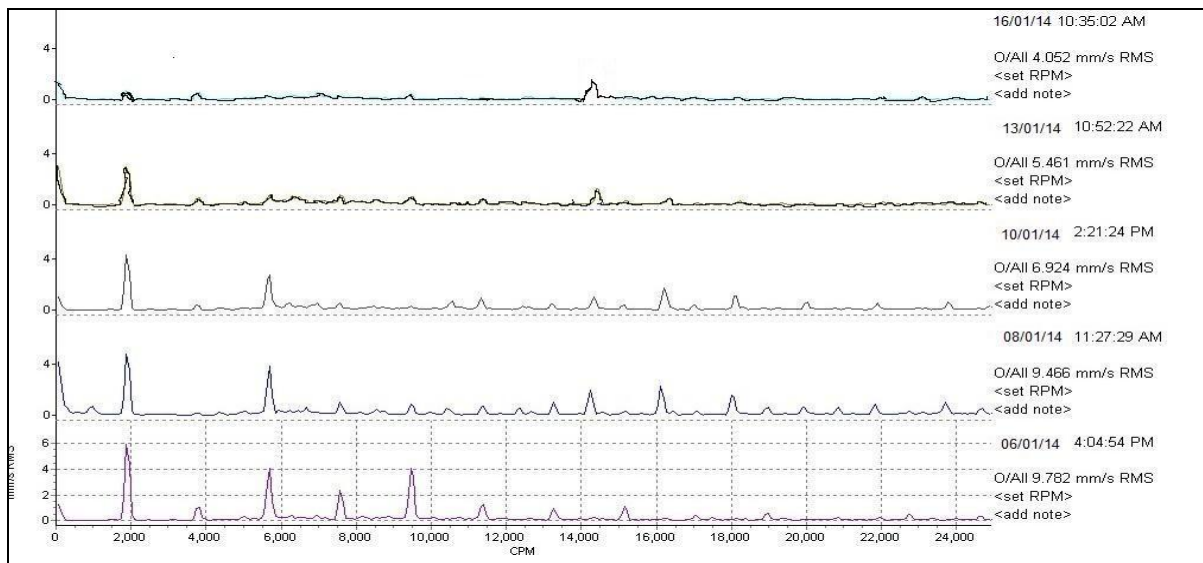
Unbalance:

Correction: Unbalance was corrected by adding weights to the pulley which would lead to balancing of equipment.

A Point for Vertical Measurement on a Pump Base

SPECTRUM ANALYSIS:

Observations:
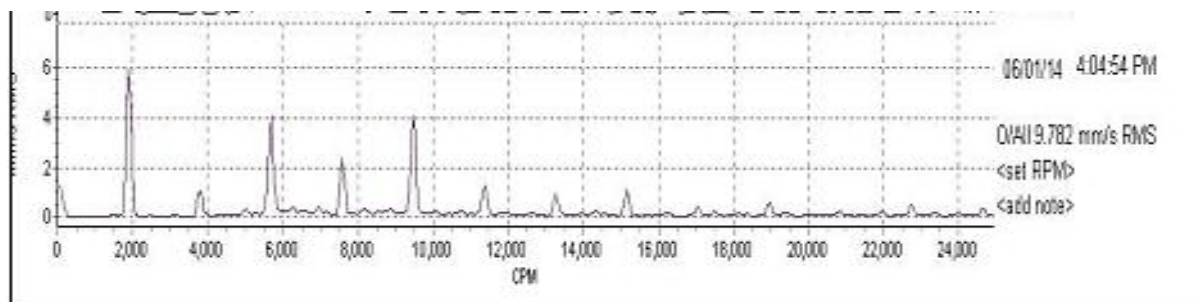
The pump developed looseness due to the bearing clearance which was beyond the limit recommended.
On further study it was seen that it also developed misalignment.
On through study of spectrum we see that it has developed unbalance also.

Corrections:

Bearing Clearance:
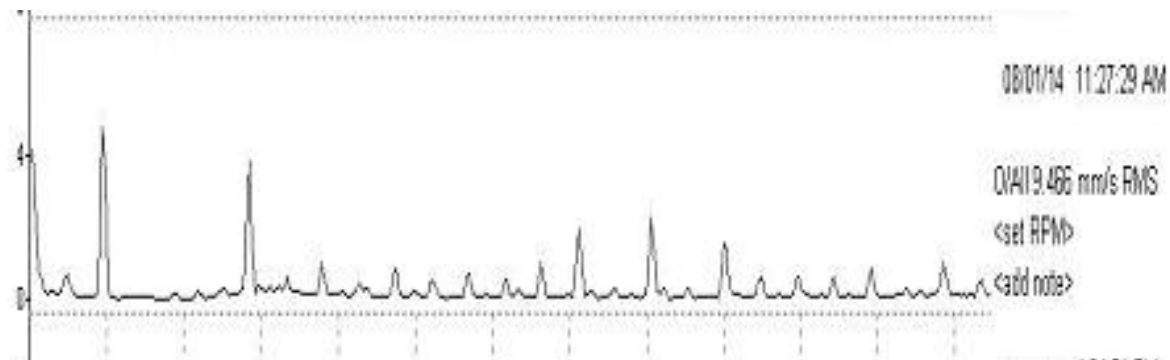
The peaks 2x, 4x,5x, 6x indicate mechanical looseness which is due to bearing clearance. The bearing clearance was corrected by the use of shims, due to this correction the rms value has not changed but the peaks 2x,4x, 5x, 6x etc. vanish, indicating that looseness has been eliminated.

Misalignment:

From the spectrum the peaks 3x, 1x indicate misalignment. So by radial adjustment/alignment of the pump shaft with the pulley shaft was done . By this, the rms value reduced from 9.466 to6.924 where the peak 3x vanishes and 1x has reduced.

Unbalance:

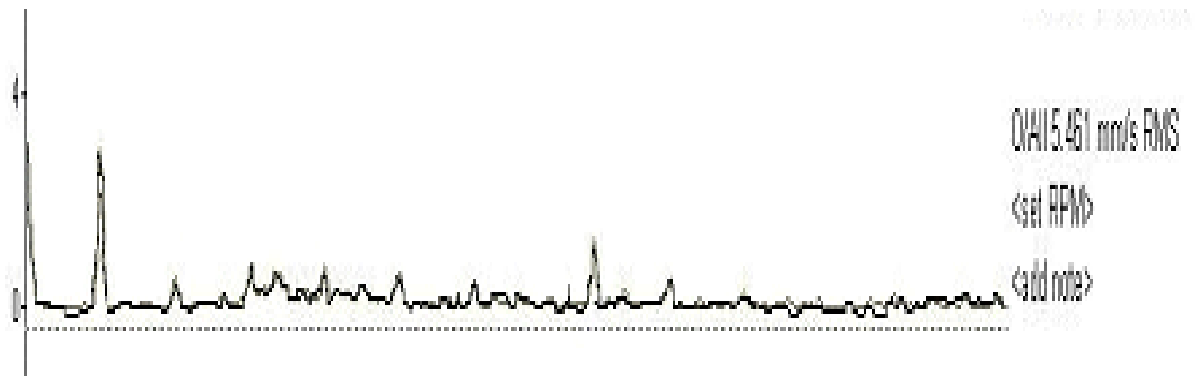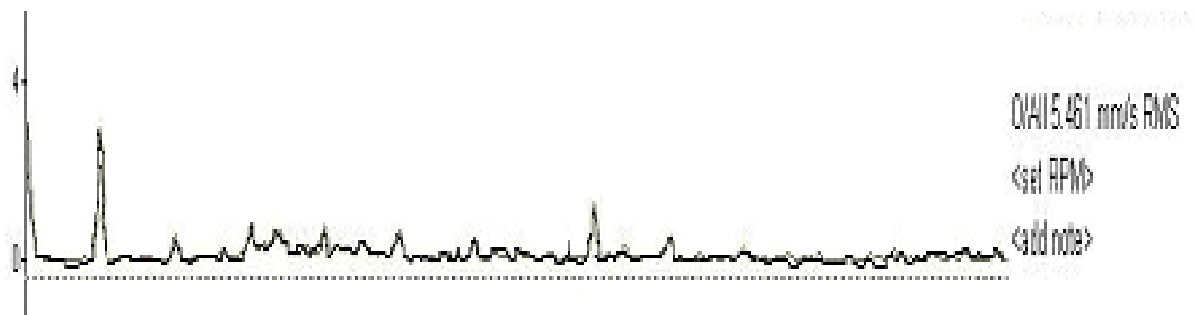The Unbalance was corrected. The correction is done by balancing the pulley by adding weight to it. By this, the rms value shifts from 6.924 to 4.0 and the 1x peak vanished. The overall value has come below the norm.

Spectrum of the machine in normal condition (corrected spectrum):
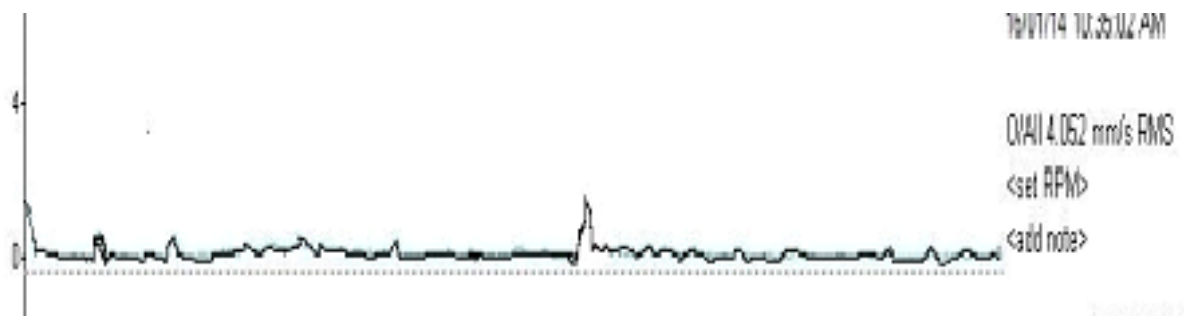
Thus by performing all the above techniques using Condition Monitoring, the Equipment was protected from likely Breakdown.

III.   Conclusion

A timely detection of problem and attending to by taking necessary corrective action prevent major break down and increasing productivity. Further I will continue to take projects and try to increase condition monitoring diagnostics and its cost effectiveness.

REFERENCES

[1.] NREL conference paper.
[2.] Prof Jeans T Broch, Mechanical Vibrations and Shock measurements, Burel & Kjaer ,1984.
[3.] CM Harris and A G Piersol, Shock and Vibration Hand Book, 1990.
[4.] P G Agashe , 'Lub Oil analysis for predictive maintenance', Proc . Of National Conference on Condition Monitoring, 2006.
[5.] Roylance.B and T. Hunt,1999.THE WEARDEBRISANALYSIS HANDBOOK,OXFORD, UK:COXMOOR
[6.] Alfredson, R.J. 1982. A computer based system for condition monitoring, Symposium on Reliability of Large Machines, The Institute of Engineers Australia, Sydney, pp. 39–46.
[7.] http://turbolab.tamu.edu/proc/pumpproc/P8/P863-70.pdf
[8.] http://hpac.com/piping-pumping/examining-causes-pump-vibration

Design Of Hand-Held Alert System Providing Security For Individuals Using Vehicular Ad-Hoc Network

Sharvika Paliwal[1], Ms. V. N. Katkar[2]

Department of Computer Science and Engineering G. H. Raisoni Institute of Engineering and Technology for Women's, Nagpur, Maharashtra, India

Abstract: *Vehicular Ad-hoc Network (VANET) and Mobile Ad-hoc Network (MANET) provide a distinguish approach for Intelligent Transport System (ITS). The existing applications in VANET provide secure message passing and circulation of data within the range, but there are very few applications where individual's security is taken into consideration. In new applications we can make one which provides safety for individuals on road or indirectly related to roads or vehicles. For making such an application we will be using Radio Frequency (RF) signals, VANET network, GPS and GSM techniques. RF signals will be generating input signals; vehicles for making an alarm for generated signals; VANET network to spread the information about panic area to the other vehicles in range; GPS & GSM to track the location & position of victim and send this information to authorized helping system respectively. Thus using all above techniques and principles we are designing a scheme which provides safety using VANET protocols.*

Keywords: *RF signals; VANET; GSM; GPS.*

I. Introduction

VANETs are the subgroup of MANETs with the distinguishing property that the nodes are vehicles like cars, trucks, buses and motorcycles. Such systems aim to provide communications between individual vehicles said as V2V (IVC) and between vehicles and nearby fixed equipment, or roadside units said as (V2R/V2I). This implies that node movement is restricted by factors like road course, encompassing traffic and traffic regulations. Because of the restricted node movement it is a feasible assumption that the VANET will be supported by some fixed infrastructure that assists with some services and can provide access to stationary networks. The fixed infrastructure will be deployed at critical locations like slip roads, service stations, dangerous intersections or places well-known for hazardous weather conditions. Thus the goal of VANET, is to improve traffic safety by providing timely information to drivers and concerned authorities. VANET provides Inter Vehicular Communication (IVC), Hybrid Vehicle Communication (HVC) and Roadside Vehicle Communication (RVC). But with respect to project only IVC is beneficial, so that the message of panic area is given to the other vehicles of that area i.e. the broadcasting of panic or alert message to the vehicles present in the vicinity of victim.

We have also witnessed a significant increase in the number of attacks on public, in recent years, but we haven't yet managed to restrict those attacks. Due to such street attacks on people, it has become difficult for people to travel safely on roads. To have a helping hand in restricting the attacks, we are introducing a new concept of "Alarm scheme using VANET protocols for safety applications". This is executed by using the electronic devices and new technologies. To implement this concept, in practice, a person has to carry a small safety unit equipped with RF(Radio Frequency) Communication system and GSM/GPS(Global System for Mobile/Global Positioning System) services.

Radiofrequency signals are the most widely used means of wireless communication, next to Infrared light. Unlike infrared light, RF-signals have advantage in the fact that the signal can travel around obstacles to reach the destination. RF-signals allow reliable communications across wide range of distances. Radio technology is as reliable and almost as inexpensive as Infrared light. The frequency band which is selected for the worldwide is the available 2.4 GHz (known from Bluetooth and Wi-Fi) and the protocol is based on the IEEE 802.15.4 standard.

GSM i.e. Global System for Mobile Communications, originally Groupe Spécial Mobile, is a standard set developed by the ETSI to describe protocols for second generation digital cellular networks used by mobile phones. The GSM standard was developed for replacing the first generation analog cellular networks, and originally described a digital circuit-switched network optimized for full duplex voice telephony.

Using GPS (Global Positioning System) and a GPS tracking unit we can determine the precise location of a vehicle, person, or other asset to which it is attached and to record the position of the asset at regular

intervals. The recorded location data can be stored within the tracking unit, or it may be transmitted to a central location data base, or internet-connected computer, using a cellular GPRS or SMS, radio or satellite modems embedded in the unit. This allows the asset's location to be displayed against a map backdrop either in real time or when analyzing the track later, using GPS tracking software.

The problem statement says: VANET provides us with road safety measures, secure message passing, traffic jam updates, services like e-mail, audio/video sharing and internetworking. But nowhere individual's security is not taken into consideration, we are designing an alarming system for those individuals using VANET protocols.

The objectives to overcome the problems are as follows: 1. To create a technique which helps an individual, who is in non secure state, to communicate to the nearest communicative station, using technologies and VANET protocols & principles for proper help. 2. Uses a gadget which produces a panic alarm through the vehicles, using RF signals.

II. Literature Survey

Vaishak P., T. Sivakumar [1], has described in this paper about the efficient network connectivity because, when data is send from vehicle , it is possible that the track of node or vehicle may change, so for secure transfer of message a reliable network has to be maintained. Interoperability between VANET module and WiMAX are possible for achieving reliable network connectivity and for secure data transfer and also to obtain high end to end ratio. This paper proposes a protocol has been made which constitutes the combination of WiMAX and VANET technologies. So using this combination we can send message either through WiMax or VANET module.

Iman M. Almomani, Nour Y. Alkhalil, Enas M. Ahmad and Rania M. Jodeh [2], has described in this paper about the transferring of data or information or messages via GSM (Global System for Mobile) and GPRS (General Packet Radio Service) between the vehicles and the internet environment. It also comprises about the working architectures of vehicle positioning and vehicle tracking using GPS (Global Positioning System). This system is useful for fleet operators in monitoring driving behavior of employees or parents monitoring their teen drivers. Moreover, this system can be used in theft prevention as a retrieval device in addition of working as a security system combined with car alarms. The main contribution of this paper is providing two types of end user applications, a web application and a mobile application. This way the proposed system provides a ubiquitous vehicle tracking system with maximum accessibility for the user anytime and anywhere.

Zongwei Luo, Tianle Zhang and Chunlu Wgan [3], has explained about the architectures using a mobile relay network or a connected network which is made for a node to node communication, for an Intelligent Transport System, for the purpose of travelling information. RFID enabled Vehicular Ad hoc Network (VANET) emerges as an alternative which can leverage mobile nodes to bridge the gap between information isolated islands often existing in mobile and wireless networks.

Sae Fujii, Atsushi Fujita, Takaaki Umedu Hirozumi Yamaguchi, Teruo Higashino and Shigeru KanedaandMineo Takai [4], has described in this paper about the vehicle to vehicle communication (V2V), which is the primary goal of VANET, using GPS services and other communication techniques. The proposed system operates in a distributed manner and works even if all vehicles nearby do not or cannot participate in the system. Each vehicle acquires various pieces of positioning information with different degrees of accuracies depending on the sources and regency of information

Ghassan Samara, Wafaa A.H. Al-Salihy and R. Sures [5], has described in this paper about the security issues related to VANET. In simple words, the problems and solutions to keep data safe and secure are provided in this paper, for authenticated message passing. The need for a robust VANET networks is strongly dependent on their security and privacy features, which will be discussed in this paper. In this paper a various types of security problems and challenges of VANET been analyzed and discussed; we also discuss a set of solutions presented to solve these challenges and problems.

Vasilis Verroios, Carmen Ruiz Vicente and Alex Delis [6], In this paper, we propose a broadcasting protocol that alerts drivers about the presence of moving vehicles demonstrating hazardous driving behavior. In order to limit the volume of redundant transmissions, our approach selects the vehicles to be responsible for transmitting the emergency information for a hazardous vehicle. In this context, we provide mechanisms to create and maintain a chain of transmitters. This chain "covers" the road sections on which a hazardous vehicle is moving.

Our protocol attempts to increase the probability that an endangered vehicle does obtain timely information about a hazardous vehicle and reduce the total communication traffic imposed in urban environments where the vehicles' density is often high.

III. Proposed Research And Methodology To Be Employed

A. Proposed Research:

   The concept of this project mainly focuses on the safety measures of public on streets. Whenever a person carrying a safety unit with himself is attacked by someone on a street, he has to press the panic button of the Safety Unit. As soon as the panic button is pressed, a noisy alarm will get activated in the nearby vehicles with the help of RF Communication. After that, this alarm will also get activated in other vehicles. Here, VANET Technology is used. Eventually, a message will be sent to the nearby Police station to inform the police about the incident. The proposed architecture is shown in fig a.

   Since a noisy alarm is activated in the vehicles, the driver of the vehicle will stop the vehicle and check for the fault. Due to this, automatically, a crowd will be created and attention will be gathered towards the happening incident. Also with the help of GPS system, police can locate the victim and help him in the best way they can. Because of all these actions, the attacker might get caught and the motive of restricting the attacks can be achieved at a certain extent.

B. Proposed Methodology:

   In the research methodology we will consider the following steps for complete working of application:
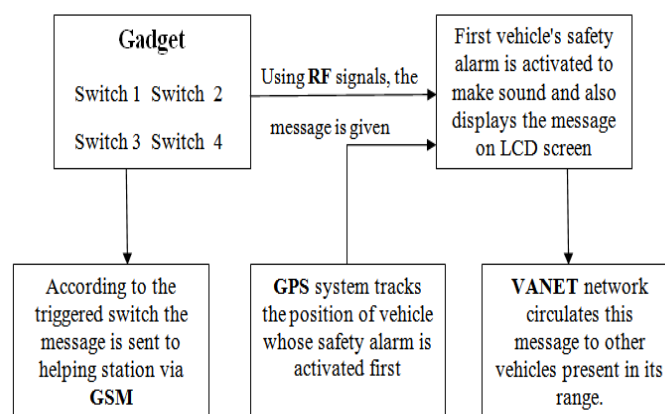

fig a : Proposed Architecture

Step1: Communication between gadget and first vehicle will be done using RF signaling technique; out of four switches, when any of the switch is triggered, the safety alarm of nearest vehicle get's activated, the signal reaches till vehicle using RF signals

Step2: The position of victim will be located using GPS of the nearest vehicle whose safety alarm was generated; the location of alarming vehicle is obtained, so that the area of troubled person is noted.

Step3: Communication between vehicle to vehicle i.e. V2V will be done using VANET technique; this is required to circulate the message of panic situation to the vehicles who are in range and can help.

Step4: Communication between vehicle and authorized help like police will be done via GSM technology; when the switch is triggered by person at that same time the message is given to the authorized helping station using GSM technology.

IV. Expected Outcome

   This paper helps in proposing a new methodology for designing an alarming system for individuals on roadside or in vehicles using the RF technology and VANET system for making the alarm work. The sending of messages to the authorized station via the GSM network and also locating the victim's area with the help of the alarming vehicle. In future we will work with the GPS to locate the exact position and location of victim and VANET communication for communicating with the nearby vehicles present in the range of victim's gadget. This paper concentrates on the public safety measures using electronic gadgets. This concept includes new invented technologies such as VANET which proves advantageous to the system. This paper also covers the literature survey of all the technologies involved in the system.

REFERENCES

[1]   Vaishak.P, T.Sivakumar, "An Efficient Routing Protocol for Minimizing Multi-hop in VANET using WiMAX " , International Journal of Scientific & Engineering Research, Volume 4, Issue 6, June-2013, ISSN 2229-5518.

[2]   Iman M. Almomani, Nour Y. Alkhalil, Enas M. Ahmad and Rania M. Jodeh, "Ubiquitous GPS Vehicle Tracking and Management System", IEEE Jordan Conference on Applied Electrical Engineering and Computing Technologies (AEECT), 2011.

[3]   Zongwei Luo, Tianle Zhang and Chunlu Wgan, "RFID Enabled Vehicular Wireless Query for Travel Information in Intelligent Transportation System", IEEE International   Conference on RFID-Technologies and Applications, 2011.

[4]   Sae Fujii, Atsushi Fujita, Takaaki Umedu Hirozumi Yamaguchi, Teruo Higashino, Shigeru KanedaandMineo Takai, "Cooperative Vehicle Positioning via V2V Communications and Onboard Sensors", IEEE 2011.

[5]   Ghassan Samara, Wafaa A.H. Al-Salihy and R. Sures, "Security Analysis of Vehicular Ad Hoc Networks", Second International Conference on Network Applications, Protocols and Services, 2010.

[6]   Vasilis Verroios, Carmen Ruiz Vicente and Alex Delis, "Alerting for Vehicles Demonstrating Hazardous Driving Behavior", MobiDE '12, Scottsdale, Arizona, USA, 2012 ACM 978-1- 4503-1442-8/12/05.

International Journal of Modern Engineering Research (IJMER)

Contents :

OPEN ACCESS

A Note on a Three Variables Analogue of Bessel Polynomials

Bhagwat Swaroop Sharma

Abstract: *The present paper deals with a study of a three variables analogue of Bessel polynomials. Certain representations, a Schlafli's contour integral, a fractional integral, Laplace transformations, some generating functions and double and triple generating functions have been obtained.*

I. Introduction

In 1949 Krall and Frink [12] initiated a study of simple Bessel polynomial

$$Y_n(x) = {}_2F_o\left[-n, 1+n; -; -\frac{x}{2}\right] \tag{1.1}$$

and generalized Bessel polynomial

$$Y_n(a, b, x) = {}_2F_o\left[-n, a-1+n; -; -\frac{x}{b}\right] \tag{1.2}$$

These polynomials were introduced by them in connection with the solution of the wave equation in spherical coordinates. They are the polynomial solutions of the differential equation.

$$x^2 y''(x) + (ax + b) y'(x) = n(n + a - 1) y(x) \tag{1.3}$$

where n is a positive integer and a and b are arbitrary parameters. These polynomials are orthogonal on the unit circle with respect to the weight function

$$\rho(x, \alpha) = \frac{1}{2\pi i} \sum_{n=0}^{\infty} \frac{\Gamma(\alpha)}{\Gamma(\alpha + n - 1)} \left(-\frac{2}{x}\right)^n. \tag{1.4}$$

Several authors including Agarwal [1], Al-Salam [2], Brafman [3], Burchnall [4], Carlitz [5], Chatterjea [6], Dickinson [7], Eweida [9], Grosswald [10], Rainville [15] and Toscano [19] have contributed to the study of the Bessel polynomials.

Recently in the year 2000, Khan and Ahmad [11] studied two variables analogue $Y_n^{(\alpha,\beta)}(x, y)$ of the Bessel polynomials $Y_n^{(\alpha)}(x)$ defined by

$$Y_n^{(\alpha)}(x) = {}_2F_o\left[-n, \alpha + n + 1; -; -\frac{x}{2}\right] \tag{1.5}$$

The aim of the present paper is to introduce a three variables analogue $Y_n^{(\alpha,\beta,\gamma)}(x, y, z; a, b, c)$ of (1.2) and to obtain certain results involving the three variables Bessel polynomial $Y_n^{(\alpha,\beta,\gamma)}(x, y, z; a, b, c)$.

II. The Polynomials

$Y_n^{(\alpha,\beta,\gamma)}(x, y, z; a, b, c)$: The Bessel polynomial of three variables $Y_n^{(\alpha,\beta,\gamma)}(x, y, z; a, b, c)$ is defined as follows:

$$Y_n^{(\alpha,\beta,\gamma)}(x, y, z; a, b, c)$$

$$= \sum_{r=0}^{n} \sum_{s=0}^{n-r} \sum_{j=0}^{n-r-s} \frac{(-n)_{r+s+j}(\alpha + n + 1)_j (\beta + n + 1)_s (\gamma + n + 1)_r}{r!\, s!\, j!} \left(-\frac{x}{a}\right)^j \left(-\frac{y}{b}\right)^s \left(-\frac{z}{c}\right)^r \tag{2.1}$$

For z = 0, a = b = 2, (2.1) reduces to the two variables analogue $Y_n^{(\alpha,\beta)}(x, y)$ of Bessel polynomials (1.5) as given below :

$$Y_n^{(\alpha,\beta,\gamma)}(x, y, 0; 2, 2, c) = Y_n^{(\alpha,\beta)}(x, y) \tag{2.2}$$

Similarly

$$Y_n^{(\alpha,\beta,\gamma)}(x, 0, z; 2, b, 2) = Y_n^{(\alpha,\gamma)}(x, z) \tag{2.3}$$

$$Y_n^{(\alpha,\beta,\gamma)}(0, y, z; a, 2, 2) = Y_n^{(\beta,\gamma)}(y, z) \tag{2.4}$$

Also for $\alpha = -n-1$, and $b = c = 2$

$$Y_n^{(-n-1,\beta,\gamma)}(x, y, z; a, 2, 2) = Y_n^{(\beta,\gamma)}(y, z) \tag{2.5}$$

Similarly,

$$Y_n^{(\alpha,-n-1,\gamma)}(x, y, z; 2, b, 2) = Y_n^{(\alpha,\gamma)}(x, z) \tag{2.6}$$

$$Y_n^{(\alpha,\beta,-n-1)}(x, y, z; 2, 2, c) = Y_n^{(\alpha,\beta)}(x, y) \tag{2.7}$$

where

$$Y_n^{(\alpha,\beta)}(x, y) = \sum_{r=0}^{n} \sum_{s=0}^{n-r} \frac{(-n)_{r+s}(\alpha+n+1)_s(\beta+n+1)_r}{r!\,s!}\left(-\frac{x}{2}\right)^s\left(-\frac{y}{2}\right)^r \tag{2.8}$$

Also, for $y = z = 0$, $a = 2$, (2.1) reduces to the Bessel polynomials $Y_n^{(\alpha)}(x)$ as given below:

$$Y_n^{(\alpha,\beta,\gamma)}(x, 0, 0; 2, b, c) = Y_n^{(\alpha)}(x) \tag{2.9}$$

where $Y_n^{(\alpha)}(x)$ is defined by (1.5).
Similarly

$$Y_n^{(\alpha,\beta,\gamma)}(0, y, 0; a, 2, c) = Y_n^{(\beta)}(y) \tag{2.10}$$

$$Y_n^{(\alpha,\beta,\gamma)}(0, 0, z; 2, 2, c) = Y_n^{(\gamma)}(z) \tag{2.11}$$

Also, for $\beta = \gamma = -n-1$, $a = 2$, we have

$$Y_n^{(\alpha,-n-1,-n-1)}(x, y, z; 2, b, c) = Y_n^{(\alpha)}(x) \tag{2.12}$$

Similarly

$$Y_n^{(-n-1,\beta,-n-1)}(x, y, z; a, 2, c) = Y_n^{(\beta)}(y) \tag{2.13}$$

$$Y_n^{(-n-1,-n-1,\gamma)}(x, y, z; a, b, 2) = Y_n^{(\gamma)}(z) \tag{2.14}$$

III. Integral Representations

It is easy to show that the polynomial $Y_n^{(\alpha,\beta,\gamma)}(x, y, z; a, b, c)$ has the following integral representations:

$$\frac{1}{\Gamma(\alpha+n+1)\Gamma(\beta+n+1)\Gamma(\gamma+n+1)}\int_0^\infty \int_0^\infty \int_0^\infty u^{\alpha+n}v^{\beta+n}w^{\gamma+n}\left(1+\frac{xu}{a}+\frac{yv}{b}+\frac{zw}{c}\right)^n e^{-u-v-w}\,du\,dv\,dw$$

$$= Y_n^{(\alpha,\beta,\gamma)}(x, y, z; a, b, c) \tag{3.1}$$

For $z = 0$, $a = b = 2$, (3.1) reduces to

$$\frac{1}{\Gamma(\alpha+n+1)\Gamma(\beta+n+1)}\int_0^\infty \int_0^\infty u^{\alpha+n}\,v^{\beta+n}\left(1+\frac{xu}{2}+\frac{yv}{2}\right)^n e^{-u-v}\,du\,dv$$

$$= Y_n^{(\alpha,\beta)}(x, y) \tag{3.2}$$

a result due to Khan and Ahmad [11].
For $y = z = 0$, α replaced by $a - 2$ and a replaced by b, (3.1) becomes

$$Y_n(a, b, x) = \frac{1}{\Gamma(a-1+n)}\int_0^\infty t^{a-2+n}\left(1+\frac{xt}{b}\right)^n e^{-t}\,dt \tag{3.3}$$

a result due to Agarwal [1].

$$\int_0^t \int_0^s \int_0^r x^\alpha (r-x)^{n-1} y^\beta (s-y)^{n-1} z^\gamma (t-z)^{n-1} Y_n^{(\alpha,\beta,\gamma)}(x, y, z; a, b, c)\,dx\,dy\,dz$$

$$= \frac{r^{\alpha+n}\,s^{\beta+n}\,t^{\gamma+n}\,\{\Gamma(n)\}^3}{(\alpha+1)_n\,(\beta+1)_n\,(\gamma+1)_n} Y_n^{(\alpha-n,\beta-n,\gamma-n)}(r, s, t; a, b, c) \tag{3.4}$$

$$\int_0^1 \int_0^1 \int_0^1 u^{\delta-1}(1-u)^{\lambda-1}\,v^{\eta-1}(1-v)^{\mu-1}\,w^{\xi-1}(1-w)^{\nu-1}\,Y_n^{(\alpha,\beta,\gamma)}(xu, yv zw; a, b, c)\,du\,dv\,dw$$

$$= \frac{\Gamma(\delta)\Gamma(\lambda)\Gamma(\eta)\Gamma(\mu)\Gamma(\xi)\Gamma(\nu)}{\Gamma(\delta+\lambda)\Gamma(\eta+\mu)\Gamma(\xi+\nu)} F^{(3)} \begin{bmatrix} -n :: -;-;- : \alpha+n+1, \delta; \beta+n+1, \eta; \gamma+n+1, \xi; & \\ -::-;-;- : & \delta+\lambda & ; & \eta+\mu & ; & \xi+\nu & ; \end{bmatrix} -\frac{x}{a}, -\frac{y}{b}, -\frac{z}{c} \end{bmatrix}$$

(3.5)

where $F^{(3)}$ [ ] is in the form of a general triple hypergeometric series $F^{(3)}$ [x, y, z] (cf. Srivastava [18], p. 428).

$$\int_0^1 \int_0^1 \int_0^1 u^{\delta-1}(1-u)^{\lambda-1} v^{\eta-1}(1-v)^{\mu-1} w^{\xi-1}(1-w)^{\nu-1} Y_n^{(\alpha,\beta,\gamma)}(x(1-u), y\,v\,z\,w; a, b, c)\,du\,dv\,dw$$

$$= \frac{\Gamma(\delta)\Gamma(\lambda)\Gamma(\eta)\Gamma(\mu)\Gamma(\xi)\Gamma(\nu)}{\Gamma(\delta+\lambda)\Gamma(\eta+\mu)\Gamma(\xi+\nu)} F^{(3)} \begin{bmatrix} -n :: -;-;- : \alpha+n+1, \lambda; \beta+n+1, \eta; \gamma+n+1, \xi; & \\ -::-;-;- : & \delta+\lambda & ; & \eta+\mu & ; & \xi+\nu & ; \end{bmatrix} -\frac{x}{a}, -\frac{y}{b}, -\frac{z}{c} \end{bmatrix}$$

(3.6)

$$\int_0^1 \int_0^1 \int_0^1 u^{\delta-1}(1-u)^{\lambda-1} v^{\eta-1}(1-v)^{\mu-1} w^{\xi-1}(1-w)^{\nu-1} Y_n^{(\alpha,\beta,\gamma)}(xu, y(1-v), zw; a, b, c)\,du\,dv\,dw$$

$$= \frac{\Gamma(\delta)\Gamma(\lambda)\Gamma(\eta)\Gamma(\mu)\Gamma(\xi)\Gamma(\nu)}{\Gamma(\delta+\lambda)\Gamma(\eta+\mu)\Gamma(\xi+\nu)} F^{(3)} \begin{bmatrix} -n :: -;-;- : \alpha+n+1, \delta; \beta+n+1, \mu; \gamma+n+1, \xi; & \\ -::-;-;- : & \delta+\lambda & ; & \eta+\mu & ; & \xi+\nu & ; \end{bmatrix} -\frac{x}{a}, -\frac{y}{b}, -\frac{z}{c} \end{bmatrix}$$

(3.7)

$$\int_0^1 \int_0^1 \int_0^1 u^{\delta-1}(1-u)^{\lambda-1} v^{\eta-1}(1-v)^{\mu-1} w^{\xi-1}(1-w)^{\nu-1} Y_n^{(\alpha,\beta,\gamma)}(xu, y\,v, z(1-w); a, b, c)\,du\,dv\,dw$$

$$= \frac{\Gamma(\delta)\Gamma(\lambda)\Gamma(\eta)\Gamma(\mu)\Gamma(\xi)\Gamma(\nu)}{\Gamma(\delta+\lambda)\Gamma(\eta+\mu)\Gamma(\xi+\nu)} F^{(3)} \begin{bmatrix} -n :: -;-;- : \alpha+n+1, \delta; \beta+n+1, \eta; \gamma+n+1, \nu; & \\ -::-;-;- : & \delta+\lambda & ; & \eta+\mu & ; & \xi+\nu & ; \end{bmatrix} -\frac{x}{a}, -\frac{y}{b}, -\frac{z}{c} \end{bmatrix}$$

(3.8)

$$\int_0^1 \int_0^1 \int_0^1 u^{\delta-1}(1-u)^{\lambda-1} v^{\eta-1}(1-v)^{\mu-1} w^{\xi-1}(1-w)^{\nu-1} Y_n^{(\alpha,\beta,\gamma)}(x(1-u), y(1-v), zw; a, b, c)\,du\,dv\,dw$$

$$= \frac{\Gamma(\delta)\Gamma(\lambda)\Gamma(\eta)\Gamma(\mu)\Gamma(\xi)\Gamma(\nu)}{\Gamma(\delta+\lambda)\Gamma(\eta+\mu)\Gamma(\xi+\nu)} F^{(3)} \begin{bmatrix} -n :: -;-;- : \alpha+n+1, \lambda; \beta+n+1, \mu; \gamma+n+1, \xi; & \\ -::-;-;- : & \delta+\lambda & ; & \eta+\mu & ; & \xi+\nu & ; \end{bmatrix} -\frac{x}{a}, -\frac{y}{b}, -\frac{z}{c} \end{bmatrix}$$

(3.9)

$$\int_0^1 \int_0^1 \int_0^1 u^{\delta-1}(1-u)^{\lambda-1} v^{\eta-1}(1-v)^{\mu-1} w^{\xi-1}(1-w)^{\nu-1} Y_n^{(\alpha,\beta,\gamma)}(x(1-u), y\,v, z(1-w); a, b, c)\,du\,dv\,dw$$

$$= \frac{\Gamma(\delta)\Gamma(\lambda)\Gamma(\eta)\Gamma(\mu)\Gamma(\xi)\Gamma(\nu)}{\Gamma(\delta+\lambda)\Gamma(\eta+\mu)\Gamma(\xi+\nu)} F^{(3)} \begin{bmatrix} -n :: -;-;- : \alpha+n+1, \lambda; \beta+n+1, \eta; \gamma+n+1, \nu; & \\ -::-;-;- : & \delta+\lambda & ; & \eta+\mu & ; & \xi+\nu & ; \end{bmatrix} -\frac{x}{a}, -\frac{y}{b}, -\frac{z}{c} \end{bmatrix}$$

(3.10)

$$\int_0^1 \int_0^1 \int_0^1 u^{\delta-1}(1-u)^{\lambda-1} v^{\eta-1}(1-v)^{\mu-1} w^{\xi-1}(1-w)^{\nu-1} Y_n^{(\alpha,\beta,\gamma)}(xu, y(1-v), z(1-w); a, b, c)\,du\,dv\,dw$$

$$= \frac{\Gamma(\delta)\Gamma(\lambda)\Gamma(\eta)\Gamma(\mu)\Gamma(\xi)\Gamma(\nu)}{\Gamma(\delta+\lambda)\Gamma(\eta+\mu)\Gamma(\xi+\nu)} F^{(3)} \begin{bmatrix} -n :: -;-;- : \alpha+n+1, \delta; \beta+n+1, \mu; \gamma+n+1, \nu; & \\ -::-;-;- : & \delta+\lambda & ; & \eta+\mu & ; & \xi+\nu & ; \end{bmatrix} -\frac{x}{a}, -\frac{y}{b}, -\frac{z}{c} \end{bmatrix}$$

(3.11)

$$\int_0^1 \int_0^1 \int_0^1 u^{\delta-1}(1-u)^{\lambda-1} v^{\eta-1}(1-v)^{\mu-1} w^{\xi-1}(1-w)^{\nu-1} Y_n^{(\alpha,\beta,\gamma)}(x(1-u), y(1-v), z(1-w); a, b, c)\,du\,dv\,dw$$

$$= \frac{\Gamma(\delta)\Gamma(\lambda)\Gamma(\eta)\Gamma(\mu)\Gamma(\xi)\Gamma(\nu)}{\Gamma(\delta+\lambda)\Gamma(\eta+\mu)\Gamma(\xi+\nu)} F^{(3)} \begin{bmatrix} -n :: -;-;- : \alpha+n+1, \lambda; \beta+n+1, \mu; \gamma+n+1, \nu; & \\ -::-;-;- : & \delta+\lambda & ; & \eta+\mu & ; & \xi+\nu & ; \end{bmatrix} -\frac{x}{a}, -\frac{y}{b}, -\frac{z}{c} \end{bmatrix}$$

(3.12)

$$\int_0^1 \int_0^1 \int_0^1 u^{\delta-1}(1-u)^{\lambda-1} v^{\eta-1}(1-v)^{\mu-1} w^{\xi-1}(1-w)^{\nu-1} Y_n^{(\alpha,\beta,\gamma)}(x\,v\,w, y\,u\,w, z\,u\,v; a, b, c)\,du\,dv\,dw$$

$$= \frac{\Gamma(\delta)\Gamma(\lambda)\Gamma(\eta)\Gamma(\mu)\Gamma(\xi)\Gamma(\nu)}{\Gamma(\delta+\lambda)\Gamma(\eta+\mu)\Gamma(\xi+\nu)} F^{(3)} \begin{bmatrix} -n :: \delta \; ; \; \eta \; ; \; \xi : \alpha+n+1; \beta+n+1; \gamma+n+1; & \\ -:: \delta+\lambda \; ; \eta+\mu \; ; \xi+\nu : & -; & -; & - & ; \end{bmatrix} -\frac{x}{a}, -\frac{y}{b}, -\frac{z}{c} \end{bmatrix}$$

(3.13)

$$\int_0^1 \int_0^1 \int_0^1 u^{\delta-1}(1-u)^{\lambda-1} v^{\eta-1}(1-v)^{\mu-1} w^{\xi-1}(1-w)^{\nu-1} Y_n^{(\alpha,\beta,\gamma)}\big(xv(1-w), yw(1-u), zu(1-v); a,b,c\big) du\, dv\, dw$$

$$= \frac{\Gamma(\delta)\Gamma(\lambda)\Gamma(\eta)\Gamma(\mu)\Gamma(\xi)\Gamma(\nu)}{\Gamma(\delta+\lambda)\Gamma(\eta+\mu)\Gamma(\xi+\nu)} F^{(3)}\begin{bmatrix} -n :: -;-;- : \alpha+n+1, \delta, \mu; \beta+n+1, \lambda, \xi; \gamma+n+1, \eta, \nu; & -\dfrac{x}{a}, -\dfrac{y}{b}, -\dfrac{z}{c} \\ -:: \quad \delta+\lambda \quad ; \quad \eta+\mu \quad ; \quad \xi+\nu \quad : \quad -; \quad\quad -; \quad\quad - \quad ; & \end{bmatrix}$$

$$(3.14)$$

Particular Cases:

Some interesting particular cases of the above results are as follows :

(i) Taking $\delta = \alpha+1$, $\eta = \beta+1$, $\xi = \gamma+1$, $\lambda = \mu = \nu = n$ in (3.5), we obtain

$$\int_0^1 \int_0^1 \int_0^1 u^{\alpha}(1-u)^{n-1} v^{\beta}(1-v)^{n-1} w^{\gamma}(1-w)^{n-1} Y_n^{(\alpha,\beta,\gamma)}(xu, yv\, zw; a,b,c) du\, dv\, dw$$

$$= \frac{\{\Gamma(n)\}^3}{(\alpha+1)_n (\beta+1)_n (\gamma+1)_n} Y_n^{(\alpha-n, \beta-n, \gamma-n)}(x, y, z; a, b, c)$$

$$(3.15)$$

which is equivalent to (3.4)

(ii) Taking $\delta = \eta = \xi = n+1$, $\lambda = \alpha$, $\mu = \beta$, $\nu = \gamma$ in (3.5), we get

$$\int_0^1 \int_0^1 \int_0^1 u^n (1-u)^{\alpha-1} v^n (1-v)^{\beta-1} w^n (1-w)^{\gamma-1} Y_n^{(\alpha,\beta,\gamma)}(xu, yv\, zw) du\, dv\, dw$$

$$= \frac{(n!)^3}{(\alpha)_{n+1} (\beta)_{n+1} (\gamma)_{n+1}} Y_n^{(0,0,0)}(x, y, z)$$

$$(3.16)$$

(iii) Replacing δ by $\alpha+n+1-\delta$, η by $\beta+n+1-\eta$, ξ by $\gamma+n+1-\xi$, and putting $\lambda = \delta$, $\mu = \eta$ and $\nu = \xi$ in (3.5), we get

$$\int_0^1 \int_0^1 \int_0^1 u^{\alpha-\delta+n}(1-u)^{\delta-1} v^{\beta-\eta+n}(1-v)^{\eta-1} w^{\gamma-\xi+n}(1-w)^{\xi-1} Y_n^{(\alpha,\beta,\gamma)}(xu, yv\, zw; a,b,c) du\, dv\, dw$$

$$= \frac{\Gamma(\alpha-\delta+n+1)\Gamma(\delta)\Gamma(\beta-\eta+n+1)\Gamma(\eta)\Gamma(\gamma-\xi+n+1)\Gamma(\xi)}{\Gamma(\alpha+n+1)\Gamma(\beta+n+1)\Gamma(\gamma+n+1)} Y_n^{(\alpha-\delta, \beta-\eta, \gamma-\xi)}(x, y, z; a, b, c)$$

$$(3.17)$$

Similar particular cases hold for (3.6), (3.7), (3.8), (3.9), (3.10), (3.11) and (3.12).

(iv) For $z = 0$, $a = b = 2$, results (3.4), (3.5), (3.6), (3.7) and (3.9) become

$$\int_0^s \int_0^r x^{\alpha}(r-x)^{n-1} y^{\beta}(s-y)^{n-1} Y_n^{(\alpha,\beta)}(x, y) dx\, dy$$

$$= \frac{r^{\alpha+n} s^{\beta+n} t^{\gamma+n} \{\Gamma(n)\}^2}{(\alpha+1)_n (\beta+1)_n} Y_n^{(\alpha-n, \beta-n)}(r, s)$$

$$(3.18)$$

$$\int_0^1 \int_0^1 u^{\delta-1}(1-u)^{\lambda-1} v^{\eta-1}(1-v)^{\mu-1} Y_n^{(\alpha,\beta)}(xu, yv) du\, dv$$

$$= \frac{\Gamma(\delta)\Gamma(\lambda)\Gamma(\eta)\Gamma(\mu)}{\Gamma(\delta+\lambda)\Gamma(\eta+\mu)} F_{-:1;1}^{1:2;2}\begin{bmatrix} -n : \alpha+n+1, \delta; \beta+n+1, \eta; & -\dfrac{x}{2}, -\dfrac{y}{2} \\ -: \quad \delta+\lambda \quad ; \quad \eta+\mu \quad ; & \end{bmatrix}$$

$$(3.19)$$

$$\int_0^1 \int_0^1 u^{\delta-1}(1-u)^{\lambda-1} v^{\eta-1}(1-v)^{\mu-1} Y_n^{(\alpha,\beta)}(x(1-u), yv) du\, dv$$

$$= \frac{\Gamma(\delta)\Gamma(\lambda)\Gamma(\eta)\Gamma(\mu)}{\Gamma(\delta+\lambda)\Gamma(\eta+\mu)} F_{-:1;1}^{1:2;2}\begin{bmatrix} -n : \alpha+n+1, \lambda; \beta+n+1, \eta; & -\dfrac{x}{2}, -\dfrac{y}{2} \\ -: \quad \delta+\lambda \quad ; \quad \eta+\mu \quad ; & \end{bmatrix}$$

$$(3.20)$$

$$\int_0^1 \int_0^1 u^{\delta-1}(1-u)^{\lambda-1} v^{\eta-1}(1-v)^{\mu-1} Y_n^{(\alpha,\beta)}(x(1-u), y(1-v)) du\, dv$$

$$= \frac{\Gamma(\delta)\Gamma(\lambda)\Gamma(\eta)\Gamma(\mu)}{\Gamma(\delta+\lambda)\Gamma(\eta+\mu)} F_{-:1;1}^{1:2;2}\begin{bmatrix} -n : \alpha+n+1, \lambda; \beta+n+1, \mu; & -\dfrac{x}{2}, -\dfrac{y}{2} \\ -: \quad \delta+\lambda \quad ; \quad \eta+\mu \quad ; & \end{bmatrix}$$

$$(3.21)$$

Results (3.18), (3.19), (3.20) and (3.21) are due to Khan and Ahmad [11].
Also, using the integral (see Erdelyi et al. [8], vol. I, p. 14),

$$2\,i\,\sin\pi\,z\,\Gamma(z) = -\int_{\infty}^{(0+)} (-t)^{z-1}\,e^{-t}\,dt \tag{3.22}$$

and the fact that

$$(1-x-y-z)^n = \sum_{r=0}^{n}\sum_{s=0}^{n-r}\sum_{j=0}^{n-r-s} \frac{(-n)_{r+s+j}\;x^j\,y^s\,z^r}{r!\;s!\;j!} \tag{3.23}$$

we can easily derive the following integral representations for $Y_n^{(\alpha,\beta,\gamma)}(x,y,z;a,b,c)$:

$$-\int_{\infty}^{(0+)}\int_{\infty}^{(0+)}\int_{\infty}^{(0+)} (-u)^{\alpha+n}(-v)^{\beta+n}(-w)^{\gamma+n}\,e^{-u-v-w}\left(1+\frac{xu}{a}+\frac{yv}{b}+\frac{zw}{c}\right)^n du\,dv\,dw$$

$$=8\,i\,(-1)^n \sin\pi\alpha\,\sin\pi\beta\,\sin\pi\gamma\,\Gamma(\alpha+n+1)\Gamma(\beta+n+1)\Gamma(\gamma+n+1)\,Y_n^{(\alpha,\beta,\gamma)}(x,y,z;a,b,c) \tag{3.24}$$

$$\frac{(-1)^{n+1}\sin\pi\alpha\,\sin\pi\beta\,\sin\pi\gamma\,\Gamma(1+\alpha+n)\Gamma(1+\beta+n)\Gamma(1+\gamma+n)}{\pi^3}$$

$$\int_0^\infty\int_0^\infty\int_0^\infty u^{-\alpha-n-1}\,v^{-\beta-n-1}\,w^{-\gamma-n-1}\,e^{-u-v-w}\,Y_n^{(\alpha,\beta,\gamma)}\left(\frac{ax}{u},\frac{by}{v},\frac{cz}{w};a,b,c\right)du\,dv\,dw$$

$$=(1-x-y-z)^n \tag{3.25}$$

IV. Schlafli's Contour Integral

It is easy to show that

$$\int_{-\infty}^{(0+)}\int_{-\infty}^{(0+)}\int_{-\infty}^{(0+)} u^{\alpha+n}\,v^{\beta+n}\,w^{\gamma+n}\,e^{u+v+w}\left(1-\frac{xu}{a}-\frac{yv}{b}-\frac{zw}{c}\right)^n du\,dv\,dw$$

$$=8\,i\,(-1)^n \sin\pi\alpha\,\sin\pi\beta\,\sin\pi\gamma\,\Gamma(1+\alpha+n)\Gamma(1+\beta+n)\Gamma(1+\gamma+n)\,Y_n^{(\alpha,\beta,\gamma)}(x,y,z;a,b,c) \tag{4.1}$$

Proof of (4.1) : We have

$$\frac{1}{(2\pi i)^3}\int_{-\infty}^{(0+)}\int_{-\infty}^{(0+)}\int_{-\infty}^{(0+)} u^{\alpha+n}\,v^{\beta+n}\,w^{\gamma+n}\,e^{u+v+w}\left(1-\frac{xu}{a}-\frac{yv}{b}-\frac{zw}{c}\right)^n du\,dv\,dw$$

$$=\sum_{r=0}^{n}\sum_{s=0}^{n-r}\sum_{j=0}^{n-r-s} \frac{(-n)_{r+s+j}}{r!s!j!}\left(\frac{x}{a}\right)^j\left(\frac{y}{b}\right)^s\left(\frac{z}{c}\right)^r \frac{1}{(2\pi i)^3}\int_{-\infty}^{(0+)}\int_{-\infty}^{(0+)}\int_{-\infty}^{(0+)} u^{\alpha+n+j}v^{\beta+n+s}w^{\gamma+n+r}e^{u+v+w}du\,dv\,dw$$

$$=\sum_{r=0}^{n}\sum_{s=0}^{n-r}\sum_{j=0}^{n-r-s} \frac{(-n)_{r+s+j}\left(\frac{x}{a}\right)^j\left(\frac{y}{b}\right)^s\left(\frac{z}{c}\right)^r}{r!s!j!\;\Gamma(-\alpha-n-j)\Gamma(-\beta-n-s)\;\Gamma(-\gamma-n-r)}$$

using Hankel's formula (see A. Eerdelyi et al. [8], 1.6 (2)).

$$\frac{1}{\Gamma(z)}=\frac{1}{2\pi i}\int_{-\infty}^{(0+)} e^t\,t^{-z}\,dt \tag{4.2}$$

Finally (4.1) follows from (2.1) after using the result

$$\Gamma(z)\Gamma(1-z) \;=\; \pi\,\operatorname{cosec}\pi\,z \tag{4.3}$$

for $z = 0$, $a = b = 2$, (4.1) reduces to

$$\int_{-\infty}^{(0+)}\int_{-\infty}^{(0+)} u^{\alpha+n}\,v^{\beta+n}\,e^{u+v+w}\left(1-\frac{xu}{a}-\frac{yv}{b}\right)^n du\,dv$$

$$=-4\sin\pi\alpha\,\sin\pi\beta\,\Gamma(1+\alpha+n)\Gamma(1+\beta+n)\,Y_n^{(\alpha,\beta)}(x,y) \tag{4.4}$$

which is due to Khan and Ahmad [11].

V. Fractional Integrals

Let L denote the linear space of (equivalent classes of) complex – valued functions f(x) which are Lebesgue – integrable on [0, α], α < ∞. For f(x) εL and complex number μ with Rl μ > 0, the Riemann – Liouville fractional integral of order μ is defined as (see Prabhakar [13], p. 72)

$$I^{\mu} f(x) = \frac{1}{\Gamma(\mu)} \int_0^x (x-t)^{\mu-1} f(t) \, dt \qquad \text{for almost all } x \in [0, \alpha] \qquad (5.1)$$

Using the operator I^{μ}, Prabhakar [14] obtained the following result for Rl μ > 0 and Rl α > −1.

$$I^{\mu} \left[x^{\alpha} Z_n^{\alpha}(x; k) \right] = \frac{\Gamma(kn+\alpha+1)}{\Gamma(kn+\alpha+\mu+1)} x^{\alpha+\mu} Z_n^{\alpha+\mu}(x; k) \qquad (5.2)$$

where $Z_n^{\alpha}(x; k)$ is Konhauser's biorthozonal polynomial.

Khan and Ahmad [11] defined a two variable analogue of (5.1) by means of the following relation :

$$I^{\lambda, \mu} \left[f(x, y) \right] = \frac{1}{\Gamma(\lambda)\Gamma(\mu)} \int_0^x \int_0^y (x-u)^{\lambda-1} (y-v)^{\mu-1} f(u, v) \, du \, dv \qquad (5.3)$$

and obtained the following result :

$$I^{\lambda, \mu} \left[x^{\alpha+n-\lambda} y^{\beta+n-\mu} Y_n^{(\alpha,\beta)}(x, y) \right] = \frac{x^{\alpha+n} y^{\beta+n} \Gamma(\alpha-\lambda+n+1)\Gamma(\beta-\mu+n+1)}{\Gamma(\alpha+n+1) \Gamma(\beta+n+1)} Y_n^{(\alpha-\lambda,\beta-\mu)}(x, y)$$

$$(5.4)$$

In an attempt to obtained a result analogous to (5.4) for the polynomial $Y_n^{(\alpha,\beta,\gamma)}(x, y, z \,; a, b, c)$ we first seek a three variable analogue of (5.1).

A three variable analogue of I^{μ} may be defined as

$$I^{\lambda, \mu, \eta} \left[f(x, y, z) \right] = \frac{1}{\Gamma(\lambda)\Gamma(\mu)\Gamma(\eta)} \int_0^x \int_0^y \int_0^z (x-u)^{\lambda-1} (y-v)^{\mu-1} (z-w)^{\eta-1} f(u, v, w) \, du \, dv \, dw$$

$$(5.5)$$

Putting $f(x, y, z) = x^{\alpha+n-\lambda} y^{\beta+n-\mu} z^{\gamma+n-\eta} Y_n^{(\alpha,\beta,\gamma)}(x, y, z; a, b, c)$ in (5.5), we obtain

$$I^{\lambda, \mu, \eta} = \left[x^{\alpha+n-\lambda} y^{\beta+n-\mu} z^{\gamma+n-\eta} Y_n^{(\alpha,\beta,\gamma)}(x, y, z; a, b, c) \right]$$

$$= \frac{x^{\alpha+n} y^{\beta+n} z^{\gamma+n} \Gamma(\alpha-\lambda+n+1)\Gamma(\beta-\mu+n+1)\Gamma(\gamma-\eta+n+1)}{\Gamma(\alpha+n+1) \Gamma(\beta+n+1)\Gamma(\gamma+n+1)} Y_n^{(\alpha-\lambda,\beta-\mu,\gamma-\eta)}(x, y, z; a, b, c)$$

$$(5.6)$$

VI. Laplace Transform

In the usual notation the Laplace transform is given by

$$L \{f(t): s\} = \int_0^{\infty} e^{-st} f(t) \, dt, \, Rl(s-a) > 0 \qquad (6.1)$$

where f ε L (0, R) for every R > 0 and f(t) = 0(e^{at}), t → ∞.

Khan and Ahmad [11] introduced a two variable analogue of (6.1) by means of the relation:

$$L \{f(u, v): s_1, s_2\} = \int_0^{\infty} \int_0^{\infty} e^{-s_1 u - s_2 v} f(u, v) \, du \, dv \qquad (6.2)$$

and established the following results :

$$L \left\{ u^{-\alpha-n-1} v^{-\beta-n-1} Y_n^{(\alpha,\beta)} \left(\frac{2x}{us_1}, \frac{2y}{vs_2} \right) : s_1, s_2 \right\}$$

$$= \frac{\pi^2 s_1^{\alpha+n} s_2^{\beta+n}}{\sin \pi\alpha \, \sin \pi\beta \, \Gamma(\alpha+n+1)\Gamma(\beta+n+1)} (1-x-y)^n \qquad (6.3)$$

and

$$L \left\{ u^{\alpha+n} v^{\beta+n} \left(1 + \frac{xus_1}{2} + \frac{yvs_2}{2} \right)^n : s_1, s_2 \right\}$$

$$= \frac{\Gamma(\alpha+n+1)\Gamma(\beta+n+1)}{s_1^{\alpha+n+1}\,s_2^{\beta+n+1}}\,Y_n^{(\alpha,\beta)}\,(x,\,y) \tag{6.4}$$

In an attempt to obtain results analogous to (6.3) and (6.4) for $Y_n^{(\alpha,\beta,\gamma)}(x,\,y,z;a,\,b,\,c)$ we define a three variable analogue of (6.1) as follows

$$L\{f(u,\,v,\,w):s_1,s_2,s_3\}=\int_0^\infty\int_0^\infty\int_0^\infty e^{-s_1 u\,-s_2 v\,-s_3 w}\,f(u,\,v,\,w)\,du\,dv\,dw \tag{6.5}$$

Now, we have

$$L\left\{u^{-\alpha-n-1}\,v^{-\beta-n-1}\,w^{-\gamma-n-1}\,Y_n^{(\alpha,\beta,\gamma)}\left(\frac{ax}{us_1},\frac{by}{vs_2},\frac{cz}{ws_3}\,;a,\,b,\,c\right):s_1,\,s_2,\,s_3\right\}$$

$$=\frac{(-1)^{n+1}\,\pi^3\,s_1^{\alpha+n}\,s_2^{\beta+n}\,s_3^{\gamma+n}}{\sin\pi\alpha\,\sin\pi\beta\,\sin\pi\gamma\,\Gamma(\alpha+n+1)\Gamma(\beta+n+1)\Gamma(\gamma+n+1)}\,(1-x-y)^n \tag{6.6}$$

Similarly, we obtain

$$L\left\{u^{\alpha+n}\,v^{\beta+n}\,w^{\gamma+n}\left(1+\frac{xus_1}{a}+\frac{yvs_2}{b}+\frac{zws_3}{c}\right)^n:s_1,\,s_2,\,s_3\right\}$$

$$=\frac{\Gamma(\alpha+n+1)\Gamma(\beta+n+1)\Gamma(\gamma+n+1)}{s_1^{\alpha+n+1}\,s_2^{\beta+n+1}\,s_3^{\gamma+n+1}}\,Y_n^{(\alpha,\beta,\gamma)}\,(x,\,y,z;a,\,b,\,c) \tag{6.7}$$

VII. Generating Functions

It is easy to derive the following generating functions for $Y_n^{(\alpha,\beta,\gamma)}(x,\,y,z;a,\,b,\,c)$:

$$\sum_{n=0}^\infty\frac{t^n}{n!}\,Y_n^{(\alpha-n,\beta-n,\gamma-n)}(x,\,y,z;a,\,b,\,c)=e^t\left(1-\frac{xt}{a}\right)^{-\alpha-1}\left(1-\frac{yt}{b}\right)^{-\beta-1}\left(1-\frac{zt}{c}\right)^{-\gamma-1} \tag{7.1}$$

$$\sum_{n=0}^\infty\frac{t^n}{n!}\,Y_n^{(\alpha,\beta-n,\gamma-n)}(x,\,y,z;a,\,b,\,c)$$

$$=\left(1-\frac{4xt}{a}\right)^{-\frac{1}{2}}\left[\frac{2}{1+\sqrt{1-\dfrac{4xt}{a}}}\right]^\alpha\left[1-\frac{\dfrac{2yt}{b}}{1+\sqrt{1-\dfrac{4xt}{a}}}\right]^{-\beta-1}\left[1-\frac{\dfrac{2zt}{c}}{1+\sqrt{1-\dfrac{4xt}{a}}}\right]^{-\gamma-1}e^{\dfrac{2t}{1+\sqrt{1-\dfrac{4xt}{a}}}}$$

$$\tag{7.2}$$

$$\sum_{n=0}^\infty\frac{t^n}{n!}\,Y_n^{(\alpha-n,\beta,\gamma-n)}(x,\,y,z;a,\,b,\,c)$$

$$=\left(1-\frac{4yt}{b}\right)^{-\frac{1}{2}}\left[\frac{2}{1+\sqrt{1-\dfrac{4yt}{b}}}\right]^\beta\left[1-\frac{\dfrac{2xt}{a}}{1+\sqrt{1-\dfrac{4yt}{b}}}\right]^{-\alpha-1}\left[1-\frac{\dfrac{2zt}{c}}{1+\sqrt{1-\dfrac{4yt}{b}}}\right]^{-\gamma-1}e^{\dfrac{2t}{1+\sqrt{1-\dfrac{4yt}{b}}}}$$

$$\tag{7.3}$$

$$\sum_{n=0}^\infty\frac{t^n}{n!}\,Y_n^{(\alpha-n,\beta-n,\gamma)}(x,\,y,z;a,\,b,\,c)$$

$$= \left(1 - \frac{4zt}{c}\right)^{-\frac{1}{2}} \left[\frac{2}{1 + \sqrt{1 - \frac{4zt}{c}}}\right]^{\gamma} \left[1 - \frac{\frac{2xt}{a}}{1 + \sqrt{1 - \frac{4zt}{c}}}\right]^{-\alpha-1} \left[1 - \frac{\frac{2yt}{b}}{1 + \sqrt{1 - \frac{4zt}{c}}}\right]^{-\beta-1} e^{\frac{2t}{1 + \sqrt{1 - \frac{4zt}{c}}}} \quad (7.4)$$

$$\sum_{n=0}^{\infty} \frac{t^n}{n!} Y_n^{(\alpha-2n, \beta-n, \gamma-n)}(x, y, z; a, b, c)$$

$$= e^{\frac{at}{a+xt}} \left(1 + \frac{xt}{a}\right)^{\alpha} \left\{1 - \frac{ayt}{b(a+xt)}\right\}^{-\beta-1} \left\{1 - \frac{azt}{c(a+xt)}\right\}^{-\gamma-1} \quad (7.5)$$

$$\sum_{n=0}^{\infty} \frac{t^n}{n!} Y_n^{(\alpha-n, \beta-2n, \gamma-n)}(x, y, z; a, b, c)$$

$$= e^{\frac{bt}{b+yt}} \left(1 + \frac{yt}{b}\right)^{\beta} \left\{1 - \frac{bxt}{a(b+yt)}\right\}^{-\alpha-1} \left\{1 - \frac{bzt}{c(b+yt)}\right\}^{-\gamma-1} \quad (7.6)$$

$$\sum_{n=0}^{\infty} \frac{t^n}{n!} Y_n^{(\alpha-n, \beta-n, \gamma-2n)}(x, y, z; a, b, c)$$

$$= e^{\frac{ct}{c+zt}} \left(1 + \frac{zt}{c}\right)^{\gamma} \left\{1 - \frac{cxt}{a(c+zt)}\right\}^{-\alpha-1} \left\{1 - \frac{cyt}{b(c+zt)}\right\}^{-\beta-1} \quad (7.7)$$

$$\sum_{k=0}^{\infty} (-\lambda)^k Y_n^{(\alpha, \beta, k-n)}(x, y, z; a, b, c) = \frac{1}{1+\lambda} Y_n^{(\alpha, \beta, -n)}(x, y, z; a, b, c(1+\lambda)) \quad (7.8)$$

$$\sum_{k=0}^{\infty} (-\lambda)^k Y_n^{(\alpha, k-n, \gamma)}(x, y, z; a, b, c) = \frac{1}{1+\lambda} Y_n^{(\alpha, -n, \gamma)}(x, y, z; a, b(1+\lambda), c) \quad (7.9)$$

$$\sum_{k=0}^{\infty} (-\lambda)^k Y_n^{(k-n, \beta, \gamma)}(x, y, z; a, b, c) = \frac{1}{1+\lambda} Y_n^{(-n, \beta, \gamma)}(x, y, z; a(1+\lambda), b, c) \quad (7.10)$$

Using (3.1), we can also derive the following results :

$$\sum_{k=0}^{\infty} \frac{(-\lambda)^k}{k!} Y_n^{(\alpha, \beta, k-n)}(x, y, z; a, b, c)$$

$$= \frac{1}{\Gamma(\alpha+n+1)\Gamma(\beta+n+1)} \int_0^{\infty} \int_0^{\infty} \int_0^{\infty} u^{\alpha+n} v^{\beta+n} \left(1 + \frac{xu}{a} + \frac{yv}{b} + \frac{zw}{c}\right)^n e^{-u-v-w} J_0\left(2\sqrt{\lambda w}\right) du\, dv\, dw$$

$$(7.11)$$

$$\sum_{k=0}^{\infty} \frac{(-\lambda)^k}{k!} Y_n^{(\alpha, k-n, \gamma)}(x, y, z; a, b, c)$$

$$= \frac{1}{\Gamma(\alpha+n+1)\Gamma(\gamma+n+1)} \int_0^{\infty} \int_0^{\infty} \int_0^{\infty} u^{\alpha+n} w^{\gamma+n} \left(1 + \frac{xu}{a} + \frac{yv}{b} + \frac{zw}{c}\right)^n e^{-u-v-w} J_0\left(2\sqrt{\lambda v}\right) du\, dv\, dw$$

$$(7.12)$$

$$\sum_{k=0}^{\infty} \frac{(-\lambda)^k}{k!} Y_n^{(k-n, \beta, \gamma)}(x, y, z; a, b, c)$$

$$= \frac{1}{\Gamma(\beta+n+1)\Gamma(\gamma+n+1)} \int_0^{\infty} \int_0^{\infty} \int_0^{\infty} u^{\beta+n} w^{\gamma+n} \left(1 + \frac{xu}{a} + \frac{yv}{b} + \frac{zw}{c}\right)^n e^{-u-v-w} J_0\left(2\sqrt{\lambda u}\right) du\, dv\, dw$$

$$(7.13)$$

$$\sum_{k=0}^{\infty} (-1)^k \ \lambda^{2k} \ Y_n^{(\alpha,\beta,2k-n)}(x,y,z;a,b,c)$$

$$= \frac{1}{\Gamma(\alpha+n+1)\Gamma(\beta+n+1)} \int_0^{\infty} \int_0^{\infty} \int_0^{\infty} u^{\alpha+n} v^{\beta+n} \left(1 + \frac{xu}{a} + \frac{yv}{b} + \frac{zw}{c}\right)^n e^{-u-v-w} \cos \lambda w \ du \ dv \ dw$$

(7.14)

$$\sum_{k=0}^{\infty} (-1)^k \lambda^{2k} \ Y_n^{(\alpha,2k-n,\gamma)}(x,y,z;a,b,c)$$

$$= \frac{1}{\Gamma(\alpha+n+1)\Gamma(\gamma+n+1)} \int_0^{\infty} \int_0^{\infty} \int_0^{\infty} u^{\alpha+n} w^{\gamma+n} \left(1 + \frac{xu}{a} + \frac{yv}{b} + \frac{zw}{c}\right)^n e^{-u-v-w} \cos \lambda v \ du \ dv \ dw$$

(7.15)

$$\sum_{k=0}^{\infty} (-1)^k \ \lambda^{2k} \ Y_n^{(2k-n,\beta,\gamma)}(x,y,z;a,b,c)$$

$$= \frac{1}{\Gamma(\beta+n+1)\Gamma(\gamma+n+1)} \int_0^{\infty} \int_0^{\infty} \int_0^{\infty} u^{\beta+n} w^{\gamma+n} \left(1 + \frac{xu}{a} + \frac{yv}{b} + \frac{zw}{c}\right)^n e^{-u-v-w} \cos \lambda u \ du \ dv \ dw$$

(7.16)

$$\sum_{k=0}^{\infty} (-1)^k \ \lambda^{2k+1} \ Y_n^{(\alpha,\beta,2k+1-n)}(x,y,z;a,b,c)$$

$$= \frac{1}{\Gamma(\alpha+n+1)\Gamma(\beta+n+1)} \int_0^{\infty} \int_0^{\infty} \int_0^{\infty} u^{\alpha+n} v^{\beta+n} \left(1 + \frac{xu}{a} + \frac{yv}{b} + \frac{zw}{c}\right)^n e^{-u-v-w} \sin \lambda w \ du \ dv \ dw$$

(7.17)

$$\sum_{k=0}^{\infty} (-1)^k \ \lambda^{2k+1} \ Y_n^{(\alpha,2k+1-n,\gamma)}(x,y,z;a,b,c)$$

$$= \frac{1}{\Gamma(\alpha+n+1)\Gamma(\gamma+n+1)} \int_0^{\infty} \int_0^{\infty} \int_0^{\infty} u^{\alpha+n} w^{\gamma+n} \left(1 + \frac{xu}{a} + \frac{yv}{b} + \frac{zw}{c}\right)^n e^{-u-v-w} \sin \lambda v \ du \ dv \ dw$$

(7.18)

$$\sum_{k=0}^{\infty} (-1)^k \ \lambda^{2k+1} \ Y_n^{(2k+1-n,\beta,\gamma)}(x,y,z;a,b,c)$$

$$= \frac{1}{\Gamma(\beta+n+1)\Gamma(\gamma+n+1)} \int_0^{\infty} \int_0^{\infty} \int_0^{\infty} u^{\beta+n} w^{\gamma+n} \left(1 + \frac{xu}{a} + \frac{yv}{b} + \frac{zw}{c}\right)^n e^{-u-v-w} \sin \lambda u \ du \ dv \ dw$$

(7.19)

VIII. Double Generating Functions

The following double generating functions for $Y_n^{(\alpha,\beta,\gamma)}(x,y,z;a,b,c)$ can easily be derived by using (3.1)

$$\sum_{m=0}^{\infty} \sum_{k=0}^{\infty} (-\lambda)^m (-\mu)^k \ Y_n^{(m-n,k-n,\gamma)}(x,y,z;a,b,c)$$

$$= \frac{1}{(1+\lambda)(1+\mu)} \ Y_n^{(-n,-n,\gamma)}(x,y,z;a(1+\lambda),b(1+\mu),c)$$

(8.1)

$$\sum_{m=0}^{\infty} \sum_{k=0}^{\infty} (-\lambda)^m (-\mu)^k \ Y_n^{(m-n,\beta,k-n)}(x,y,z;a,b,c)$$

$$= \frac{1}{(1+\lambda)(1+\mu)} \ Y_n^{(-n,\beta,-n)}(x,y,z;a(1+\lambda),b,c(1+\mu))$$

(8.2)

$$\sum_{m=0}^{\infty} \sum_{k=0}^{\infty} (-\lambda)^m (-\mu)^k \; Y_n^{(\alpha, \, m-n, \, k-n)} (x, y, z; a, b, c)$$

$$= \frac{1}{(1+\lambda)(1+\mu)} \; Y_n^{(\alpha, \, -n, \, -n)} (x, y, z; a, b(1+\lambda), c(1+\mu)) \tag{8.3}$$

$$\sum_{m=0}^{\infty} \sum_{k=0}^{\infty} \frac{(-\lambda)^m (-\mu)^k}{m! \; k!} Y_n^{(m-n, \, k-n, \gamma)} (x, y, z; a, b, c)$$

$$= \frac{1}{\Gamma(\gamma+n+1)} \int_0^{\infty} \int_0^{\infty} \int_0^{\infty} w^{\gamma+n} \left(1+\frac{xu}{a}+\frac{yv}{b}+\frac{zw}{c}\right)^n e^{-u-v-w} J_0\left(2\sqrt{\lambda u}\right) J_0\left(2\sqrt{\mu v}\right) du \, dv \, dw \tag{8.4}$$

$$\sum_{m=0}^{\infty} \sum_{k=0}^{\infty} \frac{(-\lambda)^m (-\mu)^k}{m! \; k!} Y_n^{(m-n, \, \beta, \, k-n)} (x, y, z; a, b, c)$$

$$= \frac{1}{\Gamma(\beta+n+1)} \int_0^{\infty} \int_0^{\infty} \int_0^{\infty} v^{\beta+n} \left(1+\frac{xu}{a}+\frac{yv}{b}+\frac{zw}{c}\right)^n e^{-u-v-w} J_0\left(2\sqrt{\lambda u}\right) J_0\left(2\sqrt{\mu w}\right) du \, dv \, dw \tag{8.5}$$

$$\sum_{m=0}^{\infty} \sum_{k=0}^{\infty} \frac{(-\lambda)^m (-\mu)^k}{m! \; k!} Y_n^{(\alpha, \, m-n, \, k-n)} (x, y, z; a, b, c)$$

$$= \frac{1}{\Gamma(\alpha+n+1)} \int_0^{\infty} \int_0^{\infty} \int_0^{\infty} u^{\alpha+n} \left(1+\frac{xu}{a}+\frac{yv}{b}+\frac{zw}{c}\right)^n e^{-u-v-w} J_0\left(2\sqrt{\lambda v}\right) J_0\left(2\sqrt{\mu w}\right) du \, dv \, dw \tag{8.6}$$

$$\sum_{m=0}^{\infty} \sum_{k=0}^{\infty} (-1)^{m+k} \; \lambda^{2m} \mu^{2k} \; Y_n^{(2m-n, \, 2k-n, \gamma)} (x, y, z; a, b, c)$$

$$= \frac{1}{\Gamma(\gamma+n+1)} \int_0^{\infty} \int_0^{\infty} \int_0^{\infty} w^{\gamma+n} \left(1+\frac{xu}{a}+\frac{yv}{b}+\frac{zw}{c}\right)^n e^{-u-v-w} \cos \lambda u \cos \mu v \; du \, dv \, dw \tag{8.7}$$

$$\sum_{m=0}^{\infty} \sum_{k=0}^{\infty} (-1)^{m+k} \; \lambda^{2m} \mu^{2k} \; Y_n^{(2m-n, \, \beta, \, 2k-n)} (x, y, z; a, b, c)$$

$$= \frac{1}{\Gamma(\beta+n+1)} \int_0^{\infty} \int_0^{\infty} \int_0^{\infty} v^{\beta+n} \left(1+\frac{xu}{a}+\frac{yv}{b}+\frac{zw}{c}\right)^n e^{-u-v-w} \cos \lambda u \; \cos \mu w \; du \, dv \, dw \tag{8.8}$$

$$\sum_{m=0}^{\infty} \sum_{k=0}^{\infty} (-1)^{m+k} \; \lambda^{2m} \mu^{2k} \; Y_n^{(\alpha, \, 2m-n, \, 2k-n)} (x, y, z; a, b, c)$$

$$= \frac{1}{\Gamma(\alpha+n+1)} \int_0^{\infty} \int_0^{\infty} \int_0^{\infty} u^{\alpha+n} \left(1+\frac{xu}{a}+\frac{yv}{b}+\frac{zw}{c}\right)^n e^{-u-v-w} \cos \lambda v \; \cos \mu w \; du \, dv \, dw \tag{8.9}$$

$$\sum_{m=0}^{\infty} \sum_{k=0}^{\infty} (-1)^{m+k} \; \lambda^{2m+1} \mu^{2k} \; Y_n^{(2m+1-n, \, 2k-n, \gamma)} (x, y, z; a, b, c)$$

$$= \frac{1}{\Gamma(\gamma+n+1)} \int_0^{\infty} \int_0^{\infty} \int_0^{\infty} w^{\gamma+n} \left(1+\frac{xu}{a}+\frac{yv}{b}+\frac{zw}{c}\right)^n e^{-u-v-w} \sin \lambda u \cos \mu v \; du \, dv \, dw \tag{8.10}$$

$$\sum_{m=0}^{\infty} \sum_{k=0}^{\infty} (-1)^{m+k} \; \lambda^{2m+1} \mu^{2k} \; Y_n^{(2m+1-n, \, \beta, \, 2k-n)} (x, y, z; a, b, c)$$

$$= \frac{1}{\Gamma(\beta+n+1)} \int_0^\infty \int_0^\infty \int_0^\infty v^{\beta+n} \left(1 + \frac{xu}{a} + \frac{yv}{b} + \frac{zw}{c}\right)^n e^{-u-v-w} \sin \lambda u \cos \mu w \; du \, dv \, dw$$

<div align="right">(8.11)</div>

$$\sum_{m=0}^\infty \sum_{k=0}^\infty (-1)^{m+k} \; \lambda^{2m+1} \, \mu^{2k} \, Y_n^{(\alpha, \, 2m+1-n, \, 2k-n)} \left(x, \, y, z; a, b, c\right)$$

$$= \frac{1}{\Gamma(\alpha+n+1)} \int_0^\infty \int_0^\infty \int_0^\infty u^{\alpha+n} \left(1 + \frac{xu}{a} + \frac{yv}{b} + \frac{zw}{c}\right)^n e^{-u-v-w} \sin \lambda v \cos \mu w \; du \, dv \, dw$$

<div align="right">(8.12)</div>

$$\sum_{m=0}^\infty \sum_{k=0}^\infty (-1)^{m+k} \; \lambda^{2m} \, \mu^{2k+1} \, Y_n^{(2m-n, \, 2k+1-n, \, \gamma)} \left(x, \, y, z; a, b, c\right)$$

$$= \frac{1}{\Gamma(\gamma+n+1)} \int_0^\infty \int_0^\infty \int_0^\infty w^{\gamma+n} \left(1 + \frac{xu}{a} + \frac{yv}{b} + \frac{zw}{c}\right)^n e^{-u-v-w} \cos \lambda u \sin \mu v \; du \, dv \, dw$$

<div align="right">(8.13)</div>

$$\sum_{m=0}^\infty \sum_{k=0}^\infty (-1)^{m+k} \; \lambda^{2m} \, \mu^{2k+1} \, Y_n^{(2m-n, \, \beta, \, 2k+1-n)} \left(x, \, y, z; a, b, c\right)$$

$$= \frac{1}{\Gamma(\beta+n+1)} \int_0^\infty \int_0^\infty \int_0^\infty v^{\beta+n} \left(1 + \frac{xu}{a} + \frac{yv}{b} + \frac{zw}{c}\right)^n e^{-u-v-w} \cos \lambda u \sin \mu w \; du \, dv \, dw$$

<div align="right">(8.14)</div>

$$\sum_{m=0}^\infty \sum_{k=0}^\infty (-1)^{m+k} \; \lambda^{2m} \, \mu^{2k+1} \, Y_n^{(\alpha, \, 2m-n, \, 2k+1-n)} \left(x, \, y, z; a, b, c\right)$$

$$= \frac{1}{\Gamma(\alpha+n+1)} \int_0^\infty \int_0^\infty \int_0^\infty u^{\alpha+n} \left(1 + \frac{xu}{a} + \frac{yv}{b} + \frac{zw}{c}\right)^n e^{-u-v-w} \cos \lambda v \sin \mu w \; du \, dv \, dw$$

<div align="right">(8.15)</div>

$$\sum_{m=0}^\infty \sum_{k=0}^\infty (-1)^{m+k} \; \lambda^{2m+1} \, \mu^{2k+1} \, Y_n^{(2m+1-n, \, 2k+1-n, \, \gamma)} \left(x, \, y, z; a, b, c\right)$$

$$= \frac{1}{\Gamma(\gamma+n+1)} \int_0^\infty \int_0^\infty \int_0^\infty w^{\gamma+n} \left(1 + \frac{xu}{a} + \frac{yv}{b} + \frac{zw}{c}\right)^n e^{-u-v-w} \sin \lambda u \sin \mu v \; du \, dv \, dw$$

<div align="right">(8.16)</div>

$$\sum_{m=0}^\infty \sum_{k=0}^\infty (-1)^{m+k} \; \lambda^{2m+1} \, \mu^{2k+1} \, Y_n^{(2m+1-n, \, \beta, \, 2k+1-n)} \left(x, \, y, z; a, b, c\right)$$

$$= \frac{1}{\Gamma(\beta+n+1)} \int_0^\infty \int_0^\infty \int_0^\infty v^{\beta+n} \left(1 + \frac{xu}{a} + \frac{yv}{b} + \frac{zw}{c}\right)^n e^{-u-v-w} \sin \lambda u \sin \mu w \; du \, dv \, dw$$

<div align="right">(8.17)</div>

$$\sum_{m=0}^\infty \sum_{k=0}^\infty (-1)^{m+k} \; \lambda^{2m+1} \, \mu^{2k+1} \, Y_n^{(\alpha, \, 2m+1-n, \, 2k+1-n)} \left(x, \, y, z; a, b, c\right)$$

$$= \frac{1}{\Gamma(\alpha+n+1)} \int_0^\infty \int_0^\infty \int_0^\infty u^{\alpha+n} \left(1 + \frac{xu}{a} + \frac{yv}{b} + \frac{zw}{c}\right)^n e^{-u-v-w} \sin \lambda v \sin \mu w \; du \, dv \, dw$$

<div align="right">(8.18)</div>

IX. Triple Generating Functions

The following triple generating functions can easily be obtained by using (3.1):

$$\sum_{m=0}^{\infty} \sum_{k=0}^{\infty} \sum_{j=0}^{\infty} (-\lambda)^m (-\mu)^k (-\eta)^j \, Y_n^{(m-n, \, k-n, \, j-n)} (x, \, y, z; a, b, c)$$

$$= \frac{1}{(1+\lambda)(1+\mu)(1+\eta)} Y_n^{(-n, \, -n, \, -n)} (x, \, y, z; a(1+\lambda), b(1+\mu), c(1+\eta)) \qquad (9.1)$$

$$\sum_{m=0}^{\infty} \sum_{k=0}^{\infty} \sum_{j=0}^{\infty} \frac{(-\lambda)^m (-\mu)^k (-\eta)^j}{m! \, k! \, j!} \, Y_n^{(m-n, \, k-n, \, j-n)} (x, \, y, z; a, b, c)$$

$$= \int_0^{\infty} \int_0^{\infty} \int_0^{\infty} \left(1 + \frac{xu}{a} + \frac{yv}{b} + \frac{zw}{c}\right)^n e^{-u-v-w} J_0\left(2\sqrt{\lambda u}\right) J_0\left(2\sqrt{\mu v}\right) J_0\left(2\sqrt{\eta w}\right) du \, dv \, dw \qquad (9.2)$$

$$\sum_{m=0}^{\infty} \sum_{k=0}^{\infty} \sum_{j=0}^{\infty} (-1)^{m+k+j} \, \lambda^{2m} \mu^{2k} \eta^{2j} \, Y_n^{(2m-n, \, 2k-n, \, 2j-n)} (x, \, y, z; a, b, c)$$

$$= \int_0^{\infty} \int_0^{\infty} \int_0^{\infty} \left(1 + \frac{xu}{a} + \frac{yv}{b} + \frac{zw}{c}\right)^n e^{-u-v-w} \cos \lambda u \, \cos \mu v \, \cos \eta w \, du \, dv \, dw \qquad (9.3)$$

$$\sum_{m=0}^{\infty} \sum_{k=0}^{\infty} \sum_{j=0}^{\infty} (-1)^{m+k+j} \, \lambda^{2m+1} \mu^{2k+1} \eta^{2j+1} \, Y_n^{(2m+1-n, \, 2k+1-n, \, 2j+1-n)} (x, \, y, z; a, b, c)$$

$$= \int_0^{\infty} \int_0^{\infty} \int_0^{\infty} \left(1 + \frac{xu}{a} + \frac{yv}{b} + \frac{zw}{c}\right)^n e^{-u-v-w} \sin \lambda u \, \sin \mu v \, \sin \eta w \, du \, dv \, dw \qquad (9.4)$$

$$\sum_{m=0}^{\infty} \sum_{k=0}^{\infty} \sum_{j=0}^{\infty} (-1)^{m+k+j} \, \lambda^{2m+1} \mu^{2k+1} \eta^{2j} \, Y_n^{(2m+1-n, \, 2k+1-n, \, 2j-n)} (x, \, y, z; a, b, c)$$

$$= \int_0^{\infty} \int_0^{\infty} \int_0^{\infty} \left(1 + \frac{xu}{a} + \frac{yv}{b} + \frac{zw}{c}\right)^n e^{-u-v-w} \sin \lambda u \, \sin \mu v \, \cos \eta w \, du \, dv \, dw \qquad (9.5)$$

$$\sum_{m=0}^{\infty} \sum_{k=0}^{\infty} \sum_{j=0}^{\infty} (-1)^{m+k+j} \, \lambda^{2m} \mu^{2k} \eta^{2j+1} \, Y_n^{(2m-n, \, 2k-n, \, 2j+1-n)} (x, \, y, z; a, b, c)$$

$$= \int_0^{\infty} \int_0^{\infty} \int_0^{\infty} \left(1 + \frac{xu}{a} + \frac{yv}{b} + \frac{zw}{c}\right)^n e^{-u-v-w} \cos \lambda u \, \cos \mu v \, \sin \eta w \, du \, dv \, dw \qquad (9.6)$$

X. Bessel Polynomials Of M-Variables

The Bessel polynomials of m-variables $Y_n^{(\alpha_1, \alpha_2, ----, \alpha_m)} (x_1, x_2, ----, x_m; a_1, a_2, ----, a_m)$ can be defined as follows:

$$Y_n^{(\alpha_1, \alpha_2, ----, \alpha_m)} (x_1, x_2, ----, x_m; a_1, a_2, ----, a_m)$$

$$\sum_{r_1=0}^{n} \sum_{r_2=0}^{n-r_1} \sum_{r_3=0}^{n-r_1-r_2} ---- \sum_{r_m=0}^{n-r_1-r_2----r_{m-1}} \frac{(-n)_{r_1+r_2+---+r_m} \prod_{i=0}^{m} (\alpha_i + n + 1)_j}{\prod_{i=0}^{m} r_i!} \prod_{i=0}^{m} \left(-\frac{x_i}{a_i}\right) \qquad (10.1)$$

All the results of this paper can be extended for this m-variable Bessel polynomials. The only hinderance in their study is the representation of results in hypergeometric functions of m-variables.

REFERENCES

[1.] R. P. Agarwal: On Bessel polynomials, **Canadian Journal of Mathematics,** Vol. 6 (1954), pp. 410 – 415.

[2.] W. A. Al-Salam: On Bessel polynomials, **Duke Math. J.,** Vol. 24 (1957), pp. 529 – 545.

[3.] F.Brafman: A set of generating functions for Bessel polynomials, **Proc. Amer. Math Soc.,** Vol. 4 (1953), pp. 275 – 277.

[4.] J. L. Burchnall: The Bessel polynomials, **Canadian Journal of Mathematics,** Vol. 3 (1951), pp 62 – 68.

[5.] L. Carlitz: On the Bessel polynomials, **Duke Math. Journal**, Vol. 24 (1957), pp. 151 – 162.

[6.] S. K. Chatterjea: Some generating functions, **Duke Math. Journal**, Vol. 32 (1965), pp. 563 – 564.

[7.] D. Dickinson: On Lommel and Bessel polynomials, **Proc. Amar. Math. Soc.**, Vol. 5 (1954), pp. 946 – 956.

[8.] A. Erdelyi et. al: Higher Transcendal Functions, I, **McGraw Hill, New York (1953).**

[9.] M. T. Eweida: On Bessel polynomials, **Math. Zeitsehr.,** Vol. 74 (1960), pp. 319 – 324.

[10.] E. Grosswald: On some algebraic properties of the Bessel polynomials, **Trans. Amer. Math. Soc.**, Vol. 71 (1951), pp. 197 – 210.

[11.] M. A. Khan and K. Ahmad: On a two variables analogue of Bessel polynomials, **Mathematica Balkanica**, New series Vol. 14, (2000), Fasc. 1 – 2, pp. 65 – 76.

[12.] H. L. Krall: and O. Frink A new class of orthogonal polynomials, the Bessel polynomials, **Trans. Amer. Math. Soc.**, Vol. 65 (1949), pp. 100 – 115.

[13.] T. R. Prabhakar: Two singular integral equations involving confluent hypergemetric functions, **Proc. Camb. Phil. Soc.**, Vol. 66 (1969), pp. 71 – 89.

[14.] T. R. Prabhakar: On a set of polynomials suggested by Laguerre polynomials, **Pacific Journal of Mathematics**, Vol. 40 (1972), pp. 311 – 317.

[15.] E. D. Rainville: Generating functions for Bessel and related polynomials, **Canadian J. Math.**, Vol. 5 (1953), pp. 104 – 106.

[16.] E. D. Rainville: Special Functions, MacMillan, New York, Reprinted by **Chelsea Publ. Co., Bronx – New York (1971).**

[17.] H. M. Srivastava: Some biorthogonal polynomials suggested by the Laguerre polynomials, **Pacific J. Math.**, Vol. 98, No. 1 (1982), pp. 235 – 249.

[18.] H. M. Srivastava and H. L. Masnocha: A treatise on Generating Functions, J. Waley & Sons (Halsted Press), New York; **Ellis Horwood, Chichester (1984).**

[19.] L. Toscano: Osservacioni e complementi su particolari polinomiipergeometrici, **Le Matematiche**, Vol. 10 (1955), pp. 121 – 133.

Enhancing Power Quality in Transmission System Using Fc-Tcr

Abhishek Kumar Pashine[1], Satyadharma Bharti[2]

Electrical Engineering Department, Rungta College of Engineering and Technology,
Bhilai., India

Abstract*: FACTS methodology is totally based on power electronics devices which are used to increase the transmission capability. To make the power system flexible, FACTS technology is used to attain entire control of power system i.e. transmission, distribution and generation. This paper is mainly concerned about the significance of Fixed Capacitor Thyristor Control Reactor (FC-TCR) acquiring automatic power and steady state voltage stability with the help of fuzzy logic controller. In transmission systems, the fuzzy rules are set to generate the required firing angle of FC-TCR to maintain a flat profile of steady state voltage and stability. The fundamental model is simulated in MATLAB along with the fuzzy logic control strategy. The results obtained are trust worthy and it can be used for controlling the voltage and reactive power in any electrical transmission system.*
Keywords*: Facts, Fc-Tcr, Flc.*

I. INTRODUCTION

Electrical energy is the superior form of energy out of all energy forms in the world. It is easily controllable and transformable into various others forms (light, heat etc.) of energy. The basic control objectives of a power system are system voltage control, frequency control and protection. A power system is said to be well designed if it provides improve quality of reliable supply. It is said to be of good quality when the voltage levels are maintained within the reasonable limits [1].

In this thesis the first generation FACTS controller SVC type FC-TCR is considered with the fuzzy controller. The transmission line distributed parameters throughout the line, on at no loads or at no load become predominant and consequently the line applied charging VAR. In order to sustain the both side terminal voltage at the load bus bar adequate, reactive reserves are needed. FACTS devices like SVC can maintain voltage or absorb the reactive power at load end bus or at load end bus in transmission line, which helps in attaining economy in power transfer and distribution. The fuzzy control strategy has emerged as one of the most active and fruitful areas for research in the applications of fuzzy set theory [1].

Fuzzy control is based on fuzzy logic and is a logical system which is much closer in spirit to human thinking and nature language than traditional logical system. The fuzzy logic controller (FLC) provides a means for converting a linguistic control strategy based on an expert knowledge into an automatic control strategy. Based on observed results for receiving side voltage variations for various values of load inductance, resistance and capacitance a fuzzy logic controller is designed which controls the triggering angle of FC-TCR in order to automatically maintain the receiving end voltage constant [4].

II. OPERATING PRINCIPLE OF FC-TCR

A basic type VAR generator arrangement using a fixed (permanently connected) capacitor with a Thruster-controlled reactor (FC-TCR) is shown in fig 1.

The current in reactor is varied by firing delay angle control. The fixed capacitor in practice is generally substituted, wholly or partially, by a filter network that has the necessary capacitive impedance at the fundamental frequency to provide the reactive power required, but it generates low impedance at selected frequencies to shunt the dominant harmonics [1].
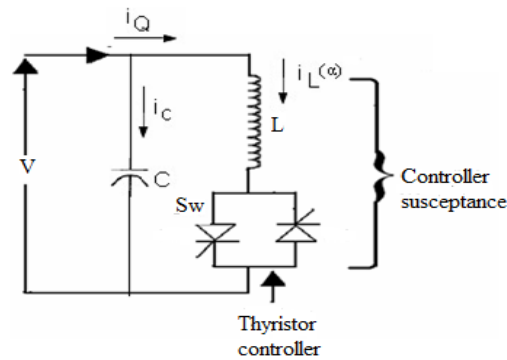
Fig.1 FC-TCR type VAR generator

The FC-TCR type VAR generator may be considered essentially to consist of a variable reactor and a fixed capacitor, with characteristics of overall VAR demand versus VAR output shown in fig 2.
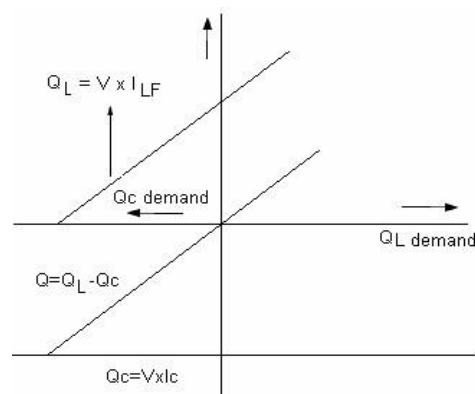

Fig.2 VAR demand versus VAR output characteristics

As seen the capacitive VAR generation of the fixed capacitor is opposed by the variable VAR absorption of the Thruster controlled reactor, to provide the entire VAR output required. At capacitive VAR output, when (α=90) the Thruster Controlled Reactor is off. To reduce the capacitive output, the current in the reactor is raised by decreasing delay angle α. When VAR output is zero, the capacitive and inductive currents become equal and thus capacitive and inductive current cancel out. With a further decrease of angle (assuming that the rating of the capacitor is lesser than that of reactor), the capacitive current becomes lower than the inductive current, resulting in a net inductive VAR output. At (zero) delay angle, the Thruster Controlled Reactor conducts current over the full180° time duration, resulting in maximum inductive VAR output that is equal to the difference between the VARs generated by capacitance and those absorbed by the fully conducting reactor. The control of Thruster controlled reactor in the FC-TCR Type VAR generator needs to provide following basic functions [3].
- Synchronous timing
- Reactive current to triggering angle converter
- Computation of required fundamental reactor current
- Thruster firing pulse generation

The first function is synchronous timing which is generally provided by a phase locked loop circuit that runs in synchronism with the ac system voltage and generates appropriate pulses with respect to the peak of that voltage.

The second function is the reactive current to firing angle conversion. This can be a real time circuit implementation of the mathematical relationship between the amplitude of the fundamental TCR current versus delay angle alpha relationship. The another is a digital "look up table" for the normalized fundamental TCR current versus alpha function which is read at t regular intervals starting from α=0 until the requested value is found, at which instant a firing angle the delay angle corresponding to the required fundamental TCR current. The actual firing instant is then determined by a timing circuit 'measuring' alpha from the peak of the voltage. The current in the reactor is varied by the method of triggering delay angle control.

A filter network that has the mandatory capacitive impedance at the frequency to generate the reactive power required generally substitutes the fixed capacitor in practice, wholly or partially, but it generates low

impedance at selected frequencies to shunt the dominant harmonics produced by the TCR [7].
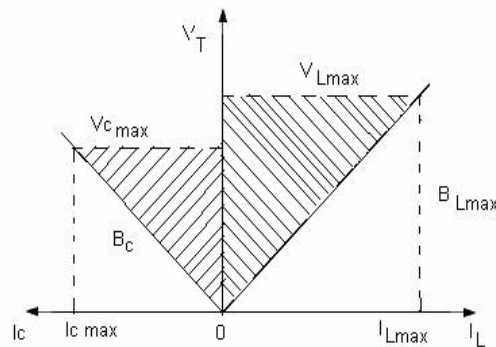

Fig.3 V-I characteristics

In Fig 3 the voltage defines the V-I operating area of the FC-TCR VAR and current rating of the major power components. In the dynamic V-I Characteristics of FC-TCR along with the Load lines showed in the Fig.4. The load characteristics are assumed to be straight lines for Dynamic studies as easily seen that the voltage is improved with compensation when compared without compensation.

III. PROPOSED FUZZY LOGIC CONTROLLER

Fuzzy logic is an advanced control approach with great potential for real time applications and fuzzy inference system in MATLAB Fuzzy logic toolbox. Load voltage and load current are taken as input to fuzzy system. For a closed loop control, error and change in error input can be selected as current or voltage according to control type. To acquire the linearity triangular membership function is taken with fifty percent overlap [2]. The output of fuzzy controller taken as the control signal and the pulse generator provides synchronous firing pulses to thrusters as shown in fig 5.
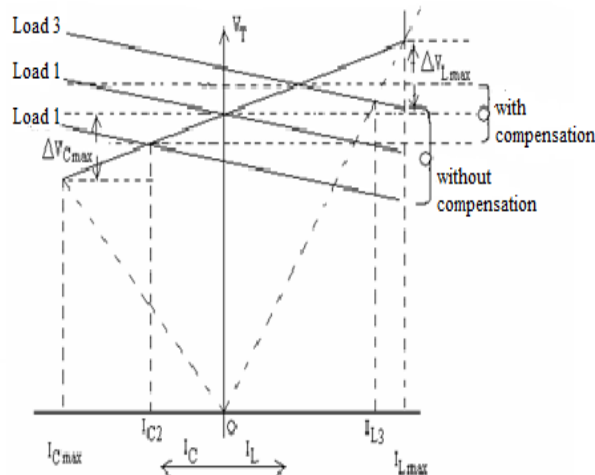

Fig.4 Dynamic V-I characteristics

The Fuzzy Logic control technique is a rule based technique, where a set of rules presents a control decision mechanism to correct the effect of definite causes coming from power system. In fuzzy logic, the seven linguistic variables expressed by fuzzy sets defined on their respective universes of discourse. Table-I shows the proposed membership function rules of FC-TCR controller. The rules chosen for this table are totally based on practical experience of experts and engineers and MATLAB simulation results observed from the behavior of the system around its stable equilibrium points [4].
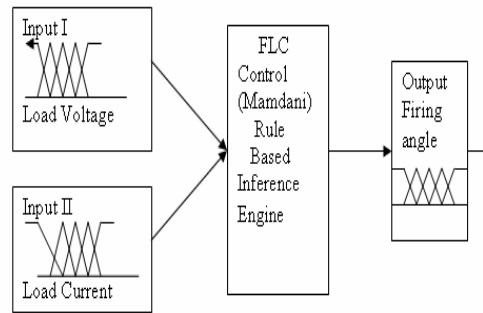
Fig.5 Proposed Fuzzy Logic Controller

TABLE I. Rules for the fuzzy logic controller

		LOAD VOLTAGE						
	ce \ e	NL	NM	NS	Z	PS	PM	PL
L O A D C U R R E N T	NL	NB	NB	NB	NB	NM	NS	Z
	NM	NB	NB	NB	NM	NS	Z	PS
	NS	NB	NB	NM	NS	Z	PS	PM
	Z	NB	NM	NS	PM	PS	PM	PB
	PS	NM	NS	Z	PS	PM	PB	PB
	PM	NS	Z	PS	PM	PB	PB	PB
	PL	Z	PS	PM	PB	PB	PB	PB

IV. FIRING ANGLE GENERATION

The control circuits discussed so far were discrete in nature. But present days specially develop ICs like IC TCA 785 can replace all the discrete circuitry. This IC can be used for triggering the SCR as well as TRIAC in different applications. It can be used in applications such as single phase semiconductor or full converters etc. That facilities like multiple pulse triggering, pulse width adjustment, variation in the firing angle etc. The same IC can be used for triggering the three 2 phase line commutated converter as well a n d for this three IC's are used. Fig.6 shows the fundamental diagram of firing scheme for Thruster with TCA785. The synchronizing signals should be generated by using step down transformers. Fig 6 shows Firing Scheme with TCA 785 IC for SCRs. This IC 785 having output current of 250 mA and a fuzzy logic trainer kit with two input variables and having seven linguistic sets is used. This can generate 7 X 7 rules.
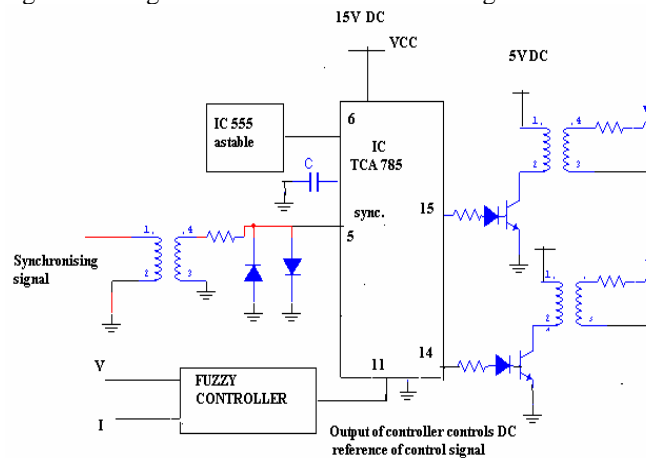

Fig.6 Fundamental diagram of firing scheme for Thruster with TCA785

V. CONTROL STRUCTURE FOR FC-TCR

The control system consists of:

- A measurement system measuring the positive-sequence and negative sequence voltage control.
- A voltage regulator that manipulates the voltage error (difference between the reference voltage and the measured voltage) to determine the FC-TCR susceptance needed to maintain the system voltage constant.
- Fuzzy logic is a computing based or rule based controller with set of rules which represents control decision mechanism to correct the effect of certain cause coming from power system [5].
- A distribution unit that regulate eventually FC-TCR must be switched in and out, and calculate the firing angle of TCRs.
- A synchronizing system synchronizes the secondary voltages and a pulse generator that send appropriate pulses to the thruster [5].

VI. HARDWARE IMPLEMENTATION

The TCR (Thruster Controlled Reactor) block consists of two thrusters in an anti-parallel connection. This setup is connected to a reactor of a fixed value. By changing the firing angles the effective value of inductance is also changed, thus the reactive power absorbed by the reactor is changed which leads to a change in the receiving end voltage. The transmission line used in the network is λ/8 transmission line. A π model is used for representing the transmission line. There are four π sections for long transmission line. Fig.8 shows the long transmission line representation. The firing pulses are generated by the block "firing circuit" which gives the firing angle α for one cycle and 180 − α during the negative cycle. The inputs to this block are the receiving end voltage of the line and a control value (firing angle). The fuzzy toolbox in the MATLAB is used to design the fuzzy controller. The designing of the fuzzy controller is done on the basis of the rules given before. The load current is taken as an input for the fuzzy controller. The firing angle is obtained as the output [7].
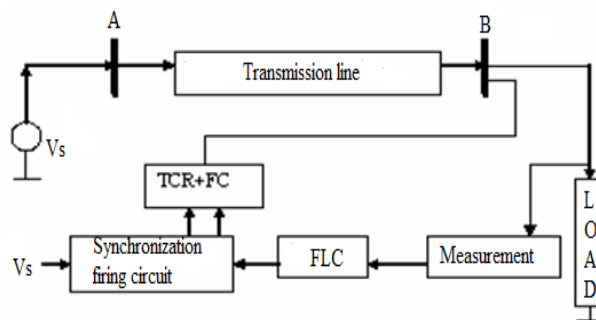

Fig.7 Single phase equivalent circuit with fuzzy control structure of FC-TCR
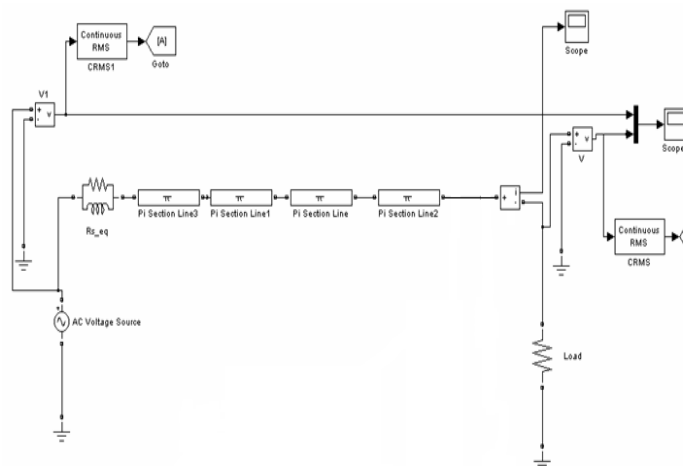

Fig.8 Transmission line representation

VII. RESULTS

The transmission system without any compensation was not fulfilling the required condition of maintaining the voltage within the reasonable limits. At low loads, the receiving end voltage is greater than the sending end voltage as the reactive power produced is greater than absorbed. Fig. 9 shows the voltage before compensation at load 400Ω and fig.10 shows instantaneous voltage after compensation at load 400Ω. Fig11 and 12 shows the RMS voltage before and after compensation at load 400Ω.

VIII. CONCLUSION

This paper deals with a "fuzzy control scheme for FC-TCR" and it can be concluded that the use of fuzzy controlled FC-TCR compensating device with firing angle control is effective, continuous and it is a simplest way of controlling the power and voltage of transmission line. It is observed that FC-TCR device was able to compensate both over and under voltages. Compensating voltages are shown in wave forms. The use of fuzzy logic has facilitated the closed loop control of system, by designing a set of rules, which decides the firing angle given to FC-TCR to attain the required voltage. With MATLAB simulations and actual testing it is observed that SVC type FC-TCR provides an effective reactive power control irrespective of load variation
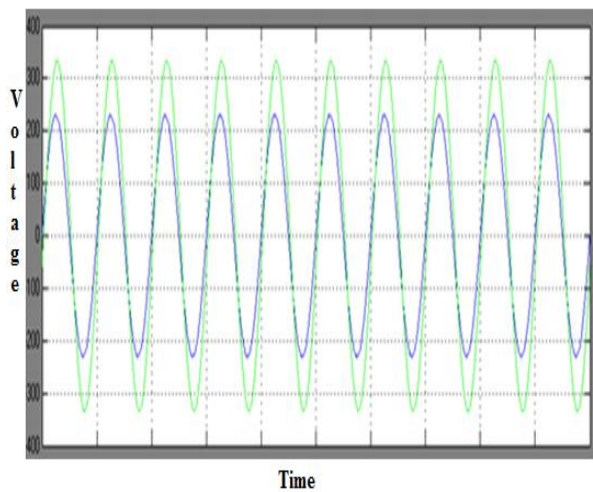

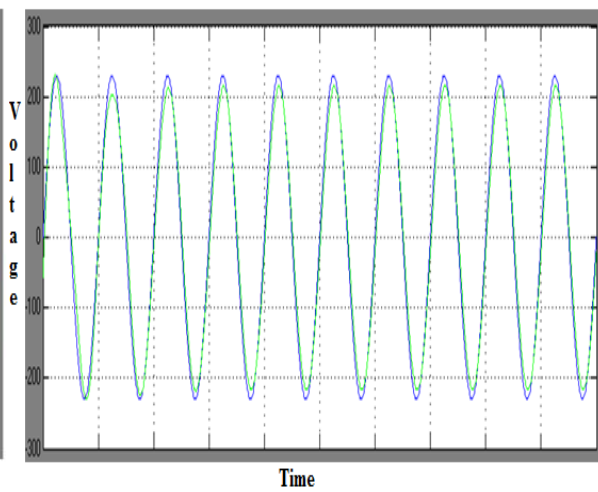Fig. 9 Voltage waveforms before compensation at load R= 400Ω

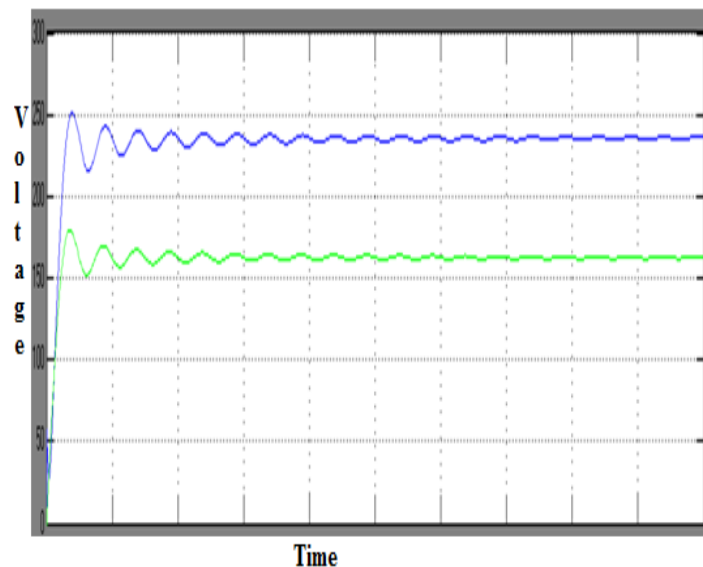Fig. 10 Voltage waveforms after compensation at load R= 400Ω

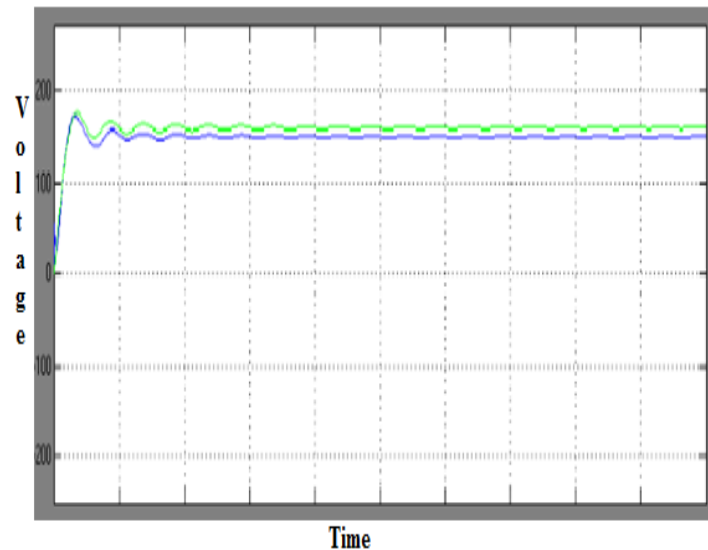
Fig. 11 Voltage waveforms before compensation at load R= 400Ω

Fig. 12 RMS Voltage waveforms before compensation at load R= 400Ω

REFERENCES

[1]   J. J. Peserba, How FACTS Controllers Benefits AC Transmission Systems, IEEE Power Engineering Society General Meeting, 2004, 1257-1262.

[2]   Shilpy Agarwal and Vijay Bhuria, Shunt Active Power Filter for Harmonic Mitigation by Using Fuzzy Logic Controller, International Journal of Advanced Research in Computer Engineering & Technology (IJARCET), 2013, 1950-1954.

[3]   D. Devraj and N. Karpagam, Fuzzy Logic Control of Static VAR Compensator for Power System Damping, International Journal of Electrical and Electronics Engineering, 2009, 625-631.

[4]   Avneesh Kumar Vishwakarma and Dhaneswari Sahu, Efficient Transmission Line Voltage   Regulation Using Fuzzyfied Soft Static VAR Compensator, International Journal of Latest Trends in Engineering and Technology (IJLTET), 2013, 50-57.

[5]   Javid Akhtar and P. M. Shamsudheen, Power Quality Improvement using Fuzzy Logic Control Static VAR Compensator in Power System Networks, ISOR Journal of engineering, 2012, 01-08.

[6]   T. X. Wang, S. S. Choi and E.K.K. Sng, Series Compensation Method to Mitigate Harmonics and Voltage Sags and Swells, IET Generation Transmission Distribution, 2007, 96-103.

[7]   D.Harikrishna, R.S.Dhekekar and N.V.Srikanth, A Novel Approach to Small Signal Stability Enhancement using Fuzzy Logic Controller of   SVC, IEEE Transactions on Power Systems, 2000, 1360-1366.

[8]   Mark Ndubuka Nwohu, Voltage Stability Improvement Using Static Var Compensator in Power Systems,Federal university of Technology Nigeria, 2009, 167-172.

[9]   Sakshi Bangia, Maneesha Garg and P. R. Sharma, Simulation of Fuzzy Logic Based Shunt Hybrid Active Filter for Power Quality Improvement, I. J. Intelligent Systems and Applications MECS, 2013, 96-104.

A Novel Technique for Enhancing Active and Reactive Power Quality for Renewable Energy Sources at Low Voltage Grid

Aiman Saleh Alamin[1], Surya Prakash[2]

1,2 (Libyan water of Ministry, Electrical Engineering Department, University SHIATS, India)

Abstract: *Renewable energy resources (RES) are being increasingly connected in distribution systems utilizing power electronic converters. This paper presents a novel control strategy for achieving maximum benefits from these grid-interfacing inverters when installed in 3-phase 4-wire distribution systems. The inverter is controlled to perform as a multi-function device by incorporating active power filter functionality. The inverter can thus be utilized as: 1) power converter to inject power generated from RES to the grid, and 2) shunt APF to compensate current unbalance, load current harmonics, load reactive power demand and load neutral current. All of these functions may be accomplished either individually or simultaneously. With such a control, the combination of grid-interfacing inverter and the 3-phase 4-wire linear/non-linear unbalanced load at point of common coupling appears as balanced linear load to the grid. This new control concept is demonstrated with extensive MATLAB/Simulink simulation studies and results.*

Keywords: *Power, Technique Grid, wind turbine, Renewable Energy sources.*

I. INTRODUCTION

ELECTRIC utilities and end users of electric power are becoming increasingly concerned about meeting the growing energy demand. Seventy five percent of total global energy demand is supplied by the burning of fossil fuels. But increasing air pollution, global warming concerns, diminishing fossil fuels and their increasing cost have made it necessary to look towards renewable sources as a future energy solution. Since the past decade, there has been an enormous interest in many countries on renewable energy for power generation. The market liberalization and government's incentives have further accelerated the renewable energy sector growth. Renewable energy source (RES) integrated at distribution level is termed as distributed generation (DG). The utility is concerned due to the high penetration level of intermittent RES in distribution systems as it may pose a threat to network in terms of stability, voltage regulation and power-quality (PQ) issues. Therefore, the DG systems are required to comply with strict technical and regulatory frameworks to ensure safe, reliable and efficient operation of overall network. With the advancement in power electronics and digital control technology, the DG systems can now be actively controlled to enhance the system operation with improved PQ at PCC.

However, the extensive use of power electronics based equipment and non-linear loads at PCC generate harmonic cur rents, which may deteriorate the quality of power [1], [2]. Generally, current controlled voltage source inverters are used to interface the intermittent RES in distributed system. Recently, a few control strategies for grid connected inverters incorporating PQ solution have been proposed. In [3] an inverter operates as active inductor at a certain frequency to absorb the harmonic current. But the exact calculation of network inductance in real-time is difficult and may deteriorate the control performance. A similar approach in which a shunt active filter acts as active conductance to damp out the harmonics in distribution network is proposed in [4]. In [5], a control strategy for renewable interfacing inverter based on – theory is proposed. In this strategy both load and inverter current sensing is required to compensate the load current harmonics.

The non-linear load current harmonics may result in voltage harmonics and can create a serious PQ problem in the power system network. Active power filters (APF) are extensively used to compensate the load current harmonics and load unbalance at distribution level. This results in an additional hardware cost. However, in this paper authors have incorporated the features of APF in the, conventional inverter interfacing renewable with the grid, without any additional hardware cost. Here, the main idea is the maximum utilization of inverter rating which is most of the time underutilized due to intermittent nature of RES. It is shown in this paper that the grid-interfacing inverter can effectively be utilized to perform following important functions: 1) transfer of active power harvested from the renewable resources (wind, solar, etc.); 2) load reactive power demand support; 3) current harmonics compensation at PCC; and 4) current unbalance and neutral current compensation in case of 3-phase 4-wire system. Moreover, with adequate control of grid-interfacing inverter, all the four objectives can

be accomplished either individually or simultaneously. The PQ constraints at the PCC can therefore be strictly maintained within the utility standards without additional hardware cost.
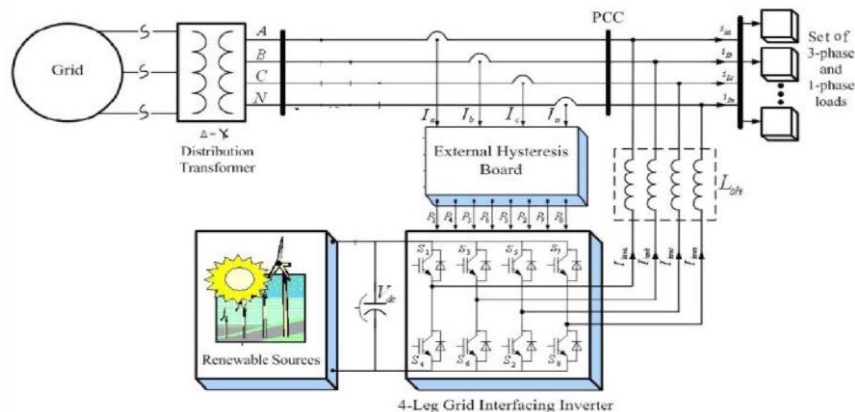

Fig. 1: Schematic of proposed renewable based distributed generation system

The paper is arranged as follows: Section II describes the system under consideration and the controller for grid interfacing inverter. A digital simulation study is presented in Section III. Section IV concludes the paper.

II. SYSTEM DESCRIPTION

The proposed system consists of RES connected to the dc-link of a grid-interfacing inverter as shown in Fig. 1. The voltage source inverter is a key element of a DG system as it interfaces the renewable energy source to the grid and delivers the generated power. The RES may be a DC source or an AC source with rectifier coupled to dc-link. Usually, the fuel cell and photovoltaic energy sources generate power at variable low dc voltage, while the variable speed wind turbines generate power at variable ac voltage. Thus, the power generated from these renewable sources needs power conditioning (i.e., dc/dc or ac/dc) before connecting on dc-link [6]–[8]. The dc-capacitor decouples the RES from grid and also allows independent control of converters on either side of dc-link.

A. DC-Link Voltage and Power Control Operation

Due to the intermittent nature of RES, the generated power is of variable nature. The dc-link plays an important role in transferring this variable power from renewable energy source to the grid. RES are represented as current sources connected to the dc-link of a grid-interfacing inverter. Fig. 2 shows the systematic representation of power transfer from the renewable energy resources to the grid via the dc-link. The current injected by renewable into dc-link at voltage level V_{dc} can be given as:

$$I_{dc1} = \frac{P_{RES}}{V_{dc}} \qquad (1)$$
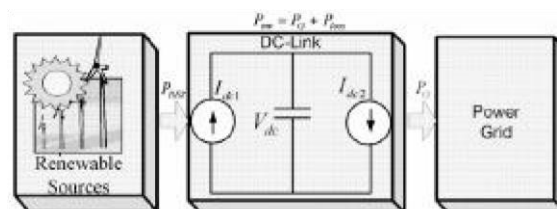
Fig. 2 : DC-Link equivalent diagram

Where press is the power generated from RES. The current flow on the other side of dc-link can be represented as:

$$I_{dc2} = \frac{P_{inv}}{V_{dc}} = \frac{P_G + P_{Loss}}{V_{dc}} \qquad (2)$$

Where P_{inv}, P_G and P_{loss} are total power available at grid interfacing inverter side, active power supplied to the grid and inverter losses, respectively. If inverter losses are negligible then

$$PRES = PG$$

B. Control of Grid Interfacing Inverter

The control diagram of grid- interfacing inverter for a 3-phase 4-wire system is shown in Fig. 3. The fourth leg of inverter is used to compensate the neutral current of load. The main aim of proposed approach is to regulate the power at PCC during:

1) $P_{RES}=0$,
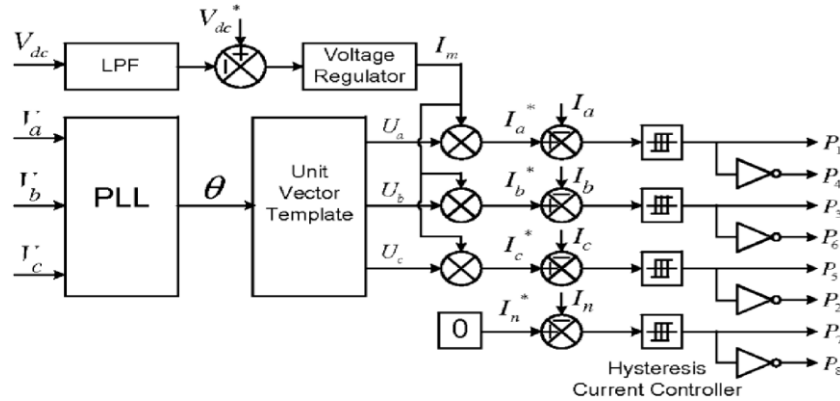2) $P_{RES}<$ Total load power (P_L) and
3) $P_{RES}>P_L$

Fig. 3 : **Block diagram representation of grid-interfacing inverter control**

While performing the power management operation, the inverter is actively controlled in such a way that it always draws/ supplies fundamental active power from/ to the grid. If the load connected to the PCC is non-linear or unbalanced or the combination of both, the given control approach also appears as balanced resistive load to the grid. The regulation of dc-link voltage carries the information regarding the exchange of active power in between renewable source and grid. Thus the output of dc-link voltage regulator results in an active current I_M The multiplication of active current component (I_M) With unity grid voltage vector templates (U_a , U_b and U_c). Generates the reference grid currents I_a^* , I_b^* and I_{c^*} the reference grid neutral current (I_n^*) is set to zero, being the instantaneous sum of balanced grid currents. The grid synchronizing angle θ obtained from phase locked loop (PLL). Compensates the harmonics, unbalance, and neutral current. Such that the combination of load and inverter injected power. The duty ratio of inverter switches are varied in a power cycle is used to generate unity vector template as [9]–[11]

$$U_a = \sin\theta \qquad (3)$$
$$U_b = \sin(\theta - \tfrac{2\pi}{3}) \qquad (4)$$
$$U_c = \sin\left(\theta + \tfrac{2\pi}{3}\right) \qquad (5)$$

The actual dc-link voltage is sensed and passed through a first order low pass filter (LPF) to eliminate the presence of switching ripples on the dc-link voltage (V_{dc})   and in the generated reference current signals. The difference of this filtered dc-link voltage and reference dc-link voltage(V_{dc}^*) is given to a discrete- PI regulator to maintain a constant dc-link voltage under varying generation and load conditions.
The dc-link voltage error ($V_{dcerr\,(n)}$)at the sampling instant is given as:

$$V_{dcrr(n)} = V_{dc\,(n)}^* - V_{dc\,(n)} \qquad (6)$$
$$I_{m(n)} = I_{m(n-1)} + K_{PVdc}V_{dcerr(n)} - V_{dcerr(n-1)} + K_{IVdc}V_{dcerr(n)} \qquad (7)$$

Where $K_{pvdc} = 10$ and $K_{ivdc} = 0.05$ are proportional and integral gains of dc-voltage regulator. The instantaneous values of reference three phase grid currents are computed as:

$$I_a^* = I_m.U_a \qquad (8)$$
$$I_a^* = I_m.U_a \qquad (9)$$
$$I_a^* = I_m.U_a \qquad (10)$$

The neutral current, present if any, due to the loads connected to the neutral conductor should be compensated by forth leg of grid-interfacing inverter and thus should not be drawn from the grid. In other words, the reference current for the grid neutral current is considered as zero and can be expressed as:

$$I_n^* = 0 \qquad (11)$$

The reference grid currents I_a^* , I_b^* , I_c^* and I_n^* are compared with actual grid currents I_a, I_b, I_c and I_n to compute the current errors as:

$$\boldsymbol{Iaerr = I*a - Ia} \qquad (12)$$
$$\boldsymbol{Iberr = Ib* - Ib} \qquad (13)$$
$$\boldsymbol{I_{cerr} = I_c^* - I_c} \qquad (14)$$

These current errors are given to hysteresis current controller. The hysteresis controller then generates the switching pulses (P_1 to P_8) for the gate drives of grid-interfacing inverter. The average model of 4-leg inverter can be obtained by the following state space equations

$$\frac{dI_{inva}}{dt} = \frac{V_{inva} - V_a}{L_{sh}} \qquad (16)$$
$$\frac{dI_{invb}}{dt} = \frac{V_{invb} - V_b}{L_{sh}} \qquad (17)$$
$$\frac{dI_{invc}}{dt} = \frac{V_{invc} - V_c}{L_{sh}} \qquad (18)$$
$$\frac{dI_{invn}}{dt} = \frac{V_{invn} - V_n}{L_{sh}} \qquad (19)$$
$$\frac{dV_{dc}}{dt} = \frac{I_{invad} + I_{invbd} + I_{invcd} + I_{invnd}}{C_{dc}} \qquad (20)$$

Where $Vinva$, $Vinvb$, $Vinvc$ and $Vinvn$ and are the three-phase ac switching voltages generated on the output terminal of inverter. These inverter output voltages can be modeled in terms of instantaneous dc bus voltage and switching pulses of the inverter as:

$$V_{inva} = \frac{(P_1 - P_4)}{2} V_{dc} \qquad (21)$$
$$V_{invb} = \frac{(P_3 - P_6)}{2} V_{dc} \qquad (22)$$
$$V_{invc} = \frac{(P_5 - P_2)}{2} V_{dc} \qquad (23)$$
$$V_{invn} = \frac{(P_7 - P_8)}{2} V_{dc} \qquad (24)$$

Similarly the charging currents I_{inva} , I_{invb} , I_{invc} and I_{invn} and on dc bus due to the each leg of inverter can be expressed as:

$$I_{invad} = I_{inva}(P_1 - P_4) \qquad (25)$$
$$I_{invbd} = I_{invb}(P_3 - P_6) \qquad (26)$$
$$I_{invcd} = I_{invc}(P_5 - P_2) \qquad (27)$$
$$I_{invnd} = I_{invn}(P_7 - P_8) \qquad (28)$$

The switching pattern of each IGBT inside inverter can be formulated on the basis of error between actual and reference current of inverter, which can be explained as:

if $I_{inva} < (I_{inva}^* - h_b)$ then upper switch S_1 will be OFF (P_1=0) and lower switch S_4 will be on ($P_4 = 1$) in the phase "a" leg of Inverter

If $I_{inva} > (I_{inva}^* - h_b)$ then upper switch S_1 will be ON (P_1=1) and lower switch S_4 will be OFF $P_4 = 0$ in the phase "a" leg of Inverter Where h_b is the width of hysteresis band. On the same principle , the switching pulses for the other remaining three legs can be derived.

III. SIMULATION RESULTS

In order to verify the proposed control approach to achieve multi-objectives for grid interfaced DG systems connected to a 3-phase 4-wire network, an extensive simulation study is carried out using MATLAB/Simulink. A 4-leg current controlled voltage source inverter is actively controlled to achieve balanced sinusoidal grid currents at unity power factor (UPF) despite of highly unbalanced nonlinear load at PCC under varying renewable generating conditions. A RES with variable output power is connected on the dc-link of grid interfacing inverter. An unbalanced 3-phase 4-wire nonlinear load, whose unbalance, harmonics, and reactive power need to be compensated, is connected on PCC. The waveforms of grid voltage(V_a, V_b, V_c) , grid currents (I_a, I_b, I_c and I_n), unbalanced load current and inverter currents I_{la}, I_{lb}, I_{lc} and I_{ln} are shown in Fig. 4. The corresponding active-reactive powers of grid (P_{load} , Q_{load}), load and inverter(P_{inv} Q_{inv}) are shown in Fig. 5. Positive values of grid active-reactive powers and inverter active-reactive powers imply that these powers flow from grid side towards PCC and from inverter towards PCC, respectively. The active and reactive powers absorbed by the load are denoted by positive signs. Initially, the grid interfacing inverter is not connected to the network (i.e., the load power demand is totally supplied by the grid alone). Therefore, before time t=0.72 s, the grid current profile in Fig. 4(b) is identical to the load current profile of Fig. 4(c). At s, the grid-interfacing inverter is connected to the network. At t=0.72 s, this instant the inverter starts injecting the current in such a way that the profile of grid current starts changing from unbalanced non linear to balanced sinusoidal current as shown in Fig. 4(b). As the inverter also supplies load neutral current demand, the grid neutral current (I_{n})

becomes zero after s t=0.72 s At t=0.72 s, the inverter starts injecting active power generated from RES $P_{RES} \backsimeq P_{inv}$. Since the generated power is more than the load power demand the additional power is fed back to the grid.

The negative sign of P_{grid} , after time 0.72 s suggests that the grid is now receiving power from RES. Moreover, the grid-interfacing inverter also supplies the load reactive power demand locally. Thus, once the inverter is in operation the grid only supplies/receives fundamental active power. At t=0.82 s, the active power from RES is increased to evaluate the performance of system under variable power generation from RES. This results in increased magnitude of inverter current. As the load power demand is considered as constant ,this additional power generated from RES flows towards grid, which can be noticed from the increased magnitude of grid current as indicated by its profile. At t=0.92 s, the power available from RES is reduced. The corresponding change in the inverter and grid currents can be seen from Fig. 4. The active and reactive power flows between the inverter, load and grid during increase and decrease of energy generation from RES can be noticed from Fig. 5. The dc-link voltage across the grid- interfacing inverter (Fig. 5(d)) during different operating condition is maintained at constant level in order to facilitate the active and reactive power flow. Thus from the simulation results, it is evident that the grid interfacing inverter can be effectively used to compensate the load reactive power, current unbalance and current harmonics in addition to active power injection from RES.
This enables the grid to supply/ receive sinusoidal and balanced power at UPF.
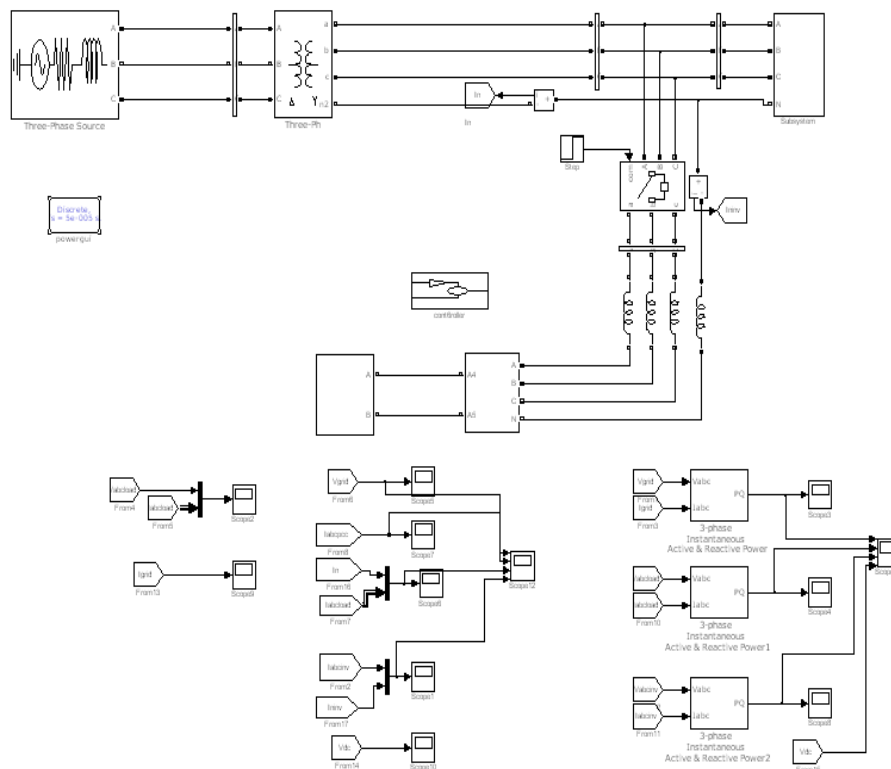
MATLAB DESIGN OF CASE STUDY AND RESULTS

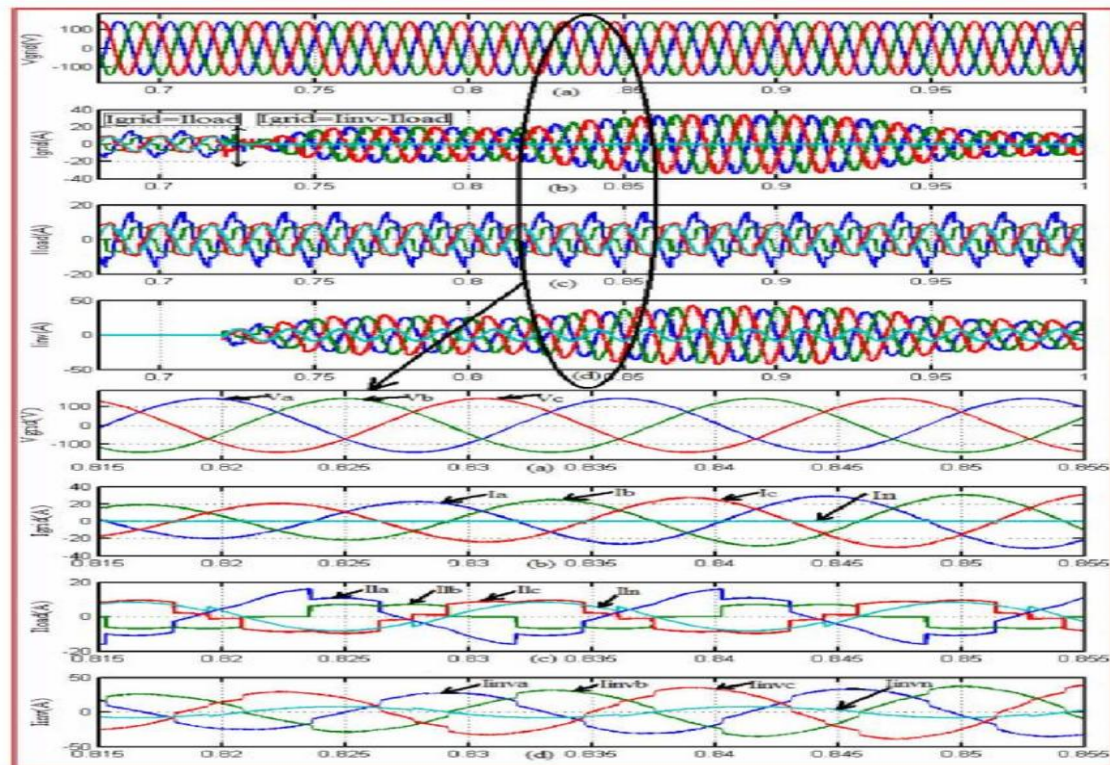**Fig. 4 : DESIGN OF CASE STUDY AND RESULTS**

Fig.5. Simulation results: (a) Grid voltages, (b) Grid Currents (c) Unbalanced load currents, (d) Inverter Currents
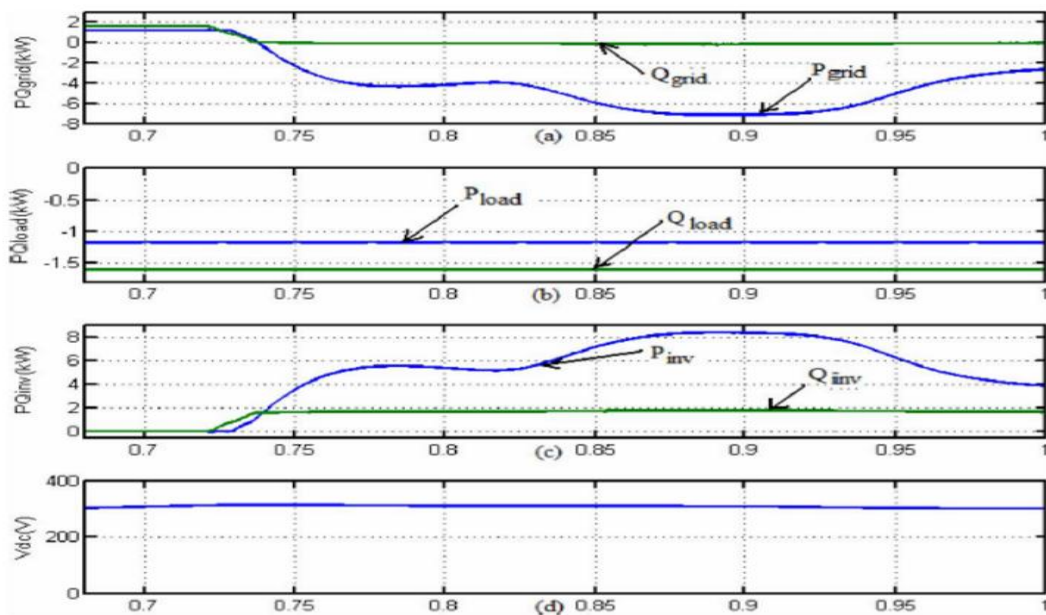
Fig. 6 Simulation results: (a) PQ-Grid, (b) PQ-Load, (c) PQ Inverter, (d) dc-link voltage

IV. CONCLUSION

This paper has presented a novel control of an existing grid interfacing inverter to improve the quality of power at PCC for a 3-phase 4-wireDGsystem. It has been shown that the gridinterfacing inverter can be effectively utilized for power conditioning without affecting its normal operation of real power transfer. =The grid-interfacing inverter with the proposed approach can be utilized to:

- ➢ inject real power generated from RES to the grid, and/or,
- ➢ Oprate as a shunt Active Power Filter (APF).

This approach thus eliminates the need for additional power conditioning equipment to improve the quality of power at PCC. Extensive MATLAB/Simulink simulation as well as the DSP based experimental

results have validated the proposed approach and have shown that the grid-interfacing inverter can be utilized as a multi-function device.

It is further demonstrated that the PQ enhancement can be achieved under three different scenarios: 1) $P_{RES} = 0$, 2) $P_{RES} < P_{Load}$, and 3) $P_{RES} > P_{Load}$. The current unbalance , current harmonics and load reactive power, due to unbalanced and non-linear load connected to the PCC, are compensated effectively such that the grid side currents are always maintained as balanced and sinusoidal at unity power factor. Moreover, the load neutral current is prevented from flowing into the grid side by compensating it locally from the fourth leg of inverter. When the power generated from RES is more than the total load power demand, the grid-interfacing inverter with the proposed control approach not only fulfills the total load active and reactive power demand (with harmonic compensation) but also delivers the excess generated sinusoidal active power to the grid at unity power factor.

REFERENCES

[1]   J. M. Guerrero, L. G. de Vicuna, J. Matas, M. Castilla, and J. Miret, "A wireless controller to enhance dynamic performance of parallel inverters in distributed generation systems," IEEE Trans. Power Electron., vol. 19, no. 5, pp. 1205–1213, Sep. 2004.

[2]   J. H. R. Enslin and P. J. M. Heskes, "Harmonic interaction between a large number of distributed power inverters and the distribution network ",IEEE Trans. Power Electron., vol. 19, no. 6, pp. 1586–1593, Nov. 2004.

[3]   U. Borup, F. Blaabjerg, and P. N. Enjeti, "Sharing of nonlinear load in parallel-connected three-phase converters," IEEE Trans. Ind. Appl., vol. 37, no. 6, pp. 1817–1823, Nov./Dec. 2001.

[4]   P. Jintakosonwit, H. Fujita, H. Akagi, and S. Ogasawara, "Implementation and performance of cooperative control of shunt active filters for harmonic damping throughout a power distribution system," IEEE Trans. Ind. Appl., vol. 39, no. 2, pp. 556–564, Mar./Apr. 2003.

[5]   J. P. Pinto, R. Pregitzer, L. F. C. Monteiro, and J. L. Afonso, "3-phase 4-wire shunt active power filter with renewable energy interface," presented at the Conf. IEEE Renewable Energy & Power Quality, Seville,Spain, 2007

[6]   F. Blaabjerg, R. Teodorescu, M. Liserre, and A. V. Timbus, "Overview of control and grid synchronization for distributed power generation systems," IEEE Trans. Ind. Electron., vol. 53, no. 5, pp. 1398–1409, Oct. 2006.

[7]   J. M. Carrasco, L. G. Franquelo, J. T. Bialasiewicz, E. Galván, R. C. P. Guisado, M. Á. M. Prats, J. I. León, and N. M. Alfonso, "Power electronic systems for the grid integration of renewable energy sources: A survey," IEEE Trans. Ind. Electron., vol. 53, no. 4, pp. 1002–1016, Aug. 2006.

[8]   B. Renders, K. De Gusseme, W. R. Ryckaert, K. Stockman, L. Vandevelde, and M. H. J. Bollen, "Distributed generation for mitigating voltage dips in low-voltage distribution grids," IEEE Trans. Power. Del., vol. 23, no. 3, pp.1581–1588, Jul. 2008.

Er. Aiman saleh Alamin , Libya, Sebha, Tragen,(Bs.c) Electrical Engineering (power system) Hoon institute , Master of Technology in Electrical Engineering (Power System) , SHIATS, Allahabad , UP,India .

Dr. Surya Prakash Belongs to Allahabad, DOB is 01.05.1971, Received his Bachelor of Engineering degree from The Institution of Engineers (India) in 2003, He obtained his M.Tech. In Electrical Engg. (Power System) from KNIT, Sultanpur. UP-India in 2009. Presently he is Pursuing Ph. D in Electrical Engg. (Power System). SSET, SHIATS (Formerly Allahabad Agriculture Institute, Allahabad-India). His field of interest includes power system operation & control, Artificial Intelligent control.

Optimization of Capacity Utilization in a Manufacturing Industry – A Case Study

N. Jayanth[1], S. Vidyashankar[2]

[1]*Associate Professor, Dept. of MECH ENGG, B.M.S College of Engg., BANGALORE – 19*
[2]*Professor, Dept. of MECH ENGG, B I T, BANGALORE-2*

Abstract: *In today's competitive market, every organization is striving hard to excel to utilize capacities effectively which determines the position of the organization in the Market. To achieve effective utilization a lot of planning is required with respect to capacity utilization. Capacity Planning and Capacity Management are today's modern organization requirement. The capacity plans needs to be executed flawlessly without unpleasant surprises .To match the capacity with the plans, an attempt has been made to evaluate capacity utilization index in a cement manufacturing industry. Overall equipment effectiveness is calculated with three separate but measurable components availability, performance and quality. Many manufacturing companies benchmark their industry to set challenging target at 85% capacity utilization, even though 100% OEE is possible.*

Keywords: *Capacity Utilization, Capacity Index, Capacity Utilization, Capacity Management, OEE*

I. Introduction

The present work has been aimed to determine capacity index in a cement industry with respect to capacity plan. The following aspects are considered while conducting the study:

1. Utilization of machines in a cement industry.
2. Utilization of labour in a cement industry.
3. Combined utilization of machines as well as labour in a cement industry.
4. Calculation of the overall capacity index of the cement industries.
5. Recommendations and inferences drawn by analyzing the data.

Analysis of this work will be helpful to know the capacity utilization of cement manufacturing industry, since it is going to be helpful for all kinds of economic activities .corporate needs to control the types and quantities of materials they purchase, plan which products are to be produced and what quantities and ensure they are able to meet the current and future demand. Making a bad decision in any of these areas will make the company lose money. Hence capacity planning is a tool to deal these types of problems.

The common steps involved in cement manufacturing are:

1. Procurement of raw materials.
2. Preparation of raw materials for the pyro-processing system.
3. Pyro-processing raw materials to form Portland cement clinker.
4. Cooling of Portland cement clinker.
5. Storage.
6. Packing and loading.

II. Methodology

The methodology adopted in the present work is to study the layout of the industry and collecting suitable data with respect to utilization of machines and man power. The human effort is judged, wastage identified and bottlenecks are identified to eliminate the same .The daily data is collected which is converted to weekly, monthly to calculate capacity indexes, which are charted. To study the comparison the same details are plotted mainly to give recommendations to the issues.

The capacity index is calculated by taking one machine in a cement industry mainly to design index value so that the decision makers can take qualitative decision on capacity. Dumper 1 has been identified for the above purpose. The details of working time, idle time, percentage of utilization calculated for the month of January.

WEEK	WORKING TIME	IDLE TIME	TOTAL TIME	% UTILIZATION	% IDLE TIME
1	2580	4440	7020	58.10	41.90
2	1620	5400	7020	23.07	76.93
3	3660	3360	7020	52.13	47.87
4	2220	4800	7020	31.62	68.38
MONTH	WORKING TIME	IDLE TIME	TOTAL TIME	% UTILIZATION	% IDLE TIME
JAN	10080	18000	28080	35.89	64.11

Similarly the labour details are calculated for the same month and the same are as follows

WEEK	WORKING TIME	IDLE TIME	TOTAL TIME	% UTILIZATION	% IDLE TIME
1	5943	1077	7020	84.65	15.34
2	6054	966	7020	86.23	13.77
3	5982	1038	7020	85.21	14.79
4	5963	1057	7020	84.94	15.06

III.   Analysis

As we know in modern day competitive world every organization demands an effective utilization of capacity. In this work the researcher selected cement manufacturing plant to calculate and evaluate capacity index. In simple words Cement manufacturing starts with raw material acquisition to milling of raw materials to pyro processing where raw mix is heated to produce port land cement clinkers to cooling and storage, finally finish milling to packing and storing.

The machines slelected for the above work are dumpers (where 10 dumpers were available), Excavators (where 5 excaveters were available), Drilling Machines (Where 02 were available) and one crusher. The capacity index calculated machine wise, month wise and tabulated as follows.

IV.   Average Capacity Index Of Machineries

MACHINE / WEEK	1	2	3	4	AVERAGE MACHINE C.I
DRILLING MACHINE 1	0.2322	0.2200	0.3305	0.2542	0.2592
DRILLING MACHINE 2	0.2596	0.2969	0.2869	0.2801	0.2809
EXCAVATOR 1	0.4730	0.4023	0.3837	0.4195	0.4196
EXCAVATOR 2	0.3640	0.4409	0.5272	0.5849	0.4793
EXCAVATOR 3	0.6420	0.6083	0.6867	0.5993	0.6341
EXCAVATOR 4	0.7681	0.7695	0.7494	0.6809	0.7420
EXCAVATOR 5	0.5285	0.5946	0.4222	0.5349	0.5201
DUMPER 1	0.5196	0.5943	0.5545	0.5338	0.5506
DUMPER 2	0.4923	0.4831	0.4620	0.5339	0.4928
DUMPER 3	0.5386	0.5537	0.5453	0.6727	0.5776
DUMPER 4	0.6433	0.5542	0.6806	0.6512	0.6323
DUMPER 5	0.6439	0.7442	0.7683	0.7144	0.7177
DUMPER 6	0.6802	0.9153	0.8477	0.6917	0.7837
DUMPER 7	0.6420	0.7579	0.6183	0.7232	0.6854
DUMPER 8	0.6228	0.6883	0.6639	0.4544	0.6074
DUMPER 9	0.8358	0.8549	0.8707	0.8757	0.8593
DUMPER 10	0.7572	0.8507	0.8594	0.8787	0.8315
CRUSHER	0.7920	0.7811	0.8493	0.7905	0.8032

V.   Conclusion

In this work OEE and Labour Sheet is set to determine C I which will be used to measure and study the capacity planning. Even though every calculation involves variables and accuracy of that calculation is dependent of the choice and number of variables. As we increase the number of relevant variables the accuracy of the CI increases. By creating C I charts of cumulative data by considering only the bottleneck in particular plant.

Application of Weighted Centroid Approach in Base Station Localization for Minimization of Multipath Losses in Wireless Sensor Networks

Archna Singh Yadav[1], Saifur Rahman[2]

[1, 2] *(Department of ECE, Integral University, Lucknow, India)*

Abstract: *A Wireless Sensor Networks (WSNs) consisting of sensor with strategic locations, and a base-stations (BSs) whose locations are relatively flexible. A sensor cluster consists of many small sensor nodes (SNs) that capture, encode, and transmit relevant information from a designated area. This article is focused on the topology of positioning process for BSs in WSNs. Heterogeneous SNs are battery-powered and energy-constrained, their node lifetime directly affects the network lifetime of WSNs. We have proposed an algorithmic approach to locate BSs optimally such that we can maximize the topological network lifetime of WSNs deterministically, even when the initial energy provisioning for SNs is no longer always proportional to their average bit-stream rate. The obtained optimal BS locations are under different length of area field and number of nodes according to the mission criticality of WSNs. By studying energy consumption due to space loss and amplification losses in WSNs, we establish the upper and lower bounds of maximal topological parameters of area and number of nodes, which enable a quick assessment of energy provisioning feasibility and topology necessity. Numerical results and surface plot are given to demonstrate the efficiency and optimality of the proposed topology of BSs positioning approaches designed for maximizing network lifetime of WSNs.*

Keywords: *Network topology, sensor networks, wireless communications, algorithm design, positioning algorithms.*

I. INTRODUCTION

WIRELESS Sensor Networks (WSNs) [1] have attracted intensive attention in audio streams, temperature readings, motion measures, and so on. In WSNs there is at least one application node (AN) in each cluster responsible for receiving raw data sent from sensor nodes (SNs), creating a local-view by exploring application-specific correlations among these data and forwarding the composite bit-stream toward a base-station (BS). The BS has much better processing and storage capabilities to further increase the value of local views. The BS also serves as a gateway for WSNs to exchange data and control information. SNs and ANs are battery-powered; it is unlikely to recharge them economically once they have been deployed in field. If a single SN runs out of energy, it's AN may still have the capability to reconstruct data sent from other correlated SNs. However, if an AN runs out of energy, the whole cluster coverage is completely lost. In this paper we have discussed these energy constraint of ANs is the foremost concern for WSNs. The location and communication arrangement can be determined before WSN initialization, or can be adjusted throughout a mission.

II. RELATED WORK

From last two decades there are tremendous research and design goals are chassed in the field of WSNs. Elizabeth M. Royer described an adhoc mobile network as a collection of mobile nodes that are dynamically located with the interconnections between nodes are capable of changing on a continual basis. The primary goal of such an ad hoc network routing protocol is correct and efficient route establishment between a pair of nodes so that messages may be delivered in a timely manner [3]. Katayoun Sohrabi present gave algorithms for self-organization of wireless sensor networks having scalably large number of mainly static nodes with highly constrained energy resources. [4].Ram Ramanathan consider the problem of adjusting the transmit powers of nodes in a multi hop wireless network (also called an ad hoc network) to create a desired topology. They formulated a constrained optimization problem with two constraints - connectivity and bi connectivity, and one optimization objective - maximum power used. [5].Further Wendi B. Heinzelman discussed the networking using hundreds or thousands of cheap Micro sensor nodes that allows users to accurately monitor a remote environment by intelligently combining the data from the individual nodes. These networks require robust wireless communication protocols that are energy efficient and provide low latency [6]. Jim Chou and Dragan

Petrovic proposed a novel approach to reducing energy consumption in sensor networks using a distributed adaptive signal processing framework and efficient algorithm. They also compared results with the topic of energy-aware routing to alleviate energy consumption in sensor networks has received attention recently .In this work they proposed an orthogonal approach to previous methods [7]. Jianping Pan designed a generic two-tiered Wireless Sensor Networks (WSNs) consisting of sensor clusters deployed around strategic locations, and base-stations (BSs) whose locations are relatively flexible. Numerical results were demonstrating the efficacy and optimality of the proposed topology control approaches designed for maximizing network lifetime of WSNs [8].

In this paper we have worked on the base station placement in a two-tiered wireless sensor network (WSN) field. The objective is to minimize the overall energy consumption in a WSN. Our results prove that the overall energy consumption is minimized at the centroid of the nodes and proposed point of the node as the compare of the minimum enclosing circle of the centre of the nodes. We know that most of the nodes are close to the base station, whereas a few nodes are far from it. Therefore these far-off sensors nodes use more energy than nearer ones. We have used a weighted centroid method for finding the optimal base station location and investigating how to find the base station location to reduce energy consumption and hence to increase network lifetime.

III. ENERGY CONSUMPTION IN WSNS

WSN are a self configured network formed using a large numbers of sensor nodes distributed over a geographical area with either predefined location or randomly deployed. Individual sensor nodes posses limited processing, communicating and energy recourses. These sensor nodes can sense, measure, and gather information from the vicinity and transmit the sensed information (data) to the user or information sink. Communication of sensed data from the sensor nodes to information sink happens to be the main cause of energy depletion in sensor nodes. In order to extend the active life of WSN, it is required to process data locally and send the processed information to sink node. One of possible solution for optimal use of available energy is by using cluster based routing protocols. Hierarchical or cluster based routing is well known technique for scalability and efficient communication. Clustering enables bandwidth re-use and thus can improve the system capacity. Clustering enables efficient resource allocation and helps in designing better power control. In the hierarchical routing the data collected by sensor nodes in the proximity of the event is routed to the sink nodes through cluster heads. These selected head nodes are responsible for routing the information from the sensor nodes to the sink node after application of proper data aggregation or fusion [2].Overall system scalability, life time and efficiency depend upon the creation of optimal number of clusters and the spatial position of cluster head.

IV. METHODOLOGY OF POSITIONING OF BS IN WSN

Wireless sensor network (WSN) has self-organizing wireless sensor nodes with limited energy resource, and usually a base station to collect and process the data from sensor nodes. A sensor node consumes energy for event sensing, coding, modulation, transmission, reception and aggregation of data. Data transmission has the highest share in total energy consumption [1, 2]. The required transmission power of a wireless radio is proportional to square or an even higher order exponent of distance in the presence of obstacles. Thus, the distance between transmitter and receiver is the main metric for energy consumption in a WSN. Base station location affects the lifetime of the sensor network as all the data are finally transmitted to the base station for processing and decision making for various applications. We can reduce transmission energy by reducing the distance between the sensor nodes and the base station. This can be achieved by placing the base station at an optimal location. In the literature so far, many heuristic algorithms have been proposed to find sub-optimal solutions of the optimum base station positioning in two-tiered WSN. Although these heuristics are shown to be effective, their algorithms depend on the topology and are based on structural metrics.

In this work we have searched the optimal location of a base station with respect to minimum energy expenditure or maximum lifetime of a sensor network.

The centre of a minimum enclosing circle, is the optimal location for the N-of-N lifetime. N-of-N lifetime means the time after which the first node dies or the time up to which N out of N nodes remain alive. The minimum enclosing circle is equivalent to minimizing the maximum distance between the base station and any sensor node in the network. The overall energy consumption [2] is minimized at the centroid of the nodes, when path loss exponent n is 2. In this method, average energy expenditure is minimized, but the first nodes may die earlier compared with the min max approach, as energy contributions of the sensor nodes, are rather uneven. For example, it may happen that most of the nodes are close to the base station, whereas a few nodes are far from it. Therefore these far-off sensors use more energy than nearer ones and hence deplete their energy at a faster rate and die sooner. This approach is known as minimum average or min avg. The Pan et al. approach consist of

location of station based on only free space energy model but in our work we will consider multipath losses along with free space losses to assign different weightage to the sensors which follow a multipath loss. In our approach we have defined a proposed position of BS using weighted positioning of centroid of the sensor nodes as described below:

Step 1: Find centroid (Cx, Cy) of the nodes distributed in the field. This is the point, where energy consumption is minimized, and is given by summation of location of sensor nodes.
Step 2: Find the nodes that are at less than d0 distance from the centroid.
Step 3: Calculation of weights using centroid for all the nodes.
Step 4: Determine the weighted average of nodes' positions as proposed optimal position (xp, yp) for the base station.

V. SIMULATION RESULTS

In this section we have described our WSN model design using the MATLAB. Using this model we have determined the energy consume by sensors during the force of data transmission from WSN sensor to base station. We have analyzed three different scheme of determining the location of base station with respect to minimum energy expenditure of a sensors network.

VI. DESIGN OF WSN MODEL

The transmitter dissipates energy to run the transmitter radio electronics and the power amplifier, and the receiver dissipates energy to run the receiver radio electronics. If the distance between the transmitter and the receiver is less than a threshold (d_0), the 'free space (fs) loss' model is used; otherwise, the 'multipath (mp) loss' model is used. Here, we are assuming that a suitable power control mechanism exists to regulate transmit power depending on the distance to the receiver. In a transmission amplifier .we used path loss exponent, n= 2, for free space loss model and n = 4 for multi-path loss model. The consumed amplifier energy E_{amp}, of a sensor node is $E_{fs}.d^2$ or $E_{mp}.d^4$ depending on the distance d between node and base station.
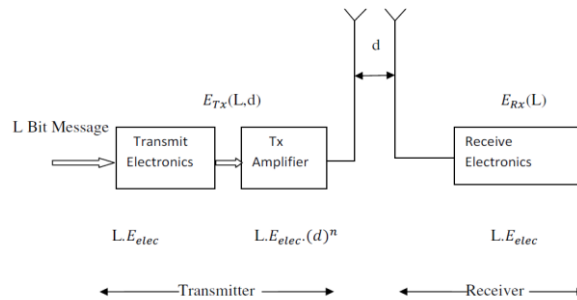

Fig. 1: Radio Model

$$E_{amp} = \begin{cases} E_{fs}.d^2 & d < d_0 \\ E_{mp}.d^4 & d \geq d_0 \end{cases} \qquad (1)$$

Here, threshold distance d0 for swapping amplification model is calculated by equating E_{amp}(fs) to E_{amp}(mp) [6].

$$E_{fs}.d^2 = E_{mp}.d^4 = d_0 = \sqrt{\frac{E_{fs}}{E_{mp}}} \qquad (2)$$

Where E_{fs} is free space loss constant measured in J/bit/m2 and E_{mp} is multi-path loss constant measured in J/bit/m4. If a node transmits L number of bits, the energy used in transmission will be

$$E_{TX}(L,d) = E_{TX-ele}(L) + E_{amp}(L,d) = \begin{cases} LE_{ele} + LE_{fs}.d^2 & d < d_0 \\ LE_{ele} + LE_{mp}.d^4 & d \geq d_0 \end{cases} \qquad (3)$$

To receive L message bits, the radio spend

$$E_{RX}(L) = E_{RX-ele}(L) = LE_{elc} \qquad (4)$$

Here, E_{ele} is the energy, in J/bit in transmission and reception electronics. Most of the earlier work had considered only free space loss (n = 2) as the model of radio communication. We are not aware of any work that considers multi-path loss (n =4) in their radio model or multi-path radio models for analyzing optimal base station positioning. We have designed WSN model having large number of wireless sensor nodes with limited energy resources model having a base station that can collect and process the data obtained from sensor nodes. For this purpose an algorithm using MATLAB 10 software is developed. In this algorithm we have generated randomly distributed sensor node in a given field having square area M×M meter square. The number of nodes are varied from 5 to 200 nodes for a given area .We have also considered field area of different dimensions having length of square area 30 to 500 meters. Every time we have increment of 10 and nodes are increment of 10 also. In this way we have generated about 48×20 random distributed WSN cluster with different areas and different number of nodes. Let we have N sensor nodes randomly distributed in a rectangular field at a location (Px, Py) where ;

Px=X1,X2,X3................Xn
Py=Y1,Y2,Y3...............Yn

After that we have calculated the location of centroid for given randomly distributed wireless sensor nodes. Fig 2 are shown below where x and y axis represents the length of square field and stars shown the location of wireless sensor and a circle shown the location of centroid.
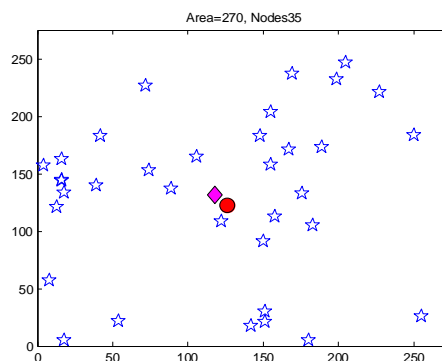

Fig. 2: WSN sensor node cluster for area =270 and node=35

Fig 2 shows the cluster of nodes (blue stars), centroid (mageta diamond) and proposed position of base station (red circle) for area field of length=120 and number of nodes=175 in this Fig. Here area is small hence centroid and proposed position are approximately same with centroid and proposed base station location.
We have shown the surface plot obtained from value of average percent reduction in energy on using proposed point with respect to centroid as BS position (%Ecp) in fig 3(a) using this surface plot we can visualize how does percentage energy reduction varies with different configuration of WSN nodes and field area. In the surface plot the colour of the surface changes from red to blue shades where red shades represents high values, yellow represents medium values and blue represents low values.
In Fig 3(a) we have shown %Ecp on the z-axis, nodes and area are on the x-axis and y-axis. As we can see that x-axis varying from 0-200 and Here we have in circle the portion where %Ecp is significantly larger than the other cluster. for more clearly we have clipped the negative part to zero such that the surface plot becomes blue in the regions having Ec=Ep.
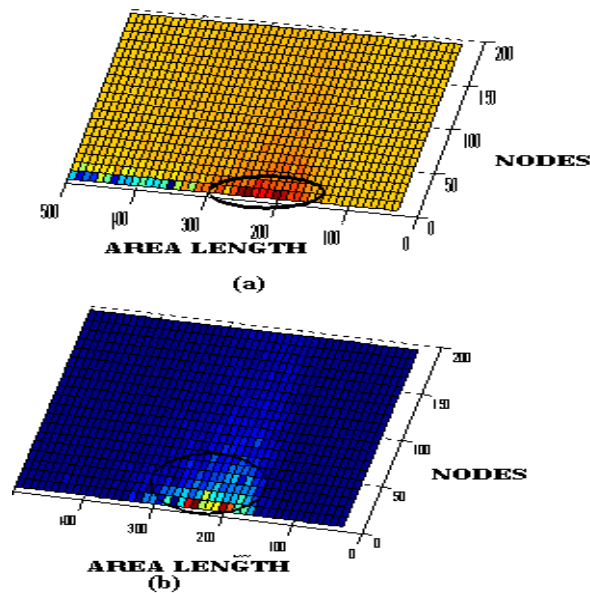
Fig. 3: Top view of Percentage reduction in average amplifier energy for the proposed point compared with centroid (a) without clipping negative part (b) with clipping negative part.

In the Fig 3(b) we can see that a yellow line is drawn in the portion having %Ecp as positive in this region area varies from 100 to 350 meter and number of nodes are varying from 5 to 180. It represents that for area less than 100 the performance of both algorithm are same. However since our threshold distance is 80 for area of length 100 all the nodes will be at a distance less than d_0. So there will be no case of amplification loss there will be only the free path losses that is why for area less than 100 our proposed point and centroid point is similar. For large area above than 350 both algorithm are giving same performance. So we can say that our proposed base station location is good for area of field length less than 150 and for all combination of number of sensor nodes. We have also in circle the region where the surface value is significantly larger for %Ecp with black circle in fig 3(b). This region is under the range 150-300 meter field length with new nodes 5-50. Similarly we have run our algorithm about three times and generated an average % Ecp for 20 results for all three time simulation results .We have also calculated energy consumption on taking centroid as position of BS (Ec) and center of minimum enclosing circle as BS position Em. Using the results we have determined %EM and %EMP. Every time we have found that %Ecp is largest in comparison to %EMP and %EMC.

VII. CONCLUSION

We investigated energy consumption minimization for different schemes of positioning BS in WSNs with variation of area and number of nodes .for area we are considered field length of 30-500 meter and number of nodes 5-200 and nodes and the average percentage reduction in energy consumption for each defined area and nodes evaluated. We found that proposed weighted centroid based approach is best for giving highest percent of reduction in energy consumption compare to centroid and minimum enclosing circle base positioning of base station .maximum percentage reduction approximately 4-6 % compare to percentage reduction when centroid is taken as position of base station .Proposed schemes is better than centroid specially for the region varies from length 100-350 meter and number of nodes 5-180 otherwise the proposed scheme is giving result equivalent to result coming from centroid .We have also design the table for node ratio for calculating the ratio of nodes lies inside the threshold distance where only free space losses occur to number of nodes where both free space and amplification losses occur.

It has been observed that number of nodes are increases as this node ratio decreases and as we increases the area this node ratio again decreases , and it has been found that if we take number of nodes above than 75 for area above than 210 meter length , we can get node ratio less than one. We can reduced the multi-path losses for area 210 meter for the case the proposed schemes but for centroid same result are found from a slightly higher area.

REFERENCES

[1] Blumenthal, J., Grossmann, R., Golatowski, F., Timmermann, D.'Weighted centroid localization in Zigbee-based sensor networks'.*IEEE Int. Symp. on Intelligent Signal Processing, 2007, pp. 1–6*

[2] Pan, J., Cai, L., Hou, T., Shi, Y., Shen, S.X.: 'Optimal base-station locations in two-tiered wireless sensor networks', *IEEE Trans. Mob. Comput., 2005, 4, (5), pp. 458–473.*

[3] Elizabeth M. Royer, "A Review of Current Routing Protocols for Ad Hoc Mobile Wireless Networks" University of California, Santa Barbara Chai-Keong Toh, Georgia Institute of Technology.

[4] Katayoun Sohrabi, Jay Gao, Vishal Ailawadhi, and Gregory J. Pottie, "Protocols for Self-Organization of a Wireless Sensor Network". *UCLA*

[5] Ram Ramanathan, "Topology Control of Multihop Wireless Networks using Transmit Power Adjustment." *Regina Rosales-Hain Internetwork Research Department BBN Technologies (A Division of GTE) Cambridge, Massachusetts, USA*

[6] Wendi B. Heinzelman, Member, IEEE, Anantha P. Chandrakasan, "An Application-Specific Protocol Architecture for Wireless Microsensor Networks". *Senior Member, IEEE, and Hari Balakrishnan, Member, IEEE*

[7] Jim Chou"A Distributed and Adaptive Signal Processing Approach to Reducing Energy Consumption in Sensor Networks". *Department of EECS University of California at Berkeley Berkeley, CA 94709*

[8] Jianping Pan, "Optimal Base-Station Locations in Two-Tiered Wireless Sensor Networks" *Member, IEEE, Lin Cai, Student Member, IEEE, Y. Thomas Hou, Senior Member, IEEE, Yi Shi, Student Member, IEEE, and Sherman X. Shen, Senior Member, IEEE*

Isolated Wind Hydro Hybrid Generation System with Battery Storage

Nirmal S.[1], Rinku Scaria[2]

[1](Student, Department of Electrical and Electronics, FISAT, MG University, Kerala, India)
[2](Assistant Professor, Department of Electrical and Electronics, FISAT, MG University, Kerala, India)

Abstract: In this paper, a new isolated wind- hydro hybrid generation system comprising one squirrel - cage induction generator (SCIG) driven by a variable-speed wind turbine and another synchronous generator driven by constant power hydro turbine feeding three phase four wire local loads is proposed. The system utilizes two back to back connected voltage-source converters (VSCs) with a battery energy storage system at their dc link. The main objective of the control algorithm for the VSC is to achieve control of the magnitude and the frequency of the load voltage. The proposed wind-hydro hybrid system has a capability of bidirectional active- and reactive-power flow, by which it controls the magnitude and the frequency of the load voltage. The proposed electromechanical system is modelled and simulated in MATLAB using Simulink.

Keywords: Battery energy storage system (BESS), squirrel cage induction generator (SCIG), synchronous generator, wind energy conversion system (WECS), voltage source converter (VSC).

I.   INTRODUCTION

Renewable energy sources have attracted attention worldwide due to soaring prices of fossil fuels. Renewable energy sources are considered to be important in improving the security of energy supplies by decreasing the dependence on fossil fuels and in reducing the emissions of greenhouse gases. The viability of isolated systems using renewable energy sources depends largely on regulations and stimulation measures. Renewable energy sources are the natural energy resources that are inexhaustible, for example, wind, solar, geothermal, biomass, and small hydro generation. Among the renewable energy sources, small hydro and wind energy have the ability to complement each other.

Hybrid power systems are combinations of two or more energy conversion devices (e.g., electricity generators or storage devices), or two or more fuels for the same device, that when integrated, overcome limitations that may be inherent in either. System efficiencies are typically higher than that of the individual technologies used separately, and higher reliability can be accomplished with redundant technologies and/or energy storage. Some hybrid systems include both, which can simultaneously improve the quality and availability of power.

In general, well-designed hybrid systems will substantially reduce diesel fuel consumption while increasing system reliability. In addition to the diesel generator and the renewable energy generator, hybrid systems consist of a battery bank for energy storage, a control system and particular system architecture that allows optimal use of all components. Hybrid systems are potentially very cost-effective solutions to rural AC electricity needs. For low load applications (< 10 kWh/day), wind/PV hybrid systems are very attractive. For larger applications, wind/diesel hybrids are very attractive as long as a reasonable wind resource is available. Bilateral and multilateral finance and market stimulation programs should be based on best service at least cost.

There exists a wide collection of literatures on the modeling of WECS, specifically on the modeling of individual components in the system which is mainly comprised of two subsystems, namely a wind turbine part and an electric generator part. Detailed descriptions of these concepts can be found in references [5],[6],[7].The conversion of mechanical power of the wind turbine into electrical power can be accomplished by an electrical generator which can be a DC machine, a synchronous machine, or an induction machine. DC machines were used widely until 1980s in smaller installations below 100 kW, because of its extremely easy speed control. The presence of commutators in DC machines has low reliability and high maintenance.

The second kind of electric generators are synchronous generators suitable for constant speed systems. Another choice for the electric generator in a WECS is a permanent magnet synchronous generator PMSG.

But PMSGs have the weakness of uncontrollable magnetic field decaying over a period of time. Induction generators on the the other hand have many advantages over conventional synchronous generators due to their ruggedness, no need for DC field current, low maintenance requirements and low cost.

Many wind power systems for economy and reliability reasons used induction machines driven by a wind turbine through a gear box as an electrical generator. Based on the rotor construction induction machine can be one of two types based on the rotor construction, squirrel cage type or wound rotor type. Squirrel cage rotor construction is popular because of its ruggedness, lower cost and simplicity of construction. Hence, nowadays it is most commonly used.

In the case of stand-alone or autonomous systems, the issues of voltage and frequency control (VFC) are very important. In references [17]–[18], the issues of VFC for stand-alone systems using SCIGs have been addressed. However, maximum power tracking (MPT) could not be realized in this battery-based isolated system employing SCIG operated at fixed speed. Reference [4] proposes an electronic load controller for VFC at the stator terminals, and the controller transfers excess power from the hydropower generator to a dump load, whenever the load is less than the generated power.

In this paper, a new three-phase four-wire autonomous (or isolated) wind–small hydro hybrid system is proposed for isolated locations, which cannot be connected to the grid and where the wind potential and hydro potential exist simultaneously. One such location in India is the Andaman and Nicobar group of islands [24].The proposed system utilizes variable speed wind-turbine-driven SCIG and a constant-speed/constant-power small hydro-turbine-driven synchronous generator.

A schematic diagram of a three-phase four-wire autonomous system is shown in Fig. 1.Two back-to-back-connected pulse width modulation (PWM)-controlled insulated-gate-bipolar transistor (IGBTs)-based
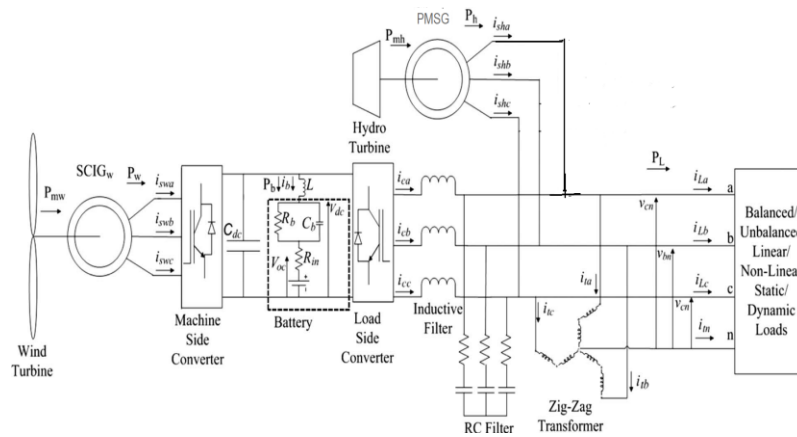

Figure 1: Schematic of wind hydro hybrid system

voltage-source converters (VSCs) are connected between the stator windings of SCIG and the stator windings of the PMSG to facilitate bidirectional power flow. The stator windings of the PMSG are connected to the load terminals. The two VSCs can be called as the machine side converter and the load-side converter. The system employs a battery energy storage system (BESS), which performs the function of load leveling in the wake of uncertainty in the wind speed and variable loads. The BESS is connected at the dc bus of the PWM converters. The advantage of using BESS on the dc bus of the PWM converters is that no additional converter is required for transfer of power to or from the battery. Further, the battery keeps the dc-bus voltage constant during load disturbances or load fluctuations. An inductor is connected in series with the BESS to remove ripples from the battery current. A zigzag transformer is connected in parallel to the load for filtering zero-sequence components of the load currents. Further, the zigzag windings trap triplen harmonic (third, ninth, fifteenth, etc.) currents. As shown in Fig. 1, the zigzag transformer consists of three single-phase transformers with a turn ratio of 1 : 1. The zigzag transformer is to be located as near to the load as possible. The neutral terminal of the consumer loads is connected to the neutral terminal of the zigzag transformer.

In the conventional control of variable-speed SCIGs, the objective of the load-side converter (called as grid-side converter in the grid-connected systems) is to maintain the dc-bus voltage constant at the dc link of two back-to-back connected VSCs. Because in the proposed system the dc-bus voltage is kept constant by the battery, the control objective of the load-side converter is different, i.e., to maintain an active power balance in the system by transferring the excess power to the battery or for providing deficit power from the battery. Further, the load-side converter provides the requisite reactive power for the load. .

A novel control strategy using indirect current control is proposed for the load-side converter. The control signals for switching of the load-side converter are generated from the error of the reference and the sensed stator currents of SCIG rather than by the errors of the load-side converter currents. With this control strategy, the switching of the load-side converter is controlled to make the SCIG currents balanced and sinusoidal at the nominal frequency. Any unbalance and harmonics in the load currents are compensated by the zigzag transformer and the load-side converter. The proposed control algorithm for load-side converter requires sensing of the load voltage and stator currents of SCIG.For the control purpose, sensing of load-side-converter currents and load currents is not required, thus reducing the requirement of current sensors for the control of load-side converter.
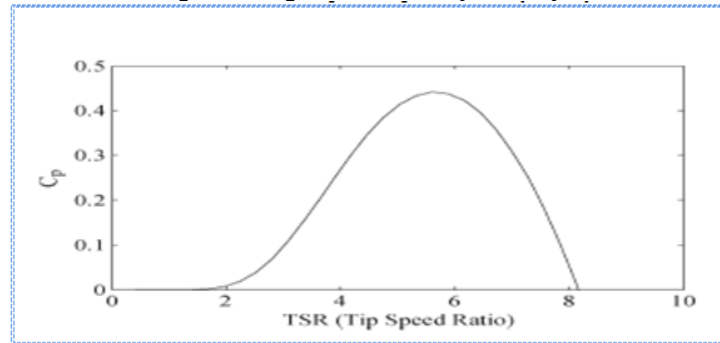
II.   Principle Of Operation Of Hybrid System

Figure 2: Coefficient of performance versus tip speed ratio

The proposed system uses two back to-back-connected VSCs. These VSCs are referred to as the machine side converter and load-side converter.The objective of the load-side converter is VFC at the load terminals by maintaining active- and reactive-power balance. To achieve MPT, the SCIG is required to be operated at optimal tip speed ratio as shown in Fig. 2. The tip speed ratio determines the SCIGw rotor-speed set point for a given wind speed, and the mechanical power generated at this speed lies on the maximum power line of the turbine.

The load-side converter is controlled for the regulation of load-voltage magnitude and load frequency. Further, for maintaining the load-frequency constant, it is also essential that any surplus active power in the system is diverted to the battery. Alternatively, the battery system should be able to supply any deficit in the generated power. Similarly, the magnitude of the load voltage is maintained constant in the system by balancing the reactive-power requirement of the load through the load side converter.

For the proposed system, there are three modes of operation. In the first mode, the required active power of the load is less than the power generated by the synchronous generator and the excess power generated by the PMSG is transferred to the BESS through the load-side converter. Moreover, the power generated by the SCIG is transferred to the BESS. In the second mode, the required active power of the load is more than the power generated by the PMSG but less than the total power generated by SCIG and PMSG. Thus, portion of the power generated by SCIG is supplied to the load through the load-side converter and remaining power is stored in BESS. In the third mode, the required active power of the load is more than the total power generated by SCIG and PMSG. Thus, the deficit power is supplied by the BESS, and the power generated by PMSG and the deficit met by BESS are supplied to the load through the load-side converter.

2.1 Control of Load-Side Converter
The objectives of the load-side converter are to maintain rated voltage and frequency at the load terminals irrespective of connected load. The power balance in the system is maintained by diverting the surplus power generated to the battery or by supplying power from the battery in case of deficit between generated power and load requirement. Similarly, the required reactive power for the load is supplied by the load-side converter to maintain constant value of the load voltage.
1) Generation of Reference Three-Phase SCIGw Currents:
The reference voltages (V*an, V*bn, and V*cn) for the control of the load voltages at time t are given as

$$V^*_{an} = \sqrt{2}\, V_t\ \sin(2\pi f t) \tag{1}$$

$$V^*_{bn} = \sqrt{2}\, V_t\ \sin(2\pi f t - 120) \tag{2}$$

$$V^*_{cn} = \sqrt{2}\, V_t\ \sin(2\pi f t + 120) \tag{3}$$

where *f* is the nominal frequency, which is considered as 50 Hz, and *Vt* is the rms phase-to-neutral load voltage, which is considered as 240 V. The load voltages (van, vbn, and vcn) are sensed and compared with the reference voltages. The error voltages (v_{anerr}, v_{bnerr} and v_{cnerr}) at the *n*th sampling instant are calculated as

$$V_{anerr(n)}) = V_{*an(n)} - V_{an(n)} \tag{4}$$
$$V_{bnerr(n)} = V_{*bn(n)} - V_{bn(n)}. \tag{5}$$
$$V_{cnerr(n)} = V_{*cn(n)} - V_{cn(n)} \tag{6}$$

The reference three-phase SCIG*w* currents (i_{*swa}, i_{*swb}, i_{*swc}) are generated by feeding the voltage error signals to PI voltage voltage controller with proportionate gain K_{pv} and integral gain K_{iv}. The reference three-phase SCIGw currents are then compared with the sensed SCIGw currents (i_{swa}, i_{swb}, and i_{swc}) to compute the SCIGw current errors as

$$i_{swaerr} = i_{*swa} - i_{swa} \tag{7}$$
$$i_{swberr} = i_{*swb} - i_{swb} \tag{8}$$
$$i_{swcerr} = i_{*swc} - i_{swc} \tag{9}$$

These current errors are amplified with gain (*K*=5), and the amplified signals are compared with a fixed-frequency (10 kHz) triangular carrier wave of unity amplitude to generate gating signals for IGBTs of the load-side converter. The sampling time of the controller is taken as 50μs, as this time is sufficient for completion of calculations in a typical DSP controller.

III. DESIGN

3.1 Turbine
The wind hydro hybrid system being considered has a wind turbine of 55kW and a hydro turbine of 60 kW respectively. The rating of the SCIG$_w$ is equal to the rating of the wind turbine, ie 55 kW.

3.2 Selection of Voltage of Dc Link And Battery Design
The dc-bus voltage (Vdc) must be more than the peak of the line voltage for satisfactory PWM control as
$$Vdc > 2\sqrt{(2/3)}V_{ac} m_a \tag{10}$$
where ma is the modulation index normally with a maximum value of one and Vac is the rms value of the line voltage on the ac side of the PWM converter .The maximum rms value of the line voltage at the load terminals is 415 V. Substituting this value in (10), Vdc should be more than 677.7 V. The voltage of the dc link and the battery bank is selected as 700 V. The maximum rms value of the line voltage at the load terminals is 415 V. Substituting this value in V_{dc} should be more than 677 V.The voltage of the dc link and the battery bank is selected as 700 V.

Considering the ability of the proposed system to supply electricity to a load of 60 kW for 10 h, the design storage capacity of the battery bank is taken as 600 kWh. . The commercially available battery bank consists of cells of 12 V. The nominal capacity of each cell is taken as 150 A.h. To achieve a dc-bus voltage of 700 V through series connected cells of 12 V, the battery bank should have (700/12) = 59 number of cells in series. Since the storage capacity of this combination is 150 A · h, and the total ampere hour required is (600 kW · h/700 V) = 857 A · h, the number of such sets required to be connected in parallel would be (857 A.h /150 A.h) = 5.71 or 6 (selected). Thus, the battery bank consists of six parallel-connected sets of 59 series connected battery cells.

Thevenin's model is used to describe the energy storage of the battery in which the parallel combination of capacitance (Cb) and resistance (Rb) in series with internal resistance (Rin) and an ideal voltage source of voltage 700 V are used for modelling the battery.
$$Cb = (Kw.h*3600*1000)/0.5 (V_{2ocmax} - V_{2ocmin}) \tag{11}$$
Taking the values of V_{ocmax} = 750 V, V_{ocmin} = 680 V, and Kw.h = 600, the value of Cb obtained is 43156 F.

3.3 Selection of Rating of Ac Inductor And Rc Filter On Ac Side Of Load-Side Converter
An inductor is used on the ac side of the load-side converter for boost function. inductance (Lf) of the inductive filter can be calculated as
$$Lf = \{(\sqrt{3}/2)m_a V_{dc} /(6a f_s Ir_{(p-p)}I_{sc}\} \tag{12}$$
where fs is the switching frequency and is equal to 10 kHz and Ir(p−p)lsc is the peak-to-peak ripple current in the load-side converter and inductive filter. During transients, the current in the inductive filter is likely to be more than the steady-state values. For calculation of inductance, current rating of 120% (a = 1.2) of steady-state current is taken; modulation index ma is taken as one. Thus, the value of inductance of the filter is

0.76mH . A high-pass first-order filter tuned at half the switching frequency is used to filter out the noise from the voltage at the load terminals. The time constant of the filter should be very small compared with the fundamental time period (T), or

$$RC << T/10. \tag{13}$$

When T = 20 ms, considering, C = 5μF, R can be chosen as 5 Ω. This combination offers a low impedance of 8.1 Ω for the harmonic voltage at a frequency of 5 kHz (half of the switching frequency).

3.4 Selection of Specifications Of Wind Turbine And Gear   Ratio

The wind turbine is designed for 55 kW at 11.2 m/s, which is considered as rated wind speed. For wind speeds below the rated wind speed, the mechanical power *Pm* captured by the turbine is a function of wind speed *Vw*, radius of turbine *rw*, density of air *ρ*, and coefficient of performance *Cp*, and is given

$$Pm = 0.5Cp\pi r^2\rho V^3 \tag{14}$$

The relationship between the coefficient of performance and tip speed ratio for a typical wind turbine is shown in Fig. 3.The maximum coefficient of performance (*Cp*max) is achieved optimum tip ratio ($\lambda *_w$). The values of *Cp*max and $\lambda *_w$ obtained from the Figure. 3.1 are 0.4411 and 5.66, respectively. Substituting, *Pm* = 55 kW, *Cp* = 0.4411, wind speed *Vw* = 11.2 m/s, and density of air *ρ* = 1.1544 kg/m3 in 4.1, the radius of the wind turbine *rw* is obtained as 7.5m.

At 11.2 m/s wind speed, the generator rotor speed is considered as 100 rad/s. Substituting the value of tip speed ratio = 5.66, radius of the wind turbine = 7.5 m,wind speed = 11.2 m/s, and generator speed = 100 rad/s, the gear ratio is obtained as

$$\eta w = \omega_{rw}r_w/\lambda wVw \tag{15}$$
$$=100*7.5/5.66*11.2$$
$$= 11.811 \sim=12 \text{ (selected)}.$$

Above equations are used to simulate wind turbine. In the real turbines above the rated wind speed, the blade-pitch control comes in operation, and the turbine blades are pitched slightly out of the wind to limit power. Conversely, the blades are turned back into the wind whenever the wind drops again. The ratings and the specifications of the selected components of the hybrid system based on the aforementioned design procedure are used for simulation purpose.

IV.   Simulation Results

The performance of the wind hydro hybrid system is demonstrated in figure 2.1. A balanced linear load and a secondary dynamic load at wind speed of 11m/s is connected to the above network. At this speed the wind turbine generates 55 kW and the hydro generates 60 kW. So the total power generation is 115 kW. The model is tested for the following loads.
1. Half load of 57.5 kW
2. Full load of 115 kW
3. Overload of 10%

In each case the output waveforms of load voltage, load current and load frequency are studied. The model is working satisfactorily for the above mentioned loads. The waveforms are purely sinusoidal as expected for the above three conditions. Also, under the above conditions both the magnitude and frequency of the load voltage are maintained constant. The obtained waveforms are shown in figures.
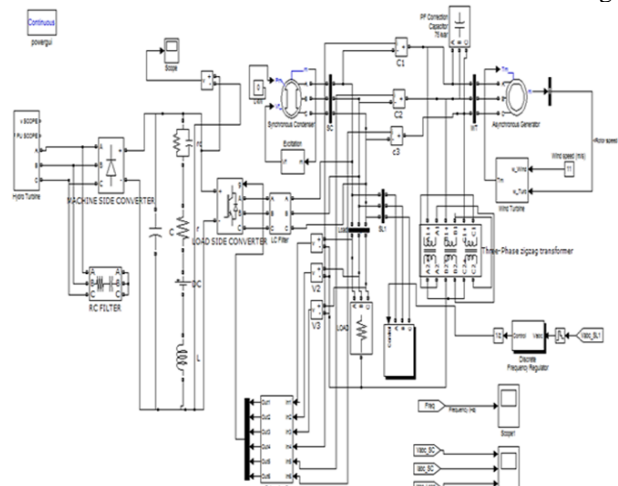

Figure 4.1: Simulink Block diagram of proposed system
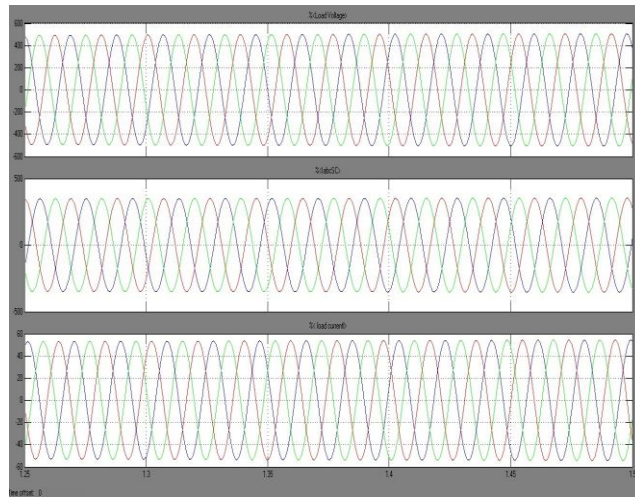
Figure 4.2 Output voltage and current waveforms for half load
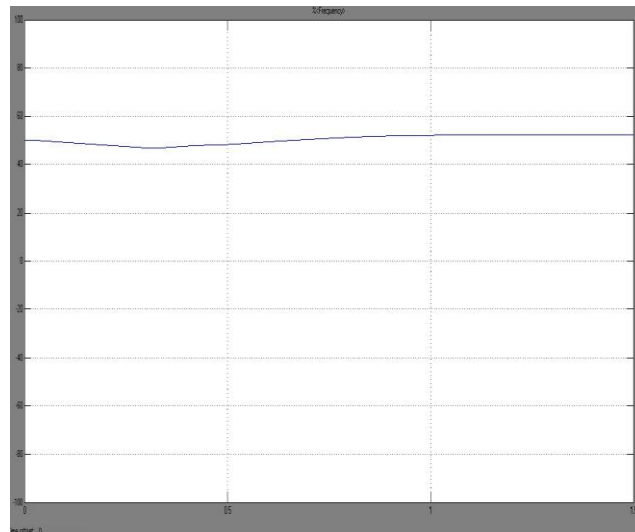

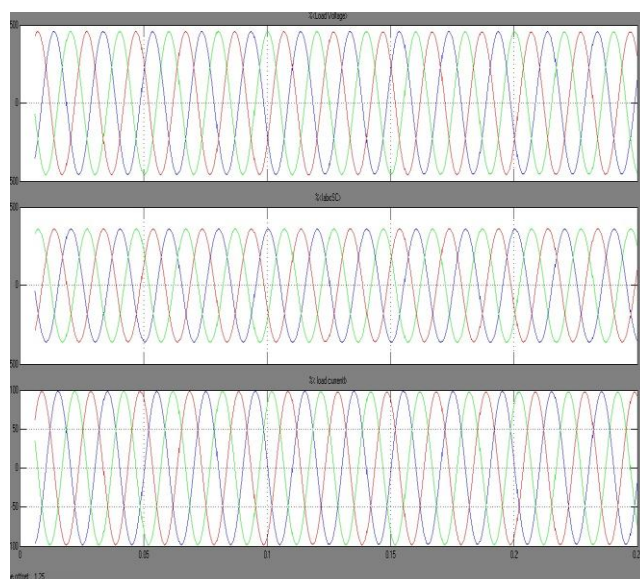Figure 4.3: Frequency waveform for half load

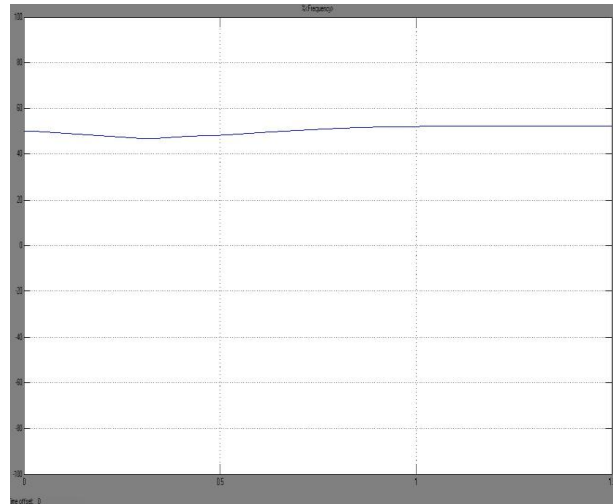Figure 4.4 Output voltage and current waveforms for full load

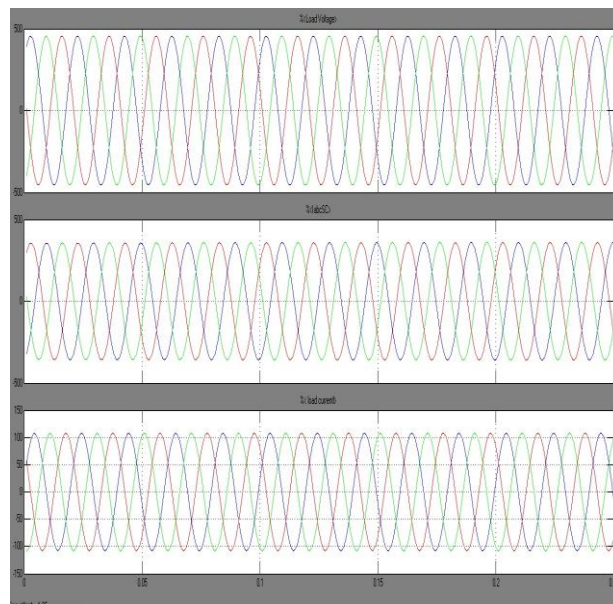Figure 4.5: Frequency waveform for full load

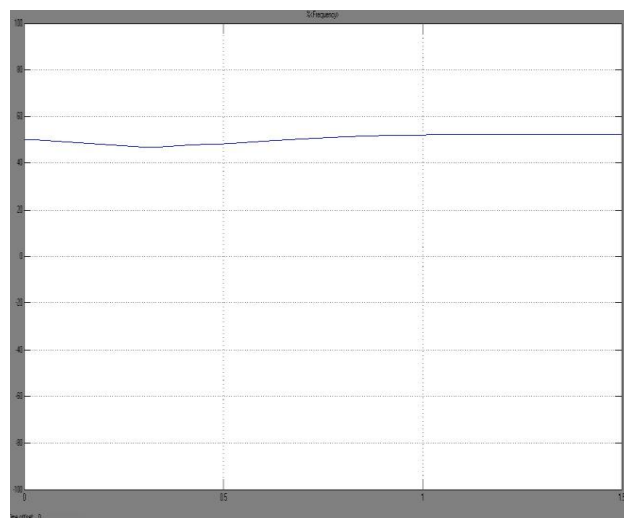Figure 4.6: Output voltage and current waveforms for over load

Figure 4.7: Frequency waveform for over load

V. Conclusion

Among the renewable energy sources, small hydro and wind energy have the ability to complement each other. Further, there are many isolated locations which cannot be connected to the grid and where the wind potential and hydro potential exist simultaneously. For such locations, a new three-phase four wire autonomous wind-hydro hybrid system, using one cage generator driven by wind turbine and another synchronous generator driven by hydro turbine along with BESS, has been modeled and simulated in MATLAB using Simulink and Sim Power System tool boxes. The design procedure for selection of various components has been demonstrated for the proposed hybrid system. The performance of the proposed hybrid system has been demonstrated under different electrical (consumer load variation) and mechanical (with wind-speed variation) dynamic conditions. It has been demonstrated that the proposed hybrid system performs satisfactorily for linear loads while maintaining constant voltage and frequency.

REFERENCES

[1]   Puneet.K.Goel, Bhim Singh, S.S Murthy and Navin Kishore "Isolated Wind-Hydro Hybrid System Using Cage Generators and Battery Storage", In IEEE Trans, Industrial Electronics.vol 58, no.4, April 2011.

[2]   L. L. Lai and T. F. Chan, *Distributed Generation: Induction and Permanent Magnet Generators*. West Sussex, U.K.: Wiley, 2007, ch. 1.

[3]   E. D. Castronuovo and J. A. Pecas, "Bounding active power generation of a wind-hydro power plant," in *Proc. 8th Conf. Probabilistic Methods Appl. Power Syst.*, Ames, IA, 2004, pp. 705–710.

[4]   B. Singh, S. S. Murthy, and S. Gupta, " An improved electronic load controller for self-excited induction generator in micro-Hydel applications," in *Proc. IEEE Annu. Conf. Ind. Electron. Soc.*, Nov. 2003, vol. 3,pp. 2741–2746.

[5]   J. B. Ekanayake, "Induction generators for small hydro schemes," *IEEE Power Eng. J.*, vol. 16, no. 2, pp. 61–67, 2002.

[6]   M. Molinas, J. A. Suul, and T. Undeland, "Low voltage ride through of wind farms with cage generators: STATCOM versus SVC," *IEEE Trans.Power Electron.*, vol. 23, no. 3, pp. 1104–1117, May 2008.

[7]   S. Ganesh Kumar, S. Abdul Rahman, and G. Uma, "Operation of selfexcited induction generator through matrix converter," in *Proc. 23rd Annu. IEEE APEC*, Feb. 24–28, 2008, pp. 999–1002.

[8]   G. Quinonez-Varela and A. Cruden, "Modelling and validation of a squirrel cage induction generator wind turbine during connection to the local grid," *IET Gener., Transmiss. Distrib.*, vol. 2, no. 2, pp. 301–309,Mar. 2008.

[9]   E. Diaz-Dorado, C. Carrillo, and J. Cidras, "Control algorithm for coordinated
reactive power compensation in a wind park," *IEEE Trans. Energy Convers.*, vol. 23, no. 4, pp. 1064–1072, Dec. 2008.

[10]   L. Tamas and Z. Szekely, "Modeling and simulation of an induction drive with application to a small wind turbine generator," in *Proc. IEEE Int. Conf. Autom., Quality Test., Robot.*, May 22–25, 2008, pp. 429–433.

[11]   A. Luna, P. Rodriguez, R. Teodorescu, and F. Blaabjerg, "Low voltage ride through strategies for SCIG wind turbines in distributed power generation systems," in *Proc. IEEE Power Electron. Spec. Conf.*, Jun. 15–19, 2008,pp. 2333–2339.

[13]   B. Fox, D. Flynn, L. Bryans, N. Jenkins, D. Milborrow, M. O'Malley,R. Watson, and O. Anaya-Lara, *Wind Power Integration Connection and System Operational Aspects*. London, U.K.: IET, 2007, ch. 3.

[14]   S. S. Murthy, B. Singh, P. K. Goel, and S. K. Tiwari, "A comparative study of fixed speed and variable speed wind energy conversion systems feeding the grid," in *Proc. IEEE PEDS*, Nov. 2007, pp. 736–743.

[15]   G. Poddar, A. Joseph, and A. K. Unnikrishnan, "Sensorless variable speed controller for existing fixed-speed wind power generator with unity-power-factor operation," *IEEE Trans. Ind. Electron.*, vol. 50, no. 5,pp. 1007–1015, Oct. 2003.

[16]   M. G. Simoes, B. K. Bose, and R. T. Spiegel, "Fuzzy-logic-based intelligent control of a variable speed cage machine wind generation system,"*IEEE Trans. Power Electron.*, vol. 12, no. 1, pp. 87–95, Jan. 1997.

[17]   D. Joshi, K. S. Sindhu, and M. K. Soni, "Constant voltage constant frequency operation for a self-excited induction generator," *IEEE Trans.Energy Convers.*, vol. 21, no. 1, pp. 228–234, Mar. 2006

[18]   B. Singh, S. S. Murthy, and S. Gupta, "Analysis and design of STATCOM based
voltage regulator for self-excited induction generators," *IEEE Trans. Energy Convers.*, vol. 19, no. 4, pp. 783–790, Dec. 2004.

[19]   J. G. Slootweg, S. W. H. Haan, H. Polinder, and W. L. Kling, "General model for representing variable speed wind turbines in power system dynamics simulations," *IEEE Trans. Power Syst.*, vol. 18, no. 1, pp. 144–151, Feb. 2003.

Implementation of Six Sigma Using DMAIC Methodology in Small Scale Industries for Performance Improvement

Ivan Sunit Rout[1], Dipti Ranjan Patra[2], Smruti Snigdha Patro[3],
Madhusmita Pradhan[4]

[1,2,3,4]*(Assistant Professor, Department of Mechanical Engineering, C.V.Raman College of Engineering, Bhubaneswar, India)*

Abstract: *The fast changing economic conditions such as global completion, declining profit margin, customer demand for high quality product, product variety and reduced lead time etc had a major impact on manufacturing industries. To respond to these needs a new paradigm in this area of manufacturing strategies is six sigma. The six sigma has been increasingly adopted world wide in the manufacturing sector in order to enhance productivity and quality performance and to make the process robust to quality variations. This paper deals with an application of six sigma using DMAIC methodology in a gas industry which provides a frame work to identify, quantify and eliminate sources of variation in an operational process in question, to optimize the operation variables, improve and sustain performance viz process yield with well executed control plans. Six sigma improves the process performance of the critical operational process, leading to better utilization of resources, decreases variations and maintains consistent quality of the process output.*

Keywords: *Control process, DMAIC, Improvement, Gas cylinder, Six sigma.*

I. INTRODUCTION

Six Sigma is business performance improvement strategy that aims to reduce the number of mistakes/defects to as low as 3.4 occassions per million opportunities. Sigma is a measure of "variation about the average" in a process which could be in manufacturing or service industry. Six sigma improvement drive is the latest and most efficient technique in quality engineering and management spectrum. It enables organizations to make substantial improvements in their bottom line and quality line by designing and monitoring everday business activities in ways which minimize customer satisfactions. While all the quality improvemet drives are useful in their own ways, they often fail to make breakthrough improvement in bottom line and quality. Voelkel, J.G contents that six sigma blends correct management, financial and methodological elements to make improvement in process and products in ways that surpass other approaches. Six sigma has a major impact on the quality management approach, while still based in the fundamental methods and tools of quality management. Six sigma is a strategic initiative to boost profitability, increases market a share and improve customer satisfaction through statistical tools that can lead to breakthrough quantum gains in quality.

Six sigma is a disciplined, data-driven methodology for eliminating defects in any process. To achieve six sigma quality a process must produce no more than 3.4 defects per million opportunities. Six sigma's basic value propositions is that principle for process improvement, statistical methods, a customer focus, attention to process and management system focusing on high return improvement project results in continuous improvement and significant gains. Six sigma is highly disciplined process that helps on focus on developing and delivering near-perfect products and service. The central idea behind six sigma is that it can measure how many "defects" you have in process, you can systematically figure out how to eliminate them and gets as close to "zero defects" as possible. Sigma is a measurement that indicates how a process is performing. Six sigma stands for six standard deviations from mean. Six sigma methodology provides the technique and tools to improve the capability and reduce defects in any process. Six sigma is fact-based, data-driven philosophy of improvement that values defect prevention over defect detection.

1.1 Concepts of Six Sigma

The word " Sigma" is a statistical term that measures how far a given process deviates from perfection as a new methodology using old tools. Six sigma is a comprehensive system for achieving, maintaining and maximizing business success. The basics of six sigma is a detailed knowledge of customer requirements, disciplined use of facts and objective data, statistical analysis and ongoing efforts focused on optimizing business processes. Six sigma revolves around a few key concepts:

1. Critical to Quality: Attributes most important to the customer;
2. Defect: Failing to deliver what the customer wants;
3. Process Capability: What your process can deliver;
4. Variation: What the customer sees and feels;
5. Stable operations: Ensuring consistent, predictable processes to improve what the customer sees and feels;
6. Design for six sigma: Designing to meet customer needs and process capability.

1.2 DMAIC methodology

It is a process for continued improvement. It is systematic, scientific and fact based. This closed loop process eliminates unproductive steps, often focuses on new measurements, and applies technology for improvement. It is in the six sigma methodology being used as the standard routine for planning and implementation in the gas industry.DMAIC forms the five major phases of any six sigma project:

1.2.1 Phase I: Define
The purpose of this phase is to clarify the goals and value of a project.

1.2.2 Phase II: Measure
The purpose of this phase is to gather data on the problem

1.2.3 Phase III: Analyze
The purpose of this phase is to examine the data and process maps to characterize the nature and extent of the defect.

1.2.4 Phase IV: Improve
The purpose of this phase is to eliminate defects in both quality and process velocity.

1.2.5 Phase V: Control
The purpose of this phase is to lock in the benefits achieved by doing the previous phases.
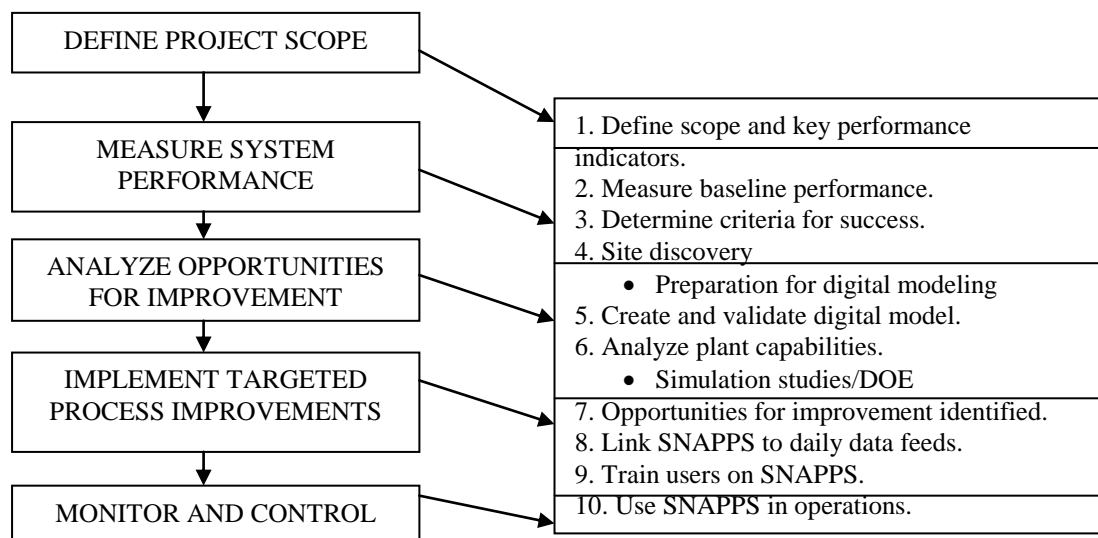

Fig 1: The abetment for Six Sigma projects

II. IMPLEMENTING DMAIC IN GAS INDUSTRY

2.1 Define

The gas cylinder plant is one of the most unique plant in country where both high pressure and low pressure cylinders are manufactured. These are used for both domestic as well as industrial purposes. The cylinders manufactured in gas cylinder plant are seamless gas cylinder, welded gas cylinder, liquefied petroleum gas cylinder and porous mass plant.

2.1.1 Seamless gas cylinder
These are made by two methods: closing the pipe end on CNC hot roller spinning machine and piercing billet to from shell and close the end on hot spinning machine.

2.1.2 Processes involved in manufacturing of seamless gas cylinder
2.1.2.1 Cutting of pipe
The pipes are first cut to required dimensions using gas cutting machines.

2.1.2.2 Dooming
After the cutting of the pipe to suitable length, it is loaded on the hot spinning CNC machines. End part of the pipe is heated in induction furnace at same time it is rolled and dome is formed.

2.1.2.3 Bottom forming
After dooming of cylinder end, it is loaded on tile HMT-press machine. HMT press is used to make bottom by pressing it with dies. It is done according to requirement, sometime footing is also provided.

2.1.2.4 Necking
It is the operation of making neck at the cylinder. This operation is done on the hot spinning CNC machine with roller. Some part of neck is cut after necking completion because at end material becomes oxidized.

2.1.3 Heat treatment of cylinders
The stresses are developed during dooming, bottom forming and necking. To remove these stresses two heat treatment operations are performed on cylinders.

2.1.3.1 Hardening
It is the process in which steel is heated above its critical temperature. It is then held at this temperature for a considerable time and then allowed to cool by quenching in water, oil or brine solution.
Temperature   : 860^0C
Quenching media: Oil
Time required   : 22 minutes for temperature rise and 23 minutes for soaking

2.1.3.2 Tempering
Steel after hardening becomes brittle, develops non visible micro cracks and is strained due to residual stresses. This undesired stresses are removed by tempering. Steel is heated below lower critical temperature followed by slow cooling.
Temperature   : 560^0C
Time required   : 45 minutes for temperature rise and 45 minutes for soaking

2.1.4 Machining operations
These operations are carried out for giving final shape to the gas cylinders:
 1. Turning and facing
 2. Neck ring jamming by cold press
 3. Drilling in neck by straight drill
 4. Hob milling (14 TPI and 1:8 taper in thread)
 5. Rimming
 6. Hob threading

2.1.5 Cleaning
Wire brushing is done for removal of scales that are formed during heat treatment processes. Steam cleaning is also preferred.

2.1.6 Testing
2.1.6.1 Hydro-stress Test
After cleaning the cylinders it is loaded for hydro-test to check their capability. Cylinder filled with water and put in the water jacket which is already filled with water. Jacket is connected with burette when cylinder is put in it extra water is filled in burette. After closing the jacket hydraulic press fills the water in it. Pressure inside the cylinder normally it is about 1.5 times of the working pressure. In case of CNG cylinder it is about 469 Kg/cm^2.

2.1.6.2 Pneumatic test

This is performed at working pressure. In case of CNG cylinder these are manufactured at a pressure of 205 Kg/cm^2.

2.1.7 Shot blasting
For painting and stamping on the outer surface a finished surface is achieved. This is done by using a mixture of short and small abrasive particles to blast on cylinder in shot blasting machines.

2.1.8 Colour coding
After finishing the surface vacuum cleaning is done. Colour coding is done to recognize the cylinder which gas is filled in it without testing.

2.1.9 Stamping
After colour coding, stamping is the final step that is done to write working pressure, testing pressure, batch number and gas filled etc. At end these cylinders are tested by ISI members. They confirm their quality and safety measures.
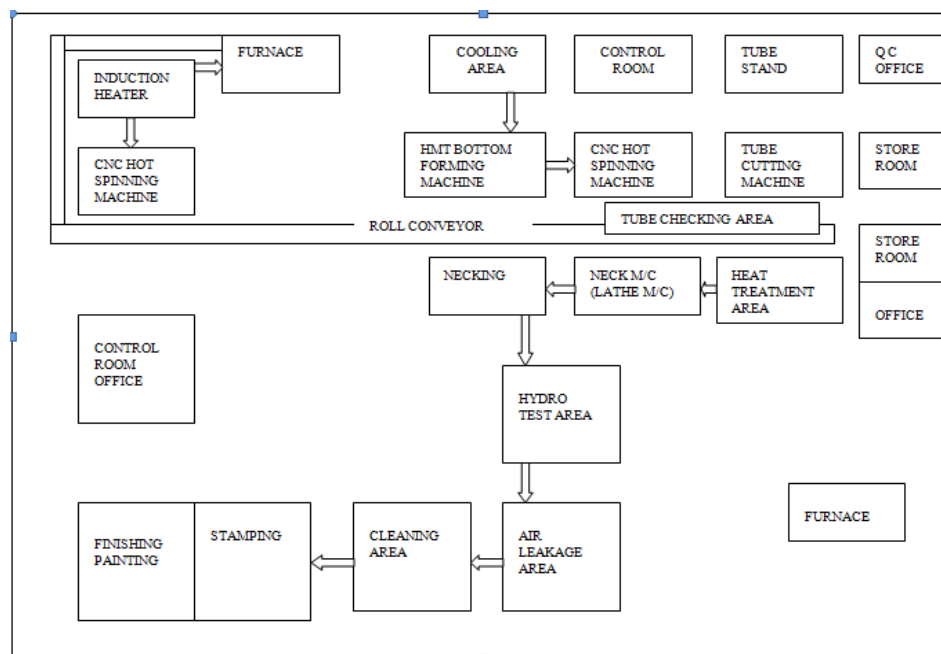
2.2 Measure

Fig 2: Gas Cylinder Manufacturing layout

2.3 Analyze
The cylinders that were manufactured had defects due to the irresponsibility of the worker and operator. The tube cutting process is not very good in industry because operator cuts the taper by hand which takes very much time in the process. According to tube cutting process, workers are few. The supply of material is not in proper condition so much time is lost during this period. Due to improper heat treatment process, the operator or worker makes mistakes and failure is obtained. Many of the work is done by the manual operation which is not suitable for production. This decreases the production rate and cost of the cylinder increases. All the machines are not working properly due to which production per capita is less. The plant layout even does not facilitate fast production due to improve arrangement of working stations. Due to unavailability of studied and experienced workers, defects are increasing as a result much scrap and waste are being obtained. Proper maintenance and repair of machines are being lacked due to which much machines are in overhaul condition.

2.4 Improve
The processing of the cylinders and for improving the production rate should be based upon the modern technology because it is impossible to increase the production rate by manual operation on the machine. Better technique is to be adopted such as modern CNC lathe machines for taper tube cutting and automatic belt

conveyors for moving cylinders inside the manufacturing workshop. The production rate will be enhanced by taking these steps. The operator and worker must take great responsibility and care while performing the jobs. The stamping and finishing of the manufacturing product must not be done manually instead it should be replaced by automatic presses and punches to do work faster and economically.

2.5 Control
      The following steps are to be implemented for enhancing the production rate and improving quality of the gas cylinders thereby reducing the cost of manufacturing:

1. The plant layout should be revised.
2. The work floor space should be used economically.
3. Skilled workers are to be employed for doing work.
4. Automatic lathe machines and chain conveyor belts should be adopted.
5. Time saving must be the prime factor.
6. Faster production rate and economic irresponsibility of the products must be considered.
7. Machines should be repaired and maintained as soon as it fails to perform operation.
8. Accuracy and dimensional tolerances of the machine should be checked.

III. REMEDIES AND DISCUSSION

      The graph shows the production rate of gas cylinder in the plant. In this graph we can see that production rate of gas cylinder by using lathe machine is less than by using CNC machine. The production rate of gas cylinder by using lathe machine is 1.08 lakhs/year while the production rate of gas cylinder by using CNC machine nearly 2.5 lakh/year. The preference to use CNC machine should be optimum for good production rate. CNC machines can be used continuously 24 hours a day, 365 days a year and only need to be switched off for occasional maintenance. CNC machines are programmed with a design which can then be manufactured hundreds or even thousands of times. Each manufactured product will be exactly the same. One person can supervise CNC machines as once they are programmed they can usually left to work unlike lathe machines which needs trained technicians for handling. A skilled technician on lathe machine can make the same component many times. However, if each component is carefully studied, each one will have minute defects unlike CNC machines which will manufacture each component exactly.
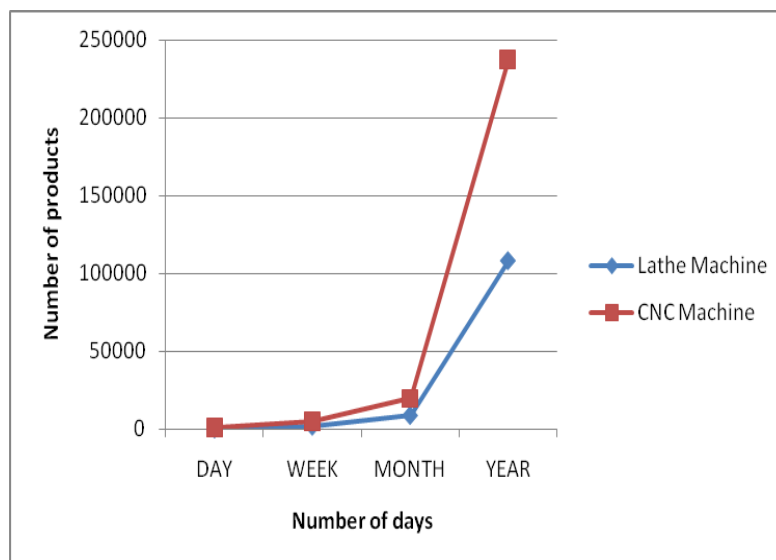

Fig 3 The production rate of gas cylinders

IV. CONCLUSION

      The maturity of a manufacturing process can be described by a sigma rating indicating its yield, or the percentage of defect free products it creates. A Six sigma process is one in which 99.99966% of the products manufactured are statistically expected to be free of defects. As can be seen from the study that Six Sigma can be very successfully implemented in any manufacturing unit. It also shows the importance of strong supplier base with Six sigma product quality. The breakthrough improvement using Six sigma can be achieved, however, to sustain this, the organization will have to continue with rigorous implementation and sustanance of the same.

Six Sigma DMAIC projects ideally should concentrate on a specific area of interest. Larger projects, or projects targeting more than one area of concentration and taking more than three to six months, should be divided into separate projects with the spin-offs to be completed later or worked on in parallel as separate projects. As Six sigma project experience increases, person will become better at using the right tools to develop project scopes that meet the description of a Six Sigma project while simultaneously producing quantifiable benefits.

Acknowledgements

REFERENCES

[1]   J.Antony, Six-Sigma in the UK Service Organizations: Results from a Pilot Survey, Managerial Auditing Journal, 19(8), 2004, 1006-1013.

[2]   S.G.Deshmukh, N.Seth and P.Virat, Service Quality Models: A Review, International Journal of Quality and Reliability Management, 22(9), 2005, 941-949.

[3]   L.G.Gutierrez, F.J.Montes and O.B.Sanchez, Six Sigma: from a goal theoretic perspective to shared division development, International Journal of Operations and production managemen, 29(2),2009, 151-169.

[4]   J.S.Oakland and J.A.Dotchin, Total Quality Management in Services Part 1: Understanding and Classifying Services, International journal of Quality and reliability Management,29 September,1994.

[5]   M.Rusko and R.Kralikova, Application of Six Sigma method to EMS design, 30, 2011.

[6]   A.Chakrabarty and T.K.Chuan, An explatory qualitative and quantitative analysis of six sigma in service organizations in Singapore, Management research new, 32(7),2009, 614-632.

[7]   C.H.Lovelock, Classifying services to gain strategic marketing insights, Journal of Marketing, 47(3),1983, 9-20.

[8]   M.Schimdt and S.Aschkenase, The building blocks of service, Supply chain management review, july-aug,2004, 34-40.

[9]   T.Woodall, Six sigma and service quality: Christian Gronroos revisited, Journal of Marketing Management, 17,2001, 595-607.

[10]   P.Kaushik and D.Khanduja, Utilising six sigma for improving pass percentage of students: a technical institute case study, Educational research and review, 5(9), 2010, 471-483.

[11]   P.Stephen, Application of DMAIC to integral lean manufacturing and six sigma, June 4, 2011.

[12]   H.C.Hung and M.H.Sung, Applying six sigma to manufacturing processes in the food industry to reduce quality cost, 4 February, 2011.

Review on Adsorption Refrigeration System

B. k. Manmode[1], S A. Borikar[2]

Kavikuguru Institute of Technology and Science, Ramtek.District-Nagpur (Maharashtra) India.

Abstract: *"Energy can neither be created nor be destroyed"- first law of thermodynamics. the energy potential of the world is constant , so we have to save the energy as much as possible .as the refrigeration is needed everywhere in the world and it is the major user of energy. The energy that could be used for the adsorption refrigeration is powered by low grade heat. the low grade heat can be obtain from industrial waste heat, exhaust gases from the engines or heat from solar thermal collector. Moreover it uses environment kindly refrigerants and avoids the global warming and ozone depletion.*

Keywords: *Adsorption, adsorption system working pairs, waste heat.*

I. INTRODUCTION

Everywhere in our world, refrigeration is a major energy user. In poor areas off grid refrigeration is a critically important need. Refrigeration is an interesting application of solar energy because the incident radiation and the need for cold production both reach maximum levels in the same period. All of these considerations point the way toward refrigeration using renewable energy, as part of a sustainable way of life. Solar-powered refrigeration is a real and exciting possibility. Due to the increasing concentration of green house gases and climate changes, the need for renewable energy sources is greater than ever. This has now attracted attention from the countries that has set up targets to increase the share of renewable energy supply in the world in order to reduce greenhouse gas emissions.

Nomenclature	
GHG	Green house gases
CCHP	combine cooling and heating
SCP	Specific Cooling Power
COP	coefficient of performance
GDP	global warming potential
h_{fg}	latent heat of vaporization

II. Sorption Refrigeration Cycle

The sorption refrigeration cycle is a thermodynamic cycle with two sources and two sinks, which operates using three temperature levels. Two of them are used to drive the thermal compressor "Reactor" that replaces the mechanical compressor in a vapour compression refrigeration cycle, The sorption refrigeration cycle operates between two pressures and two refrigerant / sorbent concentration levels.[1]
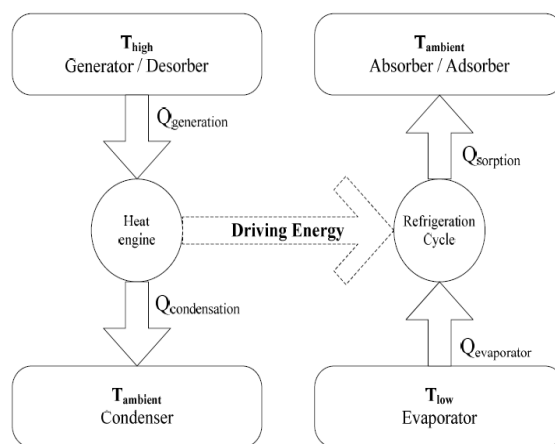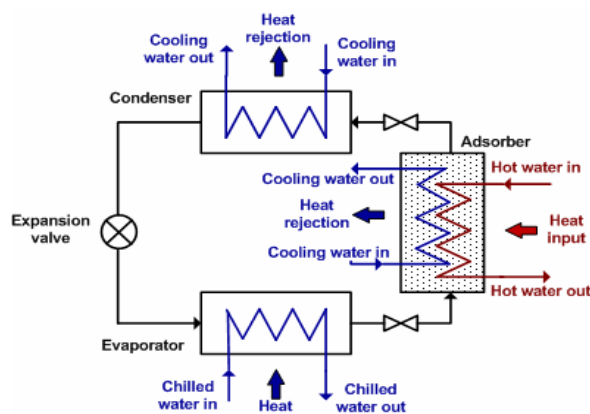

Figure 1 sorption cycle

Figure 2 Simple Adsorption cooling system

Simple adsorption refrigeration system consist of a generator that is the adsorption bed which is nothing but a heat exchanger having the adsorbent such as silica gel activated carbon , zeolite etc. Material sticking on the outer side of heat exchanger tubes and fins which increases the rate of heat transfer. It also consist of the evaporator condenser expansion device similar to an conventional VCRS. The solid adsorber adsorbs the refrigerant vapour when the cooling fluid is passed through the adsorption bed. These are the vapours of refrigerant that are form by taking the heat load from the evaporator and produce the cooling effect in the evaporator. After the adsorption of vapours in next phase of cycle the hot fluid is again send to the adsorption bed which creates the desorption of vapours which are passed through the expansion device through the condenser and then to the evaporator and the cycle can be repeated.

III.   Working Pairs

Working pairs are essential and critical in adsorption refrigeration system. The requirement for appropriate working pairs and status of current research into this topic were reviewed by Wang et al. (2009).Two aspects was reviewed: firstly, refrigeration performance requirements; and secondly, basic natural property requirements. In regard to the formed requirements, a refrigerant should have large latent heat of vaporization and little adsorption heat so that a high COP can be achieved, while an adsorbent should have significant and varied adsorption capacity that corresponds with temperature change, in order to generate high specific cooling power (SCP). Ideally with regard to requirements for natural properties, being environmental friendly, appropriate working pressure and temperature, and having thermal stability are aimed for.[2]

In investigations of common working pairs, numerous adsorbent/adsorbate combinations have been applied and compared. Most research has been done using activated carbon/methanol, activated carbon/ammonia, zeolite/water, silica gel/methanol, silica gel/water as working as working pairs. Various comparative studies were conducted by Critoph (1988), San and Lin (2008) and Wang et al.(2009).

According to these comparative studies, activated carbon/methanol an silica gel/water have been recognized as two appropriate working pairs in the application of a low temperature driven system, because both of these two working pairs can normally be driven by a low temperature heat source (below 100° C), while a working pair with zeolite normally needs the temperature of heat source to be 200° C. Some physical methods were employed to improve and change the working pairs properties so they worked better. Tamainot-Telto and Critoph (2000) investigated the thermo physical properties of monolithic carbon that is manufactured by compressing and firing solid carbon with an organic binder. Three critical parameters of the monolithic carbon were significantly improved: max concentration increased from 0.29 to 0.36 kg/kg; thermal conductivity rose from 0.16 to 0.60 W/mk; and density increased by 50% to 750 kg/m^3. Research into composite working pairs mainly focuses on improving thermal conductivity and enhancing the adsorption capacity of adsorbents. Currently, there are two main ways to produce composite adsorbents, namely simple mixture and impregnation.[2]

The first method is simply the process of mixing the chemical adsorbent and porous physical adsorbent. The chemical adsorbent is applied as an impregnated salt while the physical adsorbent is added as a host matrix to form an internal porous structure and enhance thermal conductivity.

The second method is known as impregnation in which a compound adsorbent is extracted from a mixed solution, whereby both the physical adsorbent (additive) and

Chemical adsorbent are dissolved and mixed in a solution. In order to further increase the thermal conductivity and physical density, a composite adsorbent that is made using the above two methods can be

compressed to form adsorbent blocks, known collectively as solidified composite adsorbent. Some of the working pairs are shown in table below.[2]

Adsorbent	Adsorbate(refrigerant)
Activated carbon	Water
Activated carbon fiber	Ammonia
Silica-gel	Ethanol
Zeolite	Hydrogen, methanol

Table 1 The working pairs in adsorption refrigeration.

IV.   Development In The Adsorption System

Adsorption system are invented with different focus , for one bed machine , simple structure and low cost are pursued it can be used in applications when continuous cooling or higher cooling capacity is not required ,such as cooling drinks, storage of vaccine. Multi-bed systems are suggested to provide steady refrigeration and higher energy performance .in order to increase system COP and SCP .

It is the object of several inventions to provide an improved sorption cooling system for use in various applications which are not limited by the desorption efficiency of the adsorbent. Methods are sought which provide low cost heat recovery with sorption cooling systems integrated in such a manner to provide an overall stable , continuous operation.

Three main technologies to improve the process have been extensively developed: regenerative processes with temperature front (also named thermal wave process)-heat transfer fluid is circulated through the system by a reversible pumping means , the beds are cycled between an upper and lower operating temperature, creating the thermal wave within the bed of solid adsorbent. [5]

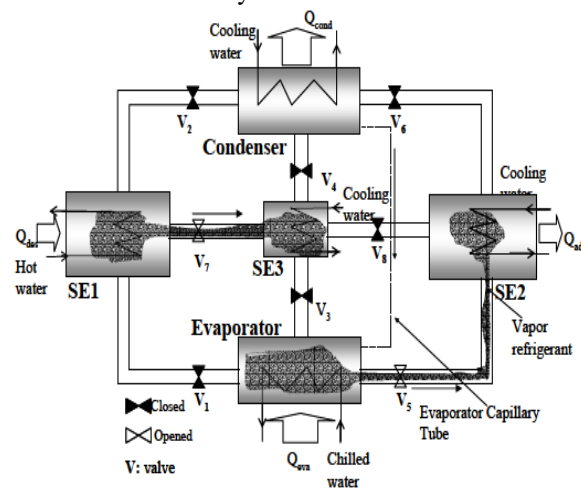Regenerative processes with heat and mass recovery-

Figure 3 three bed chiller with mass recovery

The system includes a condenser , an evaporator and number of reactor, each being able to operate in adsorption and desorption modes and having a coolant inlet to directly or indirectly receive coolant when operating in adsorption mode before after or simultaneous with the condenser. A waste heat inlet for directly or indirectly receive thermal energy from a waste heat source when operating in desorption mode. Each adsorber alternately operates in adsorption and desorption modes for substantially identical time intervals. Each adsorber has an equal chance of being first adsorber to receive the coolant when operating in adsorption mode, and the waste heat from the waste heat source when operating in desorption mode.

Third technology involving rotating adsorbers-rotary structure has been used for heat regeneration in adsorption system and provides continuous cooling effect. A rotary thermal regenerative adsorption system which has a number of adsorption module circumferentially about a rotary axis partly within toroidal conduit. A heat transfer fluid flows from an inlet of the conduit to the outlet in counter flow with respect to the rotational movement of the adsorbent modules. Separate fluid channels encase the evaporation /condensation zones of the vessels to enable transfer of heat between the vessels and the fluid flowing in channels. In this system heat is generated in particularly simple and convenient manner. As a result the compressive device is capable of achieving higher efficiencies than existing adsorption devices. [5]

V. Heat Pipe Technology

There are three vacuum chambers in this type of adsorption chiller two adsorption or desorption (or evaporation or condensation) vacuum chambers and one heat pipe working vacuum chambers as the evaporator. One adsorber, one condenser and one evaporator are housed in the same chamber to constitute an adsorption or desorption unit. The evaporators of two adsorption or desorption units are combined together by a heat pipe heat exchanger to obtain continuous cooling effect.

VI. Conclusion

The technologies for adsorption refrigeration have been extensively studied in academic as well an industry. For adsorption refrigeration system, significant achievement have been obtained on the use of various technologies to reduce the complexity of system structure, initial cost, to increase the system operation reliability as well as energy performance. Use of the solar energy in the adsorption system is a great alternative as the system is compatible with low grade heat energy. Nearly all waste heat resources can be coupled up with the adsorption refrigeration system to get a refrigeration effect. Incorporation of the consolidate adsorbents, coated adsorbents and improvement in the heat transfer process make the adsorption system an great alternative to the future refrigeration need.

REFERENCES

[1] R.Z. wang, R.G. Oliveira, adsorption refrigeration-an efficient way to make good use of waste heat and solar energy, progress in energy and combustion science 32(2006) pp 424-458.
[2] L.W.Wang , R.Z. Wang, R.G.Oliveira, A review on adsorption working pairs for refrigeration, renewable and sustainable energy reviews 13(2009) pp 518-534.
[3] LI Yong and Ruzhu Z. Wang, adsorption refrigeration:A survey of novel technologies.
[4] Ahmed Rezk Masoud Rezk, theoretical and experimentalinvestigation of silica gel / water Adsorption refrigeration systems, University of Birmingham Research Archive.(2012) pp 9-217.
[5] K. Sumathy, K.H.Yeung, Li Yong, Technology development in the solar adsorption refrigeration systems, Progress in Energy and Combustion Science 29 (2003) pp 301–327.
[6] Zisheng Lu, Ruzhu Wang,Zaizhong Xia, Experimental analysis of an adsorption air conditioning with micro-porous silica gel water, Applied Thermal Engineering 29 (2009) 2100-2105.
[7] R.Z.Wang, R.G. Oliveira, An analysis of the performance of a novel solar silica gel water adsorption air conditioning ,progress in energy and combustion science 32(2006) pp 424-458.